

INIS-EG--006



EG9700096

# *Proceedings of* Third Radiation Physics Conference

Organized by  
Atomic Energy Authority - National  
Network of Radiation Physics  
and  
Al-Minia University, Egypt

## Editorial Board

Prof. Mohammad A. Gomaa  
Prof. Amin Z. El-Behay  
Prof. Gaber M. Hassib  
Prof. Anas M. El-Naggar

Faculty of Science, Al-Minia  
University  
Al-Minia - Egypt

13 - 17 Nov. 1996

POOR QUALITY  
ORIGINAL

28 No 20



# Proceedings 2

## Third Radiation Physics Conference

Organized by

Atomic Energy Authority - National Network of Radiation Physics  
And  
Al-Minia University, Egypt



المؤسسة العامة للطاقة الذرية



المعهد القومي للمعايير



مركز البحوث النووية شاذول  
طرابلس - ليبيا

Sponsored by

Arab Atomic Energy Agency, Tunis  
Nuclear Research Center, Libya  
National Institute of Standards, Egypt

Faculty of Science, Al Minia University  
13-17 Nov. 1996 Al-Minia - Egypt

Under the Auspices of

His Excellency Engineer Mohammad Maher Abaza  
Minister of Electricity and Energy.

His Excellency Hussein Kamel Bahaa El. Din Minister of Education,

Prof. Gamal Abu Al-Makarim Rizk  
President, Al-Minia University

CONFERENCE HONORARY CHAIRMAN

Prof. Hisham Fouad Aly  
President, Atomic Energy Authority

### CONFERENCE HONORARY BOARD

**Prof. Samira M. Morsal**  
*Vice - President, Atomic Energy Authority*

**Prof. Maher Moustafa Kamel**  
*Vice President, Al-Minia University*

**Prof. Mahmoud Fouad Barakat**  
*Dirac. Gen. Arab Atomic Energy Agency*

**Prof. Mohammad M. El- Neamy**  
*Director, Nuclear Research Center*

**Prof. Mohammad Abdel Halim El-Fiki**  
*Chairman, National Institute of Standards.*

### CONFERENCE CHAIRMEN

**Prof. Mohammad A. Gomas**  
*Atomic Energy Authority*  
101 Kasr El-Elmi St.,  
Cairo, Egypt

**Prof. Fouad T. Abdel- Haleem**  
*Dean Faculty of Science*  
Al-Minia University  
Al-Minia, Egypt

### ORGANIZING COMMITTEE

**Atomic Energy Authority**  
Prof. Amin Zaki El-Behay  
Prof. Gaber M. Hassib  
Prof. Anas M. El-Naggar

*Executive Secretariat*  
*Scientific Secretariat*

**Al-Minia University**  
Prof. Abu El-Fotouh E. Mourad  
Prof. Abdel Rahman A. Ahmad  
Prof. Kamal A. Mohammed

### LOCAL ORGANIZING COMMITTEE

*Faculty of Science Al- Minia University*

**Kamal Abdel-Hady Mohammad**  
**Mamdouh A. Abdel- Rahman**

**Tharwat Girgis Abdel-Malak**  
**All Mohammad All El-Sayed**  
**Amr Mohammad Abu El-Hussain**

### SCIENTIFIC COMMITTEE

**Atomic Energy Authority**  
Prof. Mohammad A. Gomas  
Prof. Amin Z. El-Behay  
Prof. Gaber M. Hassib  
Prof. Anas M. El-Naggar

**Al-Minia University**  
Prof. Fouad T. Abdel Halim  
Prof. Abu El- Fotouh E. Mourad  
Prof. Abdel- Rahman A. Ahmad  
Prof. Kamal A. Mohammed

#### **Arab Atomic Energy Agency**

**Dr. Saleh El-Mashry**

#### **Nuclear Research Center - Libya**

**Dr. Yehia S. Khrish**

#### **National Institute of Standards**

**Prof. Mohammad A. El-Fiki**

#### **National Network of Radiation Physics**

**Prof. Samira M. Rabie**  
**Prof. Amr M. I. Kani**

**KEYNOTE LECTURES (2)**

**Hall A**

**Date: 16/11/ 96**

**Time: 9:00 - 11:00**

**Chairman Prof. Mohammad N. Comsan**

**Co-Chairman Prof. E. A. Krasavin**

**K.L. 4- STATUS REPORT OF INSHAS CYCLOTRON**

**M. N. H. Comsan**

**K.L. 5- HIGH ENERGY PARTICLE ACCELERATORS  
AS RADIATION SOURCES**

**Mohamed E. Abdelaziz**

**K.L. 6- ACCELERATORS OF THE JINR AND  
RADIOBIOLOGICAL RESEARCH**

**E. A. Krasavin**

**K. L. 7- DESIGN PRINCIPLES AND CLINICAL POSSIBILITIES  
WITH A NEW GENERATION OF RADIATION  
THERAPY EQUIPMENT**

**B.P Rudén**

**SCIENTIFIC SESSION (7)**

**Hall B**

**Date: 16/11/ 96**

**Time: 11:30 - 13:30**

**Chairman Prof. Mohammad Ezzat Abel Aziz**

**Co-Chairman Prof. B. P. Rudèn**

**PLASMA AND ACCELERATORS**

**7.1 MOTION OF CHARGED SUSPENDED PARTICLE IN A  
NON-NEWTONIAN FLUID BETWEEN TWO LONG PARALLEL PLATES**

**M. M. Abd El Khalek**

**7.2 NUMERICAL SIMULATION OF THE MOTION OF CHARGED  
SUSPENDED PARTICLE IN MULTI-PHASE FLOW**

**M. M. Abd El Khalek**

**7.3 ION OPTICS IN AN ION SOURCE SYSTEM**

**F. W Abdel Salam, O. A. Moustafa, and H. El- Khabeary**

**7.4 SHEATH FORMATION AND EXTRACTION  
OF IONS FROM A CONSTRICTED R.F ION SOURCE**

**F. W Abdel Salam, A. G. Helal, H. El-Khabeary, and N. T. El- Merai**

**7.5 THE BROAD BEAM ION IMPLANTER WITH THE USE OF  
RADIO FREQUENCY ION SOURCE**

**M. E. Abdelaziz, S. G. Zakhary, and A.A. Ghanem**

7.6                    **ELECTRON BEAM INTERACTION WITH  
INHOMOGENEOUS WARM PLASMA  
AND WAVE RADIATION**

**N. G. Zaki, and Kh. H. El-Shorbagy**

7.7                    **COEFFICIENTS OF VISCOSITY FOR HEAVY  
IMPURITY ELEMENT IN TOKAMAK**

**R. N. El - Sharif, A. M. Bekhit**

**SCIENTIFIC SESSION (8)**

**Hall C**

**Date: 16/11/ 96**

**Time: 11:30 - 13:30**

**Chairman Prof. Mohammad A. Gomaa**

**Co-Chairman Prof. Rifaat M. K. El-Shinawy**

**RADIATION PROTECTION**

***Keynote Lecture***

**RELEVANT DOCUMENTS TO IAEA REGULATIONS  
FOR THE SAFE TRANSPORT OF RADIOACTIVE MATERIALS**

**R. M. K. EL-Shinawy , M. G. Sabek , and M. A. Gomaa**

***Contributed Papers***

**8.1 EXPOSURES FROM NATURAL AND ARTIFICIAL SOURCES  
OF IONIZING RADIATION IN ROMANIA**

**Olga Iacob**

**8.2 OUTLINES ON DATA BASE FOR THE USE OF RADIOACTIVE  
SOURCES, AND ENVIRONMENTAL IMPACT IN EGYPT**

**A. M. Hathout , E. Amin , Kh. M. El-Said , and M.A. Gomaa**

**8.3 COLLECTIVE DOSE OF EGYPTIAN ATOMIC  
ENERGY WORKERS DURING THE PERIOD 1991 - 1995**

**M.A. Gomaa, and S.K. Youssef.**

**8.4 CALCULATIONS ON SAFE STORAGE AND TRANSPORTATION  
OF RADIOACTIVE MATERIALS**

**A.M. Hathout, A. M. El Messiry, and E. Amin**

8.5            **A LOGIC SCHEME FOR REGULATING SAFE OPERATION  
                 OF RESEARCH REACTORS**

Ensherah E. Ahmad , Ahmad Effat , and F.A. Rahman

8.6            **STUDY OF <sup>124</sup>I CONTAMINATION IN  
                 <sup>123</sup>I USED IN MEDICAL APPLICATIONS**

H. El Samman , and W. Arafa

**SCIENTIFIC SESSION (9)**

**Hall B**

**Date: 16/11/ 96**

**Time: 15:30 - 17:30**

**Chairman Prof. M. H. S. Bakr**

**Co-Chairman Prof. Rifaat M. Maayouf**

**RADIATION DETECTION -1**

*Keynote Lecture*

**USE OF SSNTD FOR MEASURING NUCLEAR REACTIONS**

**M. H. S. Bakr**

*Contributed Papers*

**9.1 TOTAL AND PEAK EFFICIENCIES OF SCINTILLATION  
GAMMA DETECTORS, PART-I: AXIAL-POINT**

**Younis S. Selim, Mahmoud I. Abbas, and Mohammad A. Fawzy**

**9.2 DETERMINATION OF K-CAPTURE PROBABILITIES IN  
THE DECAY OF <sup>133</sup>Ba**

**A. Abd El-Haliem, and KH. M. Hella**

**9.3 OPTIMIZATION OF A NEUTRON DETECTOR SYSTEM FOR  
THE FOURIER RTOF-DIFFRACTOMETER  
FACILITY AT THE ET-RR-1 REACTOR**

**R. M. A. Maayouf, A.S.I. El- Kady, and Y. H. El- Shaer**

**9.4 NEUTRON SPECTRUM MEASUREMENTS FROM A NEUTRON  
GUIDE TUBE FACILITY AT THE ET-RR-1 REACTOR**

**R. M A. Maayouf, L. A. A. El-Sayed, and A. S. I. El-Kady**

9.5            **A REVERSE TIME OF FLIGHT ANALYZER FACILITY AT  
                 THE ET-RR-1 REACTOR**

**R. M.A. Maayouf, A.S. El-Shafey, and M. I. Khalil**

9.6            **AN ARC DETECTOR FOR NEUTRON CRYSTAL STRUCTURE  
                 INVESTIGATIONS**

**N. Habib**

**SCIENTIFIC SESSION (10)**

**Hall C**

**Date: 16/11/ 96**

**Time: 15:30 - 17:30**

**Chairman Prof. Kazuaki Katoh**

**Co-Chairman Prof. Gaber M. Hassib**

**RADIATION DOSIMETRY -1**

***Keynote Lecture***

**A NUMERICAL ANALYSIS OF ASPECTS OF ABSORBED DOSE IN THE VICINITY OF THE INTERFACE OF DIFFERENT MATERIALS**

**JunIchiro Tada , Hideo Hirayama , and Kazuaki Katoh**

***Contributed Papers***

**10. 1 DETERMINATION OF DOSES TO DIFFERENT ORGANS AND PREDICTION OF HEALTH DETRIMENT, AFTER HYPOTHETICAL ACCIDENT IN MTR REACTOR CORE**

**E. A. Amin, and A.H. Abd El- Ghani**

**10. 2 CALCULATION OF THE RELATIVE DOSE RATE OF COBALT-60 BY COMPUTER CODE**

**J. Mashina**

**10. 3 NEUTRON DOSIMETRY IN PARAFFIN BLOCK BY ACTIVATION FOIL TECHNIQUE**

**M. El-Khatib , M. Bassiouny , M. Adel Fawzy ,  
and Mahmoud I. Abbas**

10. 4      **RADIATION ABSORBED DOSE AND EXPECTED RISK  
IN HEAD AND NECK TISSUES AFTER THYROID  
RADIOIODINE THERAPY**

**A. Hamed , H. I.Farag , and A. Saleh**

10. 5      **A TECHNIQUE OF EVALUATING MOST PROBABLE  
STOCHASTIC VALUABLES FROM A SMALL NUMBER OF SAMPLES  
AND THEIR ACCURACIES AND DEGREES OF CONFIDENCE**

**Kazuaki Katoh**

**SCIENTIFIC SESSION (11)**

**Hall B**

Date: 17/11/ 96

Time: 9:00 - 11:00

Chairman Prof. Mamdouh Adeeb

Co-Chairman Prof. Salah El- Konsul

**RADIATION DETECTION -2**

**11.1 LIFETIME MEASUREMENTS OF THE EXCITED STATES IN  $^{145}\text{Sm}$**

A. M. El- Badry , Sh. Abdel Samie , A. A. Ahmad ,  
T. Kuroyanagi , S. Mitarai , A. Odahara , Y. Gono , and S. Morinobu

**11.2 A COMPUTER SIMULATION  
OF AUGER ELECTRON SPECTROSCOPY**

M. S. Ragheb, and M. H. S. Bakr

**11.3 A PREPARATION OF THIN FLAT TARGET FOR RD  
LIFETIME MEASUREMENTS**

Azza M. El-Badry , Sh. Abdel Samie , A. A. Ahmad  
T. Kuroyanagi , and S. Morinobu

**11.4 STUDY OF VARIATION OF TRACK DENSITY IN IRRADIATED  
CR-39 AS A FUNCTION OF DIFFERENT PARAMETERS**

M. S. Garawi

**11.5 ETCHING PROPERTIES AND EFFICIENCY STUDIES  
OF LR - 115 TYPE II DETECTOR**

H. EL-Samman, A. Hussein, and Kh. Shnishin

**11.6 A NEW METHOD FOR DETERMINING THE RADON EMANATION  
COEFFICIENTS AND RADON PRODUCTION RATES FROM DIFFERENT  
BUILDING MATERIALS USING SOLID STATE NUCLEAR  
TRACK DETECTORS.**

M. A. Misdag. H. Moustaidine, K. Fahde, A. Ktata, and H. Khajmi

**SCIENTIFIC SESSION (12)**

**Hall C**

**Date: 17/11/ 96**

**Time: 9:00 - 11:00**

**Chairman Prof. B. Slowinski**

**Co-Chairman Prof. Mohammad S. Ellid**

**HIGH ENERGY PHYSICS**

***Keynote Lecture***

**INTERMEDIATE AND HIGH ENERGY NUCLEAR REACTIONS AT  
THE HADRONIC STRUCTURAL LEVEL**

**B. Slowinski**

***Contributed Papers***

**12.1 DISTRIBUTION, SCALING, AND CORRELATIONS  
IN PROTON - EMULSION INTERACTIONS AT 400 GEV**

**M. El-Nadi , M.S. El-Nagdy , S.M. Abdel Halim  
and M.N. Yasin**

**12.2 EMISSION OF INTERMEDIATE ENERGY NEUTRONS FROM  
PION NUCLEUS REACTIONS AT SEVERAL GEV**

**N. Hassan , B. Slowinski**

**12.3 ELASTIC SCATTERING OF  $^{12}\text{C}$  BY  $^{12}\text{C}$  AT  
INTERMEDIATE ENERGIES**

**S. A. E. Khallaf , M. A. Abdel- Rahman , S. k. Abdel - Raheem  
And S. W. Z. Mahmoud**

12.4 **CHARACTERISTICS OF THE COSMIC RAY SOLAR DIURNAL  
VARIATION ASSUMING TWO-WAY ANISOTROPY**

I. Sabbah, A.A. Darwish, and A.A. Bishara

12.5 **AN EXPECTATION OF A BACKBENDING FOR  $N \geq 98$   
OF A RARE EARTH NUCLEI**

M. M. Salah , and H. Elgebaly

**SCIENTIFIC SESSION (13)**

**Hall B**

**Date: 17/11/ 96**

**Time: 11:30 - 13:30**

**Chairman Prof. Sayed A. Marie**  
**Co-Chairman Prof. Abdallah Abdel - Halim**

**ENVIRONMENT**

***Keynote Lecture***

**COMPARATIVE ASSESSMENT OF ENVIRONMENTAL IMPACT OF  
DIFFERENT ELECTRICITY SOURCES**

**S. M. Rashad**

***Contributed Papers***

**13.1 KINETIC STUDY ON THE SORPTION OF CESIUM  
ON SOME EGYPTIAN SOILS**

**A. S. Ibrahim\*, W.S. Hegazi\*, W. E. W. Abdel Malik \*\*,  
and N. H. M. Kamel\*\***

**13.2 PARTITIONING OF RADIOACTIVE CESIUM IN  
AQUATIC ENVIRONMENT**

**Tarek A. Ewais\*, Alaistar Grant,\*\* and A. T., Abdel Fattah**

**13.3 LEACHING OF RA-226 CONTAMINATED  
GRAVEL USING DIFFERENT AQUEOUS TREATMENTS**

**Abdel Megid Mamoon, Waleed H. Abulfaraj, and Moustafa A. Sohsah,**

**13.4 OPERATION OF TEMPORARY RADIOACTIVE WASTE  
STORAGE FACILITY**

**Abdul Raheem A. Kinsara, Waleed H. Abulfaraj, Moustafa A. Sohsah,  
Salah El-Din M. Kamal, and Abdel Megid Mamoon**

**13.5 INFLUENCE OF HUMIC SUBSTANCES OF FIXATION OF FISSION  
PRODUCTS IN SILICATE MEDIA**

**I. S. Shaban, F. Macàsek**

**13.6 TESTING OF A GAMMA- SPECTROMETRIC SYSTEM  
USED IN ENVIRONMENTAL CONTROL**

**A. Luca , R. Radwan , Ana-Maria Razdulescu , C. Ivan**

**SCIENTIFIC SESSION (14)**

**Hall C**

**Date: 17/11/ 96**

**Time: 15:30 - 17:30**

**Chairman Prof. Mohammad A. El- Fiki**

**Co-Chairman Prof. Ahmad M. Eid**

**RADIATION DOSIMETRY -2**

- 14.1 APPLICATIONS OF DEVELOPED TECHNIQUES FOR OBTAINING TRAP PARAMETERS OF OVERLAPPED THERMOLUMINESCENCE GLOW PEAKS**

**M. S. Rasheedy**

- 14.2 CONSTRUCTING ISODOSE CURVES USING TL DOSIMETERS**

**M. A. El- Fiki, Nadia R. Khalil, H. Soliman**

- 14.3 RADIATION DOSE TO PATIENT IN SOME DIAGNOSTIC X-RAY PROCEDURES**

**N. El-Sherbiny\*, A. Hamed \*\*, and M. H. Nassef\*\***

- 14.4 COMPARISON OF SOME PHYSICAL PARAMETERS OF HIGH ENERGY PHOTON BEAMS**

**N. A. El-Sherbini, \*A.A. El Said\*\*, and M. A. Sherif\*\*\***

- 14.5 APPLICATION OF TLD IN RADIOTHERAPY TREATMENT PLANNING**

**M.A. El- Fiki, Nadia R. Khalil, H. Soliman**

**KEYNOTE LECTURES (2)**

**K.L. 4- STATUS REPORT OF INSHAS CYCLOTRON  
M. N.H. Comsan**

**Nuclear Research Center, Atomic Energy Authority  
Calro, Egypt**

**ABSTRACT**

The 1996 status of the Cyclotron complex under erection at NRC site at Inshas Egypt is given. The complex is based on a compact AVF cyclotron of Russian type MGC-20 with  $K=20$ . The accelerator is intended to be used for multidisciplinary purposes. The layout of the complex is approved and contains provisions for radioisotope production, fast neutron research and applications, use of cyclotron beams in nuclear analytical techniques, biomedical and nuclear medicine application, and surface modification, and treatment. Shielding design of walls, floors and ceilings are done in accordance with ICRP-60 recommendations with dose limit rates to the public 1 mSv/y. Building construction is undertaken and is expected to end by August 1997.

**K.L. 5- HIGH ENERGY PARTICLE ACCELERATORS  
AS RADIATION SOURCES**

**Mohamed E. Abdelaziz**

**National Center for Nuclear Safety and Radiation Control  
Atomic Energy Authority-Egypt**

**ABSTRACT**

Small accelerators in the energy range of few million electron volts are usually used as radiation sources for various applications, like radiotherapy, food irradiation, radiation sterilization and in other industrial applications. High energy accelerators with energies reaching billions of electron volts also find wide field of applications as radiation sources. Synchrotrons with high energy range have unique features as radiation sources. This review presents a synopsis of cyclic accelerators with description of phase stability principle of high energy accelerators with emphasis on synchrotrons. Properties of synchrotron radiation are given together with their applications in basic and applied research.

K.L. 6-

**ACCELERATORS OF THE JINR AND  
RADIOBIOLOGICAL RESEARCH**

**E. A. Krasavin**

**Joint Institute for Nuclear Research, Dubna, Moscow Region,  
141980, Russia**

**ABSTRACT**

The availability of various nuclear-physical facilities at JINR provides a unique possibility to generate different types of radiation fields with wide energy range, linear energy transfer (LET), and complex component composition.

This situation on one hand creates difficulties for adequate radiation monitoring and personnel dosimetry, but on the other hand it gives great opportunities for health physics research in the field of radiation protection, radiation biology and for improvement of techniques and instruments of radiation monitoring. The actuality and necessity of such investigations change the conceptual approach to consequences of human exposure to different types of ionizing radiation.

The regulation of personnel exposure is connected with the problem of stochastic radiation-induced effects, which result from some change in the genetic structures. These are mutations, chromosomal abnormalities. That is why investigations of ionizing radiation-induced mutation mechanisms are very crucial problems, since it is known that several mutations induce cell malignant transformations.

Nuclear physical facilities which generate radiation with different LET are very important tools for radiation mutagenesis, in general, and for stochastic radiation-induced effects in particular. This situation allows to take JINR into consideration as a unique scientific center for such researches. The physical characteristics of the charged particles generated by the JINR accelerators and the basic results of the radiobiological experiments are considered.

**K. L. 7- DESIGN PRINCIPLES AND CLINICAL POSSIBILITIES  
WITH A NEW GENERATION OF RADIATION  
THERAPY EQUIPMENT**

**B.P Rudén**

**Department of Hospital Physics  
Karolinska Institute, Sweden**

**ABSTRACT**

The main steps in the development of isocentric megavoltage external beam radiation therapy machines are briefly reviewed identifying three principal types or generations of equipment to date. The new fourth generation of equipment presented here is characterized by considerably increased flexibility in dose delivery through the use of scanned elementary electron and photon beams of very high quality. Furthermore, the wide energy range and the possibility of using high resolution multileaf collimation with all beam modalities makes it possible to simplify irradiation techniques and increase the accuracy in dose delivery. The main design features are described including a dual magnet scanning system, a photon beam purging magnet, a helium atmosphere in the treatment head, a beam's eye view video read-out system of the collimator setting and a radiotherapeutic computed tomography facility. Some of the clinical applications of this new type of radiation therapy machine are finally reviewed, such as the ease of performance, beam flattening, beam filtering and compensation, and the simplification of many treatment techniques using the wide spectrum of high quality electron and photon beams. Finally, the interesting possibility of doing conformal and more general isocentric treatments with non-uniform beams using the multileaf collimator and the scanning systems are demonstrated.



EG9700097

s Conf., Al-Minia, 13 - 17 Nov., 1996

## HIGH ENERGY PARTICLE ACCELERATORS AS RADIATION SOURCES

MOHAMED E. ABDELAZIZ

NATIONAL CENTER FOR NUCLEAR SAFETY AND RADIATION PROTECTION  
(LIFE MEMBER IEEE)

### ABSTRACT

Small accelerators in the energy range of few million electron volts are usually used as radiation sources in various applications, like radiotherapy, food irradiation, radiation sterilization and in many industrial applications. However, high energy accelerators with energies which may reach billions of electron volts find a wide field of uses as radiation sources. In particular, synchrotrons in this energy range have unique features as radiation sources.

This lecture presents a review of cyclic accelerators, a description of phase stability principle and of high energy accelerators-with emphasis on synchrotrons. Properties of synchrotron radiation are given together with their applications in basic and applied research.

### INTRODUCTION

Low energy accelerators in the range of millions of electron volts (MeV) are widely used as radiation sources in various fields of applications. Some examples are : radiation processing of materials as in crosslinking, curing and polymerization; radiation sterilization of medical and pharmaceutical supplies; radiation treatment of food to reduce food losses; treatment of waste water and of sewage; applications in radiotherapy and in biological research.

However, high energy accelerators in the energy range of hundreds of MeV, or even billions of electron volts (BeV) find a wide field of applications as radiation sources. Some examples are: nuclear research and high energy and elementary particle physics; nuclear material testing and breeding of fissionable materials, inertial fusion research .

High energy accelerators are usually cyclic synchronous accelerators whose principle is based on phase stability. Thus, we will start by describing the phase stability principle, then we give a review of different types of high energy accelerators and energy limitations in each type. Synchrotrons, in particular, will be considered as radiation sources having unique features. Thus, properties of synchrotrons as radiation sources used in various applications will be treated.

## I. High Energy Cyclic Accelerators

### 1.1 Cyclotrons

Cyclic accelerators start with the simple cyclotron whose principle depends on synchronism between rotation frequency  $f_r$  of ions injected from an ion source at the centre of two semicircular hollow electrodes (the dees) in a vacuum chamber, and the frequency of a.c. accelerating potential applied to the dees under the influence of a perpendicular magnetic field  $B$ , (Fig 1A),

$$f_r = \frac{eB}{2\pi M} = f_{a.c.}, \text{ where } M \text{ is mass of accelerated ion. Energy}$$

limitation of the conventional cyclotron results from disruption of synchronism since  $f_r$  is reduced as energy is increased due to relativistic increase of  $M$  and reduction of  $B$  (negative gradient of  $B$  needed for focusing), Fig 1B>

Accordingly, a maximum energy of 50 MeV could be achieved in an ordinary cyclotron without disruption of synchronism.

### 1.2 Isochronous Cyclotron :

A development to meet the contradicting requirements in a cyclotron; that  $B$  must increase with the relativistic increase of  $M$  to maintain constant  $f$ , and that  $B$  must decrease with  $R$  to maintain particle focusing, was made possible by the use of alternately high and low regions of magnetic field around the orbit obtained with radial sectors of iron fastened to the pole faces, Fig 2, thus yielding the "azimuthally varying field" (AVF) cyclotron. (1) Maximum energy could thus be increased to few hundreds of MeV, especially when high charge state beams are used, as seen from the energy equation :  $E = K \frac{q^2}{M}$ , where  $K$  = characteristic number of accelerator,  $q$  = charge number of ions.

High energy accelerators are usually cyclic synchronous accelerators whose principle is based on phase stability. Thus, we will start by describing the phase stability principle, then we give a review of different types of high energy accelerators and energy limitations in each type. Synchrotrons, in particular, will be considered as radiation sources having unique features. Thus, properties of synchrotrons as radiation sources used in various applications will be treated.

## 1. High Energy Cyclic Accelerators

### 1.1 Cyclotrons

Cyclic accelerators start with the simple cyclotron whose principle depends on synchronism between rotation frequency  $f_r$  of ions injected from an ion source at the centre of two semicircular hollow electrodes (the dees) in a vacuum chamber, and the frequency of a.c. accelerating potential applied to the dees under the influence of a perpendicular magnetic field  $B$ , (Fig 1A),

$$f_r = \frac{eB}{2\pi M} = f_{a.c.}, \text{ where } M \text{ is mass of accelerated ion. Energy}$$

limitation of the conventional cyclotron results from disruption of synchronism since  $f_r$  is reduced as energy is increased due to relativistic increase of  $M$  and reduction of  $B$  (negative gradient of  $B$  needed for focusing), Fig 1B>

Accordingly, a maximum energy of 50 MeV could be achieved in an ordinary cyclotron without disruption of synchronism.

### 1.2 Isochronous Cyclotron :

A development to meet the contradicting requirements in a cyclotron; that  $B$  must increase with the relativistic increase of  $M$  to maintain constant  $f$ , and that  $B$  must decrease with  $R$  to maintain particle focusing, was made possible by the use of alternately high and low regions of magnetic field around the orbit obtained with radial sectors of iron fastened to the pole faces, Fig 2, thus yielding the "azimuthally varying field" (AVF) cyclotron. (1) Maximum energy could thus be increased to few hundreds of MeV, especially when high charge state beams are used, as seen from the energy equation :  $E = K \frac{q^2}{M}$ , where  $K$ =characteristic number of accelerator,  $q$ =charge number of ions.

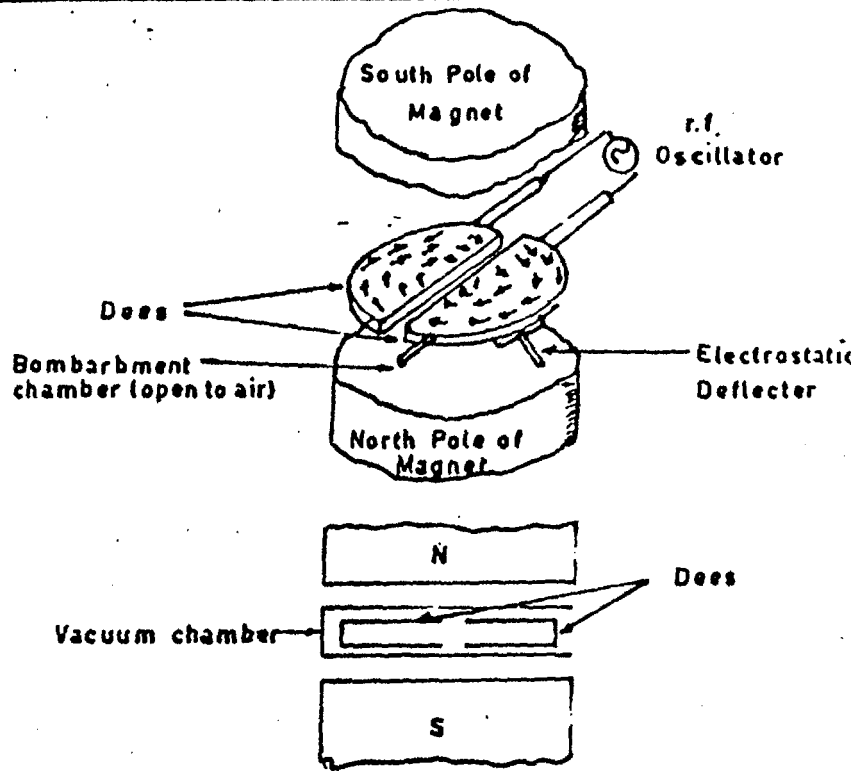
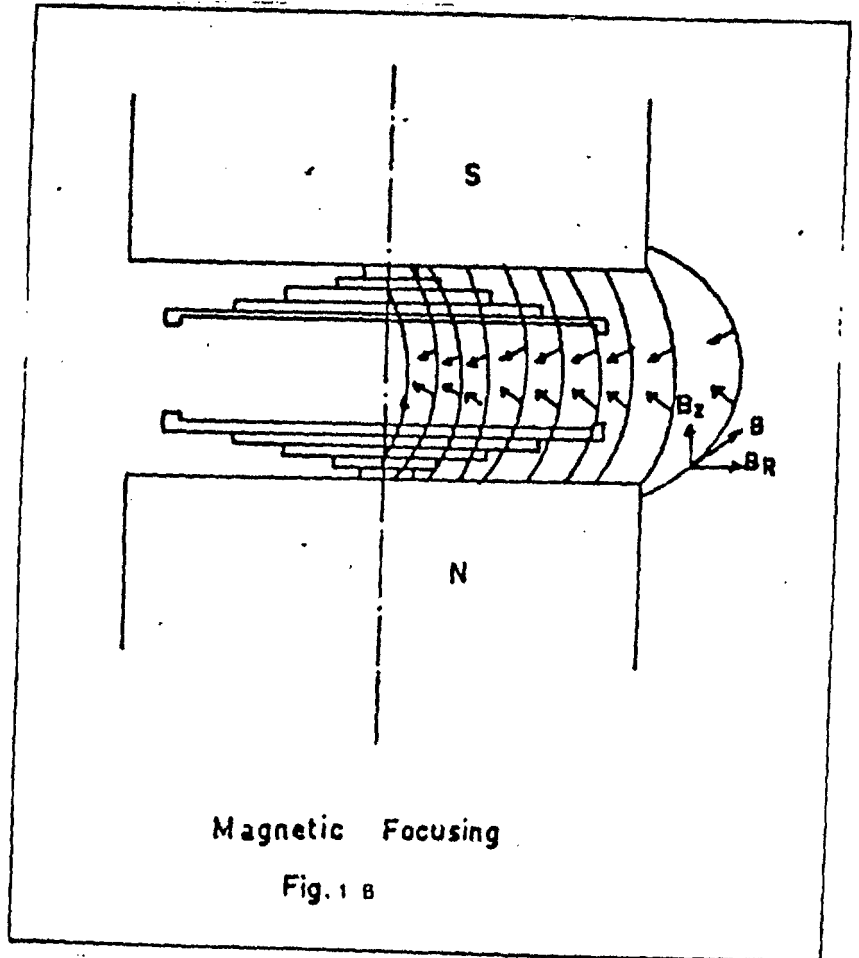


Fig. 1 A Schematic of a Cyclotron.





### I.3 The Synchrotron :

An accelerator concept without energy limitation has been made possible by utilizing ring-shaped magnets and constant-orbit radius in the synchrotron after the discovery of the phase stability principle. It states briefly that particles with phase or energy errors will continue to be accelerated with minor oscillations in phase and energy around the correct equilibrium phase and energy, Fig 3A, and Fig 3B (2).

A proton synchrotron, Fig4, therefore, consists basically of an injector to produce a well-defined beam, and annular-shaped magnet whose magnetic field can be pulsed from a very small value- (needed for injection) to many kilogauss in a short time, and resonant cavity whose accelerating r.f. voltage can be produced at a frequency which is kept in synchronism with the particle rotation frequency.

Thus, as B begins to rise, protons are injected when B has reached the value at which protons can just go around the machine ( $Mv=Ber$ ), then as orbit radius R shrinks, protons are allowed to enter the resonant cavity and receive energy such that R increases. By correctly adjusting the voltage and frequency the position of the orbit of the particles can be kept fixed as B and energy rise.

Accordingly, the proton energy keeps in step with B until B reaches its maximum value. Finally, high energy protons can either be extracted from the synchrotron or be directed into a target within the ring to produce secondary particles. Different types of synchrotrons differ in the way that the circulating beam is focused due to particle oscillations.

With no limitation on energy increase in the synchrotron, it was possible to build a 500 BeV accelerator complex at Fermilab in the U.S.A., Fig5, which started operation in 1972, and a 400 BeV complex at CERN in Switzerland. The two atom smashers were basically the same with some differences in their injection system. The need arose, therefore, and attempts continued to develop super-high energy machines.

### I.3 The Synchrotron :

An accelerator concept without energy limitation has been made possible by utilizing ring-shaped magnets and constant-orbit radius in the synchrotron after the discovery of the phase stability principle. It states briefly that particles with phase or energy errors will continue to be accelerated with minor oscillations in phase and energy around the correct equilibrium phase and energy, Fig 3A, and Fig 3B (2).

A proton synchrotron, Fig4, therefore, consists basically of an injector to produce a well-defined beam, and annular-shaped magnet whose magnetic field can be pulsed from a very small value-(needed for injection) to many kilogauss in a short time, and resonant cavity whose accelerating r.f. voltage can be produced at a frequency which is kept in synchronism with the particle rotation frequency.

Thus, as B begins to rise, protons are injected when B has reached the value at which protons can just go around the machine ( $Mv=Ber$ ), then as orbit radius R shrinks, protons are allowed to enter the resonant cavity and receive energy such that R increases. By correctly adjusting the voltage and frequency the position of the orbit of the particles can be kept fixed as B and energy rise.

Accordingly, the proton energy keeps in step with B until B reaches its maximum value. Finally, high energy protons can either be extracted from the synchrotron or be directed into a target within the ring to produce secondary particles. Different types of synchrotrons differ in the way that the circulating beam is focused due to particle oscillations.

With no limitation on energy increase in the synchrotron, it was possible to build a 500 BeV accelerator complex at Fermilab in the U.S.A., Fig5, which started operation in 1972, and a 400 BeV complex at CERN in Switzerland. The two atom smashers were basically the same with some differences in their injection system. The need arose, therefore, and attempts continued to develop super-high energy machines.

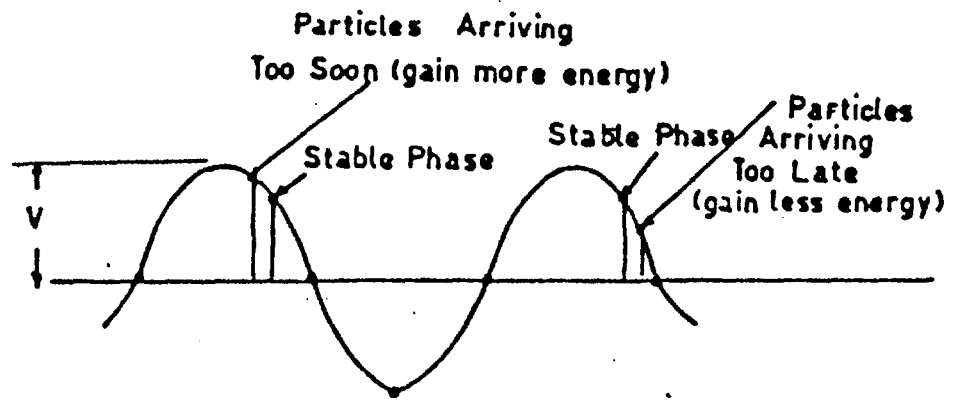


Fig. 3 A Phase Oscillations

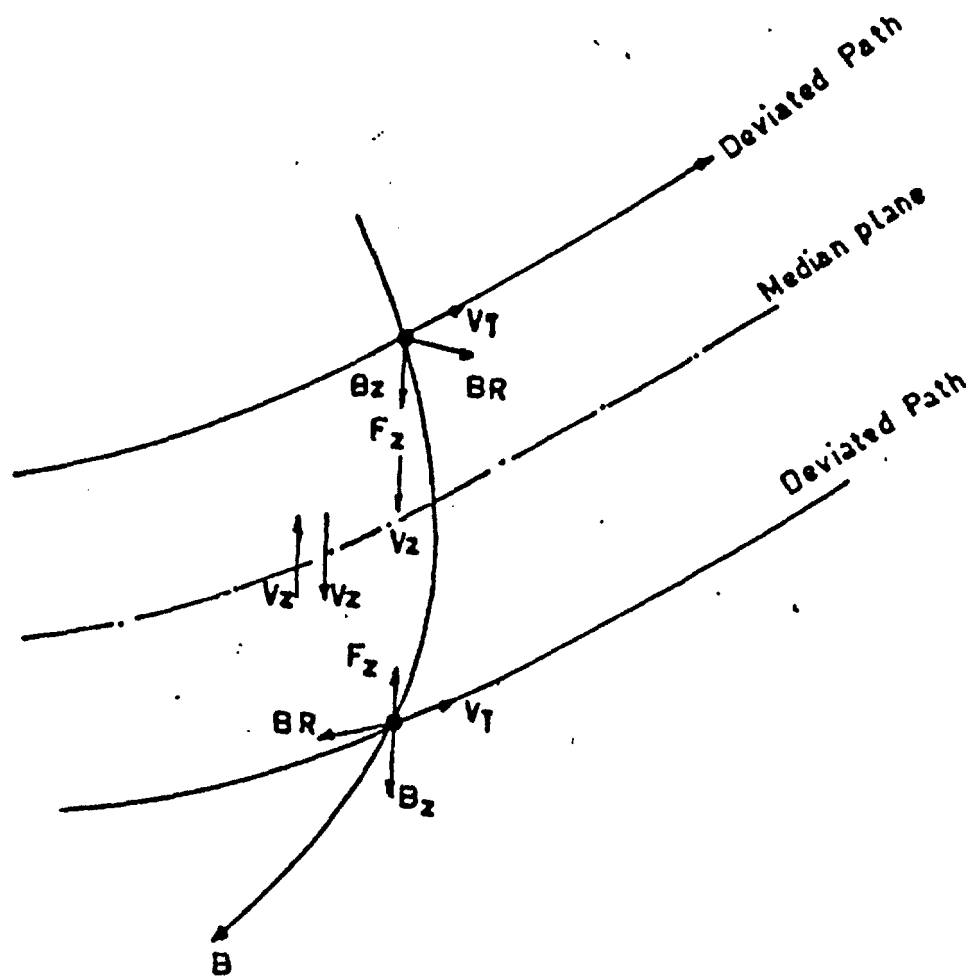


Fig. 3B Axial Oscillations

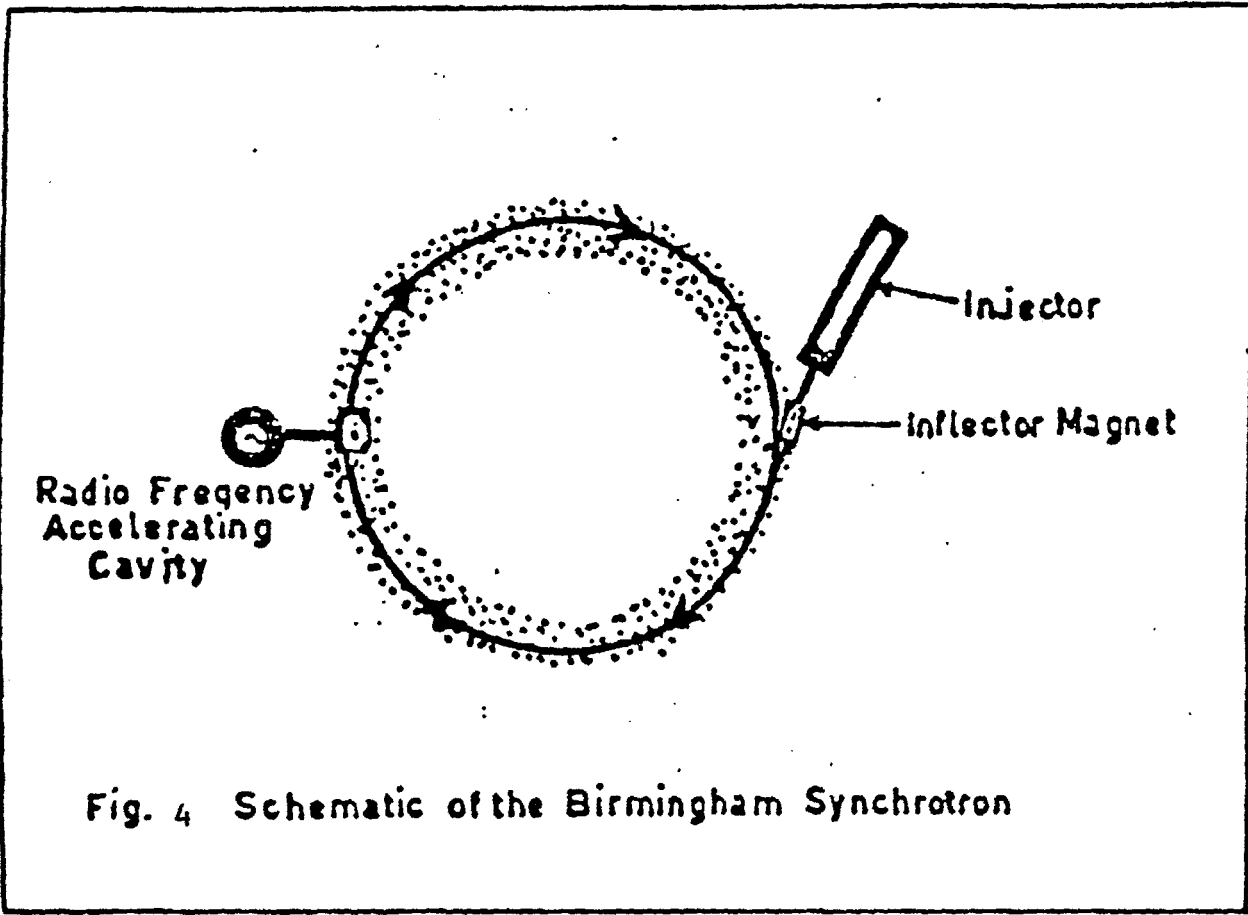


Fig. 4 Schematic of the Birmingham Synchrotron

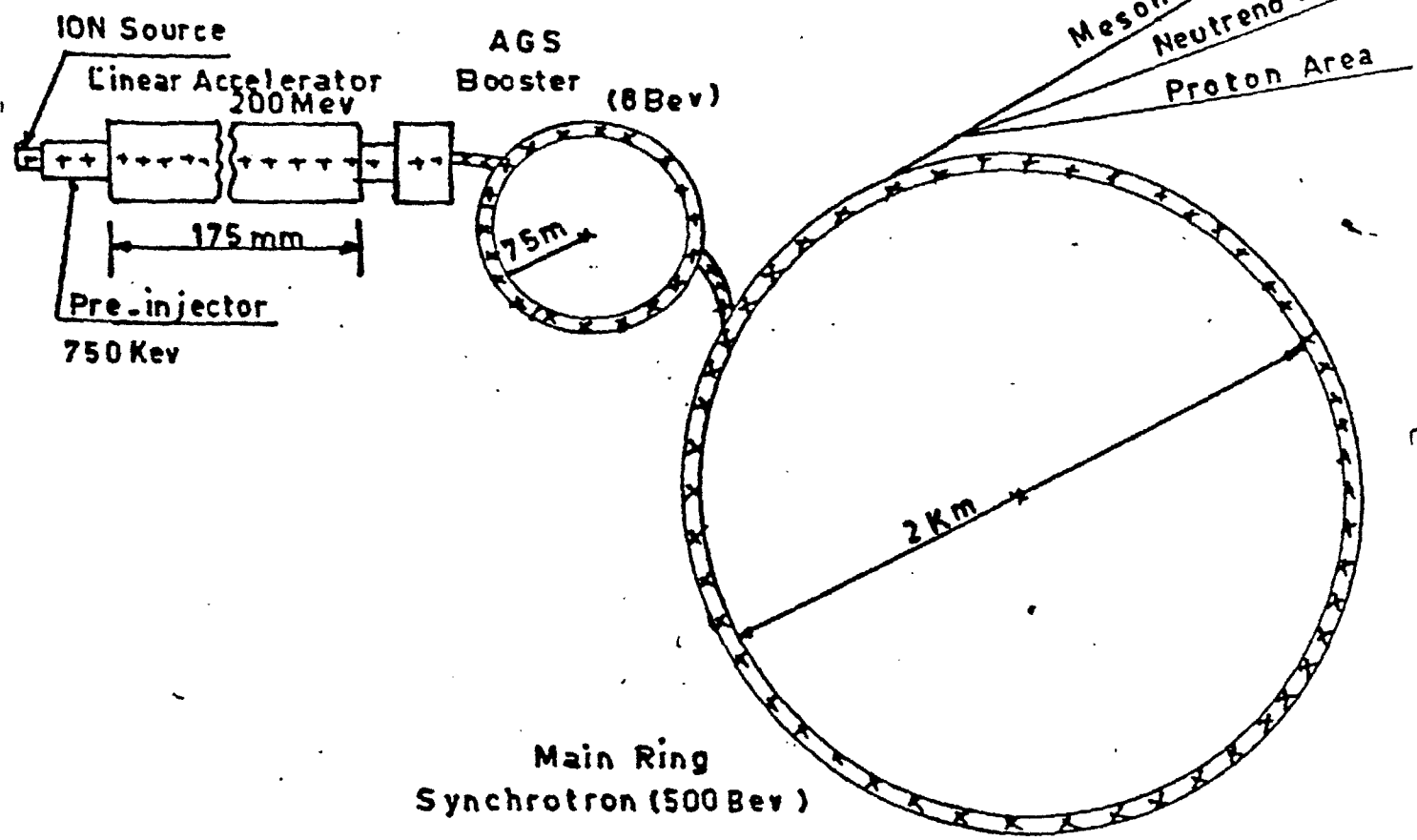


Fig. 5 Schematic of Accelerator Complex at Fermilab

### COLLIDER ACCELERATORS

A new development based on colliding beams, the Energy Doupler/Saver (ED/S) (3) ring, in the same tunnel with the main 500-BeV Fermilab ring, but using superconducting magnets to increase B to a much higher value and reduce the size of vacuum chamber at a great saving in magnet power.

The 500-BeV beam was injected into the ED/S ring to ultimately raise the energy to 1000 BeV. The proximity of two accelerated beams in the same tunnel made the prospect of colliding these beams an obviously attractive possibility. Thus, in fixed target accelerators the center-of-mass energy  $E = \sqrt{1.88 W}$ , while for colliding beams  $E = 2W$ , (W being laboratory energy of each of the beams in head-on collision). A development in this direction is the POPAE project, Fig 6, which aims at the construction of a facility consisting of 1000-BeV on 1000-BeV proton-proton colliding beams to yield the Tevatron 2000-BeV center-of-mass energy which, if in a fixed-target accelerator, would require a beam of more than  $2 \times 10^6$  BeV, Fig 7.

### The Large Electron-Positron Collider (LEP) :

LEP, which started operation in 1989, is a super high energy accelerator which is thought to be one of the grandest and most costly undertakings in the history of science so far. It is a mammoth particle racetrack residing in a ring-shaped tunnel 27 kilometers in circumference that runs 110 meters on the average beneath landscape of villages and farms at CERN, along the French-

Swiss border. LEP is built on a pharonic scale, its excavation and that of four huge experimental halls, required the removal of 1.4 million cubic meters of earth, roughly half the volume of the Great Pyramid of Cheops.

### Operation of the LEP is as Follows (Fig 8) <sup>(4)</sup>

1. Positrons are created in a linear accelerator and then stored in a storage ring,
2. Electrons and positrons are accelerated in synchrotron,

### COLLIDER ACCELERATORS

A new development based on colliding beams, the Energy Douler/Saver (ED/S) (3) ring, in the same tunnel with the main 500-BeV Fermilab ring, but using superconducting magnets to increase B to a much higher value and reduce the size of vacuum chamber at a great saving in magnet power.

The 500-BeV beam was injected into the ED/S ring to ultimately raise the energy to 1000 BeV. The proximity of two accelerated beams in the same tunnel made the prospect of colliding these beams an obviously attractive possibility. Thus, in fixed target accelerators the center-of-mass energy  $E = \sqrt{1.88 W}$ , while for colliding beams  $E = 2W$ , (W being laboratory energy of each of the beams in head-on collision). A development in this direction is the POPAE project, Fig 6, which aims at the construction of a facility consisting of 1000-BeV on 1000-BeV proton-proton colliding beams to yield the Tevatron 2000-BeV center-of-mass energy which, if in a fixed-target accelerator, would require a beam of more than  $2 \times 10^6$  BeV, Fig 7.

### The Large Electron-Positron Collider (LEP) :

LEP, which started operation in 1989, is a super high energy accelerator which is thought to be one of the grandest and most costly undertakings in the history of science so far. It is a mammoth particle racetrack residing in a ring-shaped tunnel 27 kilometers in circumference that runs 110 meters on the average beneath landscape of villages and farms at CERN, along the French-

Swiss border. LEP is built on a pharonic scale, its excavation and that of four huge experimental halls, required the removal of 1.4 million cubic meters of earth, roughly half the volume of the Great Pyramid of Cheops.

### Operation of the LEP is as Follows (Fig 8) <sup>(4)</sup>

1. Positrons are created in a linear accelerator and then stored in a storage ring,
2. Electrons and positrons are accelerated in synchrotron,

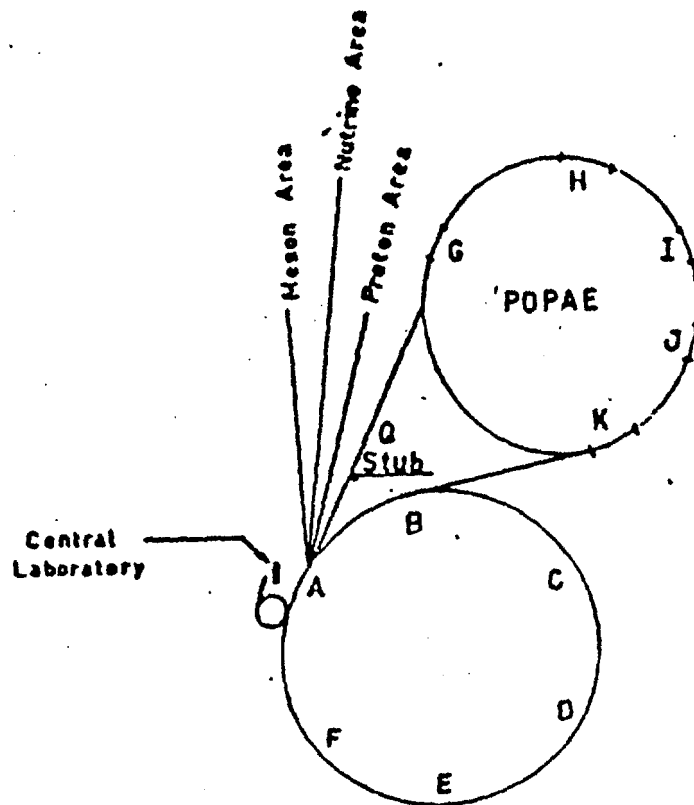
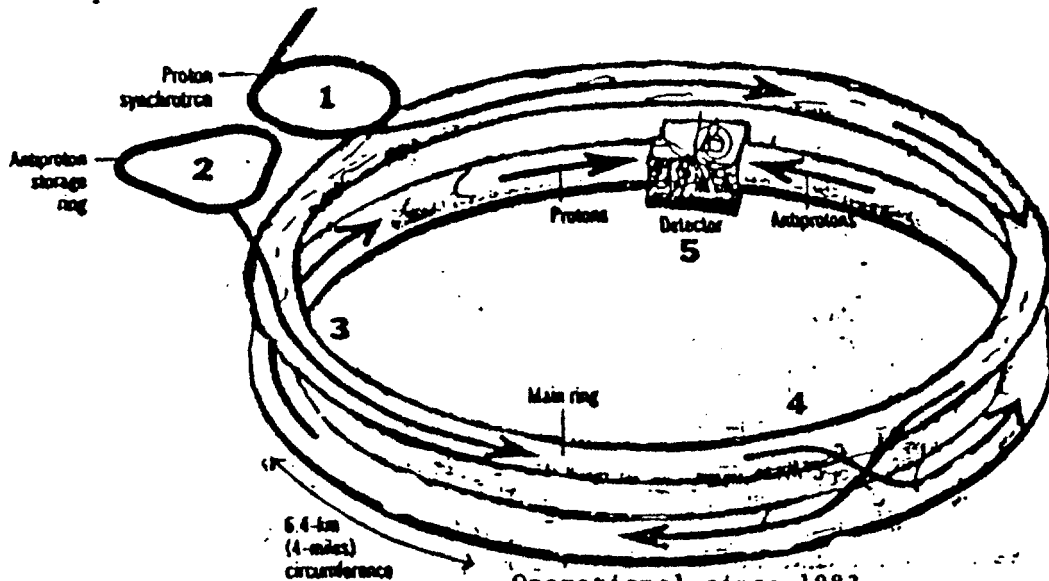
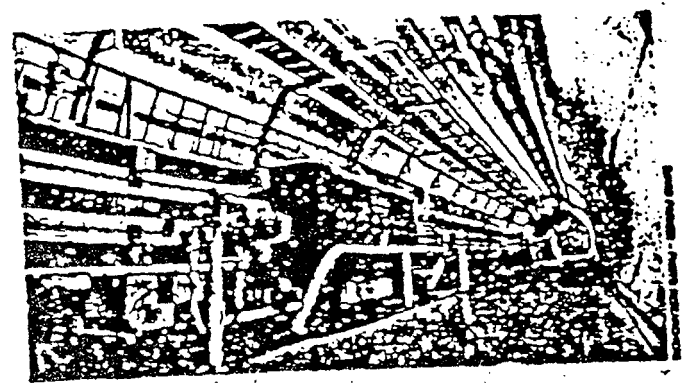


Fig. 6 Location of POPAE on the Fermilab site (Reference 5)

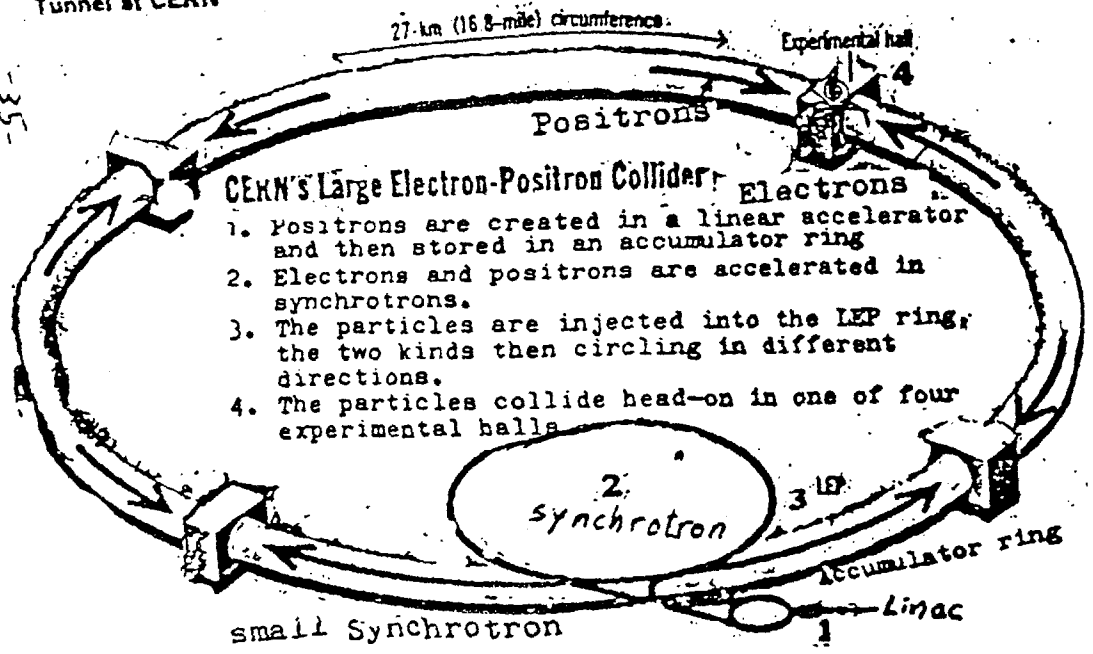


Operational since 1983 .  
 Maximum collision energy :  
 2 trillion electron volts .  
 Type : proton-antiproton collider  
 1 protons are created and then  
 accelerated in a small synchrotron .  
 2 Antiprotons are created and then put  
 into ring .  
 3 The particles are injected into the  
 main ring , where they are accelerated  
 to high energies .  
 4 They are then diverted and further  
 accelerated in the Tevatron . It is a  
 more powerful ring , using superconducti  
 magnet , installed below the main ring.  
 5 The counterrotating beams smash  
 together in the detector .

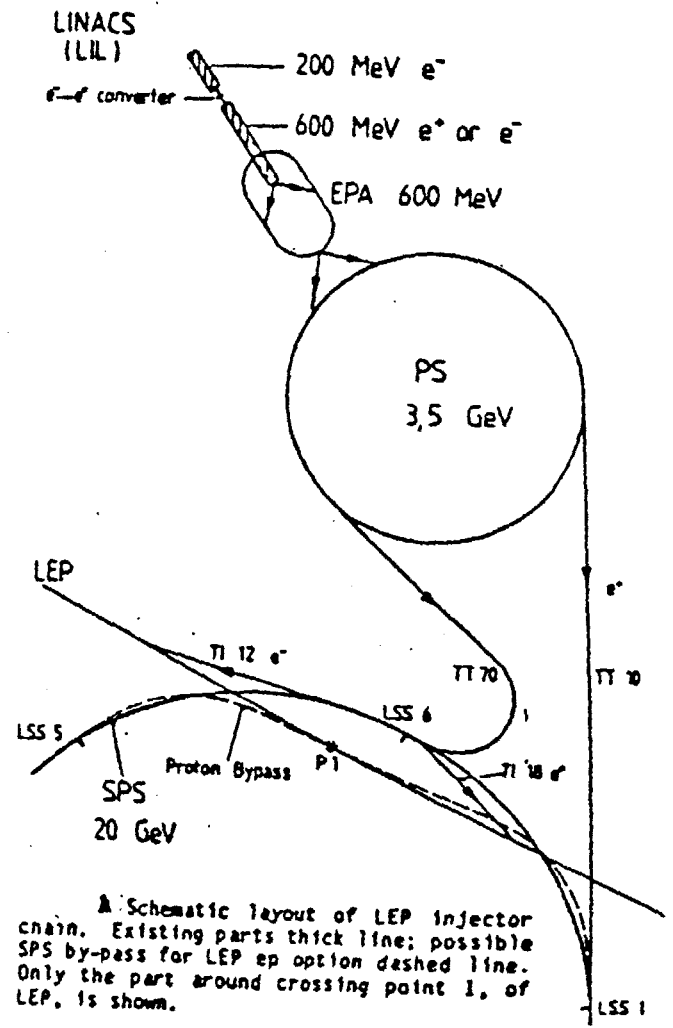
( Fig 7 Schematic of Fermilab Tevatron )



Tunnel at CERN



- CERN'S Large Electron-Positron Collider:**
1. Positrons are created in a linear accelerator and then stored in an accumulator ring
  2. Electrons and positrons are accelerated in synchrotrons.
  3. The particles are injected into the LEP ring; the two kinds then circling in different directions.
  4. The particles collide head-on in one of four experimental halls.



A Schematic layout of LEP injector chain. Existing parts thick line; possible SPS by-pass for LEP ep option dashed line. Only the part around crossing point 1, of LEP, is shown.

Fig 8 Schematic of Large-Electron-Positron Collider (LEP)

3. The particles are injected into the LEP ring, the two kinds then circling in opposite directions, and
4. The particles collide head-on in one of the four experimental halls.

The real work is conducted in the main four experimental halls spaced equidistantly around the 27-km central loop.

They are dedicated to the same research goal: capturing and analyzing the feathery traces left by short-lived collision products in hopes of discovering something new and unexpected.

#### **The Superconducting Supercollider:**

Still higher-energy atom smashers seem to be needed in an attempt to make possible an understanding of the development of the universe, the evolution of the elements and behaviour of atomic nuclei.

U.S. scientists have, therefore, taken the bold decision of building a colossal collider that will dwarf today's accelerators. This is the Superconducting Supercollider which will have a tunnel that circle for 87 kilometers under the cotton and cattle country surrounding Waxahachie, Texas, it will have a maximum collision energy of 40 TeV. Being a proton-proton collider, an injector accelerator (Fig 9) injects a high energy proton beam into two rings to be accelerated in opposite directions. The beams will cross at experimental halls. The counter-rotating beams of protons which are strongly focused to an extremely small diameter contain quadrillions of particles, will whip around the ring-shaped tunnel 3000 times producing up to 100 million collisions every second. The magnets amount to 10000, using superconducting wire enough to circle the earth's equator 25 times.

#### **Properties of Synchrotron Radiation**

Synchrotron radiation (SR) is the electromagnetic radiation of charged particles travelling in a magnetic field at a velocity close to the velocity of light. Electrons and positron storage rings are the main synchrotron radiation sources.

3. The particles are injected into the LEP ring, the two kinds then circling in opposite directions, and
4. The particles collide head-on in one of the four experimental halls.

The real work is conducted in the main four experimental halls spaced equidistantly around the 27-km central loop.

They are dedicated to the same research goal: capturing and analyzing the feathery traces left by short-lived collision products in hopes of discovering something new and unexpected.

#### **The Superconducting Supercollider:**

Still higher-energy atom smashers seem to be needed in an attempt to make possible an understanding of the development of the universe, the evolution of the elements and behaviour of atomic nuclei.

U.S. scientists have, therefore, taken the bold decision of building a colossal collider that will dwarf today's accelerators. This is the Superconducting Supercollider which will have a tunnel that circle for 87 kilometers under the cotton and cattle country surrounding Waxahachie, Texas, it will have a maximum collision energy of 40 TeV. Being a proton-proton collider, an injector accelerator (Fig 9) injects a high energy proton beam into two rings to be accelerated in opposite directions. The beams will cross at experimental halls. The counter-rotating beams of protons which are strongly focused to an extremely small diameter contain quadrillions of particles, will whip around the ring-shaped tunnel 3000 times producing up to 100 million collisions every second. The magnets amount to 10000, using superconducting wire enough to circle the earth's equator 25 times.

#### **Properties of Synchrotron Radiation**

Synchrotron radiation (SR) is the electromagnetic radiation of charged particles travelling in a magnetic field at a velocity close to the velocity of light. Electrons and positron storage rings are the main synchrotron radiation sources.

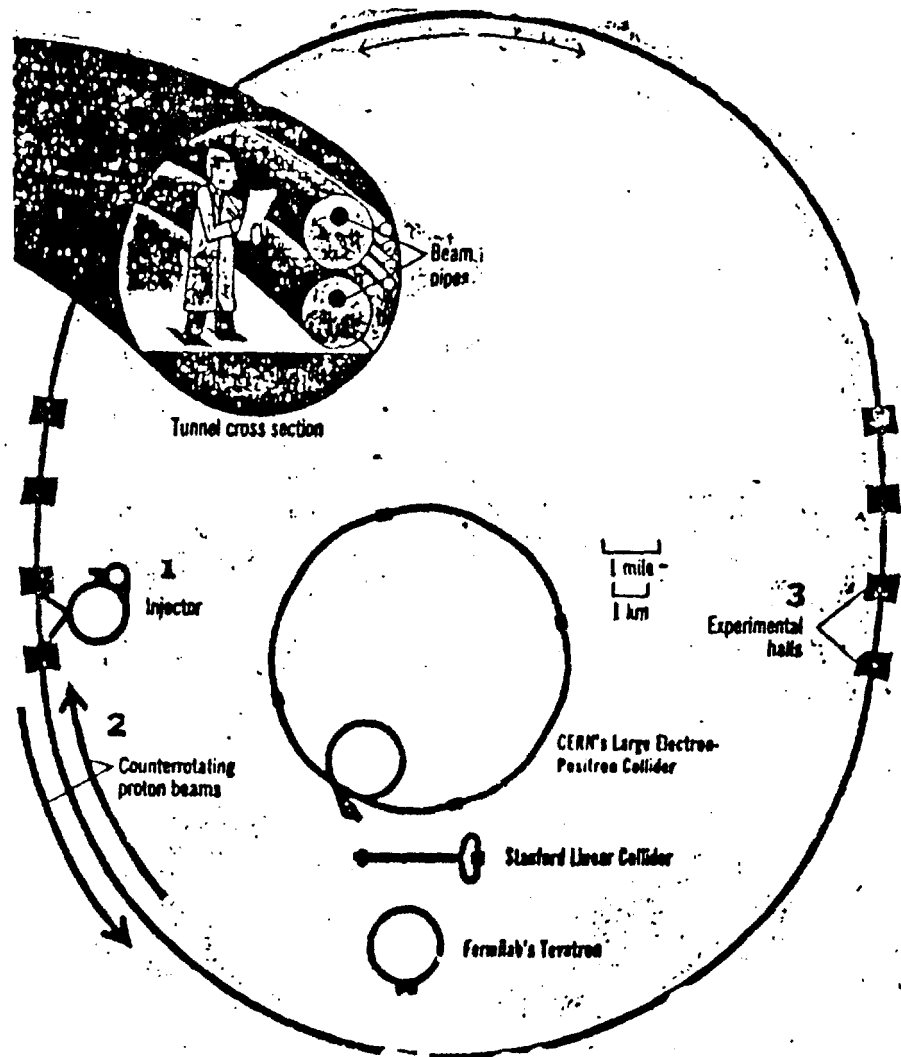


Fig 9

**Superconducting Supercollider**  
 Operational by about 2000  
 Maximum collision energy.  
 40 trillion electron volts  
 Type : proton-proton collider  
 1 protons will be collected in  
 the injector .  
 2 They will be sent into two pipes  
 and will circle in opposite directions .  
 3 The beams will cross at experimental  
 halls .

The following features are unique for synchrotron radiation:

1. Small angular divergence of the SR beam (for an electron energy of 2.5 GeV. SR power is mainly concentrated within an angle of about 30 angular seconds; at a distance of 10 m, the SR beam increases in size by 2 mm);
2. Wide spectral range covering the infrared, visible, ultraviolet, and X-ray regions of electromagnetic waves;
3. High intensity, high spectral brightness of the source. In all spectral regions, except for the range covered by lasers the intensity and brightness of synchrotron radiation exceeds those of the conventional sources by a factor of  $10^4$  to  $10^5$ ;
4. Time modulation of the SR intensity (regular bunches of nanosecond and sub-nanosecond duration);
5. Natural polarization of the radiation;
6. Exactly calculable characteristics;
7. High temporal stability;
8. Chemical purity with superhigh-vacuum conditions in the source.

These properties of synchrotron radiation make it attractive for various fields of science. Synchrotron radiation is widely used for research in physics, chemistry, biology, and materials science, for the development of new technologies, and also for solving applied problems in microelectronics, geology and medicine.

#### **Synchrotron Radiation Centers**

The rapid growth in the number of experimental teams using synchrotron radiation (SR) calls for special forms of research such as establishment of synchrotron radiation centers.

We will refer to one of such centers as an example. This is the Siberian Center of Synchrotron Radiation which has been created on the basis of the laboratories of the Institute of Nuclear Physics provided with three storage rings. At present the institute has completed a project of storage rings developed specially for SR generation, a so called Dedicated Synchrotron Radiation Source which consists of two storage rings; a small storage ring - "Siberia 1" - intended for research in the soft X-ray and vacuum ultra violet regions, and a large storage ring - "Siberia 2" - to be used for experiments in the range of hard X-rays. The small storage ring is used as an injector for the large one, Fig 10.

The following features are unique for synchrotron radiation:

1. Small angular divergence of the SR beam (for an electron energy of 2.5 GeV. SR power is mainly concentrated within an angle of about 30 angular seconds; at a distance of 10 m, the SR beam increases in size by 2 mm);
2. Wide spectral range covering the infrared, visible, ultraviolet, and X-ray regions of electromagnetic waves;
3. High intensity, high spectral brightness of the source. In all spectral regions, except for the range covered by lasers the intensity and brightness of synchrotron radiation exceeds those of the conventional sources by a factor of  $10^4$  to  $10^5$ ;
4. Time modulation of the SR intensity (regular bunches of nanosecond and sub-nanosecond duration);
5. Natural polarization of the radiation;
6. Exactly calculable characteristics;
7. High temporal stability;
8. Chemical purity with superhigh-vacuum conditions in the source.

These properties of synchrotron radiation make it attractive for various fields of science. Synchrotron radiation is widely used for research in physics, chemistry, biology, and materials science, for the development of new technologies, and also for solving applied problems in microelectronics, geology and medicine.

#### **Synchrotron Radiation Centers**

The rapid growth in the number of experimental teams using synchrotron radiation (SR) calls for special forms of research such as establishment of synchrotron radiation centers.

We will refer to one of such centers as an example. This is the Siberian Center of Synchrotron Radiation which has been created on the basis of the laboratories of the Institute of Nuclear Physics provided with three storage rings. At present the institute has completed a project of storage rings developed specially for SR generation, a so called Dedicated Synchrotron Radiation Source which consists of two storage rings; a small storage ring - "Siberia 1" - intended for research in the soft X-ray and vacuum ultra violet regions, and a large storage ring - "Siberia 2" - to be used for experiments in the range of hard X-rays. The small storage ring is used as an injector for the large one, Fig 10.

The basic specifications of the two storage rings are shown in table 1. They are provided with special devices for generation of radiation, namely, the "Snakes", Fig 11, and "undulatory", Fig 12, which incorporate a large number of identical magnets. The "Snakes" and "Undulatory" are installed in the storage ring by radiation extraction channels.

A layout of the complexes of the small storage ring (Siberia 1) and the large storage ring (Siberia 2), is shown in the schematic diagram of Fig 13 which shows the microtron injector which injects its beam into the small storage ring. Electron-optical channels are used for beam transfer to the small storage ring and for its re-injection from the small storage ring to the large one. In order to extract synchrotron radiation, the storage rings are equipped with:

- Vacuum channels with differential pumping and quick acting emergency valves for work with vacuum ultraviolet and soft X-ray radiation;
- SR channels with vacuum-tight aluminum windows, 1.5  $\mu\text{m}$  thick and  $80 \times 10 \text{ mm}^2$  in size. These channels enable radiation at wavelengths ranging from 5 to 20  $\text{\AA}$  to be extracted from vacuum into a helium atmosphere under a pressure of down to 10 mm of mercury.
- SR channels with superhigh-vacuum heatable windows made of 50-300  $\mu\text{m}$  thick beryllium to extract powerful SR beams at wavelengths of less than 5  $\text{\AA}$  into the atmosphere.

## References :

1. M.E Abdelaziz, "Particle Accelerators", Publisher: Arab development Institute, T.P.M., 1980
2. A.V.Crew, D.R.Getz, R.H.Hilderbrand, L.S.Markheim, D.A.Garlson, "high Energy Physics at Argonne National laboratory", Book published by Arg.Nat.Lab., Sept.1963.
3. P.Livdahl, "Status of the Fermilab Energy Doubler/Saver Project", IEEE Transactions On Nuclear Science, Vol.NS-24, No.3, June 1977.
4. G.Plass, "The LEP Project, Status and Plans" IEEE Trans. On Nucl. Sci, Vol NS-30, No 4, Aug. 1983, P 1978.
5. "Dedicated Synchrotron Radiation Sources", Report by The Institute of Nuclear physics, Siberian Division of the Academy of Sciences, Novosibirsk, Russia, 1986.

Table (1)

**The basic specifications of the storage rings  
"Siberia-1" and "Siberia-2"**

Parameters	"Siberia-1"	"Siberia-2"
Operating electron energy, GeV	0.45	2.5
Current, mA		
single-bunch mode of operation	100	100
multi-bunch mode of operation	-	300
Magnetic field in bending magnets, kGs	15	4.25; 8.5; 17
Injection energy, GeV	0.06	0.45
Injector	microtron	"Siberia-1"
Circumference, m	8.68	115.73
Overall dimensions (circle diameter), m	3	37-38
Power consumption, MW	1.1	5.2
Heat power, MW (removed by cooling water)	0.3	2.5
Ventilation-total heat output extracted into the atmosphere by main and auxiliary equipment, MW	~ 0.15	0.45
Atmosphere parameters indoors:		
winter	$t = 20 \pm 3 \text{ }^\circ\text{C}$ humidity $\leq 75 \%$	$t = 20 \pm 3 \text{ }^\circ\text{C}$ humidity $\leq 75 \%$
summer	$t = 23 \pm 3 \text{ }^\circ\text{C}$ humidity $\leq 75 \%$	$t = 23 \pm 3 \text{ }^\circ\text{C}$ humidity $\leq 75 \%$
Beam lifetime, hours	> 2	~ 10

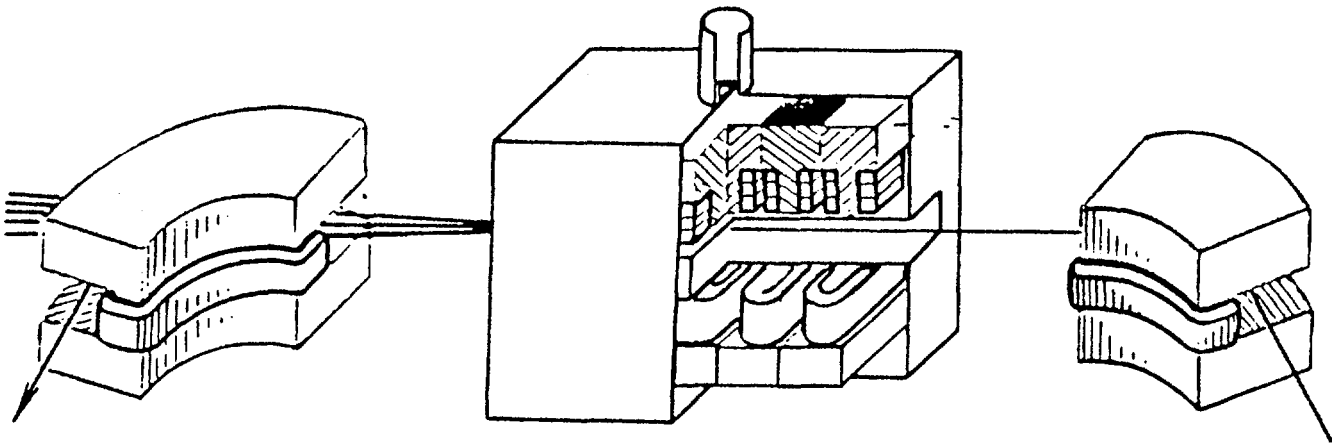


Fig 11 Superconducting "snake"

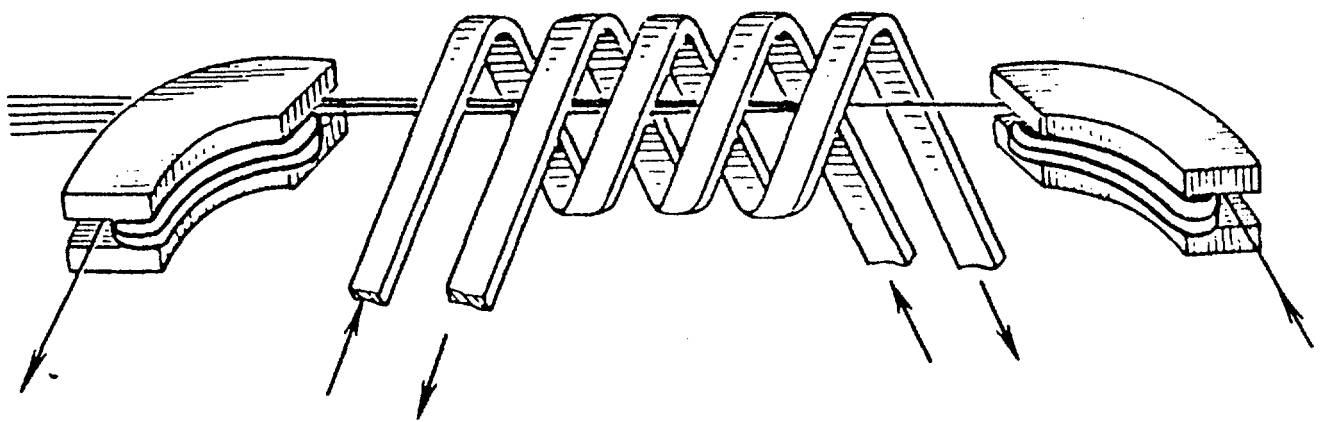


Fig 12 Spiral undulator

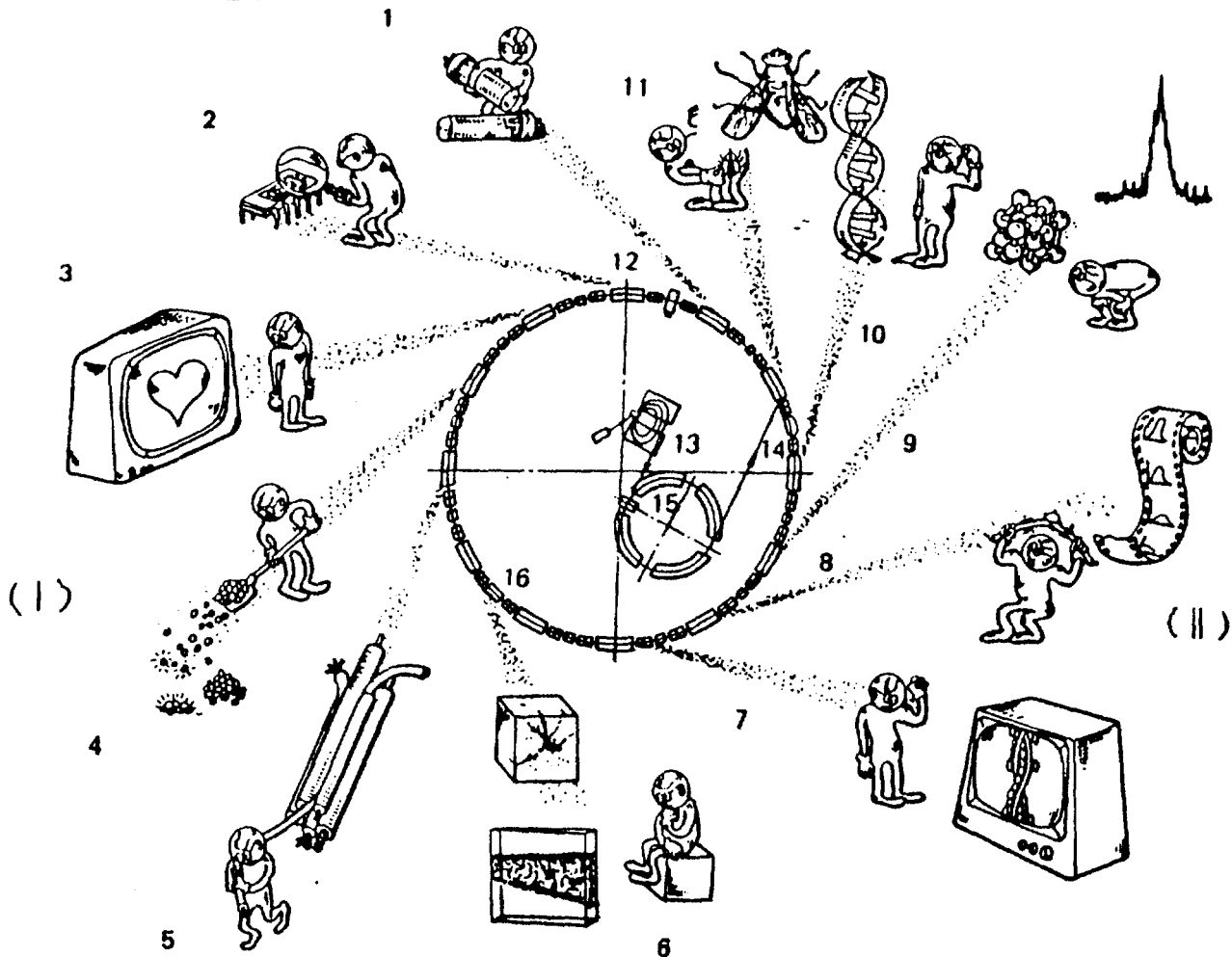


Fig 10

Technological and research capabilities of synchrotron radiation:  
 (I)- technological capabilities; (II)- scientific capabilities;  
 1 - radiometry; 2 - X-ray lithography - manufacture of super-large and super-fast integrated circuits; 3 - medicine; 4 - element express analysis  $10^{-3}$  s,  $10^{-4}$  g/g; 5 - X-ray technology of thick-wall products; 6 - study of X-ray resistance of materials; 7 - investigations of structure transformations of living objects; 8 - X-ray "movie" (resolution 1-10 ns); 9 - studies of amorphous material structures; 10 - microobject structure analysis; 11 - contact microscopy; 12 - storage ring; 13 - microtron; 14 - "snake"; 15 - booster; 16 - undulator

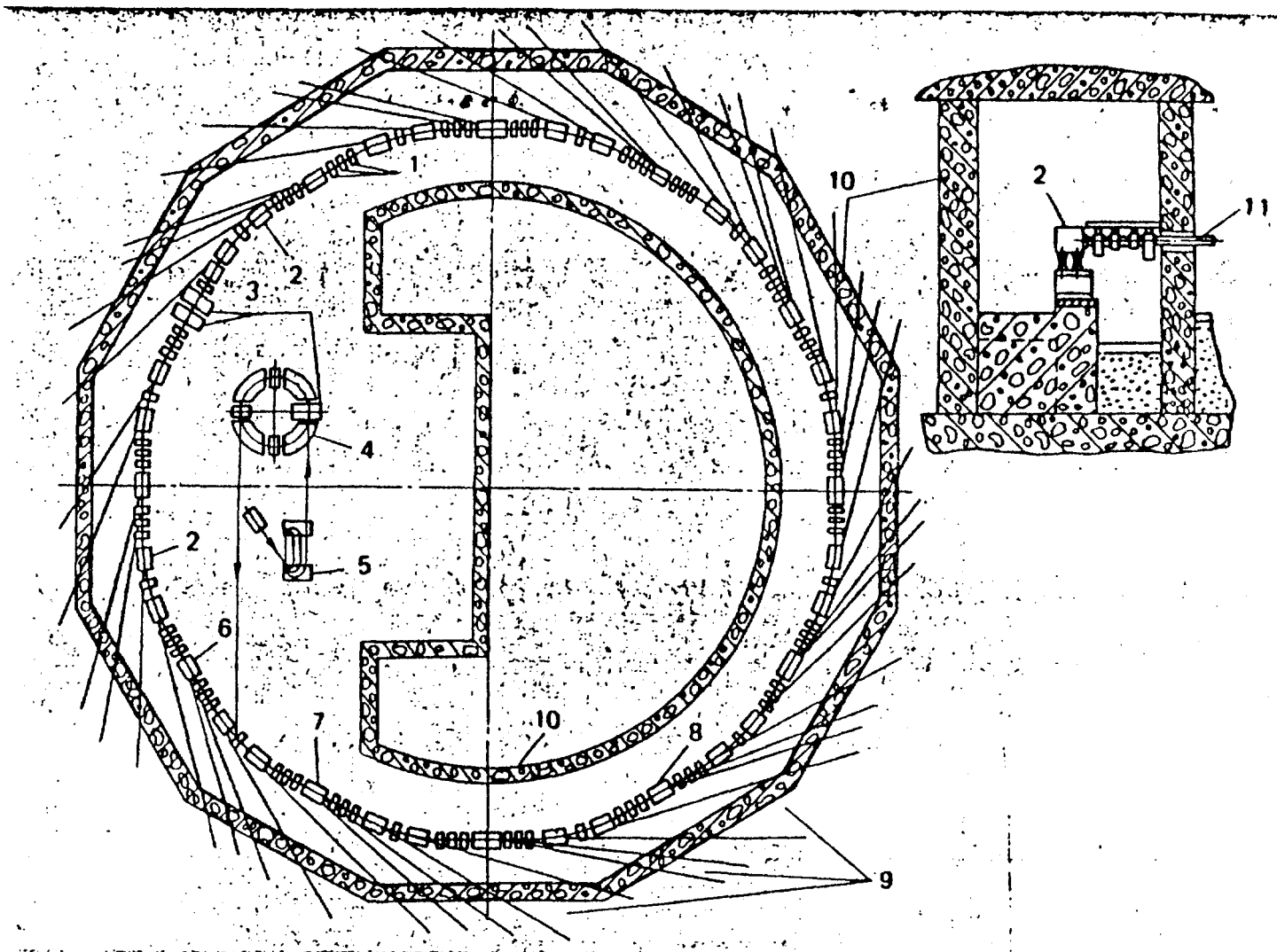


Fig 13

Lay-out of the complexes "Siberia-1" and "Siberia-2": 1 - lenses; 2 - bending magnets; 3 - RF cavity; 4 - small storage ring; 5 - microtron; 6 - "snakes" for lithography; 7 - superconducting "snakes"; 8 - undulators; 9 - SR beams; 10 - biological protection; 11 - SR extraction channel



EG9700098

*tion Physics Conf., Al-Minia, 13 - 17 Nov., 1996*

## Design principles and clinical possibilities with a new generation of radiation therapy equipment

Bengt-Inge Rudén

Department of Hospital Physics

Karolinska Hospital

S-171 76 STOCKHOLM, Sweden

The development of radiation oncology has to a significant degree been associated with the development of new techniques for radiation therapy. The megavoltage era started in the late 30's by introducing 1-2 MV photon beams from van der Graff generators for clinical use.

The first generation of truly isocentric megavoltage external beam treatment units appeared in the early 50's when the first  $^{60}\text{Co}$  units and low megavoltage (4-6 MV) linear accelerators were taken into clinical use (Fig. 1).

Simultaneously the first betatrons were developed for electron and photon beam therapy, but they were generally not truly isocentric even though they could simulate isocentric movements by coupled translational and rotational movements.

Not until 10 years later, in the mid 60's, the second generation of truly isocentric equipment appeared with medium megavoltage (6-14 MV) photon and electron beams, for the first time combined in a single treatment unit. This second generation of equipment was not fully developed, especially with the small maximum field sizes that were initially available

The third generation of isocentric radiation therapy equipment is delivering a wider spectrum of high quality electron and photon beams, and it first appeared about a decade later during the mid 70's (Fig. 1). The treatment units already then fulfilled most of the properties today required by state of the art equipment, such as multiple photon beam

energies, independent collimator jaw movements, automatic wedge systems, and high quality photon and electron beams of large field sizes. Of course a classification of isocentric treatment units in a few well-defined generations is not strictly possible as some machines will fall between the groups. However, it may be useful to indicate the principal steps in equipment development.

The development of the presently discussed fourth generation of treatment units (Fig. 1) was commenced during the later half of the 70's. The initial motivation was to investigate the radiation beam qualities obtainable from a newly developed compact 3-55 MeV electron accelerator.

The research on the radiotherapeutic beams resulted in a number of new universal solutions of the traditional problems in the formation of high quality electron and photon beams for radiation therapy (Table). The most interesting property of many of these solutions is their equally well applicability for photon and electron beam therapy thereby making the treatment unit well optimized for both treatment modalities. Previous treatment units were primarily designed for photon therapy with electron therapy as an additional modality often available under a number of compromises.

Before going into more details about these solutions the main problem areas associated with the shaping of high quality electron and photon dose distributions for radiation beam properties and clinical possibilities are briefly reviewed.

CLASSIFICATION OF ISOCENTRIC MEGAVOLTAGE EXTERNAL BEAM TREATMENT UNITS				
Generation	I	II	III	IV
Radiation modality	Low energy photons	Medium energy photons/electrons	High energy photons/electrons	Very high energy photons/electrons
Characteristic features	① Straight through beam ② Fixed flattening filter ③ External wedges ④ Book end collimator	① Bent beam ② Movable target/flattening filter ③ Dual transmission monitors ④ Electron tube/cone applicators	① Dual photon energies ② Dual scattering foils/scanned beam ③ Automatic dual wedge selector ④ Electron filter ⑤ Independent collimator jaws	① Scanned photon/electron beams ② Photon beam purging magnet ③ Dose distribution monitor ④ Multileaf collimator/Video readout ⑤ Helium atmosphere
Typical treatment head design diagram				
Prototype unit Energies In operation year	Gimmert Johns Vickers 60Co 4 MV 1951 1954	Applied radiation, Mullard 6-8 MV 3-10MeV 1985	Scanditronix MM22 6-21MV 2-22MeV 1976	Scanditronix MM50 5-50MV 2.5-50MeV 1985
Representative units	Theratron 780 LUE 5 Mevaltron 60 Neptun Dynaray 4-6 Clinac 4-6	Clinac 12, 18 Mevaltron 74, 77 LME 13, 15 LUE 15, 22 BJ-10 Dynaray 12 SL75-12, 20	Saturn 20, 25 Clinac 1800, 2500 SL75 25	

Fig 1. Schematic illustration of the main features of the 4 existing generations of isocentric megavoltage equipment. The beta-

trons have purposely been left out because they generally were not truly isocentric.

## Problems in therapy beam formation

The principal problem in the design of high quality photon beams is often the substantial electron contamination which will decrease in depth of dose maximum and reduce the sparing of superficial tissue.

The problem in the formation of high quality electron beams is generally associated with a significant contamination by scattered low energy, oblique electrons and by bremsstrahlung photons originating in the photon collimators, heavy auxiliary electron applicators and scattering foils. At low energies the influence of multiple scattering of electron beam and patient also complicates the flattening and collimation of the electron beam (Table).

Nearly as important as the physical factors are the ergonomical ones. These include adaption of the therapy machine to the patient and the various types of personnel that operate the treatment units. Heavy electron

applicators necessary for electron therapy indicate a poor ergonomical design and are time consuming particularly when used in complex clinical set-ups. It is well known that the shape of most tumours are far from rectangular, and probably in 80-95% of the treatments some type of beam blocking would be desirable. In many of these treatments, however, simple rectangular fields are used today, since this is the collimation system that is generally available on all treatment units. In many cases beam blocks, custom made inserts, compensators, bolus, wedges, and auxiliary electron applicators are necessary to use. However, they are auxiliary tools that require special equipment and personnel for their manufacture. Furthermore such devices always slow down the treatments because of their considerable weight and extra care and time needed in patient set-up.

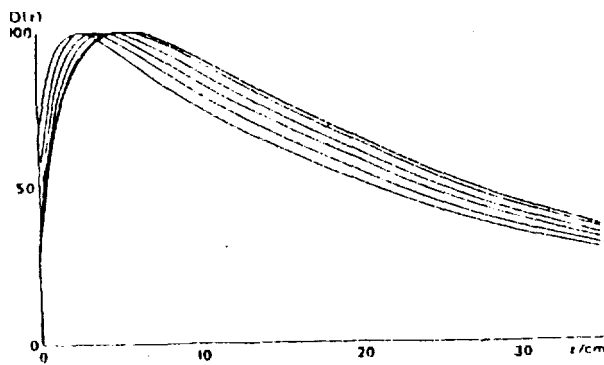


Fig 5 Illustration of the effect of the purging magnet on a 50 MV photon beam at a field size of 30 cm by 30. The magnetic field integrals are about 1, 2, 3, 5 and 7 Tesla cm in order of increasing half value depths

### Clinical applications

The wide range of electron and photon beam qualities available in the treatment unit makes it of very general use in radiation therapy, specially when different beam qualities are needed for the same patient. In general a wide choice of beam qualities will also allow a more optimal dose delivery, with fewer fields and simpler irradiation techniques. This will most often increase the accuracy of the treatment and improve the precision in dose delivery.

The very high energy beams of outstanding quality are naturally very useful for treating deep seated tumours. In particular the high energy electron beams above some 30 MeV open up a wide range of applications using multiple fields or small angle arc treatments. In Fig 6 this is illustrated by a parallel opposed electron beam technique on a tumour of the bladder. It is noticed that the absorbed dose in the entrance regions is about 70% which is considerably lower than that with high energy photons and almost as good as with proton beams. If only low megavoltage photon beams were available, a four-field box technique would generally be required.

The coincidence of the irradiation geometry for electron and photon therapy with the multileaf collimator opens new possibilities for the abutment of irregular electron and photon beams, the delivery of multiple irregular photon fields to complex target volumes, and use of shrinking field or even concomitant boost techniques. The multileaf collimator also allows a number of moving beam techniques,

The main purpose of the purging magnet is to produce very pure photon beams with deep dose maxima and low surface doses. However, it may equally well be switched off or used at a reduced setting, for example when a more superficial tumour should be treated with a given beam quality. This will allow some or most of the electron and positron contamination to reach the patient and increase the surface dose substantially. A similar result is sometimes achieved with a bolus or so called beam spoilers.

such as photon conformation therapy or electron arc therapy. It should be pointed out that the helium atmosphere in the treatment head allows electron collimation above about 10 MeV at an SSD of up to 100 cm with a penumbra  $P_{80/20}$  of about 15 mm. This implies that the complex patient mounted electron collimators in electron arc therapy are no longer needed. The present multileaf collimator is therefore the most practical device, e.g. for electron arc therapy of the postoperative chest wall in mammary carcinoma.

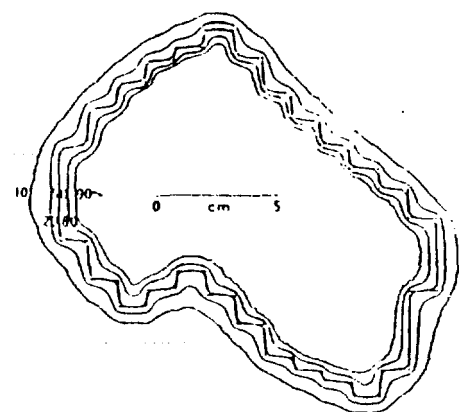


Fig 4 Illustration of the shape of the transversal isodose at dose maximum with a multileaf collimator on a 20 MeV bremsstrahlung beam. The fairly smooth of the 90% isodose demonstrates that a leaf width of about 1 cm is generally sufficient

The most exciting application of the multi-leaf collimator and the scanning system is probably on the recently developed generalized moving beam radiation therapy technique. This is the optimal irradiation of an arbitrary target volume with external beams when a minimal dose to surrounding normal tissues is the objective. The method employs angular dependent non-uniform incident radiation beams in a moving beam treatment, as illustrated in Fig. 7. The most practicable technique to deliver such time dependent non-uniform beams is by scanning an elementary beam in a time dependent patten.

For high energy photon beams it is quite reasonable that the optimal incident beam on an irregular target volume in the first approximation should be proportional to the projected beam path through the target volume (Fig. 7.). This will increase the dose delivery in directions where the beam is most efficient as the beam is passing a long distance through the target and often a short distance in normal tissues. However, in low energy beams the considerable photon attenuation and scatter introduces increasing deviations from this simple rule.

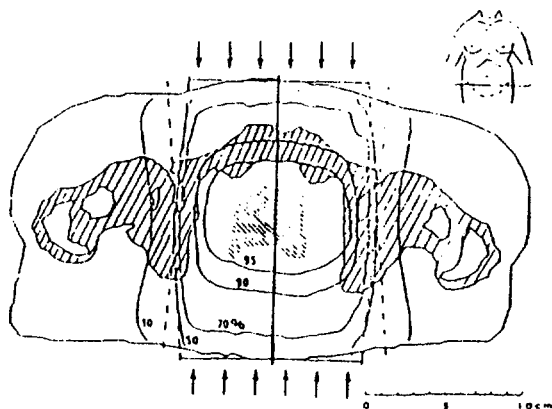


Fig. 6. Dose plan for the treatment of a bladder tumor by two parallel opposed 40 MeV electron beams. Due to the high electron energy the penumbra is quite good and the dose in the entrance regions is fairly low.

The resemblance of the generalized moving beam irradiation technique with the back-projections used in computed tomography is striking. The calculated isodose distributions for the target volume in Fig. 7. are shown in Fig. 8, clearly illustrating the merits of this new irradiation technique. The resultant isodoses very accurately follow the shape of the desired absorbed dose distributions inside the target volume (the jagged 95, 100, 105 and 110% isodose lines shaped in this way due to the finite size of the input matrix used in the calculations) and the mean dose to points at a given distance from the target volume is as rapidly as possible brought to low values.

This generalized moving beam irradiation technique is particularly interesting for complex irregular target volumes where the desired dose delivery can be calculated using simple algorithms, recently developed to determine the incident beam profiles. It is even possible to consider in detail possible organs at risk near the target volume. This development of the simple conformation technique has the potential of substantially improving radiation therapy. This concerns not least deep complex target volumes, that are difficult to treat adequately with present techniques.

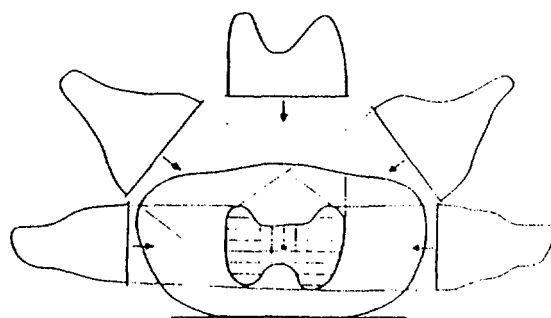


Fig. 7. Illustration of the recently developed generalized moving beam irradiation technique. The dose profile is strongly dependent on the angle of incidence on the target volume (shaded) and it is therefore most effectively realized by a scanning beam irradiation technique.

**Beam properties**

Due to the wide energy range of the race-track microtron and the flexibility of the beam scanning system, high quality photon beams at any energy from 5 to 50 MV, in 5 MV steps, can be generated. This is of special value in treatment optimization as the photon energy could be used as an independent variable covering a wide range of values when trying to find the best possible beam combination. A wide energy range is naturally as important for treatment optimization as a wide modulation transfer function is for an imaging system, or a broad frequency response for an amplifier. The same argument is even more applicable for the electron beams due to their more pronounced change in spatial energy deposition with a change in beam energy. The availability of wide range of photon and electron beams' energies on the same treatment unit in addition opens up the field for the optimal combination of electron and photon dose distributions. This technique has interesting clinical advantages as a low entrance and exit dose can be obtained at the same time as irradiation technique is simple and the dose in the target volume is high and uniform.

*Beam collimation.* The strong need for a flexible collimation system capable of adjusting the beam cross section to the shape of the target volume and the requirement to avoid heavy electron applicators have led to the design of a high resolution double focused multileaf collimator, as shown in Fig. 2. As this type of collimator is placed in the lower part of the treatment head with an internal helium atmosphere, it also allows the shaping of irregular electron fields without external applicators. For the first time this is a practical clinical collimation system which is equally well suited for electron and photon beam collimation.

To maximize the flexibility in collimation and minimize the area outside the target volume which is irradiated to a high dose, a narrow leaf width and a collimator edge, accurately aligned with the effective radiation source, are important design considerations. Therefore, all the leaves are double focused,

which means that they are wedge shaped in cross section and move on circular orbits. In this way the front and side edges are always accurately aligned with the radiation source to minimize the penumbra.

A typical multileaf collimated photon field is shown in Fig. 4. As seen from the rather smooth shape of the 90% isodose, which approximately determines the projection of the volume with a high therapeutic effect, a leaf spacing in the patient of about 1 cm is generally sufficient with high energy photon beams. The present collimator has two parallel opposed groups of 32 leaves, each with a projected width at isocentre of 1.25 cm covering field size up to 40 by 32 cm<sup>2</sup>. All 64 leaves are individually motordriven and computer controlled. The clinical advantages gained by using a high resolution double focused multileaf collimator instead of conventional collimation techniques has been proven.

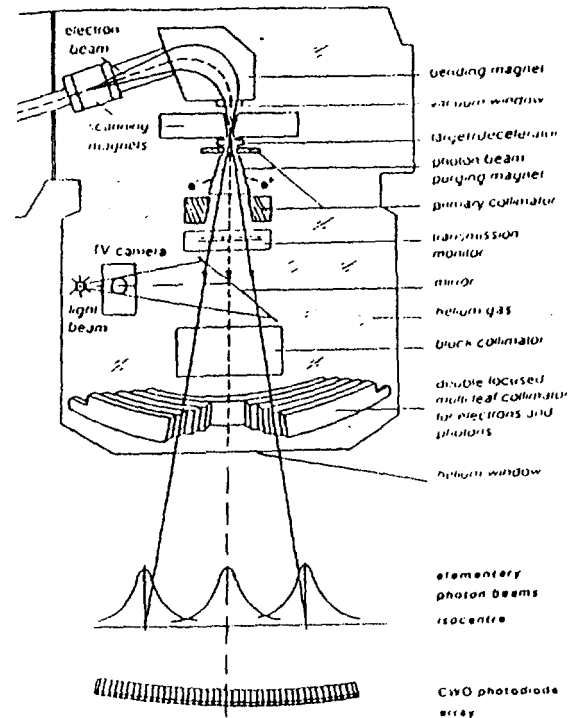


Fig 2. Crosssection through the scanning system and treatment head of the new generation of treatment units. The conceptually most important design features are that the same components are used for electron and photon beam formation. The flattening system, the dose distribution monitor, the collimation system and the patient monitor and verification system are all used for both radiation modalities. The detector array below the patient may be used both to make CT images of the patient with the therapy beam and for verification and interlock purposes.

Table  
*Problems and solutions in radiation therapy beam shaping*

Traditional problems	Energy range	Solutions in different equipments		
		Generation I+II	Generation III	Generation IV
<i>Photon beams (MV)</i>				
Electron contamination from air	<6	-	Thin electron filter + scattering foil	Helium atmosphere in treatment head
Compton scatter in patient	<6	Over flattened beams	Separate small and large field size filters	Continuously variable beam flattening by computer scanning system
Electron and positron contamination from filters	>10	-	Low atomic filter base or magnetic flattening filter	Photon beam purging magnet
Variation of energy spectrum across beam	>10	(Auxiliary compensators)	Spectral compensation in flattening filter	Scanned elementary photon beams
Energy degradation in flattening filters	>20	Low atomic number filter	Magnetic flattening filter without filter	Scanned photon beams
Beam compensation wedge filters		External wedges and material compensators	Automatic wedge selectro	Computer controlled non-uniform scanning patterns
<i>Electron beams (MeV)</i>				
Multiple scatter in air, etc.	<15	Smaller electron fields	Minimal material thickness in monitors	Helium in head, beryllium vacuum window
Bremsstrahlung	>15	Long SSD	Dual scattering foil system Q-pole scanning system	Dual dipole scanning system
Collimator weight	>20	-	Optimized electron jaw shape	Same multileaf collimator as for photons
Scattered electrons from collimator system		Smaller electron fields	Optimized balloon collimator	Tungsten multileaf collimator
Beam compensation wedge filters		-	-	Computer controlled scanning pattern

### Design principles of the IV generation of therapy beams

The fourth generation of isocentric radiation therapy equipment (Fig. 1.) has been developed to cover a wide energy range from 2.5 to 50 MeV electrons and 5 to 50 MV photons but also to solve the above mentioned traditional problems in the design of high quality therapy beams. The principal design idea was to use the same universal solutions for both electron and photon beam generation in order to accomplish the following principal tasks:

- Beam flattening
- Beam compensation
- Beam filtration
- Beam collimation
- Beam shape monitoring
- Patient position monitoring
- Absorbed dose monitoring
- Dose distribution monitoring
- Treatment verification

All these major tasks in the generation and monitoring of the radiation therapy beams have been solved by new technological approaches. As a result treatment beams of outstanding quality and physical properties are generated and accurately supervised under computer control.

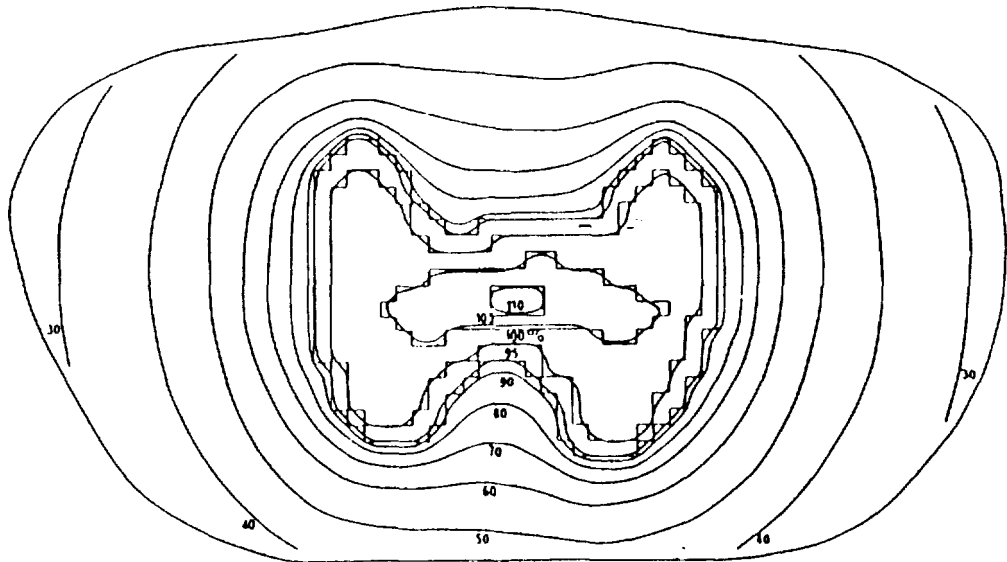
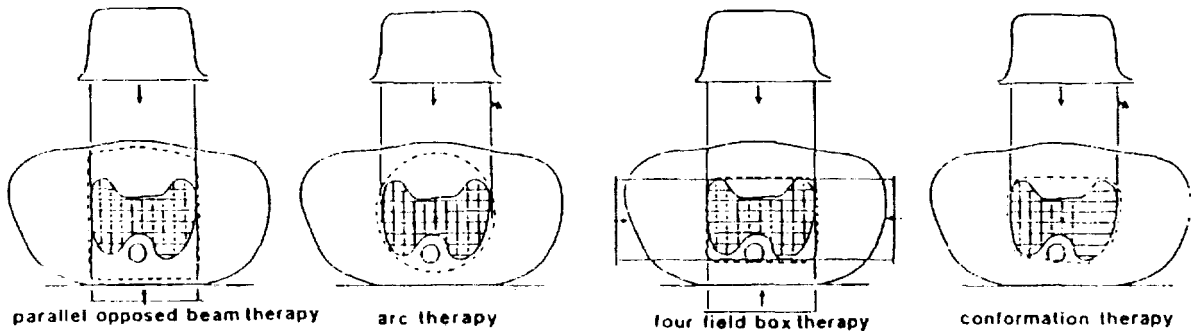


Fig 8 The resultant dose distribution in the patient when using the target volume and the irradiation technique presented in Fig 7. It is seen that the isodoses very accurately follow the shape of the target volume which is practically coincident with the 95% isodose. With this irradiation technique the desired absorbed

dose distribution inside the target volume is accurately produced and in addition the absorbed dose in surrounding normal tissues is in average as low as possible. The jagged shape of the isodoses inside the target volume are due to the finite voxel size (6 mm x 6 mm) used in the calculation and definition of the target volume

**CONVENTIONAL UNIFORM BEAM RADIOTHERAPY**



**NON UNIFORM BEAM RADIOTHERAPY**

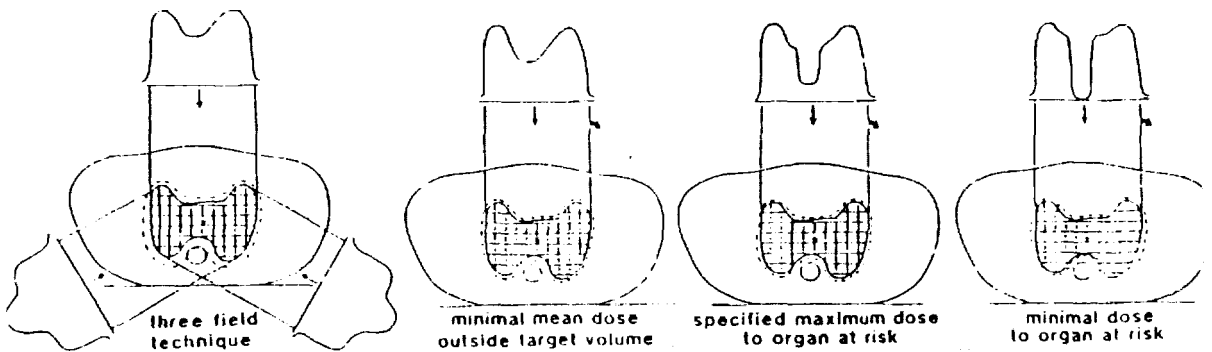


Fig 9 Schematic comparison of different external beam irradiation techniques. It is seen that non uniform dose delivery using inverse therapy planning will in general allow a better matching of the treatment volume (dashed line) to the target volume (shaded)

**SCIENTIFIC SESSION (7)**

**PLASMA AND ACCELERATORS**

**MOTION OF CHARGED SUSPENDED PARTICLE IN A  
NON-NEWTONIAN FLUID BETWEEN TWO LONG PARALLEL PLATES**

**M. M. Abd El Khalek**

**Nuclear Research Center- Atomic Energy Authority, Cairo - Egypt**

**ABSTRACT**

The motion of charged suspended particle in a non-Newtonian fluid between two long parallel plates is discussed. The equation of motion of a suspended particle was suggested by Clooskin. The equations of motion are reduced to ordinary differential equations by similarity transformations and solved numerically by using Runge-Kutta method. The trajectories of particles are calculated by integrating the equation of motion of a single particle. The present simulation requires some empirical parameters concerning the collision of the particles with the wall. The effect of solid particles on flow properties are discussed. Some typical results for both fluid and particle phases and density distributions of the particles are presented graphically.

**NUMERICAL SIMULATION OF THE MOTION OF CHARGED  
SUSPENDED PARTICLE IN MULTI-PHASE FLOW**

**M. M. Abd El Khalek**

**Nuclear Research Center - Atomic Energy Authority, Cairo - Egypt**

**ABSTRACT**

A method for computing Numerical simulation of the motion of charged suspended particle in multi-phase flow between two-long parallel plates is described in detail. The equation of motion of a suspended particle was suggested by Clooskin. The equations of motion are reduced to ordinary differential equations by similarity transformations and solved numerically by using Runge-Kutta method. The Trajectories of particles are calculated by integrating the equation of motion of a single particle. Numerical solutions of the resulting ordinary differential equations provide velocity distributions for

both fluid and solid phases and density distributions for the solid. The present simulation requires some empirical parameters concerning the collision of the particles with the wall. Some typical results for both fluid and particle phases and density distributions of the particles are presented graphically.

### **ION OPTICS IN AN ION SOURCE SYSTEM**

**F. W Abdel Salam, O. A. Moustafa, and H. El- Khabeary**

**Accelerators Dept., Nuclear Research Center,  
Atomic Energy Authority, Cairo, Egypt.**

#### **ABSTRACT**

An analysis of ion beams from an ion source which consisted of a hemispherical anode, a plane earthed cathode, and a focusing electrode has been carried out. The focal properties of such electrode arrangement were studied using axially symmetric fields. Axial and radial electric fields were obtained as functions of the axial distance. It was found that the radial component of the gradient of potential pushes the ions towards the axis, which indicates the convergent action of the system. The effect of voltage variation between the plasma boundary and the focusing electrode on the position of the plasma boundary are given using the experimental data of the ion source characteristics and its geometrical parameters. The advantages of plasma diffusing outside the source through a small aperture were used by applying a potential to the focusing electrode. It was possible to extract a large ion current from the expanded plasma. The system constituted a lens with a focal length of 29.4 mm.

### **SHEATH FORMATION AND EXTRACTION OF IONS FROM A CONSTRICTED R.F ION SOURCE**

**F. W Abdel Salam, A. G. Helal, H. El-Khabeary, and N. T. El- Merai**

**Accelerators Dept., Nuclear Research Center,  
Atomic Energy Authority, Cairo, Egypt.**

#### **ABSTRACT**

The present work investigates the plasma characteristics in a constricted R. F. ion source. The extraction of ions from the plasma boundary and sheath

formation were studied. The ion source physical parameters are discussed in order to understand the physical processes occurring within the discharge region up to the extraction system. Electron temperature and density were determined using Langmuir probe. The probe current-voltage characteristics were measured for different extraction voltages  $V(\text{ext.}) = 0, 500, 1000, \text{ and } 1250$  volt at various constant R.F. powers. The effect of R.F. power on electron temperature was deduced for a beam-plasma discharge. This revealed that for a quasi-neutral (plasma) region the electron temperature increased linearly with the R.F. power which leads to substantial electron heating and efficient electron energy transport in this region. Applying extraction voltage, the electron temperature drops as the ionization rate increases. The sheath thickness was obtained at constant extraction voltages. The curves show that if the ion current density increased, the sheath thickness decreased while it increases by increasing extraction voltage, and it is negligible in the plasma region.

### **THE BROAD BEAM ION IMPLANTER WITH THE USE OF RADIO FREQUENCY ION SOURCE**

**M. E. Abdelaziz, S. G. Zakhary, and A.A. Ghanem**

**Accelerators Dept., Nuclear Research Center,  
Atomic Energy Authority, Cairo, Egypt**

#### **ABSTRACT**

The project started with the design of the broad beam RF ion source and the single gap accelerating column. The preliminary results of the source show that the ion current extracted from the source could reach  $\approx 30\text{mA}$  with extraction voltage = 2kV. The beam uniformity was made by the use of multiapertures graphite cathode designed to make perveance matching to the normal Gaussian distribution of the ion beam. The beam uniformity could reach  $\approx 66\%$  of the beam width of  $\approx 6$  cm. The design of the single gap accelerating column based on tracing of beam lines inside the accelerating gap and estimation of the minimum value of the electric field required to contain the beam against space charge expansion in order to achieve minimum beam emittance without aberrations. The preliminary results of the acceleration of the ion beams up to 20 KeV show an increase of the extracted ion current with increase of the extraction voltage. This increase is due to decrease of the angular divergence of the beam due to the effect of increasing the axial velocity component of the accelerated field.

**ELECTRON BEAM INTERACTION WITH  
INHOMOGENEOUS WARM PLASMA  
AND WAVE RADIATION**

**N. G. Zaki, and Kh. H. El-Shorbagy**

**Plasma Physics Dept. Nuclear Research Centre  
Atomic Energy Authority, Cairo - Egypt**

**ABSTRACT**

The beam - plasma heating due to a relativistic electron beam (REB) under the effect of an external static magnetic field was investigated. A longitudinal 1-D oscillations in a plasma, which is inhomogeneous and bounded in the direction of the beam motion was considered.

It was observed that the REB acts as a mechanism responsible for putting more power into magnetized plasma and not only for amplifying the waves. Besides, more energy is absorbed from this beam due to plasma electron warmness. It was also found that nonlinear effects associated with the generation of second harmonics, play an important role in the process of energy transfer from the beam to the plasma as compared with linear stage.

**COEFFICIENTS OF VISCOSITY FOR HEAVY  
IMPURITY ELEMENT IN TOKAMAK**

**R. N. El - Sharif, A. M. Bekhit**

**Plasma Physics Dept., NRC, Atomic Energy Authority,  
Cairo, Egypt**

**ABSTRACT**

The transport of heavy impurity element in tokamak was studied theoretically. The viscosity coefficients of Chromium impurities has been calculated in 13 and 21 moment approximation, in the limit of strong fields ( $\omega_{c\alpha} \tau_{\alpha} \gg 1$ ) where  $\omega_{c\alpha}$  is the gyrofrequency of species  $\alpha$  ( $\alpha = e$  &  $i$ ). It was found that the off-diagonal viscosity coefficient approximately tends to zero. This means that the friction force in the off-diagonal direction is very small, for the perpendicular viscosity coefficient the two approximations coincide with each other.



24

## MOTION OF CHARGED SUSPENDED PARTICLE IN A NON-NEWTONIAN FLUID BETWEEN TWO LONG PARALLEL PLATES -

M.M.ABD EL KHALEK

Nuclear Physics Department-Nuclear Research Centre - Atomic Energy Authority

### ABSTRACT

The motion of charged suspended particle in a non-Newtonian fluid between two long parallel plates is discussed. The equation of motion of a suspended particle was suggested by Cioskin. The equations of motion are reduced to ordinary differential equations by similarity transformations and solved numerically by using Runge-Kutta method. The trajectories of particles are calculated by integrating the equation of motion of a single particle. The present simulation requires some empirical parameters concerning the collision of the particles with the wall. The effect of solid particles on flow properties are discussed. Some typical results for both fluid and particle phases and density distributions of the particles are presented graphically.

### INTRODUCTION

Suspensions of small particles in fluids are common nature and in several engineering fields, and it is desirable to know how they respond to imposed forces or motions at their boundaries. The problem is to determine the rheological properties of this equivalent homogeneous fluid from a knowledge of the properties of the particles and the ambient fluid in which they are suspended. The particles and ambient fluid will be supposed to be incompressible of uniform temperature and permanent in constitution. It will also be assumed that the ambient fluid is non-Newtonian. Research on suspension rheology has been directed towards extensions of these well known results, in particular for the cases of (a) more concentrated suspensions of spherical particles, (b) deformable particles with both viscous and elastic properties, (c) non-spherical rigid particles. Hence much effort has been directed towards the problem of particle-wall collisions { Matsumats et al. 1976<sup>(1)</sup>; Tsuji & Morikawa 1978<sup>(2)</sup>; Tsuji et al. 1983<sup>(3)</sup>, 1985<sup>(4)</sup> and Tsuji et al. 1987<sup>(5)</sup> }. The most difficult problem in calculating trajectories in pipes and ducts is the effect of particle collisions with the wall. When a spherical particle collides with a flat plate, the relations between the velocities before and after the collision are obtained by the impulsive equations. If the spherical particles do not collide too frequently, these relations are sufficient to consider the effect of collisions even in a horizontal channel. However if a perfect sphere collides with a perfect plane wall with a coefficient of restitution  $<1$ , this results in all particles sliding along the bottom of the wall after a number of collisions. A major difficulty in the study of rheology is that one's intuition about the form of the constitutive stress relation appropriate to given circumstances is so poorly developed. It is hard to know even in broad terms how a given material will behave, chiefly because we have at our disposal so few definite and well-understand constitutive relations for non-Newtonian fluids to provide guidance. In a material element of the suspension large enough to contain many particles, there will be at any instant a certain statistical distributions of particles with respect to shape, orientation, size and relative position, and this information we can regard as included in a specification of the instantaneous "state" of the element of the suspension. The configuration of the particles, and so also the state of an element of the suspension, is changing in a way which depends on the nature of the instantaneous motion of the

element ; and in general a calculation of the state of an element at an arbitrary time after some given initial instant requires a knowledge of the history of the motion of the element .Richardson<sup>[6,7]</sup> studied the behavior of two-dimensional solitary bubbles in a purely straining flow , a simple shearing flow , and a parabolic flow ; Buckmaster and co-workers<sup>[8,9]</sup> studied the deformation and burst of two-dimensional slender drops with pointed ends in a purely straining flow ; and Zahalek et al.<sup>[10]</sup> computed the deformation of a cylindrical liquid capsule which is enclosed by an inextensible membrane in a simple shearing flow . In the context of two- dimensional flow , one configuration that received attention on several occasions consists of a suspension of two-dimensional particles that are arranged in a single file within a channel that is bounded by two parallel plane walls . The motion may be driven either by the relative motion of the two walls or by an axial pressure gradient . Studies of these flows furnish useful information . On the behavior of ordered suspensions and illustrate the significance of solid boundaries . Moreover , they allow direct comparisons with experimental observations and standard rheological measurements based on the plane-couette viscometric flow<sup>[11,12]</sup> . Louis J. Durlofsky and John F. Brady<sup>[13]</sup> have studied a general method for computing the hydrodynamic interactions among an infinite suspensions of particles immersed between two infinite plane boundaries , under the condition of vanishing particle Reynolds number , many previous investigators have considered the problem of particle motion near one , or between two-plane walls in Stoke's flow . The early for field asymptotic solutions for one sphere near a single plane wall or between two plane walls computed by Faxe'n and others are discussed by Happel & Brenner (1973)<sup>[14]</sup> . Exact solutions now exist for the general motion of a single sphere near a single plane wall with the fluid at infinity quiescent ( Brenner 1961<sup>[15]</sup> ; Maude 1961<sup>[16]</sup> ; Goldman , Cox & Brenner 1967a<sup>[17]</sup> ; Dean & O'Neil 1963<sup>[18]</sup> ; O'Neil 1964<sup>[19]</sup> ) as do near - field asymptotic results (Cox & Brenner 1967<sup>[20]</sup> ; Goldman , Cox & Brenner 1967a<sup>[17]</sup> ; O'Neil & Stewartson 1967<sup>[21]</sup> ) . The more general problem involving sphere motion near a plane wall subject to an imposed shear flow has also been solved ( Goldman , Cox & Brenner 1967 b<sup>[22]</sup> ; O'Neill 1968<sup>[23]</sup> ) . B.V.R. Vihall and W. Tabakoff<sup>[24]</sup> present a numerical solution for the fundamental problem of solid particles suspended in a viscous incompressible flow over a cylinder at low Reynolds number . A method for computing Stokes flow interactions in suspensions of spherical objects is described in detail and applied to the suspensions of porous particles , drops , and bubbles to determine their hydrodynamic transport coefficient by Guobiao Mo and Ashok S. Sangani<sup>[25]</sup> . The flow of a periodic suspension of two-dimensional viscous drops between two parallel plane walls were studied by Hua Zhou and C. Pozrikidis<sup>[26]</sup> and a framework for performing dynamic simulations with suspensions of increasingly complex structure is developed .

This paper describes a new method for studying the path lines of a solid suspended charged particle in a non-Newtonian fluid . The particle is considered to move with a velocity equal to the velocity of the fluid and initially starting from the mid point of the channel . The effect of some parameters such as particle volume , fluid density , fluid viscosity on the path lines are also investigated . The present simulation requires some emperical parameters concerning the collision of the particles with the wall .

## FORMULATION OF THE PROBLEM

In this paper , we study the path lines of a solid charged suspended particle in a non-Newtonian fluid . The flow is take place in a long channel under constant magnetic field normal to the plane of the motion . The particle is assumed initially moving from the mid point of the channel with a velocity equal to the velocity of the fluid . We consider a plane steady laminar flow of n-power non-Newtonian electrically conducting fluid of constant viscosity and constant electrical

conductivity between two parallel plates in the x-direction . Also , we consider that there is a small external magnetic field  $H_0$  in the Y-direction . The upper plate is at  $Y=h$  and is moving with a speed  $U_0$  in the X-direction while the lower plate is at rest at  $y=0$  . For a non-Newtonian fluid the continuity equation and the equation of motion are ,

$$\frac{d}{dy}(\rho v) = 0 \quad (1)$$

$$\rho v \frac{du}{dy} = \mu \frac{d}{dy} \left( \frac{du}{dy} \right)^n - \sigma B_0^2 u \quad (2)$$

$$0 = - \frac{dp}{dy} + \sigma B_0 u B_z \quad (3)$$

$$0 = \frac{\partial p}{\partial x} \quad (4)$$

The induced magnetic field  $H_x$  may be determined from

$$\frac{dH_x}{dy} = \epsilon \sigma B_0 u \quad (5)$$

The energy equation is

$$\rho c_p v \frac{dT}{dy} = k \frac{d^2 T}{dy^2} + \mu \left( \frac{du}{dy} \right)^{n+1} + \sigma B_0^2 u^2 \quad (6)$$

and the boundary conditions are

$$u(0) = 0, T(0) = T_w, H_x(0) = B_z(0) = 0, u(h) = 1, T(h) = T_w(1+x) \quad (7)$$

Introducing non-dimensional quantities defined by

$$y = hy', u = U_0 u', v = U_0 v', p' = \frac{p}{\rho U_0^2}, H_x' = \frac{H_x}{H_0}, T' = T/(U_0^2/c_p) \quad (8)$$

Substituting from (8) in equations (2,3,5,6 and 7) , we get after dropping dashes , we get

$$\frac{d}{dy} \left( \frac{du}{dy} \right)^n - R_n v \frac{du}{dy} = H_n^2 u \quad (9)$$

$$\frac{dp}{dy} = R_o R_H u H_x \quad (10)$$

$$\frac{dH_x}{dy} = - R_o u \quad (11)$$

$$\frac{d^2 T}{dy^2} = - R_n p_n v \frac{dT}{dy} = - p_n \left[ \left( \frac{du}{dy} \right)^{n+1} + H_n^2 u^2 \right] \quad (12)$$

With the boundary conditions

$$u(0) = 0, T(0) = 1, H_x(0) = 0, u(1) = 1, T(1) = 1 + x \quad (13)$$

where,  $R_n = \frac{\rho h^n U_0^{2-n}}{\mu}$  is the Reynolds number of the non-Newtonian fluid ,

$H_n^2 = \frac{\sigma B_0^2 h^{n+1} U_0^{1-n}}{\mu}$  : is its Hartmann number ,  $p_n = \frac{c_p \rho}{\mu} \left( \frac{U_0}{h} \right)^{n-1}$  : is Prandtl number ,  $R_o = \frac{\mu_o H_0^2}{\rho U_0^2}$  :

is the magnetic Reynolds number .

$$\text{Let , } \epsilon = \nu R_n, H_n^2 = a \quad (14)$$

where , a : is a constant .

To solve equation (9) , we consider

$$u(y) = u_0(y) + \epsilon u_1(y) \quad (15)$$

Where terms of  $O(\epsilon^2)$  and higher orders may be neglected . Substituting from (14,15) into (9,13) , equating terms free of  $\epsilon$  and terms of order  $(\epsilon)$  in both sides of the resulting equations , after some simple calculations , we get

$$u(y) = y + \epsilon \frac{y(y-1)}{6n} [a(y+1) + 3] \quad (16)$$

The equation of motion of the suspended particle was suggested by Clooskin N.A.<sup>[21]</sup> in the form

$$\rho_p \frac{dc}{dt} = -g(\rho_p - \rho_f) j^z - k_v(c^z - u_f^z) + k(u_f^z - c^z) \wedge \text{rot } u_f^z - \text{grad } p \quad (17)$$

where,  $\rho_p$  : is the particle's density ,  $\rho_f$  : is the density of the fluid ,  $\vec{c}$  : is the particle velocity ,  $\vec{u}_f$  : is the fluid velocity ,  $p$  : is the pressure ,  $g$  : is the gravitational acceleration which is vertical ,  $k_v$  : is the resistance coefficient of motion in viscous fluid and  $k$  : is the so called the form coefficient .

Therefore , the equation of motion is

$$\rho_p \frac{d\vec{c}}{dt} = -g(\rho_p - \rho_f)\vec{j} - k_v(\vec{c} - \vec{u}_f) + k [c_x \frac{\partial u}{\partial y} \vec{i} + (u - c_x) \frac{\partial u}{\partial y} \vec{j}] + \frac{e}{v} [c_x H_0 \vec{i} - c_y H_0 \vec{j}] - \text{grad } p \quad (18)$$

Introducing non-dimensional quantities defined by :

$$u = U_0 u', y = hy', t = \frac{U_0}{g} t', c_x = u_0 c_x', c_y = u_0 c_y' \quad (19)$$

Therefore ,

$$u' = \frac{hy'}{U_0} + \frac{e}{6nU_0} [ah^3 y'^3 + 3h^2 y'^2 - hy'(a+3)] \quad (20)$$

substituting from (19) and (20) in (18) and after dropping dashes we get ,

$$\frac{dx}{dt} = c_x \quad (21)$$

$$\frac{dy}{dt} = c_y \quad (22)$$

$$\frac{dc_x}{dt} = -\alpha_v c_x + \alpha_1 \{hy + \frac{e}{6n} [ah^3 y^3 + 3h^2 y^2 - hy(a+3)]\} + \alpha_m c_y \{1 + \frac{e}{6n} [3ah^2 y^2 + 6hy - (a+3)]\} - \alpha_H c_y - \alpha_{sp} \quad (23)$$

$$\frac{dc_y}{dt} = -\alpha_d - \alpha_v c_y + \alpha_2 \{hy + \frac{e}{6n} [ah^3 y^3 + 3h^2 y^2 - hy(a+3)]\} \{1 + \frac{e}{6n} [3ah^2 y^2 + 6hy - (a+3)]\} - \alpha_m c_x \{1 + \frac{e}{6n} [3ah^2 y^2 + 6hy - (a+3)]\} - \alpha_H c_x - \alpha_{sp} \quad (24)$$

where ,  $\alpha_v = \frac{k_v U_0}{\rho_p g}$  : is a parameter dependent on the fluid viscosity ,  $\alpha_1 = \frac{kv}{\rho_p g}$  ,  $\alpha_m = \frac{kU_0}{\rho_p g}$  : is a parameter dependent on the shape of the particle ,  $\alpha_H = \frac{eU_0 H_0}{\rho_p g v}$  : is a parameter dependent on the magnetic force ,  $\alpha_2 = \frac{k}{g\rho_p}$  ,  $\alpha_d = 1 - \frac{\rho_f}{\rho_p}$  : is a parameter dependent on the fluid density and  $\alpha_{sp} = \frac{g \text{grad } p}{g\rho_p}$  : is a parameter dependent on the pressure gradient .

## NUMERICAL SOLUTIONS AND RESULTS

The equations (21-24) are a system of differential equations , which can be solved using the method of fourth order Runge-Kutta method .

### The dependence on fluid density :-

The solution is shown graphically in figure (1) . As conclusion the results show that when ( $\alpha_d$ ) is increased :

- (1) The motion of the particle is directed downward , it collides the lower plate .
- (2) The number of collisions with the lower plate is decreased .
- (3) The particle continue to repeat the bouncing motion .
- (4) The particle distribution is too close to the lower plate .
- (5) No particle collides with the upper plate .
- (6) The width and maximum height are decreased .

## The dependence on fluid viscosity :-

The solution is shown graphically in figure (2) . As conclusion the results show that when ( $\alpha_v$ ) is decreased :

- (1) The motion of the particle is directed downward and the number of collisions with the lower plate is increased .
- (2) The particle continue to repeat the bouncing motion .
- (3) The particle distribution is too close to the lower plate .

And when ( $\alpha_v$ ) is increased :

- (1) The motion of the particle is directed upward , the particle collides with the upper plate and the number of collisions with the upper plate is increased .
- (2) The particle continue to repeat the bouncing motion .
- (3) The particle distribution is too close to the upper plate .

## The dependence on particle shape :-

The solution is shown graphically in figure (3) . As conclusion the results show that when ( $\alpha_s$ ) is decreased :

- (1) The motion of the particle is directed upward , the particle collides with the upper plate and the number of collisions with the upper plate is increased .
- (2) The particle continue to repeat the bouncing motion .
- (3) The particle distribution is too close to the upper plate .

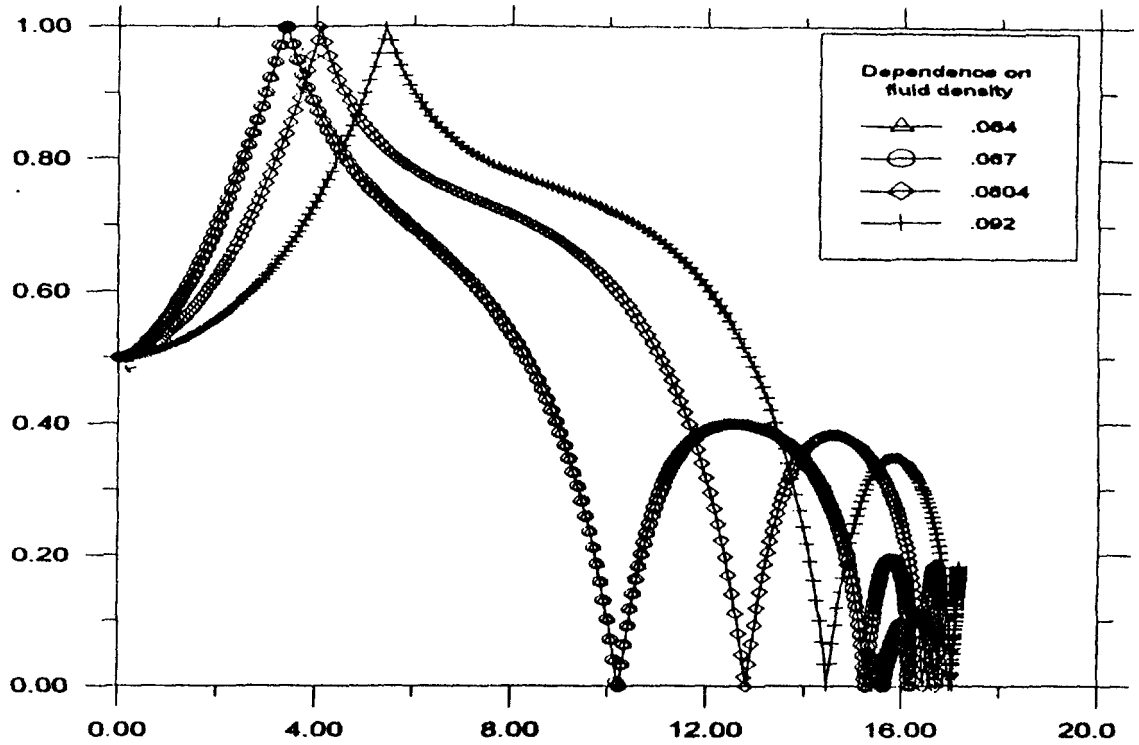
And when ( $\alpha_s$ ) is increased :

- (1) The motion of the particle is directed downward , the particle collides with the lower plate and the number of collisions with the lower plate is increased .
- (2) The particle continue to repeat the bouncing motion .
- (3) The particle distribution is too close to the lower plate

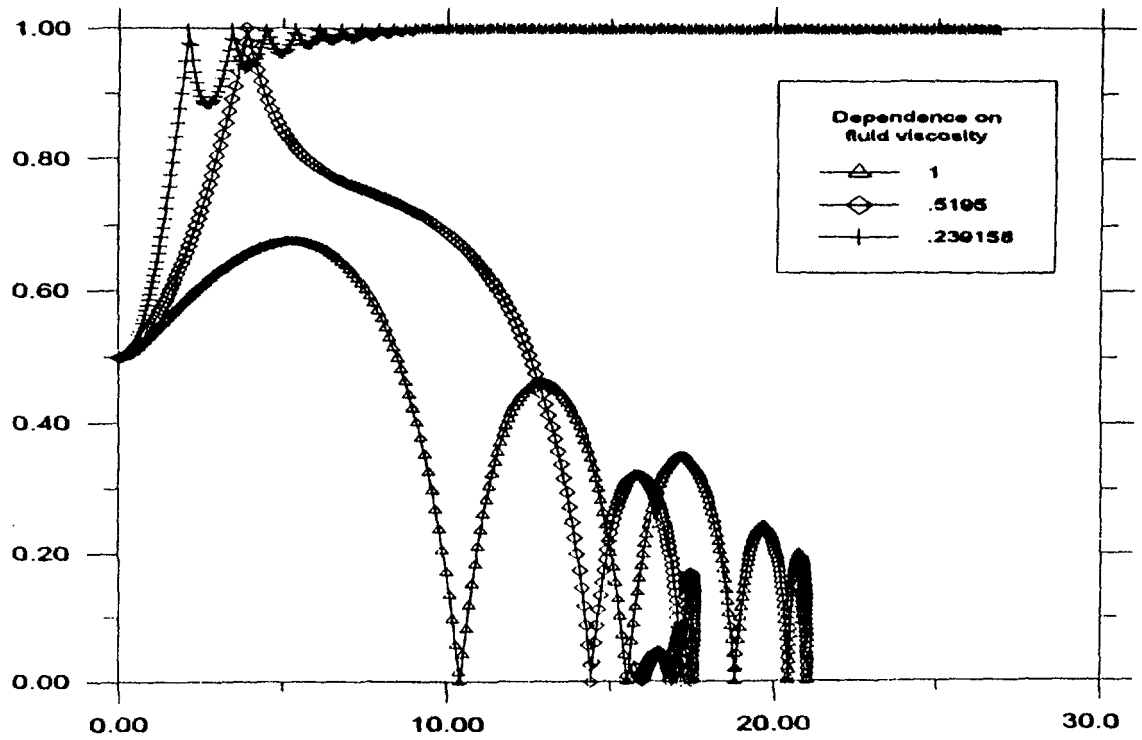
## The dependence on magnetic force :-

The solution is shown graphically in figure (4) . As conclusion the results show that when ( $\alpha_m$ ) is increased :

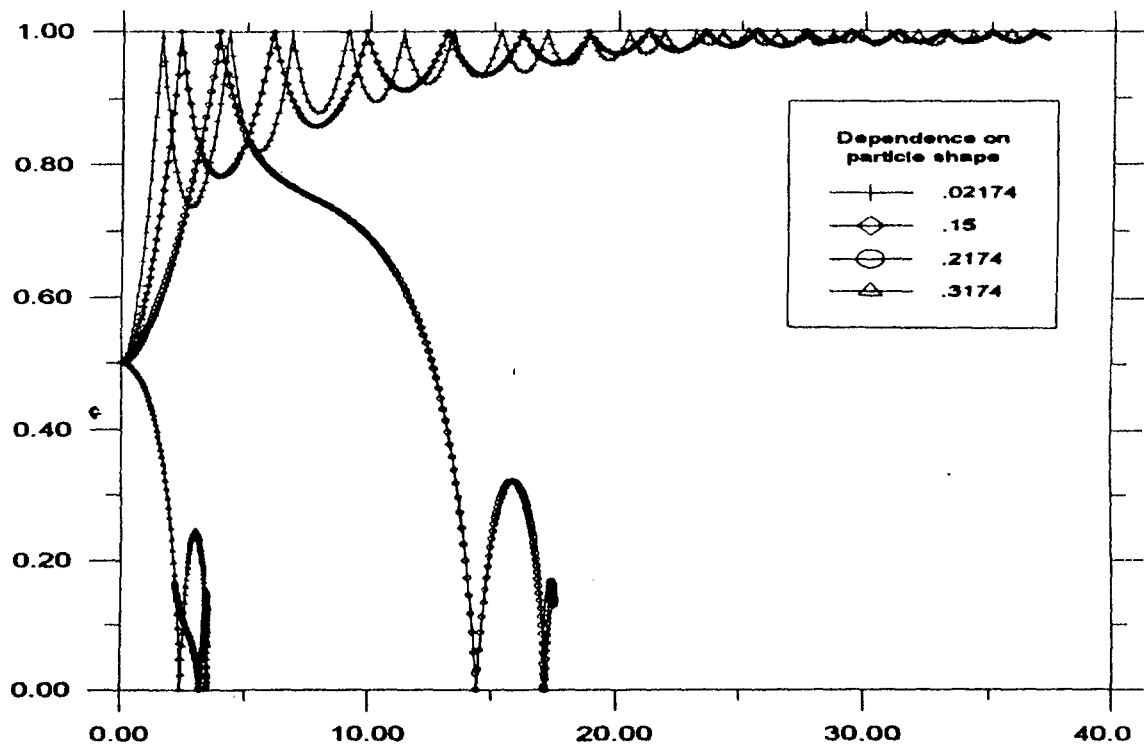
- (1) The motion of the particle is directed to the lower plate , the particle collides with the lower plate and the number of collision with the lower plate is decreased .
- (2) The particle continue to repeat the bouncing motion .
- (3) The particle distribution is too close to the lower plate .
- (4) No particle collides with the upper plate .
- (5) The width and maximum height are decreased .



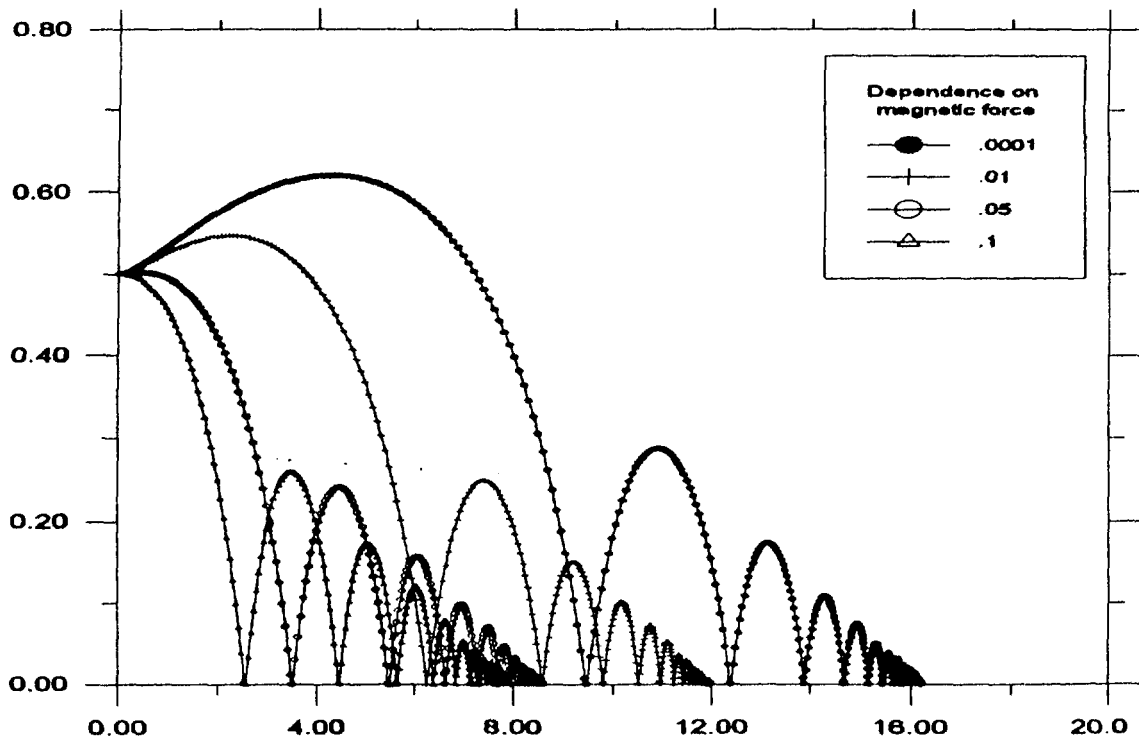
Figure(1) Particle trajectories for different  $\alpha_d$



Figure(2) Particle trajectories for different  $\alpha_v$



Figure(3) Particle trajectories for different  $\alpha_{\delta}$



Figure(4) Particle trajectories for different  $\alpha_H$

## REFERENCES

- [1] Matsumoto S. , Saito S. & Maeda S. , *J. Chem. Engng. Japan* 9, 23- 28 . (1976).
- [2] Tsuji Y. , *BHRA Fluid Engineering , cranfield , U.K. Paper B1.*(1978) .
- [3] Tsuji Y., Seki W. & Morikawa Y., *J. Soc. Powder Tech . Japan* 20, 270-278 (1983)•  
(In Japanese) .
- [4] Tsuji Y. , Oshima T. & Morikawa Y. , *KONA* 3, 38-51 (1985) .
- [5] Tsuji Y. , Morikawa Y. , Tanaka T., Nakatsukasa N. and Nakatani M., *Int. J. Multiphase Flow* Vol .13, No.5, P. 671-684 (1987) .
- [6] Richardson S., *J. Fluid Mech.* 33,476(1968).
- [7] Richardson S., *J. Fluid Mech.* 58,115(1973).
- [8] Buckmaster J.D., *J. Fluid Mech.* 55,385(1972).
- [9] Buckmaster J.D. and Flaherty J.E., *J. Fluid Mech.* 60,625(1973).
- [10] Zahalak G.I. , Rao P.R. and Suter S.P. , *J. Fluid Mech.* 179,283(1987).
- [11] Karnis A. , Goldsmith H. L. , and Mason S.G. , *J. Colloid Interface Sci* 22,531(1966)
- [12] Masliyah J.H. and Van de Ven T.G.M. , *Int. J. Multiphase Flow* 12,791(1986).
- [13] Louis Durlofsky J. and John Brady F., *J. Fluid Mech.* Vol.200,p.39-67(1989).
- [14] Happel J. & Brenner H. , " low Reynolds number hydrodynamics" 2 nd. edn.  
Noorhoof (1973) .
- [15] Brenner H., *Chem. Engng. Sci.* , 16, 242-251 (1961).
- [16] Maude A.D. , *Brit. J. Appl. Phys.* 12, 293-295 (1961).
- [17] Goldman A.J. , Cox R.G. & Brenner H. , *Chem. Engng. Sci.* 22, 637 -651(1967a).
- [18] Dean W.R. & O'Neil M.E. , *Mathematika* 10, 13-24 (1963) .
- [19] O'Neil M.E. , *Mathematika* 11, 67-74 (1964) .
- [20] Cox R.G. & Brenner H. , *Chem. Engng. Sci.* 22, 1753-1777 (1967) .
- [21] O'Neil M.E. & Stewartson K.J., *Fluid Mech.* 27 , 705-724 (1967).
- [22] Goldman A.J., Cox R.G. & Brenner H. , *Chem. Engng. Sci.* 22, 653 -660 (1967b).
- [23] O'Neil M.E. , *Chem. Engng. Sci.* 23, 1293-1298 (1968) .
- [24] Vittal B.V.R. and Tabakoff W. , *AIAA J.* , Vol. 25, No.5, P.648-654 (1987) .
- [25] Guobiao Mo and Ashok Sangani S. , *Phys. Fluids* , Vol.6, No. 5, P.1637-1652 ,  
(1994) .
- [26] Hua Zhou and Pozrikidis C. , *Phys. Fluids A* , Vol.5 , No.2, P. 311-324 (1993).
- [27] Cioskin N.A. " Dynamics of viscous flow", Moscow (1958).



# NUMERICAL SIMULATION OF THE MOTION OF CHARGED SUSPENDED PARTICLE IN MULTI-PHASE FLOW

M.M.ABD EL KHALEK

*Nuclear Physics Department- Nuclear Research Centre- Atomic Energy Authority*

## ABSTRACT

A method for computing Numerical simulation of the motion of charged suspended particle in multi-phase flow between two-long parallel plates is described in detail. The equation of motion of a suspended particle was suggested by Clooskin. The equations of motion are reduced to ordinary differential equations by similarity transformations and solved numerically by using Runge-Kutta method. The trajectories of particles are calculated by integrating the equation of motion of a single particle. Numerical solutions of the resulting ordinary differential equations provide velocity distributions for both fluid and solid phases and density distributions for the solid. The present simulation requires some empirical parameters concerning the collision of the particles with the wall. Some typical results for both fluid and particle phases and density distributions of the particles are presented graphically.

## INTRODUCTION

The flow of suspensions of flexible particles, such as drops, cells, and capsules, involves a variety of motions whose understanding requires fundamental studies in several fields of two phase flow. The problem of computing Stokes flow interactions among randomly placed particles has been treated by a number of investigators<sup>[1-11]</sup>. In particular Ladd<sup>[11]</sup> has developed a method based on multipole expansion that accounts for these interactions quite accurately, while in principal his method can be extended to treat non rigid spherical particles as well. Guobiao Mo and Ashok S. Sangani<sup>[12]</sup>, studied a method for computing Stokes flow interactions in suspensions of spherical objects in detail and applied to the suspension of porous particles, drops and bubbles to determine their hydrodynamic transport coefficient. One of the most important factors in dealing with collisions is that collisions accompany irregularity. This irregularity plays an important role as the necessary mechanism by which particles are conveyed in horizontal pipe. Hence much effort has been directed towards the problem of particle-wall collisions { Matsumats et al. 1976<sup>[13]</sup>; Tsuji & Morikawa 1978<sup>[14]</sup>; Tsuji et al. 1983<sup>[15]</sup>, 1985<sup>[16]</sup> and Tsuji et al. 1987<sup>[17]</sup> }. The most difficult problem in calculating trajectories in pipes and ducts is the effect of particle collisions with the wall. When a spherical particle collides with a flat plate, the relations between the velocities before and after the collision are obtained by the impulsive equations. If the spherical particles do not collide too frequently, these relations are sufficient to consider the effect of collisions even in a horizontal channel. However if a perfect sphere collides with a perfect plane wall with a coefficient of restitution  $< 1$ , this results in all particles sliding along the bottom of the wall after a number of collisions. Richardson<sup>[18,19]</sup> studied the behavior of two dimensional solitary bubbles in a purely straining flow, a simple shearing flow, and a parabolic flow; Buckmaster and co-workers<sup>[20,21]</sup> studied the deformation and burst of two-dimensional slender with pointed ends in a purely straining flow; and Zahalak et al.<sup>[22]</sup> computed the deformation of a cylindrical liquid capsule which is enclosed by an inextensible membrane in a simple shearing flow. The motion may be either by the relative motion of the two walls or by an axial pressure gradient. Studies of these flows furnish useful information on the behavior of ordered suspensions and illustrate the

significance of solid boundaries . Moreover , they allow direct comparisons with experimental observations and standard rheological measurements based on the plane Couette viscometric flow . Masliyah and Van de Ven<sup>[23]</sup> studied the motion of two-dimensional periodic arrays of cylindrical rods in plane-Couette flow , with an objective to gain insights on the dynamics of ordered structures that have been observed to develop spontaneously in a dense sheared suspension . Their results include illustrations of the streamline pattern and the distribution of shear stress along the walls , and predictions for the shear force distribution on the walls and the effective viscosity of the suspension . Sugihara-Seki and Skalak<sup>[24]</sup> performed similar numerical investigations with an objective to model the motion of red blood cells in the micropillaries . The cells are represented by cylindrical rods in a single or double file arrangement . Hua Zhou and C. Pozrikidis<sup>[25]</sup> performed a computational framework for studying the flow of ordered and random suspensions of two dimensional deformable particles in channels . Specifically , they consider a model configuration which consists of a suspension of viscous drops with periodic structure flowing between two parallel plate in a Couette flow device . Each flow cell contain one or more suspended drops which are arranged in an ordered or random fashion . Vittal B.V.R. and Tabakoff W<sup>[26]</sup> present a numerical solution for the fundamental problem of solid particles suspended in viscous incompressible flow over a cylinder at low flow Reynolds number . The effect of solid particles on flow properties , such as streamline pattern , coefficient of drag of the cylinder , separation angle , and recirculation eddy , are discussed .

This paper describes a new method for studying the trajectories of a solid charged suspended particle in multi-phase flow between two long parallel plates . The particle is considered to move with a velocity equal to the velocity of the fluid and initially starting from the mid point of the channel . The effect of some parameters such as particle shape , fluid density , fluid viscosity on the path lines are also investigated . The present simulation requires some empirical parameters concerning the collision of the particles with the wall .

### FORMULATION OF THE PROBLEM

Consider a mixture consists of two-phase flow and suspended in it a solid particle . The fluid is placed between two plates , one is fixed and is taken as the X-axis and the other is at a distance h from the first and is moving with a constant velocity  $U_0$  . Let phase one has the velocity  $u_1$  and phase two the velocity  $u_2$  , and let the viscosities and densities of the phases be considered constants . The steady motion of phases between the two-plates can be described by the equations ,

$$f_1 \mu_1 \frac{\partial^2 u_1}{\partial y^2} + k(u_1 - u_2) = f_1 \frac{\partial p}{\partial x} \quad (1)$$

$$f_2 \mu_2 \frac{\partial^2 u_2}{\partial y^2} + k(u_2 - u_1) = f_2 \frac{\partial p}{\partial x} \quad (2)$$

$$\frac{\partial p}{\partial x} = N = \text{constant}$$

Under the boundary conditions

$$\text{at } y = 0 , u_1 = u_2 = 0 \quad (3)$$

$$\text{at } y = h , u_1 = u_2 = U_0 \quad (4)$$

$$\text{if } u_1 = u_0 u'_1 , u_2 = u_0 u'_2 , y = h y'$$

The equations (1,2) under the boundary conditions (3,4) will be

$$\frac{d^2 u_1}{dy^2} + \beta(u_1 - u_2) = \frac{Nh^2}{\mu_1 u} \quad (5)$$

$$\frac{d^2 u_2}{dy^2} + \beta\beta'(u_2 - u_1) = \frac{Nh^2}{\mu_2 u} \quad (6)$$

$$\text{at } y = 0, \quad u_1 = u_2 = 0 \quad (7)$$

$$\text{at } y = 1, \quad u_1 = u_2 = 1 \quad (8)$$

$$\text{where, } \beta = \frac{kh^2}{f_1 \mu_1}, \quad \beta' = \frac{f_2 \mu_1}{f_2 \mu_2}$$

Now, we consider the case when  $\beta$  is a small quantity, such that  $\beta^2 \ll 1$  and take

$$u_1 = u_1^{(0)} + \beta u_1^{(1)}$$

$$u_2 = u_2^{(0)} + \beta u_2^{(1)}$$

The system of equations (5,6) under the conditions (7,8) has the solution

$$u_1 = \frac{Nh^2}{2\mu_1 U_0} (y^2 - y) + y - \frac{Nh^2 \beta}{24U_0} \left(\frac{1}{\mu_1} - \frac{1}{\mu_2}\right) y [y^2 (y - 2) + 1] \quad (9)$$

$$u_2 = \frac{Nh^2}{2\mu_2 U_0} (y^2 - y) + y + \frac{Nh^2 \beta \beta'}{24U_0} \left(\frac{1}{\mu_1} - \frac{1}{\mu_2}\right) y [y^2 (y - 2) + 1] \quad (10)$$

The equation of motion of the suspended particle was suggested by Closkin N.A. <sup>[20]</sup> in the form

$$\rho_1 \frac{dc}{dt} = -g(\rho_1 - \rho) \vec{j} - k_1(\vec{c} - \vec{u}_2) + k_2(\vec{u}_2 - \vec{c}) \wedge \text{rot } \vec{u}_2 - \text{grad } p$$

where,  $\rho_1$  : is the particle's density,  $\rho$  : is the density of the fluid,  $\vec{c}$  : is the particle velocity,  $\vec{u}_2$  : is the fluid velocity,  $p$  : is the pressure,  $g$  : is the gravitational acceleration which is vertical,  $k_1$  : is the resistance coefficient of motion in viscous fluid and  $k_2$  : is the so called the form coefficient.

Therefore, the equation of motion is

$$\begin{aligned} \rho_p \frac{dc}{dt} = & -g(\rho_p - \rho) \vec{j} - g(\rho_p - \rho) \vec{j} - k_v(\vec{c} - \vec{u}_1) - k_v'(\vec{c} - \vec{u}_2) \\ & + k[c_v \frac{\partial u_1}{\partial y} \vec{i} + (u_1 - c_x) \frac{\partial u_1}{\partial y} \vec{j}] + k'[c_v \frac{\partial u_2}{\partial y} \vec{i} + (u_2 - c_x) \frac{\partial u_2}{\partial y} \vec{j}] \\ & + \frac{\epsilon}{v}[c_v H_0 \vec{i} - c_x H_0 \vec{j}] - \text{grad } p \end{aligned} \quad (11)$$

Introducing non-dimensional quantities defined by

$$u_1 = U_0 u_1', \quad u_2 = U_0 u_2', \quad y = hy', \quad c_x = U_0 c_x', \quad c_y = U_0 c_y', \quad t = \frac{U_0}{g} t' \quad (12)$$

Substituting from (12) in equation (11) and after dropping dashes we get,

$$\frac{dx}{dt} = c_x \quad (13)$$

$$\frac{dy}{dt} = c_y \quad (14)$$

$$\begin{aligned} \frac{dc_x}{dt} = & -\alpha_v c_x + \alpha_v \{ \alpha_1 (y^2 - y) + y - \alpha_2 \alpha_3 y [y^2 (y - 2) + 1] \} - \alpha_v c_x + \alpha_v \{ \alpha_1 (y^2 - y) \\ & + y + \alpha_2 \alpha_3 y [y^2 (y - 2) + 1] \} + \alpha_v c_y \{ \alpha_1 (2y - 1) + 1 - \alpha_2 \alpha_3 (4y^3 - 6y^2 + 1) \} \\ & + \alpha_v c_y \{ \alpha_1 (2y - 1) + 1 + \alpha_2 \alpha_3 (4y^3 - 6y^2 + 1) \} + \alpha_v c_y - \alpha_{pp} \end{aligned} \quad (15)$$

$$\begin{aligned} \frac{dc_y}{dt} = & \alpha_v - \alpha_v c_y - \alpha_v c_y + \alpha_v \{ \alpha_1 (y^2 - y) + y - \alpha_2 \alpha_3 y [y^2 (y - 2) + 1] \} \{ \alpha_1 (2y - 1) \\ & + 1 - \alpha_2 \alpha_3 (4y^3 - 6y^2 + 1) \} - \alpha_v c_x \{ \alpha_1 (2y - 1) + 1 - \alpha_2 \alpha_3 (4y^3 - 6y^2 + 1) \} + \\ & \alpha_v \{ \alpha_1 (y^2 - y) + y + \alpha_2 \alpha_3 y [y^2 (y - 2) + 1] \} \{ \alpha_1 (2y - 1) + 1 + \alpha_2 \alpha_3 (4y^3 - 6y^2 \\ & + 1) \} - \alpha_v c_x \{ \alpha_1 (2y - 1) + 1 + \alpha_2 \alpha_3 (4y^3 - 6y^2 + 1) \} - \alpha_v c_x - \alpha_{pp} \end{aligned} \quad (16)$$

Where,  $\alpha_v = \frac{k_v U_0}{\rho_p g}$  : is a parameter dependent on the viscosity of phase one,  $\alpha_1 = \frac{N h^2}{2 \mu_1 U_0}$ ,  $\alpha_2 = \frac{N h^2 \beta}{24 U_0}$ ,  $\alpha_3 = \left( \frac{1}{\mu_1} - \frac{1}{\mu_2} \right)$ ,  $\alpha_4 = \frac{k_v U_0}{\rho_p g}$  : is a parameter dependent on the viscosity of phase two,  $\alpha_5 = \frac{N h^2}{2 \mu_2 U_0}$ ,  $\alpha_6 = \frac{N h^2 \beta \beta'}{24 U_0}$ ,  $\alpha_{sh} = \frac{k U_0^2}{\rho_p g h}$  : is a parameter dependent on the shape of phase one,  $\alpha_7 = \frac{k U_0^2}{\rho_p g h}$  : is a parameter dependent on the shape of phase two,  $\alpha_H = \frac{e U_0 H_0}{\rho_p g v}$  : is a parameter dependent on the magnetic force,  $\alpha_d = \frac{2 \rho_p - \rho_{f1} - \rho_{f2}}{\rho_p}$  : is a parameter dependent on the fluid density, and  $\alpha_{pp} = \frac{grad p}{g \rho_p}$  : is a parameter dependent on the pressure gradient.

## NUMERICAL SOLUTIONS AND RESULTS

Equations (13-16) are a system of differential equations, which can be solved using the method of fourth order Runge-Kutta method.

### The dependence on fluid viscosity :-

The solution is shown graphically in figure (2). As conclusion the results show that when ( $\alpha_v$ ) is decreased :

- (1) The motion of the particle is oscillatory.
- (2) The number of collisions with the upper and the lower plates is increased
- (3) The particle continue to repeat the bouncing motion.
- (4) The width and maximum height are increased.

And when  $\alpha_v$  is increased

- (1) The motion of the particle is slow.
- (2) The motion of the particle is too close to the centre line tube.
- (3) No particle collides with the upper plate nor the lower plate.

### The dependence on fluid density:-

The solution is shown graphically in figure (3). As conclusion the results show that when ( $\alpha_d$ ) is increased :

- (1) The motion of the particle is directed upward and collides with the upper plate.
- (2) The particle continue to repeat the bouncing motion.
- (3) No particle collides with the lower plate.
- (4) The width and maximum height are increased.

And when ( $\alpha_d$ ) is decreased :

- (1) The particle motion is slow.
- (2) The particle motion is too close to the centre line of the tube.
- (3) The particle does not collide with the upper nor the lower plate.

### The dependence on Particle Shape:-

The solution is shown graphically in figure (4). As conclusion the results show that when ( $\alpha_{sh}$ ) is decreased :

- (1) The particle motion is too close to the lower plate.
- (2) The particle does not collide with the upper nor the lower plate.
- (3) The width and maximum height are decreased.

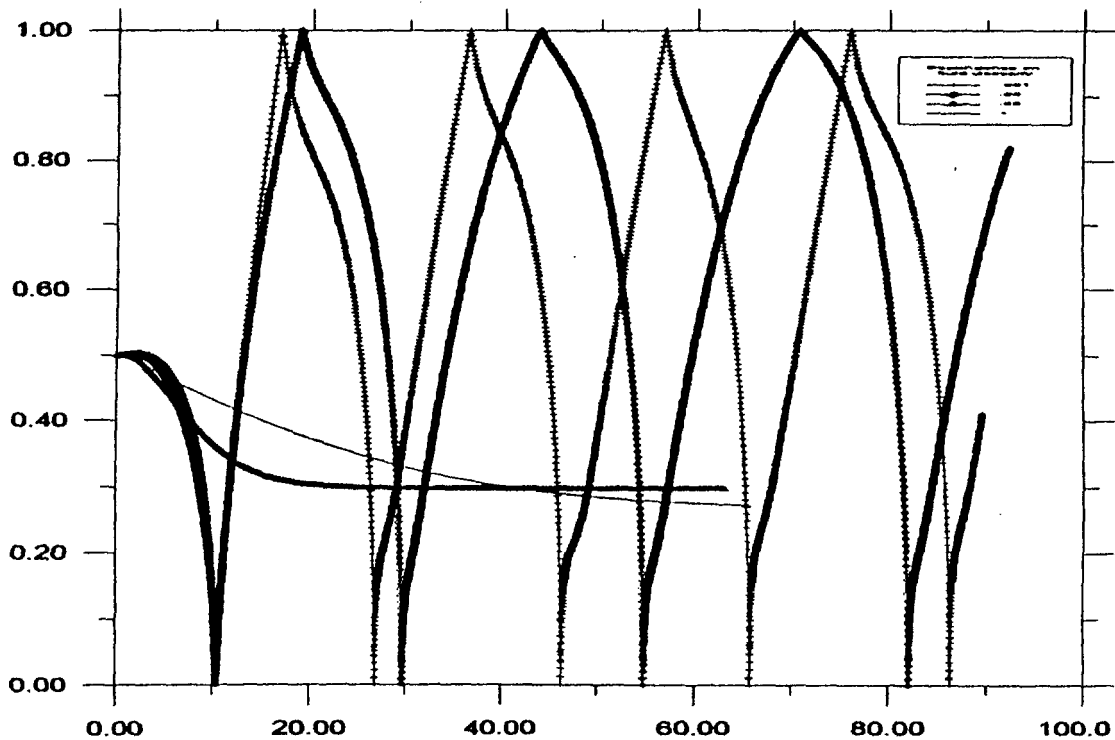
The dependence on Magnetic Force:-

The solution is shown graphically in figure ( 5 ) . As conclusion the results show that when (  $\alpha_H$  ) is increased :

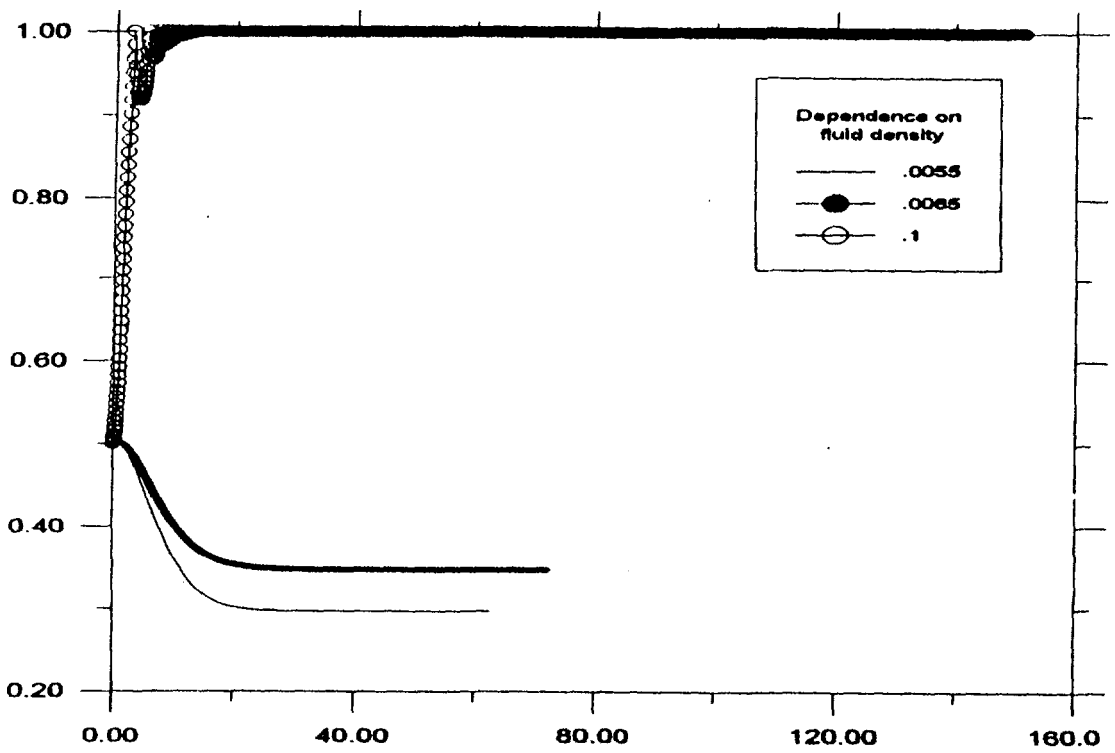
- (1) The motion of the particle is directed downward .
- (2) The particle motion is too close to the lower plate .
- (3) The particle motion is slow .
- (4) No particle collides with the upper nor lower plates.
- (5) The width and maximum height are decreased .

And when (  $\alpha_H$  ) is decreased :

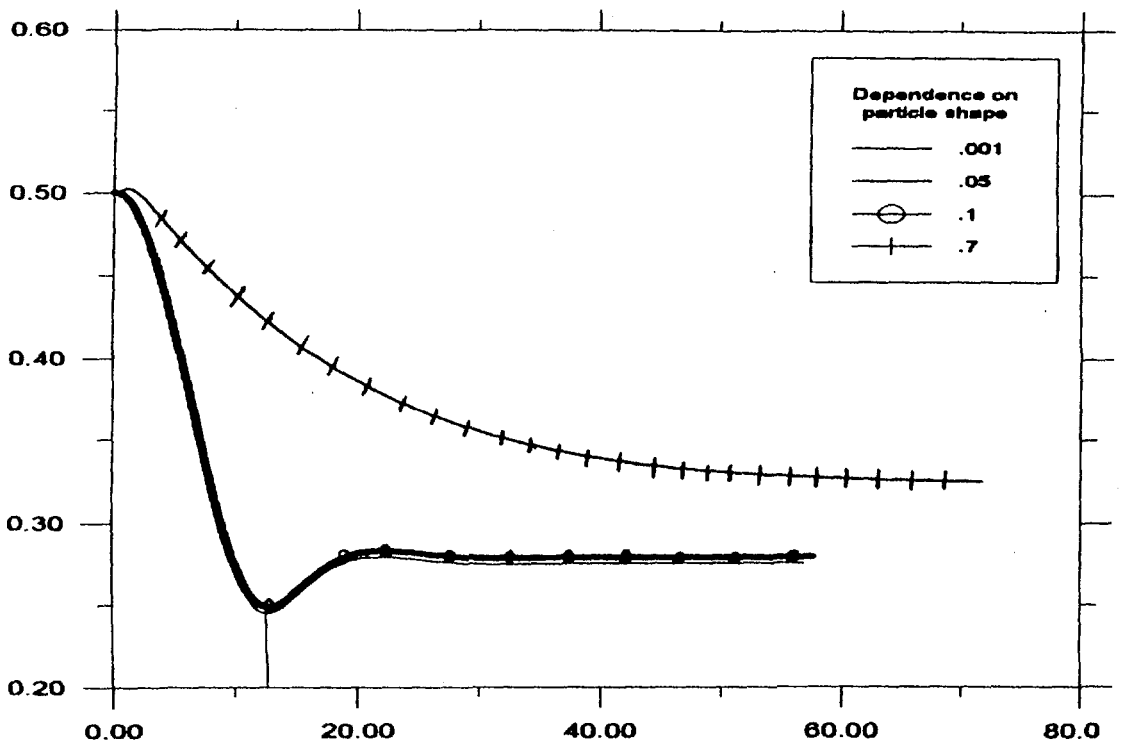
- (1) The motion of the particle is directed upward and it collides with the upper plate .
- (2) The number of collisions with the upper plate is increased .
- (3) The particle continue to repeat the bouncing motion .
- (4) The particle motion is too close to the upper plate .
- (5) The width and maximum height are increased .



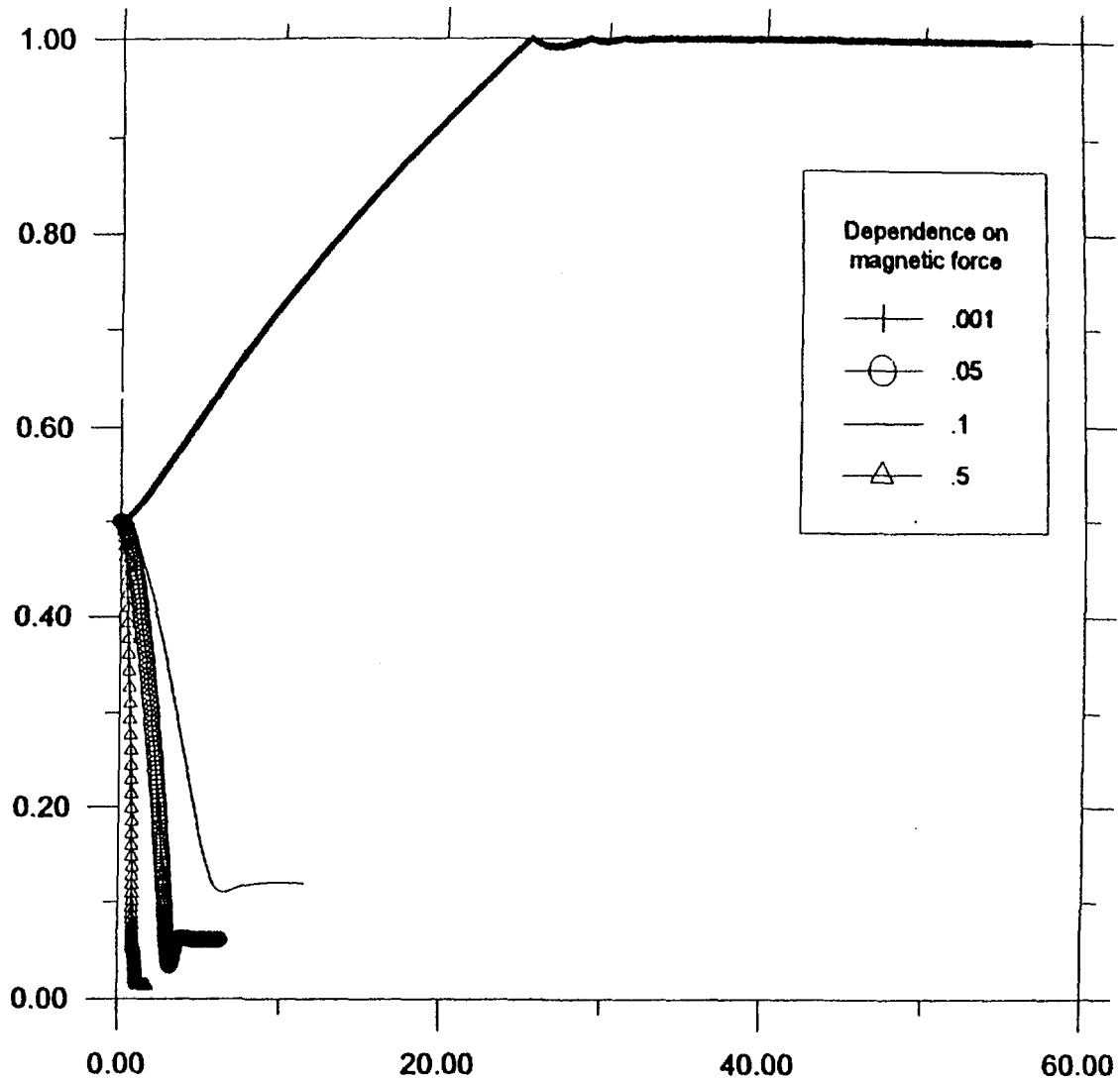
Figure(1) Particle trajectories for different  $\alpha_H$ .



Figure(2) Particle trajectories for different  $\alpha_d$



Figure(3) Particle trajectories for different  $\alpha_d$



Figure(4) Particle trajectories for different  $\alpha_H$

### REFERENCES

- [1] Ganatos P., Pfeffer R., and Weinbaum S., *J. Fluid Mech.* 84, 79 (1978).
- [2] Mazur P. and Van Ssaarloos W., *Physica A*, 115, P.21(1982).
- [3] Van Saarloos W. and Mazur P., *Physica A* 120, P.77(1983).
- [4] Beenakker C.W.J., *Physica A* 128, P.48(1984).
- [5] Beenakker C.W.J. and Mazur P., *Physica A* 126, P.349 (1984).
- [6] Bossis G. and Brady J.F., *J. Chem. Phys.* 80, P.5141 (1984).
- [7] Durlofsky L., Brady J.F., and Bossis G., *J. Fluid Mech.* 180, P.121 (1987).
- [8] Brady J.F. and Bossis G., *Annu. Rev. Fluid Mech.* 20, P.111(1988).
- [9] Ladd A.J.C., *J. Chem. Phys.* 88, P.5051 (1988).
- [10] Ladd A.J.C., *J. Chem. Phys.* 90, P.1149 (1989).

- [11] Ladd A.J.C. , J. Chem. Phys. 93 , P.3484 (1990).
- [12]Guobiao Mo and Ashok Sangani S., Phys. Fluids , Vol. 6, No.5 , P.1637-1652 (1994).
- [13] Matsumoto S. , Saito S. & Maeda S. , J. Chem. Engng. Japan 9, 23- 28 . (1976).
- [14]Tsuji Y.&Morikawa Y., BHRA Fluid Engineering , cranfield ,U.K.Paper B1. (1978).
- [15] Tsuji Y., Seki W. & Morikawa Y., J. Soc. Powder Tech . Japan 20, 270-278 (1983) (In Japanese) .
- [16] Tsuji Y., Oshima T. & Morikawa Y. , KONA 3, 38-51 (1985) .
- [17]Tsuji Y. , Morikawa Y., Tanaka T. , Nakatsukasa N. and Nakatani M. Int. J. Multiphase Flow Vol. 13, No.5, PP. 671-684 (1987) .
- [18]Richardson S. , J.Fluid Mech. 33, P.476 (1968) .
- [19]Richardson S. , J.Fluid Mech. 58, P.115(1973) .
- [20] Buckmaster J.D., J. Fluid Mech. 55,385 (1972).
- [21] Buckmaster J.D. and Flaherty J.E. , J.Fluid Mech. 60,625(1973).
- [22] Zahalak G.I. , Rao P.R. , and Sutera S.P., J. Fluid Mech. 179, P.283(1987) .
- [23]Masliyah J.H. and Van de Ven T.G.M. , Int. J. Multiphase flow 12, P.791 (1986).
- [24]Sugihara-Seki M. and Skalk R., Microvascular Res. 36 , P.64 (1988) .
- [25] Sugihara-Seki M. and Skalk R., Biorheology 26 , P.261 (1989) .
- [26] Hua Zhou and Pozrikidis C. , Phys. Fluids A , Vol.5, No.2,P.311-324(1993).
- [27] Vittal B.V.R. and Tabakoff W. , AIAA J. , Vol.25,No.5,P.648-654 (1987).
- [28] Closkin N.A. " Dynamics of Viscous Flow " Moscow (1958) .



EG9700101

# THE BROAD BEAM ION IMPLANTER WITH THE USE OF RADIO FREQUENCY ION SOURCE

M. E. ABDELAZIZ, S. G. ZAKHARY AND A. A. GHANEM

Accelerators Dept., Nuclear Research Center,  
Atomic Energy Authority, P.O. Box 13759 Cairo, Egypt

## ABSTRACT

The project starts with the design of the broad beam RF ion source and the single gap accelerating column. The preliminary results of the source show that the ion current extracted from the source could reach  $\approx 30\text{mA}$  with extraction voltage  $\approx 2\text{kV}$ . The beam uniformity is made by the use of multiapertures graphite cathode designed to make perveance matching to the normal Gaussian distribution of the ion beam. The beam uniformity could reach  $\approx 66\%$  of the beam width of  $\approx 6\text{ cm}$ . A design is made of the single gap accelerating column based on tracing of beam lines inside the accelerating gap and estimation of the minimum value of the electric field required to contain the beam against space charge expansion in order to achieve minimum beam emittance without aberrations. The preliminary results of the acceleration of the ion beams up to  $20\text{ keV}$  show an increase of the extracted ion current with the increase of the extraction voltage.

## 1. INTRODUCTION:

Wide-aperture intense ion beams formed by ion sources based on multiapertures extracting system are wide spread in fusion research and in beam technology. The features of the AC discharge besides cleanliness results from the absence of the metallic elements, ease of maintenance and operation make it preferable on other ion sources. Both types of the AC discharge RF ( $f=10 - 100\text{MHz}$ ) & microwave ( $f= 2.45- 20\text{GHz}$ ) occur in the low pressure range  $10^{-3} - 10^{-4}\text{ torr}$ . The former is based on the principle of secondary electrons emitted from the tube

walls and accelerated in the RF field to gain energy (12- 15 eV) sufficient for ionization of gas atoms and molecules. The latter is based on the electron cyclotron resonance in the plasma.

## 2. THE EXPERIMENTAL SETUP

The broad beam accelerator system is shown in Fig 1. The main components of the system are

- a- the broad beam RF ion source<sup>1</sup>
- b- the single gap accelerating column<sup>2</sup>
- c- the target chamber and the vacuum line.

## 3 - THE BROAD BEAM RF ION SOURCE

### 3.1 The source construction

It consists of a Pyrex cylindrical vessel  $\phi = 8$  cm,  $L = 6$  cm with both anode probe  $\phi = 1$  mm and tungsten filament (6V-10A) joined to the vessel. Axial magnetic field (70 - 300 G) is produced around the filament. The cathode is made from a graphite planar target its thickness is 1 mm and it has multiapertures. These apertures are arranged to produce a wide and uniform beam density distribution with the use of perveance matching to the normal Gaussian distribution of the beam. This matching is achieved with the holes in the cathode arranged at equal distances on consequent circular orbits. The diameters of these holes are 1,2,3,4 mm which increase with the increase of the orbit radius. This allows an increase of the source's perveance at the outer edges and its decrease at the source's inner region. Fig.2 shows the beam profiles traced at 1kV extraction voltage with and without perveance matching. The profiles show that the Gaussian distribution of the beam profile for a single aperture  $\phi = 5$  mm is modulated due to the effect of perveance matching to produce a uniform distribution which could reach  $\approx 66\%$  of the beam width of 6 cm.

### 3.2 The source characteristics

Fig.3 shows the variation of the extraction current with the extraction voltage at different values of RF power. This variation does not obey the Child's law which says:

$$I = \frac{4}{9} \pi \epsilon_0 S^2 \sqrt{2 \frac{q}{m}} V^{3/2}, \quad (1)$$

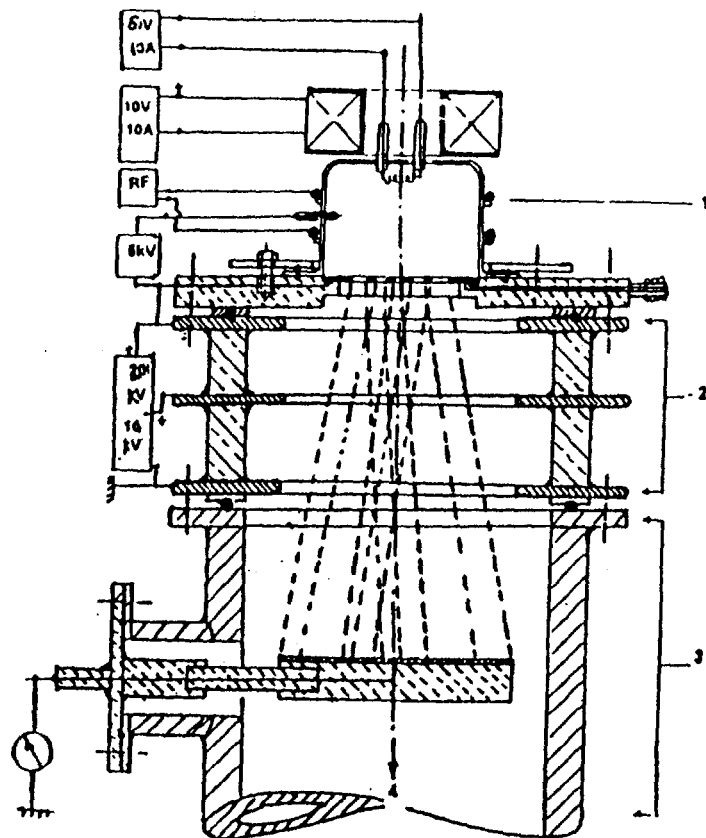


Fig.1 The broad beam ion implanter project with broad beam RF ion sources. 1- the source, 2- the accelerating tube, 3- the target chamber, 4- the vacuum line

$I$  is the extracted current,  $\epsilon_0$  is the permittivity,  $S$  is the aspect ratio  $=a/d$  where  $a$  the aperture radius,  $d$  the electrode distance and  $V$  is the extraction voltage. The increase of  $S$  with the increase of the distance from the source axis affects the deviation of the extraction characteristics from the Child's law. Fig.4 shows an increase of the extracted current with an increase of the discharge pressure which is limited by the breakdown. It also shows the magnetic field has the same effect on increasing the extracted ion current like the effect of increasing the discharge pressure. This effect is greater at low pressure than at high pressure due to the increase of the mean free path at low pressure and increase of the energy gained by the particle between collisions<sup>3,4</sup> Fig.5 shows the influence of electron injection into the plasma on increasing the extracted ion current due to the increase of ionization efficiency. The increase in the extracted ion current could reach four times its value without electron injection into the plasma.

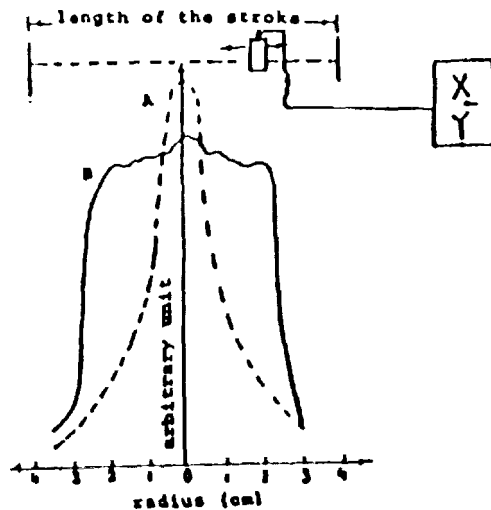


Fig 2 Influence of the pervasance matching of the beam profiles A- without matching, B- with matching.

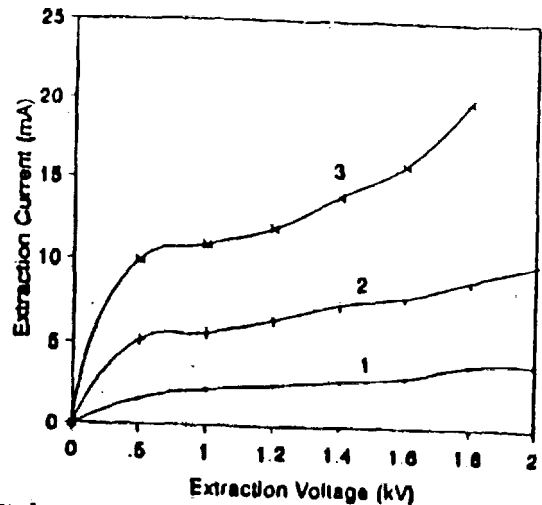


Fig 3 Influence of the extracting voltage and RF power on the extracted ion current,  $B=1400$ ,  $P_r=7.5 \times 10^{-4}$  torr. 1- $P_{rf}=100W$ , 2- $P_{rf}=350W$ , 3- $P_{rf}=500W$

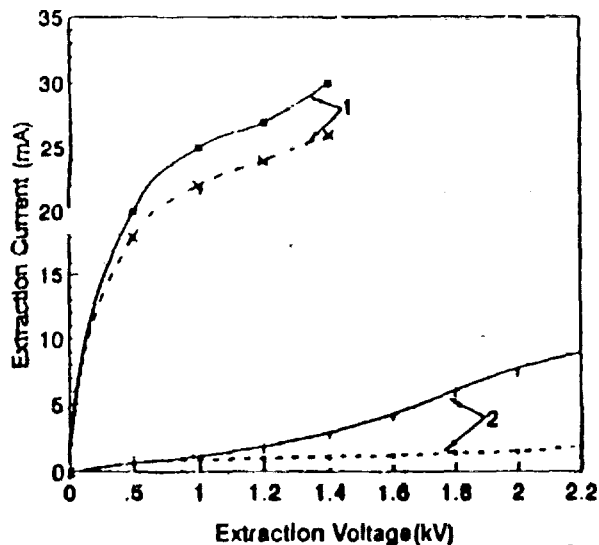


Fig 4 Influence of the discharge pressure and the magnetic field on the extracted ion current  $P_{rf}=100W$ , 1- $P_r=1.5 \times 10^{-4}$  torr,  $B=1400$ , 2- $P_r=9 \times 10^{-4}$  torr

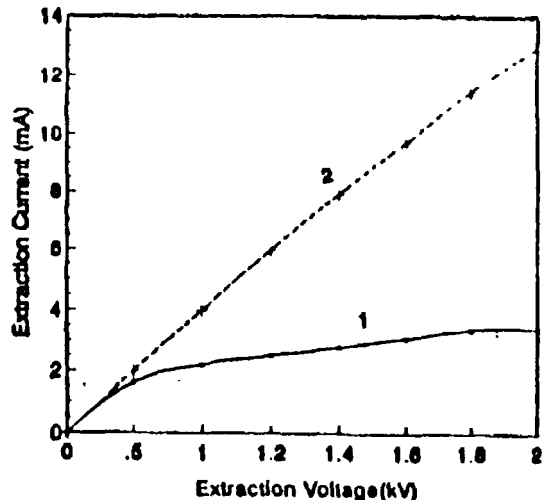


Fig 5 Influence of the electron injection into the plasma on the extracted ion current  $B=1400$ ,  $P_{rf}=100W$ ,  $P_r=7.5 \times 10^{-4}$  torr. 1-Without injection, 2-With injection  $P_{rf}=50W$ .

#### 4. DESIGN OF A SINGLE GAP ACCELERATING COLUMN.

##### 4.1 Tracing of the beam line within the gap.

The variation of the cross section of a beam propagating along the Z axis of an accelerating section of a single gap accelerating column shown in Fig 6, can be determined using Eq 2<sup>67</sup>

$$\frac{d^2 r}{dz^2} + \frac{V'_0}{2V_0} \frac{dr}{dz} + \frac{V''_0 r}{4V_0} = -\frac{Q}{4V_0 \epsilon_0} r, \quad (2)$$

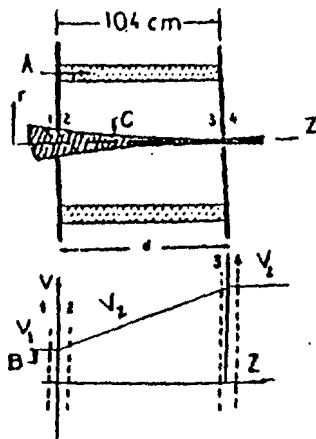


Fig.6 Schematic diagram of the single gap accelerating column(A-the gap,B-the potential distribution,C-the beam line(1,2 represents the input condition, 3,4 the output condition))

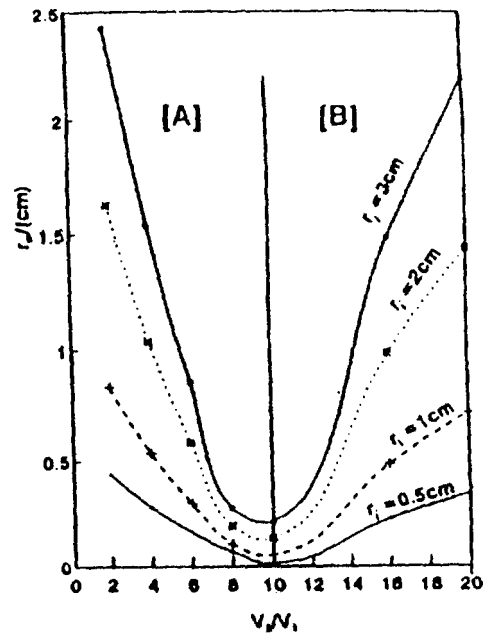


Fig.7 Variation of beam output radius with the accelerating ratio (the zone of beam transport without aberration, B- (the aberration zone))

where  $V_0$  is the potential on the Z axis and the primes denote the derivatives with respect to Z,  $Q$  represents the space charge density (which is assumed to be uniform over the beam cross section) and  $\epsilon_0$  is the dielectric permittivity of the free space. Neglecting the space charge effect, the right hand side of Eq.2 is set equal to zero. This equation was solved to determine the ray path between two planes representing the input and output of the accelerating column shown in Fig.6, located at a given distance apart ( $d$ ) along the Z axis. Defining the input and output of an ion optical element,  $(r_1, r_1', V_1)$  refer to condition of beam radius, half angle of beam divergence, and the voltage at the input.  $(r_4, r_4', V_4)$  are the conditions of the beam at the outlet. The solution is given by

$$\begin{bmatrix} r_4 \\ \sqrt{V_2} r_4' \end{bmatrix} = M_{14} \begin{bmatrix} r_1 \\ \sqrt{V_1} r_1' \end{bmatrix} \quad (3)$$

where

$$M_{14} = \begin{bmatrix} \frac{3\sqrt{V_1} - \sqrt{V_2}}{2\sqrt{V_1}} & 2 \frac{d}{\sqrt{V_1} + \sqrt{V_2}} \\ \frac{3(V_2 - V_1)(\sqrt{V_1} - \sqrt{V_2})}{8d\sqrt{V_1}\sqrt{V_2}} & \frac{3\sqrt{V_2} - \sqrt{V_1}}{2\sqrt{V_2}} \end{bmatrix} \quad (4)$$

and  $d$  is the gap distance.

Fig 7 shows the variation of the beam outlet radius with the accelerating ratio. The optimal value of the accelerating ratio is found to be equal to 10 for the gap length  $d = 10.4$  cm. Beyond the optimal ratio the beam transport without aberration and higher than the optimal value the beam transport with aberration.

#### 4.2 Estimation of the minimum value of the electric field required to contain the beam against space charge expansion

It is of interest to have a guide relating the rate of acceleration of the ion beams to the space charge (i.e., beam current). From such a guide an approximate value of the electric field which prevents beam expansion could be obtained. Consider an ion beam to be accelerated by an electric field  $E$ . Poisson's equation in cylindrical coordinates is written as\*

$$\frac{1}{r} \frac{\partial}{\partial r} (rE_r) + \frac{\partial E_z}{\partial z} = \frac{\rho}{\epsilon_0} = \frac{J}{\epsilon_0 \sqrt{2} \eta V/M} \quad (5)$$

and the solution is found to be<sup>2</sup>

$$E_z = -4/3 \left[ \frac{9J}{4\epsilon_0 \sqrt{2} \eta/M} \right]^{2/3} Z^{1/3} \\ = 9.25 \times 10^4 M^{1/3} J^{2/3} Z^{1/3} \text{ (V/m)} \quad (6)$$

where  $J$  the current intensity in ( $A/cm^2$ ),  $M$  = atomic weight,  $Z$  = gap distance (m). Fig. 8 shows the variation of  $Ez$  with the current density  $J$  of single charge for different gaseous ions ( $H_2, N_2, Ar$ ). For an optimal acceleration corresponding to the minimum beam output radius ( $V_2/V_1=10$ ), we can deduce the optimum electric field  $Ez$  and draw a horizontal line to deduce the current density limit for best beam focusing.

#### 5. TARGET CHAMBER

It consists mainly of a stainless steel holder carrying the specimen of 4cm diameter to receive the uniform distribution part in the beam. The target is placed behind the accelerating column at  $\approx 30$  cm from the source outlet. The pressure in the vacuum chamber could reach  $\approx 10^{-4}$  torr

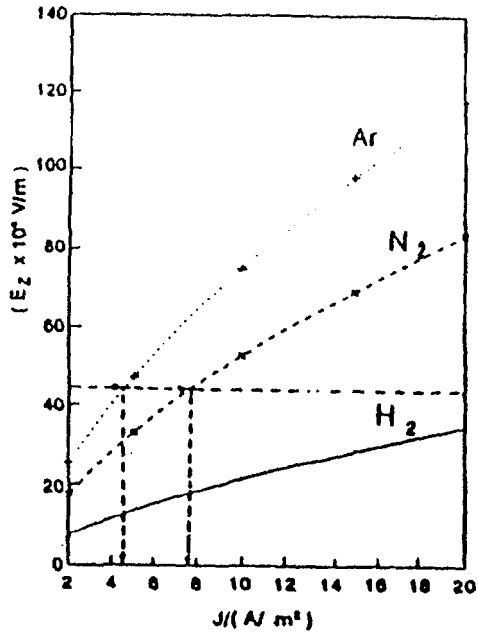


Fig. 8 Variation of the optimal value  $E_z$  with the current intensity  $J$  for  $Ar, N_2$ , and  $H_2$

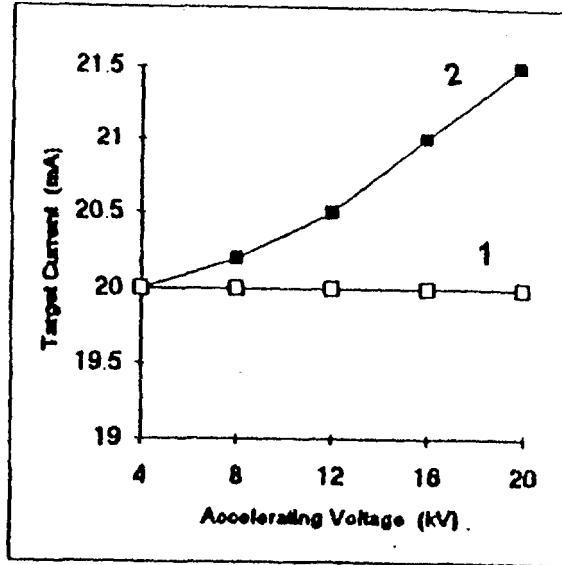


Fig. 9 Influence of the accelerating voltage on the target current (Prf= 200W,  $P_{ra} = 2 \times 10^{-4}$  torr.) 1- without acceleration, 2- with acceleration

## 6. TARGET CURRENT TEST

Fig. 9 shows the influence of the accelerating voltage on the target current test. The accelerating voltage produces a slight increase of the extracted ion current. This can be explained due to the decrease of the angle of the beam divergence as described by the Eq. 7:

$$\omega \propto \sqrt{\frac{kT_i}{2eV}} \quad (7)$$

where  $\omega$  is the angle of beam divergence,  $kT_i$  is the transverse kinetic energy ( $k$  is the Planck's constant,  $T_i$  is the ion temperature) and  $eV$  is the accelerating energy.

REFERENCES

- [1] M.E. Abdelaziz, S.G. Zakharyan, A.A. Ghanem, *Rev. Sci. Instrum.* 67(2), 1996.
- [2] M.E. Abdelaziz, S.G. Zakharyan, A.A. Ghanem, *Rev. Sci. Instrum.*, 67(2) 1996.
- [3] M.M. Abdelbaki, S.G. Zakhary, *Nucl. Instrum and Methods* 154, 509 (1978).
- [4] G. Francis, *Ionization Phenomena in Gases* (Butterworths, London) Chapter 4 (1960).
- [5] M.E. Abdelaziz, M.M. Abdelbaki and S.G. Zakhary, *IEEE Trans. on Nucl. Science*, Vol NS30(4) 2699 (1983).
- [6] P.T. Kirstein, C.S. Kino, and W.E. Water, *Space charge flow* (McGraw-Hill, New York (1967).
- [7] M. Reiser, *IEEE Trans. Nucl. Sci.* 32, 2201 (1985).
- [8] R.G. Wilson and G.R. Brewer, *Ion beam application to ion implantation*, (Wiley, New York), (1973).
- [9] T.S. Green, *IEEE Trans. Nucl. Sci.* NS. 23, 918-925 (1976).



## ION OPTICS IN AN ION SOURCE SYSTEM

F.W.Abdel Salam , O.A.Moustafa and H.EL-Khabeary.T.

Accelerators Dept., Basic Nuclear Science Division, Nuclear Research Center, Atomic Energy Authority, P.O.13759 Cairo, Egypt .

### Abstract

An analysis of ion beams from an ion source consisted of a hemispherical anode, a plane earthed cathode and a focusing electrode has been carried out. The focal properties of such electrode arrangement are studied using axially symmetric fields. Axial and radial electric fields are obtained as functions of the axial distance. It is found that the radial component of the gradient of potential pushes the ions towards the axis, which indicates that the action of the system is convergent. The effect of variation of the voltage between the plasma boundary and the focusing electrode on the position of the plasma boundary has been given using the experimental data of the ion source characteristics and its geometrical parameters. The advantages of plasma diffusing outside the source through a small aperture are used and by applying a potential to the focusing electrode, it is possible to extract a large ion current from the expanded plasma. The system constitute a lens with a focal length of 29.4 mm.

### Introduction

The first application of ion optical principles to practical problems [1,3] was concerned with the formation of narrow beams of high intensity. The focal length of an electric lens does not depend on the mass of the particles. This makes electric lenses the natural imaging means for high voltage ions. If ions, in spite of their smaller diffraction effects, have not been used to any extent for imaging purposes, this is without doubt, due primarily to the greater difficulty of generating ions beams of very small divergence.

An electrostatic ion source which consists of a hemispherical electrode and a plane earthed cathode was constructed before [4] in order to meet the requirements for applications of low energy ion surface interaction Theoretical analysis had been carried out in a previous work [5] for the purpose of designing the ion source which produces an electrostatic confined discharge.

In this paper ion beam optics has been studied carefully using this ion source and the electrostatic focusing of the beam is determined using a focusing electrode near the ion exit aperture. We use a simple model which considers the geometrical parameters of the system. The distance between the plasma boundary and the focusing electrode is a fundamental value, since the extraction regimes are classified according to the relative position of the plasma boundary in the ion source [6]. Also two problems are considered, the examination of the nature of the electrostatic field and the determination of the focusing properties from this field.

### Adjustment of the distance between the plasma boundary and the focusing electrode

Fig.1 shows a diagram for the electrodes arrangement in the ion source system. An analysis for the position and plasma boundary shape in the ion source is given. It is a fact that they change as the extraction potential does and that they are a function of the geometrical parameters of the system. Our analysis is based on the experimental data for the ion source characteristics.

Fig.2 shows the variation of the voltage between the plasma boundary and the focusing electrode with beam current  $I_b$  at constant values of current and voltage discharges ( $I_d = 350$  mA,  $V_d = 5.7$  K.V) respectively and at a pressure of  $2.2 \times 10^{-4}$  torr for both nitrogen and argon gases. These linear relations are used to determine the distance between the plasma boundary and the focusing electrode by introducing the geometrical parameters of the system. For practical purposes, when the ion source system is constructed, it is necessary to determine the position of the plasma boundary which could modify the extraction regime.

The expression which allows us to calculate the focusing electrode -plasma boundary distance is [7]:-

$$d = \frac{3.7 \times 10^{-2} D V^{3/4} I_b^{-1/2} - (\rho + \delta)}{1 + 3.7 \times 10^{-2} (D - \phi) \ell^2 V^{3/4} I_b^{-1/2}} \quad (1)$$

where  $V$  is the plasma - focusing electrode voltage in K.V,  $I_b$  is the output ion current in amperes,  $D$  is the plasma cone cross diameter at the focusing electrode,  $\phi$  is the cathode diameter,  $\ell$  is the cathode- focusing electrode distance,  $\rho$  is the radius of the focusing electrode aperture and  $\delta$  is the cathode thickness. Here the geometrical parameters are:-  $D=1.93$ mm,  $\phi = 1.3$ mm,  $\ell = 2$ mm,  $\rho = 0.75$  mm and  $\delta = 5$  mm. The formula (1) gives a description of the experimental data obtained using the ion source.

Fig.3 shows the effect of variation of the plasma -focusing electrode voltage on the position of the plasma boundary in the ion source. To extract the ions from the plasma boundary ( ion emitting surface ), the extraction mechanism with prestudied geometry [5] is used. The ions have low velocities equivalent to the potential difference between plasma boundary and walls ( few volts ) and they have a random motion due to thermal impacts with gas. So the focusing electrode is kept at high potential [4] relative to the walls for focusing the output beam. From fig. 3 it is seen that with the increase of the potential, the plasma boundary layer is extended to the cathode and the ion beam is diffused out of the discharge through cathode exit hole. As the voltage between the plasma boundary and the focusing electrode increases, the plasma takes a concave shape and this leads to bigger plasma boundary which results in a large ion current.

### The focusing properties of the beam

Referring to fig.1, we obtain the axial potential  $V ( Z , 0 )$  where  $r = 0$  as [5]:-

$$V ( Z , 0 ) = \frac{V_{anode}}{\left[ \frac{1}{a} \sqrt{2ah} + \frac{1}{2L-a} (\sqrt{4L^2 - 4Lh + 2ah} - 2L) \right] \cdot \left[ \frac{1}{a-Z} (\sqrt{Z^2 - 2Zh + 2ah - Z}) - \frac{1}{a-(2L-Z)} (\sqrt{(2L-Z)^2 - 2(2L-Z)h + 2ah - (2L-Z)}) \right]} \quad (2)$$

Using the hemispherical anode with a radius of curvature "a" and depth "h" equal to 17.5 mm which is placed at a distance  $L = 25.5$  mm from the plane cathode, one can get the potential  $V( Z , 0 )$  along the axis  $Z$  using equation ( 2 ).

Fig.4 shows how  $V_T = V(Z, 0) / V_{anode}$  varies with the axial distance  $Z$ . It is seen that at  $Z = 25.5$  mm,  $V(Z,0) = 0$  which indicates that at the cathode  $Z = 25.5$  mm. For an axially symmetric field :

$$\frac{V(Z, r)}{V_{anode}} = \frac{V(Z, 0)}{V_{anode}} - \frac{r^2}{4} \frac{V''(Z, 0)}{V_{anode}} + \frac{r^4}{64} \frac{V''''(Z, 0)}{V_{anode}} + \dots \quad (3)$$

where  $V''(Z, 0)$  and  $V''''(Z, 0)$  are the second and fourth derivatives of the axial potential with respect to  $Z$  respectively . The axial electric field  $E(Z)$  and the radial electric field  $E(r)$  are given by :

$$E(Z) = \frac{\partial V(Z, r)}{\partial Z} = 0.02302 + 0.00178 Z - 0.00003 Z^2 + 0.000015 r^2 \quad (4)$$

$$E(r) = \frac{\partial V(Z, r)}{\partial r} = (0.00003 Z - 0.00089) r \quad (5)$$

Fig.5 shows the variation of the axial electric field with the axial distance at  $r = 0$  and  $r = 5$  mm using equation ( 4 ). Fig.6 shows the variation of the radial electric field with the axial distance at  $r = 1, 2, 3, 4, 5$  mm using equation ( 5 ). It is seen that  $E(r)$  is always negative for all values of  $Z$  and  $E(r)$  is always positive. The radial component of the gradient of potential is directly proportional to the second derivative of the axial potential as long as the distance from the axis is not too great [see equation ( 3 )]. As a result of this the radial force on an ion is directed towards the axis. So the action of this system is convergent.

To find the focal length of this system, we know that the focal length of a ray passing through the system parallel to the axis is given by [8]:

$$\frac{1}{F} = \frac{-2.5}{\sqrt{V_{\text{anode}}}} \int_0^{25.5} \frac{V''(Z, 0)}{\sqrt{V(Z, 0)}} dZ \quad (6)$$

plotting the relation between  $V''(Z, 0) / \sqrt{V(Z, 0)}$  and  $Z$ , we obtain the curve shown in fig. 7. By measuring the area under the curve and then multiply by  $(-2.5 / \sqrt{V_{\text{anode}}})$ , one can find the reciprocal of the focal length where ;

$$\frac{V''(Z, 0)}{\sqrt{V(Z, 0)}} = \frac{0.00006 Z - 0.00178}{\sqrt{1 - 0.02302 Z - 0.00089 Z^2 + 0.00001 Z^3}} \quad (7)$$

So the focal length of the system is equal to 29.4 mm. Accordingly, for ion etching of materials, the specimen can be put at a distance of about 29.4 mm from the cathode in order to be exposed to a well focused beam. This is quite satisfactory, since the specimen will be far away from the effect of the temperature of the cathode .

### Conclusion

The exact adjustment of the beam focusing to the required value is usually carried out by the adjustment of some voltage or current or other parameters within the control of the operator of the device. Therefore the trip of the ion beam extracted from the ion source to the target through ion optical system has to be studied carefully to accumulate enough fragments of information about all aspects of lens fields so that the whole picture can be pieced together rather well. The focal length of the ion source system is 29.4 mm. So the specimen can be subjected to large ion current at a reasonable distance away from the effect of the cathode temperature.

In the presence of space charge limitation of the beam current, the attainment of the maximum intensity in a spot of prescribed size makes it desirable to apply a strong electrostatic field in the immediate neighborhood of the cathode.

### References

- [1] Whitson J., Smith J. and Whealton J., *Journal Comput. Phys.*, 28, 408 (1978).
- [2] Whealton J. and Whitson J., *Particle Accelerator* , 10 , 235 ( 1980 ) .
- [3] Hofmann I., Laslett L.J., Smith L. and Harber I., *Particle Accelerators*, 13, 145 ( 1983 )
- [4] Abdel Salam F.W. and Moustafa O.A., *Nucl. Sci. J., Chung Hua. Nuclear Energy Society*, 29 ( 5 ), 325 Oct . ( 1992 ).
- [5] Abdelaziz M.E., Abdel Salam F.W. and Moustafa O.A. *Proceedings of the Ninth National Radio Science Conf., Cairo, Egypt, Feb. 18 - 20 (1992).*
- [6] Gabovich M.D., "Physics and Tecnology of Plasma Ion Source" Transl. FTDH. T 23 - 1690, U.S. Air Force (1972).
- [7] Ortiz T. and Munoz Castro A., in *Proceedings XIII Yugoslav Summer School and International Symposium on Physics of Ionized Gases*, edited by M.V.Kurepa (Department of Physics and Meteorology University of Beograd, Sibenik, Yugoslavia) , 233 ( 1986 ) .
- [8] Spangenberg K., "Vacuum Tubes", Mc Graw - Hill Book Company, Inc. 351, (1948) .

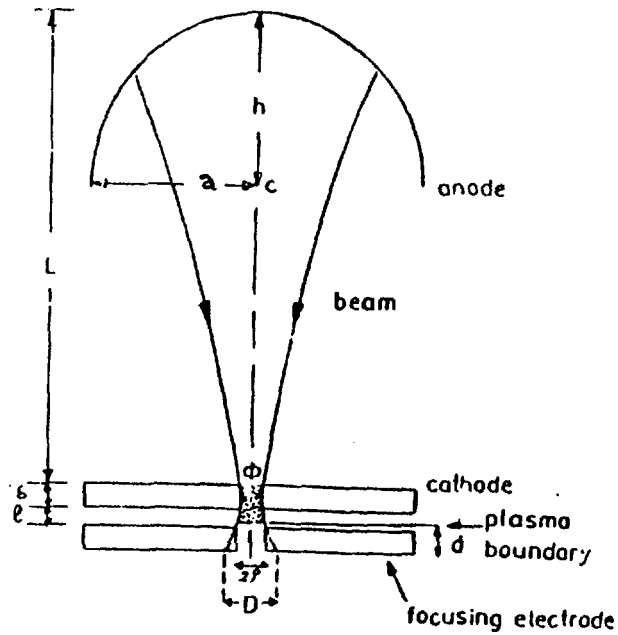


Fig.1 Electrodes arrangement in the ion source system.

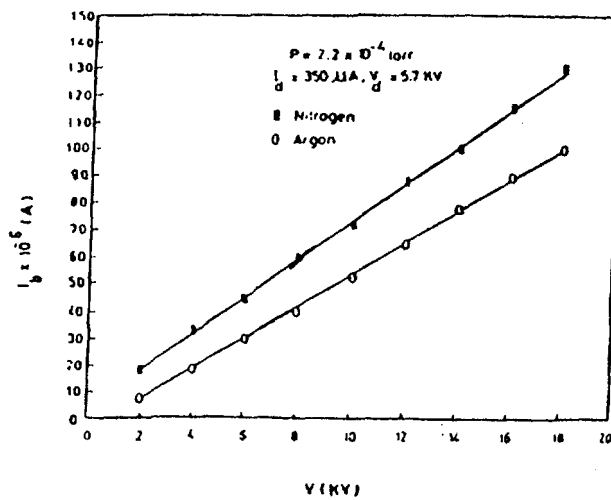


Fig. 2 Variation of the voltage between the plasma boundary and the focusing electrode with the beam current at constant discharge power and pressure for both argon and nitrogen gases.

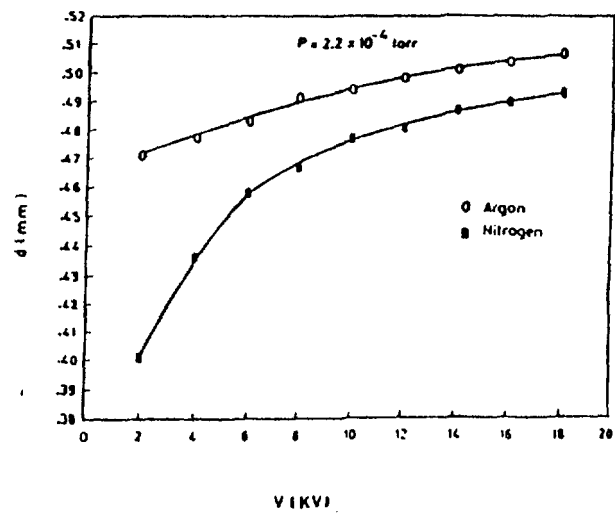


Fig.3 Effect of variation of plasma -focusing electrode voltage on the position of the plasma boundary in the ion source.

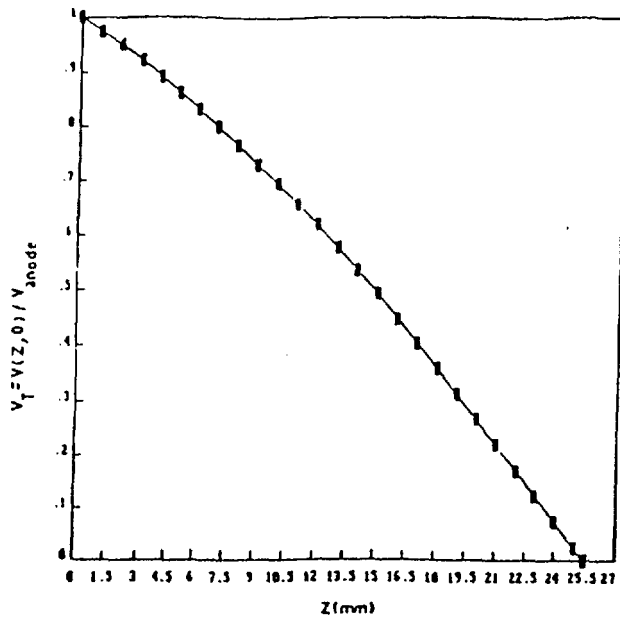


Fig. 4 The potential distribution along the axial distance z

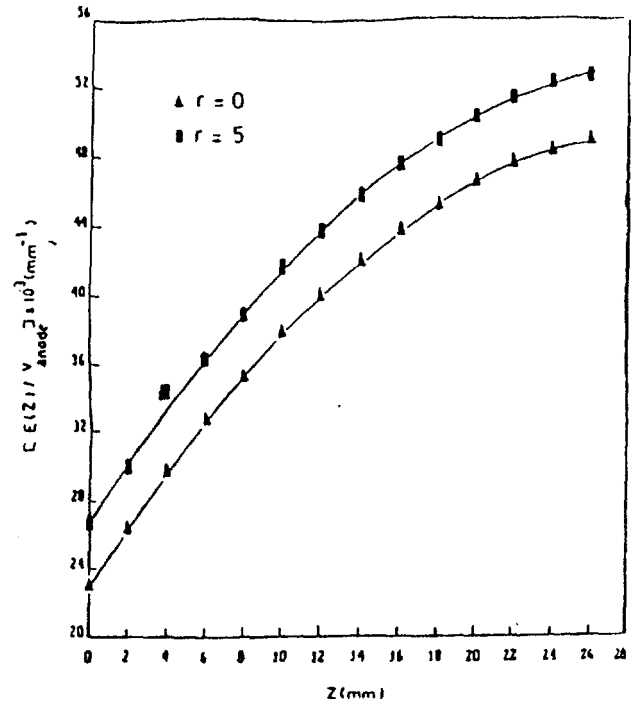


Fig. 5 Axial electric field.

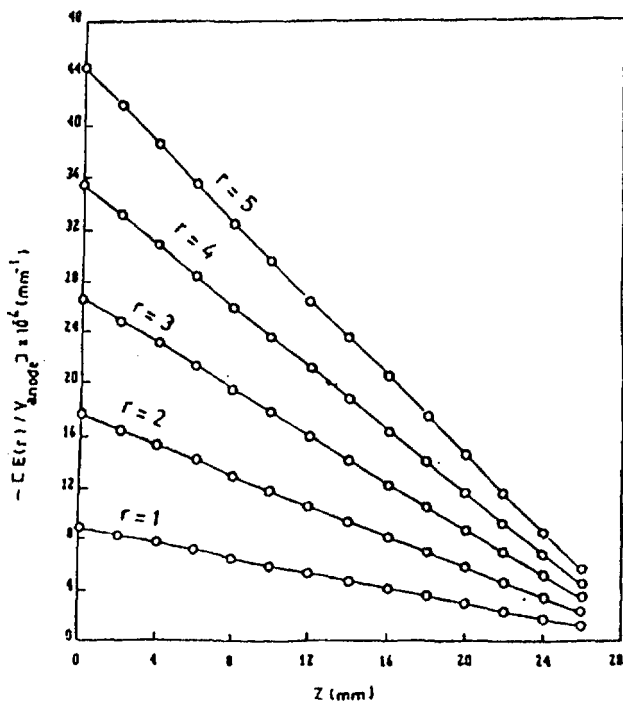


Fig. 6 Radial electric field .

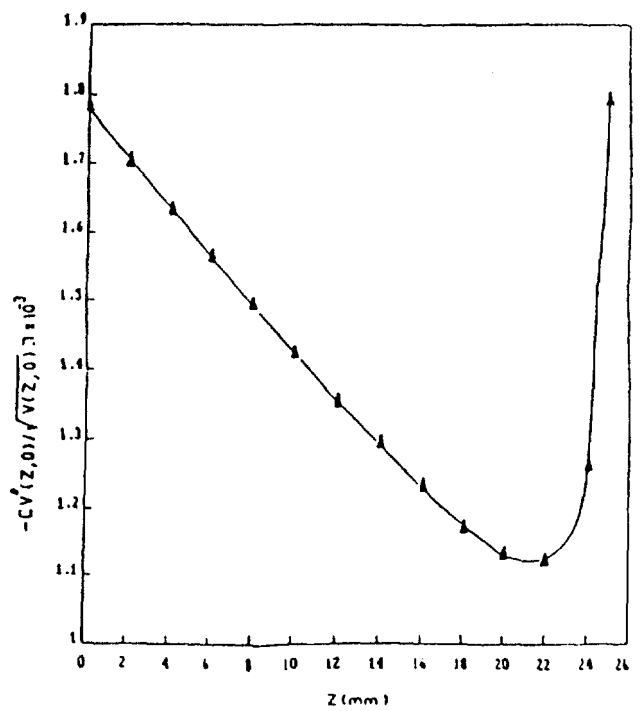


Fig. 7 Determination of the local length.



EG9700103

# SHEATH FORMATION AND EXTRACTION OF IONS FROM A CONSTRICTED R.F. ION SOURCE

F.W.Abdel Salam, A.G.Helal, H.EL-Khabeary T. and N.T.EL-Merai

Accelerators Dept., Basic Nuclear Science Division, Nuclear Research Center,  
Atomic Energy Authority, P.O.13759, Cairo, Egypt.

## Abstract

The present work investigates the plasma characteristics in a constricted axial R.F. ion source. The probe current - voltage characteristics are measured for different extraction voltages  $V(\text{ext.}) = 0, 500, 1000$  and  $1250$  volt at various constant R.F. powers.

The measurements show that at a pressure of  $40\mu\text{Hg}$ , the electron temperature increases linearly with the increase of R.F power without using extraction voltage. It is  $7\text{eV}$  for  $25$  watt and  $20\text{eV}$  for  $90$  watt. At constant R.F power and gas pressure, the electron temperature increases with the increase of the extraction voltage. The electron density varies between  $4.5 \times 10^{15} \text{ m}^{-3}$  and  $7.5 \times 10^{15} \text{ m}^{-3}$  at R.F power equal  $77$  watt, for extraction voltage  $500$  and  $1250$  volt respectively. The performance of the constricted axial R.F ion source shows that it can be used to draw higher current where the electron temperature and density within the source play an important role.

## Introduction

All types of ion sources create a gas discharge to form a plasma from which the specified ions are extracted. In this work, the plasma is created using a constricted R.F ion source with an axial extraction. The high frequency source is applied to a coil surrounding the discharge chamber which contains a gas at a pressure about ( $10^{-3}$  to  $10^{-2}$  torr). The ions are extracted by a positive potential applied to an extraction electrode fixed at the top of the chamber [1]. Fig.(1) shows a schematic diagram of the axial constricted R.F ion source. The plasma produced by electrical discharges are characterized by their electron energy  $KT_e$  and their electron density  $n_e$ . Here the plasma is generated in a high frequency discharge at low pressure. In this type, the electron temperature is very high, but the heavy particles remain at relatively low temperature, due to small rate of collisions with them. The technological and physical aspects are discussed before [2] in order to increase the source efficiency. As a consequence of the of ion sources, better understanding of the factors which affect the formation of ion beam by extraction from the plasma boundary have been done.

## Experimental Results and Discussion

After the ion source has been thoroughly cleaned and normalized, and the vacuum in the system becomes stable, the following results are obtained using nitrogen gas.

### 1. Probe measurements:

It is required to probe deeply in the produced plasma inside the ion source to understand the physical processes occurring within the discharge region up to the extraction system. The measurements are taken using nitrogen gas at pressure =  $4 \times 10^{-2}$  torr. For R.F discharge the electric probe will be affected by the discharge frequency below 20MHz and it needs additional circuit to compensate the R.F current. In this study R.F frequency was greater than 20MHz and it has been found that the electric probe current is slightly affected by the R.F power, and I-V characteristic curves has been obtained without any additional circuits. Fig.(2) shows the probe current versus the probe voltage at constant R.F powers ( 50, 77, 105 watt ). These measurements are taken without using extraction voltage. From the figure, it is seen that there are three regions, the saturation ion and electron current are represented by region I and III in the figure. It has been found that the saturation current of the ions is affected by the R.F frequency where it increases by decreasing of the probe potential below the floating potential.

The deviation of the electron current from the saturation value is mainly due to secondary ionization processes. The electron temperature  $T_e$  is equal to the inverse slope of the region II in eV as given in Fig.(3) for natural logarithmic probe current versus probe voltage. The calculated electron temperature in the R.F discharge using nitrogen gas at pressure  $4 \times 10^{-2}$  torr, see Fig.(3) has a value of  $T_e = 11.1$  eV,  $T_e = 15$  eV,  $T_e = 20$  eV. for R.F power = 50, 77, 105 watt respectively.

Figs. (4),(5) and (6) show natural logarithmic probe current versus probe voltage for different extraction voltages (  $V_{ext} = 500, 1000, 1250$  volt ) respectively at constant R.F powers ( 50, 60, 77 watt ) for nitrogen gas at pressure equal  $4 \times 10^{-2}$  torr.

Figs. (7) and (8) show the same probe characteristics in case of using R.F power equal 90 and 105 watt respectively at constant  $V_{ext} = 500, 1000$  and 1205 volts. Therefore the electron temperature  $T_e$  can be obtained in each case using the above figures.

### 2. Determination of the electron temperature:

Fig.(9) shows the relation between the extraction voltage and electron temperature at constant value of R.F power ( 50, 60 and 77 watt ). At constant R.F power, the extraction voltage increases the electron temperature ( $T_e$ ) of the plasma inside the R.F source in the extraction voltage region up to 1500 volt. This increase can be due to the acceleration of the electrons by the electric field of the extraction voltage. The electron temperature increase will be accompanied normally with density increase, so one may increase the saturation current density.

So for a beam - plasma discharge in which a beam of electrons interacting with a dense plasma at a temperature (11 to 15 eV) can give rise to a second group of electrons with a near thermal distribution at a higher temperature (22 to 30 eV).

Fig.(10) shows the variation of electron temperature with R.F power at constant extraction voltages (  $V_{ext} = 500, 1000$  and 1250 volts ). From the figure it is seen that by increasing the power, the electrons temperature rises rapidly as secondary electrons originating at the cathode surface due to ion bombardment, are accelerated in the sheath field, then drops as the ionization rate increases.

Ionization is a highly endothermic process and therefore reduces the electron temperature. Most of the discharge power is expended in accelerating the ions through the cathode sheath. There are two cooling mechanisms that cause the electron temperature to drop, the endothermic nature of ionization and the energy loss to the electron cloud from heating the created electrons to the local temperature.

In case of  $V_{ext} = 0$  ( see Fig.11 ), i.e a quasi-neutral ( plasma ) region of approximately equal number of positive and negative charged ions and electrons, the electron temperature increases linearly with the R.F power. This leads to substantial electron heating and efficient electron energy transport in this region.

### 3. Determination of the electron density :

To determine the electron density, one can make use of the equation [3]

$$n_e = \frac{J}{0.45e} \left( \frac{2KT}{m_e} \right) \quad (1)$$

Where  $m_e$  is the mass of electron,  $T_e$  is the electron temperature,  $K$  is Boltzman constant,  $e$  is electronic charge and  $J$  is the saturation ion current density, i.e the saturation ion current divided by the area of the probe. Therefore by substituting with the values of electron temperature and saturation ion current obtained from the above mentioned figures, in equation (1), one can determine the electron density in each case. Where :  $m_e = 9.1 \times 10^{-31}$  Kg.,  $K = 1.38 \times 10^{-23}$  Joule / deg.k,  $e = 1.6 \times 10^{-19}$  Columb and probe area =  $0.785 \times 10^{-6}$  m<sup>2</sup>. The electron density has been estimated within the R.F discharge vessel for nitrogen gas at pressure =  $4 \times 10^{-2}$  torr.

Fig.(12) shows the variation of electron density  $n_e$  with ion current density at constant R.F power equals 77 watt. It is seen that the electron density increases linearly with the ion current density. The density varies between  $4.5 \times 10^{15}$  m<sup>-3</sup> and  $7.5 \times 10^{15}$  m<sup>-3</sup> for R.F power = 77 watt.

### 4. Determination of the sheath thickness of the plasma :

The actual sheath thickness formed on the probe is given by [4] :

$$X = \beta \frac{2}{3} \left( \frac{\epsilon_0}{J} \right)^{1/2} \left( \frac{2e}{M} \right)^{1/4} \sqrt{3/4} V_{ext} \quad (2)$$

Where  $\epsilon_0$  is permittivity of free space =  $8.859 \times 10^{-12}$  F/m,  $M$  is the ionic mass and  $V$  is the extraction voltage. The sheath thickness given by  $X$  is increased by the factor  $\beta$  over that for the case of an ion sheath containing only positive ions. The value of the constant  $\beta$  is approximately [4] equals 1.36. This equation assumes that the field terminates abruptly at the plasma boundary. Using the measured voltages in the above equation, one can determine the sheath thickness in each case.

Fig.(13) shows the variation of sheath thickness  $X$  with ion current density  $J$  at various extraction voltages ( 500, 1000 and 1250 volts ). From the figure, it is seen that by increasing the ion current, the sheath thickness decreases but, it is increased by increasing the extraction voltage  $V_{ext}$ . In case of  $V_{ext} = 0$ , the sheath thickness is negligible. Most of the ionization in the R.F power case has shifted from the sheath to

the plasma region. The cathode sheath ionization is highly modulated. There is substantial modulation in the ionization at the edges of the plasma region because of the increase in electron temperature at the appropriate points in the R.F period.

## Conclusion

The effect of R.F power on electron temperature is deduced for a beam-plasma discharge. It reveals that for a quasi-neutral ( plasma ) region, the electron temperature increases linearly with the R.F power which leads to substantial electron heating and efficient electron energy transport in this region. By applying extraction voltage, the electron temperature drops as the ionization rate increases. The sheath thickness is obtained at constant extraction voltages. The curves show that if the ion current density is increased, the sheath thickness decreases while it is increased by increasing extraction voltage and it is negligible in the plasma region.

## References

- [1] Abdel Salam F.W., Helal A.G. and EL-khabeary H.T., *AL-azhar Eng. Fourth Inter. Conf.* . P.233 Dec. 16-19 (1995).
- [2] Abdel Salam F.W., Helal A.G., EL-khabeary H.T. and EL-merai N.T., *Proc. of the 13th. NRSC., Military Tech. college, Mar. 19-21 (1996).*
- [3] Freeman J.H., Gard G.A. and Temple W., *AERE Report 6758 (1971).*
- [4] Cooper W.S., Berkner K.H. and Pyle R.V., *2nd Int. Conf. on Ion Sources, Vienna, P.264 (1972).*

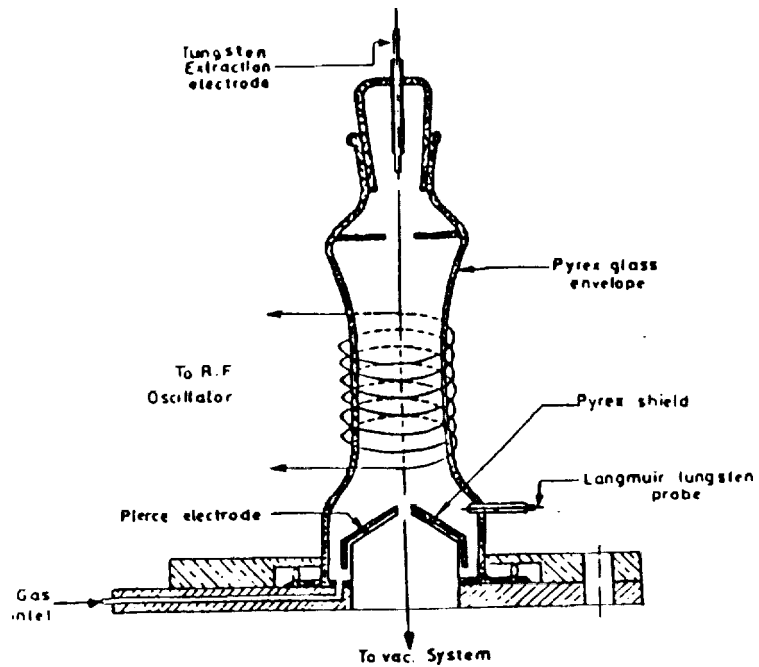


Fig.(1) Axial constricted R.F. ion source.

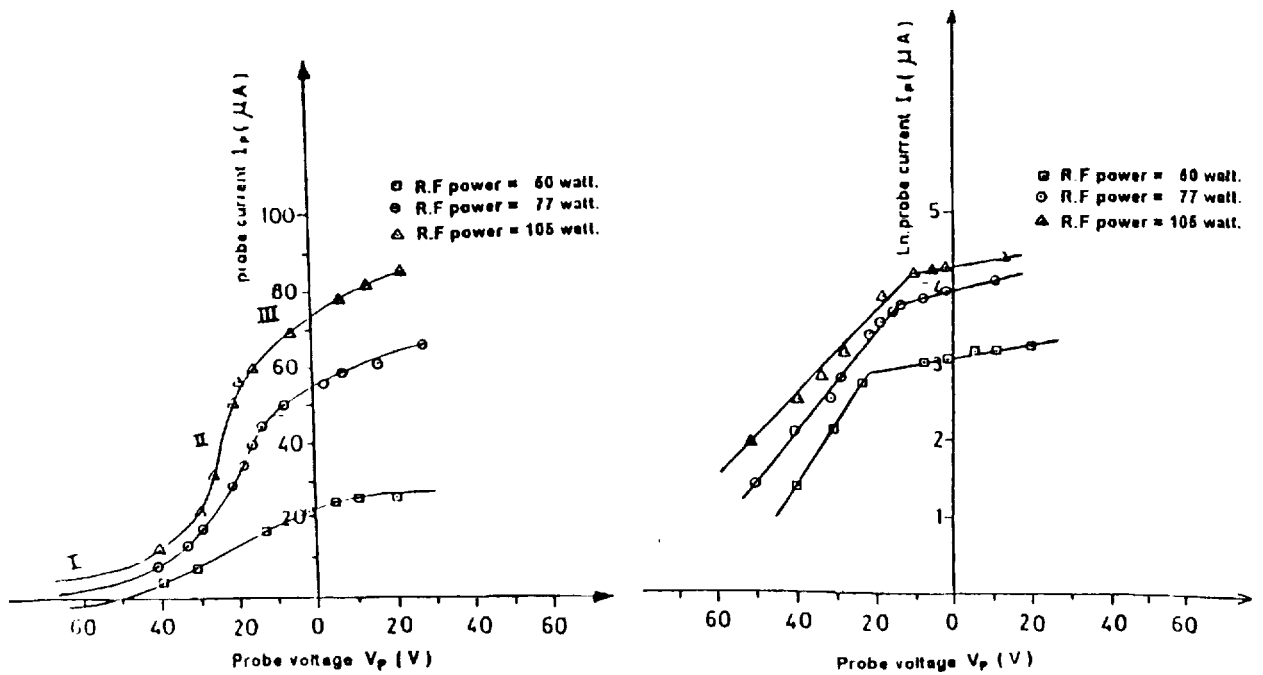


Fig ( 2 ) The probe current versus the probe voltage for different R.F powers at  $V_{ext} = 0$

Fig ( 3 ) The natural logarithmic probe current versus probe voltage for different R.F power at  $V_{ext} = 0$

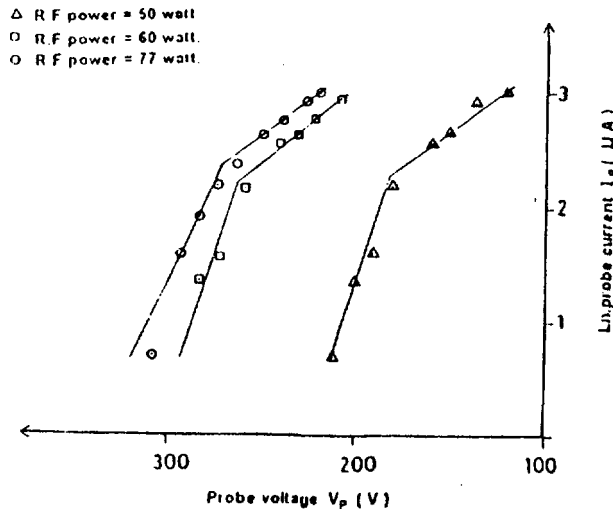


Fig.( 4 ) The natural logarithmic probe current versus probe voltage for different R.F power at  $V_{ext} = 500$  volt.

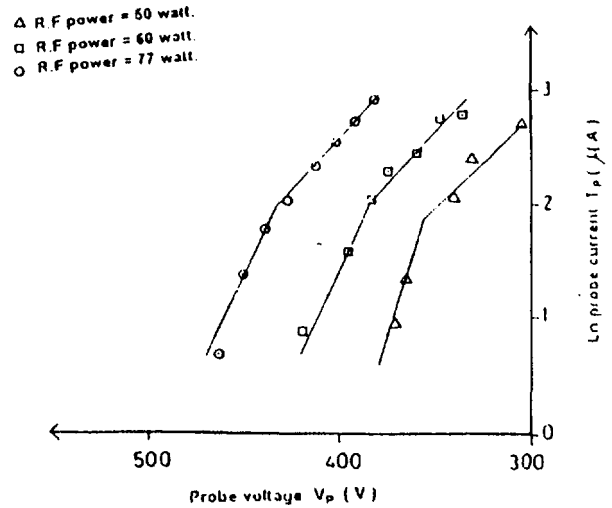


Fig.( 5 ) The natural logarithmic probe current versus probe voltage for different R.F power at  $V_{ext} = 1000$  volt.

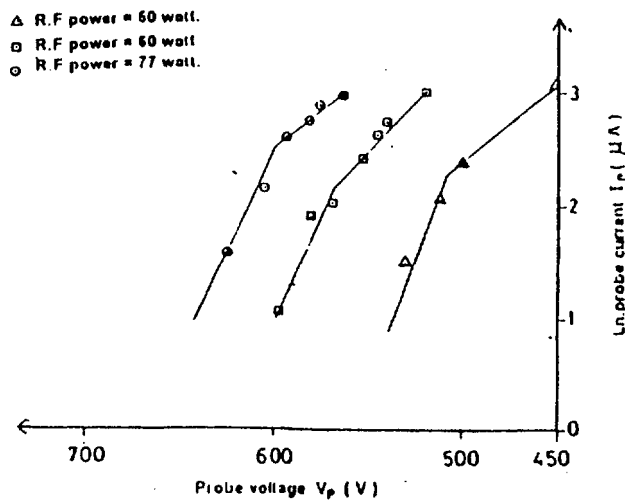


Fig.( 6 ) The natural logarithmic probe current versus probe voltage for different R.F power at  $V_{ext} = 1250$  volt.

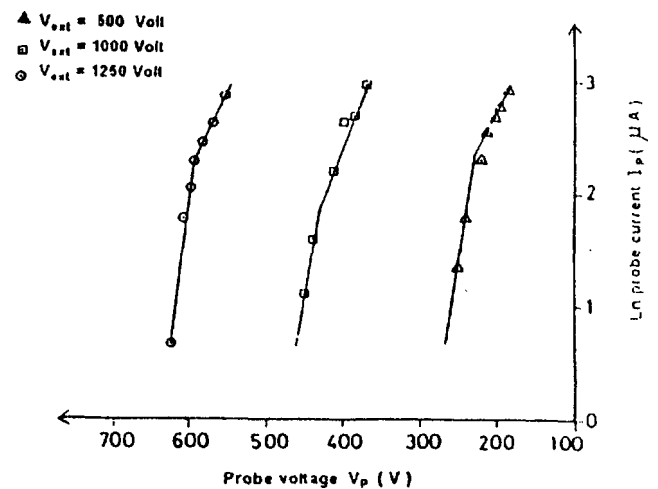


Fig.( 7 ) The natural logarithmic probe current versus probe voltage for different extraction voltage at R.F power = 90 watt.

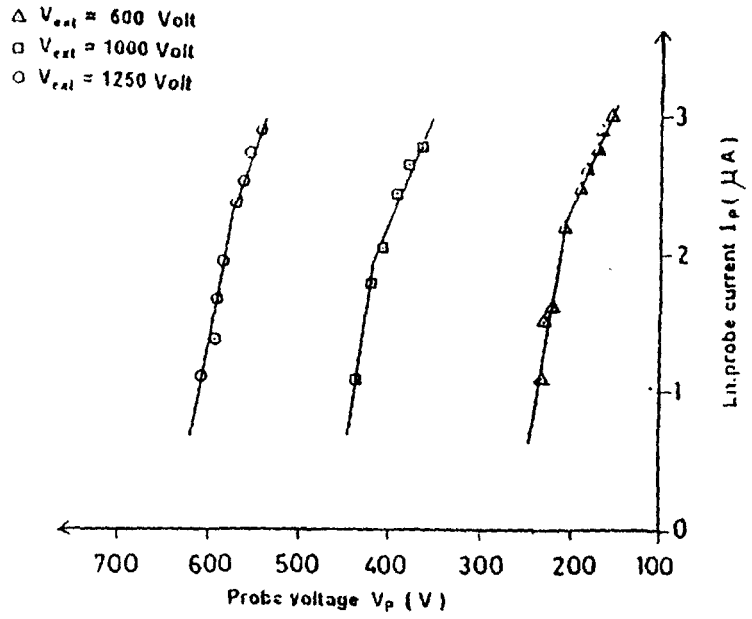


Fig.( 8 ) The natural logarithmic probe current versus probe voltage for different extraction voltage at R.F power = 105 watt.

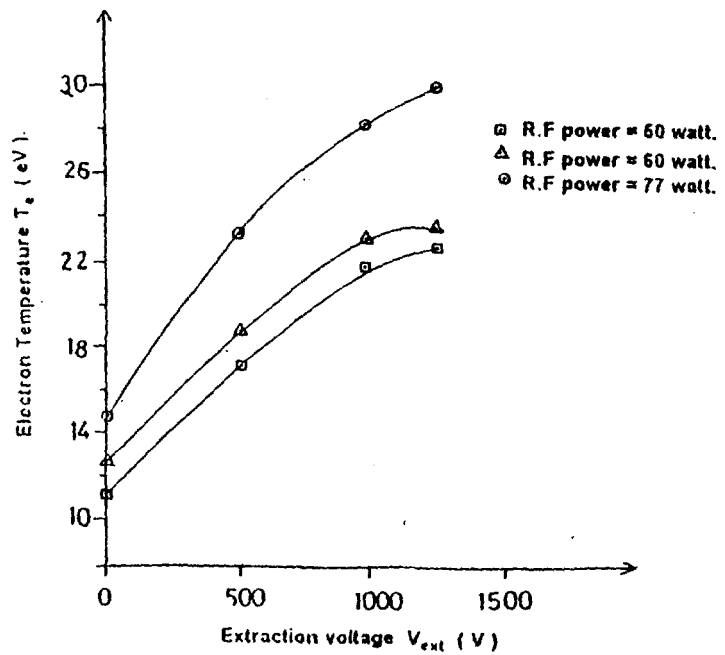


Fig.( 9 ) The relation between the electron temperature and extraction voltage at constant values of R.F power.

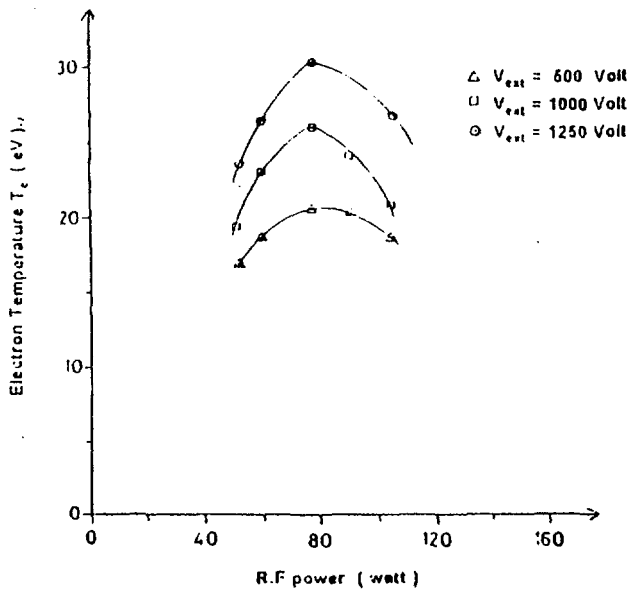


Fig.( 10 ) The variation of electron temperature with R.F power at constant extraction voltages.

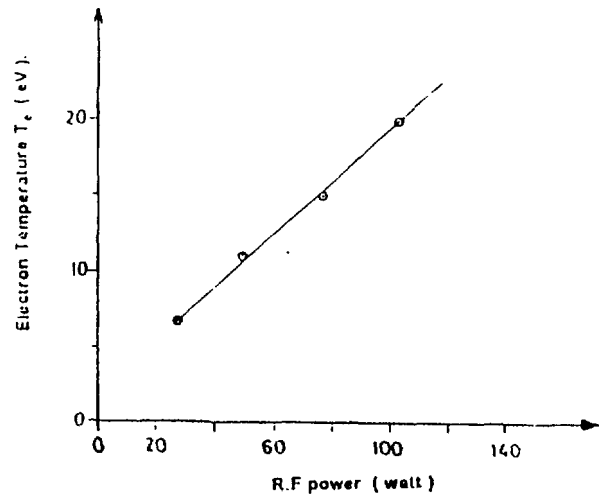


Fig.( 11 ) The variation of electron temperature with R.F power at  $V_{ext} = 0$ .

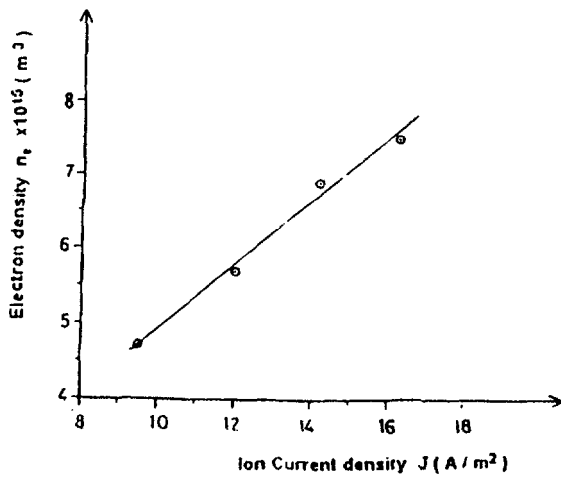


Fig.( 12 ) The variation of electron density with ion current density at constant R.F power = 77 watt.

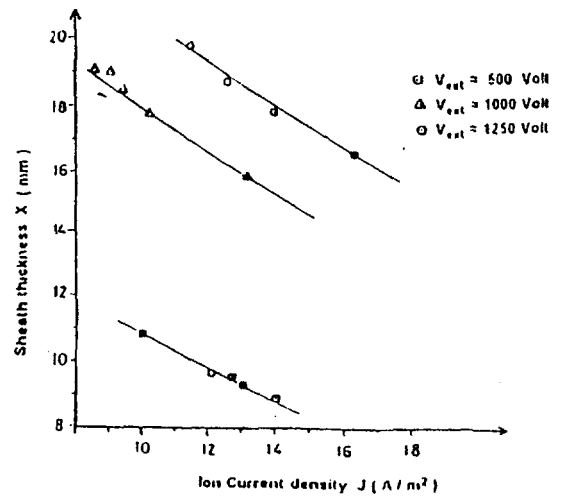


Fig.( 13 ) The variation of sheath thickness  $x$  with ion current density at various extraction voltages.

## **ELECTRON BEAM INTERACTION WITH AN INHOMOGENEOUS WARM PLASMA AND WAVE RADIATION**



EG9700104

**N. G. Zaki and Kh. H. El-Shorbagy**

Plasma Physics and Nuclear Fusion Dept.

Nuclear Research Centre

Atomic Energy Authority

Cairo - Egypt .

### **ABSTRACT**

The linear and nonlinear interaction of an electron beam with an inhomogeneous semi-bounded warm plasma is investigated . The amount of energy absorbed by the plasma is obtained . The formation of waves at double frequency at the inlet of the beam into the plasma is also considered .

### **1. INTRODUCTION**

Electron beams has many applications in areas like material studies , compact tours formation , generation of x-ray and microwave , ion acceleration , etc... , where it is desirable to have energy source supplied over a long duration of time . As a potential application , use of an electron beam to heat the plasma to a high temperature has attracted a lot of attention , both theoretically ( e.g. , [1-3] ) and experimentally ( e.g. , [4-6] ) in the recent past .

The problem of electron beam linear interaction with cold with unmagnetized plasma was studied by many authors ( e.g. , [7-8] ) . In these cases , a beam - plasma interaction takes the form of an amplification of waves by beam . It is shown that due to the resonance rise of the wave field with plasma dielectric permeability reducing to zero , the power absorbed by the plasma is finite and independent of the value of the dissipation .

In this case the beam not only amplifies waves in the plasma , but also provides for effective absorption of these waves by the plasma .

In the present work we investigate the same problem treated in references [7-9] but under the following considerations ; (i) warm plasma electrons , and (ii) the nonlinear interaction of the

type of wave generation at double frequency . The interest in these considerations are that recent investigations related to the beam - cold plasma interaction have shown that within the frame of linear theory only limited statements about the energy transfere is possible . Moreover , the spatial dispersion of the plasma electrons can not be neglected in these interactions due to the fact that the plasma electrons practically are not absolutely cold .

For simplicity we shall consider a one - dimensional electrostatic oscillations when the directions of beam propagation , plasma density gradient and wave electric field coincide with x-axis .

Our investigation will be made under the following mathematical formulation :

- a) The hydrodynamic model applies to both the beam and the plasma .
- b) A plasma layer of width  $a$  is considered so that the plasma density  $n_0(x)$  , unperturbed by the wave fields , is an arbitrary function of  $x$  in the region  $0 \leq x \leq a$  , equal to zero in the region  $x \leq 0$  and a constant w. r. t.  $x$  in the region  $x \geq a$  .
- c) The wavelengths are large if compared with the width of the plasma layer .
- d) Plasma electrons are warm , cold beam while ions are infinitely heavy and serving as a neutralizing background .

## 2. FUNDAMENTAL WAVES

On the basis of above assumptions , the linearized equation of motion , the continuity equation and poisson's equation are written for the beam as well as the plasma electrons . In the frame of reference attached to the plasma , these equations have the following form :

$$\frac{\partial v_{1b}}{\partial x} - i \frac{\omega}{v_{0b}} v_{1b} = - \frac{e}{m v_{0b}} E_1 \quad (1)$$

$$-i\omega n_{1b} + \frac{\partial}{\partial x} (n_{0b} + n_{1b})(v_{0b} + v_{1b}) = 0 \quad (2)$$

$$v_{1p} = - \frac{i}{\omega} \left[ \frac{eE_1}{m} + \frac{v_{Te}^2}{n_{0p}} \frac{\partial}{\partial x} n_{0p}(x) \right] \quad (3)$$

$$n_{1p} = -\frac{e}{m\omega^2} \frac{\partial}{\partial x} (n_{0p} E_1) - \frac{v_{T_e}^2}{\omega^2} \frac{\partial^2 n_{0p}(x)}{\partial x^2} \quad (4)$$

$$\frac{\partial E_1}{\partial x} = -4\pi e (n_{1b} + n_{1p}) \quad (5)$$

$$v_{T_e} = \sqrt{\frac{T_e}{m_e}}$$

Where , the subscripts 0 and 1 denotes the unperturbed and first order perturbation quantities respectively , and subscripts b and p refer to the beam and plasma parameters respectively . In deriving equations (1) - (4) we considered an  $\exp(-i\omega t)$  variation in time for all of the first order quantities . Furthermore , we considered

$$E = E_1 + E_2 ,$$

$$n_b = n_{0b} + n_{1b} + n_{2b} , v_b = v_{0b} + v_{1b} + v_{2b}$$

$$n_p = n_{0p} + n_{1p} + n_{2p} , v_p = 0 + v_{1p} + v_{2p}$$

The subscript 2 indicates the second order perturbations (second harmonics) .

A combination of equation (1) through (5) yields the following results :

$$v_{1b} = -\frac{e}{mv_{0b}} e^{i(\omega/v_{0b})x} \int e^{-i(\omega/v_{0b})x} E_1 dx \quad (6)$$

$$n_{1b} = \left(\frac{en_{0b}}{m v_{0b}^2}\right) e^{i(\omega/v_{0b})x} \int e^{-i(\omega/v_{0b})x} dx [E_1 + (i\omega/v_{0b}) e^{i(\omega/v_{0b})x} \int e^{-i(\omega/v_{0b})x} E_1 dx'] dx' \quad (7)$$

$$(v_{0b} \frac{\partial}{\partial x} - i\omega)^2 [\epsilon_1(x) E_1(x)] + \omega_p^2 E_1(x) = R_1(x) \quad (8)$$

$$\text{where ; } \epsilon_1(x) = 1 - \frac{\omega_{pe}^2}{\omega^2} , \quad \omega_{pe}^2 = \frac{4\pi e^2 n_{0p}(x)}{m} ,$$

$\epsilon_1$  is the fundamental dielectric constant of the plasma , and

$$R_1(x) = \frac{4 \pi e v_{Te}^2}{\omega^2} \frac{\partial}{\partial x} \left[ (v_{0b} \frac{\partial}{\partial x} - i\omega)^2 n_{0p}(x) \right] \quad (9)$$

$R_1(x)$  represent a source term due to taken into consideration the warmness of plasma electrons

The differential equation (8), cannot be solved without assuming further relations among the components of the electric field. Therefore, we first use the substitutions:

$$E_1(x) = \frac{F_1(x)}{\epsilon_1(x)} e^{i(\omega/v_{0b})x}, \quad (10)$$

hence (8) reduces to:

$$\frac{d^2 F_1(x)}{dx^2} + \frac{k^2}{\epsilon_1} F_1(x) = R_1'(x) \quad (11)$$

$$R_1'(x) = \frac{R_1(x)}{v_{0b}^2} e^{-i(\omega/v_{0b})x}, \quad k^2 = \frac{\omega_b^2}{v_{0b}^2}$$

In our case we consider a semi - bounded plasma, and it will be convenient to choose a linear profile density:

$$n_{0p}(x) = N_0 \frac{x}{a},$$

so that at  $x \leq 0$ ,  $n_{0p}(x) = 0$ , at  $x \geq 0$ ,  $n_{0p}(x) = N_0 = const.$

In the regions  $x \leq 0$ ;  $\epsilon_1 = 1$ ,  $R_1'(x) = 0$ , and equation (11) have the solutions:

$$F_1(x) = c_1 e^{ikx}, \quad x \leq 0 \quad (12)$$

while in the region  $x \geq 0$ ;  $\epsilon_1 = 1 - \frac{\omega_0^2}{\omega^2} = \epsilon_{01}$ ,  $R_1'(x) = 0$ , and solution of (11) is

$$\left( \omega_0^2 = \frac{4 \pi e^2 N_0}{m} \right):$$

$$F_1(x) = c_2 e^{-i(k/\sqrt{\epsilon_{01}})(x-a)}, \quad x \geq a \quad (13)$$

A solution of (11) in the inhomogeneous plasma region  $0 \leq x \leq a$  can be sought by using the method of successive approximation using the condition when the wavelengths are large compared with the width of the plasma layer;  $|ka / \sqrt{\epsilon_{01}}| \ll 1$ .

Accordingly we have:

$$F_1(x) \equiv c_1 + iv_r^2 \left(\frac{\omega_0}{\omega}\right) \left(\frac{m}{e}\right) \left(\frac{\omega_0}{v_{01}}\right) \left(\frac{x}{a}\right) \quad , \quad 0 \leq x \leq a \quad (14)$$

$c_1, c_2$  are the integration constants, which can be determined by matching the solutions (12) - (14) in the different regions.

For cold plasma  $F_1(x) \equiv c_1$  which again in agreement with case investigated in references [7,10].

### 3. PLASMA HEATING

From (10) and (14) it follows that, just as in the case of electromagnetic wave propagation in inhomogeneous plasma in the absence of a beam, the interval value  $\varepsilon \approx 0$  (i. e., when  $\omega \rightarrow \omega_p$ ) is that of resonance rise of electric field of the wave. Accordingly:

$$|E_1|^2 \equiv \frac{1}{|\varepsilon_1|^2} \left(1 + |1 - \varepsilon_1|^2 v_r^4 \left(\frac{m\omega}{ev_{0b}}\right)^2\right) \quad (15)$$

Expression (15), with the second term on R. H. S. due to warmness of plasma electrons, is still valid for any relation of beam and plasma density [2].

The amount of energy absorbed by the plasma per unit time  $S$  is determined by the expression:-

$$S = \int dx (J_1 E_1^* + J_1^* E_1) = \frac{\omega}{2\pi} \int dx \operatorname{Im} \varepsilon |E_1|^2 \quad (16)$$

where  $J$  is the electric current density created by the plasma electrons, and (\*) denotes the conjugate.

It is clear from (15) and (16) that resonance increase of the field within the interval  $\omega_p \rightarrow \omega$ , (i. e.,  $\varepsilon_1 \approx 0$ ) should involve the resonance rise of the power absorbed by the plasma.

If  $S_c$  is the energy absorbed in the case when  $v_r = 0$  (i. e., for cold plasma), and  $S_w$  is the energy absorbed in the case of warm plasma. Then we obtain  $S_w = S_c + \Delta S$ ;

$$\Delta S \approx \varepsilon \frac{a}{2\pi} \left(\frac{m}{e}\right) \left(\frac{v_r}{v_{0b}}\right)^2 \left(\frac{\omega_0^2}{\omega^2 - \omega_0^2}\right)^2 > 0, \quad \varepsilon \ll 1 \quad (17)$$

Relation (17) shows that more power is transferred to the plasma due to the warmness of plasma electrons.

#### 4. SECOND HARMONIC WAVES

In the next approximation of the perturbation theory, and for the interaction of cold beam and warm plasma, we shall consider a  $e^{-2i\omega t}$  variation in time for all the second order quantities.

Accordingly, we can derive the following expressions:

$$v_{2b} = -\frac{1}{v_{0b}} e^{i(2\omega/v_{0b})x} \int \left[ \frac{e}{m} E_2 + v_{1b} \frac{\partial v_{1b}}{\partial x} \right] e^{-i(2\omega/v_{0b})x} dx \quad (18)$$

$$n_{2b} = -\frac{1}{v_{0b}} e^{i(2\omega/v_{0b})x} \int e^{-i(2\omega/v_{0b})x} \left[ n_{0b} \frac{\partial v_{2b}}{\partial x} + \frac{\partial}{\partial x} (n_{1b} v_{1b}) \right] dx \quad (19)$$

we can derive the part with frequency  $2\omega$ :

$$v_{2p} = -\frac{i}{2\omega} \left[ \frac{eE_2}{m} + v_{1p} \frac{\partial v_{1p}}{\partial x} + \frac{v_{Te}^2}{n_{0p}} \frac{\partial}{\partial x} n_{0p}(x) \right] \quad (20)$$

$$n_{2p} = \frac{\partial}{\partial x} \left[ -\frac{en_{0p}}{4m\omega^2} E_2 + -\frac{3e^2 n_{0p}}{4m^2 \omega^4} E_1 \frac{\partial E_1}{\partial x} + \left( \frac{e^2 E_1^2}{2m^2 \omega^4} - \frac{v_{Te}^2}{4\omega^2} \right) \frac{\partial n_{0p}(x)}{\partial x} \right] \quad (21)$$

The equation describing the electric field at second harmonics for arbitrary dependence of  $n_{0p}(x)$  on  $x$  can be derived in the form:

$$\frac{d^2 F_2(x)}{dx^2} + \frac{k^2}{\epsilon_2} F_2(x) = R_2(x) \quad (22)$$

where,  $\epsilon_2(x) = 1 - \frac{\omega_{pe}^2}{4\omega^2}$ ,  $E_2(x) = \frac{F_2(x)}{\epsilon_2(x)} e^{i(2\omega/v_{0b})x}$ ,  $R_2(x) = e^{-i(2\omega/v_{0b})x} (R_b + R_p)$ ;

$$R_b = -\frac{1}{v_{0b}} \int e^{i(2\omega/v_{0b})x} \frac{\partial}{\partial x} \left[ \frac{m\omega_b^2}{e} e^{-i(2\omega/v_{0b})x} \frac{\partial v_{1b}^2}{\partial x} + 2 \frac{im\omega_b^2 \omega}{e v_{0b}^2} e^{-i(2\omega/v_{0b})x} \right. \\ \left. \frac{\partial}{\partial x} (e^{i(2\omega/v_{0b})x} \int v_{1b}^2 e^{-i(2\omega/v_{0b})x} dx) + 4\pi e e^{-i(2\omega/v_{0b})x} \frac{\partial}{\partial x} (n_{1b} v_{1b}) \right] dx \quad (23)$$

$$R_p = -\int e^{i(2\omega/v_{0b})x} \frac{\partial}{\partial x} \left\{ \frac{\partial}{\partial x} [e^{-i(2\omega/v_{0b})x} \frac{\partial}{\partial x} \left( \frac{e\omega_{pe}^2}{2m\omega^4} E_1 \frac{\partial E_1}{\partial x} + \frac{e^2 E_1^2}{2m^2 \omega^4} \frac{\partial n_{0p}}{\partial x} \right)] \right\} dx + \\ + \frac{\pi e v_{Te}^2}{\omega^2} \frac{\partial}{\partial x} \left[ (v_{0b} \frac{\partial}{\partial x} - i2\omega)^2 n_{0p} \right] \quad (24)$$

As it clear from (23), (24) the source terms  $R_b$  and  $R_p$  can be described in terms of the ground waves.

To find the solution of equation (22), i. e., the fields associated with waves of frequency  $2\omega$ , we consider the semi-bounded plasma, so that:

In region  $x \leq 0$  ;

$\omega_p = 0, R_p = 0, R_2 = R_b, \epsilon_2(x) = 1$   
and we have a solution in the form :

$$F_2(x) \equiv \frac{e^{ikx}}{2ik} \left\{ \int_0^x R_b e^{-ikx} dx - e^{-2ikx} \int_0^x R_b e^{ikx} dx \right\}, \quad x \leq 0 \quad (25)$$

In region  $x \geq a$  ;

$\omega_p = \omega_0^2, R_p = R_{pa}, R_2 = R_{pa} + R_b = R_a; \epsilon_2(x) = \epsilon_{a2} = 1 - \frac{\omega_0^2}{4\omega^2} = \text{const.}$

where ;

$$R_{pa} = -\frac{e\omega_0^2}{2m\omega^4} \int e^{i(2\omega/v_0)x} \frac{\partial}{\partial x} \left\{ \frac{\partial}{\partial x} [e^{-i(2\omega/v_0)x} \frac{\partial}{\partial x} (E_1 \frac{\partial E_1}{\partial x})] \right\} dx \quad (26)$$

and we have a solution in the form

$$F_2(x) \equiv \frac{\sqrt{\epsilon_{a2}}}{2ik} e^{\frac{ik}{\sqrt{\epsilon_{a2}}}(x-a)} \left\{ \int_0^x R_a e^{-\frac{ik}{\sqrt{\epsilon_{a2}}}(x-a)} dx - e^{-\frac{12k}{\sqrt{\epsilon_{a2}}}(x-a)} \int_0^x R_a e^{\frac{ik}{\sqrt{\epsilon_{a2}}}(x-a)} dx \right\}, \quad x \geq a \quad (27)$$

Following the same method used to solve equation (11) in the inhomogeneous plasma region  $0 \leq x \leq a$ , and after neglecting all terms of the  $(ka/\sqrt{\epsilon_2})$  - order, we can obtain the electric field with double frequency :

$$E_2(x) \equiv \left[ \int_0^x dx' \int_0^{x'} dx'' e^{-i\frac{2\omega}{v_0}x''} (R_b + R_p) + c \right] \frac{e^{i\frac{2\omega}{v_0}x}}{\epsilon_2(x)} \quad (28)$$

where ;  $c$  is constant of integration .

First term on R. H. S. of equation (28) indicate the solution corresponding to nonlinear interaction of the beam and the plasma and it is clear that it proportional to waves oscillates with frequency  $2\omega$ . The second term on R. H. S. indicate again the solution for the case when the beam interact with cold plasma and for waves oscillates with frequency  $\omega$ . It is clear from (28) that the electric field  $E_2$  associated with second harmonics waves, and hence the power absorbed - different from the linear case - will depend on the relation of beam and plasma densities. Accordingly, taking into consideration nonlinear effect, this leads to an increase in the amplitude of electric field in the inhomogeneous region, and in turn to more power absorption.

## 5. CONCLUSIONS

An analysis of the linear and nonlinear interaction of an electron beam with an inhomogeneous semi - bounded warm plasma. It is shown that power absorption by the inhomogeneous plasma layer may be increased in the linear stage when taking into consideration that plasma electrons are warm (equation (17)). In practice, the thermal velocity of the beam is usually quite negligible compared with its directed velocity.

It is also shown that the nonlinear effects associated with the generation of second harmonics, play an important role in the process of energy transfer from the beam to the plasma as compared with linear stage [7,10]. This is due to the fact that the electric field intensity at double frequency - equation (28) - is stronger than that of basic frequency.

## 6. ACKNOWLEDGMENTS

The authors are indebted to Prof. Dr. Sh. M. Khalil for valuable advice and providing facilities.

## 7. REFERENCES

- [1] Thode, L. E., *Phys. Fluids*, **20** (1977) 2121.
- [2] Janssen, G. C. A. M.; Bonnie, J. H. M.; Granneman, E. H. A.; Kremontsov, V. I. & Hopman, H. J., *Phys. Fluids*, **27** (1984) 726.
- [3] Gupta, G. P.; Vijayan, T. & Rohatgi, V. K., *Phys. Fluids*, **31** (1988) 606.
- [4] Hammer, D. A.; Gerber, K. A. & Ali, A. W., *IEEE Trans. Plasma Sci.*, **Ps-7** (1986) 83.
- [5] De Hann, P. H.; Janssen, G. C. A. M., Hopman, H. J. & Granneman, E. H. A., *Physics Fluids*, **25** (1982) 592.
- [6] Friedman, M.; Serlin, V.; Dorbot, A. & Mondelli, A., *IEEE Trans. Plasma Sci.*, **Ps-14** (1986) 201.
- [7] Amein, W. H.; Dolgoplov, V. V.; Hussein, A. M. & Zayed, K. E.
  - a) *Plasma Physics* **17** (1975) 497.
  - b) *Physica* **79c** (1975) 628.
- [8] Ivanov, A. A.; Popkov, N. G.; Wilhelm, J. & Winkler, R., *Beitr. Plasma Phys.*, **7** (1984) 23.
- [9] Bohmer, H.; Jackson, E. A.; Rather, M., *Phys. Fluids*, **16** (1973) 1064.
- [10] Khalil, Sh. M. & Zaki, N. G., "XIX International Conference on Phenomena in Ionized Gases", Belgrade, Yugoslavia, 10-14 July, **4** (1989) 906.



# COEFFICIENTS OF VISCOSITY FOR HEAVY IMPURITY ELEMENT IN TOKAMAK

R. N. EL - SHARIF , A. M. BEKHIT  
PLASMA PHYSICS DEPT., NRC, ATOMIC ENERGY  
AUTHORITY, CAIRO , EGYPT

## ABSTRACT

The transport of heavy impurity element in tokamak was studied theoretically . The viscosity coefficients of Chromium impurities has been calculated in 13 and 21 moment approximation , in the limit of strong fields ( $\omega_{c\alpha} \tau_{\alpha} \gg 1$ ) where  $\omega_{c\alpha}$  is the gyrofrequency of species  $\alpha$  ( $\alpha \equiv e \text{ \& \ } i$ ) it was found that the off-diagonal viscosity coefficient approximately tends to zero . This means that the friction force in the off -diagonal direction is very small , for the perpendicular viscosity coefficient the two approximation coincide to each other.

## INTRODUCTION

The existence of energetic particles and electromagnetic radiation in plasma requires consideration of their interaction with the exposed surfaces . The physical interactions, which takes place at any surface exposed to the plasma , have a significant effect on the results of the plasma treatment. The plasma contains energetic electrons and positive ions and also energetic neutrals . Bombardment of the solid surfaces with these particles can impart energy to the solid . When an energetic ion collides with a solid surfaces , the ion energy is transferred to the lattice atoms , creating impurities . The plasma - surface

interaction can be divided into two categories. One type of interaction takes place far from the surface in which the electronic excitation energy of the particles dominates . The second type of interaction requires a much closer proximity to the surface or even penetration of the particles from the plasma into the Crystal lattice and therefore , involves the kinetic energy of the particles [1-3]. The plasma impurity ions have higher sputtering and desorption yield than the hydrogen ions, contamination makes it, more difficult to achieve net fusion energy condition [3,5]. Neutral particles refuel the plasma as they ionize, adding also to the plasma's momentum and energy . The process of charge - exchange alters the plasma momentum and energy as the plasma ions, momentum and energy are replaced with those of the neutrals plasma electrons lose energy as they excite and ionize neutral particles and dissociate molecules , and , in very hot plasma , ions lose energy through the same processes . Neutral particles also transmit energy to the confinement device's wall in the form of radiation and ,as they collide with the wall , heat. Walls absorbing the atom's momenta may suffer damage as material is sputtered off. Neutral particles may stay in wall for times which vary from a few milliseconds to a few years , so that , for example , the wall acts as a pump as well as a repository of tritium in reactors [7]

## THEORETICAL STUDY

Using the result of ref.[6] . Starting from distribution function  $f_{\alpha}$  .

$$f_{\alpha} = f_{\alpha}^{(0)} (1 + \varphi_{\alpha}) \quad (1)$$

$\varphi_\alpha$  is the perturbation from equilibrium  $f_\alpha^{(0)}$ . Then the kinetic equation takes the form:

$$\frac{\partial f_\alpha}{\partial t} + \vec{V} \cdot \vec{\nabla} f_\alpha + \frac{e_\alpha}{m_\alpha} (\vec{E} + \frac{1}{c} [\vec{V} \times \vec{B}]) \cdot \frac{\partial f_\alpha}{\partial \vec{V}} = C_\alpha \quad (2)$$

$$C_\alpha \text{ is the collision term, } C_\alpha = (f_\alpha - f_\alpha^{(0)}) \nu \quad (3)$$

and  $\nu$  is collision frequency. Expanding the perturbation function in irreducible Hermmit Polynomials [6].

$$\varphi_\alpha^{(13)} = \sum_{P=0}^1 h_r^{(2P+1)}(\vec{X}, t) H_r^{(2P+1)}(\vec{\xi}) + h_{rs}^{(2)}(\vec{X}, t) H_{rs}^{(2)}(\vec{\xi}) \quad (4)$$

$$\varphi_\alpha^{(21)} = \sum_{P=0}^2 h_r^{(2P+1)}(\vec{X}, t) H_r^{(2P+1)}(\vec{\xi}) + \sum_{P=1}^2 h_{rs}^{(2P)}(\vec{X}, t) H_{rs}^{(2P)}(\vec{\xi}) \quad (5)$$

equations (4), (5) describes the 13 and 21 moment approximations respectively.

$$\text{Where : } r, s = x, y, z, \vec{\xi} = \left(\frac{m_{\alpha s}}{T_{\alpha s}}\right)^{1/2} (\vec{V} - \vec{U}_{\alpha s}(X, t)) ; \left(\frac{m_{\alpha s}}{T_{\alpha s}}\right)^{1/2} = \frac{1}{V_{r, s}} \quad (6)$$

$m_\alpha$  is the mass of species  $\alpha$ ,  $T_\alpha$  is its temperature.

$$\left. \begin{aligned} H_r^{(1)}(\vec{\xi}) &= \xi_r \\ H_r^{(3)}(\vec{\xi}) &= \frac{1}{\sqrt{10}} \xi_r (\xi^2 - 5) \\ H_r^{(5)}(\vec{\xi}) &= \frac{1}{2\sqrt{70}} \xi_r (\xi^4 - 14\xi^2 + 35) \end{aligned} \right\} \quad (7)$$

$$\text{and } \xi_r = \sqrt{\gamma} \xi_r^* \quad \gamma = \frac{m_\alpha}{T_\alpha}$$

$$\left. \begin{aligned} h_r^{(1)}(\vec{X}, t) &= \sqrt{\gamma} W_r(\vec{X}, t) \\ h_r^{(3)}(\vec{X}, t) &= \frac{2\sqrt{\gamma}}{\sqrt{10} P} h_r(\vec{X}, t) \\ h_r^{(5)}(\vec{X}, t) &= \frac{2}{\sqrt{70}} \frac{\sqrt{\gamma}}{P} Y_r(\vec{X}, t) \end{aligned} \right\} \quad (9)$$

$$\left. \begin{aligned} W_r(\vec{X}, t) &= \frac{1}{n} \int d^3\xi \cdot \xi_r \cdot f(\vec{X}, t) \\ h_r(\vec{X}, t) &= \frac{m}{2} \int d^3\xi \cdot \xi_r \cdot \left( \xi_r^2 - \frac{5}{\gamma} \right) f(\vec{X}, t) \\ Y_r(\vec{X}, t) &= \frac{m}{4} \int d^3\xi \cdot \xi_r \cdot \left( \xi_r^4 - \frac{14}{\gamma} \xi_r^2 + 35 \right) f(\vec{X}, t) \end{aligned} \right\} \quad (10)$$

$$\left. \begin{aligned} H_{rs}^{(2)}(\xi) &= \frac{1}{\sqrt{2}} \left( \xi_r \xi_s - \frac{\xi^2}{3} \delta_{rs} \right) \\ H_{rs}^{(4)}(\xi) &= \frac{1}{2\sqrt{7}} \left( \xi_r \xi_s - \frac{\xi^2}{3} \delta_{rs} \right) (\xi^2 - 7) \\ h_{rs}^{(2)}(\vec{X}, t) &= \frac{\pi_{rs}(\vec{X}, t)}{P} \\ h_{rs}^{(4)}(\vec{X}, t) &= \frac{\gamma}{\sqrt{7}P} \sigma_{rs} \end{aligned} \right\} \quad (11)$$

$$\left. \begin{aligned} \pi_{rs}(\vec{X}, t) &= m \int d^3 \xi \left( \xi_r^* \xi_s^* - \frac{\xi^{*2}}{3} \delta_{rs} \right) f(\vec{X}, t) \\ \sigma_{rs}(\vec{X}, t) &= \frac{m}{2} \int d^3 \xi \left( \xi^{*2} - \frac{7}{\gamma} \right) \left( \xi_r^* \xi_s^* - \frac{\xi^{*2}}{3} \delta_{rs} \right) f(\vec{X}, t) \\ \text{and } P &= nkT \end{aligned} \right\} \quad (12)$$

The rate of change of tensorial moment in 13 and 21 moment approximation will be.

$$\frac{\partial h_{rs}^{(2)}}{\partial t} = \omega_c ( \epsilon_{rnm} h_{sm}^{(4)} + \epsilon_{smn} h_{rm}^{(2)} ) - \frac{1}{\tau} ( A_1 h_{rs}^{(2)} + B_1 h_{rs}^{(4)} ) + \frac{1}{\tau} C_{rs}^{(2)} \quad (13)$$

$$\frac{\partial h_{rs}^{(4)}}{\partial t} = \omega_c ( \epsilon_{rnm} h_{rs}^{(4)} + \epsilon_{smn} h_{rm}^{(4)} ) - \frac{1}{\tau} ( A_2 h_{rs}^{(2)} + B_2 h_{rs}^{(4)} ) \quad (14)$$

where  $\omega_c = \frac{ZeB}{mc}$ ,  $Z = 24$  for Cr  $\epsilon_{smn}$  is permutation tensor and given by:

$$\epsilon_{smn} = \begin{cases} 1 & s, m, n \text{ are cyclic} \\ 0 & \text{if two indices are equal} \\ -1 & s, m, n \text{ are not cyclic} \end{cases} \quad (15)$$

$C_{rs} = -\sqrt{2} \mathfrak{I}_{r,spq} \nabla_p U_q$   $\tau$  is collision time,  $\mathfrak{I}_{r,spq}$  is symmetrization operator is defined as:

$$\mathfrak{I}_{r,spq} = \frac{1}{2} ( \delta_{rp} \delta_{sq} + \delta_{rq} \delta_{sp} - \frac{2}{3} \delta_{rs} \delta_{pq} ) \quad (16)$$

$A_1, B_1, A_2, B_2$  are constants evaluated in [6] and equal to

$$A_1 = \frac{3\sqrt{2}}{5}, \quad B_1 = A_2 = -\frac{9\sqrt{7}}{70}, \quad B_2 = \frac{4\sqrt{2}}{56}$$

For slowly varying in time  $\frac{\partial}{\partial t} = 0$  in equation (13) and (14) and then solve equations (13) and (14) for  $h_{rs}^{(2)}$  and  $h_{rs}^{(4)}$  and substitute in the pressure tensor  $\pi_{rs}$  defined by:

$$\pi_{rs} = \sqrt{2} n_{\alpha z} T_{\alpha z} h_{rs}^{(2)} v_{rs} \quad v_{rs} = 2 \mathfrak{J}_{rs/pq} \nabla_p U_q \quad (17)$$

we have the viscosity coefficient of Cr impurity element in tokamak plasma . By using simulation process we get the following result shown in Fig.(1), (2), (3). Equation (17) gives us the values of viscosity coefficients as follows

$$\pi_{rs} = -\eta_B^\alpha v_{rs}$$

B stand for parallel , perpendicular and off-diagonal components. As shown in Fig.(1), (2), (3).

## CONCLUSION

plasma. Contaminate makes it more difficult to achieve net fusion energy condition. The occurrence of heavy (Cr) impurities was Plasma surface interaction impurities which contaminate the monitored spectroscopically. The aim of this work is, calculation of viscosity coefficient of one of the heavy impurity elements, in EGYPTOR tokamak plasma, such as chromium "Cr" [8] . In summary , an analysis of the existing results in Fig.(1-3) of viscosity coefficients of Chromium impurities in tokamak plasma , it is found that the parallel viscosity coefficient for Chromium is approximately the same as the light impurity element. For perpendicular viscosity coefficient for Chromium ion increased with increasing the confinement magnetic field and there is no difference between 13 and 21 moment approximation . The off-diagonal viscosity coefficient for " Cr" is approximately zero for EGYPTOR range . The most effective viscosity coefficient is the perpendicular.

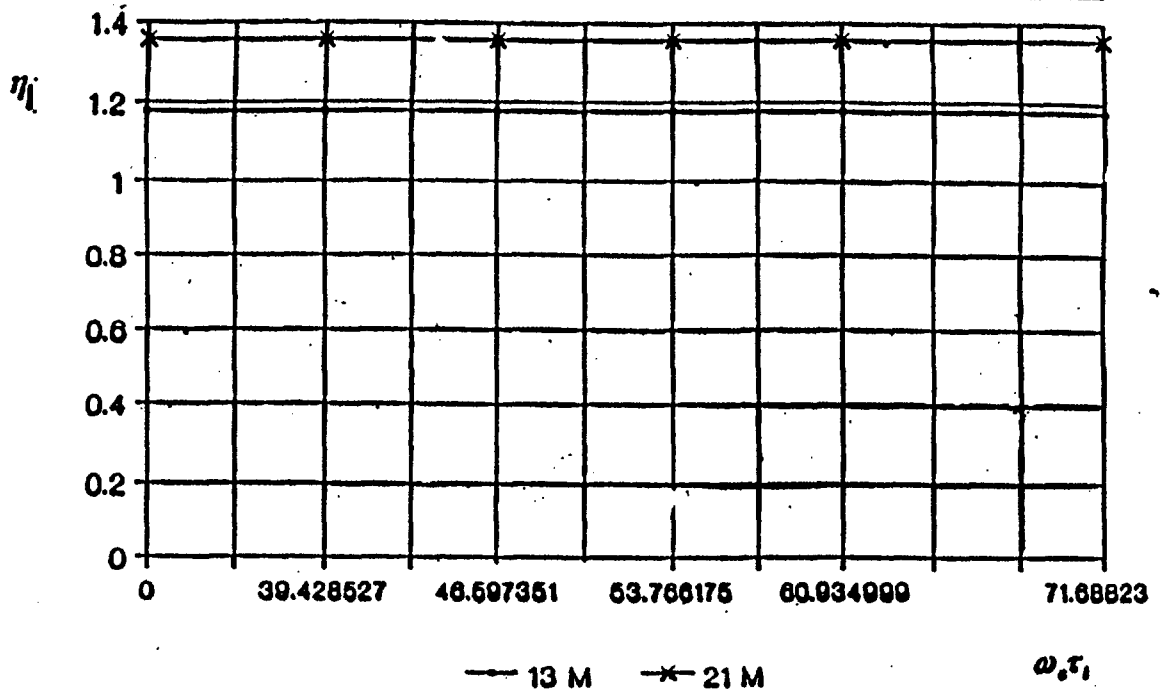


Fig. (1) Parallel Viscosity Coefficient.

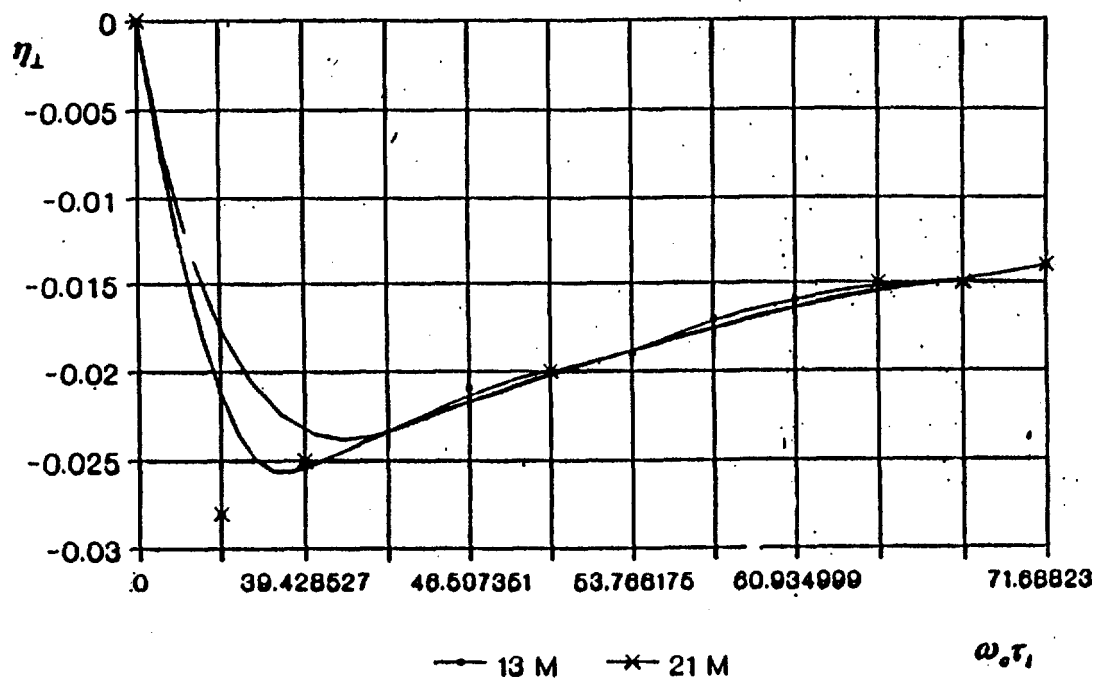


Fig. (2) Perpendicular Viscosity Coefficient.

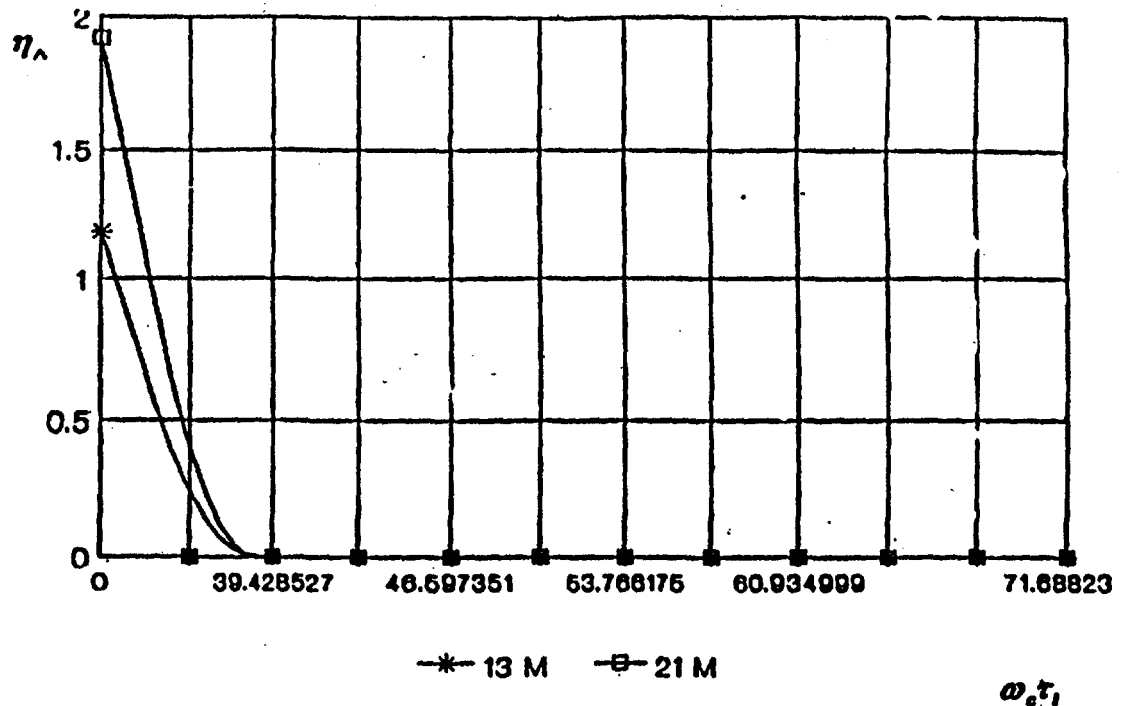


Fig (7) Off-Diagonal Viscosity Coefficient.

## Reference

- [1] Winters, H.F, In Topics In Current Chemistry , Plasma Chemistry III ,eds. S.Veprek and Venugopalan, M., P. 69. Berlin : Springer- verlage , (1980)
- [2] Gaber, F. A. and El-Sharif, R. N., J.FIZ. Mal. 16 , 19, (1995).
- [3] Nedospasove , A. V. and Tokar, Reviews of Plasma Physics 18. P.(176) (1994).
- [4] Claassen, H. A. and Repp, H., Proceeding of the International Symposium on Plasma Wall Interaction."CEC" P.(25) (1977).
- [5] Dong , J. Q., Phys. Plasma 2,september (1995).
- [6] El-Sharif , R. N. and Bakhit , Sixth Conference of Nuclear Sciences and Applications ( Cairo, 15-20 , March 1996) .
- [7] Post P.E. et al, Atomic and Nuclear Date Table 20, 397, (1977) .
- [8] Hackmann, J., Uhlenbusch, J., Nuclear Fusion, vol. 24. no. 5, (1984) .

**SCIENTIFIC SESSION (8)**

**RADIATION PROTECTION**

***Keynote Lecture***

**RELEVANT DOCUMENTS TO IAEA REGULATIONS  
FOR THE SAFE TRANSPORT OF RADIOACTIVE MATERIALS**

**R. M. K. EL-Shinawy \*, M. G. Sabek\*\*, and M. A. Gomaa\***

\* National Research Center, AEA, Cairo, Egypt

\*\* National Center for Nuclear Safety and Radiation Control, AEA,  
Cairo, Egypt

**ABSTRACT**

IAEA regulations for the safe transport of radioactive materials provide standards for insuring a high level of safety of people, property, and environment against radiation, contamination, and criticality hazards as well as thermal effects associated with the transport of radioactive materials. IAEA routinely published technical reports which are relevant to radioactive material transportation such as INTERTRAN, Directory of Transport Packaging Test Facilities, and others. A case study was performed to assess the impact of transporting radioactive materials through the Suez Canal using the two computer codes namely INTERTRAN and RADTRAN-4 which are part of IAEA Technical Documents. A comparison of the results of these two codes is given.

***Contributed Papers***

**EXPOSURES FROM NATURAL AND ARTIFICIAL SOURCES  
OF IONIZING RADIATION IN ROMANIA**

**Olga Iacob**

**Institute of Public Health and Medical Research, Iasi,  
Iasi, Romania**

**ABSTRACT**

An updated review of the data available for assessing the Romanian population exposure from the following natural and artificial sources of ionizing radiation is presented.

- External natural sources: Cosmic rays (ionizing and neutron components) and terrestrial gamma radionuclides ( $^{40}\text{K}$ ,  $^{238}\text{U}$  and  $^{232}\text{Th}$  series) .
- Internal natural sources: Naturally- occurring radionuclides inhaled or ingested in the body ( $^{222}\text{Rn}$  and  $^{220}\text{Rn}$  short lived decay products) and ( $^{40}\text{K}$ ;  $^{238}\text{U} \rightarrow ^{226}\text{Ra}$ ,  $^{210}\text{Pb} \rightarrow ^{210}\text{Po}$ ;  $^{232}\text{Th}$ ) .
- Diagnostic X-ray and Nuclear medicine procedures- as man-made sources of population exposure.

The methods used to estimate the exposures from these sources were specific to each type of radiation source and exposure pathway are described. The results, expressed in terms of average annual per caput effective doses, are 0.33 mSv from cosmic rays, 0.550 mSv from terrestrial gamma radiation, 0.31 mSv from ingestion of long - lived natural radionuclides, 2.08 mSv and 0.28 mSv from inhalation of  $^{222}\text{Rn}$  and  $^{220}\text{Rn}$  Short - lived decay products respectively, 0.62 mSv from diagnostic radiology and 0.06 mSv from diagnostic use of radiopharmaceuticals. Consequently, the annual per caput effective dose from all these these source of ionizing radiation is 4.18 mSv with a corresponding collective dose of about 95, 500 manSv. It is clear that natural sources have the main contribution to the annual average dose ( 83%) and radon progeny inhalation is the dominant source of human exposure. The aim of our periodic reviews is to keep the overall level of population exposure under control in accordance with requirements of the Romanian Legislation for radiological protection of man and his environment.

#### **OUTLINES ON DATA BASE FOR THE USE OF RADIOACTIVE SOURCES, AND ENVIRONMENTAL IMPACT IN EGYPT**

**A. M. Hathout\*, E. Amin\*, Kh. M. El-Said\*, and M.A. Gomaa\*\***

\* National Center for Nuclear Safety and Radiation Control, AEA,

\*\* Reactors Division Nuclear Research Center, AEA Cairo, Egypt.

#### **ABSTRACT**

Radio isotopes and radioactive sources have shown increase applications in scientific research, agriculture, medicine and industry. The prime concern in regulating activities involving the release of radioactive materials into the environment, is ensuring the safety of individuals and population. The

management of radioactive wastes generated from medical centers, research institutes, industrial facilities, mining operations, and research reactors caused serious accidents. Radiation sources mismanagement resulted in injuries or fatalities to individuals. The objectives of this work is to develop the required data base and establish the necessary rules for safe management of radioactive sources.

**COLLECTIVE DOSE OF EGYPTIAN ATOMIC  
ENERGY WORKERS DURING THE PERIOD 1991 - 1995**

**M.A. Gomaa, and S.K. Youssef.**

**Reactors Division, and Radiation Protect. Dept., Nuclear Research Center  
Atomic Energy Authority, Cairo, Egypt**

**ABSTRACT**

The collective dose to Egyptian Atomic Energy Authority workers during the period from 1991 - 1995 were statistically evaluated. The personnel dosimetry in use since 1957 for evaluating external exposure doses was mainly the Harwell blue badge and kodak radiation monitoring Film for X and Gamma photons. The calibration sensitivity of the badge system was evaluated under the 'AL' and/or "Pb/Sn alloy" Filters. The results of calibration showed  $\pm 15\%$  errors in the predicted values for whole body effective doses. The statistical survey showed that the annual collective dose ranged between 0.83-1.54 man Sv. The annual limit of exposure presented 25-58% of the recommended annual limit by ICRP- 60 (1991). Details of the study will be considered in the text.

**CALCULATIONS ON SAFE STORAGE AND TRANSPORTATION  
OF RADIOACTIVE MATERIALS**

**A.M., Hathout, A. M., El Messiry, and E. Amin**

**National Center for Nuclear Safety and Radiation Control and AEA, Cairo, Egypt**

**ABSTRACT**

In this work the safe storage and transportation of fresh fuel as a radioactive material is studied. Egypt planned ET RR 2 reactor which is of relatively high power and would require adequate handling and

transportation. Therefore, the present work is initiated to develop a procedure for safe handling and transportation of radioactive materials. The possibility of reducing the magnitude of radiation transmitted on the exterior of the packages is investigated. Neutron absorbers are used to decrease the neutron flux. Criticality calculations are carried out to ensure the achievement of subcriticality so that the inherent safety can be verified. The discrete ordinate transport code ANISN was used. The results show good agreement with other techniques.

### **A LOGIC SCHEME FOR REGULATING SAFE OPERATION OF RESEARCH REACTORS**

**Ensherah E. Ahmad\*, Ahmad Effat\*\*, and F.A. Rahman\*\***

\* Reactor Department, Nuclear Research Centre, Atomic Energy Authority

\*\* Operational Safety Dept, National Center of Nuclear Safety and Radiation Control  
Atomic Energy Authority, Cairo Egypt.

#### **ABSTRACT**

This investigation presents a logic scheme for regulating the safe operation of research reactor in accordance with the new revision of SS-35 and revised by the 10 CFR. It emphasizes the regulatory inspection and enforcement (RI&E) during the reactor operation phase. It is developed to provide information, guidance and recommendations to be taken when constructing the RI & E program that could be applied to the operational phase of the Egyptian Research Reactors. In the operational phase, the Regulatory inspection (RI) means an examination, observation, measurement, or test undertaken or on behalf of the Nuclear Regulatory Body (NRB) during operation to verify that the nuclear materials, components, systems and structures as well operational activities, processes, procedures and personnel competence and performance are in accordance with the requirements established or the provisions approved by NRB or specified in the operational license or contained in regulations. Regulatory inspection includes both routine and non-routine ones. Any of them may be announced or unannounced. The problems identified by the RI must be resolved by the proper RE actions. The RE actions include investigative and corrective RE actions. These RI & E procedures for regulating safe operation of research reactors are presented as flow charts and then developed as a computer logic



EG9700106

sceme. The software program is very efficient, very friendly, very simple and is interactive in nature such that the program asks the user certain questions about essential steps that guide the (RI & E) for research reactors, and the user responds. The program proceeds based on this response until all the necessary steps for (RI & E) are accomplished.

### STUDY OF $^{124}\text{I}$ CONTAMINATION IN $^{123}\text{I}$ USED IN MEDICAL APPLICATIONS

H. El Samman\*, and W. Arafa\*\*

\* Faculty of Science, Menoufia University, Shbin El kom, Egypt

\*\* Physics Department, Faculty of Women, Ain Shams University, Cairo, Egypt

#### ABSTRACT

The decay of 0.2 mCi capsules of sodium iodide ( $^{123}\text{I}$ ) used for diagnostic purpose and delivered to Hamad hospital in QATAR, was studied using HPGe detector of (30% efficiency and 1.8 KeV energy resolution), coupled to a computer based 4096 multichannel analyzer. The acquisition parameters were controlled by computer program. The gamma spectra were analyzed using well developed gamma spectrum analysis program gamanl. Results showed that the isotope used is not pure  $^{123}\text{I}$  but it is a mixture of  $^{123}\text{I}$  and  $^{124}\text{I}$ . The percentage of the unwanted  $^{124}\text{I}$  isotope was estimated to be 15%. The dose taken by the patient due to the unwanted  $^{124}\text{I}$  isotope was estimated. Half-lives time of the  $^{123}\text{I}$  and  $^{124}\text{I}$  isotopes were determined with high accuracy and compared to the published values.

## **I- INTRODUCTION**

The IAEA regulations for the safe transport of radioactive material provide standards for insuring a high level of safety of people, property, and environment against radiation, contamination, and criticality hazards as well as thermal effects associated with the transport of radioactive materials.

Safety in the transport of radioactive materials is dependent on packaging appropriate for the contents being shipped, rather than on operational and/or administrative actions required on the package. The greater the risk posed by the material being moved, the more stringent become the performance standards for the packaging that can be authorized to contain it.

These principles have been expanded since 1961 into a set regulations that have been responsible for safely moving the ever-growing number and complexity of radioactive material shipments throughout the world.

Safety series No. 6 elaborates requirements for the design, fabrication and maintenance of packaging as well as those for preparation, consigning, handling, carriage, storage in transit, and receipt of the packages at final destination. Approval is required for the design or shipment of consignments and is issued in the form of certificates.

## **II- RELEVANT DOCUMENTS**

The IAEA routinely publishes technical reports in a series named **TEChnical DOCuments** or **TECDOC's**, and there are several **TECDOC's** which are relevant to radioactive material transportation. Each of these **TECDOC** publications is recommended as a valuable reference document on particular aspects of transport safety and of the IAEA regulations.

**1) INTERTRAN (IAEA-TECDOC-287) : A System for Assessing the Impact from transporting radioactive Material, IAEA, Vienna, 1983, [1].** The IAEA's Standing Advisory Group on Safe Transport of Radioactive Materials (SAGSTRAM) at its meetings in Oct. 1978 and April 1980 recommended that the IAEA initiate a risk assessment program intended to develop a simple method of risk analysis that could be applied to the transport of radioactive materials throughout the world. In August 1980, it was decided that the American computer code **RADTRAN II** should be the basis for the development of an international code **INTERTRAN**. **RADTRAN II** is an extended version of the earlier **RADTRAN** which was used in performing the **USNUREG-0170** study. **RADTRAN** and **RADTRAN II** were both developed by Sandia National Laboratories, Albuquerque, NM., USA. The **RADTRAN II** computer code was changed and reworked to meet the needs of this special project. The methodology as well as formatting and data of the input and output were changed to make the code more internationally oriented.

The computer code **INTERTRAN** calculates the radiological impact from incident-free transports and vehicular accidents involving radioactive materials. The code also addresses accident which may occur during handling operations.

**2) RADTRAN-4 (August 1993, SAND89-2370 . TTC-0943 . UC-722, also will be published as IAEA-TECDOC report):** Sandia National Laboratories (SNL) developed the original **RADTRAN-I** code in 1977 in conjunction with the preparation of **NUREG-170**. The analytical capabilities of the code were expanded

and refined in subsequent versions (RADTRAN-II in 1982, RADTRAN-III in 1986, and finally the more advanced one RADTRAN-4 in 1993). RADTRAN-4 [2] is a FORTRAN 77 computer code and used to estimate radiological risks associated with incident-free transportation of radioactive materials and with accidents that might occur during transportation. Incident-free (or normal) transportation is defined as transportation during which no accident, packaging, or handling abnormality or malevolent attack occurs. RADTRAN-4 contains idealized mathematical models of transportation environments; these models have been formulated to yield conservative estimates of integrated population dose in a way that can be supported by available data. An internal library of isotope-related parameter values has been added, which contains data on over 50 of the most commonly transported radioisotopes. The user, however, may continue to independently define isotopes.

**3) Directory of Transport Packaging Test Facilities (IAEA-TECDOC-295), IAEA, Vienna, 1983.**

The directory [4] lists the facilities and services existing in some Member States which can be made available for use by other states by arrangement. Also, it gives the technical information on the facilities, the services, the tests that can be done and in some cases even the financial arrangement is included.

This directory is useful for those with an interest in package testing who do not have their own facilities.

**4) Transport of Radioactive Materials by Post (IAEA-TECDOC-318); IAEA, Vienna, 1984.[5]**

As its title implies, this deals with the postal traffic of radioactive material.

**5) Discussion of and Guidance on the Optimization of Radiation Protection in the Transport of Radioactive Material(IAEA-TECDOC-374),IAEA, Vienna, 1986.[6].**

The application of the optimization process is a requirement of Safety Series No.6 and Safety Series No.80. This document provides guidance on the second component of the system of dose limitation (optimization) as it applies to the transport of radioactive material. Also, it represents the first step in providing guidance for this process. It is planned that after suitable review, use and revision, this material will be published as one of a set of Safety Series on radiation protection optimization.

**6) International Studies on Certain Aspects of the Safe Transport of Radioactive Materials (IAEA-tecdoc-375), IAEA, Vienna, 1986.**

This document [7] contains final summary reports on the Agency's Coordinated Research Program on Safe Transport of Radioactive Material which started in 1980. It includes a discussion of research on:

- the basis of activity limits used in the regulations;
- the structural and thermal response of packages to various environments;
- the development of INTERTRAN; and
- the risks and exposures resulting from radioactive material transport.

- 7) **Directory of National Component Authorities Approval Certificates for Packages, Shipments, Special Arrangements and special Form Radioactive Material (IAEA-TECDOC-389) 1986, (IAEA-TECDOC-442) 1987, (IAEA-TECDOC-552) 1990, (IAEA-TECDOC-617) 1991, and (IAEA-TECDOC-662) 1992, IAEA, Vienna, [8,9,10, and 11].**

The purpose of this directory is to facilitate the transfer of information to competent authorities on the packaging, authorized contents or special conditions pertinent to any package or shipment. It enables competent authorities to be aware of the state of any certificate submitted for validation. It also, indicates any change in status of any certificate already validated.

- 8) **Assessment of the Radiological Impact of the Transport of Radioactive Materials, (IAEA-TECDOC-398), IAEA, Vienna, 1986.**

This document [12] is of particular importance in presenting the results of the technical committee which met in October 1985 to examine the evidence on the radiation exposure of the public and workers due to transport of radioactive material, including accidents. A very significant statement was made in this report (page 27): "As an overall view, from the information currently available, it can be reasonably asserted that exposures of most workers and of the public in normal transport are low. Only in a few cases do workers receive doses which are more than a significant fraction of applicable limits. It is also believed, and this is confirmed by experience to date, that the risks to workers and the public due to potential accidents and incidents in transport are also low."

- 9) **Assessment of the Application of the IAEA Regulations for the Safe Transport of Radioactive Material (IAEA-TECDOC-399), IAEA, Vienna, 1986 [13].**

The results of an examination of the ways in which Member States implement the IAEA Regulation are presented in this report. All the Member States involved in this examination regulate the transport of radioactive material within their country on the basis of international agreements, regulations, and recommendations.

- 10) **Competent Authority Regulatory Control of the Transport of Radioactive Material (IAEA-TECDOC-413), IAEA, Vienna, 1987 [14].**

The purpose of this guide is to assist competent authorities in regulating the transport of radioactive material and to assist users of transport regulations in their interactions with competent authorities. This technical document specifically covers various aspects of the competent authority implementation of IAEA regulations for the safe transport of radioactive material. In addition, physical protection and safeguards control of the transport of nuclear materials as well as third party liability aspects are also given.

- 11) **Recommendations for Providing Protection during the Transport of Uranium Hexafluoride (IAEA-TECDOC-423), IAEA, Vienna, 1987 [15].**

The document summarizes the international regulations and standards which currently exist for controlling the packages and the transport of  $UF_6$  and the recommended additional requirements. These recommendations are currently under consideration by IAEA, its Standing Advisory Group on the Safe Transport

of Radioactive Materials, and Member States. The purpose of this document to provide guidance on the safe transport of  $UF_6$ .

**12) National Competent Authorities Responsible for Approvals and Authorizations in Respects of the Transport of Radioactive Material (IAEA-NCAL), IAEA, Vienna [16].**

The IAEA transport regulations lay down certain authorizations and approvals which have to be given an appropriate competent authority for national and international transport of radioactive material. This list of national competent authorities is based on information supplied by the respective Member States and is updated and issued annually by the IAEA. It is very useful and enables the various competent authorities to easily communicate with each other.

**III- Case Study**

In this section, the two computer codes INTERTRAN and RADTRAN-4 are good examples showing that IAEA updating always its tools for assessing the impact of transporting radioactive materials.

INTERTRAN (1983) was the first code used by IAEA and was based, as stated above, on RADTRAN II(1982). The code RADTRAN-4(1993) is the more advanced one used by IAEA risk assessment calculations for transporting radioactive materials. The two codes estimate the radiological risks associated with incident-free transportation of radioactive materials and with accidents that might occur during transportation.

RADTRAN-4 Code contains idealized mathematical models of transportation environment. Also, the code contains an internal data library for more than 50 of the most commonly transported radioisotopes. The code has an advantage that allow the program users to define any isotopes not included in the data library.

A large amount of input data were used by the two codes and the detailed description of these input data are presented in [1 and 2].

**III-1 Results and Discussions**

The calculations were based on actual records of radioactive material transported through the Suez Canal in the period 1986-1992.

Table 1 gives a comparison between the codes for the contribution percentage of each radioactive material to the total calculated value of the Incident-Free Population Exposure.

Tables 2 and 3 provide a Radiological Risks result comparison between the two codes for the contribution percentage of each radioactive material in case of the three towns of Suez Canal Area.

From the above tables there are, generally, some inconsistency between the results of the two codes. This inconsistency may be due to :

- a) Calculational models in the two codes are different.
- b) INTERTRAN code used many default values in its input data.
- c) there are great discrepancies between the isotopes data library of the two codes; e.g.:

- the value of deposition velocity for isotopes  $Co^{60}$ ,  $U^{235}$ ,  $U^{238}$ , and  $CF^{252}$  is

# PROC *Third Radiation Physics Conf., Al-Minia, 13 - 17 Nov., 1996*

equal to  $2.0 \cdot 10^{-3}$  in INTERTRAN, while in RADTRAN-4 the value is  $1.0 \cdot 10^{-4}$ .  
 - the photon energy for  $CF^{252}$  is equal to  $1.2 \cdot 10^{-3}$  in RADTRAN-4 code, while in INTERTRAN is equal to 9.00.

For these above reasons, in any risk analysis for radioactive material transportation we depend only on the results of RADTRAN-4 code.

Table 1 was given only for Ismailia town because in incident-free ( normal case ) there is no accident occur and the results for the other two towns in Suez Canal area (Port-Said, and Suez) are approximately the same.

From table 3, GE contrib.%, one can see that there are different results in the three towns and this may be due to the different of the atmospheric dispersion parameters in these towns. In LCF results, table 2 the values are approximately the same.

**Table ( 1 ) Incident-Free Population Exposure in Person-Rem Suez Canal (Ismailia, 1986-1992)**

Material	RADTRAN-4 Contrib. %	INTRETRAN Contrib. %
Co <sup>60</sup>	2.74	1.10
Cs <sup>137</sup>	9.18	0.86
UF <sub>6</sub>	42.66	19.91
U <sub>3</sub> O <sub>8</sub>	38.40	74.10
UO <sub>2</sub>	6.60	3.56
CF <sup>252</sup>	0.008	0.004
Kr <sup>85</sup>	0.216	0.100
H <sup>3</sup>	0.448	0.208

**Table ( 2 ) Radiological Risks, LCF contrib. % Suez Canal(1986-1992)**

Material	RADTRAN-4			INTERTRAN		
	Port-Said	Ismailia	Suez	Port-Said	Ismailia	Suez
Co <sup>60</sup>	5.59	5.99	6.45	12.37	12.19	15.66
Cs <sup>137</sup>	0.03	0.02	0.02	0.04	0.04	0.05
UF <sub>6</sub>	82.58	86.54	86.13	44.23	37.69	38.66
U <sub>3</sub> O <sub>8</sub>	11.26	7.05	7.13	42.04	48.38	44.26
UO <sub>2</sub>	0.42	0.27	0.27	1.29	1.56	1.42
CF <sup>252</sup>	0.00	0.00	0.00	0.00	0.00	0.00
Kr <sup>85</sup>	0.00	0.00	0.00	0.00	0.00	0.00
H <sup>3</sup>	0.01	0.02	0.02	0.01	0.01	0.01

Table ( 3 ) Radiological Risks, GE contrib. %  
Suez Canal (Ismailia, 1986-1992)

Material	RADTRAN-4			INTERTRAN		
	Port-Said	Ismailia	Suez	Port-Said	Ismailia	Suez
Co <sup>60</sup>	64.17	84.08	77.87	26.32	41.58	47.15
Cs <sup>137</sup>	0.35	0.29	0.27	0.09	0.14	0.16
UF <sub>6</sub>	22.28	10.38	15.66	65.69	52.81	47.95
U <sub>3</sub> O <sub>8</sub>	13.05	4.43	5.97	7.60	5.38	4.56
UO <sub>2</sub>	0.21	0.08	0.10	0.22	0.18	0.15
CF <sup>252</sup>	0.00	0.00	0.00	0.00	0.00	0.00
Kr <sup>85</sup>	0.00	0.00	0.00	0.00	0.00	0.00
H <sup>3</sup>	0.04	0.12	0.07	0.03	0.07	0.05

## REFERENCES

- 1) IAEA, " Regulations for the Safe Transport of Radioactive Material", Safety Series No. 6, IAEA, Vienna 1961, 1967, 1973, 1985.
- 2) IAEA, " INTERTRAN : A System For Assessing The Impact From Transporting Radioactive Material", IAEA-TECDOC-287, Vienna, 1983.
- 3) K.S. Neuhauser, F.L. Kanipe, " RADTRAN-4, vols 1-4", Sandia Report SAND89-2370 TTC-0943 UC-722 printed 1993. Also to be published as IAEA.
- 4) IAEA, " A Directory of Transport Packaging Test Facilities", IAEA-TECDOC-295, IAEA, Vienna, 1983.
- 5) IAEA, " Transport of Radioactive Materials By Post", IAEA-TECDOC-318, IAEA, Vienna, 1984.
- 6) IAEA, " Discussion of and Guidance on the Optimization of Radiation Protection in Transport of Radioactive Material", IAEA-TECDOC-374, IAEA, Vienna, 1986.
- 7) IAEA, " International Studies on Certain Aspects of the Safe Transport of Radioactive Materials", IAEA-TECDOC-375, IAEA, Vienna, 1986.
- 8) IAEA, " Directory of National Component Authorities' Approval Certificates for Packages, Shipments, Special Arrangements and Special Form Radioactive Material", IAEA-TECDOC-389, IAEA, Vienna, 1986.
- 9) IAEA, " Directory of National Component Authorities' Approval Certificates for Packages, Shipments, Special Arrangements and Special Form Radioactive Material", IAEA-TECDOC-442, IAEA, Vienna, 1987.
- 10) IAEA, " Directory of National Component Authorities' Approval Certificates for

Packages Design and Shipment of Radioactive Material", IAEA-TECDOC-552, IAEA, Vienna, 1990.

- 11) IAEA, " Directory of National Component Authorities' Approval Certificates for Packages Design, Special Form Material and Shipment of Radioactive Material", IAEA-TECDOC-617, IAEA, Vienna, 1991.
- 12) IAEA, " Assessment of the Radiological Impact of the Transport of Radioactive Materials", IAEA-TECDOC-398, IAEA, Vienna, 1986.
- 13) IAEA, " Assessment of the Application of the IAEA Regulations for the Safe Transport of Radioactive Material", IAEA-TECDOC-399, IAEA, Vienna, 1986.
- 14) IAEA, " Component Authority Regulatory Control of the Transport of Radioactive Material ", IAEA-TECDOC-4413, IAEA, Vienna, 1987.
- 15) IAEA, " Recommendations for Providing Protection during the Transport of Uranium Hexafluoride", IAEA-TECDOC-423, IAEA, Vienna, 1987.
- 16) IAEA, " National Component Authorities Responsible for Approvals and Authorizations in Respect of the Transport of Radioactive Material", IAEA-NCAL, IAEA, Vienna, (annually since 1967).



EG9700107

**OUT LINES OF A DATABASE FOR RADIOACTIVE SOURCES ,  
ITS APPLICATION AND ITS ENVIRONMENTAL  
IMPACT IN EGYPT**

**A. M. Hathout , E. Amin , Kh. M. El-Said and M. A. Gomaa\***

**National Center for Nuclear Safety and Radiation Control, NCNSRC,  
\*Nuclear Research Center , NRC,  
Atomic Energy Authority , AEA,  
Cairo , Egypt**

**ABSTRACT**

Radio-isotopes and radio-active sources have found increased applications in our scientific technical world. The extent and the variability of these applications are in scientific research , agriculture , medicine and industrial production. The prime concern , in regulating activities involving the release of radioactive materials into the environment , is ensuring the protection of human individuals and population . The management of nuclear wastes generated from medical center, research institutes , industrial facilities , mining operations and research reactors has lapses causing serious accidents. Radiation sources mismanagement has resulted in injuries or fatalities to the public.

The primary purpose of the impact analysis methodology is to provide a tool to enable determination of specific values of parameters that can be controlled and / or specified through technological or administrative action so as to assure the goals achievements . These goals are the long term and short term protection of the human environment.

The objective of this study is to develop the required database and establish the necessary rules for safe management of radioactive sources.

**INTRODUCTION**

The progress resulting , from the employment of radioactive substances in medicine , industry , mining and research has to be carefully considered against genetic and somatic radiation risk to both the individuals and the entire population. Exact knowledge of radiation burden , caused by various radioactive sources application is therefore a prerequisite.

The long term protection of the human environment may be achieved by reducing to acceptable level for :-

- 1- radiological impacts to members of the public ,

and

2- long term social commitment .

The level of radiological impact may be quantified through calculating individual and population exposures resulting from handling and disposal of sources.

Radiation sources in Egypt are divided into two main categories. The first is referred to as open sources. The Egyptian Atomic Energy Authority , EAEA , takes the responsibility of this source type. The other category , which is the responsibility of the Ministry of Health , is what is called sealed sources.

This study is aimed to promote a harmonized approach to optimizing occupational and public radiation protection by developing procedures to collect information on radioactive sources and identify parameters that done through DATABASE for radioactive sources in Egypt. The development and updating of a DATABASE for radioactive sources is a major step in the quantification of radiological impact.

A complicated and length series of activities is conducted to collect and analyze informations for all possible radiation sources , in use or out of use in Egypt. An extensive national co-operation has evolved within the country. This co-operation will prove to be of at most importance and the results of collaborative work will be utilized by all organizations dealing with radioactive sources.

#### **SCOPE ON THE PROPOSED STUDY :-**

The study will cover three major areas of work :-

- i - database ,
  - ii - methodologies ,
- and
- iii - support for implementing comparative assessments.

The DATABASE will be established. it contains numerical , textual and inventory informations on the main characteristics of radiation sources. Many parameters are taken into considerations. These parameters are covering technical, performance , costs , atmospheric emissions , wastes and other environmental burdens.

Industrial regions , hospitals , medical centers and research institutes are asked to assist in implementing the desired specific data required. Computer programmes are used for data collection , storage , search and analysis. The collection of data is done using national questionnaire. The NCNSRC is responsible for the collection of informations , quality control of data , storage and protection of the informations.

The full DATABASE will be updated annually and distributed to all national participant utilities. The dissemination of information is one of the most important task of the National Regions. For that purpose, the NCNSRC work in close collaboration with other centers using radioactive materials, shall guarantee to the participants the access of continuously updated information and install the updated computer programmes.

The long-term protection of the human environment may be achieved by reducing to acceptable levels :

1 - radiological impact to the members of public ,

and

2 - long term social commitment.

The level of radiological impacts may be quantified through calculating individuals and population exposures resulting from handling and disposal of sources. The level of long term cost for site control and surveillances.

The task of collecting the large amounts of data , to compile and evaluate them , and to make them available in formate needed by users can be done only by a well co-ordinated national efforts. This approach avoids duplication and maximize the use of specialized experts in the co-operating centres and regions [1].

## **SOURCES OF RADIATIONS**

Radiation is natural part of our environment. Natural radiation reaches earth from outer space and continuously radiates from the rocks, soil and water on the earth. Humankind discovered how to use radioactivity to strengthen products, improve medical treatment and produce energy. The pie chart (Fig. 1) shows that most radiation (82%) , people are exposed to comes from natural sources. The largest source is radon , an odorless, colorless gas given by natural radium in the earth crust. Artificial or man made radiation mostly from medical uses and consumer products , accounts for 18 % of our total exposure [2,3]. The nuclear industry is responsible for less than one percent. Table(1) gives the annual dose from natural radiation sources in the environment in the areas of normal background radiation and the long term committed dose from man made source[4].

The sources of radiation are [5,6]:

i - Environment sources such as cosmic radiation and the environmental radioactivity in air , water, soil and food products.

ii - Machine sources , as medical X-ray machines , accelerators and analytical device.

iii - Nuclear fuel cycle facilities such as:-

- a - Uranium mining ,
  - b - Fuel production and processing ,
  - c - Research reactors ,
- and
- d - Wast management.

Tables (2) and (3) give the principle activation products released from fuel assemblies during pool storage and the principal fission products released to spent fuel pool waters[7]. The need to gain greater understanding of radioactive nuclides behaviour in the environment is linked to the plans for cleaning up the environmental contamination.

source characteristics [6]:

- 1 - The probability of decay ,
  - 2 - The half-life , the time required for the activity to decay to one half of the initial value ,
  - 3 - Air kerma rate factors , where kerma is the initial kinetic energy of electrons and ions generated by interactions of photons and neutrons in unit mass of the specified material ,
  - 4 - The value of gamma-rays energy emitted and its spectrum ,
  - 5 - The availability of use , medical therapy , research , or, industrial ,
- and
- 6 - its impact on health and environment.

## METHODOLOGIES

Two main task had been undertaken on methodologies :

- 1 - The preparation of a report describing already available computer tools for comparative assessment ,
- 2- The development and updating of databases are linked to enable the costs analysis airborne emissions, radiation releases and other health and environmental burdens of different sources.

Several papers stressed the continuing need to improve databases and analytical tools , so that uncertainties in data and results can be reduced. Due to the increasing of public concern about health and environmental aspects of radioactive sources , it may be expected that such studies will have a greater influence on future descisions. The comparative assessment approaches are capable of providing decision makers with scientifically correct and understandable informations.

Scientists and analysts still have a long way to go in order to provide the type of comprehensive informations that are needed by decision-makers. The uncertainties that still prevail in data and in results from modelling studies make it impossible to give definitive answers to all the questions. Thus , there is a need for more co-

operative and exchange between analysts and decision-makers to transfere adequate informations and useful results from studies to those responsible for policy making.

The database is to examine the long and short term options and strategies for radioactive sources. Kinds of national questionnaire must be formulated and distributed to all of the users , to collect all informations and requirements.

**CONCLUSION REMARKS :**

- 1- The database is a very important source for theoretical work and mathematical modelling and can be established as reference technology.
- 2- The main frame VAX-6320 computer system is used to store all informations about radioactive sources in Egypt.
- 3- The database contain numerical , textual and visual informations on the main characteristics of radioactive sources.
- 4- The parameters taken into considerations are covering technical performance, costs atmospheric emissions ,wastes and other environmental burdens.
- 5- The collaborative work will be utilized by the organizations dealing with radioactive isotopes and sources..
- 6- The future development and extension in the application of radioactive sources is dependent on our ability to handle and dispose the radioactive waste in a safe and acceptable manner.
- 7- The technique for disposal exists, but the methods for assuring the safety still need more development, using updated databases.
- 8- The database will facilitate and decrease the time to obtain the public openion , acceptance of nuclear facilities and uses of radioactive sources.
- 9- The safety authorities require a considerable database to make a thorough safety analysis for the proposed failiity and repository.
- 10- Required data files can be obtained on a magetic tape or on computer diskettes, t together with documentation on the formal and origin of the data.

TABLE(1) : Annual Dose from Natural Radiation Sources in the Environment  
(in areas of normal background radiation)

Source	External	internal	total
Cosmic rays	380		380
Cosmogenic radionuclides		12	12
terrestrial radionuclides			
Potassium 40	130	170	300
Uranium 238 series			
<sup>238</sup> U, <sup>234</sup> U, Thorium	140	1	
Radium 226		4	1400
Radon 222, polonium 214		1200	
Lead 210, Polonium 210		50	
Thorium 232 series	190	80	270
<b>Total (rounded)</b>	<b>840</b>	<b>1520</b>	<b>2400</b>

**Long Term Committed Doses from Man Made Sources**

Source	Main radionuclides	collective effective dose (man-sv)
Atmospheric nuclear testing	Carbon-14, Caesium-137, Strontium-90, Zirconium-95	30 000 000
Chernobyl accident	Caesium 137, Caesium 134, Iodine 131	600 000
Nuclear power production	Carbon-14, Radon-222	400 000
Radioisotope production and use	Carbon-14	80 000
Nuclear weapons fabrication	Caesium 137, Ruthenium 106, Zirconium 95	60 000
Kyslym accident	Cerium 144, Zirconium 95, strontium 90	2 500
Satellite entries	Iodine 131, Polonium 210, Caesium 137	2 100
Windscale accidents	Caesium 137, Xenon 133, Cobalt 60, tridium 192	300
Underground nuclear testing	Iodine 131	200

TABLE (2) : PRINCIPAL ACTIVATION PRODUCTS RELEASED FORM FUEL ASSEMBLIES DURING POOL STORAGE

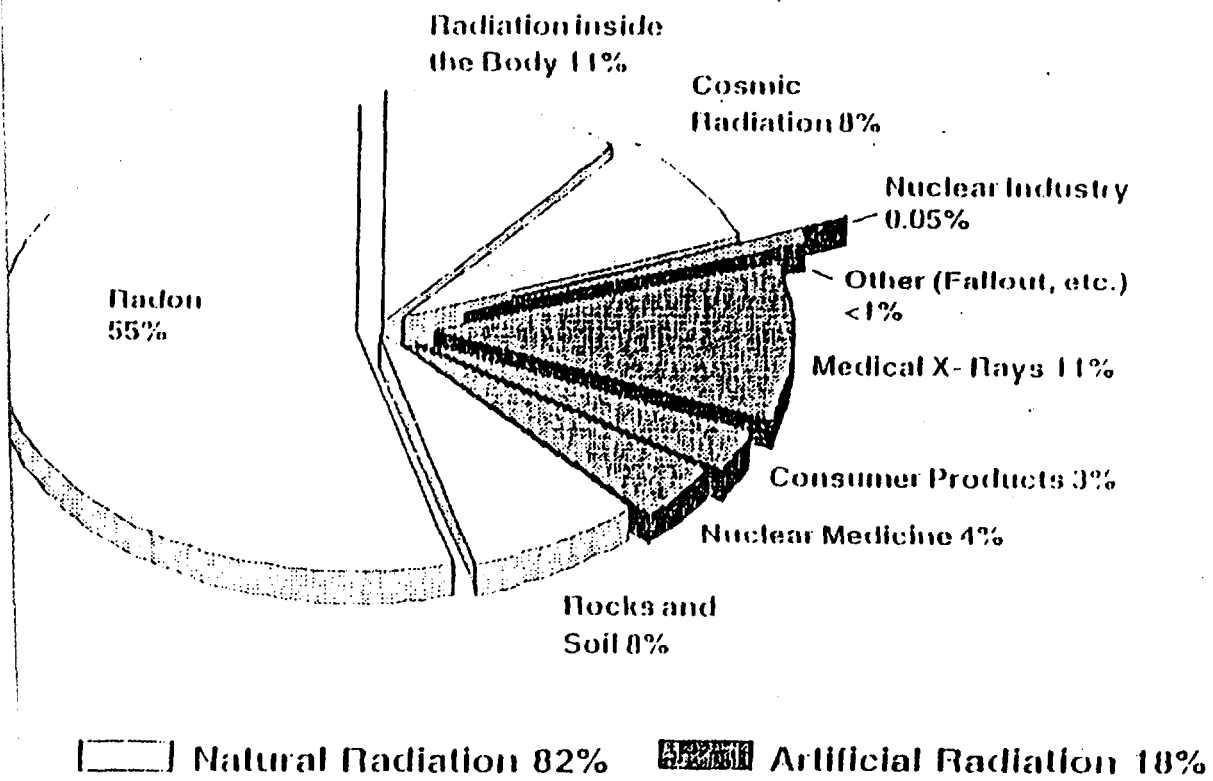
Nucleide	Half life	Production reaction
$^{184}\text{W}^a$	24 hours	$^{187}\text{W}(n-\gamma)$
$^{65}\text{Ni}^a$	25 days	$^{64}\text{Ni}(n-\gamma)$
$^{51}\text{Cr}$	28 days	$^{50}\text{Cr}(n-\gamma)$
$^{59}\text{Fe}$	45 days	$^{58}\text{Fe}(n-\gamma)$
$^{58}\text{Co}$	72 days	$^{58}\text{Ni}(n-p)$
$^{65}\text{Zn}$	243 days	$^{64}\text{Zn}(n-\gamma)$
$^{54}\text{Mn}$	310 days	$^{54}\text{Fe}(n-p)$
$^{60}\text{Co}$	53 days	$^{59}\text{Co}(n-\gamma)$

Only significant in AR pools

TABALE (3) PRINCIPAL FISSION PRODUCTS RELEASED TO SPENT FUEL POOL WATER

Isotope	Half-life
$^{131}\text{I}^a$	8.05 days
$^{126}\text{Sb}^a$	12.4 days
$^{124}\text{Sb}^a$	60.2 days
$^{95}\text{Zr}-^{95}\text{Nb}^a$	65 - 35 days
$^{144}\text{Ce}$	285 days
$^{106}\text{Ru}-^{106}\text{Rh}^a$	1.0 year to 2.2 hours
$^{134}\text{Cs}^b$	2.1 years
$^{125}\text{Sb}$	2.7 years
$^3\text{H}$	12.3 years
$^{90}\text{Sr}$	28.8 years
$^{137}\text{Cs}$	30 years

FIG (1): Common Sources of Radiation Exposure



44

# **PROC** *Third Radiation Physics Conf., Al-Minia, 13 - 17 Nov., 1996*

---

- 1- H. Lemmel, " Nuclear Data for Science and Technology : Centres for Development " IAEA Bulletin, A quarterly journal of the IAEA, Vol. 38, No.2, p. 34, 1996.
- 2- Committed Results : Doe's Environmental management Programme, An Introduction, DOE / EM - 0 152 p, 1994.
- 3- Environmental Management, Fact Sheets, U. S. DOE / EM - 0071p, 1994.
- 4- Gordon Linsley, "Environmental Impact of Radioactive Releases: Addressing Global Issues " , Topical Reports, Quarterly Journal of the IAEA, Vol. 38, No. 1, p. 36, 1996.
- 5- K. T. Thomas, W. Bucher and G. R. Plumb, "Radioactive Waste Management in Developing Countries : New Activities have been initiated to adress needs and problems", IAEA Bulletin, Quarterly Journal of the IAEA, Vienna, Austria, Vol. 31, No. 4, 1989.
- 6- A. E. Profio, "Radiation Shielding and Dosimetry", 1979.
- 7- Technical Reports Series No. 218, "Storage of Water Reactor Spent Fuel in Water Pools", Survey of World Exposure, IAEA, Vienna, Vienna, 1982.



# COLLECTIVE DOSE TO EGYPTIAN ATOMIC ENERGY WORKERS IN THE PERIOD 1991-1995

GOMAA M.A., and YOUSSEF S.K.

*ATOMIC REACTOR DIVISION,  
Radiation Protect. Dept., Nuclear,  
Research Center, Atomic Energy Authority,  
Cairo, Egypt.*

## Abstract

The collective dose to Egyptian Atomic Energy Authority workers in the period from 1991-1995 were statistically deduced. The personnel dosimetry in use since 1957 for evaluating external exposure doses is mainly the Harwell blue badge and Kodak radiation monitoring Film for x and gamma photons. The calibration sensitivity of the badge system was evaluated under the "AL" and/or "Pb/sn alloy" Filters. The results of calibration showed  $\pm 15\%$  errors in the predicted values of whole body effective exposure doses. The statistical survey showed that, the yearly annual and collective dose is respectively ranged over 0.83-1.54 man Sv, with more details is also noted in the manuscript. The annual limit of exposure presents 25-58% of the recommended limity by ICRP-60 (1991).

## (1) Introduction

In the Egyptian Atomic Energy Authority "AEA" a wide spectrum of sealed and unsealed sources are used in different research and technological programs. These sources are presented in different buildings of the various AEA Centers and their different divisions. Among radiation installations and sources are the reactor, Accelerator, gamma cell, radioisotope production laboratory, in addition to the unsealed radiation sources used by the radiobiologist, radiation protection staff members and radiochemists. The use of these wide spectrum of radiation sources in various fields subjected their users to external and/or internal radiation sources. Exposure to high level ionizing radiation might cause cancer there remain considerable uncentainty as magnitude of the risk in man following low level exposure recieved over a period of many years. Early occupational studies<sup>(1)</sup> of radiobiologist underground minors and painters

have not yield reliable dose response data at levels exposure commonly experienced to day. Mortality surveys of workers at nuclear facilities<sup>(2-8)</sup> have not provide risk estimates of usufull precesion<sup>(9,10)</sup>.

In the Egyptian AEA, radiation protection department is mainly responsible to maintain whatever relevant protection against hazards of radiation to various users. For external radiation exposures, the film badge system is in use. The Atomic Energy Program was established in 1957 and personnel occupational exposure were reported yearly as early as 1961<sup>(11-14)</sup>.

Moreover, the main objective of radiation protection program are to keep radiation doses recieved as low as reasonably achievable <sup>(16)</sup>. For the comulative person dose equivalent, and below regulatory limits, concepts of ALARA recommended by ICRP<sup>(17)</sup>. Studies of radiation worker exposures in Egypt are to follow up the utilization of the ALARA concepts recommeded by the International comission on Radiological protection "ICRP"<sup>(17)</sup>. This was achieved according to the us federal registration office, the radiation to which the occupational are exposed should be reported on an annual aggregate base. Also, personnel of employee who had recieved whole body effective comulative dose in the range of 20 mSv/y and/or 6mSv/4m. should require a utility report.

The present study presents, (a) the camulative and collective dose of the AEA study radiation workers over the period 1991-1995., (b) an existing standard dose registry system for AEA workers based on the concepts and philosophy of ALARA<sup>(16)</sup>, and (c) An intercomparison between AEA workers exposure with that recommended dose limit in ICRP-60 (1991)<sup>(15)</sup>.

## **(2) Personnel Dosimetry System**

The personnel dosimetry system in use is the Harwell blue badge and Kodak radiation monitoring Film. Fig.(1) show an schematic diagram of the blue badge and the position of the fixed filters on the badge. The calibration sensitivity of the photographic Film was estimated under different filters as shown in Figures(2 and 3) respectively. For X-ray photons of potential energy 40, 70 and 100 KVP, and gamma photons of 661 KeV; Cs-137; as well as 1250 KeV; average energy of Co-60 cascade gamma lines 1170 and 1320 KeV<sup>(18)</sup>. Detailed studies of various exposures showed that, most users exposures was due to gamma radiation. Hence forth, users doses was estimated under the lead and/or AL filters.

Both filters showed nearly flat energy response with a deviation of +6-8% when compared equivalent dose of X-ray photons of potential energies 40-100 KVP with that of gamma photons above 100 Kev<sup>(18)</sup>. The calibration sensitivity of both Filters are corrected for Film fading, angular missalignment as shown in Figure(6)<sup>(18)</sup>, in addition to the system statistical instability<sup>(18)</sup>. The overall reproducible accuracy in the evaluated users annual exposure is found to be  $\pm 15\%$ <sup>(18)</sup>.

### **(3) Personnel Dosimetry Registration System**

The effective whole body doses due to external radiation for each worker received during each unique exposure time were summed to arrive cumulative dose during the period 1991-1995. The Film badge system is mainly recorded the received cumulative effective dose to natural background, and  $\gamma$  photons of the different radiation sources.

The career average annual whole body dose  $D_a$  is

$$D_a = 1/n \sum_i N_i d_i$$

where

$i$  = is noted a group number 1,2,3,4,... who might receive respective average exposure < 1, 1-5, 5-10, 10-20,...etc.

$N_i$  = is the number of workers in each group or division and/or center.

The collective dose  $S = \sum_i N_i d_i$ .

### **(4) Users Annual and Collective Whole Body Exposure Dose**

Table(1) presents the statistical distribution of whole body collective dose to workers of the different divisional departments distributed in AEA for 1995. The data showed that, the majority of the workers are receiving an annual collective dose less than 5 mSv (i.e range over 45% in some divisional departments up to 90% in the other divisional departments). More over users received annual dose 5-10 mSv present a fraction percentage 4%-17% of the total numbers of radiation workers, in some divisional departments. This annual limit of exposure dose presents 25% of the recommended annual limit by ICRP<sup>(15)</sup>.

Table (2) presents the average annual dose in mSv and the average annual collective dose in man-Sv for the workers distributed in the various divisions of AEA. The average annual exposure is found to be in the range

2.1-4.3 mSv/y. Following ICRP recommendation, standard annual limit 20 mSv/y<sup>(15)</sup>. The average dose received by workers presented 10-21.5% of that ICRP limit. This exposure limit is also in agreement with the concepts and philosophy of ALARA<sup>(16)</sup>, i.e radiation doses received by workers as low as reasonably achievable either for annual and/or collective dose. Since, the ALARA concepts is basically a cost benefit analysis which relates the benefit gained from radiation operation with radiation injuries, collective dose and the cost of radiation operation.

Table(3) presents the yearly intercomparison of the annual and collective dose received by the workers in different AEA divisions in the period 1991-1995. The annual dose is mostly found to be ranged over 0.5-11.6 mSv. This limit of annual exposure presents 2.5-58% of the annual limit recommended by ICRP<sup>(15)</sup>. It presents a good confirmation for the applicability of the ALARA concepts in the radiation protection programs of Egypt.

Table(4) showed yearly intercomparison study for the average mean of the yearly annual dose and collective dose for the different centers of AEA in the period 1991-1995. Assuming that, the ALARA concepts is applicable to the number of workers in each center of AEA, i.e each center is considered as institute, the average mean of either the annual dose/year and/or the yearly collective dose is too low. The annual dose presented 6.0-36.5% of the recommended limit. Mean while, the collective dose approved the utility of ALARA in the Egyptian radiation protection programs.

## References

- (1) National Academy of Science on the Biological Effect of Ionizing Radiation (DEIR III). The effects on populations of exposures to low ionizing radiation. National Academy Press, Washington D.C.(1980).
- (2) Mancuso T.F., Stewart A. and Kneale G., Radiation Exposure of Hanford Workers Dying from Cancer and Other Causes, *Health Physics*, 33 (1977) 369.
- (3) Gilbert E.S. and Marks S., An Analysis of the Mortality of Workers in a Nuclear Facility, *Radiation Research*, 99 (1979) 122.
- (4) Checkoway H., Pearce N., Grawford-Borwn D.J. and Cragle D.L., Radiation Doses and Cause-Specific Mortality Among Workers at a Nuclear Materials Fabrication Plant, *Am. J. Epidemiol.* 127 (1988) 255.
- (5) Acquavella J.E., Wiggs L.D., Waxweiller R.J., McDonnell D.G., Tietjen F.L. and Wilkinson G.S., Mortality Among Worker at the Pantex Weapon Facility, *Health Physics*, 48 (1985) 735.
- (6) Beral V., Inskip H., Fraser P., Booth M., Coleman D. and Rose G., Mortality of Employee of the United Kingdom Atomic Energy Authority 1946-1079, *Br. Med. J.* 291 (1985) 440.
- (7) Smith P. and Douglas A.J., Mortality of Workers at the Sellafield Plant of British Nuclear Fuels, *Br. Med. J.* 293 (1986) 845.
- (8) Wilkinson G.S., Tietgen G.L., Wiggs L.D., Galke W.A., Aquavella J.F., Reyes M., Voelz G.L. and Waxweiller R.J., Mortality Among Plutonium Weapons Facility, *Am. J. Epidemiol.* 125 (1987) 231.
- (9) Land C.E., Estimation Cancer Risks from Low Doses of Ionizing Radiation, *Science*, 209 (1980) 1197.

- (10) Cook-Mozafri P.J., Ashmore F.L., Vincent T., Forman D. and Alderson M., Cancer incidence and Mortality in the Vicinity of Nuclear Installation, Englands and Walles 1959-80 London (1987).
- (11) A.M.El-Naggar, A.M.Sayed, S.H.El-Adawi, F.I.Saied, ARE, AEA report No. 28, Cairo, Egypt, 1968.
- (12) M.A.Gomaa, A.M.Eid, M.A.El-Kollaly, M.A.Ayad, Proc. Int. Symp. of Appl. Tech. Ion Rad., 673 King Saud. Univ., Riyad, Saudia Arabia (1983).
- (13) M.A.Gomaa, 2nd Rad. Prot. Dept. Comf., NRC, AEA, Cairo, Egypt (1991).
- (14) M.A.Gomaa, Rad. Phys. and Chem. (1995).
- (15) ICRP-60 Recommendation of the Int. Commision on Radiological Prot. Annals of ICRP 21, No. 1-3 (1991).
- (16) ICRP-Publication 51 Data for use in protection against external radiation (1988).
- (17) U.S. Office of the Federal Registration Title 10, Code of Federal Regulations Part 20, US. Goverment Printing Office, Washington D.C (1969).
- (18) Y.A.Amany, Experimental Investigation of some Aspects Affecting Personnel Dosimetry, M.Sc. Thesis", Cairo University (1996).

**Table (1): Statistical distribution of annual exposure to Egyptian AEA workers for 1995**

Devison	Department	Number of workers recieving annual exposures of ;"mSV"			
		< 1	1-5	5-10	10-20
<b>Nuclear Research Center</b>					
Atomic	Reactor	15 (67.5%)	9 (37.5%)	-	-
Reactor	Reactor	5 (10.7%)	41(89.1%)	-	-
	Physics				
	Rad. Prot.	13 (28.9%)	27(60%)	2(4.4%)	3(6.7%)
	Engineering	-	-	-	-
Material	Metallurgy	4 (16%)	4 (16%)	19(76.0%)	2(16.3%)
	Plasma	1 (4.3%)	22 (95.7%)	-	-
Basic	Expt. Physics	12(21.4%)	40(71.4%)	4 (7.2%)	-
Nuclear					
Science	Theor physics	27(100.0%)	-	-	-
	Accelerator	17 (53.2%)	15(46.8%)	-	-
Applied	Radioisotope	12(27.7%)	24(55.8%)	7 (16.3%)	-
Radio-	Agricl.				
isotope	Botomic	14(93.5%)	11 (7.6%)	-	-
	Appl. Biology	19(44.1%)	20(46.5%)	4 (9.4%)	-
	Medical unit	1 (167%)	5(83.3%)	-	-
<b>Hot Laboratories Center</b>					
	Isotope	39(100%)	-	-	-
	Production				
	Nuclear	22(100%)	-	-	-
	Chemistry				
<b>Radiation Technology Center</b>					
		15(18.8%)	60(75.0%)	3(3.75%)	2(2.5%)

**Table (2): Average annual and collective dose to workers of AEA centers for 1995**

Division	Number of workers	Average annual exposure, mSv
<b>Nuclear Research Center</b>		
Atomic Reactor	115	2.82
Material Applied	48	2.90
Radioisotope	101	2.41
Basic Nuclear Science	115	2.10
<b>Hot Laboratories Center</b>		
Nuclear chemistry	22	3.82
Isotope Production	39	4.32
<b>Radiation Technology</b>		
	82	2.99
Collective dose man Sv	255	1.437

**Table (4): Average mean of annual and collective dose to the workers of AEA Centers in the year 1991-1995**

Center Year	NRC		Hot Lab		Radiation Technology		Total No. of(1) workers	Collective (2) dose
	Number of workers	annual dose mSv	Number of workers	annual dose mSv	Number of workers	annual dose mSv		
1991	224	1.47	47	1.49	135	4.57	406	1.015
1992	331	1.18	43	4.51	70	5.31	441	0.954
1993	442	1.43	60	7.30	82	5.37	584	1.510
1994	332	1.13	77	1.80	65	4.91	474	0.831
1995	385	2.50	61	4.00	82	3.00	528	1.45

(1) Total Number of workers in Atomic Energy Authority

(2) Collective dose of the workers in Atomic Energy Authority



EG9700109

*radiation Physics Conf., Al-Minia, 13 - 17 Nov., 1996*

## CALCULATIONS ON SAFE STORAGE AND TRANSPORTATION OF RADIOACTIVE MATERIALS

*Hathout A. M., El Messiry A. M., Amin E*  
*National Center for Nuclear Safety and Radiation Control*  
*NC NSRC AEA, Cairo, EGYPT*

### ABSTRACT

In this work the safe storage and transportation of fresh fuel as a radioactive material is studied. Egypt planned ET RR 2 reactor is of relatively high power and would require adequate handling and transportation. Therefore, the present activity is initiated to develop a procedure for safe handling and transportation of radioactive materials. The possibility of reducing the magnitude of radiation transmitted on the exterior of the packages is investigated. Neutron absorbers are used to decrease the neutron flux. Criticality calculations are carried out to ensure the achievement of subcriticality so the inherent safety of these ilusters can be verified. The discrete ordinate transport code ANISN was used. The results show good agreement with other techniques.

### INTRODUCTION

Enhanced safety in the transportation and storage of fissile materials is a problem of worldwide concern (Williams F.C. and Deese D.A., 1979, Technical Report Series 218, 1982, and Technical Report Series 240, 1984). The design of wet or dry storage facility for spent fuel must include a series of technical requirements. For each design concept, the specifics may vary but the basics will remain the same.

The main nuclear safety issues that should be considered in the design of a storage facility are:

- 1- protection of fuel cladding integrity,

- 2- radiological shielding and environmental protection, and,
- 3- accidental criticality and management of nuclear waste.

Dry storage facility of any type allows also for temperature control. The heat transfer medium for the most part has been air, for higher temperature another medium should be chosen. Precaution must be taken to prevent the operators from receiving excessive radiation from irradiated components. For storage in water the problem is controlled by the thickness of the pool walls and the depth of the cooling water above the assem storage. Dry storage concepts rely upon the construction material for shielding. Various materials and combinations of materials are used such as steel, concrete, graphite and cast iron.

Spent fuels stored in dry environments have the advantage of limited moderation and therefore can be stored closer together. The design should assure that if water is present it can be evacuated. In both wet and dry storage, separation between assemblies can be reduced further by introducing neutron absorbers.

## **METHODS FOR INCREASING EXISTING POOL CAPACITY**

Expansion of existing storage pool capacities can be achieved by storage densification. The techniques being used include:

- 1 Use of design value of the effective multiplication factor of 0.95 instead of the current value 0.9 (American Standards, ANSI 210, 1976) and more sophisticated techniques for criticality calculation.
- 2 Use of stainless steel ss, boron in ss, or boron in aluminum as neutron absorber to permit greater storage density.
- 3 Filling unused pool area with fuel storage racks.
- 4 Replacing non fuel racks with racks suitable for fuel storage.
- 5 Double tiering of spent fuel storage racks has been accomplished.

In the present work the problem of criticality safety of fuel storage and transportation is addressed. The first four items above have been considered. As it is essential to assure personnel safety during handling and transportation, the shielding of casks, and pools have been studied as well.

## CRITICALITY SAFETY CALCULATION

### 1 Description of Bench Mark Experiments :

A research program funded by U.S. Nuclear Regulatory Commission to provide experimental criticality data on systems simulating packages and fuel storage pools are reported in (Bierman S.R., Clayton E.D. and Drust B.M., 1977). The experiments involve 2.35 wt % U235 enriched UO<sub>2</sub> rods about 11.176 mm diameter by 914 mm length, with 0.762 mm aluminum clad. Figure 1 shows the description of the fuel rod. The experiment consisted of determining the number of these rods required for criticality, at near optimum moderation, and then measuring the critical separation between three subcritical clusters of these rods aligned in a row.

The effect that the following fixed neutron absorber (neutron poisons) had on the critical separation between these clusters of rods, was also investigated, Boral, 304L steel, 1.1 304C steel, 1.6 wt % B-304L steel. Figure 2 gives schematic diagram of the experiment (Bierman S.R., Clayton E.D., and Drust B.M., 1977). A second critical experiment with 31 wt % uranium 235 enriched UO<sub>2</sub> rods in highly borated water lattices have been carried-out at the critical mass laboratory, operated for the U.S. Department of energy by Battle Memorial Institute. Details of the experiment are given by Drust B.M., Bierman S.R. and Clayton E.D., 1982.

### 2 The Calculation Model :

The Discrete Ordinate One Dimensional Transport Code ANISN (Engle W.W., 1967) was used to perform criticality and shielding calculation. The code has been adapted on the VAX6000 computer and validation studies have been reported (Amin E., Ashoub N. and ElKady A., 1992, and, Amin E., El Messiry A. and El Adham K., 1993).

The cell calculation code WIMSD4 is used to generate cross section for the fuel and other cell materials in the thermal energy range in the EURLIB group structure (Herrenburger V, 1982). For criticality calculations the cross section generated by WIMSD4 were used.

The criticality calculations were performed to evaluate the effective multiplication factor,  $K_{eff}$ , for different critical separations,  $X_c$ , and to show the effect on  $K_{eff}$  and  $X_c$  of different absorbers.

## RESULTS AND DISCUSSIONS

Simulation of clusters of 2.35 wt % U235 enriched UO<sub>2</sub> rods in water were performed using cylindrical geometry. The equivalent radii were generated for each region. Table 1 gives comparison of the effective multiplication factor calculated by the ANISN code with benchmark calculation using KENO IV (Whiteside G.E. and Cross N.F., 1969), for 3 array configuration with 2.032cm square pitch. The critical separation presented in this table are measured experimentally.

It is clear that the present results give the same trend and in good agreement with both the KENO IV results and experiments. The effect of steel absorber on the criticality for the same arrangement is given in the last column. The agreement is satisfactory.

Table 2 presents the effect of different concentrations of Boric acid on some critical assemblies. The critical array width is the same (40cm) while the critical array length varies from 8.92 to 30.42cm.

So, we can conclude that the present study explored a variety of phenomena affecting the criticality safety of fuel rod storage and indicated the safety conditions in each case.

Table 1: Comparison of Keff for 3-array configuration with 2.032cm square pitch ,

no.of rods	crit. separ. bet. clus.cm	Keff without absorber		Keff with absorber
		KENO IV	ANISN	
20x17	11.92 +.04	1.022 +.005	1.03037	1.02500
20x16	8.39+ .05	1.019 +.007	1.02376	1.01964
20x15	6.39 +.06	1.017+ .006	1.01767	1.01376
20x14	4.46+ .10	1.016 +.005	1.01058	1.00671

Table 2 Effect of the Boric Acid with different concentrations on the critical number of rods with 1.89 cm square lattice pitch and 40cm array width ,

Boron conc. g/l	criti. array length	critical number of rods	Keff calc.
0.0	8.92	357	0.98293
0.49 +.06	10.72	429	0.99345
1.25 +.21	14.05	562	1.00731
2.15 +.35	23.07	923	1.00662
2.55 + .07	30.42	1237	1.00670

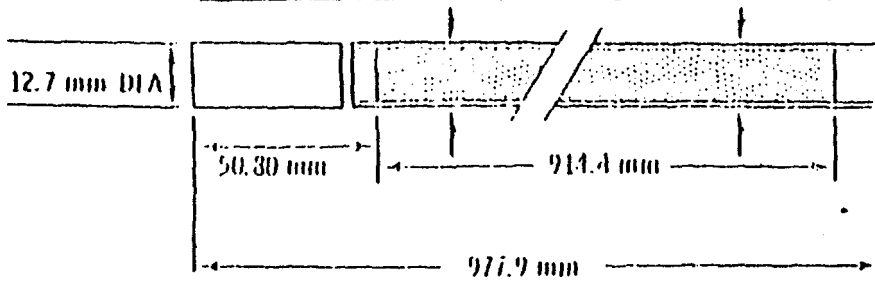


FIG. 1 DESCRIPTION OF 2.35 wt% <sup>235</sup>U ENRICHED UO<sub>2</sub> RODS

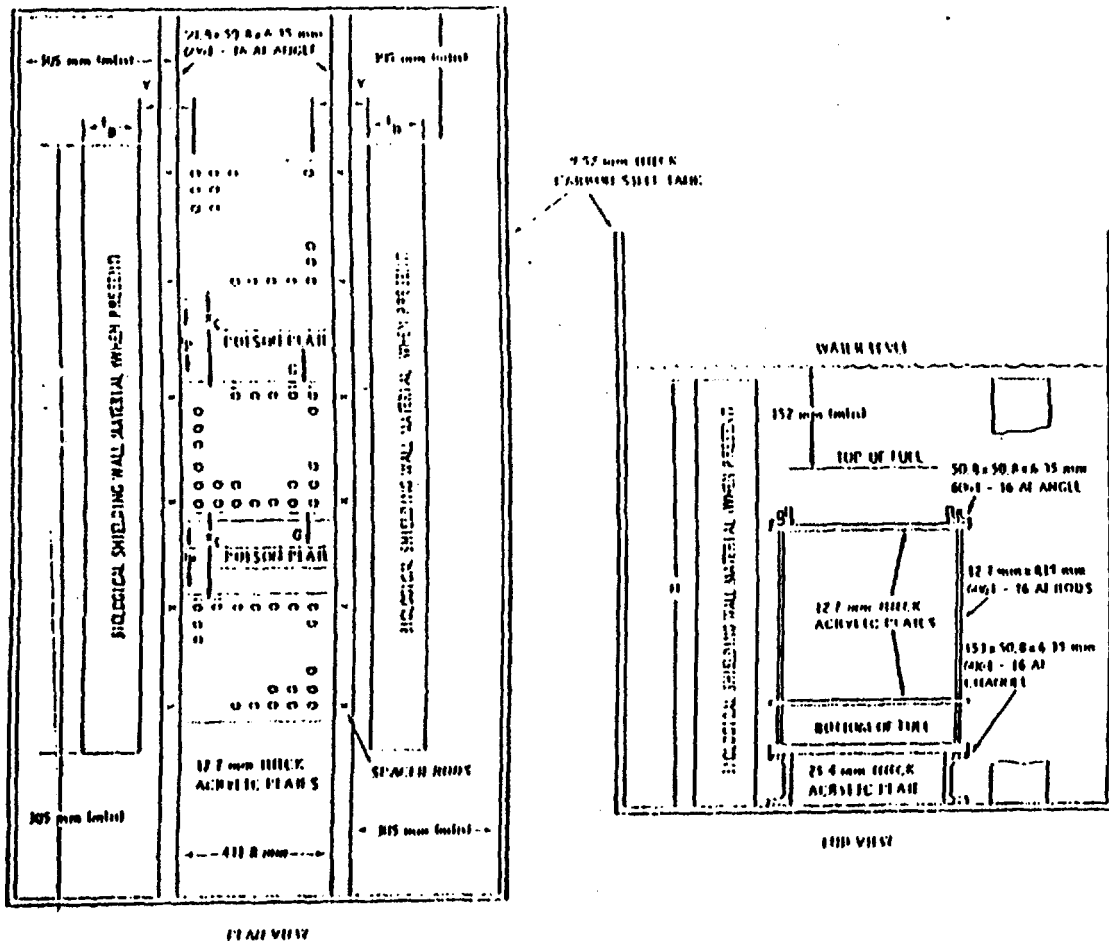


FIG. 2 GRAPHICAL ARRANGEMENT OF SHIELDED SHIPPING PACKAGE CRITICAL EXPERIMENTS

**REFERENCES**

- 1 Amin E., Ashoub N. and El Kady A.,(1992) , The 7th Annual Conference, vol.27,ISSR, Cairo Univ., Egypt. ,
- 2 Amin E., El Messiry A. and Eladham K.,(1993), NC NSRC, Rep. no. 145/1993, AEA, Egypt. ,
- 3 American Standards, (1967), ANSI No.210. ,
- 4 Bierman S.R , Clayton E.D. and Drust B.M.,(1977), PNL 2438.. ,
- 5 Drust B.M., Bierman S.R. and Clayton E.D.,(1982), Transac. 43.
- 6 Engle W.W., (1967),K 1693. ,
- 7 Herrenburger V.,(1982), Wurenlingen,NEA. ,
- 8 Technical Report Series ,(1982),No. 218.IAEA. ,
- 9 Technical Report Series ,(1984),No.240, IAEA. ,
- 10 Whitsides G.E. and Cross N.F., (1969) , CTC. ,
- 11 Williams F.C. and Deese D.A.,(1979), H.U., Pergamon Press. ,



## **A Logic Scheme For Regulating Safe Operation Of Research Reactors**

*Ensherah E.M. Ahmed \**, *Ahmed Effat \*\** and *Farouk M.A. Rahman\*\**  
ATOMIC ENERGY AUTHORITY, AEA.

### **abstract**

*This work presents a logic scheme for regulating the safe operation of research reactors in accordance with the SS-35-S2 and revised by the 10 CFR. It emphasizes the regulatory inspection and enforcement (RI&E) program in the reactor operation licensing phases. It is developed to provide information, guidance and recommendations to be taken when constructing a RI&E program to be applied in the operational phase of the Egyptian research reactors. The RI&E procedures for regulating safe operation of research reactors are presented as flow charts, and then developed as a computer logic scheme. The software program is efficient, friendly, simple and interactive in nature such that the program asks the user certain questions about essential steps that guide the RI&E for research reactors and the user responds by (yes) or (no) and the program proceeds based on this response until all the necessary RI&E steps are accomplished. Samples of results of the RI&E software execution showing some violation cases with their inspective and corrective paths throughout the program are presented and discussed.*

### **Key words**

Nuclear Safety, Logic Scheme, Enforcement & Inspection, Regulations, Reactor Operation, Reactor Operation License, Research Reactors.

### **1. Introduction**

The operation License for any nuclear facility shall include several licensing phases; sitting, design & construction, commissioning, reactor operation, utilization & modification and decommissioning<sup>(1,2)</sup>. These phases are connected to be parts of the entirely reactor operation license and regulated in a consecutive manner such that the applicant/licensee (A/L) can only obtain a phase permit if the regulatory requirements of that phase are fulfilled. So, these licensing phases are controlled by a compliance action program which includes both regulatory inspection (RI) and regulatory enforcement (RE) action programs. For example, the construction phase permit is issued after reviewing the Primary Safety Analysis Report (PSAR) by the nuclear regulatory body (NRB) before starting the construction works but after finishing the sitting and design works. The RI&E program is conducted during the construction phase to assure that all A/L works are in consistent with the technical specifications (TS) in the PSAR otherwise such construction permit is withdrawn by the NRB.

---

\* *Reactor Department, Nuclear Research Center (NRC), Atomic Energy Authority (AEA), Cairo, Egypt.*

\*\* *Operational safety Dept., National Center of Nuclear Safety and Radiation Control (NCNSRC), Atomic Energy Authority, Cairo, Egypt.*

The objective of this RI&E program is to assure that any phase permit for each license phase are in consistent with the regulatory requirements, the technical specifications of the PSAR and the licensee administrative control<sup>(3)</sup>. The RI&E program shall be conducted by the NRB which is responsible for issuing/withdrawal of phase permits and reactor operation license.

In a previous work for the authors, the safety requirements for reactor operation license in research reactors are presented, discussed and applied to Egypt's research reactors<sup>(4)</sup> showing the particular areas of inspection interest in both reactor operation and modifications phases and giving examples for the violations categorized according to their severity levels in such both phases<sup>(4)</sup>. In another work, the future prospectives for reactor operation licensing and its regulatory problems in Egyptian research reactors are also discussed<sup>(5)</sup> explaining the various phases of the RI within its cycle and the various phases of RE within its action processes. The RI report format with its contents is also given<sup>(5)</sup>.

In the present work, a logic scheme software for the compliance action program (RI&E) which regulates the safe operation of research reactors is developed. It was developed according to the requirements of the Egyptian AEA-NCNSRC- Rule No.-06<sup>(6)</sup> and based on the NCNSRC-Guide-01<sup>(7)</sup> and on the IAEA safety series SS-50-SG-S4<sup>(8)</sup>, SS-35-S1&S2<sup>(1,2)</sup> and is revised by the 10CFR-Ch1<sup>(9,10)</sup> and the NRC Inspection and Enforcement Manual<sup>(3)</sup>. It was structured under two main principles; interactive viewing between A/L and the NRB and effective communication and feed back of information resulting in a continuous evaluation for different reactor plant systems and components. So, it was developed to help in assuring coverage of all aspects to be regulatory inspected and enforced and in providing overall coordination of both RI and RE activities.

## **2. The RI&E Logic Scheme**

The RI&E is a compliance action program used for pursuing a nuclear facility from the moment of its construction to its decommissioning in order to continuously evaluate its effectiveness throughout its life time. The RI&E procedures for regulating safe operation of research reactors are presented as flow charts (shown in Figs.(1) & (2))and then developed as computer logic scheme software. This RI&E software helps in documenting all aspects of regulatory inspections and enforcement action processes for all licensing phases of any research reactor. So, it provides an easy method for collecting information, updating the detailed findings/observations histories and scheduling the RI&E activities. Consequently, it helps in selecting the optimum correction path (route) in a license phase for the sake of awarding a new permit after its withdrawal.

All these safety information of a nuclear facility can be easily pursued using the present RI&E logic scheme software. Moreover, it helps - to a great extent - in forecasting or predicting an accidental situation situation as a result of a malfunction/failure of any component/system due to the accumulation of observations/findings in that component or system. Thus, the causes leading to such accidental situation can be easily known throughout the RI&E software by following up the time history of each observation/finding occurred in that component / system even if it was a closed finding. Consequently , it helps in decision - making to withdraw the permit / license when it is felt that the safety of reactor operation is in jeopardy until the RE corrective actions are executed. On contrary,

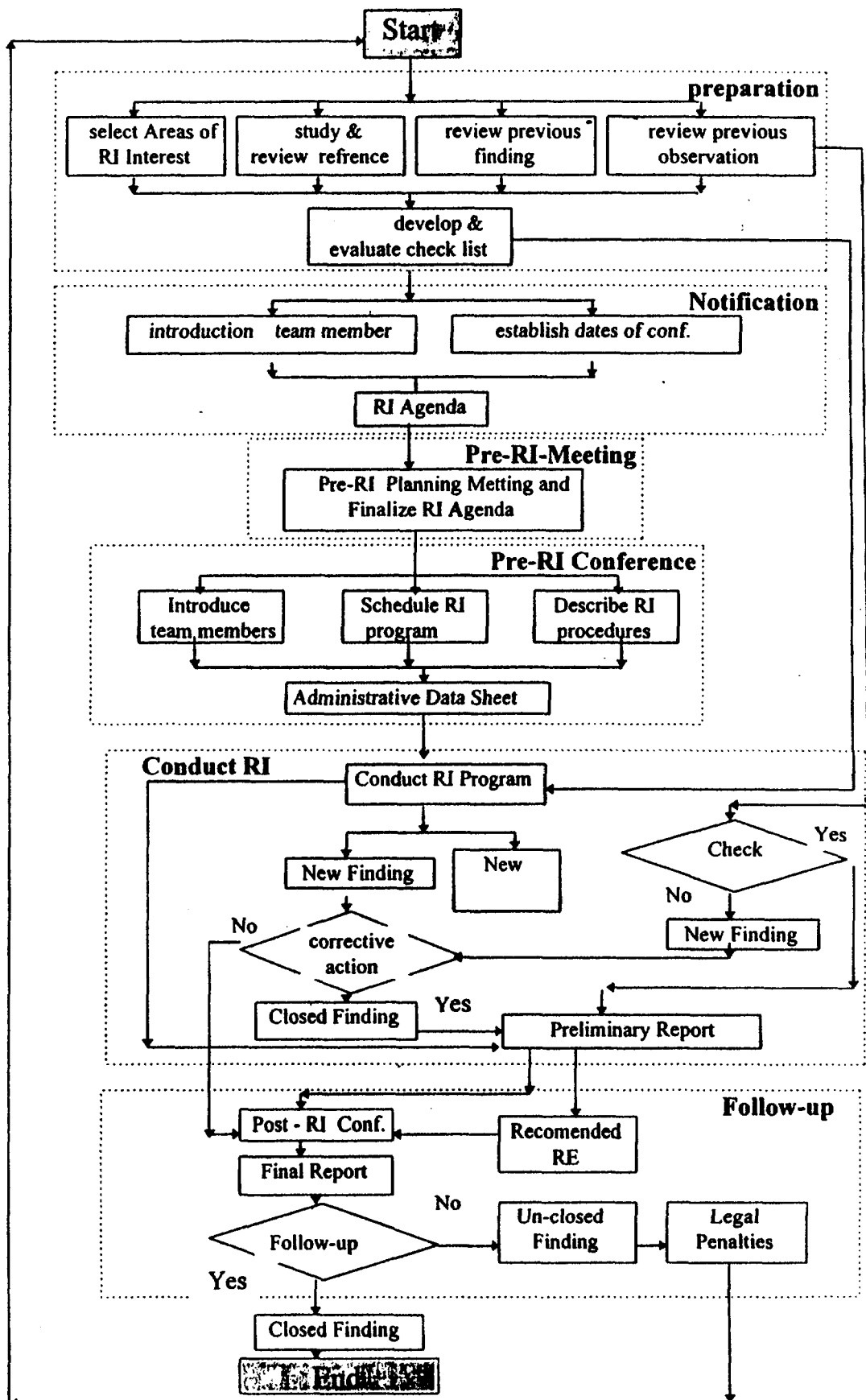


**Fig.(1) RI Program Flow chart**

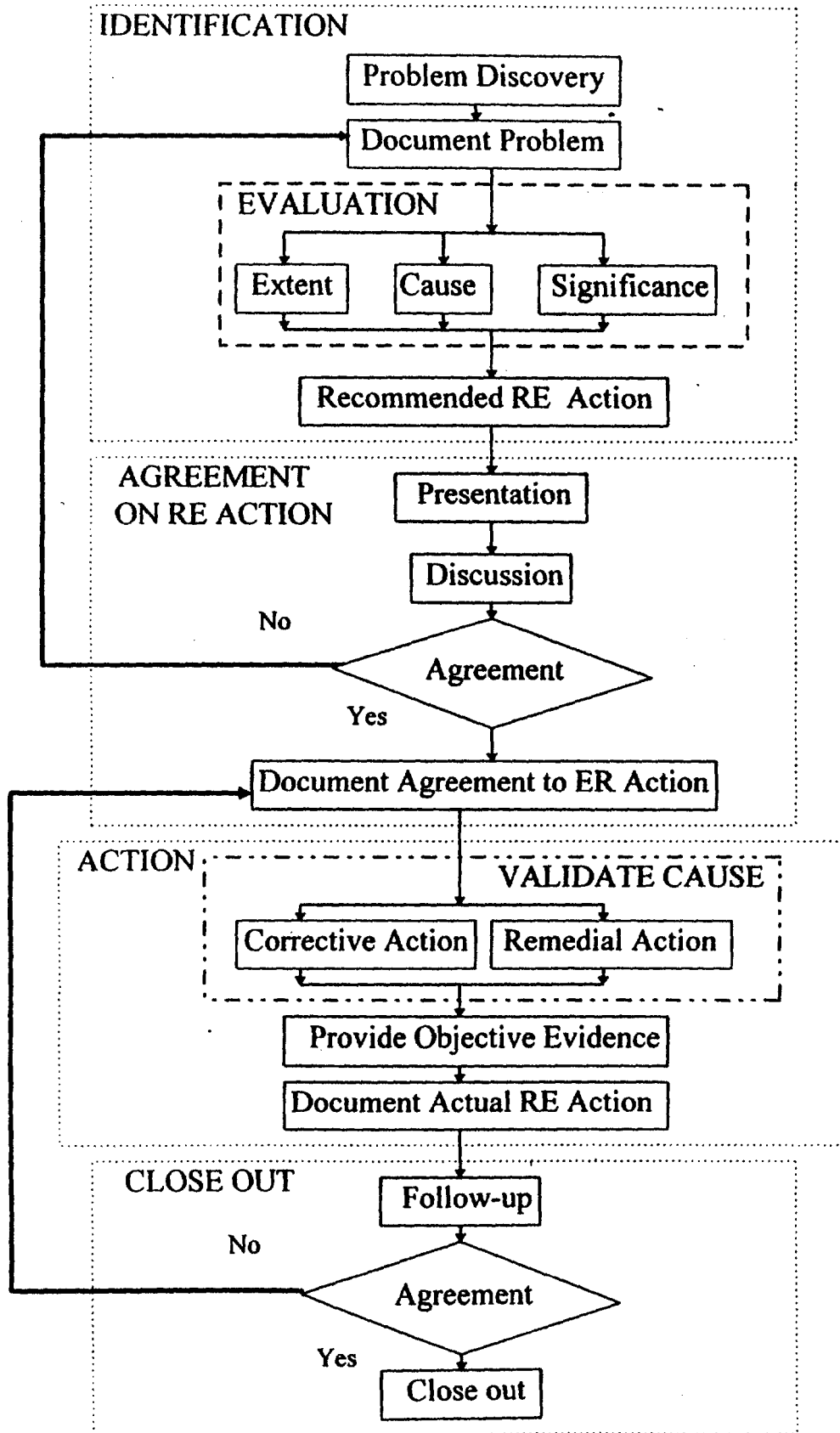


**Fig.(2) RE Program Flow Diagram**

it helps in regulating safe operation of research reactors and continuing award for reactor operation license if the reactor systems and components are consistent with regulatory requirements, technical specifications and licensee's administrative control<sup>(3)</sup>.

**3- RI&E Program Results and Discussions**

The computer program helps the user in following RE and RI instructions according to the flow charts of Figs.(1) and (2). Thus, it helps the user to regulate safe operation for any research reactor and - in turns - evaluates its effectiveness. Figure (3) shows how the RI and RE program are working when violations take place and how the re-RI shall be started again after legal penalties are punished when an unclosed finding is reached. As shown in figure, when a violation firstly takes place, it is identified and evaluated in the identification phase of the RE procedures. Then after the problem is identified, presented and discussed, an agreement on RE action is taken. The required action may be investigative, remedial or corrective action. Once the action phase is started, the RI program is called and proceeds with its all phases until the follow up action, which finally leads to either a closed finding or an unclosed finding. Based on the results of the follow up action, a violation close-out occurs or a legal penalties is forced and the RI program is rerun again. As shown from the figures, the RE program should be resulted in a close out whereas the RI program has 14 possible paths only six of them lead to a close-out which implies to re-start the RI program. So this, RI&E program helps in selecting the optimum correction path - in a licensing phase - for the sake of awarding a new phase permit if it is withdrawn.

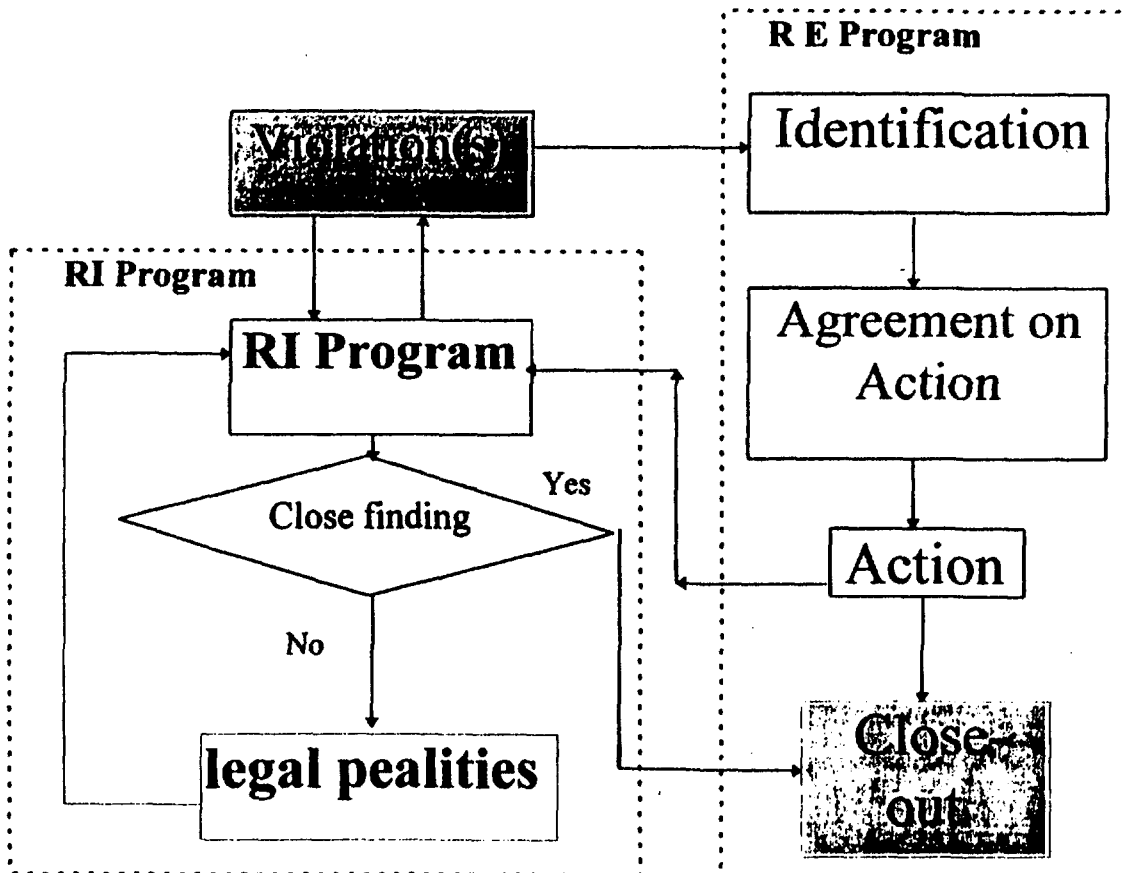


**Fig.(3) RI & E Program Layout Chart**

Output samples for the RI&E program execution are given in Figs.(4) and (5). Figure (4) shows how the RI&E program is terminated if the check lists, administrative data sheets and/or the previous preliminary reports are not fed to the RI team members to enable them to conduct the RI program. Figure (5) shows the RI procedures when the corrective action to the violational findings have not been executed and how it proceeds if an unclosed finding is reached.

START RI&E	PLAN PRE-RI MEETING
START RI	AND FINALIZE RI AGENDA
1-PREPARATION PHASE	4-PRE-RI CONFERENCE PHASE
HAS REVIEWED PREVIOUS OBSERVATIONS	HAS DESCRIBED RI PROCEDURES
RESPOND WITH (YES) OR (NO)	RESPOND WITH (YES) OR (NO)
YES	YES
HAS REVIEWED PREVIOUS FINDINGS	HAS SCHEDULED RI PROGRAM
RESPOND WITH (YES) OR (NO)	RESPOND WITH (YES) OR (NO)
YES	YES
HAS STUDIED & REVIEWED REFERENCES	HAS INTRODUCED TEAM MEMBERS
RESPOND WITH (YES) OR (NO)	RESPOND WITH (YES) OR (NO)
YES	YES
HAS SELECTED AREAS OF INTEREST	MAKE ADMINISTRATIVE DATA SHEET
RESPOND WITH (YES) OR (NO)	5-CONDUCT RI PROGRAM
YES	CONDUCT RI PROGRAM IF
DEVELOP & EVALUATE CHECK LISTS	ADMINISTRATIVE DATA SHEET WAS MADE
2-NOTIFICATION PHASE	AND CHECK LISTS WERE DEVELOPED &
HAS ESTABLISHED DATES OF CONFERENCE	CHECKED
RESPOND WITH (YES) OR (NO)	RESPOND WITH (YES) OR (NO)
YES	NO
HAS INTRODUCED TEAM MEMBERS	RI PROGRAM WILL BE STOPPED DUE TO
RESPOND WITH (YES) OR (NO)	ABSENCE
YES	OF ADMINISTRATIVE DATA SHEETS & CHECK
MAKE RI AGENDA	LISTS
3-PRE-RI MEETING PHASE	END

**Fig.(4) Example of RI&E Output Results**

#### **4. Conclusions**

- 1- This work has revealed on creating a logic scheme software for the RI&E procedures to be applied on research reactors throughout its life time to regulate its safe operation. It was developed according to the requirements of the IAEA Safety Series -S1 &S2 and revised by 10 CFR, Ch.1 and the NRC -Inspection & Enforcement Manual.
- 2- The program helps to correct a/some violation(s) happened in a nuclear facility during any of its licensing phases .
- 3- It helps in documenting all regulatory inspection and enforcement procedures and action processes for all licensing phases of a nuclear facility.
- 4- It also provides an easy method for collecting information, updating the detailed findings / observations histories and for scheduling the RI&E activities.
- 5- Consequently, it helps in selecting the optimum correction path - in a license phase - for the sake of awarding a new phase permit if it is withdrawn.

START RI

1-PREPARATION PHASE

HAS REVIEWED PREVIOUS OBSERVATIONS

RESPOND WITH (YES) OR (NO)

YES

HAS REVIEWED PREVIOUS FINDINGS

RESPOND WITH (YES) OR (NO)

YES

HAS STUDIED & REVIEWED REFERENCES

RESPOND WITH (YES) OR (NO)

YES

HAS SELECTED AREAS OF INTEREST

RESPOND WITH (YES) OR (NO)

YES

DEVELOP & EVALUATE CHECK LISTS

2-NOTIFICATION PHASE

HAS ESTABLISHED DATES OF CONFERENCE

RESPOND WITH (YES) OR (NO)

YES

HAS INTRODUCED TEAM MEMBERS

RESPOND WITH (YES) OR (NO)

YES

MAKE RI AGENDA

3-PRE-RI MEETING PHASE

PLAN PRE-RI MEETING

AND FINALIZE RI AGENDA

4-PRE-RI CONFERENCE PHASE

HAS DESCRIBED RI PROCEDURES

RESPOND WITH (YES) OR (NO)

YES

HAS SCHEDULED RI PROGRAM

RESPOND WITH (YES) OR (NO)

YES

HAS INTRODUCED TEAM MEMBERS

RESPOND WITH (YES) OR (NO)

YES

MAKE ADMINISTRATIVE DATA SHEET

5-CONDUCT RI PROGRAM

CONDUCT RI PROGRAM IF

ADMINISTRATIVE DATA SHEET WAS MADE

AND CHECK LISTS WERE DEVELOPED &

CHECKED

RESPOND WITH (YES) OR (NO)

YES

ARE NEW OBSERVATIONS SAME

AS PREVIOUS OBSERVATIONS?

RESPOND WITH (YES) OR (NO)

NO

GET NEW FINDING

HAS MADE CORRECTIVE ACTION

RESPOND WITH (YES) OR (NO)

YES

FINDINGS ARE CLOSED

WRITE PRELIMINARY REPORT

6-POST-RI CONFERENCE PHASE

HAS MADE POST-RI CONFERENCE

RESPOND WITH (YES) OR (NO)

YES

HAS TAKEN RECOMMENDATIONS OF RE

AND HAS TAKEN PRELIMINARY REPORT

RESPOND WITH (YES) OR (NO)

YES

WRITE FINAL REPORT

7-FOLLOW-UP PHASE

HAS MADE FOLLOW-UP ACTION

RESPOND WITH (YES) OR (NO)

NO

FINDINGS ARE UNCLOSED

LEGAL PENALTIES

RE-RI PROGRAM

1-PREPARATION PHASE

HAS REVIEWED PREVIOUS OBSERVATIONS

RESPOND WITH (YES) OR (NO)

YES

HAS REVIEWED PREVIOUS FINDINGS

RESPOND WITH (YES) OR (NO)

YES

HAS STUDIED & REVIEWED REFERENCES

RESPOND WITH (YES) OR (NO)

YES

HAS SELECTED AREAS OF INTEREST

RESPOND WITH (YES) OR (NO)

YES

DEVELOP & EVALUATE CHECK LISTS

2-NOTIFICATION PHASE

HAS ESTABLISHED DATES OF CONFERENCE

RESPOND WITH (YES) OR (NO)

YES

HAS INTRODUCED TEAM MEMBERS

RESPOND WITH (YES) OR (NO)

YES

MAKE RI AGENDA

3-PRE-RI MEETING PHASE

PLAN PRE-RI MEETING

AND FINALIZE RI AGENDA

4-PRE-RI CONFERENCE PHASE

HAS DESCRIBED RI PROCEDURES

RESPOND WITH (YES) OR (NO)

YES

HAS SCHEDULED RI PROGRAM

RESPOND WITH (YES) OR (NO)

YES

HAS INTRODUCED TEAM MEMBERS

RESPOND WITH (YES) OR (NO)

YES

MAKE ADMINISTRATIVE DATA SHEET

5-CONDUCT RI PROGRAM

CONDUCT RI PROGRAM IF ADMINISTRATIVE

DATA SHEET WAS MADE AND CHECK LISTS

WERE DEVELOPED & CHECKED

RESPOND WITH (YES) OR (NO)	HAS MADE POST-RI CONFERENCE
YES	RESPOND WITH (YES) OR (NO)
ARE NEW OBSERVATIONS SAME	YES
AS PREVIOUS OBSERVATIONS?	HAS TAKEN RECOMMENDATIONS OF RE
RESPOND WITH (YES) OR (NO)	AND HAS TAKEN PRELIMINARY REPORT
NO	RESPOND WITH (YES) OR (NO)
GET NEW FINDING	YES
HAS MADE CORRECTIVE ACTION	WRITE FINAL REPORT
RESPOND WITH (YES) OR (NO)	7-FOLLOW-UP PHASE
YES	HAS MADE FOLLOW-UP ACTION
FINDINGS ARE CLOSED	RESPOND WITH (YES) OR (NO)
WRITE PRELIMINARY REPORT	YES
6-POST-RI CONFERENCE PHASE	FINDINGS ARE CLOSED
	END

**FIG. (5) RI Program Output ( An Example)**

6- All safety information data needed for safe operation, inspection or enforcement , for any research reactor facility, can be easily pursued using the present RI&E logic scheme software.

7- Moreover, it helps - to a great extent - in forecasting or predicting an accidental situation as a result of malfunction / failure of any component / system due to the accumulation of the observations / findings in that component or system.

### **5. References**

1. IAEA Safety Series; "Code On The Safety Of Nuclear Research Reactors- Design", S.S.-35-S1 ,Vienna (1992).
- 2- IAEA Safety Series; "Code On The Safety Of Nuclear Research Reactors- Operation ", S.S.-35-S2 ,Vienna (1992).
- 3- NRC; "I&E Manual : Class I and Class II Non-Power Reactors", USA (1992).
- 4- Ahmed, Ensherah E.M. and Rahman, F.A.;"Nuclear Safety Requirements For Operation Licensing In Research Reactors", Under Press (1996).
- 5- Ahmed, Ensherah E.M. and Rahman, F.A.; "Future Prospectives For Licensing and Regulatory Problems In Egyptian Research Reactors", IAEA / SR- 183/53 (1993).
- 6- NRSC Safety Rule No. 6, "Nuclear Safety of Research Reactor and Critical Assemblies", NCNSRC, Cairo (1985).
- 7- Rahman, F. A. ; "Guide for Regulatory Inspection and Enforcement for Egyptian Research Reactors", NRSC Guide -01, NCNSRC, Cairo (1988).
- 8- IAEA Safety Guide , Safety Series No. 50-SG-G4, "Inspection and Enforcement by the Regulatory Body for Nuclear Power Plants", Vienna (1980).
- 9- 10 CFR Chapter 1, Part 1, Section 1.64; "Office of Inspection and Enforcement", USA (1990).
- 10- 10 CFR Chapter 1, Part 2, Appendix C; "General Statement of Policy and Procedure for NRC Enforcement Section, Supplement I - Severity Categories", USA (1990).

**SCIENTIFIC SESSION (9)**

**RADIATION DETECTION -1**

***Keynote Lecture***

**USE OF SSNTD FOR MEASURING NUCLEAR REACTIONS**

**M. H. S. Bakr**

**Division of Basic Nucl. Sc., NRC, Atomic Energy Authority  
Cairo, Egypt**

**ABSTRACT**

Solid State Nuclear Track Detectors (SSNTD) technique in nuclear reactions is reviewed. Special attention is given to the study of Makrofol-E films using a proposed optimum etching solution. The etching rate was  $\sim 10.5 \mu\text{m} / \text{hour}$ . The energy resolution was measured and estimated to be  $\sim 600$  and  $\sim 400$  KeV in the energy ranges 1 - 2 MeV and 2-3 MeV respectively. Based on these results, the sensitivity threshold for  $\alpha$ -particles in Makrofol- E is shifted up to 1 MeV, otherwise, there will be no discrimination between the etch - pits of  $\alpha$ - particles with energies ranging from 0 to 1 MeV. The full angular distribution of the  $\alpha$ -groups were measured in one run by means of a SSNTD sheel surrounding the target. A scattering chamber designed for  $\alpha$  - particle angular distribution measurements is described.

An example of the influence of energy loss in degrading Al foils in eliminating the energy angle dependence is given. The numerous curves of the range - energy dependence of  $\alpha$ - particles in Makrofol - E after passing Al foils of different thicknesses are scaled in one schematic normograph. The later simplifies the process of choosing the suitable Al foil thickness or of determining the range - energy relation. The angular distributions of five  $\alpha$  - groups from the  $^{59}\text{Co} (p, \alpha) ^{56}\text{Fe}$  reaction in the proton energy range 1.6 - 2.4 MeV have been measured using the designed chamber. A Makrofol - E film of 200  $\mu\text{m}$  thickness was exposed to the reaction products for 5 hours. This time was enough to get the angular distribution for  $(d\sigma/d\Omega)$  in the range 5-72  $\mu\text{barn} / \text{ster}$ .

Contributed Papers

**TOTAL AND PEAK EFFICIENCIES OF SCINTILLATION  
GAMMA DETECTORS, PART-I: AXIAL-POINT**

**Younis S. Selim, Mahmoud I. Abbas, and Mohammad A. Fawzy**

**Physics Department, Faculty of Science, Alexandria University  
Alexandria, Egypt**

**ABSTRACT**

Total and peak efficiencies of NaI (T) scintillation detector from an axial isotropic radiating point source was calculated by the use of rigid mathematical expressions which are very easily computed. Results are tabulated for various sources at different distances.

**DETERMINATION OF K-CAPTURE PROBABILITIES IN  
THE DECAY OF  $^{133}\text{Ba}$**

**A. Abd El-Haliem, and KH. M. Hella**

**Nuclear Physics Department, Nuclear Research Center,  
Atomic Energy Authority, Cairo, Egypt**

**ABSTRACT**

The K-capture probabilities ( $p_k$ ) in the decay of  $^{133}\text{Ba}$  to the levels 437 KeV and 384 KeV in  $^{133}\text{Cs}$  have been determined from the measurements of gamma ray intensities in conjunction with the analysis of (kx+ gamma ray) sum peaks observed using high resolution HPGe detector. The absolute efficiency of the detector was established from sum peak measurements. ( $P_k$ ) values were calculated theoretically for the two levels at energies 437 keV and 384 keV in  $^{133}\text{Cs}$ . The calculated values were found to be  $0.730 \pm 0.015$  and  $0.810 \pm 0.011$  respectively. The experimental ( $P_k$ ) values to the same levels were found to be  $0.765 \pm 0.067$  and  $0.802 \pm 0.071$  which are in a good agreement with the theoretical values and with previously reported experimental data.

**OPTIMIZATION OF A NEUTRON DETECTOR SYSTEM FOR  
THE FOURIER RTOF-DIFFRACTOMETER  
FACILITY AT THE ET-RR-1 REACTOR**

**R. M. A. Maayouf, A.S.I. El- Kady, and Y. H. El- Shaer**

**Reactor & Neutron Physics Dept., NRC, Atomic Energy Authority  
Cairo, Egypt**

**ABSTRACT**

This work deals with optimization of a detector system for use with the Fourier reverse time of flight (RTOF) diffractometer facility recently installed at the ET-RR-1 reactor. The detector system of the diffractometer was designed for detecting neutrons scattered from the sample. It consists of 4 independent scintillation detector elements arranged according to the time focusing geometry in order to increase the luminosity of the diffractometer for the given resolution. Each of the detector elements is made of 1mm thick  $^6\text{Li}$ - glass scintillator (NE-912) whose surface area is  $200\text{mm}^2$ . The present detector system ensures reliable identification and separation of thermal neutron pulses from fast neutrons and  $\gamma$ - quanta. It was found from measurements with Fe sample that it is possible to make neutron diffraction measurement, within one hour using the present detector system and with resolution  $\cong 0.5\%$ .

**NEUTRON SPECTRUM MEASUREMENTS FROM A NEUTRON  
GUIDE TUBE FACILITY AT THE ET-RR-1 REACTOR**

**R. M A. Maayouf, L. A. A. El-Sayed, and A. S. I. El-Kady**

**Reactor & Neutron Physics Dept., NRC, Atomic Energy Authority, Cairo, Egypt**

**ABSTRACT**

The present work deals with measurements of the neutron spectrum emitted from a neutron guide tube (NGT) recently installed at one of the ET-RR-1 reactor horizontal channels designed to deliver thermal neutrons, free from fast neutrons and gamma ray background, to a Fourier reverse-time-of-flight (RTOF) diffractometer. The measurements were performed using a  $^6\text{Li}$  glass scintillation detector combined with a multichannel analyzer set at channel width  $4\ \mu\text{sec}$  and installed at 3.4 m from a disc Fermi chopper. Also a theoretical model was specially developed for the neutron spectrum calculations. According to the model developed, the

spectrum calculated was found to be in good agreement with the measured one. It was found, both from measurements and calculations, that the spectrum emitted from the NGT covers, after transmission through a Fourier chopper, neutron wavelengths from 1-4 Å adequate for neutron diffraction measurements at D values between 0.71-2.9 Å respectively.

### **A REVERSE TIME OF FLIGHT ANALYZER FACILITY AT THE ET-RR-1 REACTOR**

**R. M.A. Maayouf, A.S. El-Shafey, and M. I. Khalil**

**Reactor & Neutron Physics Dept., NRC, Atomic Energy Authority  
Cairo, Egypt**

#### **ABSTRACT**

The present work deals both with the theory and performance of a reverse-time-of-flight (RTOF) analyzer designed to analyze pulses emitted from a Fourier chopper recently put into operation at the ET- RR-1 Reactor. The RTOF analyzer was found to be adequate for use with pick up pulses from the Fourier chopper which operates following a frequency window suitable for rotation rates from 0 - 9000 rpm; synchronically with neutron pulses from a  $^6\text{Li}$  glass detector set at time focusing geometry for scattering angle  $2\theta=90^\circ$ . It was possible, with the present RTOF analyzer to obtain diffraction patterns at neutron wavelength range between 1 - 4 Å within a resolution = 0.5%.

### **AN ARC DETECTOR FOR NEUTRON CRYSTAL STRUCTURE INVESTIGATIONS**

**N. Habib**

**Reactor & Neutron Physics Dept., Nuclear Research Center.  
AEA, Cairo, Egypt**

#### **ABSTRACT**

An arc detector for neutron structure investigations of powder crystals using time-of-flight technique is described. In order to enable the measurement of integral intensity from about 1/4 of the Debye-Scherrer ring and for simplicity reasons, the scattering angle  $2\theta = 90^\circ$  was chosen and a special arc

collimator was built. The arc collimator-detector had a divergency of about 20 minutes of arc, and the distance between detector-sample was 64cm. Four  $^3\text{He}$  detectors were fixed on the outer arc of the collimator. Both efficiency and space sensitivity of the detector were determined using a point neutron source. Results of measurements show that the parameters of the arc detector are acceptable for high resolution crystal structure investigations.



EG9700114

## Use of SSNTD for Measuring Nuclear Reactions

M.H.S.Bakr

Division of Basic Nucl. Sc. , NRC , Atomic Energy Authority  
13759 , EGYPT

### Abstract

The solid state nuclear track detectors (SSNTD) technique in nuclear reactions is reviewed. A special attention is paid to the study of Makrofol-E films using a proposed as an optimum etching solution. The etching rate was  $\sim 10.5 \mu\text{m} / \text{hour}$ . The energy resolution was measured and is estimated to be  $\sim 600$  and  $\sim 400$  keV in the energy ranges 1 - 2 MeV and 2 - 3 MeV respectively. Basing on these results the sensitivity threshold for  $\alpha$  - particles in Makrofol - E is shifted up to 1 MeV otherwise, there will be no discrimination between the etch - pits of  $\alpha$  - particles with energies ranging from 0 to 1 MeV. The full angular distribution of the  $\alpha$  - groups are measured in one run by means of a SSNTD sheet surrounding the target. A scattering chamber designed for  $\alpha$  - particle angular distribution measurements is described.

An example of the influence of the energy loss in degrading Al foils in eliminating the energy angle dependence is given. The numerous curves of the range - energy dependence of  $\alpha$  - particles in Makrofol - E after passing Al foils of different thicknesses are scaled in one schematic normograph. The later simplifies the process of choosing the suitable Al foil thickness or of determining the range - energy relation. The angular distributions of five  $\alpha$  - groups from the  $^{59}\text{Co} (p, \alpha) ^{56}\text{Fe}$  reaction in the proton energy range 1.6 - 2.4 MeV have been measured using the designed chamber. A Makrofol - E film of 200  $\mu\text{m}$  thickness has been exposed to the reaction products for 5 hours. This time was enough to get the angular distributions for  $d\sigma / d\Omega$  in the range 5 - 72  $\mu\text{barn} / \text{ster}$ .

### Introduction

The solid state nuclear track detectors ( SSNTD ) has proved themselves in nuclear physics research as reliable charged particle detectors. This is due to damage trail created by charged particles in the dielectric solid. The track could be etched and enlarged so as to become visible under the optical microscope.

A comprehensive study of the SSNTD was published by Somogyi et al <sup>1/</sup>, <sup>2/</sup> and Fleisher et al <sup>3/</sup>. In the present article the author will outline - the application of the Makrofol-E detectors in nuclear reactions deducing  $\alpha$  - particles.

The etching process

As a result of the investigation carried out by Somogyi et al <sup>/1/</sup> on different etching reagents, the optimum etching solution for Makrofol-E films as  $\alpha$  - particle detector is:



The optimum etching temperature for Makrofol-E detector was found to be 60-70 °C. The thickness h of the layer etched from the surface is in direct proportion with the etching time. At etching temperature 60 °C the bulk etching rate  $V_B = \Delta h / \Delta t$  is 10.5  $\mu\text{m}/\text{hour}$ . The optimum condition for track counting is at a depth h equal to the range R of the particle. At this depth the track pits are black circular pits under the microscope. After further etching processes, these pits become paler in colour and tend to be invisible.

Energy resolution:

Figure (1) shows the darkness and the diameter distribution of the track pits measured for the group  $\alpha_3$  from the nuclear reaction  $^{14}\text{N}(d, \alpha)^{12}\text{C}$  at deuteron energy  $E_d = 640$  keV at a scattering angle  $\theta = 30^\circ$ . The other two  $\alpha$  -groups are those due to Oxygen and Carbon contamination in the target. As seen in this figure a reliable selection of the  $\alpha_3$  track could be achieved on the basis of differences in darkness and diameter. The energy resolution of Makrofol-E was estimated using Th C and  $^{241}\text{Am}$   $\alpha$  - sources and Al foils of different thicknesses <sup>/4/</sup>. The results are given in table (1).

Table (1)

Energy range, ( MeV )	1 - 2	2-3	6-8 <sup>/1/</sup>
Resolution, ( keV )	600	400	200 - 150

These results with the track growing curves <sup>/1/</sup>, where it is evident that the energy resolution keeps on improving towards higher energies. The  $\alpha$  - particle groups with energy separation equal to or more than the values given for resolution in table (1) can be without measuring track pit diameters. At  $\alpha$  - energies lower than 1 MeV it is hard to distinguish the tracks of different  $\alpha$  - energies. Thus for nuclear reaction measurements the sensitivity threshold for  $\alpha$  - particles is  $\sim 1$  MeV.

The degrading foils :

The thickness of the Al - foil is chosen to eliminate the energy dependence ( the range dependence ) on the scattering angle  $\theta$  for the  $\alpha$  - group under consideration ( fig . 3 ) . Besides , such a thickness has to be enough to prevent the recoil nuclei out going from the reaction from reaching the SSNTD surface .

After passing this foil the measured  $\alpha$  - group with the highest energy must has a range less than the detector thickness . In the same time the measured  $\alpha$  - group with the lowest energy must reach the detector surface with energy not lower than the sensitivity threshold of the SSNTD .

The  $\alpha$  - particle energy  $E_d$  and range  $R_d$  in Makrofol after passing an AL foil of thickness  $d$  can be calculated using the data available in literature then plotted graphically . In order to simplify the procedure of determining  $R_d$  , the obtained curves are scaled in a single curve (fig . 4) to be used together with the simple relation :

$$R_d ( E_\alpha ) = R_0 ( E_\alpha ) - 6.0 d \quad (1)$$

where :

$R_d$  - is the range ( in  $\mu\text{m}$  ) ,

$d$  - is the Al foil thickness ( in  $\text{mg} / \text{cm}^2$  ) ,

$E_\alpha$  - is the  $\alpha$  - particle energy before entering the Al foil , and

$R_0$  - is the range ( in  $\mu\text{m}$  ) when  $d = 0$  .

In the same time a special schematic normograph ( fig . 5) is constructed to replace the same procedure described in figure (4) . The normograph makes easier the choice of the suitable Al thickness and the determination of the range - energy relation .

The angular ditribution of the  $^{59}\text{Co} ( p , \alpha ) ^{56}\text{Fe}$  reaction :

The SSNTD technique was used by Bakr et al <sup>18/</sup> to measure the angular distributions of  $\alpha$  - particles from the  $^{59}\text{Co} ( p , \alpha ) ^{56}\text{Fe}$  reaction at proton energies from 1.6 to 2.4 MeV . A round bent Makrofol-E sheets of 300  $\mu\text{m}$  thickness were fixed in the outer grove of the cylindrical scattering chamber . Thus it was possible to expose the SSNTD simultaneously to  $\alpha$  -particles out going from the reaction at angles  $30^\circ - 150^\circ$  with  $15^\circ$  intervals and entering the SSNTD at right angle . Before entering the detector , the  $\alpha$  - particles passed through Al foils of different thicknesses .

Angular distributions of the  $\alpha_0, \alpha_1, \alpha_2, \alpha_3$ , and  $\alpha_4$  - groups (  $Q = 3.24, 2.385, 1.155, 0.58$ , and  $0.3$  MeV respectively ) have been measured . These groups lead to the ground and next four excited states of  $^{56}\text{Fe}$  . The charge of the incident protons was 5000  $\mu\text{Curie}$  in each run . This lasted about 5 hours .

On etching the Makrofol detector ,  $\alpha_4$  tracks on the etched surface of the detector , then followed by  $\alpha_3, \alpha_2, \dots$  etc . groups . In order to get the number of  $\alpha$  - tracks at each angle the scanning of the irradiated area was performed at depths  $h \sim R$  of each group . The optical microscope was mostly having amplification  $40 \times 12.5$  .

The absolute values of the cross sections of the investigated groups ranged from  $5 \mu\text{barn} / \text{ster.}$  to  $72 \mu\text{barn} / \text{ster.}$  The errors in the angular distribution shape were  $\sim 14\%$  . An example of the obtained angular distributions is shown in figure (6) for proton energies 2.2 and 2.4 MeV .

#### IV . Conclusion

The insensitivity of the SSNTD , under suitable etching conditions , to protons , deuterons and tritons is one of main advantages of such technique . When  $\alpha$  - groups are separated to an extent of  $\Delta E > 500 \text{ keV}$  , the track diameter distribution is the unnecessary and consequently , the evaluation of  $\alpha$  -group intensities is a quite simple and quick procedure . Investigation of a low yield nuclear reaction is an important application of the SSNTD . The full angular distribution of  $\alpha$  - groups can be measured by a single irradiation operation of arbitrary duration .

#### References

- / 1 / Gy . Somogyi , Atomki Kozl . , 8 ( 1966 ) 218 . ; L . Mesko , B . Schlenk , Gy . Somogyi and A . Valek , Nucl. Phys. A130 ( 1969 ) 449 ; Gy . Somogyi and B . Schlenk , Radiation Effects , 5 ( 1970 ) 61 .
- / 2 / M . H . S . Bakr , I . Hunyadi , B . Schlenk , Gy . Somogyi and A . Valek , Atomki Kozl. 16 ( 1974 ) 123 .
- / 3 / R . L . Fleisher , P . B . Price and Walker , " Nuclear Tracks in Solids " , University of California Press , Berkeley , USA , ( 1975 ) .
- / 4 / M . H . S . Bakr , A . R . E . A . E . A . / Rep. 208 ( 1978 ) .
- / 5 / F . M . Membray , M . Fromm , A . E . Rahmany and A . Chambaudet , Nuclear Tracks and Radiation Measurements 21 ( 1993 ) 417 .
- / 6 / M . H . S . Bakr , F . I . Asfour , M . N . H . Comsan , T . Z . Abou Elnasr and S . A . Hassan , Arab J. of Nucl. Sc. and Appl. 14 ( 1981 ) 225 .

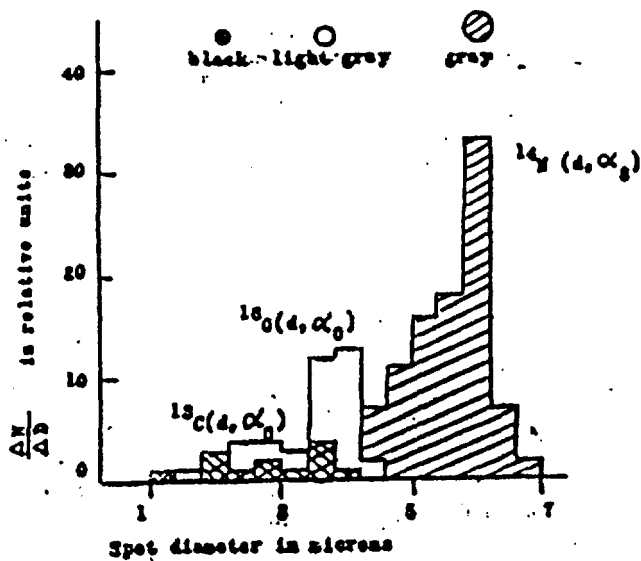


Fig (1) Diameter distribution of track pits measured for the reaction  $^{14}\text{N}(d, \alpha)^{12}\text{C}$  at  $E_d = 640$  keV and  $\Theta = 30^\circ$ .

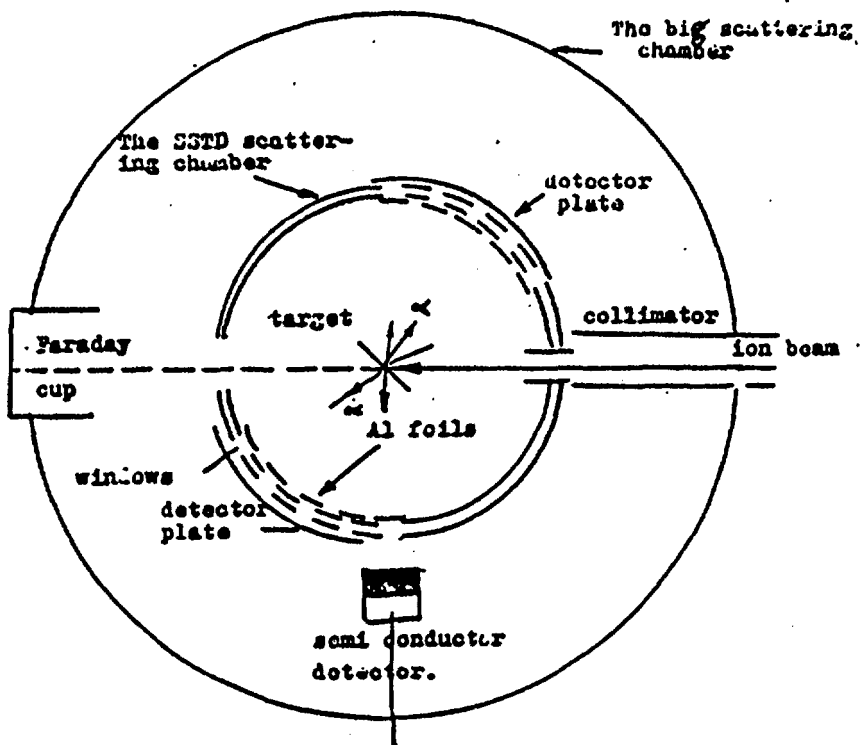


Fig (2) A schematic view of the experimental arrangement for using the SSNTD for  $\alpha$ -particle angular distribution measurements.

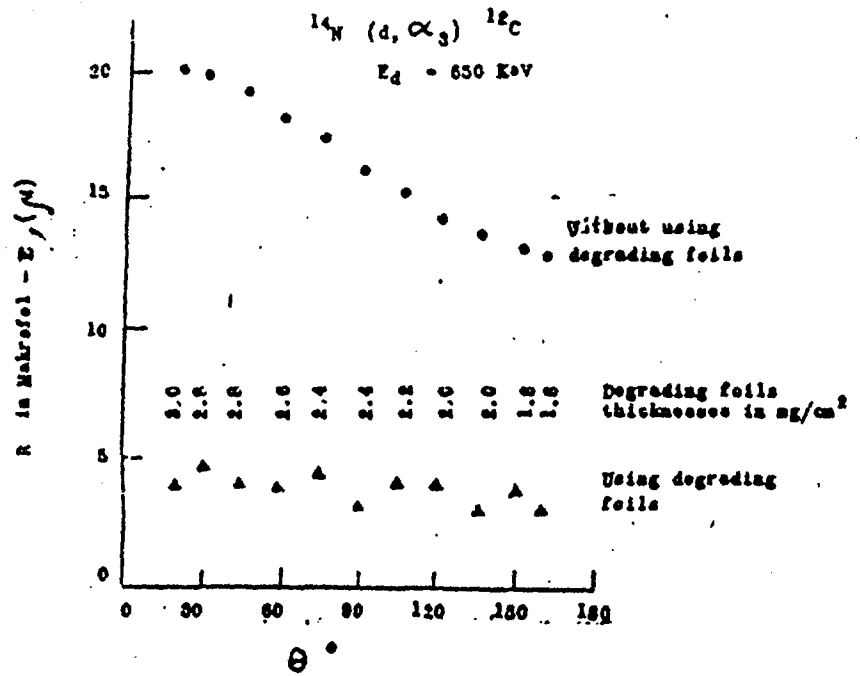
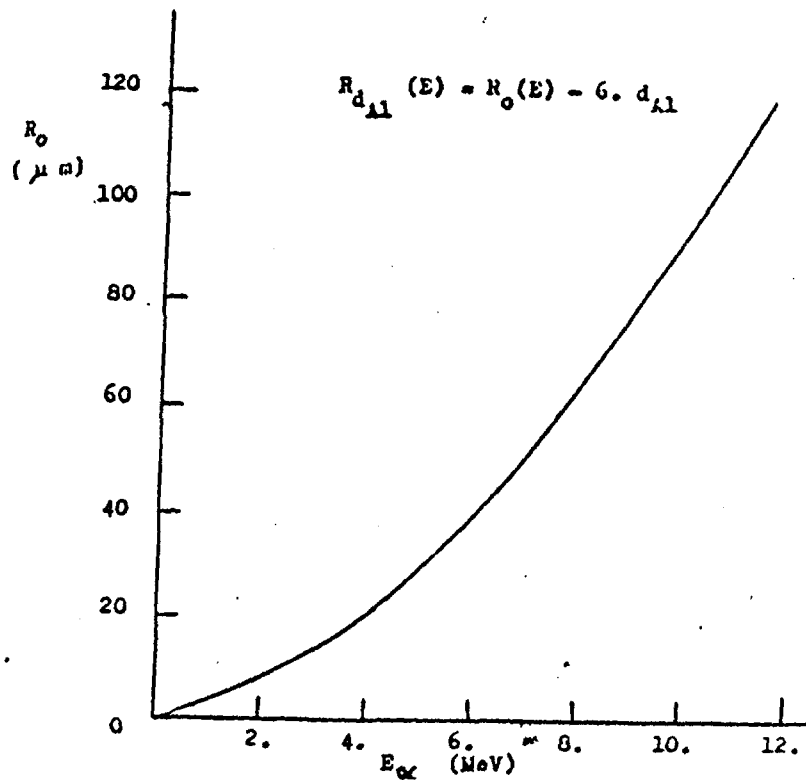


Fig. (3) The influence of degrading Al foils in eliminating the dependence of the range  $R$  on the scattering angle  $\Theta$  for the  $^{14}\text{N} (d, \alpha_3) ^{12}\text{C}^*$  reaction.



Fig(4) The scaled curve for the  $\alpha$  - particle range in Makrofol-E after passing degrading Al foils.

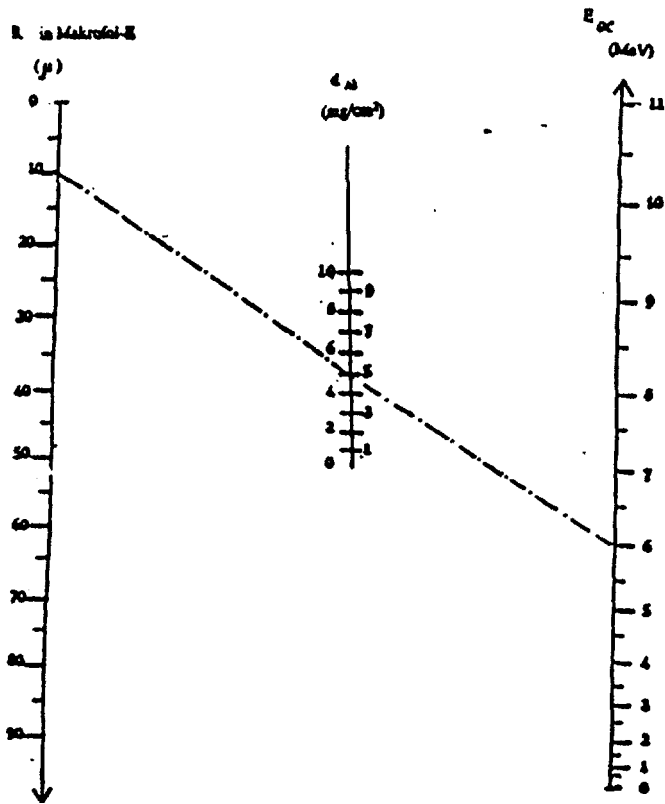


Fig.(5) A nomograph for the relation between range, energy and degrading Al thickness.

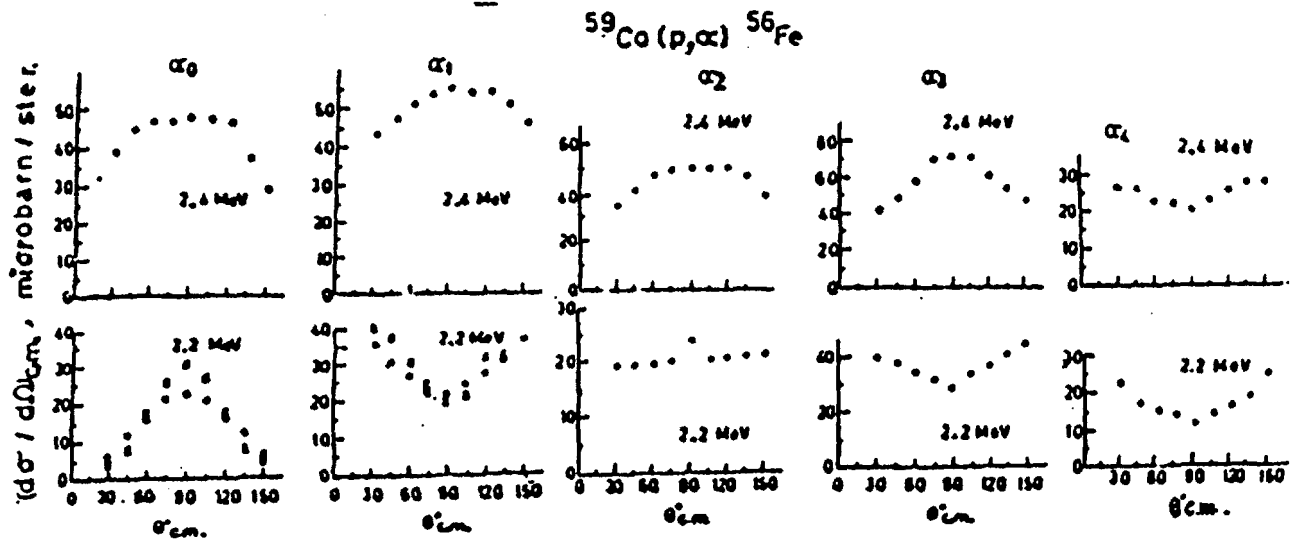


Fig.(6) Angular distributions of five  $\alpha$  - groups from the  $^{59}\text{Co}(p, \alpha)^{56}\text{Fe}$  reaction at  $E_p = 2.2$  and  $2.4$  MeV.



EG9700112

**Analytical Calculations of the efficiency of Gamma Scintillators****Part-I : Total Efficiency for Coaxial Disk Sources***Younis S. Selim, Mahmoud I. Abbas and M.A. Fawzy*

Physics Department, Faculty of Science, Alexandria University, Aleaxndria

**Abstract:**

Total efficiency of clad right circular cylindrical NaI(Tl) scintillation detector from a coaxial isotropic radiating circular disk source has been calculated by the use of rigid mathematical expressions. Results were tabulated for various gamma energies.

**Introduction:**

Total efficiency of scintillation detectors can be obtained either experimentally or theoretically. The experimental method is limited primarily to gamma energies of the common radioisotope sources. In order to obtain efficiencies for intermediate energies interpolation is required. On the other hand the theoretical calculations can provide the scintillator efficiencies at any specified energy.

The total efficiency  $\epsilon_T$  equals to the product of two efficiencies, namely the geometrical efficiency  $\epsilon_g$  and the intrinsic total efficiency  $\epsilon_{IT}$ . Treatment of  $\epsilon_g$  has been given in a previous work, Selim and Abbas (1994).

To summarize, calculations of  $\epsilon_{IT}$  have been reported by Miller *et al* (1961), Zerby *et al.* (1961), Seltzer *et al.* (1971) and Grosswendt *et al.* (1976) using Monte Carlo method, and Irfan *et al.* (1970) by the use of direct

# Analytical Calculations of the efficiency of Gamma Scintillators

## Part-I : Total Efficiency for Coaxial Disk Sources

*Younis S. Selim, Mahmoud I. Abbas and M.A. Fawzy*

Physics Department, Faculty of Science, Alexandria University, Alexandria

### **Abstract:**

Total efficiency of clad right circular cylindrical NaI(Tl) scintillation detector from a coaxial isotropic radiating circular disk source has been calculated by the use of rigid mathematical expressions. Results were tabulated for various gamma energies.

### **Introduction:**

Total efficiency of scintillation detectors can be obtained either experimentally or theoretically. The experimental method is limited primarily to gamma energies of the common radioisotope sources. In order to obtain efficiencies for intermediate energies interpolation is required. On the other hand the theoretical calculations can provide the scintillator efficiencies at any specified energy.

The total efficiency  $\epsilon_T$  equals to the product of two efficiencies, namely the geometrical efficiency  $\epsilon_g$  and the intrinsic total efficiency  $\epsilon_{IT}$ . Treatment of  $\epsilon_g$  has been given in a previous work, Selim and Abbas (1994).

To summarize, calculations of  $\epsilon_{IT}$  have been reported by Miller *et al* (1961), Zerby *et al.* (1961), Seltzer *et al.* (1971) and Grosswendt *et al.* (1976) using Monte Carlo method, and Irfan *et al.* (1970) by the use of direct

mathematical expression only for isotropic coaxial radiating point sources. In addition, Beam *et al.* (1978) and Cesana *et al.* (1977,1978) by the use of Monte Carlo program, considered the case of isotropic radiating point sources located off the axis of the detector. Recently, Selim and Abbas (1995,1996) by using efficient analytical expressions considering the previous cases, all together.

**Mathematical Viewpoint:**

In the present work we derived a direct mathematical expression in an integral form for the total efficiency of a right circular cylindrical ( $2R \times L$ ) detector using an off-axis isotropic radiating point source, by the use of the spherical coordinates system (consider the case of the lateral distance  $\rho$  to be less than the detector circular face radius  $R$ ).

The total efficiency of a cylindrical ( $2R \times L$ ) detector arising from a coaxial-isotropic radiating circular disk source (with radius  $S$ ) is obtained by averaging over  $\rho$ , see figure (1). Knowing the location of the point source which is defined by  $(\rho, h)$  and the direction of incidence of the photon which is defined by the polar angle  $\theta$  and the azimuthal angle  $\phi$ , the path of the incidence photon through the detector active volume, which is known as the traversed distance  $d$ , is obtained.

The derived analytical expression of the total efficiency of a coaxial isotropically radiating circular disk source, in which  $S < R$ , is given by:

$$\langle \epsilon_T \rangle = \frac{2}{S^2} \int_0^S \epsilon_T \rho d\rho \quad (1)$$

where,  $\epsilon_T$  is the total efficiency of an isotropic off axis radiating point source and is defined as:

$$\epsilon_T = \frac{1}{2\pi} (Y_1 + Y_2 + Y_3 + Y_4) \quad (2)$$

with,

$$Y_1 = \pi \int_0^{\theta_1} f_1 d\theta$$

$$Y_2 = \int_{\theta_1}^{\theta_2} \int_0^{\pi} f_2 d\phi d\theta$$

(3)

$$Y_3 = \int_{\theta_1}^{\theta_3} \left[ \phi'_{\max} f_1 - \int_0^{\phi'_{\max}} f_2 d\phi \right] d\theta$$

$$Y_4 = \int_{\theta_2}^{\theta_4} \int_0^{\phi_{\max}} f_2 d\phi d\theta$$

$$\theta_1 = \tan^{-1} \frac{R-\rho}{h+L}$$

$$\theta_2 = \tan^{-1} \frac{R-\rho}{h}$$

$$\theta_3 = \tan^{-1} \frac{R+\rho}{h+L}$$

$$\theta_4 = \tan^{-1} \frac{R+\rho}{h}$$

(4)

$$f_i = (1 - e^{-\mu d_i}) \sin \theta, \quad i = 1, 2$$

$$d_1 = \frac{L}{\cos \theta}, \quad d_2 = \frac{Y}{\sin \theta} - \frac{h}{\cos \theta} \quad (5)$$

$$\phi_{Max} = \cos^{-1} \frac{\rho^2 - R^2 + h^2 \tan^2 \theta}{2h\rho \tan \theta} \quad (6)$$

$$\phi'_{Max} = \cos^{-1} \frac{\rho^2 - R^2 + (h+L)^2 \tan^2 \theta}{2(h+L)\rho \tan \theta}$$

and finally

$$Y = \rho \cos \phi + \sqrt{R^2 - \rho^2 \sin^2 \phi} \quad (7)$$

$\mu$  is the total attenuation coefficient of the scintillator at corresponding energy, Hubbell *et al* (1995).

For soft rays (< 100 KeV) the attenuation in the scintillator's cap is to be considered. In this case multiply the function  $f_i$  (equation - 5) by  $e^{-\mu_c t / \cos \theta}$  where  $\mu_c$  is the total attenuation coefficient of the cap material and  $t$  its thickness.

Systematic calculations of  $\langle \epsilon_T \rangle$  of a clad right circular cylindrical 3" x 3" NaI (TI) detector for coaxial isotropically radiating circular disk source at different energies, source - to - detector distances and with different source radii were calculated see Figure (2) and Tables (1-5).

**Conclusion:**

In this paper, by the use of compact analytical expressions the total efficiency of a right circular cylindrical scintillation detector using coaxial isotropic radiating circular disk source was calculated. A forthcoming work will consider wider sources ( $S > R$ ).

**Acknowledgement:**

The authors would like to thank prof. John H. Hubbell NIST, Gaithersburg, MD, USA, for kindly providing us with comprehensive accurate tables of the attenuations coefficients.

**Figures Captions:**

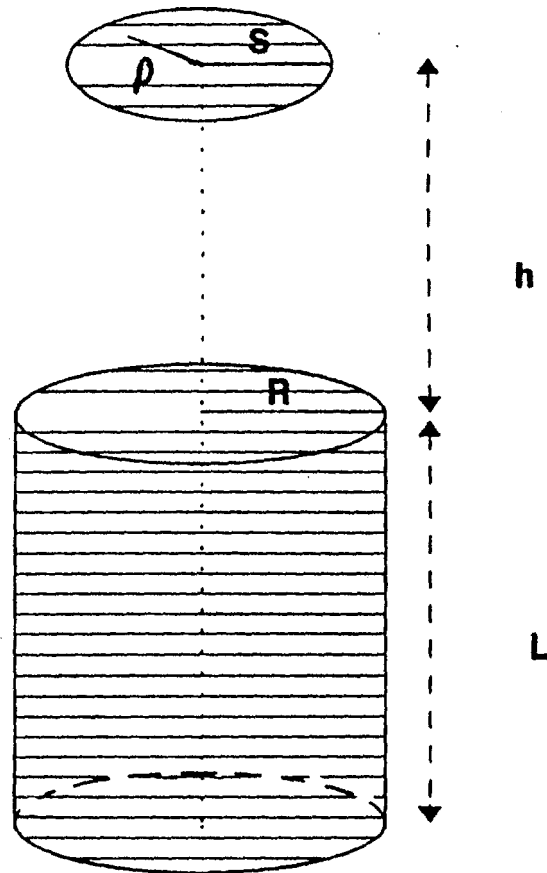
Fig. (1): Coaxial - circular disk to cylindrical NaI(Tl) scintillation detector.

Fig. (2): Variations of the total efficiency with the photon energy.

**References:**

- 1- Beam G.B., Wielopolski L., Gardner R.P. and Verghese K. (1978). Nucl. Instrum. Meth. 154, 501.
- 2- Cesana A. and Terrani M. (1977). Analytical Chem. 49, 1156.
- 3- Cesana A. and Terrani M. (1978). Energ. Nucl. 25, 3.
- 4- Grosswendt B. and Waibel E. (1976) Nucl. Instrum. Meth. 133,25.
- 5- Hubbell J.H. and Seltzer S.M. (1995). NISTIR 5632, USA.
- 6- Irfan M. and Prasad R.D.G. (1970). Nucl. Instrum. Meth. 88, 165.

- 7- Miller W.F. and Snow W.J. (1961). ANL - 6318, Argonne National Laboratory.
- 8- Selim Y.S. and Abbas M.I. (1994). Radiat. Phys. Chem. 44, 1,1.
- 9- Selim Y.S. and Abbas M.I. (1995). to be published in Egyp. J. Phys.
- 10- Selim Y.S. and Abbas M.I. (1996) to be published in Radiat. Phys. Chem.
- 11- Seltzer J.M. and Berger M.J. (1971). ANS Trans. 14, 124.
- 12- Zerby C.D. and Moran H.S. (1961). Nucl. Instrum. Meth. 14, 115.



**Fig.(1)**

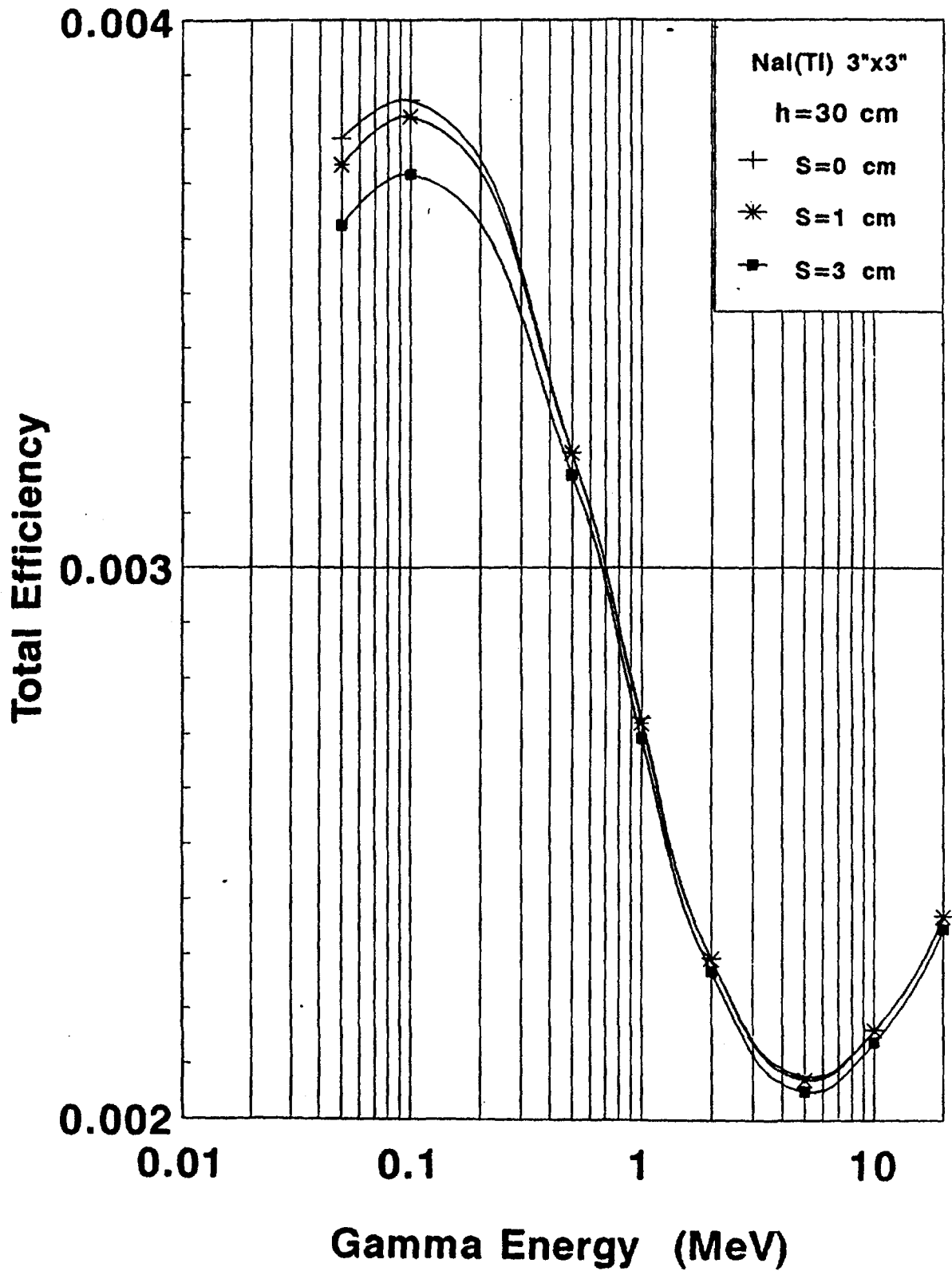


**Fig.(2)**

Table (1):  $h = 0$  cm

S cm	E <sub>γ</sub> MeV							
	0.05	0.1	0.5	1	2	5	10	20
0	0.4143	0.4517	0.3883	0.3205	0.2670	0.2416	0.2530	0.2795
.1	0.4230	0.4612	0.3963	0.3271	0.2725	0.2466	0.2582	0.2853
.5	0.4161	0.4536	0.3887	0.3207	0.2672	0.2419	0.2532	0.2797
1	0.4152	0.4526	0.3852	0.3174	0.2644	0.2394	0.2506	0.2768
1.5	0.4149	0.4523	0.3804	0.3130	0.2607	0.2361	0.2472	0.2729
2	0.4148	0.4522	0.3738	0.3069	0.2556	0.2316	0.2424	0.2676
2.5	0.4147	0.4521	0.3647	0.2988	0.2488	0.2255	0.2360	0.2605
3	0.4146	0.4520	0.3519	0.2879	0.2398	0.2175	0.2276	0.2511
3.5	0.4145	0.4508	0.3334	0.2727	0.2276	0.2067	0.2162	0.2383
3.8	0.4058	0.4327	0.3162	0.2596	0.2173	0.1976	0.2066	0.2274

Table (2) :  $h = 1$  cm

S cm	E <sub>γ</sub> MeV							
	0.05	0.1	0.5	1	2	5	10	20
0	0.3353	0.3504	0.2425	0.1936	0.1586	0.1422	0.1487	0.1648
.1	0.3457	0.3584	0.2474	0.1975	0.1617	0.1450	0.1517	0.1681
.5	0.3400	0.3526	0.2417	0.1929	0.1579	0.1416	0.1481	0.1641
1	0.3371	0.3497	0.2377	0.1896	0.1552	0.1392	0.1456	0.1614
1.5	0.3328	0.3452	0.2323	0.1853	0.1517	0.1360	0.1423	0.1577
2	0.3264	0.3383	0.2252	0.1796	0.1471	0.1319	0.1380	0.1529
2.5	0.3167	0.3278	0.2162	0.1725	0.1414	0.1268	0.1326	0.1469
3	0.3023	0.3124	0.2052	0.1640	0.1345	0.1207	0.1262	0.1398
3.5	0.2810	0.2904	0.1923	0.1543	0.1263	0.1138	0.1190	0.1317
3.8	0.2645	0.2738	0.1839	0.1481	0.1220	0.1096	0.1146	0.1267

Table (3) :  $h = 5$  cm

S cm	E <sub>γ</sub> MeV							
	0.05	0.1	0.5	1	2	5	10	20
0	X10 <sup>-1</sup>	X10 <sup>-1</sup>	X10 <sup>-1</sup>	X10 <sup>-1</sup>	X10 <sup>-1</sup>	X10 <sup>-1</sup>	X10 <sup>-1</sup>	X10 <sup>-1</sup>
.1	0.9521	0.9604	0.6278	0.5074	0.4186	0.3762	0.3930	0.4340
.5	0.9794	0.9804	0.6393	0.5167	0.4262	0.3830	0.4001	0.4419
1	0.9589	0.9606	0.6224	0.5025	0.4142	0.3721	0.3887	0.4295
1.5	0.9425	0.9474	0.6126	0.4939	0.4067	0.3651	0.3816	0.4218
2	0.9211	0.9293	0.6047	0.4881	0.4023	0.3615	0.3777	0.4172
2.5	0.8942	0.9051	0.5938	0.4797	0.3955	0.3554	0.3713	0.4101
3	0.8627	0.8754	0.5804	0.4694	0.3872	0.3479	0.3635	0.4015
3.5	0.8274	0.8415	0.5656	0.4584	0.3785	0.3402	0.3554	0.3924
3.8	0.7893	0.8044	0.5490	0.4462	0.3689	0.3318	0.3465	0.3824
3.8	0.7656	0.7812	0.5388	0.4389	0.3635	0.3272	0.3416	0.3768

# PROC *Third Radiation Physics Conf, Al-Minia, 13 - 17 Nov., 1996*

Table (4) : h = 10 cm

S cm	E <sub>γ</sub> MeV							
	0.05	0.1	0.5	1	2	5	10	20
	X10 <sup>-1</sup>	X10 <sup>-1</sup>	X10 <sup>-1</sup>	X10 <sup>-1</sup>	X10 <sup>-1</sup>	X10 <sup>-1</sup>	X10 <sup>-1</sup>	X10 <sup>-1</sup>
0	0.3111	0.3152	0.2286	0.1892	0.1582	0.1429	0.1490	0.1637
.1	0.3164	0.3196	0.2324	0.1924	0.1608	0.1453	0.1515	0.1664
.5	0.3093	0.3124	0.2255	0.1865	0.1557	0.1406	0.1466	0.1611
1	0.3052	0.3091	0.2224	0.1835	0.1529	0.1379	0.1439	0.1583
1.5	0.3007	0.3054	0.2201	0.1813	0.1509	0.1360	0.1419	0.1563
2	0.2958	0.3008	0.2179	0.1795	0.1493	0.1344	0.1403	0.1546
2.5	0.2903	0.2957	0.2157	0.1777	0.1478	0.1331	0.1389	0.1531
3	0.2845	0.2900	0.2132	0.1759	0.1464	0.1318	0.1376	0.1516
3.5	0.2782	0.2839	0.2105	0.1739	0.1449	0.1306	0.1363	0.1500
3.8	0.2744	0.2801	0.2087	0.1727	0.1440	0.1298	0.1355	0.1491

Table (5) : h = 50 cm

S cm	E <sub>γ</sub> MeV							
	0.05	0.1	0.5	1	2	5	10	20
	X10 <sup>-2</sup>	X10 <sup>-2</sup>	X10 <sup>-2</sup>	X10 <sup>-2</sup>	X10 <sup>-3</sup>	X10 <sup>-3</sup>	X10 <sup>-3</sup>	X10 <sup>-3</sup>
0	0.1375	0.1408	0.1232	0.1056	0.8954	0.8113	0.8451	0.9250
.1	0.1401	0.1433	0.1254	0.1075	0.9111	0.8255	0.8599	0.9412
.5	0.1369	0.1403	0.1227	0.1051	0.8893	0.8053	0.8391	0.9189
1	0.1355	0.1390	0.1221	0.1045	0.8841	0.8001	0.8339	0.9136
1.5	0.1344	0.1379	0.1217	0.1042	0.8817	0.7979	0.8316	0.9112
2	0.1335	0.1370	0.1214	0.1040	0.8802	0.7966	0.8302	0.9096
2.5	0.1327	0.1362	0.1211	0.1038	0.8790	0.7958	0.8292	0.9083
3	0.1320	0.1355	0.1208	0.1037	0.8781	0.7951	0.8285	0.9073
3.5	0.1315	0.1350	0.1205	0.1035	0.8772	0.7946	0.8279	0.9063
3.8	0.1312	0.1347	0.1203	0.1034	0.8767	0.7943	0.8274	0.9056



## Optimization of a Neutron Detector System for the Fourier RTOF-Diffractometer Facility at the ET-RR-1 Reactor

R.M.A.Maayouf, A.S.El-Kady and Y.H.El-Shaer

*Reactor & Neutron Physics Dept., NRC, Atomic Energy Authority,  
Cairo, Egypt*

The present work deals with the optimization of a detector system for use with the Fourier reverse time of flight (RTOF) diffractometer facility recently installed at the ET-RR-1 reactor. The detector system of the diffractometer is designed for detecting neutrons scattered from the sample at an angle  $2\theta=90^\circ$  and consists of 4 independent scintillation detector elements; arranged according to the time focusing geometry in order to increase the luminosity of the diffractometer for the given resolution. Each of the detector elements is made of 1mm thick  $^6\text{Li}$ -glass scintillator (NE-912) whose surface area is  $200 \times 200 \text{mm}^2$ . The present detector system ensures reliable identification and separation of thermal neutron pulses from those due to fast neutrons and gamma-quanta. It has been found; from measurements with a diamond powder sample, that it is possible to obtain a neutron diffraction pattern; within 30 minutes; using the present detector system and with resolution  $\approx 0.54\%$ .

Among the most acute problems in the development of a high resolution powder neutron diffraction method, are those concerned with the effective use of the available neutron beam and the instrument's luminosity. The instrument's luminosity could be increased either by using multidetector systems or position sensitive detectors (<sup>1,2</sup>). The possibilities of such instruments are limited; especially when it is concerned with the extreme action upon the sample. This makes the fixed geometry diffractometers, based on the TOF technique, the most effective set-ups. The most effective use of the neutron beam is when the Fourier correlation diffractometry is applied (<sup>3</sup>). This method is based on the Fourier analysis, since any spectrum can be composed of series of ground waves and higher order Fourier components. This technique has been improved by the idea of triggering the TOF analyzer by detected neutrons instead of by the rotor's position; known as reverse time -of flight (RTOF) method (<sup>4-5</sup>). In RTOF Fourier measurements, the incoming neutron beam is modulated periodically by a chopper so that the neutron modulation will be extended over a wide range of different frequencies. The unknown TOF distribution is then constructed by recording properly delayed sequences of the pick-up signals

representing the periodic modulation of the neutron beam. Since the detection of neutron triggers off the addition of the pick-up sequence to the analyzer's memory, the outcome of this stochastic process is a sum of many independent random variables. The origin of the correlation is obviously the contribution of every detected neutron to all channels of the TOF spectrum. In principle a measurement consists of observing the phase angle and the frequency of the beam modulation at the time of neutron detection, but because the information is recorded in the form of a pick-up sequence, the outcome of the experiment is a spectrum of correlated channels instead of a group of independent observations. One advantage of this technique is that it provides a high resolution and results in a synthesized spectrum without any off-line data manipulations.

Recently, a Fourier RTOF diffractometer facility was installed at the ET-RR-1 reactor for studying condensed matter. The facility applies a four element detector system which is set according to the time focusing geometry <sup>(6)</sup>. The present paper deals with the main characteristics of the detector system as deduced from neutron diffraction measurements with a diamond powder sample.

### The Time Focusing Geometry

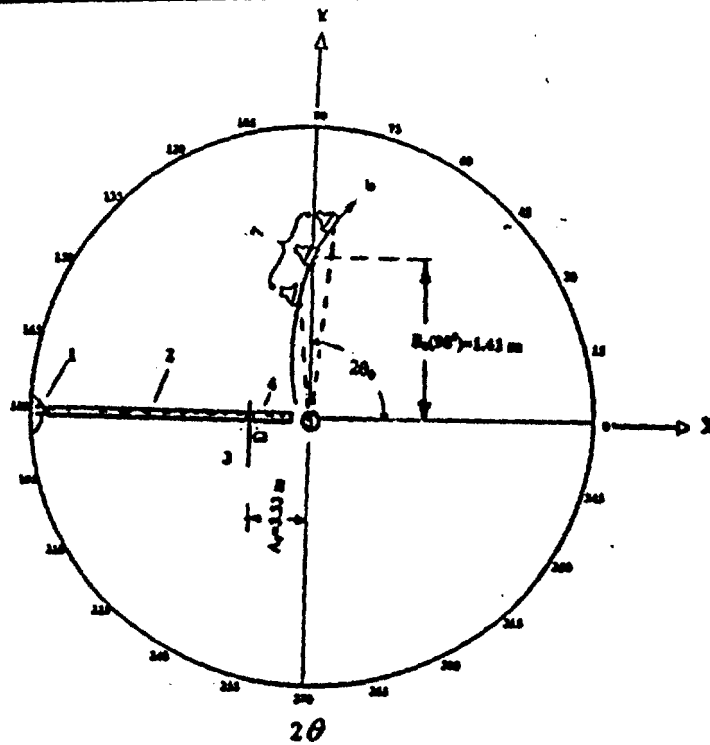
The time of flight of a chopped polyenergetic neutron beam, elastically scattered from a sample to a detector set at scattering angle  $2\theta$  is given by <sup>(6)</sup>:

$$t = 2 \left( \frac{m_n}{h} \right) \cdot D_{hkl} L(\theta) \sin(\theta) \quad (1)$$

where  $h$  is planck's constant,  $m_n$  is the neutron rest mass,  $D_{hkl}$  is the lattice plane distance and  $L(\theta)$  is the flight path of neutrons. It is clear from eq.(1) that  $t$  may be independent of  $\theta$  <sup>(6)</sup> for fixed  $D_{hkl}$  if :

$$L(\theta) \sin(\theta) = L_0 \sin \theta_0 = C_0 \quad (2)$$

Eq.(2) is the basic one for the time focusing, with  $L(\theta) = A_0 + B(\theta)$  and  $L_0 = A_0 + B_0$ , where  $A_0$  is the distance from the chopper to the sample,  $B$  and  $B_0$  are the distances from the sample to the time-focusing surface, at scattering angles  $2\theta$  and  $2\theta_0$  respectively.



- 1. Reactor core 2. Curved NGT 3. Fourier chopper 4. Straight NGT
- 5. Sample position 6. Time focusing curve (Co=3.163) 7. Detector elements

Fig.1: The locus of constant time of arrival for the detector system

The time-focusing surface is uniquely defined by the constants  $A_0$ ,  $B_0$  and  $\theta_0$ , where the locus of constant time of arrival is given by (3):

$$B(\theta) = \frac{(A_0 + B_0) \sin \theta_0}{\sin \theta} - A_0 \quad (3)$$

The angle  $\theta_1$  between the tangent to the locus(3) and the incident beam direction is then:

$$\theta_1 = 2\theta - \tan^{-1} \left[ \frac{2 B(\theta) \tan(\theta)}{A_0 + B(\theta)} \right] \quad (4)$$

The locus of detector used for the Fourier RTOF diffractometer at the ET-RR-1 reactor, at constant scattering angle  $2\theta_0 = 90^\circ$  is presented in Fig.1, for flight path lengths  $A_0 = 3.33\text{m}$  and  $B_0 = 1.14\text{m}$ . The tangent angle  $\theta_0$ , calculated for  $A_0$  and  $B_0$ , is given in Fig.2.

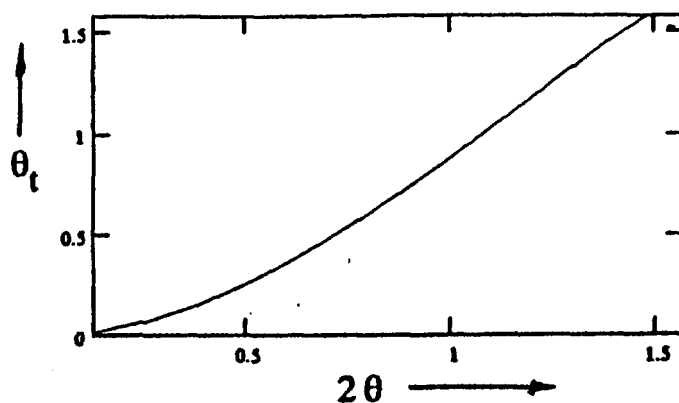


Fig.2: The dependency between the tangent angle to the time focusing curve  $\theta_t$  and the scattering angle  $2\theta$ .

### Optimization of Detector Elements

Two inferences may be drawn from eqns.(2-4). First, if a large array of detectors is placed on the locus, then the solid angle subtended by the detectors at the sample may be increased with consequent increase in the counting rate. Second, for best attainable resolution, any detector array should be situated tangentially to the locus (7). Accordingly the  $^6\text{Li}$ -glass (1mm thick) scintillator (NE-912) is used, in the detector system, for the detection of scattered neutrons as its efficiency for registering thermal neutrons is almost 100%. The detector system is made of pieces small enough to approximate the time focus surface of the scattering neutron trajectories with the desired accuracy so as to attain large solid angle for the scattered neutrons without sacrificing the TOF resolution. The detector system is set at  $90^\circ$  scattering angle and optimized for studying the internal stresses in materials; along with neutron diffraction measurements. It is an array of four independent (NE-912) scintillation elements, installed at time focusing geometry in order to increase the luminosity. Each detector element contains a light guide, photomultiplier. The sum of the pulses from each individual detector element is used as the detector signal. The detector system applies standard Nuclear Instruments Modules (NIM) for conventional pulse electronics.

The surface area of the converter scintillator (NE-912) of each detector element has the dimension  $200 \times 200 \times 1 \text{ mm}^3$ . The detector system aperture is determined by

the area of its elements, their angular position and the distance of each of the elements from the sample. The detector system aperture has been precisely calculated by a special program which calculates the detector element positions needed for the fulfillment of the time-focusing condition. Thus the angular-aperture was found equal to  $\Omega_D = 5.1 \times 10^{-2}$  steradians.

Three types of light guides are used for transmission of the light flashes from the converter scintillator to the photomultiplier (583006E type). The detector electronics discriminate the neutron pulses and form them into rectangular shape and adds up the formed pulses from the 4 detector elements. The summed up pulses are then fed to the RTOF analyzer. Fig.3 represents the pulse-amplitude distribution of each detector element, at the output of the main amplifier, as measured with neutron source (Pu- $\alpha$ -Be) whose total flux is  $6.7 \times 10^6$  n/sec. It is noticeable that good separation, between neutrons and gamma quanta, is achieved for the four detector elements at a discrimination threshold from 1.0-1.5V.

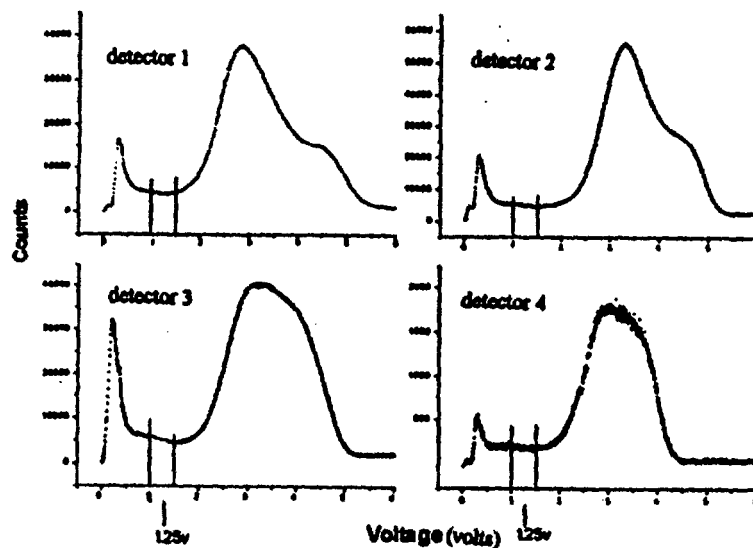


Fig.3: The pulse amplitude distributions of the four detector elements.

### Experimental Measurements

A neutron diffraction measurement was carried out for a standard diamond powder sample, with the Fourier RTOF diffractometer; schematically shown in Fig.1. The diamond sample was contained in a cylindrical Al foil (5mm in diameter and 85 mm in height) and the Fourier chopper was rotating at 8000 rpm. The intensity of the scattered neutrons at a fixed angle  $2\theta = 90^\circ$  is measured by the optimized detector

system, connected to the RTOF analyzer. Fig.4 shows the diffraction pattern of the powdered diamond measured within 30 minutes, at room temperature.

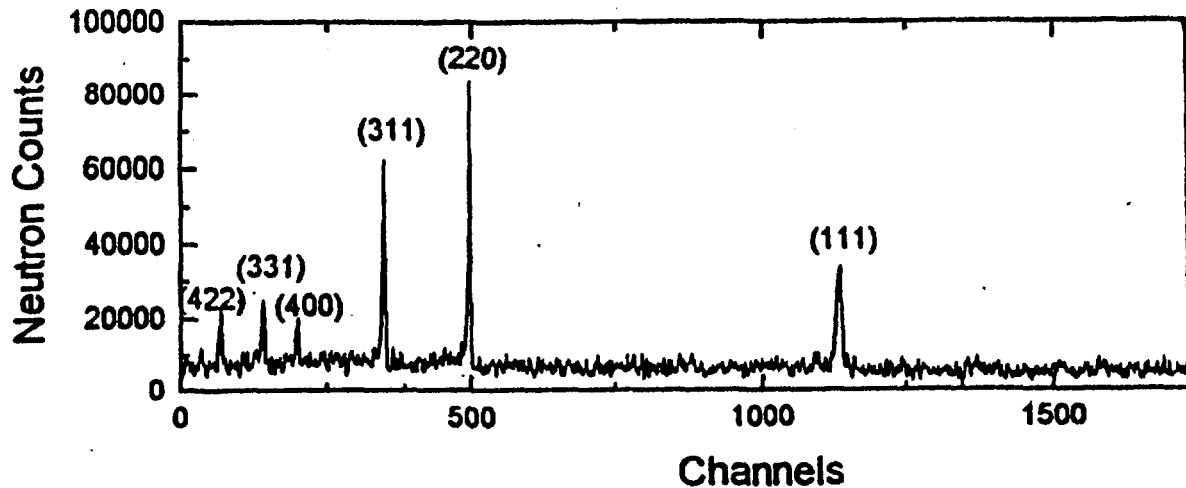


Fig.4: The diffraction pattern obtained for a diamond powder sample.

It is noticeable, from Fig.4, that a good separation between the peaks (i.e good resolution) and a high counting rate, are achieved and within short measuring time.

### Results and Discussion

A Gaussian fitting model was used to determine the diamond peaks positions and their FWHM ( $\Delta D_{hkl}$ ). Fig.5 shows an example for a fitted peak by the Gaussian model.

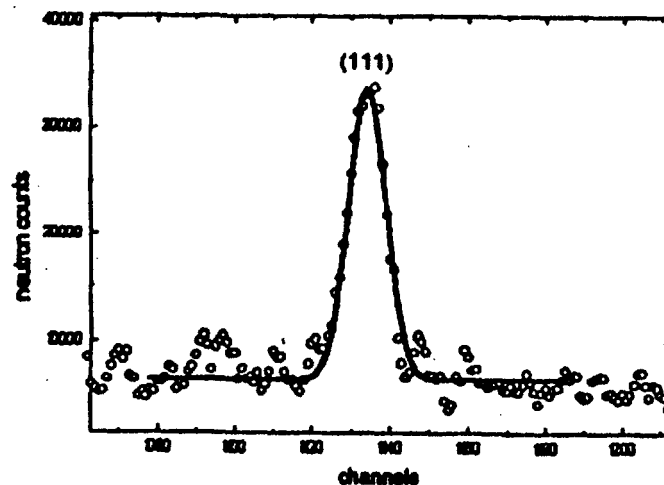


Fig.5: The diamond (111) peak as fitted by a Gaussian model.

The relative resolution  $R(\%) = \Delta D_{hkl} / D_{hkl}$  obtained from the fitted peak parameters is represented in Fig.6. The minimum of the resolution curve determines the best experimental resolution of the diffractometer. This resolution is 0.54% which is consistent with the predicted value (0.5%) according to Ref.(8).

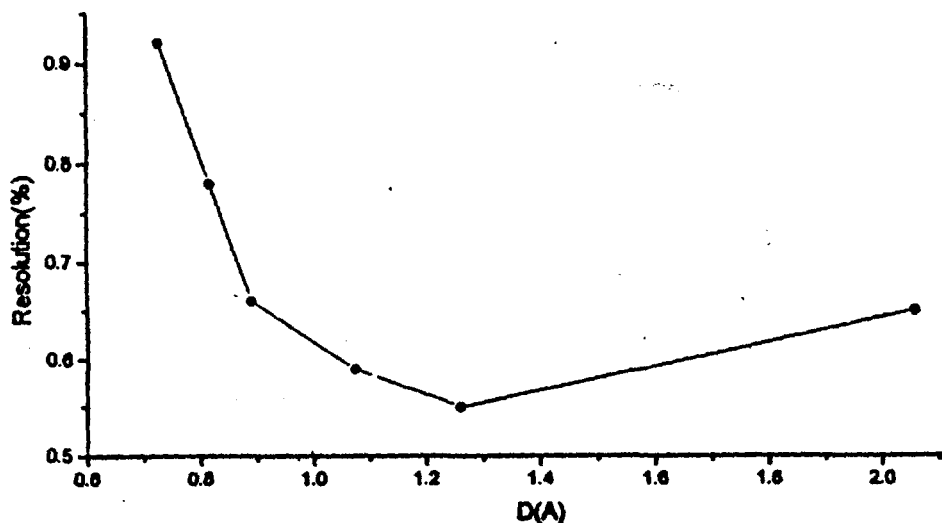


Fig.6: The measured lattice spacing resolution as a function of  $D_{hkl}$

The precise measurement of the time focusing parameter  $C_0 = L \sin \theta$  for a TOF diffractometer determines the accuracy of the obtained absolute crystal lattice dimensions from a neutron diffraction measurement. The calibration of the time focusing constant  $L \sin \theta$  was obtained from the neutron diffraction pattern of diamond. The values of  $L \sin \theta$  was deduced from the diffraction peaks of diamond with indices (111) to (422), using its known lattice parameter and found to be  $(3.154 \pm 0.009 \text{ m})$  which is consistent with the value 3.163m calculated according to eq.(2).

### Conclusions

\* The use of a Fourier chopper combined with neutron guide system and a  $^6\text{Li}$ -glass scintillation detector, arranged according to time-focusing geometry, allows high resolution neutron diffraction measurements at a high counting rate; significantly reducing the measuring time.

\* The resolution and neutron intensity of a Fourier RTOF diffractometer is a matter of careful optimization of the device parameters and a good balance must be obtained between the different contributions to the resolution.

\* The new diffractometer with the adopted geometry could be very suitable for measurements required for solving condensed matter problems; mainly high  $T_c$  superconductivity, and residual stress analysis.

**References**

1. Hewat, A.W., D2B, A New High Resolution Powder diffractometer at ILL, Grenoble, High Resolution Powder Diffraction, Edited by C.R.A. Catlow, Materials Science Forum, **9** (1986) 69-80.
2. Schefer, J., et al., Nucl. Inst. & Meth., A **288** (1990) 477-485.
3. Gompf, F., et al., IAEA Symp. Neutron Inelastic Scattering, Copenhagen, 1968, SH-104/77, p. 417-423.
4. Hiismaki, P., et al., Nucl. Inst. & Meth., **126** (1975) 435-443.
5. Poury, H., Nucl. Inst. & Meth., **156** (1978) 499-514.
6. Carpenter, J.M., Nucl. Inst. & Meth., **47**(1967) 179.
7. Kudryashev, V.A., et al., Optimization of detectors in time-focusing geometry for RTOF neutron diffractometers, Nucl. Inst. & Meth., B **93**, (1994) 355-361.
8. Maayouf, R.M.A., et al., Dual-Purpose RTOF diffractometer facility at the ET-RR-1 reactor, Technical Research Centre of Finland (VTT) Research Notes-1425, Espoo, 1992.

## Neutron Spectrum Measurements from a Neutron Guide Tube Facility at the ET-RR-1 Reactor

R.M.A.Maayouf, I.A.Abdel-Latif and A.S.El-Kady  
Reactor & Neutron Physics Dept., NRC, Atomic Energy Authority,  
Cairo, Egypt.

The present work deals with measurements of the neutron spectrum emitted from a neutron guide tube (NGT) recently installed at one of the ET-RR-1 reactor horizontal channels; designed to deliver thermal neutrons, free from fast neutrons and gamma-rays background, to a Fourier reverse-time-of-flight (RTOF) diffractometer. The measurements were performed using a  $^6\text{Li}$  galsc scintillation detector installed at 3.45 m from a disc Fermi chopper, combined with a multichannel analyzer set at channel width 4 $\mu\text{sec}$ . Also a theoretical model was especially developed for the neutron spectrum calculations. The spectrum calculated according to the developed model was found to be in good agreement with the measured one. It was found, both from measurements and calculations, that the spectrum emitted from the NGT covers, after transmission through a Fourier chopper, neutron wavelengths from 1-4  $\text{\AA}$ . The maximum of the neutron spectrum was found to be at neutron wavelength  $\lambda = 1.39 \text{\AA}$  which is consistent with the value 1.377  $\text{\AA}$  calculated for the curved NGT characteristic wavelength.

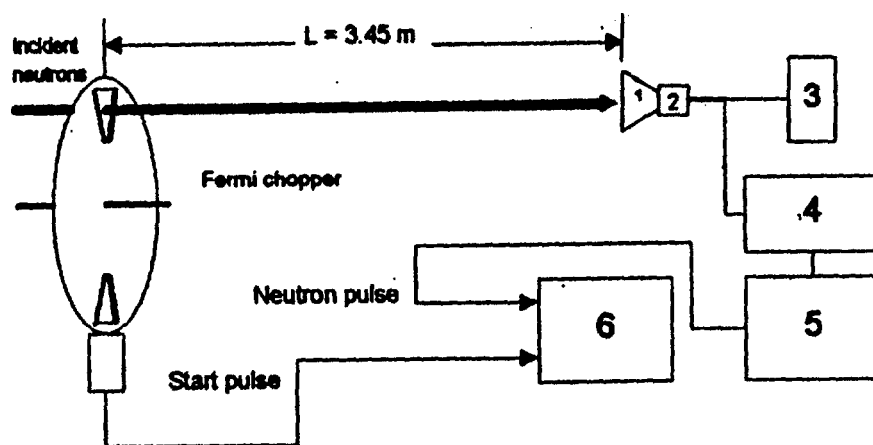
The neutron time of flight (TOF) method has proved to be one of the efficient tools for neutron diffraction studies<sup>(1)</sup>. The TOF method is based on measuring the neutron time of flight through a definite distance; using a neutron chopper which transmits short bursts of neutrons. Accordingly, neutrons of different energies, primarily present in the beam, will be sorted out; the fast neutrons will arrive at the end of the flight distance earlier than the slower ones. Most of the conventional TOF spectrometers apply the Fermi type disk chopper which makes use only of (0.1-0.5)% out of the available neutrons<sup>(2)</sup>.

The Fourier TOF method<sup>(3,4)</sup> has been of considerable interest prior to 1980<sup>(5)</sup> as a highly efficient alternative, of a Fermi chopper system, since it offers, regardless of resolution requirements, a high duty cycle combined with the possibility of exploiting a large beam area<sup>(2)</sup>. The Fourier method has been improved by the reverse time of flight (RTOF) concept<sup>(6,7)</sup> which is based on the triggering of the TOF analyzer by the detected neutrons instead of by the rotor's position. The use of the RTOF diffractometry at the ET-RR-1 reactor (2MW), was assessed in refs.<sup>(8-13)</sup>. Moreover an RTOF diffractometer was recently installed at one of the ET-RR-1 reactor horizontal channels. Such facility consists of a curved neutron guide tube (NGT) designed to deliver thermal neutrons; free from  $\gamma$ -rays and fast neutrons background, to a Fourier chopper which is followed by another straight NGT for collimation of the neutron beam before incidence on the sample. The optimized curved NGT<sup>(14)</sup> has a radius of curvature  $\rho=3388.5\text{m}$ , length  $L=22\text{m}$ , and a rectangular cross sectional area  $S=13.5\times 90\text{mm}^2$  to give a characteristic wavelength of  $\lambda^*=1.377\text{\AA}$ . The straight NGT is 3m long and with the same cross-sectional area of the curved one.  $^{58}\text{Ni}$  isotope is used as a coating layer for the mirror channel walls in both NGT.

The present paper presents neutron spectrum measurements performed at the sample's position, after the RTOF diffractometer's neutron guide system. The experimentally measured spectrum is also compared with that one theoretically calculated according to a special model.

### Neutron Spectrum Measurements

The neutron spectrum was measured after transmission through a Fermi disk type chopper. The chopper has been made of two aluminium disks attached to each other; with 0.5mm thick Cd foil pressed between them. The disk rotor has two radial slits,  $2.9 \times 80 \text{ mm}^2$  at the main radius of 200mm. The chopper was rotating at a constant speed 2840 rpm. At this speed the chopper produces approximately triangular pulses with the FWHM equals to  $48.8 \mu\text{s}$ . The pick up pulse is taken optically through two holes at the periphery. The width and timing of the pickup pulse with respect to the neutron pulse can be adjusted so that the logical "chopper open" pulse can be fully synchronized to the neutron pulse<sup>(1)</sup>. Thus the neutron spectrum was measured with a  $^6\text{Li}$ -glass scintillator detector which was set at a distance 3.45m from the Fermi chopper, being at the sample position, according to the arrangement schematically given in Fig.1.



1)  $^6\text{Li}$ -glass detector 2) Preamplifier 3) High voltage power supply  
4) Main amplifier 5) Discriminator 6) Multichannel analyzer

Fig. 1: A schematic of the arrangement used for neutron spectrum measurements

The neutron spectrum transmitted through 12cm thick beryllium filter was also measured for calibration of time of flight scale. The measured Be filtered spectrum is displayed in Fig.2, where one can notice the well known Be cut-off at 3.952A.

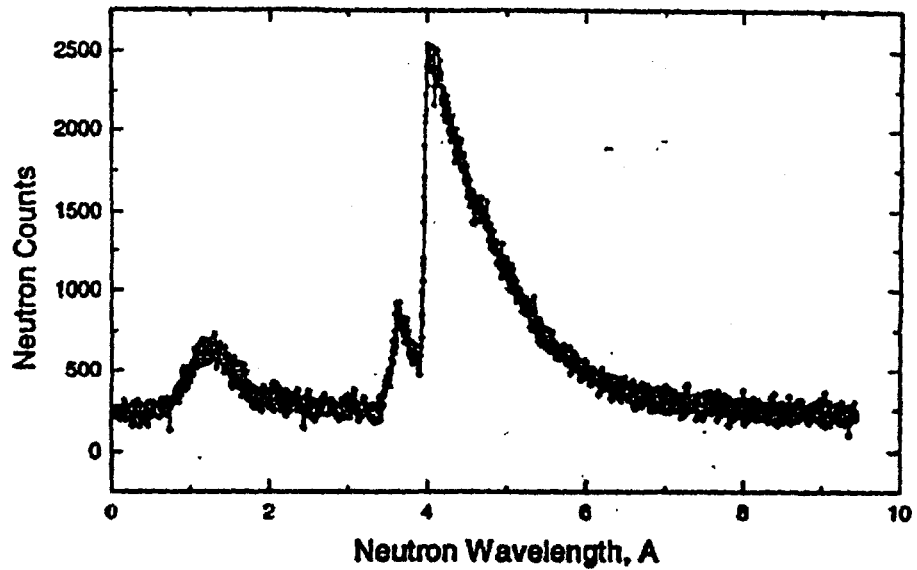


Fig.2: The spectrum transmitted through the Be filter

### Neutron Spectrum Calculations

The neutron beam spectrum at sample position was calculated, taking into account:

- The value of the neutron flux near the reactor core ( $\approx 10^{13}$  n/cm<sup>2</sup>.sec)
- Transmission through the curved NGT.
- Transmission through Fourier chopper and the straight NGT.
- Losses in the NGT system due to polygonality of the mirror channels, junction of optical sections and poor reflectivities.

The neutron spectrum from an ideal curved NGT, whose characteristic angle  $\theta_*$  and critical angle  $\theta_c(\lambda)$ ; is given by (15):

$$\Phi_c(\lambda) = \frac{\phi_m(\lambda)}{4\pi} \frac{S}{L} [4K^2 \cdot (\dots)^2 \cdot T_c(K)] \quad (1)$$

where  $\phi_m(\lambda)$  is the Maxwellian neutron flux at the entrance of the guide,  $K = \theta_c(\lambda)/\theta_*$  and  $T_c(K)$  is the curved NGT transmission coefficient;  $T_c(K)$  is given by (15):

$$T_c(K) = \begin{cases} \frac{2}{3} K^2 & \text{for } K \leq 1 \\ \frac{2}{3} K^2 \left[ 1 - \left(1 - \frac{1}{K^2}\right)^{3/2} \right] & \text{for } K > 1 \\ 4 K^2 \theta_*^2 & \text{for } K \gg 1 \end{cases} \quad (2)$$

The dependency between  $T_c(K)$  and  $K$ , calculated for the curved NGT using eq.(2), is displayed in Fig.3.

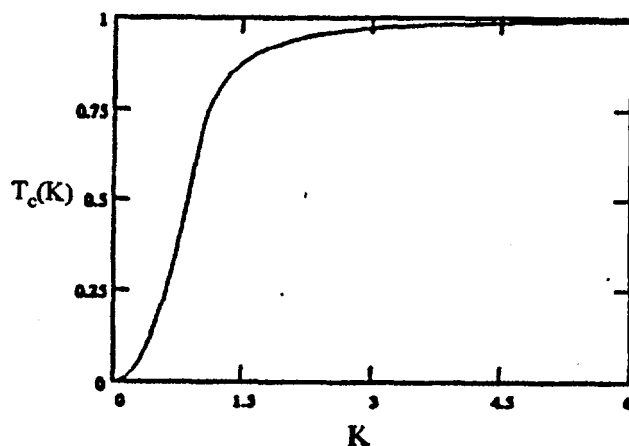


Fig.3. The dependency between  $T_c(K)$  and  $K$  for the curved NGT.

The neutron spectrum from a well-polished, straight NGT whose rectangular cross-section  $S= ab \text{ cm}^2$  and length  $L$  is given by:

$$\Phi_{st}(\lambda) = \phi_{th}(\lambda) T_{st}(K) \quad (3)$$

where  $\phi_{th}(\lambda)$  is the thermalized neutron flux introduced at the entrance of the guide,  $T_{st}(K)$  is its transmission coefficient, given by [15]:

$$T_{st}(K) = \begin{cases} T_0 & \text{for } K = 0 \\ 4 T_0 & \text{for } 0 < K < 1 \\ 4K^2 T_0 & \text{for } K \geq 1 \end{cases} \quad (4)$$

where  $T_0$  is the transmission coefficient for a conventional non-reflecting collimator. The dependency between the relative gain in transmission  $T_{st}(K)/T_0$  and  $K$  according to eq.(4), is given in Fig.4; for the straight NGT.

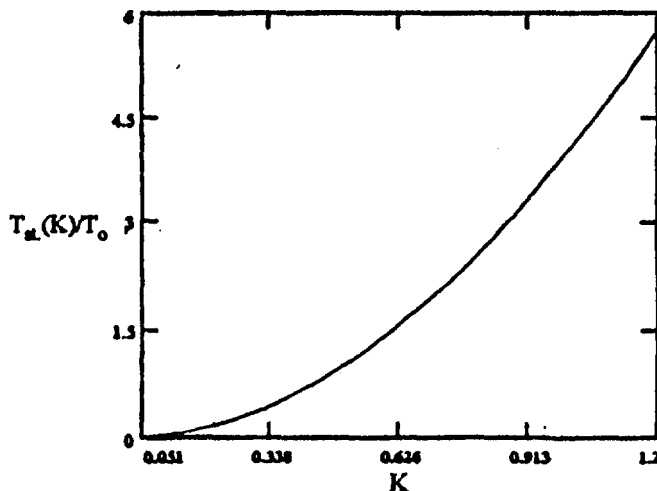


Fig.4. The dependency between  $T_{st}(K)/T_0$  and  $K$  for the straight NGT

The losses in the neutron guide system due to polygonality of the mirror channels, junction of the optical sections and poor reflectivities were calculated following the same procedure of Refs.(16,17) and found to be about 44% of the integral flux value at the entrance of the curved NGT.

A computer code based on eqs.(1-4) was especially developed for the neutron spectrum calculations, taking into account the parameters of both the neutron guide and chopper systems as well as the losses in the neutron guide system. Also, following the same procedure of Ref.(18), the measured neutron spectrum was subjected to the following corrections:

- Correction for the multichannel analyzer dead time.
- Correction for the Fermi chopper transmission function.
- Correction for absorption and scattering out of the beam in 3.45m of air molecules between the Fermi chopper and the detector.

These corrections yielded a total correction factor varying from  $1.092 \times 10^3$  -  $1.477 \times 10^3$  respectively for neutron wavelengths between 1-4Å.

### Results and Discussion

The present calculations yielded the value 1.38Å for the maximum of the neutron spectrum, at a moderator temperature 320°K. Fig.5 represents the corrected experimental neutron spectrum along with that calculated according to the present model.

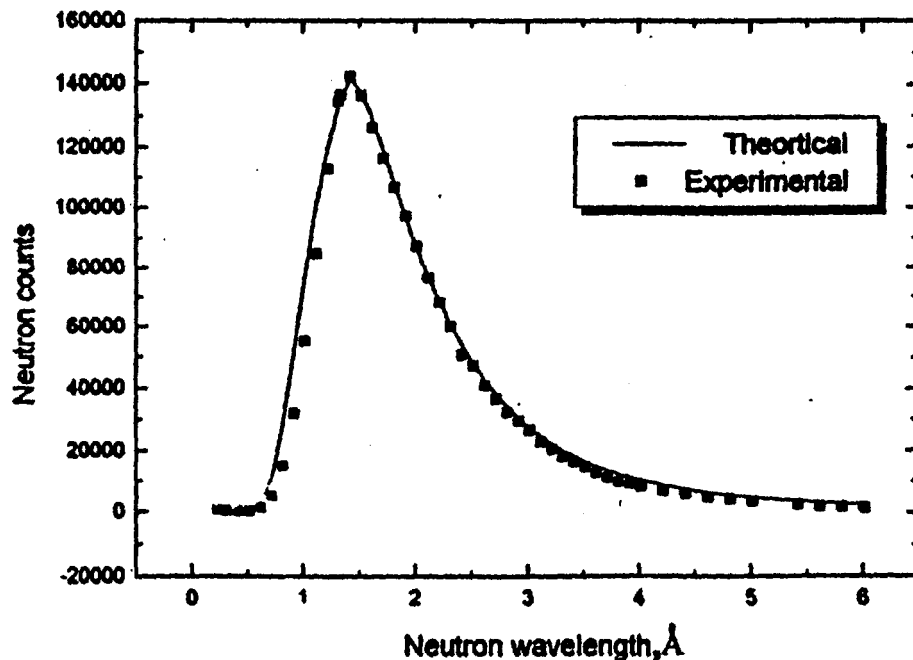


Fig.5. The neutron spectrum at the sample position

The measured neutron spectrum covers the wavelength range from 1-4Å which is adequate, according to the well known Bragg's equation, for neutron diffraction measurements at D values between 0.7-2.9Å respectively.

Two types of reflections take place, according to the value of the incident wavelength, in the curved NGT. If  $\lambda \leq \lambda^*$ , neutrons suffer only reflections from the concave wall of the NGT. The number of such type of reflections (Garland reflections) is given by<sup>(15)</sup>:

$$N_g = \frac{1}{\sqrt{K^2 + x/a}} \quad (5)$$

Where  $x$  is the entrance abscissa of neutrons in the NGT plane of curvature and  $a$  is the width of the NGT. If  $\lambda > \lambda^*$  the neutrons suffer, in addition, another type of reflections according to the value of their angle of incidence. It may be reflected alternatively from the concave and convex walls (zig-zag reflections). The number of reflections in this case is given by:

$$N_z = \frac{2}{\sqrt{K^2 + x/a} - \sqrt{K^2 + x/a - 1}} \quad (6)$$

The dependency between the total number of reflections and  $\lambda$ , calculated using eqs.(5,6), is given in Fig.6; for the curved NGT. It is noticeable, from Fig.6, that the minimum number of reflections occurs at wavelength  $\lambda = 1.38\text{\AA}$  which is consistent with the values  $1.377\text{\AA}$  and  $1.39\text{\AA}$  respectively for the characteristic wavelength of the curved NGT and the maximum of the neutron spectrum measured at sample position. It is concluded that the consistency obtained between the measured and theoretically calculated neutron spectra, ensures the reliability on the physical and optical parameters of the neutron guide system.

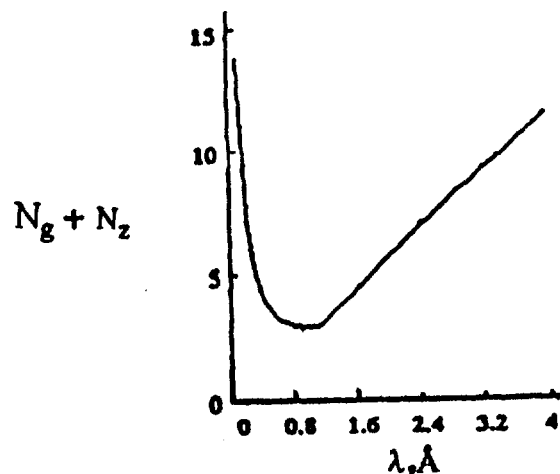


Fig. 6: The dependency between the total number of reflections and  $\lambda$ .

**References:**

1. Buras, B. and Leciejewicz, Phys. Stat. Sol. 4(1964) 349.
2. Maayouf, R.M.A., et al., GKSS report No 91/E/65, Geesthacht, 1991.
3. Colwell, J.F., Miller, P.H.; Whittemore, W.L. (1968) IAEA Symp. Neutron Inelastic Scattering Copenhagen 1968, SM-104/77 429: 437.
4. Colwell, J.F. et al., Miller, P.H.; Whittemore, W.L.; 1969, Nucl. Inst. and Meth. 77: 29-59.
5. Badureck, G., Reach, H., (1978) Proc. Symp. Neutron. Inelastic Scattering, IAEA Vienna, 1977, Vol. 1 : 211.
6. Hiismaki, P.T. (1972) IAEA Conf. Neutron Inelastic. Scattering, Grenoble SM-155/F-10: 805-807.
7. Hiismaki, P.T., et al., Nucl. Inst. & Meth., 156 (1978) 499-415.
8. Kudryashev, V.A., Trounov, V.A., Maayouf, R.M.A., et al., Report LNPI. 1732, USSR Academy of Sciences, Leningrad, 1991.
9. Maayouf, R.M.A., Tiitta, A. & Hiismaki, P., The RTOF Neutron Diffraction Facility at the ET-RR-1 Reactor, VTT Reactor Laboratory, Espoo, June, 1991.
10. Maayouf, R.M.A., et al., Report VTT (Technical Research Centre of Finland), VTT Research Notes-1425, Espoo, 1992.
11. Maayouf, R.M.A., & Tiitta, A.T., VTT Research Notes-1502, Espoo, 1993.
12. Maayouf, R.M.A., Hiismaki, P.E., & Tiitta, A.T., The Multipurpose RTOF Fourier Diffractometer at the ET-RR-1 Reactor, VTT Reactor Laboratory, Espoo, November, 1993.
13. Maayouf, R.M.A., et al., VTT Research Notes 1699, Espoo (1995).
14. Maayouf, R.M.A., El-Kady, A.S., "Optimization of a Neutron Guide Facility for the ET-RR-1 Reactor", Proceedings of the 6th Conference of Nuclear Sciences and Applications, 15-20 March, 1996, Vol.2: 265.
15. Farnoux, B. et al., Neutron Inelastic Scattering, Proc. IAEA Symp., Copenhagen; 353, (1968).
16. Maayouf, R.M.A., et al., Int. Symp. Neutron Optics and Related Research Facilities NOK96, 19-21 March, Kumatori, Osaka, Japan, 1996.
17. Leibnitz, H.M. and Springer, T., J. Nucl. Energy, 17; 217, (1963).
18. Maayouf, R.M.A., et al., Arab J. Nucl. Sci. & Appl., 2(1965) 97.



## A Reverse Time of Flight Analyzer at the ET-RR-1 Reactor

R.M.A.Maayouf, A.S.El-Shafey, M.I.Khalil and I.A.Abdel-Latif

Reactor and Neutron Physics Dept., NRC, Atomic Energy Authority,

Cairo, Egypt

The present work deals both with the theory and performance of a reverse-time of-flight (RTOF) analyzer designed to analyze pulses emitted from a Fourier chopper; recently put into operation at the ET-RR-1 Reactor. The RTOF analyzer was found to be adequate for use with pick up pulses from the Fourier chopper which operates following a frequency window suitable for rotation rates from 0-9000 rpm; synchronically with neutron pulses from a  ${}^6\text{Li}$  glass detector set at time focusing geometry for scattering angle  $2\theta = 90^\circ$ . It was possible, with the present RTOF analyzer, to obtain diffraction patterns, with reasonable accuracy at D values between 0.7-2.9Å and within short measuring time.

The Fourier time-of-flight (TOF) method has been of considerable interest prior to 1980 as a highly efficient alternative of Fermi chopper systems, for measuring the slow neutron TOF spectra<sup>(1)</sup>. The Fourier approach offers<sup>(2-5)</sup>, regardless of resolution requirements, a high duty cycle combined with the possibility of exploiting a large beam area; thus leading to an overall neutron economy which is quite unattainable with the other conventional TOF spectrometers. The Fourier TOF method has been improved by the reverse time-of-flight (RTOF) concept<sup>(6)</sup>, which is based on the triggering of the multichannel analyzer by the detected neutron pulses instead of the rotor's position<sup>(1)</sup>. The RTOF technique is particularly useful in Fourier TOF measurements as it provides an inherently on-line way of performing the required spectrum synthesis without any off-line data manipulations. The use of the Fourier RTOF diffractometry, as efficient tool for studying condensed matter at the ET-RR-1 reactor, was assessed in<sup>(1)</sup>; and the preliminary arrangement to be used at such type of reactor was also given. Further developments of the suggested arrangement were represented in<sup>(7-12)</sup>, along with the main components required for the data acquisition. Moreover, the basic stage<sup>(13)</sup> of the Cairo Fourier diffractometer facility (CFDF), based on the RTOF concept, was recently installed, as IAEA-TC Project EGY/1/022, at one of the ET-RR-1 reactor horizontal channels; it is schematically given in Fig.1.

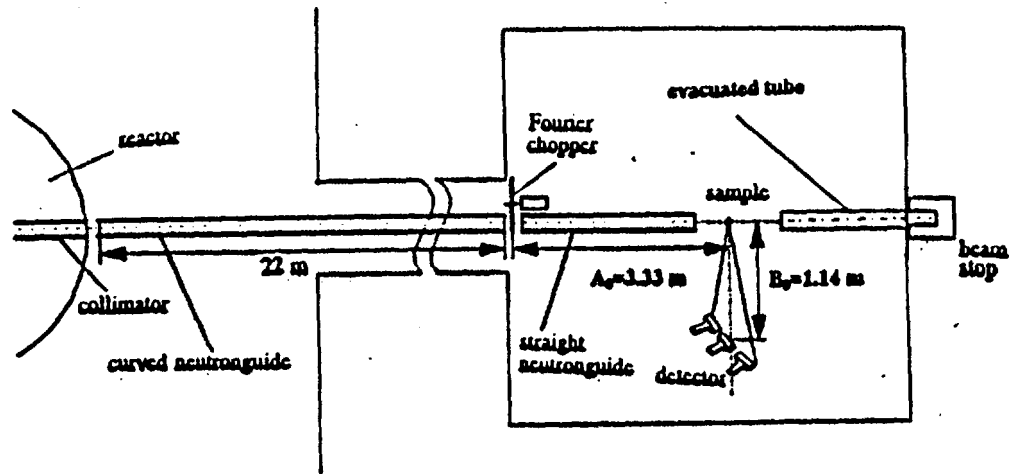


Fig.1: A schematic of the Fourier RTOF facility at the ET-RR-1 reactor

Accordingly the incoming neutron beam, is periodically modulated, as illustrated in Fig.2, by a Fourier chopper; consists of a rotating disk having 1024 periods comprising one neutron-absorbing and one neutron-transmitting sector of equal angular widths. Close to the rotating disk in the neutron beam is a stator piece having the same pattern as the disk. The disk slits pattern, sweeps over the stator pattern, during rotation, allowing the absorbing sectors of the rotor and the stator to coincide, for maximum transmission, and half of the beam intensity pass through the chopper. At its minimum transmission the absorbing sectors of the rotor and the transmitting sectors of the stator coincide; blocking the way of the neutron beam through the chopper. Both the rotor and stator are made of zero-matrix material (Ti-Zr-Mn) (13).

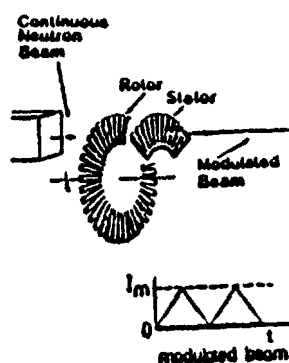
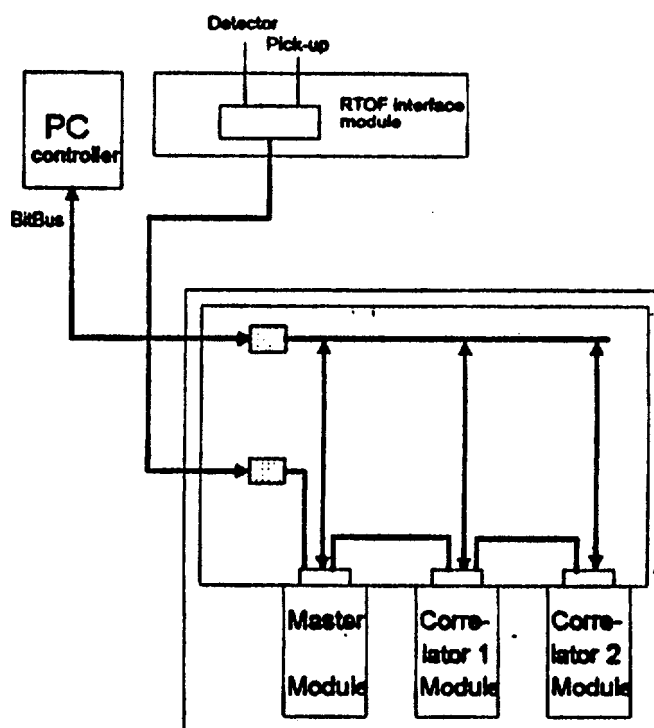


Fig.2: The Fourier chopper

The present paper deals with the theory and performance of the RTOF analyzer used specially for the CFDF.

**Principle of Operation of the RTOF Analyzer**

The block diagram of the RTOF analyzer is given in Fig.3. Accordingly, the detector and pick-up pulses are fed to the interface module; giving rise to the output pulses going to the RTOF analyzer. The RTOF analyzer consists of one master (for controlling the analyzer) and two correlator modules. Each of the two correlator modules has 1024 channel; together represent a 2048 channels shift register. The master module has a clock pulse generator to control the shifting of the pick-up pulses inside the shift register. The PC is connected with the RTOF analyzer through the BitBus communication system.



**Fig.3: Block diagram of the RTOF analyzer**

The curved neutron guide, used for the CFDF schematically shown in Fig.1, delivers thermal neutrons, free from fast neutrons and  $\gamma$ -rays background, to the Fourier chopper. The chopper modulates the beam intensity according to the  $X^{(\omega)}(t)$  law. Simultaneously the chopper optical sensor produces the  $Y^{(\omega)}(t)$  basic electrical reference pick-up signals in phase with the  $X^{(\omega)}(t)$  intensity of the neutron beam. The modulation frequency,  $\omega$ , is determined by the rotation speed of the chopper disk and changes from zero to the maximum value of  $\Omega$  according to a special frequency window,  $g(\omega)$ , during experiment. The electronic block diagram illustrating the principle of the RTOF analyzer operation principle is given in Fig.4. Accordingly, the Fourier analyzer contains an array of N counters and a

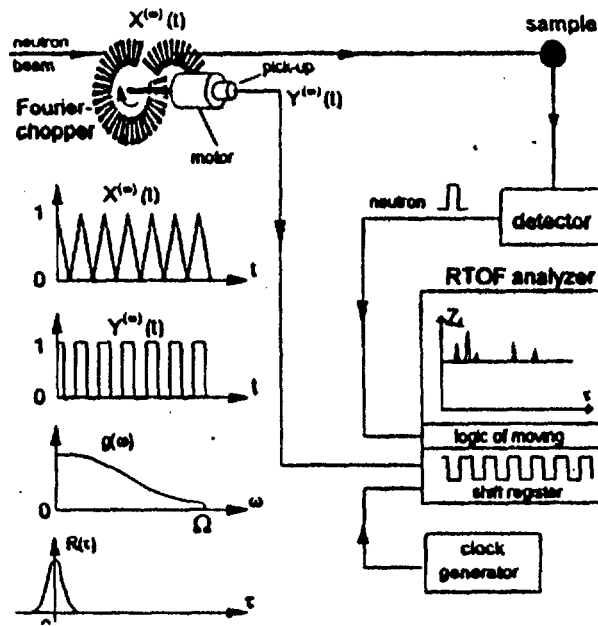


Fig.4: The block diagram illustrating the RTOF analyzer operation

special shift register with the same number of channels. The shift register is an important element of the Fourier analyzer and contains a pattern of the reference pick-up signal over the time interval from  $(t-\Delta N)$  to  $t$ , where  $t$  equals the present moment of time. The reference pick-up signal is connected to the signal input of the shift register while pulses from the clock generator with a period of  $\Delta$  are connected to the clock input. Each pulse from the clock generator shifts the contents of all the shift register channels by one channel to the right and as a result, the first channel acquires the present value of the pick-up signal (0 or 1). Thus, inside the shift register appears a running pattern of rectangular pulses, which exactly reflects the time behaviour of the pick-up signal  $Y^{(\omega)}(t-\tau_i)$ . Here  $\tau_i$  is the time delay ( $\tau_i=i\Delta$ ) where  $i$  is equal to the channel number. The period  $\Delta$  of clock pulses determines the channel width.

The accumulation of the experimental spectrum  $Z_i$  in a Fourier analyzer occurs as follows. The parallel transfer logic starts at the moment of registration of a neutron by a detector and reads out the contents of each channel of the shift register; adds up these contents to the counter corresponding to the channel. The content of the shift register is not destroyed in the process. In other words, each registered neutron causes a fast and simultaneous summation of the shift register contents to the contents of the counter array of the analyzer. The procedure is schematically shown in Fig.5, where the experimental spectrum has one diffraction peak at the time-of-flight  $\tau_0$ . This figure also assumes a uniform increase in the modulation frequency from 0 to  $\Omega$ , as well as registering 8 neutrons. The shift register contents at the registration moments  $t_1, t_2, \dots, t_8$  are shown in Fig.5a. In this case it appears that for all the 8 curves, the content of the shift register channel with the

time-of-flight  $\tau_0$  has the value of 1. The above fact is of crucial importance for forming the diffraction peak at  $\tau_0$  for the RTOF method. The values 0 and 1 are equally probable for all other points on the spectrum. As a result the level of methodical background is 1/2 of the total number of the registered neutrons. The result of the experiment is the sum of 8 curves. This result is illustrated in Fig.5b and one can easily see a single diffraction peak

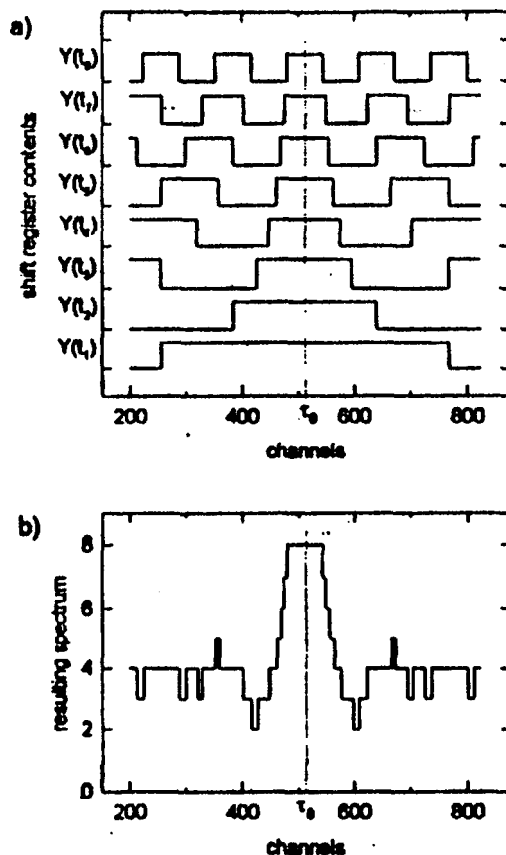


Fig.5: Illustration of the accumulation of a single spectrum

at the time-of-flight  $\tau_0$ . Using the method in a real experiment is strongly complicated by the statistical character of neutron scattering, multi-peak structure of experimental spectra, non-uniform distribution and respective non-uniform weights of different modulation frequencies. More details about the principle of operation of the RTOF diffractometer, are given in Refs.(14-17).

The program for the data acquisition and the control of the RTOF diffractometer electronic equipment is mainly written in Pascal language to be run under windows environment. The program is designed to perform the following functions:

- Control of the chopper motor rotation according to the frequency window.
- Automatic determination of the analyzer configuration; initiating the analyzer blocks via the BitBus network.

- Display the main menu which permits one to scan and, if necessary change the following parameters:

- a) Frequency window parameters (maximum motor speed, window steps number, full time of one measurement and frequency window form).
- b) RTOF analyzer parameters (number of channels, channel width and delay time).
- c) Parameters for the results of measurements (full number of measurements, file name,..).

Besides, the internal program of the RTOF analyzer makes correlation between the pickup signal coming from the chopper, and the detector signal using a shift register of 1024 channels and random access memory.

### Experimental Measurements

The chopper autocorrelation function measures the quality of the speed control system. The autocorrelation function was first measured, in 20 steps following the procedure of Ref<sup>(16)</sup>, at three maximum speeds of the chopper: 7000, 8000 and 9000 rpm; using Gaussian window with 1% of Dirichlet, and the RTOF analyser channel width=2  $\mu$ sec. The results are displayed in Fig.6A for first 20 channels(40  $\mu$ sec.). It is noticeable that the least fluctuations

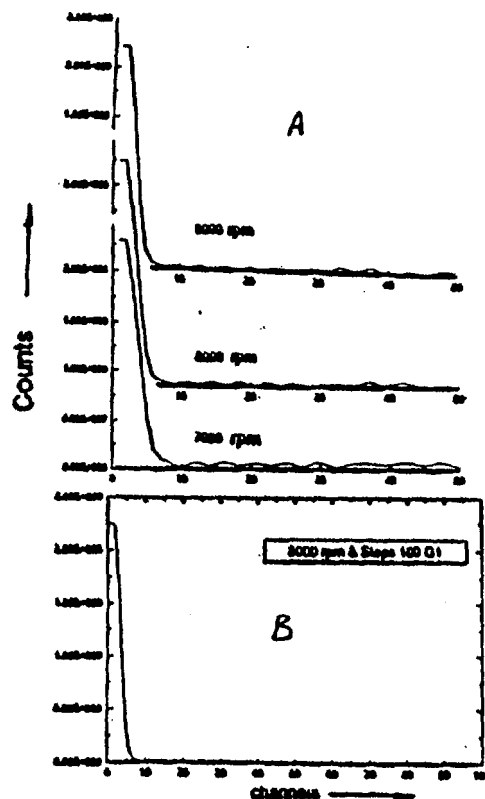
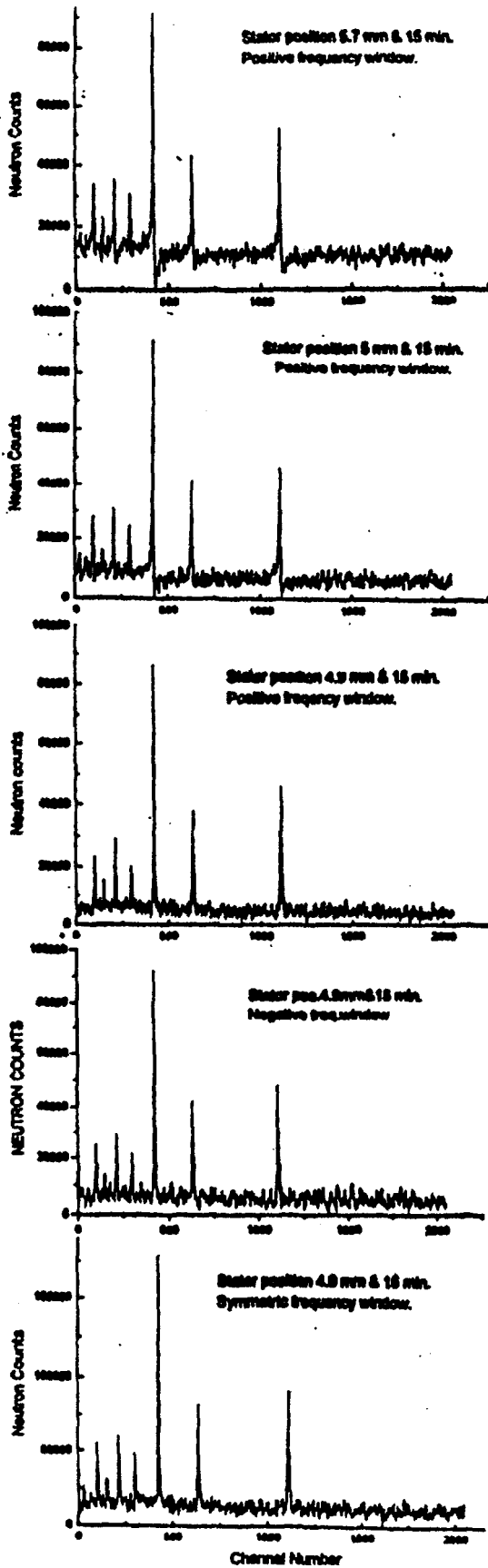


Fig.6: The Fourier chopper autocorrelation functions

A- Measured at 3 different speeds within 20 steps. B- Measured at 8000 rpm within 100 steps.



**Fig.7:** The neutron diffraction patterns measured for iron at different stator positions

are for 8000 rpm. Accordingly the autocorrelation function was measured at maximum speed of the chopper 8000 rpm using Gaussian window with 1% Dirichlet; realised by 100 steps. The result of the measurement is displayed in Fig.6B for the first 200 channels (400  $\mu$ sec) where typical small fluctuations around the main peak are observed, and the FWHM of the autocorrelation function is 7  $\mu$ sec. Besides the maximum peak-to-peak amplitude of the long-time fluctuations, observed in the measured autocorrelation function (Fig.6B) are on the level of 1% which is acceptable, since in a diffraction pattern measurement it is very seldom to press the statistical fluctuations below this level.

The pick-up signal phase  $\phi_0$ , with respect to neutron intensity modulation, depends on the positions in which the rotor and stator of the Fourier chopper are fixed relative to the pick-up sensor of the chopper. The theoretical value of  $\phi_0$  is zero when using frequency windows such as the Blackman and Gaussian ones <sup>(16)</sup>. In case of deviation of the  $\phi_0$  phase from zero the pick-up signal phase has to be adjusted. Checking and adjusting the phase of the pick-up signal should be conducted when the frequency window form parameter has positive "P" or negative "N" <sup>(16)</sup>. Thus, the phase adjustment was conducted using an iron sample (5.5mm in diameter and 85mm height); of the size standard for the CFDF and has sufficiently high scattering density. The adjustment was conducted by the method of successive approximations to the true, symmetrical Gaussian shape of the diffraction peaks. Accordingly, the position of the stator of the Fourier chopper was changed, after every test measurement using the iron sample, with the help of a micrometer screw; test measurements were carried out until the ideal shape of each diffraction peak was achieved. The phase adjusting was considered achieved when no asymmetries in the peaks are observed; at good accumulation statistics. The results of the phase adjustment measurements, with the abovementioned iron sample, are displayed in Fig.7 where diffraction patterns were obtained, during 15 minutes measurements, at three different positions of the stator.

### Results and Discussion

The specific distortion of the shape and symmetry of each of the diffraction peaks is an indicator of the phase adjustment as could be noticed from the iron patterns given in Fig.7; measured for different stator positions. The last three diffraction patterns, at the bottom of Fig.7 are the best. They were measured at stator position 4.9mm; where one finds that the peaks are symmetric and in good shape; regardless of the used window.

The iron diffraction pattern was treated with the proper software and is displayed in Fig.8; along with that one (1) which was measured for 120 minutes with the FSS diffractometer installed at the FRG1 (5MW) Reactor (GKSS-Germany). The FSS facility is also a Fourier RTOF one, with a different arrangement and is also optimized for  $2\theta=90^\circ$ . Despite the fact that the present iron diffraction pattern was obtained, with the CFDF, within 15 minutes measuring time it is superior (concerning statistics) to that one measured by the FSS facility. This offers a chance for more accurate diffraction measurements with the CFDF and within less measuring time. It is concluded that the CFDF could be used efficiently for neutron diffraction measurements at D values between  $0.7\text{\AA}$ - $2.9\text{\AA}$ .

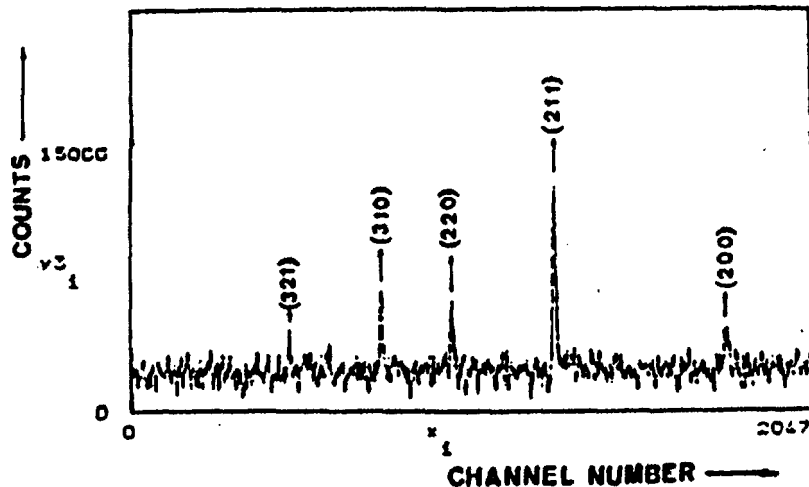
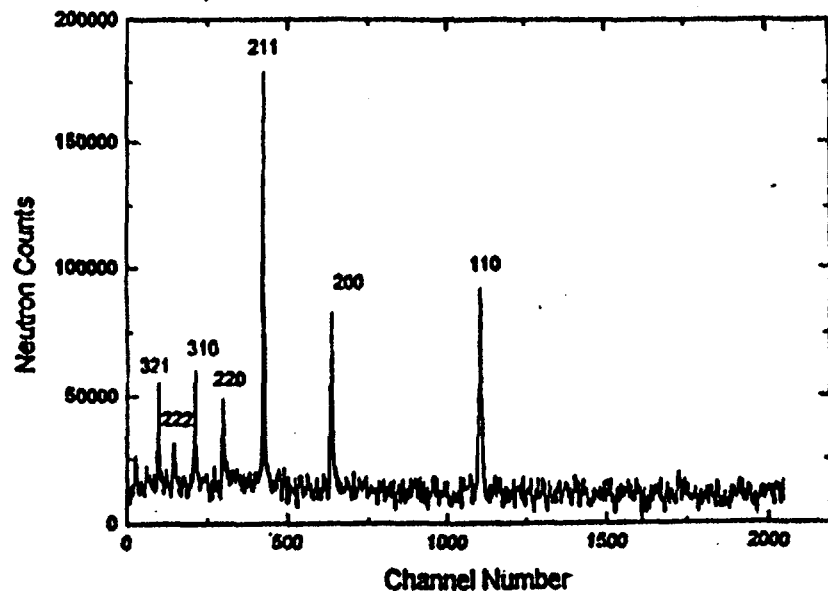


Fig.8: Iron diffraction patterns:

A- Measured with the CFDF facility    B- Measured with the FSS facility

**References**

1. Maayouf R.M.A., et al., GKSS report 91/E/96, Geesthacht, (1991).
2. Collwell, J.F.; Miller, P.H.; Whittemore, W.L., IAEA Symp. Neutron Inelastic Scattering, SH-104/647: 417 - 428, Copenhagen (1968).
3. Collwell, J.F.; Miller, P.H.; Whittemore, W.L., Nucl. Inst. & Meth. 76 135-149. (1969).
4. Collwell, J.F.; et al., Nucl. Inst. & Meth. 77 (24:39), (1970)
5. Virjo, A., Nucl. Inst. & Meth. 73:189 (1969).
6. Hiismaki, P.T., IAEA Conf. Neutron Inelastic Scattering, Grenoble SM-155/ F-10: 803-807. (1972)
7. Maayouf R.M.A., Tiitta, A., Hiismaki, P., The RTOF Neutron Diffraction Facility at the ET-RR-1 Reactor, Technical Research Centre of Finland (VTT), Reactor Laboratory Report, Espoo, Finland, June, (1991).
8. Kudryashev, V.A., Trounov, V.A., Maayouf, R.M.A., et al., Report LNPI 1732, USSR Academy of Sciences, Leningrad, (1991).
9. Maayouf, R.M.A., et al., VTT Report, Research Notes-1425, Espoo, (1992).
10. Maayouf, R.M.A., Tiitta, A.T., VTT Report, Research Notes-1502, Espoo, (1993).
11. Maayouf, R.M.A., Hiismaki, P.E., Tiitta, A.T., The Multipurpose RTOF Fourier Diffractometer at the ET-RR-1 Reactor, Report VTT, Reactor Laboratory, Espoo, Nov., (1993).
12. Maayouf, R.M.A., Tiitta, A.T., Hiismaki, P.E., VTT Report, Research Notes-1699, Espoo, (1995).
13. Maayouf, R.M.A., A Fourier RTOF Diffractometer Facility at the ET-RR-1 Reactor, IAEA-SR-198/15, Int. Seminar on Enhancement of Research Reactors Utilization, Bhabha Atomic Research Centre, Bombay, India, 11-15 March, (1996).
14. Poury, H., et al., Nucl. Inst. & Meth. 126, pp. 421-433, 1975.
15. Tiitta, A., Hiismaki, P., Nucl. Inst. & Meth. 163, pp. 427-436, (1974).
16. Tiitta, A., A Reverse time-of-flight Diffractometer using a Fourier chopper, VTT Report 27, Espoo, (1980).
17. Trounov, V.A., et al., Report GKSS 91/E/82, Geesthacht, (1991).

## محلل زمن الطيران العكسى بمفاعل البحوث المصرى الأول

أ.د. رفعت معيوف، عمرو الشافعى، مجدى خليل و ايهاب عبداللطيف  
قسم طبيعة المفاعلات والنيوترونات-مركز البحوث النووية-  
هيئة الطاقة الذرية-القاهرة-مصر.

يتناول هذا البحث كل من النظرية وطريقة عمل محلل زمن الطيران العكسى والذى صمم خصيصا لتحليل النبضات المنبعثة من قاطع نيوترونات من نوع فوربيير تم تركيبه مؤخرا امام احدى القنوات الافقية لمفاعل البحوث المصرى الأول، هذا وقد اتضح من الدراسة ان محلل زمن الطيران العكسى من المناسب استخدامه مع قاطع فوربيير عند سرعات دوران تصل الى ٩٠٠٠ دورة فى الدقيقة وحسب النافذة الترددية المناسبة. يتم ضبط نبضات البداية مع النبضات النيوترونية الناتجة من كاشف نيوترونات من الزجاج الوميسى المشبع بعنصر الليثيوم-٦ تم ضبطه عند زاوية تشتت ٠٩٠. هذا وقد أمكن باستخدام المحلل الحصول على نماذج الحيود النيوترونى عند موجات النيوترونات التى تتراوح أطوالها ما بين ١-٤ انجستروم وبقدرة تحليلية ٠,٥%.



EG9700116

## **AN ARC DETECTOR FOR NEUTRON CRYSTAL STRUCTURE INVESTIGATIONS**

By *N. HÁBIB*

Reactor & Neutron Physics Dept., Nuclear Research Center.  
AEA, Cairo, Egypt.

### **ABSTRACT**

An arc detector for neutron structure investigations of powder crystals using time-of-flight technique is described.

In order to enable the measurement of integral intensity from about 1/4 of the Debye-Scherrer ring and for simplicity reasons the scattering angle  $2\theta = 90^\circ$  was chosen and a special arc Soller collimator was built. The Soller collimator had a divergency of about 20 minutes of arc, and the distance between detector-sample was 64 cm. Four He-3 detectors were fixed on the outer arc of the collimator. The operating conditions as well as the position angular sensitivity of the detector were determined using a point neutron source. The result of the measurements shows that the parameters of the arc detector are acceptable for high resolution crystal structure investigations.

### **INTRODUCTION**

Until 1965 the procedure for neutron diffraction from polycrystalline specimens has involved the use of the double axis spectrometer (DAS). In this familiar technique the DAS is used to determine the angular distribution of scattered neutrons when a monochromatic neutron beam interacts with a polycrystalline or powdered sample. An alternative method the time-of-flight (TOF) method, has been demonstrated in several laboratories, suggested independently by Ringo [1] and by Egelstaff [2]. This method takes the advantage of the wavelength-velocity dependence of neutrons in a pulsed polychromatic beam. The wavelength distribution of neutrons scattered to a fixed angle is determined using a multichannel time analyzer and results with a pattern analogous to that obtained with the DAS. Experimental demonstration of the method was first made by Buras et al. and reported in ref. [3-6]. Buras demonstrated the usefulness of the TOF for single crystals.

The precision of the measured pattern can be increased by using a set of neutron counters which are connected to the multichannel time analyzer [5]. These counters are fixed on an arc section covering the Debye-Scherrer scattering cone.

The present work deals with the design and construction principles of an arc Soller collimator for the neutron detectors to match the TOF facility operating at ET-RR-1 reactor. The operating conditions and position angular sensitivity of the used detectors are also given.

### DESIGN PRINCIPLE OF THE ARC COLLIMATOR

If the neutrons are scattered at  $\theta_0 = 45^\circ$  then the Debye-Scherrer cone is a circular [5]. In this case it is easy to build a collimator that allows the collection of the scattering neutrons from a considerable part of Debye-Scherrer ring [5], see Fig.(1). We assume that the counter is fixed close to such a collimator and that the angle  $\phi$  does not exceed  $\pi$ .

In order to improve the part of the resolution which is connected with the spread in the Bragg angle it is customary to use Soller collimators. The detailed discussion of the theoretical basis for the use of collimators is given in [7-9] for the TOF method. As shown by Buras [5], the resolution connected with the use of Soller collimator is

$$D_c^2 = \frac{\text{ctg}^2 \theta_0}{24} \left( \frac{a_c}{L_c} \right)^2 \quad (1)$$

where  $a_c$ ,  $L_c$  width and length of a slit in the Soller collimator

If the (counter window) has a rectangular shape with height  $Z_c$  then the total angular size of it seen through the collimator from each point on the sample is in average.

$$\Delta \Omega_c = \frac{a_c}{L_c} \frac{\Delta Z_c}{L_c} \frac{1}{1 + d_c / a_c} \quad (2)$$

where  $d_c$  is the thickness of the lamellae in the Soller collimator and  $L_c$  the sample-detector distance.

As shown by Buras [6], that some new terms connected with the height of the sample and the counter must be added to resolution given by eq.(1). These terms were

negligible when the beam divergence in the direction normal to scattering plane was small, i.e. when

$$\varphi = a_c / L_c \ll 1$$

As shown by Buras [6] these new terms affecting the resolution are:

1. For a rectangular source window of dimensions

$\Delta X_s, \Delta Z_s$  is given by

$$D_{Z_s}^2 = \frac{1}{96} \left( \frac{\Delta Z_s}{L_s} \right)^2 g(\varphi) \quad (3)$$

where  $L_s$  is the sample-source distance.

And the function  $g(\varphi)$  is given by :

$$g(\varphi) = \frac{\varphi^2}{31} - \frac{\varphi^4}{51} + \dots \quad (4)$$

2. If the sample is a prism or cylinder of a height  $\Delta Z_s$  then

$$D_{Z_s}^2 = \frac{1}{96} \left[ \frac{\Delta Z_s}{L_s} \left( 1 + \frac{2L_s}{L_o} \right) \right]^2 g(\varphi) \quad (5)$$

where  $L_o$  is the analyzing flight path

The resolution of the chopper of the TOF spectrometers can be given as [10] :

$$D_{ch}^2 = \frac{1}{6} \frac{h^2 R^2}{r^2 L_o^2} \quad (6)$$

where  $2h$  is the chopper slit width

$R$  is the curvature radius

$2r$  is the chopper diameter

The total resolution connected with the use of the chopper and Soller collimator is then

$$D^2 = D_{ch}^2 + D_c^2 + D_{Z_s}^2 + D_{Z_a}^2 \dots \quad (7)$$

**CONSTRUCTION OF THE ARC COLLIMATOR SYSTEM**

The general view of the arc Soller collimator is given in Fig.(1). The circular section of the arc collimator was selected to cover the angle  $\varphi = \pi/2$  of Debye-Scherrer ring while its length was 38 cm. The inner and outer curvature radius of the circular section were 26 cm and 64 cm respectively. The number of collimator's slits was 7, while  $a_c$  and  $L_c$  were 3.5 mm and 64 cm respectively. The lamellae between the slits was made from Cd sheets and its thickness was 3 mm.

The arc collimator was mounted on a mobile platform where the sample holder can be fixed on the collimator's center. The whole collimator system can be aligned and fixed at a desired distance behind the second rotor of the TOF system at ET-RR-1 reactor using specially designed arrangements.

The horizontal view of the general arrangement of the TOF spectrometer is given in Fig. (2). The TOF facility consists of a rotating collimator (rotor 1) and a curved slot rotor (rotor 2). The rotors are suspended in magnetic fields and spinning synchronously up to maximum speed of 16,000 rpm, producing bursts of polyenergetic neutrons. The curved slot rotor 32 cm in diameter has two slots of 1 cm height and 0.7 cm width. The slot has a radius of curvature of 65.65 cm. The main parameters of the rotating collimator as well as the optimum operating conditions of double rotor facility are given in details elsewhere [11,12].

A four similar He-3 gas filled neutron detectors (type LND-2522) were fixed on the outer arc of the collimator. Each of them is 2.5 cm in diameter and 24 cm in length. The detector efficiency is 90% for neutron of energies less than 0.005 eV. A schematic circuit diagram of the detectors is given in Fig.(3). A personal computer analyzer PCA -8000 operating in its multichannel scaling (MCS) mode, was used as a 4096 multichannel time analyzer with a minimum dwell time of 10  $\mu$ s. The main parameters of the TOF facility are listed in table (1).

**Table (1): The main parameters of TOF facility**

<b>Rotor - Collimator (cm)</b>	<b>Source Window (cm)</b>	<b>Sample (cm)</b>	<b>Soller Collimator (cm)</b>
2r = 32	$\Delta X_r = 0.7$	$\Delta Z_s = 1.0$	$a_c = 0.35$
2h = 0.7	$\Delta Z_r = 1.0$	$L_o = 264$	$Z_c = 90$
H = 1.0	$L_r = 64$		$d_c = 0.3$
R = 65.65			$\varphi = 18.8^\circ$
L = 66			$L_c = 64$ cm

From the parameters listed in table (1), the terms of resolution are calculated and were found to be :

$$D_{ch}^2 = 5.64 \times 10^{-5}$$

$$D_c^2 = 1.246 \times 10^{-6}$$

$$D_{zr}^2 = 1.27 \times 10^{-11}$$

$$D_{zs}^2 = 3.0 \times 10^{-11}$$

Thus the wavelength resolution  $\Delta\lambda/\lambda$  of the TOF was calculated and found to be

$$\Delta\lambda/\lambda = 0.56 \%$$

This value is acceptable for high precision of the diffraction pattern [13].

### EXPERIMENTAL CHECK- UP OF THE DETECTOR SYSTEM

The detector plateau curve was measured using a ( $P_o - B_e$ ) neutron source. The source was inserted inside a cylinder 24 cm in diameter and 10 cm height, of pure paraffin wax. The cylinder was covered with 1 mm Cd sheet leaving a window of 1x1 cm<sup>2</sup> uncovered. Such source arrangement was used for calibration purpose to simulate the thermal reactor neutron flux transmitted through the TOF facility. Therefore the source assembly was fixed at the center of the Soller collimator with its window facing the neutron detectors.

A typical measured detector plateau curve is displayed in Fig. (4). The operating voltage was 4600 where the operating voltage range was from 4500-5000 V with plateau slope (% 100 V) < 2 %. The amplitude distributions of the output signals was measured for each detector. One of these distributions is displayed in Fig. (5). The energy resolution (% FWHM) was found to be < 15 %. From Fig. (4),(5) the detector operating conditions were selected to be V=4600 volts and the lower discriminator threshold is 0.5 volts.

The position angular sensitivity of the arc detector was measured in steps of 2° by covering the inner Soller collimator arc by 1 mm Cd sheet leaving only a window of 1 cm in width. The resulting curve was displayed in Fig. (6). The dips in the curve were found due to fact that the effective detector length is less than the geometric one. Therefore the length of the arc collimator covers slightly less than the 1/4 of the Debye-Scherrer ring. However this behaviour can be easily taken into consideration during the analysis of the diffraction pattern.

## CONCLUSION

The selected parameters of the designed and constructed arc Soller collimator with four He-3 detectors fulfill the high resolution requirements at maximum available intensity needed for crystal structure investigations using TOF technique [13]

## REFERENCES

1. Ringo G.R., Handbuch Der Physik , 23,590 (1957).
2. Egelstaff P.A., Proc. Symp. Neutron Time-of-Flight Methods Organized by EANDC Saclay, P. 69, (1961).
3. Buras B and Leciejewicz J., Nukleonika, 8, 75 (1963).
4. Buras B., Nukleonika , 8 , 259 (1963).
5. Buras B. And Leciejewicz J. Phys. Stat. Sol., 4, 349 (1964).
6. Buras B. And Holas A. , Report No. 627 (11) PS ; Inst. Nucl. Res. ,Swierk , (Poland ), (1965).
7. Holas A.,Collimators in the Neutron Time-of-Flight Powders Diffractometry , Report INR No. 747/11/PS , (1963).
8. Schmidt W., Sieger D., Tietre Jaensch H., Geick R., Nucl. Inst. & Meth. A 316, 364 (1992).
9. Schmidt W., Tietre - Jaensch H., Geick R., Will G., Grimm H., Proceeding of the Meetings ICANS - XIII and ESS-PM4, VI P 184, (1995).
10. Marseguerra M. and Panli G., Nucl. Inst. and Meth., 4, 140 (1959).
11. Wahba M., Kerntechnik 56, 183 (1991).
12. Naguib K., Habib N., Wahba M., Kilany M. and Adib M., Annals of Nuclear Energy, under Publication (1996).
13. Schefer J., Fischer P., Heer H., Isacson A., Koch M. and Thut R., Nucl. Inst. and Meth. A 288, 477 (1990).

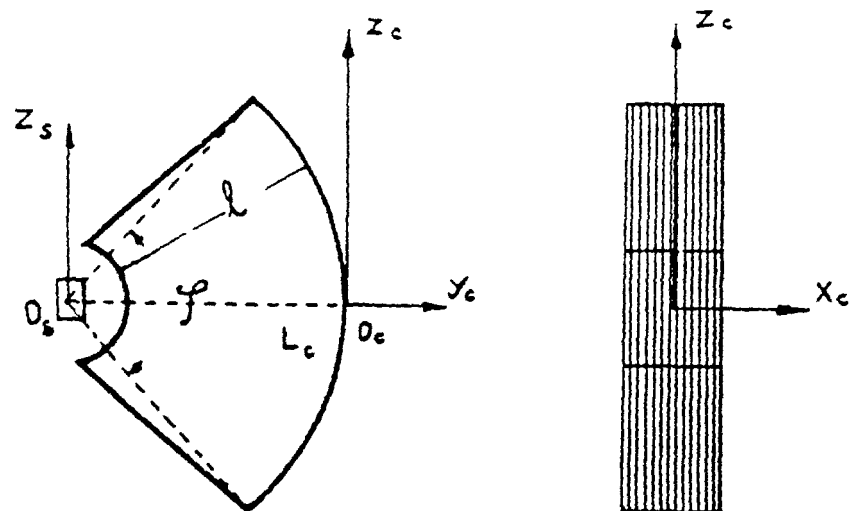


Fig. (1) The general view of the Soller arc collimator.

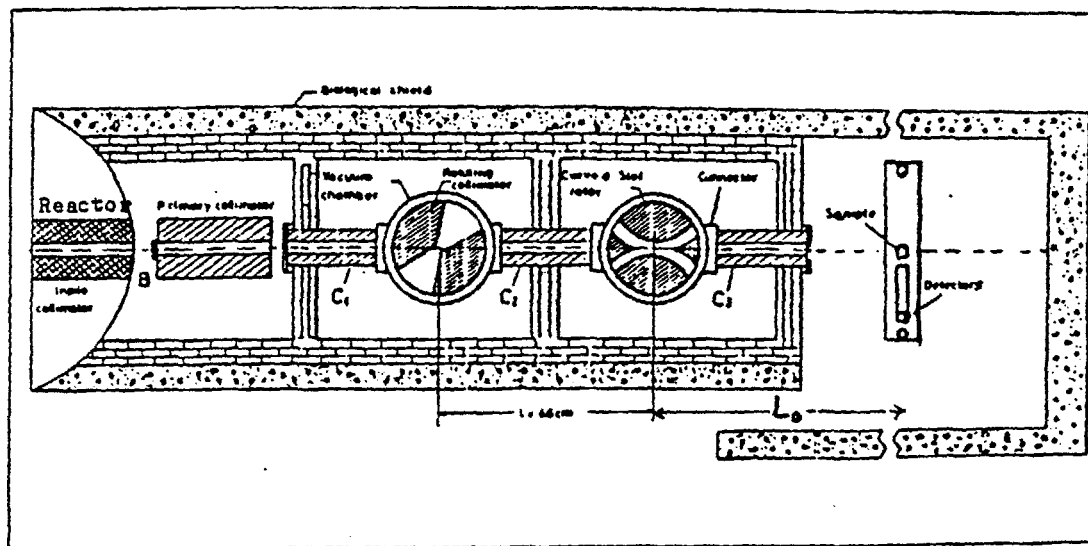


Fig. (2) The general arrangement of the TOF spectrometer.

- 212 -

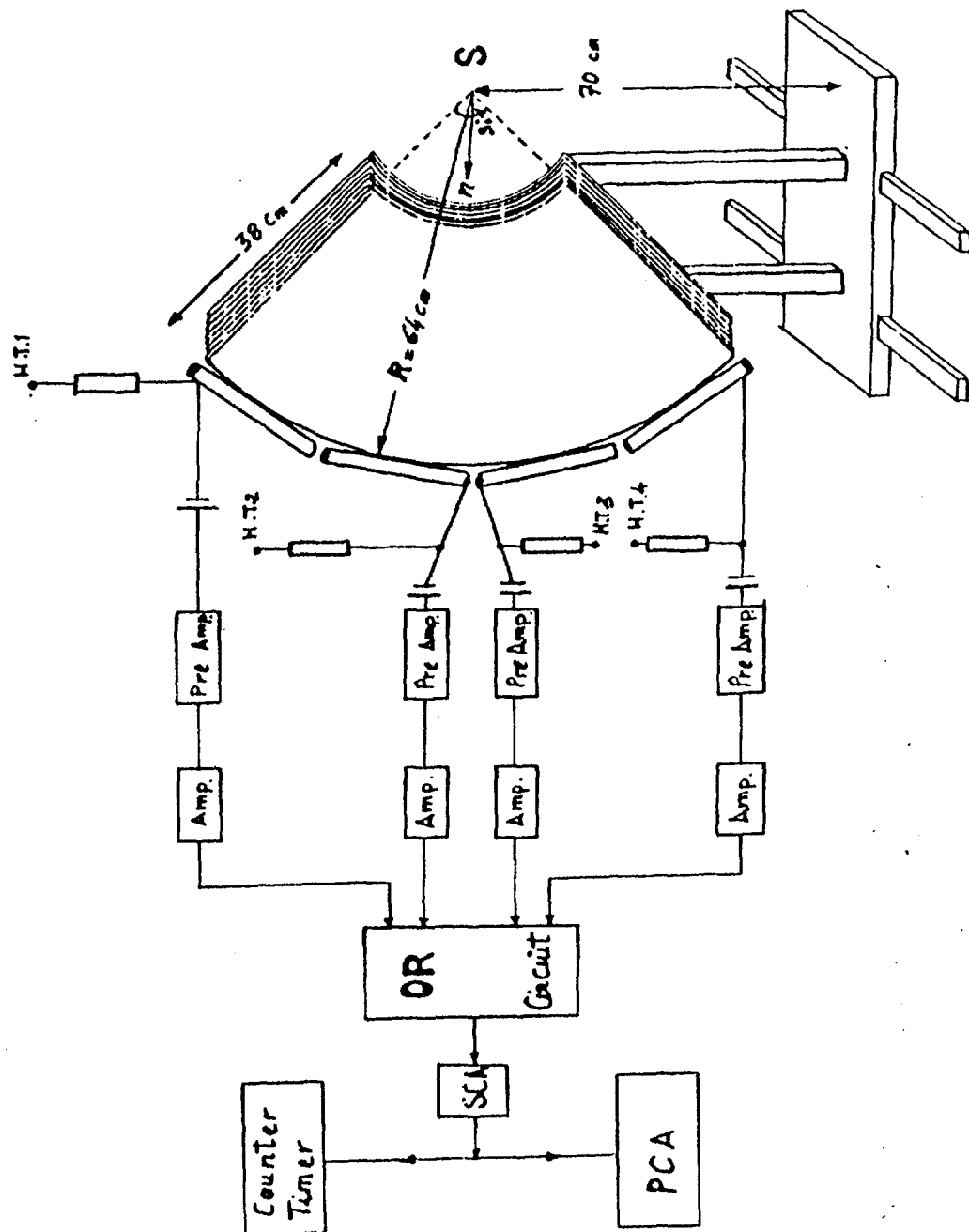
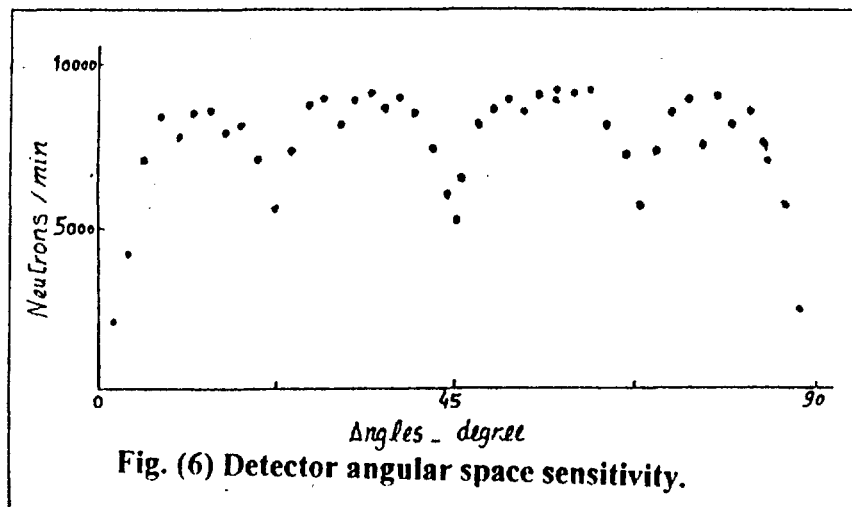
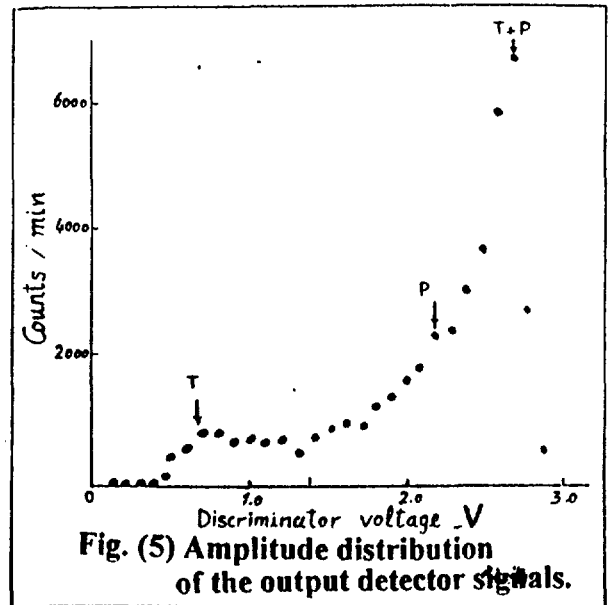
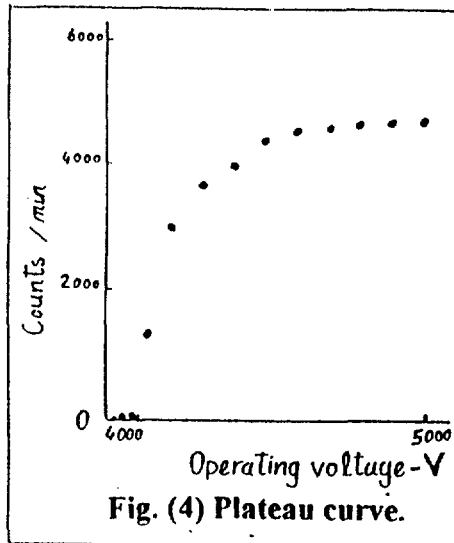


Fig. (3) The schematic diagram of the arc detector.



**SCIENTIFIC SESSION (10)**

**RADIATION DOSIMETRY -1**

***Keynote Lecture***

**A NUMERICAL ANALYSIS OF ASPECTS OF ABSORBED DOSE IN THE VICINITY OF THE INTERFACE OF DIFFERENT MATERIALS**

**Junichiro Tada\*, Hideo Hirayama\*\*, and Kazuaki Katoh\*\*\***

\* Tsukuba Univ., Japan

\*\* National Lab. High Energy Phys. (KEK), Japan

\*\*\* Ibaraki Pref. Univ. Health Sci., Japan

**ABSTRACT**

In the measurement and/or evaluation of the absorbed dose where the charged particle distribution is far from equilibrium, knowledge on the microscopic spatial distribution of the charged particle fluence is important. Spatial distribution of secondary electrons in the vicinity of an interface of materials and the values of the absorbed dose in these regions are investigated with a Monte-Carlo simulation code EGS4. There were experiments on spatial variation of the absorbed dose in the vicinity of an interface of materials. However, the behaviour of secondary electrons were discussed only broadly and qualitatively. In this study, behaviour of the secondary electrons was analysed to clarify contribution of ruling interactions to generate secondary electrons, and influence of the interface on the energy spectra of secondary electrons.

***Contributed Papers***

**DETERMINATION OF DOSES TO DIFFERENT ORGANS AND PREDICTION OF HEALTH DETRIMENT, AFTER HYPOTHETICAL ACCIDENT IN MTR REACTOR CORE**

**E. A. Amin, and A.H. Abd El- Ghani**

**National Center of Nuclear Safety and Radiation Control  
Atomic Energy Authority, Cairo, Egypt**

**ABSTRACT:**

As a result of hypothetical accidents with release of high amount of fission products, the doses to different organs consequent upon inhalation of

radioactive fission products are calculated. The processes are modeled using the ORIGIN and TIRION-4 codes: source term, containment and activity enclosure, time dependent activity behaviour in the building, and radiation exposure in the reactor building. Prediction of health detriments were calculated using ICRP-60 nominal probability coefficients and the organ doses determined for Bone, Lung, and Thyroid gland, after Whole body exposure from internal inhalation and external emmersion.

### **CALCULATION OF THE RELATIVE DOSE RATE OF COBALT-60 BY COMPUTER CODE**

**J. Mashina**

**Nuclear Research Center, Tajura - Tripoli - LYBIA**

#### **ABSTRACT**

Since 1986 CO-60 irradiation unit GB651 became available at Tajura Research Center. The original activity of 50 KCi ws distributed to 9 pencils in V shape. The first radiation field evaluation was made by Fricke solution. However, because of the variety of geometric positions of the radiation sources, the resulting radiation fields could not be determined precisely. Therefore, a computer code was developed to describe these radiation fields. According to the results obtained so far, the error of the computed absolute irradiation dose rate data is very small.

### **NEUTRON DOSIMETRY IN PARAFFIN BLOCK BY ACTIVATION FOIL TECHNIQUE**

**M. El-Khatib\*, M. Bassiouny\*\*, M. Adel Fawzy\*,  
and Mahmoud I. Abbas\***

**\*Physics Department, Faculty of Science, Alexandria University.**

**\*\* Basic and Applied Science Department, Arab Academy For Science and Technology**

#### **ABSTRACT**

Intermediate and thermal neutrons were investigated inside a paraffin block as a tissue equivalent medium. The block has a cubic shape of side length 45 cm. Neutrons were orginally emitted from D-T generator with energy 14.5 Mev. The neutron fluxes were measured using activation foil detectors with successive threshold energies. The dose equivalent rates at different planes and depths inside the block were determined. The data obtained were in fair agreement with the calculated value.

**RADIATION ABSORBED DOSE AND EXPECTED RISK IN HEAD AND  
NECK TISSUES AFTER THYROID RADIOIODINE THERAPY**

**A. Hamed\*, H. I. Farag\*\*, and A. Saleh\*\*\***

\*National Center for Nuclear Safety And Radiation Control, AEA.

\*\*National Cancer Institute, Cairo University

\*\*\* Al-Hussien Hospital, Al-Azhar University

**ABSTRACT**

Measurement of absorbed dose in head and neck phantom after applying I-131 therapeutic dose for the treatment of thyroid malignancies was conducted. The measurements were carried out at several sites of phantom using TL dosimeters.

The absorbed doses were also measured on the skin of four patients during their administration of I-131 therapeutic doses 1.332 GBq (36 mCi) I-131. The measurements were taken over 69 hours exposure at different sites of phantom. The same measurements were carried out on the four patients. At five sites of the patients head and neck, the absorbed dose were measured and compared with that measured on the phantom.

The values measured are discussed in the light of the published individual absorbed doses in the organs by ICRP tables. High absorbed doses were observed in the different sites of the head and neck during the I-131 therapy (0.14 - 9.68 mGy/ mCi).

**A TECHNIQUE OF EVALUATING MOST PROBABLE STOCHASTIC  
VALUABLES FROM A SMALL NUMBER OF SAMPLES AND THEIR  
ACCURACIES AND DEGREES OF CONFIDENCE**

**Kazuaki Katoh**

**Ibaraki Pref. Univ. Health Sci., JAPAN**

**ABSTRACT**

A problem of estimating stochastic characteristics of a population from a small number of samples is solved as an Inverse Problem, from view point of Information Theory and with the Bayesian Statistics.

For both Poisson-Process and Bernoulli-Process, the most probable values of the characteristics of the mother population and their accuracies and degrees of confidence are successfully obtained. Mathematical expressions are given to the general case where a limit amount of information and/or knowledge with the stochastic characteristics are available and a special case where no a priori information nor knowledge are available. Mathematical properties of the solutions obtained, practical appreciation to the problem to radiation measurement are also discussed.



## A Numerical Analysis of Aspects of Absorbed Dose in the Vicinity of the Interface of Different Materials

Junichiro Tada<sup>1)</sup>, Hideo Hirayama<sup>2)</sup> and Kazuaki Katoh<sup>3)</sup>

<sup>1)</sup> Tsukuba Univ., JAPAN

<sup>2)</sup> National Lab. High Energy Phys. (KEK), JAPAN

<sup>3)</sup> Ibaraki Pref. Univ. Health Sci., JAPAN

### ABSTRACT

There have been many works on the behaviour of the absorbed dose of photons near the interface of materials. However, it is rather difficult to examine the property of secondary electrons in such transient region experimentally. Recent numerical techniques enable us to analyze such kind of problems. In this paper, the spatial changes of the absorbed dose, as well as those of the fluence (spectrum) of secondary electrons, near the boundary with various combination of materials are analyzed.

### INTRODUCTION

Absorbed dose is the most fundamental dosimetric quantity in the current system of radiation dosimetry<sup>1)</sup>. As the quantity is defined as spatial density of mean energy imparted to a small volume of the matter, its value is extremely influenced by the distribution of the matter around the point of interest. It is not easy to understand the property of the absorbed dose of X- and gamma rays near the boundary of matters where charged particle equilibrium does not hold, since almost all of the energy imparted are brought by the Coulomb interaction between charged particles in the volume.

Duterix *et.al.* discussed the spatial variation of the absorbed dose of water in the vicinity of a medium with higher atomic number, based on their experimental observations<sup>2)</sup>. They reported that there is a minimum (85 % to the value at electron equilibrium) in the absorbed dose of water by <sup>60</sup>Co gamma rays at 0.2 to 0.4 mm from copper-water interface (Fig. 1). They also reported that the *underdosage* is the most significant with cadmium-water interface and disappeared for materials of atomic numbers larger than 70. They interpreted these observations by the behaviour of secondary electrons entered through the interface and those produced in the water (Fig. 2). They assumed the attenuation of the former is faster than the *build up* of the latter. Their speculation is indeed plausible, however, its pertinence is still unknown since information about the energy spectra of secondary electron fluence are not clear. Thus the ultimate interpretation of the

phenomena is not settled.

Recent development in numerical analysis provides a powerful tool for this problem. With sophisticated simulation system, we can easily obtain precise knowledge on the behaviour of secondary electrons which can not be observed, or at least very difficult to know, from experiment. The authors utilized a well established Monte Carlo simulation code system EGS-4<sup>3)</sup> to analyze the spatial variation of the electron spectrum and the energy deposition to the matter in the vicinity of material-water interface for materials with various atomic numbers.

## MATERIALS AND METHODS

In order to simulate the situation that plane parallel beam of 1 MeV photons incidents normally on the material-water interface plane, infinite slab geometry is employed (Fig. 3). In this geometry, the material and the water region, in the vicinity of the interface, are divided into eighty infinite slab whose thicknesses are approximately equal to one eightieth of the maximum CSDA range of 1 MeV electrons in the corresponding medium ( $R_{c,1MeV}^{med.}$ ). The pencil beam of 1 MeV monoenergetic photons incidents normally to the surface of the material which is parallel to the interface and is set three times of  $R_{c,1MeV}^{med.}$  upstream to the interface. As is well known, quantities summed throughout each infinite slab in this geometry correspond to those at the same distance from the interface in the case of parallel beam.

The cut off energy of both electrons and photons are set 0.01 MeV, thus electrons and photons having energies less than 0.01 MeV are considered to be absorbed at the position where they are generated. In order to take into account the photoelectric effect by L-shell electrons and emission of L X-rays, optional sub-programs of EGS-4 are employed<sup>4)</sup>. "PRESTA" option is also employed to modify spatial step size near the interface of each slab<sup>5)</sup>.

The number of histories of each simulation is  $10^7$  which is divided into fifty batches. Four kinds of materials, *i.e.*, aluminium, copper, tin and lead are used for the simulation.

## RESULTS

The spatial changes of the absorbed dose are depicted in Figs. 4 to 7. The ordinates are the absorbed dose per unit fluence of incident photon expressed in the unit of  $MeV \cdot cm^2/g$ . In the figures, the absorbed dose in the upstream side of the interface is that

of the material while in the downstream side of the interface is that of water, which cause a discontinuity at the interface corresponding to the difference of the mass stopping power of each medium. As is seen, the minimum of the absorbed dose to water in the vicinity of the material-water interface is not so significant for the case of copper and conspicuous for lead. These results are not consistent with the report of Duterix *et. al.*.

The secondary electron spectra in the region under electronic equilibrium in both material and water and those at the immediate water region to the interface are shown in Figs. 8 to 11. The ordinates are the electron fluence per unit interval of energy per unit fluence of incident photons. As seen in the figures, the larger the atomic number of the upstream material, the harder the energy spectrum of the secondary electrons in the region adjacent to the interface. This change reflects the contributions of photoelectrons.

## DISCUSSIONS

The results of the numerical analysis are not consistent with the report of Duterix *et. al.* as far as the behaviour of the absorbed dose to water in the vicinity of the material-water interface concerned. The reason of the inconsistency may be attributed to the difference of geometry between that employed in the numerical analysis and that of the experiment. However, the results of the numerical analysis with a well established simulation code system can reflect the phenomena more directly than the results of the experiment in such transient region.

As seen in Fig. 8, the energy spectrum of electron fluence at the immediate water region to the copper-water interface is not so softer than that in the region of electronic equilibrium in water. Hence the assumption used in the interpretation of Duterix *et. al.* that the electrons entered through the interface attenuate more rapidly than the build up of electrons in water dose not hold in this case. On the contrary, the electron spectrum in the water region adjacent to the lead-water interface is apparently harder than that in the region of electronic equilibrium in water due to the contribution of photoelectrons arising from lead. Moreover, the yield of electrons in the case of lead is more abundant than the case of copper. Thus, the dose minimum appears with the case of lead-water interface.

As Duterix *et. al.* did not mention the geometry of their experiment, the authors can not examine the reason of these disagreements by numerical analysis. Farther investigations are expected both in numerical and experimental analysis with this problem.

**REFERENCES**

- 1) ICRU Report 33 (1980)
- 2) Duterix, J. and Bernard, M., Br. J. Radiol., 39, 205 (1966)
- 3) Nelson, W. R., SLAC-265 UC-32 (1985)
- 4) Hirayama, H.,
- 5)

**ARABIC SUMMARY**

*Unfortunately, it is beyond the power of the authors.*

**FIGURE CAPTIONS**

[Fig. 1]

Fig. 1 of Ref. 1. "Dose distribution in water in the vicinity of an interface with copper. The ordinates correspond to the ratio of the absorbed dose  $D$  to the dose  $D_e$  in water in electronic equilibrium conditions. ..."

[Fig. 2]

Fig. 2A of Ref. 1. "... At the interface the electronic flux is reduced to  $F_{Cu}$  (forward component of the flux in copper) and this component vanishes in the water while the forward component of the water builds up. The minimum of the total flux can be explained by assuming that the decrease of the intensity of the electrons arising from copper is more rapid than the build-up of the electrons set in motion in water."

[Fig. 3]

The geometry employed in the numerical analysis. The thicknesses of each slab ( $d_1$  and  $d_2$ ) are approximately equal to one eightieth of the maximum CSDA range of 1 MeV electron in the corresponding medium ( $R_{e,1MeV}^{med.}$ ). The distance between the surface of the upstream material and the material-water interface ( $l$ ) is approximately equal to three times of the  $R_{e,1MeV}^{med.}$ .

[Figs. 4 to 7]

The spatial changes of the absorbed dose in the vicinity of material-water interface with four kinds of material, aluminium, copper, tin and lead. The ordinates are the absorbed dose per unit incidence of 1 MeV photons on the surface of the material. The dose minimum in the water is not significant with the case of copper while it is prominent with the case of lead.

[Figs. 8 to 11]

The energy spectra of electron fluence in the region under electronic equilibrium in both material and water, and those at the immediate water region to the material-water interface.

Fig. 1

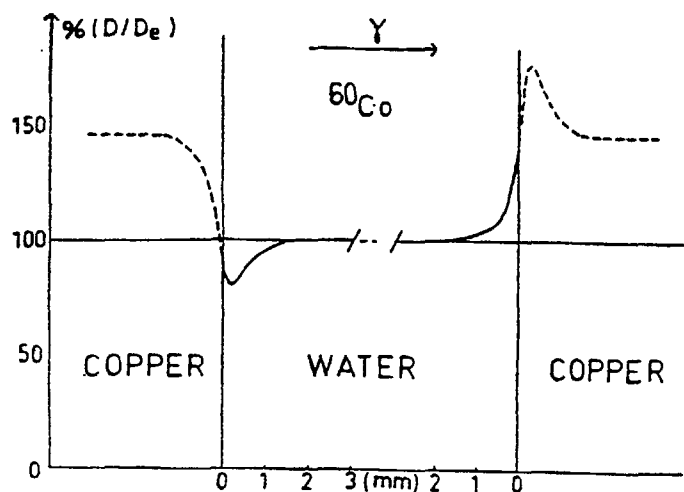


Fig. 3

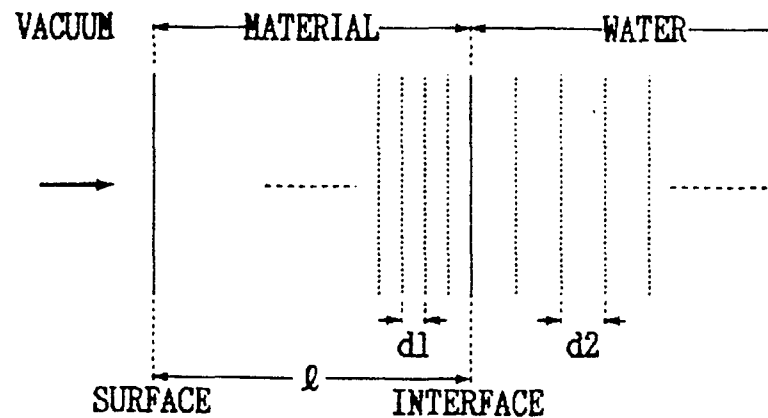
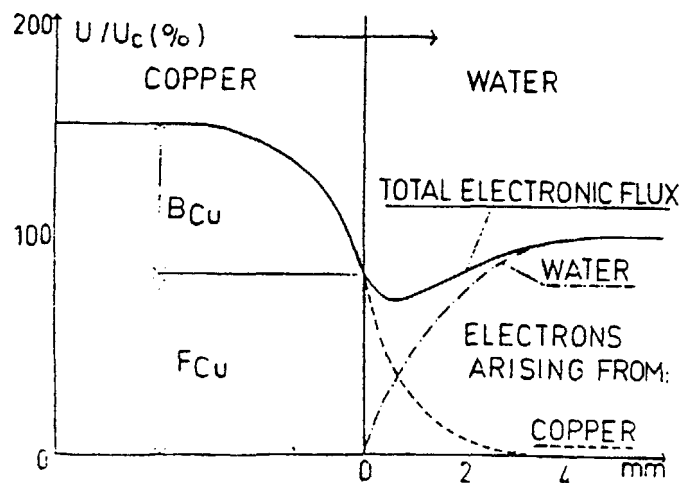


Fig. 2



223-

Fig. 4 Absorbed dose of Al and water per unit fluence of 1 MeV photon

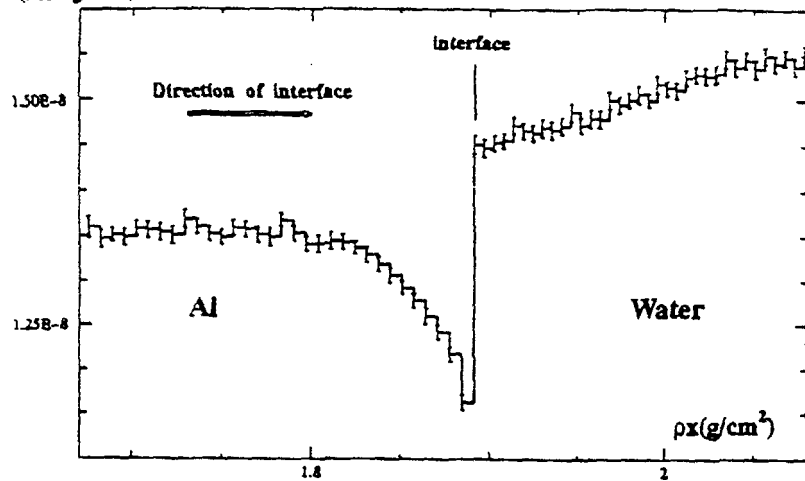


Fig. 6 Absorbed dose of Sn and water per unit fluence of 1 MeV photon

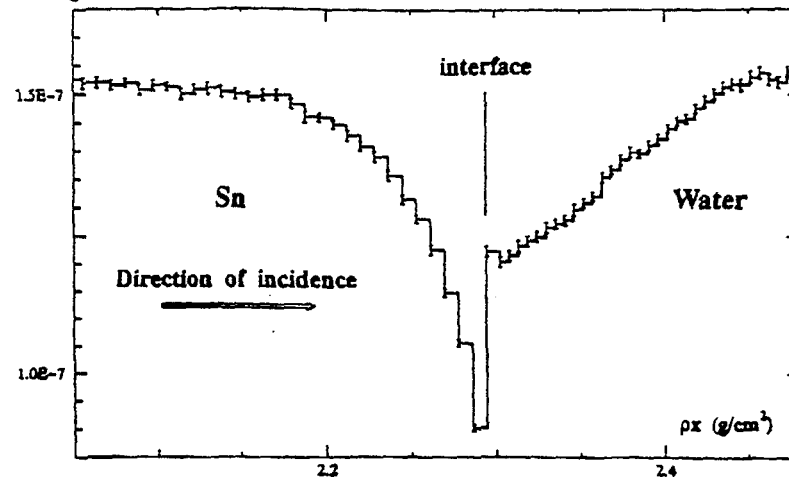


Fig. 5 Absorbed dose of Cu and water per unit fluence of 1 MeV photon

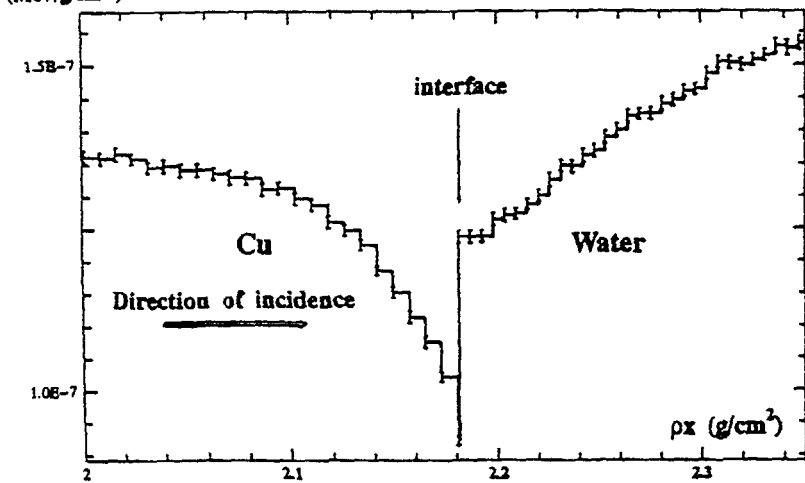
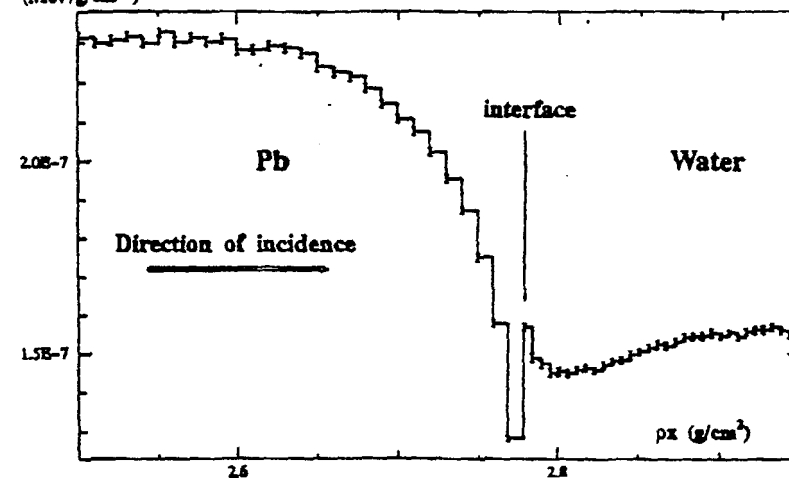


Fig. 7 Absorbed dose of Pb and water per unit fluence of 1 MeV Photon



224

Fig. 8

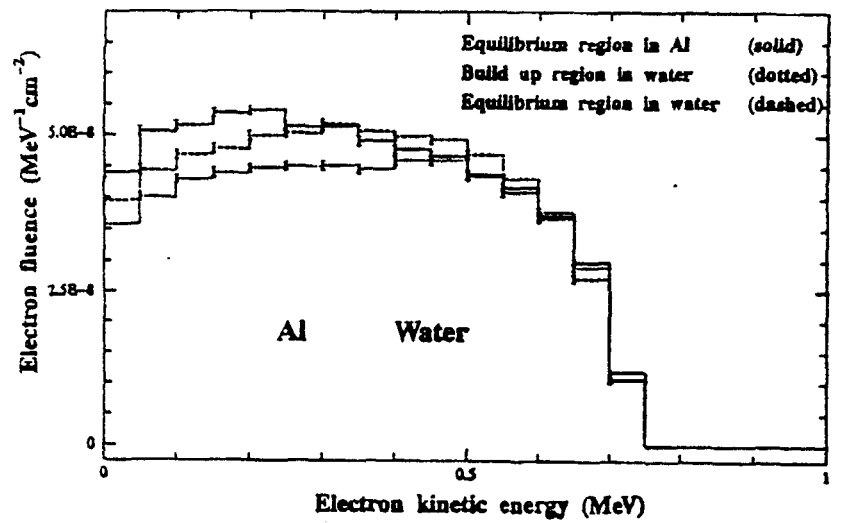
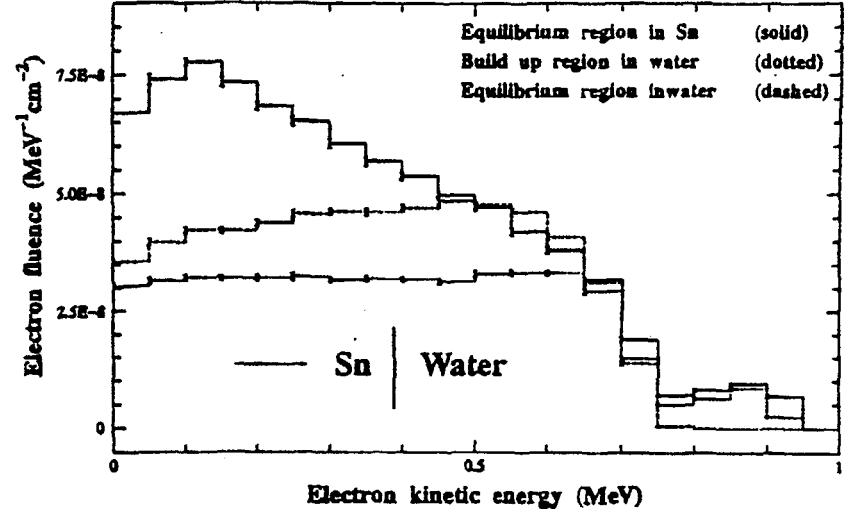


Fig. 10



- 225 -

Fig. 9

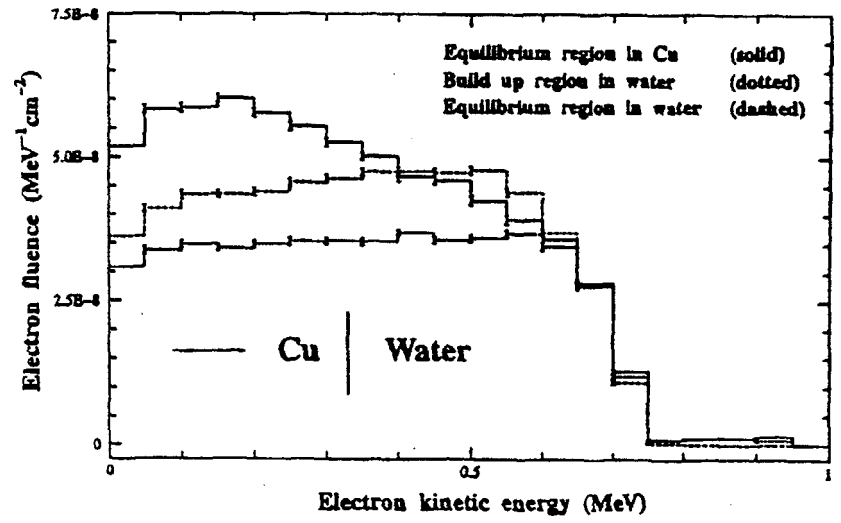
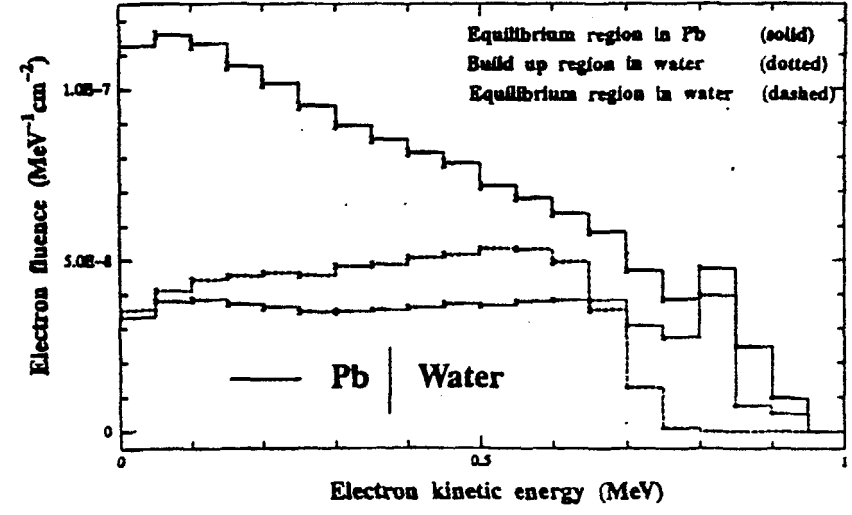


Fig. 11





EG9700118

**Determination of radiation doses to different organs and prediction of health detriment after hypothetical accident in MTR reactor core**

**E. AMIN and A.H. ABDEL GHANI**

**National Center of Nuclear Safety and Radiation Control  
Atomic Energy Authority Egypt**

**ABSTRACT**

The radiological consequences as a result of hypothetical accidents, with release of high amount of fission products are determined. The doses to different organs consequent upon inhalation of the radioactive fission products are calculated. The following processes are modeled using the ORIGINJR and TIRION-4 codes: source term, containment and activity enclosure, time dependent activity behavior in the building, radiation exposure in the reactor building, radioactivity release to the site atmosphere.

Prediction of health detriment were calculated using ICRP 60 nominal probability coefficient and the organ doses determined for bone, lung, and thyroid after whole body exposure from internal inhalation and external immersion.

**INTRODUCTION**

The standard approach in safety analysis report SAR for research and test reactors is to assume that a hypothetical accident results in the release of some portions of the inventory of radioactive materials from the fuel to the reactor building and eventually, in the release of a portion of these materials, in the atmosphere.

The consequences to the surrounding population are usually evaluated in terms of estimated radiological doses from the materials released. The calculation of radiological consequences of a postulated accident involves the determination of the fission product inventory, the release from the fuel, the calculation of the time dependent release from the reactor building, atmospheric dispersion, and the resultant individual and population doses received as a result of the release of radionuclides.

The accidental airborne release of radionuclides contributes to the following radiological doses. External whole body dose (gamma) due to submersion in the exhaust air plume, (cloudshine), external whole body (gamma) dose due to activity deposited on the ground (groundshine), internal irradiation originating from radionuclides inhaled with the air, resulting in both critical organ and whole body doses, external -radiation from the exhaust air plume (skin dose mainly) and internal irradiation due to consumption of contaminated food.

The determination of the total dose of the whole body or of a certain critical organ requires the summation of all contributions of all relevant radionuclides via the exposure path ways

Ionising radiation induces both deterministic and stochastic effects of irradiated tissue, depending on radiation dose and the radiosensitivity of the cellular population. Radiological protection aims

at avoiding deterministic effects by setting standards for the safety of radiation sources and to ensure dose levels below their thresholds.

Deterministic effects result from the killing of cells which if the dose is large enough causes sufficient cell loss to impair the function of the tissue. Above the threshold, the severity of the harm is a function of absorbed dose.

Stochastic "probabilistic" effects are believed to occur with low probability at low doses and low dose rates, therefore dose limits are always identified to bring the probability of delayed stochastic effects as low as possible.

Stochastic effects may result when the irradiated cell is not killed but is modified by a radiation induced damage to a critical molecule. Modified somatic cells may subsequently, after a prolonged delay period undergo a transformation into a malignant process. The incidence of this transformation is related to the radiation exposure at low doses and low dose rates by very complicated relationships, the most common of which is the linear proportionality relationship, the quadratic and the linear quadratic.

Radiation damage that occurs in gonadal cells whose function is to transmit genetic informations to later generations, may result in stochastic effects called ' hereditary

## **CALCULATION MODEL**

### **Fission Product Inventories :**

The computer program ORIGENJR [ 1 ] is used to estimate the inventory of fission products and actinides in the reactor fuel after a specified irradiation history. ORIGENJR has been installed, adapted and tested on the VAX6000 of the NCNSRC. The fuel cycle history in ORIGENJR is represented by a sequence of power and shutdown cycles of variable power level and duration.

The burnup / buildup is represented spatially by a point model. The entire core or fuel element is limited to a uniform distribution over each cycle.

The light water reactor LWR library is chosen which is the best choice for the MTR reactor. The appropriate parameters are set for the thermal, resonance, and fast flux data to describe the reactor in question.

The inventory of the fission products is strongly affected by the irradiation history of the reactor. The maximum inventory for a given isotope may be at the end of the maximum irradiation time for the fuel.

## Source Term

The radiological source term describes the amount of the nuclides to be released to the confinement (reactor building).

The total activity of isotope  $i$  released over time  $\tau$ ,  $Q_i(\tau)$  is obtained from

$$Q_i(\tau) = \frac{F_p F_B q_i}{\lambda_i + \lambda_r} (1 - \exp -(\lambda_i + \lambda_r)\tau) \quad (1)$$

where

$F_p$  = fraction release from fuel to building,

$F_B$  = fraction remaining airborne and available to be released from building to the atmosphere,

$q_i$  = activity of isotope  $i$  in the reactor core at time of the accident, Curies

$\lambda_i$  = leak rate parameter  $\text{sec}^{-1}$ , and

$\lambda_r$  = radioactive decay constant.

The following relevant nuclide groups are considered

- Noble gases
- Iodine (elementary and organic)
- Intermediate volatile groups Cs, Rb, Te

The release fraction  $F_p$  may be splitted into two release fractions

$$F_p = F_1 \cdot F_2$$

The data for the last two release fractions are listed in table 1. which are taken from reference [ 4].

**Table 1**  
**Release Factors for Nuclide Groups :**

	$F_1$	$F_2$	$F_1 \cdot F_2$
Noble gases	1	1	1
Iodine elementary	0.25	$10^{-4}$	$2.5 \cdot 10^{-5}$
Iodine organic	0.25	$10^{-2}$	$2.5 \cdot 10^{-3}$
Cs, Rb, Te	0.1	$10^{-4}$	$10^{-5}$

$F_1$  : release fraction from fuel into coolant

$F_2$  : release fraction from coolant into confinement/building

$F_1 \cdot F_2$  : instantaneous source term to containment atmosphere.

## The ORIGENJR

It is used to estimate  $q_i$  the activities of the different fission products. Thus the integrated source term for each significant radionuclide can be estimated. Given a confinement/reactor building leakage history, the amount of each radionuclide released to the atmospheric dispersion can be estimated.

## Modeling of Time dependent Activity Behavior in the Reactor Building:

For the assumption that an instantaneous release will occur, the following model is to be used for the estimation of time dependent airborne in the reactor building (R B).

The influence of the parent daughter activities may be neglected

The airborne activity in the RB is calculated by :

$$K_c(t) = q_i \text{ Exp}(-\lambda_c t) \quad (2)$$

$K_c(t)$  time dependent airborne activity in RB in curies .

$q_i$  Source term in Curies

$\lambda_c$  Building cleaning constant in  $\text{sec}^{-1}$ .

$$= \lambda_r + \lambda_{pl} + \lambda_1$$

$\lambda_r$ : radioactive decay constant

$\lambda_{pl}$  plate-out constant in  $\text{sec}^{-1}$

$\lambda_1$  building venting rate

$t$  time since accident in seconds.

Equation (1) is obtained from equation (2) by integrating over a period of time  $\tau$ .

## The TIRION-4 Code:

The TIRION-4 [2] code is used to evaluate of accidental releases of radioactive materials to the atmosphere. The TIRION-4 Code is a Gaussian Plume constant weather code. It contains the following models;

Release model which calculates the total activity released for each nuclide allowing for decay and daughter build up. As input to it, the nuclide involved, the release period, the initial activities and any hold up period.

The dispersion model used for atmospheric dispersion is the Gaussian Plume diffusion model incorporating Paquill weather categories A-F.

Dry deposition model allows ground deposition from the cloud dependent on parameters such as chemical form, vegetation cover, distance.

Radioactive decay model allows for decay and daughter build up during the diffusion time.

Building Wakes model allows for the effect wake dilution and gives reasonable estimate of the effect on downwind concentration but does not lead to accurate values within the wake.

Lift-Off model determines whether or not a ground level plume lift off the ground.

Plume Rise model determines the trajectory of a rising plume based on initial momentum, initial temperature and a radioactive heating of the cloud. The code includes other important models a plume breakup, inversion lids, inhalation dose, external radiation dose, consequences of absorbed doses, deposited activity.

## Concept of Detriment

To measure the total health harm eventually experienced by an exposed group and its descendents as a result of radiation exposure, the ICRP publication 26 (1977) [6] introduced the concept of detriment which is expressed by a combination of a health effect and a judgement of its severity. This approach to detriment has proved useful but is somewhat too limited.

The ICRP publication 60 (1990) [7] recommended a **Multiplicative risk projection model** and adopted an aggregate representation of detriment (a multidimensional concept) which includes four components (stochastic quantities) which are :

- 1- The probability of attributable fatal-cancer.
- 2- The weighted probability of attributable non-fatal cancer.
- 3- The weighted probability of severe hereditary effects.
- 4- The length of life lost if the harm occurs.

The multiplicative risk projection model is a simple model and does not necessarily imply multiplicative biological process. It is a convenient description of the manner in which the probability of an attributable cancer varies with time. This model is more popular than the **Additive risk projection model** [7] which has been found to be consistent with epidemiological observations.

The distribution of the detriment in organs and tissues is assessed by considering :

- a- Probability of fatal-cancer in each tissue or organ.
- b- Multiplying by an appropriate factor for non-fatal cancer, which is determined by the lethality factor for that cancer.
- c- Adding the probability of severe hereditary effects.
- d- Adjusting the probability, severity and time expression of the harm.

The distribution of aggregate detriment among organs is represented after appropriate rounding by the tissue weighting factor.

## CALCULATION AND RESULTS

Calculations have been carried out using the two codes ORIGNJR and TIRION-4. For the sake of comparison, calculation has been performed for the IAEA generic 10 Mw reactor presented in TECDOC 643 [3]. The doses are calculated for the release from the highest power fuel element (.4434 Mw) after 100 full power days (FPD) operation. The maximum doses were found to be not on site, rather some hundred meters away. The doses are considered at a distance 50 m site boundary at 2 hours and after 30 days of the release. The comparison are found in table 2. The assumptions in the calculation are : the release fraction is 100% for noble gases, 25 %

for halogens and 1% for all others and only 50% of the halogens remain available for release to the atmosphere.

A leakage rate to the atmosphere of 1% day is assumed. No credit is taken for filtering, washdown, or other engineered safety features that might be included in some designs.

After release to the atmosphere, the assumptions are made to describe the dispersion of the plume in the atmosphere are:

The wind speed is 1m/s and the atmosphere conditions is of Pasquill type F (stable)

The comparison showed that the present calculation is in good agreement with the IAEA bench mark results

bench mark results.

**Table 2**

**Comparison of Doses to Different Organs From Ref [3] with the present calculation**

Using peak element ,4434Mw ,in 10 Mw generic reactor .

**Dose at 500 m Site Boundary , rem (  $10^{-2}$  Sv )**

**Inhalation**

**Whole Body**

Case	Time	Inhalation			Whole Body	
		bone	Lung	Thyroid	Internal n	External Immersion
Ref [4 ]	2 h	.1384	.1987	4.419	1.549-02	5.305-2
100FPD	30 d	1.305	1.6	26.38	.1171	.1812
Infinite Irr		17.47	4.541	26.70	.4943	.203
PresentCal.	2h	.1403	.2001	4.622	1.613-02	5.415-02
100 FPD	30 d	1.512	1.712	27.003	.1200	.1877
Infinite Irr.		18.29	5.2511	27.110	.5012	.2140

Calculations have been then performed for a 22 Mw MTR reactor type.

The uranium 235 content per fuel element is 404.9 gr. The fuel element power is .751 Mw

Table 3 shows the values of doses to different organs due to the inventory of one fuel element or that of all fuel elements for 100 FPD operation. The first case represent an accident that resulted in partial core damage and the second corresponds to a one with 100% core damage.

**Table 3**

**Calculated Doses to Different Organs using Fuel element of .753 Mw ,in 22 Mw reactor and the Inventory of all fuel elements..**

**Dose at 500 m Site Boundary , rem (  $10^{-2}$  Sv )**

Case	Time	Inhalation			Whole Body	
		bone	Lung	Thyroid	Internal Inhalation	External Immersion
one fuel element 100FPD	2 h	.2383	.3402	7.857	.0274	0.0921
	30 d	2.5704	2.910	45.905	.204	.319
All fuel elements	2h	5.2425	7.844	1.7286+2	.603	2.0262
	30 d	56.549	64.02	1.0099+3	4.488	7.018

The results presented in table3 show that the thyroid dose is most limiting. It is useful to compare the doses obtained with limiting values as are given in 10CFR[5 ]

Organ	Reference	present all fuel element
Thyroid	300	1.0099+3
Bone	150	56.6
Lung	75	64.0

One may note that with increase of reactor operation over 100 FPD the values of the doses are expected to be larger than that given in the last table.

**Nominal probability coefficients for stochastic effects**

The average value for several calculations using the multiplicative risk projection model was taken as  $10 \times 10^{-2} \text{ Sv}^{-1}$ . This value is used as the nominal risk for acute high dose exposure. Applying the dose and dose rate effectiveness factor, DDREF, of 2 for the probability of induced fatal cancer in a population of all ages at low dose and low dose rate exposures, yields a nominal value of  $5 \times 10^{-2} \text{ Sv}^{-1}$ . For a working group of age from 20 to 65 years another value  $4 \times 10^{-2} \text{ Sv}^{-1}$  was obtained.

**Table 4**

**Nominal probability Coefficients for Stochastic effects [7]**

**Detriment ( $10^{-2} \cdot \text{Sv}^{-1}$ )**

Exposed Population	Fatal cancer	Non Fatal cancer	Severe hereditary effects	Total
Adult Workers	4.0	0.8	0.8	5.6
Whole Population	5.0	1.0	1.3	7.3

**Table 5**

**Nominal probability Coefficients for individual Tissues and Organs [7]**

Tissue or Organ	Probability of Fatal Cancer ( $10^{-2} \cdot \text{Sv}^{-1}$ )		Aggregated Detriment ( $10^{-2} \cdot \text{Sv}^{-1}$ )	
	Whole Population	Workers	Whole Population	Workers
Bone Surface	0.05	0.04	0.07	0.06
Lung	0.85	0.86	0.80	0.64
Thyroid	0.08	0.06	0.15	0.12

Table 6

Detriment ( $10^{-4}$ ) for Stochastic effects resulting from doses calculated in table 2 in case of whole body internal inhalation

Using peak element .4434 Mw , in 10 Mw generic reactor

Case	Time	Category	Fatal Cancer	Non-fatal Cancer	Hereditary Effects	Total
Ref [4]	2 h	workers	6.376 $10^{-2}$ 6.376	1.272 $10^{-2}$ 1.239	1.272 $10^{-2}$ 1.239	8.674 $10^{-2}$
	2 h	Public	7.97 $10^{-2}$ 7.745	1.549 $10^{-2}$ 2	2.014 $10^{-2}$	11308 $10^{-2}$
100 FBD	30 d	workers	.468	.094	.094	.656
	30 d	Public	.585	.117	.152	.855
Infinite Irr.		workers	1.977	.395	.395	2.768
		public	2.472	.494	.643	3.608
Present						
Cal	2 h	workers	6.452 $10^{-2}$	1.290 $10^{-2}$	1.290 $10^{-2}$	9.033 $10^{-2}$
	2 h	Public	8.065 $10^{-2}$	1.613 $10^{-2}$	2.097 $10^{-2}$	11.775 $10^{-2}$
100 FPD	30 d	workers	.48	.096	.096	.672
	30 d	Public	.60	.120	.156	.876
Infinite Irr.		workers	2.005	.401	.401	2.806
Infinite Irr.		Public	2.506	.501	.651	3.659

**Table 7**

**Detriment ( $10^{-4}$ ) for Stochastic effects resulting from doses calculated in table 2 in case of whole body external immersion**

Using Peak element .4434 Mw, in 10 Mw generic reactor

Case	Time	Category	Fatal Cancer	Non-Fatal cancer	Hereditary effects	Total
Ref [4]	2 h	workers	$31.22 \cdot 10^{-2}$	$4.244 \cdot 10^{-2}$	$4.244 \cdot 10^{-2}$	$29.708 \cdot 10^{-2}$
	2 h	Public	$26.525 \cdot 10^{-2}$	$5.305 \cdot 10^{-2}$	$6.896 \cdot 10^{-2}$	$38.726 \cdot 10^{-2}$
100 FPD	30 d	workers	.725	.145	.145	1.015
	30 d	Public	.906	.181	.236	1.323
Infinite Irr.		workers	.812	.162	.162	1.137
		Public	1.015	.203	.264	1.482
<b>Present</b>						
Cal	2 h	workers	$21.66 \cdot 10^{-2}$	$4.332 \cdot 10^{-2}$	$4.332 \cdot 10^{-2}$	$30.324 \cdot 10^{-2}$
	2 h	Public	$25.75 \cdot 10^{-2}$	$5.415 \cdot 10^{-2}$	$7.039 \cdot 10^{-2}$	$39.529 \cdot 10^{-2}$
100 FPD	30 d	workers	.751	.150	.150	1.051
	30 d	Public	.938	.188	.244	1.370
Infinite Irr.		workers	.96	.171	.171	1.198
		Public	1.07	.214	.278	1.562

**Table 8**  
**Detriment ( $10^{-4}$ ) for individual organs due to inhalation**  
**resulting from doses calculated in table 2**

Using peak element .4434 Mw , in 10 Mw generic reactor

Case	Time	y	Fatal cancer			Aggregated detriment		
			Bone	Lung	Throid	bone	Lung	Thyroid
Ref [4]	2 h	workers	.005	.135	.265	.008	.127	.530
	2 h	public	.007	.169	.353	.009	.159	.663
100FD	30 d	workers	.052	1.088	1.583	.078	1.280	3.165
	30 d	public.	.065	1.360	2.110	.091	1.280	3.957
Infinite Irr		workers	.699	3.088	1.602	1.048	2.906	3.204
		public	.873	3.860	2.136	1.223	3.632	4.005
Present								
Cal	2 h	workers	.005	.136	.277	.008	.128	.554
	2 h	public	.007	.170	.369	.009	.160	.693
100 FPD	30 d	workers	.060	1.164	1.620	.091	1.095	3.240
Infinite Irr		workers	.731	3.570	1.627	1.094	3.361	3.253
		public.	.914	4.463	2.169	1.280	4.201	4.066

**Table 9**  
**Detriment ( $10^{-4}$ ) for Stochastic effects resulting from doses calculated in table 2**  
**in case of whole body internal inhalation**

using fuel element of .735 Mw in 22 Mw reactor

Case	Time	Category	Fatal cancer	Non-Fatal cancer	hereditary effects	Total
One fuel element	2 h	workers	.109	.022	.022	.153
	2 h	Public	.137	.027	.036	.200
100 FPD	30 d	workers	.816	.163	.163	1.142
	30 d	Public	1.02	.204	.265	1.489
All fuel elements	2 h	workers	691.44	138.288	138.288	968.016
	2 h	Public	864.3	172.86	224.718	1261.878
	30 d	workers	17.952	3.590	3.590	25.133
	30 d	Public	22.44	4.488	5.834	32.762

**Table 10**  
**Detriment ( $10^{-4}$ ) for Stochastic effects resulting from doses calculated in table 2**  
**in case of whole body external immersion**

using fuel element of .735 Mw in 22 Mw reactor

Case	Time	Category	Fatal cancer	Non-Fatal cancer	hereditary effects	Total
One fuel element	2 h	workers	.368	.074	.074	.516
	2 h	Public	.460	.092	.120	.692
100 FPD	30 d	workers	1.276	.255	.255	1.786
	30 d	Public	1.595	.319	.415	2.329
All fuel elements	2 h	workers	8.105	1.621	1.621	11.347
	2 h	Public	10.131	2.026	2.634	14.791
All fuel elements	30 d	workers	28.072	5.614	5.614	39.301
	30 d	Public	35.09	7.018	9.123	51.231

**Table 11**

**Detriment ( $10^{-4}$ ) for individual organs due to inhalation**  
**resulting from doses calculated in table 2**

Fuel element of .753 Mw , in 22 Mw reactor

Case	Time	Category	Fatal cancer			Aggregated detriment		
			Bone	Lung	Throid	bone	Lung	Thyroid
One fuel element	2 h	workers	.009	.231	.471	.014	.218	.943
	2 h	public	.012	.289	.629	.017	.272	1.178
100 FPD	30 d	workers	.103	1.979	2.754	.154	1.862	5.509
	30 d	public.	.129	2.473	3.672	.180	2.328	6.886
All fuel elements	2 h	workers	.210	5.334	10.372	.315	5.020	20.743
	2 h	public	.262	6.667	13.829	.367	6.275	25.929
All fuel elements	30 d	workers	2.262	43.534	60.594	3.393	40.973	121.188
	30 d	public.	2.827	54.417	80.792	3.958	51.216	151.485

## **SUMMARY AND CONCLUSION**

The present paper estimates the doses to different organs and calculates the health detriments as a result of some HYPOTHETICAL accidents.

No details is given about the accident itself, however the accident may result to either one fuel element damage or to 100% core damage. For both cases the doses are calculated and are tabulated. No credit is given to ventilation and other engineering safety features.

For 100% core damage the Thyroid dose will exceed the dose limit.

From the results obtained of calculated detriment, it appears clearly that the thyroid has a higher probability for stochastic effects than lung while the bone has the least probability in both cases of reactor power considered.

The calculation tools used in the present work provide efficient method for dose estimation resulting from reactor radioactive release accident.

## **REFERENCES**

- 1-ORIGEN-JR , A Computer Code for Calculating Radiation Sources and Analyzing Nuclide Transmutations: Kinji Koyama et al ., JAERI-M 8229  
VAX6000 Version ,E. Amin 1992 NCNSRC AEA Cairo.
- 2- Fryer , L. S. , " A Guide to TIRION 4 " , SRD R 120 1978  
UK AEA  
VAX6000 Version , E. Amin 1994 NCNSRC,AEA Cairo.
- 3 - Research Reactor Core Conversion Guidebook  
IAEA-TECDOC-643 1992
- 4-" Assumptions used for Evaluating the potential Radiological Consequences of a Loss of Coolant for Pressurized Water Reactors "  
USAEC Regulatory Guide 4, 1970.
- 5- U.S Nuclear regulatory Commission Rules and Regulations 10 CFR part 100  
' Reactor Siting Criteria'
- 6- Recommendations of the International Commission on Radiological Protection, ICRP Publication 26. Annals of the ICRP 1 (3), Pergamon Press, Oxford , 1977 .
- 7-1990 Recommendations of the International Commission on Radiological Protection, ICRP Publication 60, Pergamon Press , Oxford , 1991 ..



## The Calculation of the Absolute Dose Rate of GB651 by Computer Code

*G.Mashina*

Tajoura Nuclear Research Center P.O.Box 30878 Tripoli-Libya

### Abstract

Since 1986 a Co-60 irradiation unit GB651 has been available at Tajoura research center , the original activity of 50 kCi was distributed to 9-v shaped pencils .

The first radiation field evaluation was made by fricke solution. Because of the variety of geometric positions of the radiation sources ,the resulting radiation fields could be determined precisely with great difficulty. Therefore , a computer code was developed to describe these radiation fields . According to the experiences obtained so far, By taking into consideration the specific correction factor , the coincidence of the computational model and experimental data was attained.

### Introduction

There are several dosimeter systems such as Fricke, ethanolchlorobenzen for dose determinations, but unfortunately these systems cannot cover wide dose ranges and they require complicated handling. Fast determination of exposure rates can be done by a series of computational procedures. The available literature provides methods only for the calculation of exposure rates belonging to relatively simple (point, line, disc, etc.) source geometries [1-5] . Therefore ,a computer code Mash1 was developed to describe the radiation fields of the GB651 unit.

### GB651 Gamma Irradiator

Gammabeam 651 irradiator (Fig. 1) was designed for research studies and pilot-scale irradiation. Source assemblies stored in a water-filled pool below floor level in the radiation room, are raised by pneumatic cylinders. These sources are enclosed in a fully shielded room.

The samples, and the products to be irradiated are arranged at the turntables located at several positions adjacent to the source. The irradiator is operated remotely from a control panel located outside the irradiation room.

Originally, the capacity was 50000 Ci, but because of natural decay of the source, the total activity at the time of measurement has decreased to 14740Ci. The cobalt-60 source configuration arranges nine source assemblies forming two lines extending at right angles from an apex.(Fig. 2).

### Experiment

To evaluate the performance of the code , the ferrous ammonium sulphate solution (Fricke) has been used as a reference dosimeter for measuring the dose rates. The Fricke solutions were prepared according to procedures described elsewhere [6]. The solution containers were placed along the

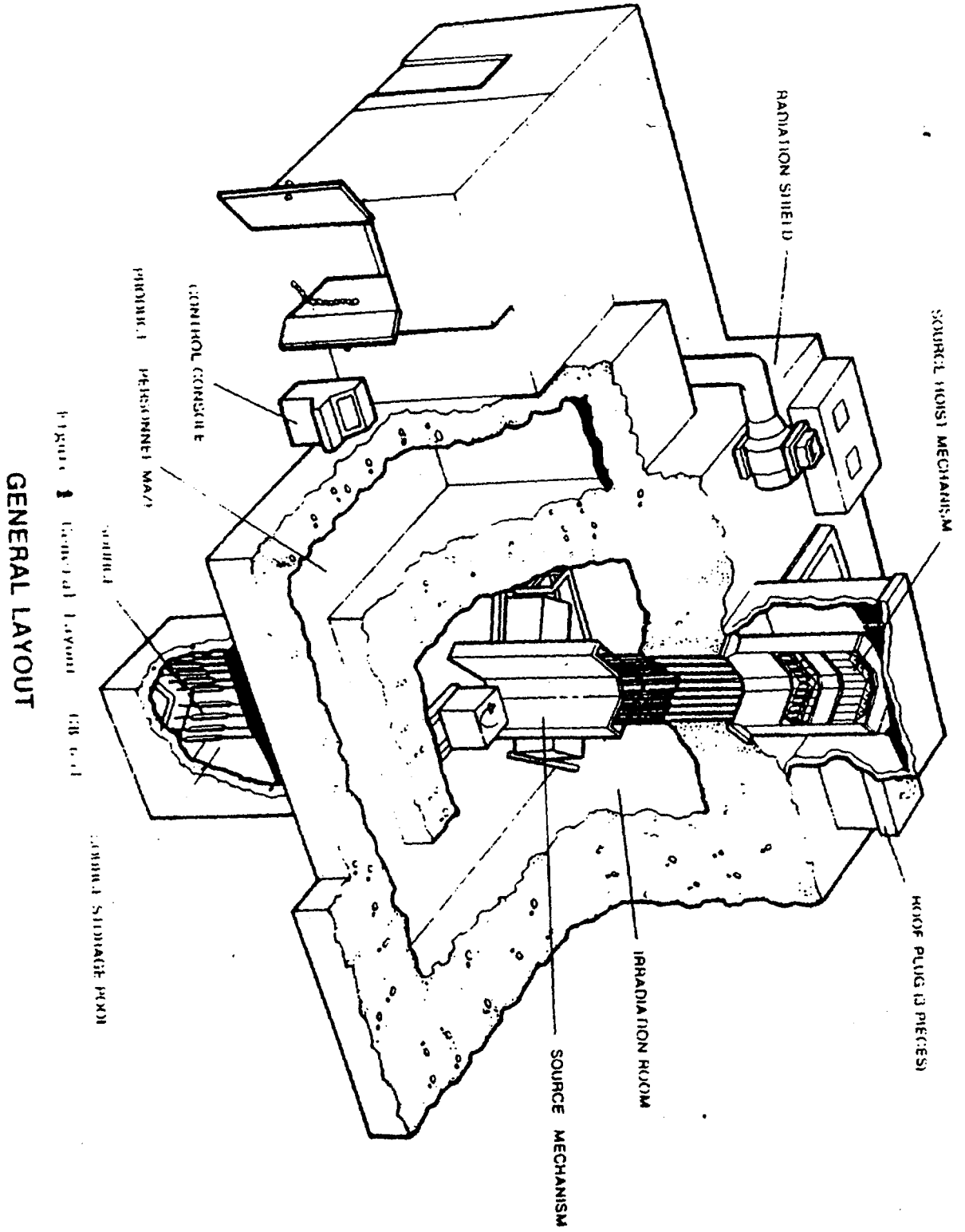


FIGURE 1 General Layout of the Cell

GENERAL LAYOUT

central normal line of the vertical source plate, There were six measurement points along a line (20cm- 60cm ) from the source apex (Fig. 2).

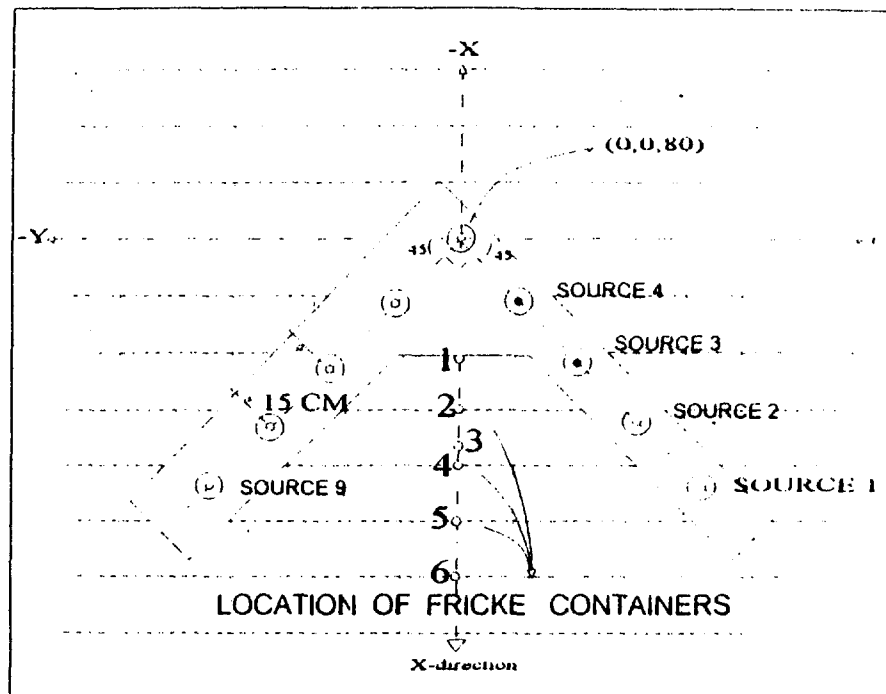


Fig. 2 Irradiation configuration - Plan View

**Basis of the Computer Model**

For exposure rate computations, simple expressions were used which could easily be processed by a computer. In the first step, the source rods were subdivided into a number of small sources in order to simulate a point source condition. The number of source subdivisions is variable and was inversely proportional to the distance between the source and the point at which the dose rate was calculated. The total dose rate was calculated as the sum of exposure rate contribution of individual sources (Fig 3) using the following formula :-

$$\dot{X} = \sum_i^n \frac{A_i * K_s * K_r}{L * B} [\theta_2 - \theta_1]$$

or

$$\dot{X} = \sum_i^n \frac{A_i * K_s * K_r}{L * B} \left[ \tan^{-1} \left( \frac{2E + L}{2B} \right) - \tan^{-1} \left( \frac{2E - L}{2B} \right) \right]$$

Where  $A_i$  is the activity (Ci) of the i-th cobalt source

$K_r$  is the dose rate constant of  $Co^{60}$  ( $1.3 \times 10^4 R \text{ cm}^2 / \text{Ci hr}$ )

$K_s$  is the correction factor ( according to experimental data )

$n$  is the number of source rods  
 $L$  is the length of source rod (cm)

$$E = \text{ABS}(Z - Z_i)$$

$$B = \sqrt{(X - X_i)^2 + (Y - Y_i)^2}$$

The geometric conditions were given by Cartesian systems of co-ordinates (x,y,z), the location of computation points was defined in relation to a fixed reference linked to the source,

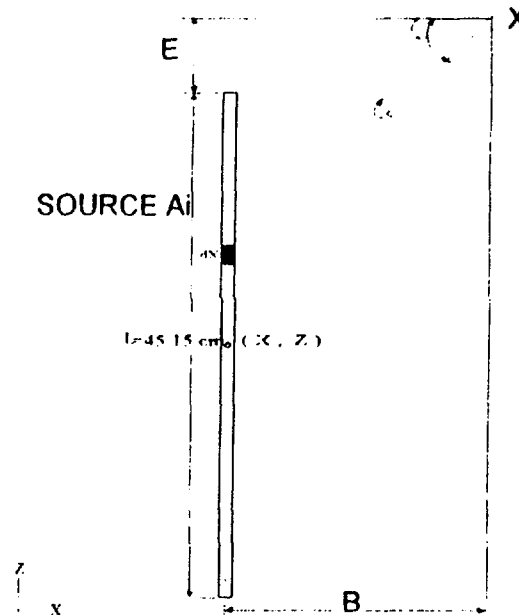


Fig. 3. Geometry for line source (one rod)

By using **MASH1** code, it is possible to chose an initial value, a step and a final value for each co-ordinate and to calculate many points of the field in one run. The basic assumptions used in these computations are:

- 1-The back scattering from the wall or other parts of the radiation chamber is not considered.
- 2-The absorption and scattering in the source itself are neglected,
- 3-The radioactive material is distributed uniformly along the line source,
- 4-The absorption in irradiated material was not taken into consideration

The computer program written in FORTRAN language was used for actual computations. The operation of this program is probably best appreciated by study of the flow chart shown in (Fig. 4), The input to the code consists of the following information :-

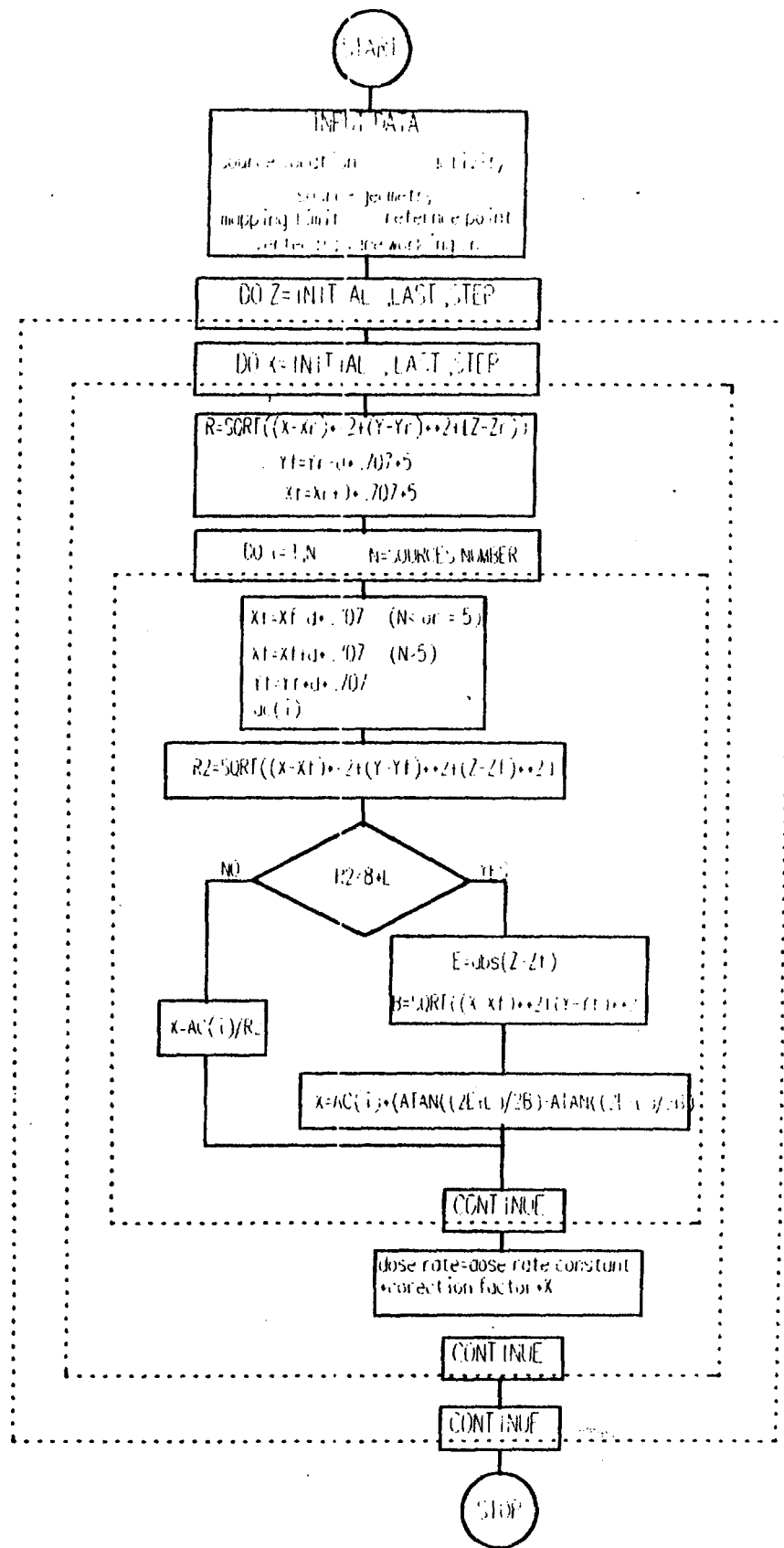


Fig. 1. FLOW CHART OF PROGRAM MATR

- Source rod length(cm).
- Individual source rod activity (Ci).
- Distance between the rods (cm).
- Number of rods
- Correction factor  $K_s$ .
- Reference point ( $x_r, y_r, z_r$ )
- Vertical plane working on ( $y$ )
- Mapping limit in x-direction ( $x_{initial}, x_{step}, x_{end}$ ).
- Mapping limit in z-direction ( $z_{initial}, z_{step}, z_{end}$ )

**Results**

Fig. 5, shows the variation of dose rate curve along the axis of symmetry of the source rods (the rods placed at height of 58.5 cm above the floor) as a function of distance from the sources, as measured with Fricke method and as calculated by computer code.

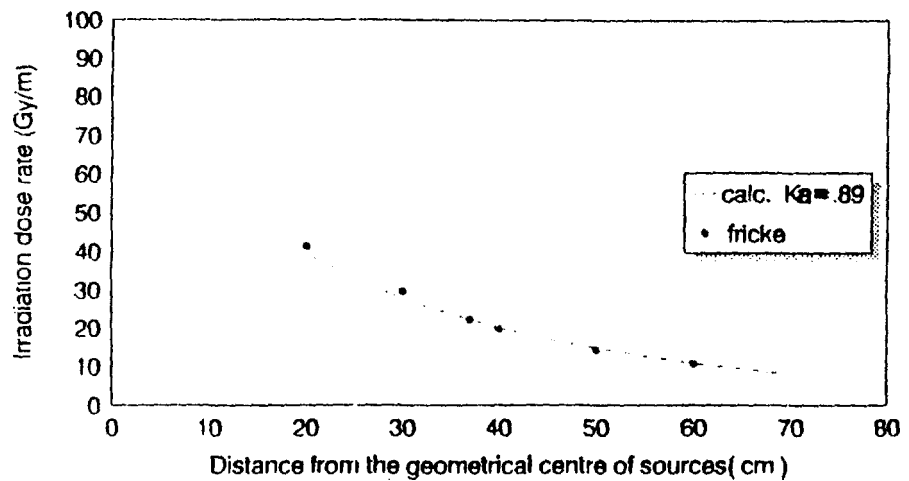


Fig. 5. Variation in dose rate, as a function of distance (x) from the sources ( $y=0, z=80\text{cm}$ )

Table 1 contains the results of such a calculation in plane  $y=0, z=80\text{ cm}$  above the floor, and at distances of 20, 30, 40, 50 and 60cm from the sources. The computed exposure rates are in good agreement with the experimental values, with the correction factor value  $k_s = 0.89$ .

**Table 1. comparison of computed and measured values**

Distance (cm)	D.R(Gy/m) cal.	D.R(Gy/m) ref.	RATIO.
20	39.6	41.4	.957
30	27.6	29.7	.929
37	22.17	22.2	.999
40	20.2	20.3	.995
50	14.77	14.3	1.033
60	10.9	10.7	1.019

### Discussion

A review of table 1 and Fig 5. shows resonable agreement between values computed using **Mash1** code and experimental data obtained by Fricke . discrepancies between computed and measured values under 7% after taking into consideration specific correction factor ( $K_s=0.89$ ) which represent the unknown parameters of the unit.

The discrepancy is due to : inherent errors associated with the code , the Fricke Dosimetry , and the errors associated with the matching of the two results together. This latter source of error reflects itself mostly on the input data to the code. In particular, imprecise position coordinates of the source rods.

The results obtained in this work recommened the application of **Mash1** code for dose rate measurements in **GB651** unit

### Acknowlegments

The author wish to tank Dr. M.Ennami , Dr. M. Abedalh, Dr. M. Sharif for their help.

### Reference

- 1- 1-G.R.Raisali,M.Sohrabpour and A.Hadjinia," **A computer code for dose rate mapping of gamma irradiators**",Radiat.Phys.Chem.Vol.35,Nos 4-6,p.831-835,(1990)
- 2- 2-P.Fejes , Zs.Horrath ,V.Stenger , " **The calculation of the relative Irradiation dose rate of a High-power Gamma-Source by digital Computer** " Isotopnpraxis,6. Jahrgang.Heft 3(1970).
- 3- H.M.B.,r,J.Reinhardt,M.Rerrer ,"**Experimental chemical Dosimetry and Computer Calculations**" , High-dose Dosimetry . (Proc. Symp.Vienna ,1984)IAEA,Vienna,p79-83( )
- 4- D.C.Mosse, J.J.M.Laizier, Y.Keraron, T.F.Lallemant, P.D.M.Perdriau, "**Experimental Qualification of a Code For Optimizing Gamma Irradiation Facilities**" , Radiat. Phys.Chem. Vol. 31, Nos 4-6, p.555-562, (1988)
- 5- G.Foldiak," **Industrial Application of Radioisotopes**"Akad,miai Kiado,Budapest , p. 498-505(1986).
- 6- 6-G.Cser,p,P.Fejes,G.Foldiak,I.Gyorgy, etc,"**Chemical Dosimetry Course** ",Institute of Isotopes of the Hungarian Academy of Sciences,Budapest,p20-24,(1971)



EG9700120

## THIRD CONFERENCE OF RADIATION PHYSICS

## RADIATION ABSORBED DOSE AND EXPECTED RISK IN HEAD AND NECK TISSUES AFTER THYROID RADIOIODINE THERAPY

A.AHAMED\*, H.I.FARAG\*\* and A.SALEH\*\*\*

\* NATIONAL CENTER FOR NUCLEAR SAFETY AND RADIATION CONTROL.

\*\* NATIONAL CANCER INSTITUTE, CAIRO UNIVERSITY.

\*\*\* AL-HUSSIEN UNIVERSITY HOSPITAL, AL-AZHER UNIVERSITY.

ABSTRACT:

A study of absorbed dose in head and neck phantom after applying I-131 therapeutic dose in the treatment of thyroid malignancies was conducted to evaluate the influence of I-131 treatment on the risk of developing cancer. The measurements were carried out at several sites of phantom using TL dosimeters.

The absorbed doses also measured on the skin surface of four patients during their administration of I-131 therapeutic doses. The measurements were taken over 69 hours exposure from 1.332 GBq (36 mCi) I-131 to the different sites of phantom. The same procedures of measurements were carried out on the four patients. At five sites of the patients head and neck, the absorbed dose were measured and compared with that measured on the phantom.

The measured values are discussed on the light of the published individual absorbed doses in the organs by ICRP tables. High absorbed doses were observed in the different sites of the head and neck during the I-131 therapy (0.14 - 9.68 mGy / mCi).

Introduction :

I-131 is still an acceptable practically method for thyroid diseases treatment. I-131 treatment is considered the treatment of choice for metastatic thyroid cancer and is also given postoperatively to iradicate remaining radioiodine accumulating tissue in the neck. The radiation dose to specific organ from I-131 depends mainly on<sup>(1)</sup>:

\* the amount of I-131 circulating in the blood, which has not been concentrated in the thyroid ( or for thyroid cancer in metastasis),

\* the quantity of organically bound I-131 released as thyroid hormones from thyroid gland,

Mailing address	Visiting address	Telephone	Telex	Telefax
Department of Medical Radiation Physics P.O. Box 260 S-171 76 STOCKHOLM Sweden	Karolinska Hospital SOLNA	+46 8 729 43 59 +46 8 729 20 00	11771 SAFERADS	+46 8 34 35 25

- \* the local accumulation of I-131 in iodine concentrating tissue (e.g. thyroid gland, salivary gland, gastrointestinal tract and urinary tract, and
- \* the radiation received from I-131 concentrated in nearby organs.

The radiation dose from I-131 derives mainly from circulating and organically bound I-131. This means that the organ doses increase with increasing 24-hours thyroid uptake values, except for the urinary tract since I-131 is excreted through the urine.

The accurate quantitation of the parameters of radioactive iodine uptake and the biological half life (BHL) of some model of therapeutic doses were determined and standardised by Rajashekharrao et al<sup>(2)</sup> to indicate the efficacy of treatment.

The most thorough way to obtain information on radiation induced cancer is through estimation study to provide the risks related to exposure dose. In the I-131 treated patients an increase risks were observed for cancers of salivary gland, female genital organs, kidney, and for tumours for the adrenal gland but an increase risk was observed for tumours of the adrenal gland in patients not treated by I-131<sup>(3)</sup>.

Lars-Erik et al<sup>(4)</sup> studied the cancer risk after I-131 therapy for hyperthyroidism after receiving 506 MBq (13.7 mCi), 360 MBq and 700 MBq as a mean total administered activity with 27% of patients received two treatments and 14% received three treatments ( Graves disease and toxic nodular goiter). and they concluded that an overall cancer risk only slightly greater 6% than that expected in the general population. Also an estimation of cancer risks after I-131 therapy. ( given dose is 4551 MBq= 123 mCi, average) are indicated by P. Hall, et al.<sup>(5)</sup> For absorbed dose calculations, an appropriate simple model describes the behaviour of administered iodine only does not include the effects of organically bound iodine and iodine produced by catabolism of organically bound iodine, which is released to the body tissues following discharge from the thyroid<sup>(5)</sup>. Different models should include values of uptake in thyroid, stomach and intestines, together urinary excretion components and describe organ and tissue retention in terms of exponential functions with up to four components<sup>(6)</sup>

In the present work the absorbed dose in different sites of the head and neck tissues of phantom were measured under the same conditions of thyroid patient treatment in addition to five corresponding sites of patients undertaken I-131 therapeutic doses. The measurements were carried out using thermoluminescence detector (TLD) and the expected risk on the patient was discussed.

#### **Material and methods:**

In order to measure the absorbed doses inside the patient head neck for risk estimation on the thyroid cancer patients treated by I-131, a typical head and neck assembly phantom (Alderson radiation therapy ART phantoms) is used. It is constructed of consistent tissue equivalent material, designed within highly sophisticated technology constraints and follow ICRU-44 standards. It is transected horizontally and each slice has holes which are plugged with soft tissue -equivalent.

There some many holes locations are distributed to include the whole body measurements. Each slic is 2.5 cm thickness with glass - smooth interfaces the soft tissue equivalent coatings which cut away over the air space of the oro-nasal pharynges. It has calcium content and the tissue simulating materials designed to have the same energy absorption as human tissue. It is matched to muscle in specific gravity, mass density and absorption coefficients. Figure (1) illustrate the slices construct to head and neck phantom.

The absorbed doses were measured by thermoluminescent dosimeters<sup>(7)</sup> in the chosen sites at the head and neck of patients and the phantom.

The absorbed doses were measured after exposing detectors 69 hr underpositioning 1332 MBq (36 mCi) I-131 in the thyroid position of the phantom (I-131 is contained in a sealed vial).

The sites of measurements were distributed in the phantom as five vertical lines as follows:

- 1- Right lateral vertical line starts from the right occipitoparital point passes through the angle of right mandible, down to the clavical bone.
- 2- Left lateral vertical line starts from the left occipito-parital point passes through the angle of left mandible, down to the clavical bone.
- 3- Anterior area vertical middle line starts from the frontal point up to the sternum bone.
- 4- posterior area vertical middle line of the occipital bone starts from the front occipital point to the end of the vertiberal neck.
- 5- Central vertical line in the contour center of the head and neck starts from the center of the frontal line into the end of the first quarter of the oesophagus and passes through cerebral tissues, posterior eye orbits, nose and tongue.

The measured sites were 45 since the head and neck phantom has 9 sections.

Table (1) represents the measured values of the absorbed doses in these 45 sites of the phantom during the first three days.

In order to evaluate these results it is important to measure the absorbed doses in head and neck of patients undergoing treatment by administering I-131 therapeutic doses (3 GBq for patient) and it is matched with the measured absorbed doses by the phantom.

On the skin surface of four patients the absorbed doses were measured in the sites of thyroid, right temporomandibular joint (TMJ), left temporomandibular joint (TMJ) and top of skull during 67 hours after administration table (2).

In histograms (1 and 2) the results are represented in groups for the nine sections of the head and neck phantom in which every column indicates a vertical line.

**Discussion and Conclusion:**

The expected risks to specific organs and tissues from therapeutic irradiation may be of stochastic or nonstochastic type<sup>(8)</sup>. While nonstochastic effects are most likely to occur within the direct treatment beams where radiation doses are greatest, the stochastic effect e.g. cancer or hereditary detriment, may result from radiation in the direct beams or from scattering or leakage radiation outside the direct beams<sup>(9)</sup>. Every organ or tissue will suffer clinically significant injury if irradiated with sufficiently high doses. Hypothyroidism is a frequent complication of radioactive iodine therapy for diffuse hyperthyroidism. It was found that with a single administration of I-131 the incidence of hypothyroidism was 22% for patients receiving less than 2 MBq (50  $\mu$ Ci) and 55% for those receiving greater than 6.5 MBq (175  $\mu$ Ci) of radioactive iodine per estimated gram of thyroid tissue. After an estimation of the absorbed dose to the thyroid of 50-120 Gy the incidence of the hypothyroidism was 7.5% within the first year with 3% becoming hypothyroid each year<sup>(10)</sup> and the incidence after 7 years was about 27% in which the incidence of hypothyroidism will rise further with time. However the younger the patients the greater the risk, and as the age at which the treatment is given decreases, the risk probably increases. For adults, external irradiation of tumours in the neck has produced hypothyroidism with conventionally fractionated cumulative thyroid doses of 26-48 Gy. Therefore to prevent chronic stimulation of thyroid from subclinical hypothyroidism with its possible effect on neoplastic transformation, it is recommended that serum thyroid stimulation hormone (TSH) measurements be obtained periodically after high dose of the thyroid area and that patient with elevated serum TSH levels be given thyroid hormone.

Also from looking on the estimated results by I. Diallo. et.al.<sup>(11)</sup> for the radiation dose delivered to any point outside the target volume per patient treated with external beam radiotherapy from target volume dose 60 Gy by irradiating field size 10 x 10 cm<sup>2</sup> in patient neck, the absorbed dose by the eye orbits is 2 Gy.

The mean absorbed doses in head and neck in this work are compared with the results of Hall P. et al.<sup>(3)</sup> in which their results indicate the mean absorbed doses in breast, stomach, kidney and bladder from I-131 for cases and controls and they estimated the risk of developing cancer in these organs. A comparison between the absorbed doses per mm<sup>3</sup> as a target volume of the head and neck tissues from I-131 therapy in the present study (mean administered activity in patient receiving I-131 is 1332 MBq) and the mean absorbed organ dose measured by Per, Hall<sup>(3)</sup> (mean administered activity in patients receiving I-131 is 1520,1225 MBq). It is clear that although the absorbed doses in breast, stomach, kidney and bladder are smaller than the absorbed doses in the head and neck tissues in the present results, they indicated 64 developed cancers in the mentioned organs from 834 patients table (3), and therefore more developed cancers in the head and neck could be expected.

Since the effective dose received from radioiodine therapy has potential mutagenic and carcinogenic effects (stochastic effect of ionizing radiation), it is necessary to

assure the recommendation that an important consideration could be taken for limiting the indicated risk of radioiodine administration for the benign disease.

**Acknowledgements:**

We thank Dr. Ashgan Mahmoud for illustration some midical aspects and our colleagues in the dept..

**References:**

- (1) Edmonds-CJ, Smith T. The long term hazerds of the treatment of thyroid cancer with radioiodine. Br. J. Radiol. 1986; 59:-45-51.
- (2) Rajashekharrao,-B. et.al. Thyroid cancer dosimetry: quantitation of radioiodine uptake and biological half life using gun monitor. Bulletin of radiation protection. v. 16(1-2), p. 92-94, 1993.
- (3)Hall-P, et. al. Tumours after radiotherapy for thyroid cancer. acase control study within a cohort of thyroid cancer patients. Acta oncology v. 31 no. 4, pp 403-407, 1992.
- (4) Lars-Erik Holm, et.al. Cancer risk after Iodine -131 therapy for hyperthyroidism, Jurnal of national cances institute Vol. 83, no. 15, aug.1991.
- (5)P.Hall, et.al. Cancer risks in thyroid cancer patients. Br. J. Cancer, 64, 159-163, 1991.
- (6)International commission on radiological protection. Radiation dose to patients from radiopharmaceuticals. Annals of the ICRP, Vol.18 publ.53. Oxford: Pergamon Press, 1988.
- (7)Farag A.h., et. al. Radiation absorbed dose for special extra oral radiography. Radiation phys. and chem. J 1995.
- (8)ICRP publication 26 para. 7.
- (9)International commission on radiological protection. Radiation. Protection of the patients in radiation therapy. Annals of the ICRP, Vol.15 No. 2 publ.44. Oxford: Pergamon Press, 1985.
- (10)Edsmyr, F and Einhorn, J. Complications in radioiodine treatment of hyperthyrodism. Acta Radiology 4, 49-54. 1966
- (11)Diallo. I. et. al. Estimation of radiation dose delivered to any point outside the target volume per patient treated with external beam radiotherapy. Radiotherapy and encology 38, 269-271, 1996.

**Measured Absorbed Dose mGy/mCi / 69 hr.**

Section no.	Rt. sites	Lt.sites	Ant. sites	Post. sites	Mid. sites	Averag dose/sect.
-------------	-----------	----------	------------	-------------	------------	-------------------

Measured Absorbed Dose mGy/mCi / 69 hr.

Section no.	Rt. sites	Lt. sites	Ant. sites	Post. sites	Mid. sites	Averag dose/sect.
1	0.133	0.127	0.167*	0.116	0.145	0.138
2	0.167	0.162	0.162	0.123	0.2	0.162
3	0.197	0.232	0.249	0.205	0.304	0.237
4	0.333	0.311	0.281	0.289	1.156	0.474
5	4.225	4.217	3.889	4.103	4.247	4.137
6	4.825	4.678	4.011	4.539	4.986	4.608
7	5.961*	5.903*	4.143	5.556	7.211	5.754
8	5.444	8.842	11.633	3.199	12.219	8.267
9	4.997	3.227	17.306*	5.005	9.675	8.043

Table (1) The measured absorbed doses in the head and neck phantom.

\* Corresponding reading on patient skull top (section 1), RT. and Lt. TMJ (section 7) and thyroid of patients (section 9).

Patient Sex	Exposur time hr	Absorbed doses $\text{c Gy/mCi hr} \times 10^{-3}$			
		Skull top	Rt. TMJ	Lt. TMJ	Thyroid
M	44.0	361.45	375.70	373.60	702.05
F	67.00	488.35	447.10	389.10	749.30
F	67.00	580.60	338.95	297.50	743.50
F	67.00	365.30	505.80	694.05	577.40

Table (2) represent the measured absorbed doses in the head and neck of patients undergoing treatment using I-131 therapeutic dose administration.

Measured Absorbed Dose mGy/mCi / 69 hr.

Section no.	Rt. sites	Lt. sites	Ant. sites	Post. sites	Mid. sites	Average dose/sect.
1	0.133	0.127	0.167*	0.116	0.145	0.138
2	0.167	0.162	0.162	0.123	0.2	0.162
3	0.197	0.232	0.249	0.205	0.304	0.237
4	0.333	0.311	0.281	0.289	1.156	0.474
5	4.225	4.217	3.889	4.103	4.247	4.137
6	4.825	4.678	4.011	4.539	4.986	4.608
7	5.961*	5.903*	4.143	5.556	7.211	5.754
8	5.444	8.842	11.633	3.199	12.219	8.267
9	4.997	3.227	17.306*	5.005	9.675	8.043

Table (1) The measured absorbed doses in the head and neck phantom.

\* Corresponding reading on patient skull top (section 1), RT. and Lt. TMJ (section and thyroid of patients (section 9).

Patient Sex	Exposure time hr	Skull top	Rt. TMJ	Lt. TMJ	Thyroid
M	44.0	0.36	0.37	0.42	0.7
F	67.00	0.18	0.45	0.38	0.75
F	67.00	0.58	0.33	0.29	0.74
F	67.00	0.36	0.5	0.69	0.58

Table (2) represent the measured absorbed doses in the head and neck of patients undergoing treatment using I-131 therapeutic dose administration expressed in cGy/mCi/m .



*An ART-210 detail*

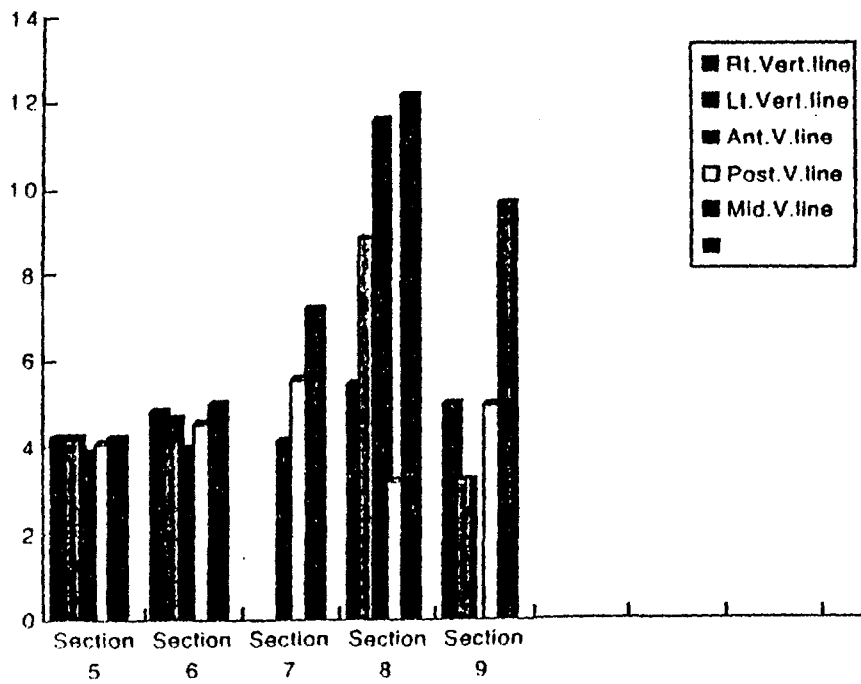
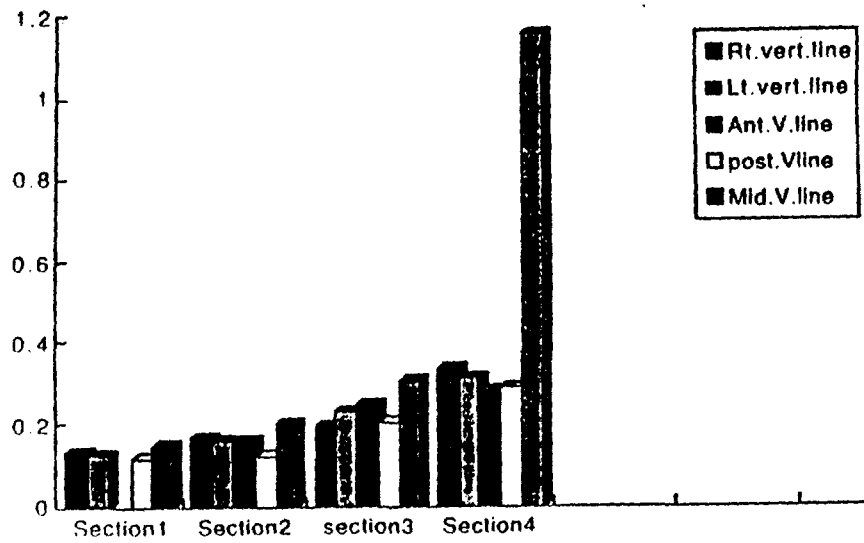
Fig(1)



L-3161-253-

	dose/mGy	mean absorbed dose per mCi/mm <sup>3</sup>
Breast	50 / 70	
Stomach	1300 / 580	
Kidney	100 / 290	
Bladder	360 / 610	
Head and neck tissues		0.138 / 8.267

Table (3) represents the absorbed doses and the indicated risks.





EG9700121

A Technique of Evaluating Most Probable Stochastic Valuables  
from a Small Number of Samples  
and their Accuracies and Degrees of Confidence

**Kazuaki KATOH**

Ibaraki Prefectural University of Health Sciences

Ami, Ibaraki-ken 300-03, Japan

**ABSTRACT**

A method of retrospective estimation of the expectation value for the number of incident stochastic signals from actually observed digital signals released from a signal-converter with extremely low conversion efficiency is proposed. The Bayesian statistics is used to solve the problem, since it is a typical *inverse problem*.

Importance of evaluating the quality of the estimate is stressed and equations are derived to calculate the mathematical expectation and its standard deviation on the premise that no other useful information to the evaluation is available. Two important stochastic processes to radiation protection dosimetry, the Poisson- and the Bernoulli- are considered as the conversion system.

**INTRODUCTION**

Radiation protection practices necessitate low level radiation dosimetry and improvement in technology has repelled classical analog measurement and techniques dealing digital (including digitalized) signals from a measuring system has become dominant.

Such systems can be regarded as a signal converting machine or system, namely input of incident radiation particles and output of detection signals. The processes of the conversion are of stochastic character and efficiencies of conversion are usually extremely low. Thus, the accuracy (or precision) and the reliability (or degree of confidence) of the estimate must be evaluated, simultaneously.

In this circumstance, the aim of measurements is to get best estimate of numbers of the incident particles for a specified condition from the actually counted numbers of the output signals. This is a typical *inverse problem*. Unfortunately, however, importance of evaluating the accuracy and reliability stated-above has been frequently neglected, and even in case evaluations are tried, the problems were treated in the scheme of the ordinary forward problem.

From view point of the science of information treatment, radiation dosimetry is

nothing but the estimating a value of a functional related to the radiation field from both pumped out information on it (experimental results) and already known knowledge about it if it exists and is available. If the information on the field in the vicinity of the point of interest is known adequately enough, there is no need to pump up information any more. The dose, a functional of the field, can be estimated without any new information. On the contrary, if no information on the field is available, a response of a detector itself cannot give any information on the quality of the estimation.

### PROBLEMS

The problem is to evaluate the most probable expectation value and its standard deviation of the incident digital signals from actually obtained number of output signals from a signal converting system with extremely low efficiency. As for stochastic processes, the Poisson- and Bernoulli- are considered, since these two are important in the practices.

#### (1) Poisson Process

In case the incident signals are generated independently each other and transforming to or yielding output signals is probabilistic, the process of converting signal numbers is that of Poisson. Namely, the system generates output signals following the Poisson formula,

$$P(m \rightarrow K) = \exp(-m) \cdot m^K / K!$$

where  $m$  is the expectation value of the number of output signals for a specified condition

$$m = p \cdot N$$

$p$  is the probability of conversion and  $N$  is the number of incident signals for the specified condition. The number  $m$  is a real while the number  $K$  is non-negative integer.

Thus the problem in this case is to calculate the expectation value of  $m$ ,  $\langle m \rangle$ , when a number  $K$  is given as the number of output signals.

#### (2) Bernoulli Process

In the system of the Bernoulli Process, trials of  $n$  times yield responses  $r$  times. The probability that a trial yield a signal is expressed as

$$P(p \rightarrow) = {}_n C_r p^r (1 - p)^{n-r}$$

where  ${}_n C_r$  stands for the combination from  $n$  to  $r$ .

The problem is to evaluate the expectation value of the probability,  $p$ , in case the figures  $n$  and  $r$  are given.

nothing but the estimating a value of a functional related to the radiation field from both pumped out information on it (experimental results) and already known knowledge about it if it exists and is available. If the information on the field in the vicinity of the point of interest is known adequately enough, there is no need to pump up information any more. The dose, a functional of the field, can be estimated without any new information. On the contrary, if no information on the field is available, a response of a detector itself cannot give any information on the quality of the estimation.

### PROBLEMS

The problem is to evaluate the most probable expectation value and its standard deviation of the incident digital signals from actually obtained number of output signals from a signal converting system with extremely low efficiency. As for stochastic processes, the Poisson- and Bernoulli- are considered, since these two are important in the practices.

#### (1) Poisson Process

In case the incident signals are generated independently each other and transforming to or yielding output signals is probabilistic, the process of converting signal numbers is that of Poisson. Namely, the system generates output signals following the Poisson formula,

$$P(m \rightarrow K) = \exp(-m) \cdot m^K / K!$$

where  $m$  is the expectation value of the number of output signals for a specified condition

$$m = p \cdot N$$

$p$  is the probability of conversion and  $N$  is the number of incident signals for the specified condition. The number  $m$  is a real while the number  $K$  is non-negative integer.

Thus the problem in this case is to calculate the expectation value of  $m$ ,  $\langle m \rangle$ , when a number  $K$  is given as the number of output signals.

#### (2) Bernoulli Process

In the system of the Bernoulli Process, trials of  $n$  times yield responses  $r$  times. The probability that a trial yield a signal is expressed as

$$P(p \rightarrow) = {}_n C_r p^r (1 - p)^{n-r}$$

where  ${}_n C_r$  stands for the combination from  $n$  to  $r$ .

The problem is to evaluate the expectation value of the probability,  $p$ , in case the figures  $n$  and  $r$  are given.

**METHOD and RESULTS**

(1) Poisson

The problems can be formulated as follows by using Bayesian statistics:

$$P(m \leftarrow K) = \omega(m) \cdot P(m \rightarrow K) / \int_0^{\infty} \omega(m) \cdot P(m \rightarrow K) \cdot dm$$

where  $P(m \leftarrow K)$  is the probability of  $m$  given  $K$  and  $\omega(m)$  is a weighting function to take in other information available on the value of  $m$ . In some cases, it might be possible to utilize such information, i.e. a certain amount of *a priori* or *a posteriori* information, prior to the measurement. However, usually in many cases, there exist no such information. Therefore, in this study, the function  $\omega(m)$  is taken independent from  $m$ ,  $\omega(m) = 1$ .

Then, the equations to calculate the expectation value of  $m$ ,  $\langle m \rangle$ , and its standard deviation,  $\sigma$ , are derived as follows:

$$\langle m \rangle = \int_0^{\infty} m \cdot P(m \leftarrow K) \cdot dm = K + 1$$

$$\sigma = \sqrt{K + 1}$$

It is interesting to see that the value of  $\langle m \rangle$  is limited to integer, and  $\sigma$  has the familiar form of  $\sigma = \sqrt{\langle m \rangle}$ .

The most probable value of  $m$ ,  $\hat{m}$ , is obtained by solving

$$\partial P(m \leftarrow K) / \partial m = 0$$

The solution is

$$\hat{m} = K$$

(2) Bernoulli

Similarly to (1), mathematical formulations are given as follows:

$$P(p \leftarrow r) = \omega(p) \cdot P(p \rightarrow r) / \int_0^1 \omega(p) \cdot P(p \rightarrow r) \cdot dp$$

With

$$\omega(p) = 1, \quad 0 \leq p \leq 1,$$

following equations are derived:

$$\langle p \rangle = (r + 1) / (n + 2)$$

$$\sigma = \sqrt{\{(n - r) \cdot r + (n + 1)\} / (n + 3) / (n + 2)}$$

$$\hat{p} = r / n$$

## DISCUSSION

The results obtained in this study show various interesting features of the matter. Listed below are some of them:

1). The expectation value of the variable  $m$  of the Poisson distribution function estimated retrospectively from an observation,  $K$ , is turned out  $K+1$  for the case where no other information is available. Values of  $\langle m \rangle$  are limited to integer, while those of  $m$  are real numbers.

2). The expectation values are not equal to the corresponding most probable values. The former is the outcome of the *retrospective analysis*, while the latter is that of *forward analysis*.

3). In the case of Poisson, the expectation differs by 1(unity) from actually obtained number. This implies special attention is needed in such a work of neutron dose measurement with a track detector in the vicinity of lower limit of detection in dose range.

4). Similarly, special attention is needed in the process of data analyses of biological dosimetry, where the death probability of cells,  $p$ , is related to dose and the probability is evaluated from an experimental result of  $r$  deaths from  $n$  trials, in the vicinity of lower limit of detection.

5). It is very interesting to see the relation

$$\sigma = \sqrt{\langle m \rangle}$$

is also hold for the case of retrospective estimation of the mean value of the variable, since except the ordinary Poisson and Gaussian (of distribution function of variables), nothing is known of which the relation holds.

## CONCLUSION

Equations to calculate the retrospective expectation values of the mean of stochastic variables are successfully derived by using the Bayesian Statistics upon the premise of absence of any other information to improve the quality of the estimation, for the two important processes in radiation protection dosimetry practices, the Poisson and the Bernoulli.

The standard deviations of these expectations are calculated also successfully. Hence, it becomes possible to evaluate the degree of confidence for the estimation of the expectation values.

## Acknowledgement

The author expresses his sincere thanks to Dr Junichiro Tada for the discussion and proof reading of the manuscripts.

**SCIENTIFIC SESSION (11)**

**RADIATION DETECTION -2**

**LIFETIME MEASUREMENTS OF THE EXCITED STATES IN  $^{145}\text{Sm}$**

**A. M. El-Badry\*, Sh. Abdel Samie\*, A. A. Ahmad\*,  
T. Kuroyanagi\*\*, S. Mitarai\*\*, A. Odahara\*\*, Y. Gono\*\*, and S. Morinobu\*\***

**\* Department of Physics, Faculty of Science, El Minia University, El Minia, Egypt  
\*\* Tandem Accelerator Laboratory, Department of Physics, Kyushu University, Japan**

**ABSTRACT**

Lifetime of the excited levels in  $^{145}\text{Sm}$  has been measured through the  $^{139}\text{La} (^{10}\text{B}, 4n) ^{145}\text{Sm}$  nuclear reaction. The optimal beam energy of 49 MeV was determined from the measurements of the excitation function and CASCADE program. With the possibility of studying lifetime of this nucleus a conventional plunger system have been designed and constructed at Kyushu University tandem accelerator laboratory.

A La target of 0.22 mg/cm<sup>2</sup> thickness which was evaporated onto a Au foil of 2 mg/cm<sup>2</sup> thickness was used. Since the recoil velocity was estimated to be 1.76 mm/ns ( $\beta = 0.00585$ ), the measurable time range resulted in the range from 5 ps to 5 ns.

The single spectra measurements were performed at the 20 plunger positions in the range from 10 $\mu\text{m}$  to 10mm. Analyses of the data were carried using hypermet and/or GF2 program to obtain the lifetimes. A new list of lifetimes for 12 excited states up to 3.922 MeV excitations for  $^{145}\text{Sm}$  were determined for the first time. Decay curves of these transitions are discussed.

The new lifetimes of excited states in  $^{145}\text{Sm}$  enabled us to understand the electromagnetic properties. The deduced transition probabilities were established and compared with that of N = 83 isotones and the closed shell nucleus  $^{144}\text{Sm}$ . In addition, a nuclear structure of  $^{145}\text{Sm}$  have been discussed and proposed in framework of the shell model.

**A COMPUTER SIMULATION  
OF AUGER ELECTRON SPECTROSCOPY**

**M. S. Ragheb, and M. H. S. Bakr**

**Dept. of Accelerators and Ion Sources,  
Division of Basic Nuclear Sciences,  
NRC, Atomic Energy Authority, Egypt**

**ABSTRACT**

A simulation study of Auger electron spectroscopy was performed to reveal how far the dependency between the different parameters governing the experimental behavior affects the peaks. The experimental procedure followed by the AC modulation technique were reproduced by means of a computer program. It generates the assumed output Auger electron peaks, exposes them to a retarding AC modulated field and collects the resulting modulated signals. The program reproduces the lock-in treatment in order to demodulate the signals revealing the Auger peaks. It analyzes the spectrum obtained giving the peak positions and energies. Comparison between results of simulation and the experimental data showed good agreement. The peaks of the spectrum obtained depend upon the amplitude, frequency and resolution of the applied modulated signal. The peak shape is affected by the rise time, the slope and the starting potential of the retarding field.

**A PREPARATION OF THIN FLAT TARGET FOR RD  
LIFETIME MEASUREMENTS**

**Azza M. El-Badry\*, Sh. Abdel Samie\*, A. A. Ahmad\*  
T. Kuroyanagi\*\*, and S. Morinobu\*\***

**\*Department of Physics, Faculty of Science, El Minia University**

**\*\* Tandem Accelerator Laboratory**

**Department of Physics, Kyushu University, Japan**

**ABSTRACT**

An extreme flatness for a target surface is the most necessary in recoil distance method (RDM). A suitable technique was used for preparing a La target. The  $^{139}\text{La}$  target of thickness  $0.22 \text{ mg/cm}^2$  was evaporated onto a very flat soft Au foil of thickness  $2 \text{ mg/cm}^2$ . This target was successively used for

lifetime measurements of the excited nuclear states in  $^{145}\text{Sm}$  nucleus through the nuclear reaction  $^{139}\text{La} (^{10}\text{B}, 4n) ^{145}\text{Sm}$ . Background  $\gamma$  rays produced by the  $^{10}\text{B}$  irradiation for the Au backing and the Pb stopper without the La target were measured. Besides that, the  $\gamma$  rays from residual activities were also measured.

### **STUDY OF VARIATION OF TRACK DENSITY IN IRRADIATED CR-39 AS A FUNCTION OF DIFFERENT PARAMETERS**

**M. S. Garawi**

Physics Department, College of Science  
King Saud University, Riyadh 11451, Saudi Arabia

#### **ABSTRACT**

In this work variation of track density in  $^{241}\text{Am}$ -irradiated CR-39 was studied as a function of different parameters. The behaviour of NaOH and KOH as etchants with different normalities was investigated. It was found that the number of tracks as a function of etching time increases gradually in both cases till saturation, keeping the other parameters (temperature and concentration of the solution) constant. In general, at lower values of etching time, concentration and etching temperature, the appearance of tracks is low, but increases gradually till saturation is reached. The effect of different etchants, temperature were examined. At higher etching temperature, the tracks density decreases slowly. This may be due to overlapping of tracks as an effect of higher etching temperature.

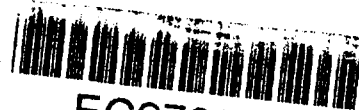
### **ETCHING PROPERTIES AND EFFICIENCY STUDIES OF LR - 115 TYPE II DETECTOR**

**H. EL-Samman, A. Hussein, and Kh. Shnishin**

Faculty of Science, Menoufia University,  
Shebin El Kom, Egypt

#### **ABSTRACT**

Chemical etching properties of LR- 115 type II track detectors have been extensively studied under different NaOH etchant conditions C (2 - 9N) and temperature T (40 - 60 °C). Bulk etch rate ( $V_B$ ) was determined by fission



EG9700122

## Lifetime measurements of the excited states in $^{145}\text{Sm}$

A.M.El-Badry, Sh. Abdel samie and A. A. Ahmed

Department of physics, Faculty of science, El Minia University,  
El Minia, Egypt

and

T.kuroyanagi, S.Mitarai, A.Odahara, Y.Gono, and S. Morinobu

Tandem Accelerator laboratory

Department of physics, Kyushu University, 812 Japan

### Abstract

Lifetimes of the excited levels in  $^{145}\text{Sm}$  have been measured using the  $^{139}\text{La}(^{10}\text{B}, 4n)^{145}\text{Sm}$  reaction. The optimum beam energy of 49 MeV has been determined from the measurements of the excitation function. A new plunger system has been designed and constructed for this purpose at the Kyushu University Tandem Accelerator Laboratory.  $^{139}\text{La}$  target of 0.22(5) mg/cm<sup>2</sup> in thickness, evaporated onto a Au foil of 2 mg/cm<sup>2</sup> in thickness, has been used. As a stopper for the recoil nuclei and the beam, a 86 mg/cm<sup>2</sup> thick Pb foil has been used. The measurable lifetime range with the present apparatus is from 5 ps to 5 ns. The singles  $\gamma$ -ray spectra have been measured at 20 separations ranging from 10  $\mu\text{m}$  to 10 mm between the target and the stopper. Analysis of the data has been carried out using GF2 programs to obtain the lifetimes. A new list of lifetimes for the 12 excited states in  $^{145}\text{Sm}$  up to 3.922 MeV is presented for the first time. The electromagnetic transition probabilities are derived for the relevant transitions by using the obtained lifetime results. The reduced transition probabilities are calculated and compared with those of theoretical single particle Weisskopf estimates.

## 1 Introduction

Recently, high-spin isomers in  $N=83$  isotones were reported [1-6] to have an oblate shape with spins and parities of  $49/2^-$  and  $27^-$  for odd and odd-odd nuclei, respectively. The origin of these isomers was attributed to sudden shape changes from a near spherical- to an oblate-shape [3]. These isomers were interpreted to have configurations with stretch couplings of angular momenta of valence nucleons. Although characteristics of the isomers were fairly well studied, the information of low lying states are still insufficient.

High-spin states of  $^{145}\text{Sm}$  were reported [3,7] previously. They were studied by in-beam gamma and electron spectroscopic techniques and were interpreted within the framework of the empirical shell model (ESM) [7] and the deformed independent particle model (DIPM) [3]. Many low-spin states of  $^{145}\text{Sm}$  were also known [8] from studies of a  $\beta$  - decay of  $^{145}\text{Eu}$  and the  $^{144}\text{Nd}(\alpha, 3n)$ ,  $^{144}\text{Sm}(d, p)$  reactions. However the lifetimes of only two excited states were known, i.e. 14 ns for the  $13/2^-$  excited state [9] and  $0.96 \mu\text{s}$  for the high-spin isomer [3]. It is essential to measure lifetimes of other known states to see if these interpretations are consistent or not. In this report, the life times of the low-lying states of  $^{145}\text{Sm}$  are presented.

## 2 Experimental procedure

The nucleus  $^{145}\text{Sm}$  was produced by the  $^{139}\text{La}(^{10}\text{B}, 4n)^{145}\text{Sm}$  reaction. The life times of excited states of  $^{145}\text{Sm}$  were measured by a recoil distance method (RDM). The  $^{10}\text{B}$  beam was provided by the Kyushu university tandem accelerator. The excitation function was taken in the energy range of the  $^{10}\text{B}$  beam from 42 to 52 MeV. The optimum energy for the 4n emission channel was determined to be 49 MeV which was consistent with that estimated by using the computer code CASCADE [10].

A La target with thickness of  $0.22(5) \text{ mg/cm}^2$  was prepared by evaporation on a  $2 \text{ mg/cm}^2$  Au foil. It was crucial to keep extremely flat surface of the target for this experimental method. A target holder was made to realize flat surface by giving a uniform tension to the target foil. A new plunger system was used for RDM [11]. A stopper for the recoil nuclei and the beam was made of a Pb foil with thickness of  $86 \text{ mg/cm}^2$ . The stopper was made to cover a movable range from  $10 \mu\text{m}$  to 10 mm with respect to the fixed target. Since the velocity

of the recoil nuclei was estimated to be 1.76(2) mm/ns, the measurable time range resulted in the time range of from 5 ps to 5 ns. The maximum distance of 58 mm was also used when it was necessary. This distance corresponds to 33 ns of the flight time.

Singles  $\gamma$ -rays spectra were taken by using a HPGe (GMX) detector of 20% relative efficiency. The detector was placed at 64 mm apart from the stopper foil and at  $0^\circ$  with respect to the beam axis. A low energy photon spectrometer (LEPS) with high energy resolution was also used to separate shifted and unshifted peaks of low energy  $\gamma$ -rays. LEPS was placed at the same position as GMX. An absorber which consisted of a 4mm Cu and a 1mm Al plate was set in front of the  $\gamma$ -ray detectors to suppress KX-rays. The  $\gamma$ -ray spectra were taken at 20 positions of various target- and stopper -distances. These data taken by GMX and LEPS at each position were collected for the integrated beam charge of 100  $\mu$ C and 400  $\mu$ C, respectively.

Singles  $\gamma$ -ray spectra were also taken at  $125^\circ$  with respect to the beam axis to obtain  $\gamma$ -ray relative intensities. In this case a La target of 1 mg/cm<sup>2</sup> was used. The background spectra originating from various reactions which were unavoidable in the present experiment were also measured. They were those from  $^{10}\text{B}$  bombardment on targets of Au, Pb,  $\text{PbO}_2$ ,  $^{27}\text{Al}$  at the same beam energy of 49 MeV. These measurements worked very effectively to subtract the background components from the  $\gamma$ -ray peaks of  $^{145}\text{Sm}$ . The  $\gamma$ -ray energy and efficiency calibrations of Ge detectors were performed by using a standard source  $^{152}\text{Eu}$ .

### 3 Spectrum analysis and results

#### 3.1 Spectrum analysis

Twelve  $\gamma$ -rays deexciting the states up to  $27/2^+$  at 3922 keV were strong enough to give information on half lives. A partial level scheme of  $^{145}\text{Sm}$ , is shown in Fig.1 which is necessary for the following discussions.

High energy parts of  $\gamma$ -ray spectra taken by GMX at various distances are shown in Fig.2. The peaks at 944.8, 1104.7 and 1331.4 keV were shifted to 950.5, 1111.5 and 1338.8 keV. These energy differences were used to extract the recoil velocity of  $^{145}\text{Sm}$ . The deduced velocity was 1.76(2) mm/ns. This value is consistent with that calculated considering the energy losses of both the projectile

and  $^{145}\text{Sm}$  in the target. It is clear from the intensity ratios of the shifted and unshifted peaks that 1105 keV deexcites a state with a relatively long half life while 945 and 1331 keV deexcite those with short half lives. Low energy parts of  $\gamma$ - ray spectra taken by LEPS are shown in Fig.3. The necessity of using LEPS with a high energy resolution is obvious.

To analyze areas of both shifted and unshifted peaks, corrections such as dead time of the data taking system and  $\gamma$  ray detection efficiencies including solid angles were taken into account. Since the target position moved depending on the distance from the stopper, it was necessary for the analysis of shifted peak areas to correct solid angle accepted by Ge detectors for each distance. In the latter case the correction depended on half lives as well.

In addition to these corrections,  $\gamma$ - rays originated from the unwanted reaction products caused severe problems in some cases. It was found that the 269 keV  $\gamma$ - ray of  $^{145}\text{Sm}$  overlaps with a  $\gamma$ - ray of the same energy emitted from Coulomb excitation of  $^{197}\text{Au}$ . This kind of accidental overlaps also occurred for other peaks such as 140, 364 and 438 keV. Contamination of  $\gamma$ - ray spectra from these reactions were unavoidable in the present experiment. These contaminant components were subtracted by multiplying factors obtained from known ratios of these  $\gamma$ - ray intensities with those of isolated peaks stemmed from the same origin.

### 3.2 Decay curves

The extraction of nuclear level lifetime from the experimental data can be obtained from the intensity changes for both unshifted (U) and shifted peaks(S) vs. the distance. In other words the ratios  $U/(U+S)$  and/or  $U/F$  decays with the distance  $d$ , where  $F$  is a normalization factor deduced from relative peak intensities of Coulomb excitation or KX ray in each spectrum. Once the mean distance value in the decay curve can be determined by means of a least square fit, and it is converted to the lifetime of such transition using the recoil velocity. All the least square fit to the experimental points were performed by DECAY SHELL program. The two independent analysis of the ratios were carried out for each transition up to the  $27/2^+$  state in  $^{145}\text{Sm}$ . The obtained lifetime results using the both method are in good agreement.

Examples of the decay curves are given in Fig.4. As can be seen in the figure good fitting is obtained in all cases. Decay curve Fig.4(a) for the first

excited  $13/2^+$  state gives the half-life of  $13.9 \pm 0.7$  ns in good agreement with the previously published result of 14 ns [9] for this state, which shows the validity of the experiment and the correct treatment of the data.

The highest excited state in the present study is the  $27/2^+$  state at 3.922 MeV which deexcites via the 438 keV transition. The decay curve, Fig 4 (a), of this transition shows single component with half-life of  $1.0 \pm 0.08$  ns. This is the first determination of the lifetime for the  $27/2^+$  state.

On the other hand, a component with long lifetime around 3 ns exists in the decay curves of U/(U+S) or U/F for the transitions in the cascades starting from  $23/2^+$  state down to the  $13/2^+$  state. These long components can be seen in Fig. 4(b) and 4(c). The weighted average of the lifetime was calculated to be  $3.1 \pm 6$  ns, which is consistent with the lifetime assigned to the transitions above  $15/2^-$  state in ref. [8]. The intensities of 3 ns components were not so intense to disturb the analysis of the short components.

In the cascade from  $27/2^+$  to  $13/2^+$  state, it was found that only the transitions of the 494, 220 and 1331 keV  $\gamma$  rays from the lowest two levels of the  $21/2^+$  and  $17/2^+$  states show to be the half-lives around 200 ps (an example can be seen for 494 transition in Fig.4(b)). Then it can be concluded that the half-life of the  $21/2^+$  state at 2.930 MeV is assigned to  $210 \pm 20$  ps which is the weighted average of the results for the above three transitions.

As can be seen in the level scheme in Fig.1, the  $23/2^+$  state not only deexcites to the  $21/2^+$  state at 2.930 MeV, but also another  $21/2^+$  state at 2.980 MeV via the 140 keV transition. The new half-life around 100 ps appears in the succeeding cascade transitions via negative parity states from  $19/2^-$  to  $15/2^-$ . The derived half-lives are 120(26), 120(20) and 130(24) ps for the 481 (see Fig. 4(b)), 181 and 945 keV transitions respectively. Then the weight average of the half-life of  $125 \pm 25$  ps is determined for the lifetime of the  $21/2^+$  state at 2.980 MeV.

The transitions of 481 and 181 keV between the negative parity states showed no indication of other lifetime components than those mentioned above. Then the half-lives of the  $19/2^-$  and the  $17/2^-$  states are considered to be less than the instrumental limit of 5 ps.

The next low lying state which is the  $15/2^-$  state at 2.050 MeV depopulates by the transition of 945 keV. The analysis of the 3 step cascade decay of this transition is shown in Fig.4(c). The flattening part of the decay curve in the distance range within 60  $\mu$ m of the decay curve gives the half-life of 16 ps as

the life time of this  $15/2^-$  state. Also the 1331 keV transition shown the same flattening at short range within  $60 \mu\text{m}$  besides the components of 2.3(10) ns and 190(30) ps. provided a signature of a component with a half-life of roughly 17 ps for the  $17/2^-$  state at 2.436 MeV. However, these flattening effects are shown by only a few data points and the results of the two transitions may not be reliable enough.

The final lifetime results for 12 transitions as shown in the level scheme (Fig. 1) and table 1 were determined for the first time. Also the deduced transition probabilities calculated from the experimental data are summarized in table 1 together with the transition energies, multipolarities and the factors of the enhancement relative to the single particle (Weisskopf) estimates.

#### 4 conclusion

The  $\gamma$  transitions in  $^{145}\text{Sm}$  were studied by applying in-beam spectroscopy to the  $^{139}\text{La}(^{10}\text{B}, 4n)^{145}\text{Sm}$  reaction. The lifetime of the excited states in  $^{145}\text{Sm}$  have been measured up to  $27/2^+$  state at 3.922 MeV excitation by RDM. The 12 lifetime of the excited states have been determined for the first time. The transition probabilities of these states have been deduced and compared with theoretical single particle (Weisskopf estimate).

Table 1: The results of the lifetime measurement  $T_{exp}$  for the excited states in  $^{145}\text{Sm}$ , the transition energies  $E_{\gamma}$ , multipolarities(MP), the experimental reduced transition probabilities ( $B_{exp}$ ), the theoretical single particle (Weisskopf) ( $B_w$ ) and the relative values of  $f = (B_{exp})/(B_w)$  are also summarized. The reduced transition probabilities are given in  $B_{exp}(E\lambda)$  in  $e^2 fm^{2\lambda}$ , B(M1) in  $\mu_N^2$ .

$E_x$ (KeV)	$I_i^{\pi} - I_f^{\pi}$	$T_{exp}$	$E_{\gamma}$ (KeV)	MP	$T_w$	$B_{exp}$	$B_w$	f
1105	$13/2^- \rightarrow 7/2^-$	13.9(7) ns	1105	E3	466 ns	$4.34(22) \times 10^4$	$1.25 \times 10^3$	35(2)
2050	$15/2^- \rightarrow 13/2^-$	16(8) ps	945	E1	0.3 fs	$3.23(162) \times 10^{-3}$	1.78	$1.81(91) \times 10^{-5}$
2231	$17/2^- \rightarrow 15/2^-$	< 5ps	181	M1	2.9ps	> 0.74	1.79	> 0.74
2436	$17/2^- \rightarrow 13/2^-$	17(5)ps	1331	E2	2.9 ps	8.07(237)	45.26	0.18(5)
2711	$19/2^- \rightarrow 17/2^-$	< 5ps	481	M1	0.2 ps	> 0.071	1.79	> 0.04
2930		210(20) ps						
	$21/2^- \rightarrow 17/2^-$	287 ps	494	E2	410 ps	67.5(63)	45.26	1.49(14)
	$21/2^- \rightarrow 19/2^-$	781 ps	220	E1	20 fs	$5.2(5) \times 10^{-3}$	1.78	$2.93(28) \times 10^{-5}$
2980	$21/2^+ \rightarrow 19/2^-$	125(25) ps	269	E1	13 fs	$2.2(4) \times 10^{-4}$	1.78	$1.25(25) \times 10^{-4}$
3120		< 5ps						
	$23/2^- \rightarrow 21/2^-$	< 10.8ps	189	M1	2.9ps	> 0.54	1.79	> 0.30
	$23/2^- \rightarrow 21/2^-$	< 9.3ps	140	M1	8.1ps	> 1.54	1.79	> 0.86
3484	$25/2^+ \rightarrow 23/2^-$	< 5ps	364	M1	0.46 ps	> 0.16	1.79	> 0.09
3922	$27/2^- \rightarrow 25/2^-$	1.0(1) ns	438	M1	0.3 ps	$4.69(47) \times 10^{-4}$	1.79	$2.76(28) \times 10^{-4}$

## References

- [1] T. Murakami et al., Z. Phys. A345,123(1993)
- [2] A. Ferragut et al., Z. Phys.Soc.Jpn. 62,3343(1993)
- [3] A. Odahara et al., Z. Phys. A350,185(1994)
- [4] E. Ideguchi et al., Bull. Phys.Soc.Jpn.,108(1993)
- [5] M. W. Drigert et al., Nucl. Phys. A515,466(1990).
- [6] E. Ideguchi et al., Z. Phys.A352,363(1995)
- [7] M. Piiparinen et al., Z. Phys. A338, 417(1991)
- [8] L. K. Peker, Nuclear Data sheets, 49,1(1986)
- [9] Z. Haratym et al. Nucl. Phys. 276.299(1977)
- [10] F. Puhlhofer, Nucl. Phys.A280,267(1977)
- [11] Azza M. El-Badry et al. KUTL Report5,137(1995)

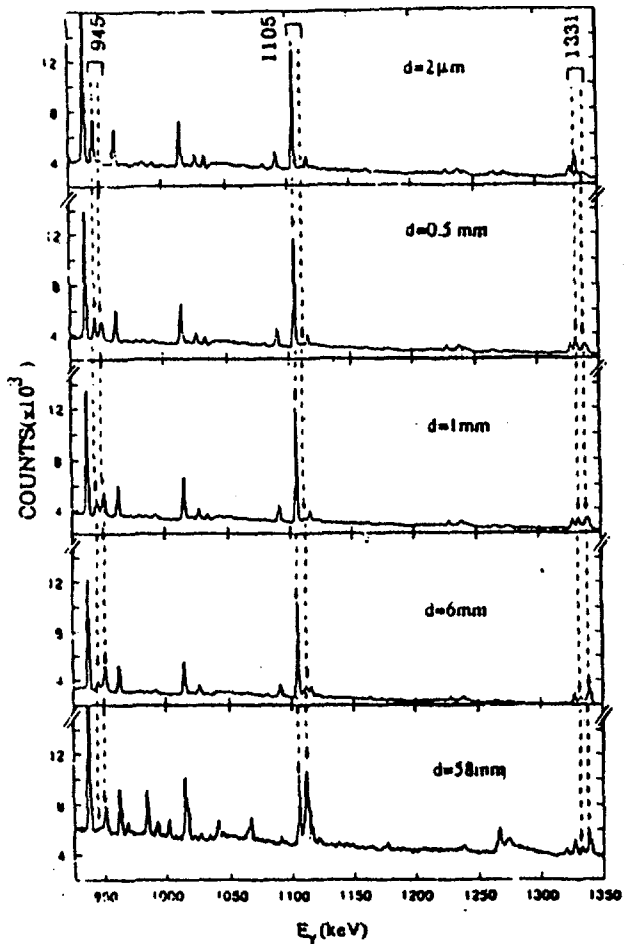


Figure 1 The high energy parts of the  $\gamma$  ray spectra taken by GMX. The separation distance  $d$  from the target to the stopper are indicated. The energies of the unshifted peaks are given in keV at the top of the figure. The location of the shifted and unshifted peaks are indicated by the dotted lines.

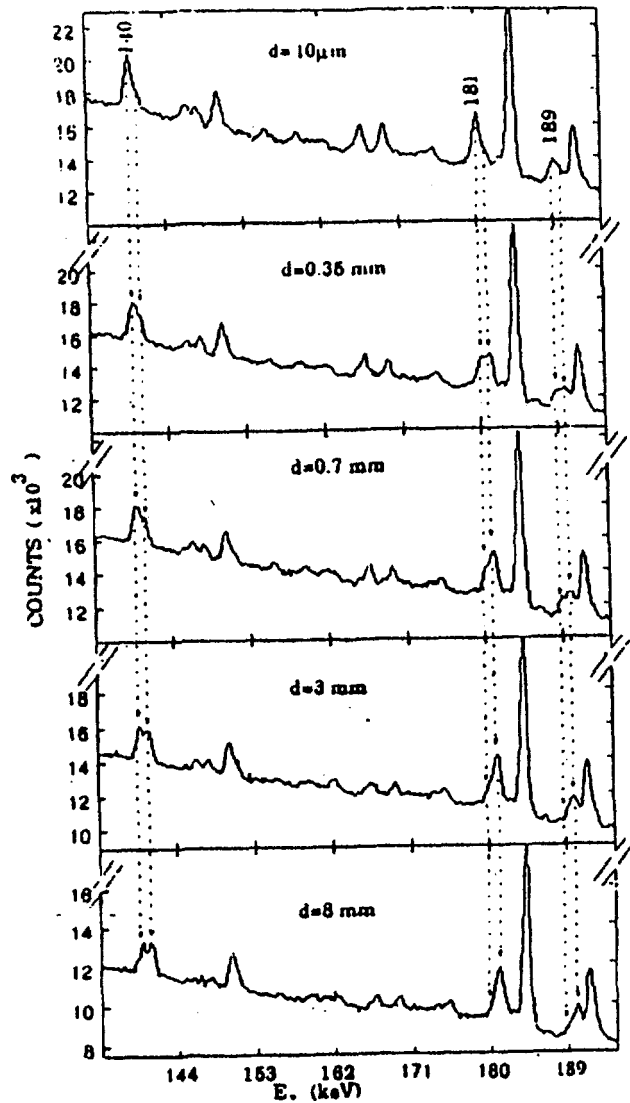


Figure 3 The RD spectra for low energy  $\gamma$  rays, taken by LEPS at various distances  $d$ , showing the 140, 181 and 189 keV  $\gamma$  rays in  $^{145}\text{Sm}$ . The shifted and unshifted peak positions are indicated by dotted lines.

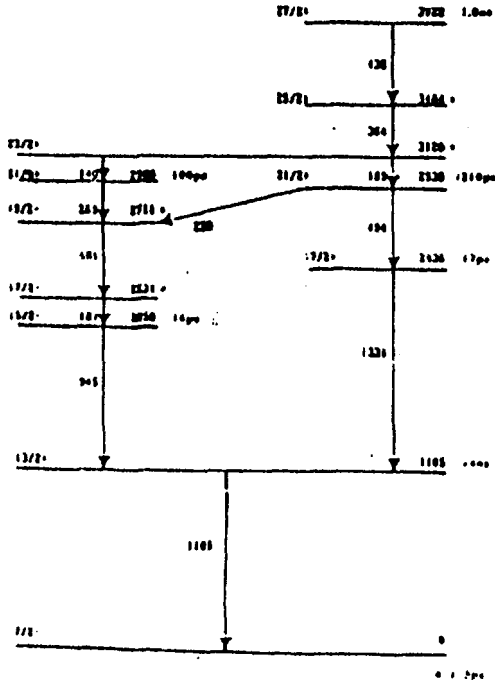


Figure 2 Level scheme for  $^{145}\text{Sm}$  and RD lifetime results

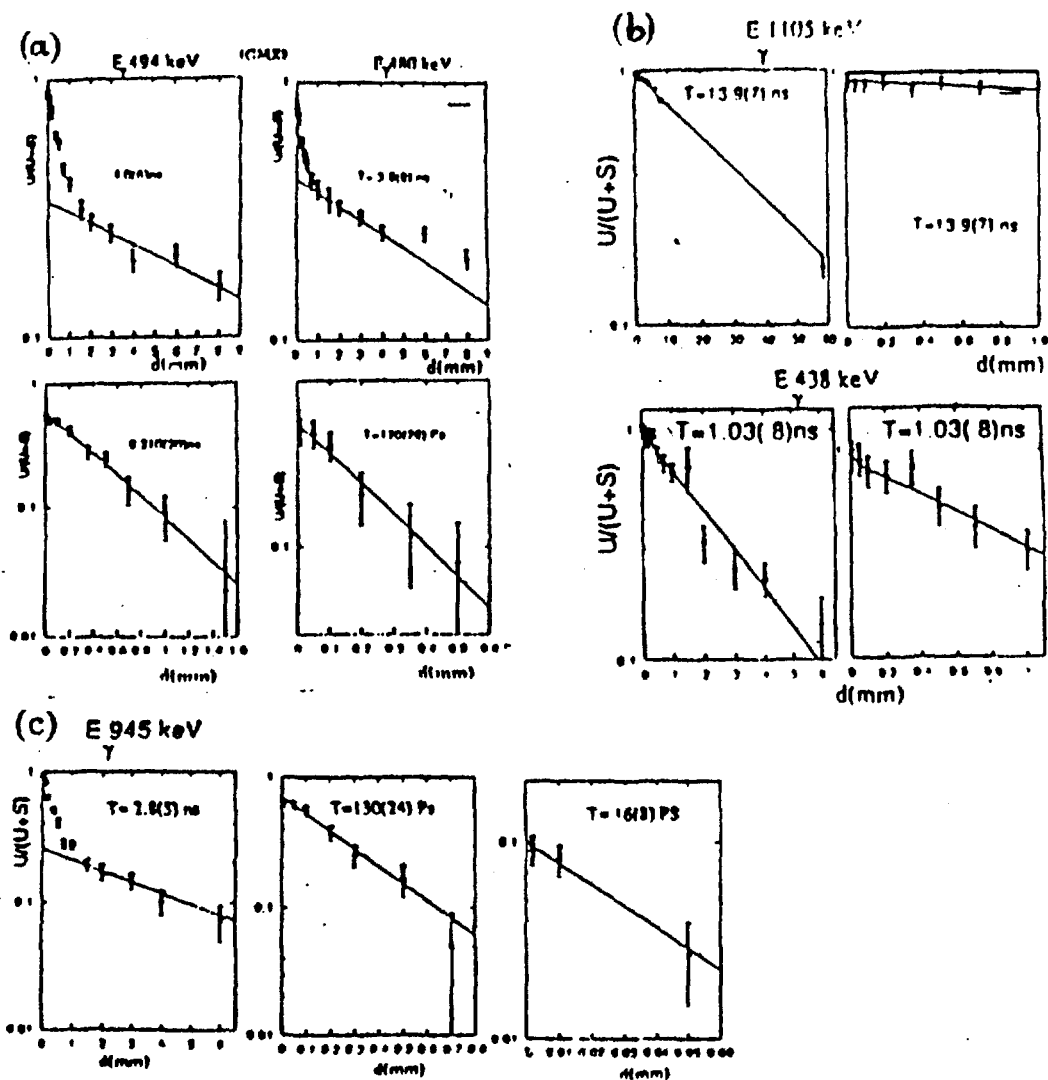
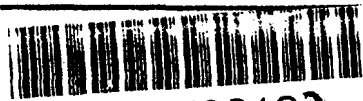


Fig.4. Some examples for the decay curves of the different transitions in  $^{145}\text{Sm}$ . (a) Single lifetime component for the 1105 and 438 keV, (b) two components case for the 480 and 494 keV transitions, (c) three components for 945 keV transitions.



EG9700123

## *A computer Simulation of Auger Electron spectroscopy*

**M.S.Ragheb and M.H.S.Bakr**

Dept. of Accelerators and Ion Sources, Division of Basic Nuclear Sciences, NRC,  
Atomic Energy Authority, 13759, Egypt.

### Abstract

A simulation study of Auger electron spectroscopy has been performed to reveal how far the dependency between the different parameters governing the experimental behavior affects the peaks. The experimental procedure, followed by the AC modulation technique, has been reproduced by means of a computer programme. It generates the assumed output Auger electron peaks, exposes them to a retarding AC modulated field and collects the resulting modulated signals. The program reproduces the lock-in treatment in order to demodulate the signals revealing the Auger peaks giving the peak positions and shapes.

The peak shape and position are affected by the slope of the retarding field, the starting potential, the amplitude the frequency of the applied modulated signal and the resolution of the retarding field analyzer. The simulation has revealed some new aspects that were not considered experimentally.

### Introduction:

Investigations of the behavior of complex physical systems has been carried out through the application of two techniques, the experimental techniques in which one disturbs the system in some controlled manner and observes its behavior, and the theoretical approach in which one uses

analytical mathematical technique to determine the behavior consistent with well established physical laws . The great advances in physics have become through the combined application of these two approaches.

Recently, a powerful new method for both types of investigation has been possible through the advent of modern high speed computers . This is the method of computer simulation or modeling . We believe, we understand what the fundamental laws that govern the system are ,but we are simply unable to work out their consequence. The simulation techniques try to give a comprehensive coverage of all the work that has been done which would involve confusion . It extends the work study and reveals the different aspects of physical knowledge that are obscured.

The Auger electron spectroscopy provides a comprehensive picture about the elemental composition of surfaces . Bombarding the specimen with accelerated electrons , an inner electron is ejected out and a hole is created in a core electronic state. The electronic transition that recombines the hole can take place via radiation less process by means of emission of an Auger electron . Each element has characteristic Auger energy . This can serve as a kind of chemical signature of the element . Only the Auger electron coming from the few outermost layers of the specimen will be detected as a part of the Auger peak in question. The detection is accomplished through a retarding field analyzer, a lock-in amplifier and AC modulation technique<sup>(1)</sup>.

The AC modulation is to ensure that the obtained Auger current will not be disturbed or affected by the background noises. Typically an experiment is excited at a fixed frequency( reference frequency ) and the lock-in detects the response from the experiment at the reference frequency. This lock-in amplifier serves to detect and measure very

small AC currents and signals in a narrow range of frequencies centered around the reference frequency. Noise signals at frequencies other than the reference frequency are rejected and do not affect the measurement. The lock-in uses a multiplier or a demodulator to translate the signal from the reference frequency down to DC where it can be filtered and amplified to give the first and second derivatives of the measured current.

Too many parameters affect the peaks in the spectrum. These parameters have to be studied precisely in order to explain the behavior of the obtained Auger spectra. The optimum values of these parameters ensure the more reliable spectrum.

A numerical run of the simulation can be carried out allowing the system to evolve from some initial situation of interest (in accordance with the laws used) , to a final request situation . Comparison can be made between the simulation results and experimental observations on the phenomena in question in order to obtain new physical insights.

**Simulation procedure :**

A mathematical technique is used to simulate the experimental spectrum and to determine the most appropriate values of the parameters governing its detection . The program represents the Auger electrons in function of their energies in a spectrum with the possible species influencing the collected electrons. The whole procedure is shown in figure(1). It begins by forming a complete spectrum involving Auger electron peaks and background . Interfering noises as well as free channels can also be introduced. The electrons are then controlled ,arranged according to their

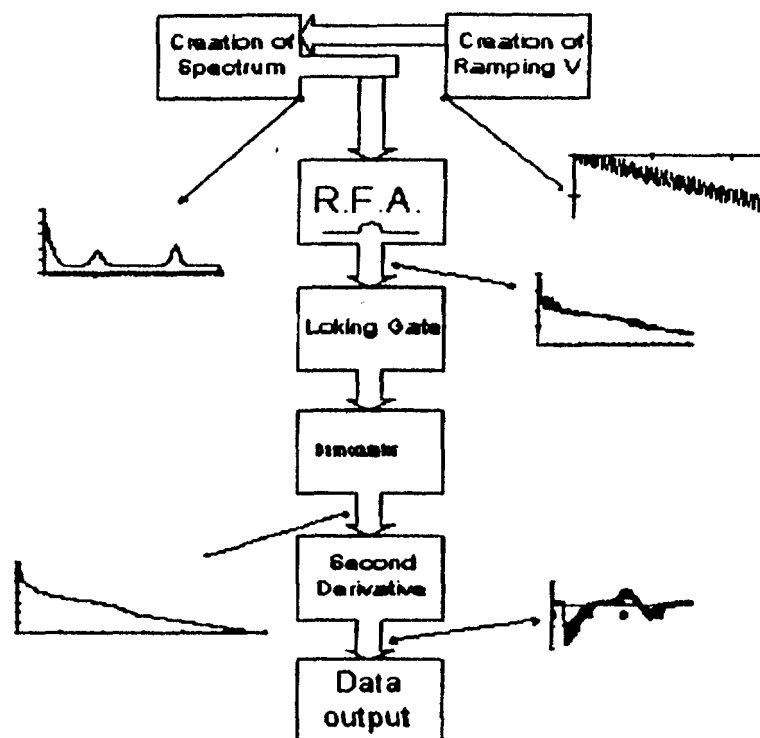


Fig.1 Block diagram of the computer programme showing the spectrum obtained by each stage.

energies by means of a retarding field process in a daughter spectrum . The retarding field comprises a scanning ramped voltage modulated by a sine wave as seen in figure(1). The amplitude ( $A_m$ ) and the frequency ( $F$ ) of the sine wave , the slope ( $a$ ) and the value ( $b$ ) of the starting ramping voltage can be easily varied . The obtained daughter spectrum represents the modulated Auger electrons that have the same frequency as the sine wave of the retarding field (which is the reference frequency).

In a real spectrum the Auger electron peaks have very small intensities and need to be accentuated from the background levels . In order to reveal the Auger electron peaks we have to demodulate the obtained spectrum and filter out the background levels and the unwanted noises. Two

blocks of the program perform this routine and the obtained spectrum is shown in figure(1). The first block detects the peaks and then the frequency is compared with the reference frequency by means of a locking gate. The demodulation is performed according to the gate result by a second block.

The spectrum is then treated by a third block which performs the second derivative (SD) routine <sup>[2]</sup>. This SD has the property to define with great accuracy the center of the peak. This is accomplished by giving a positive kink joined to a negative one intersecting the x-axis at the center of the peak.

**Results and discussions:**

The slope of the ramping retarding voltage is varied in

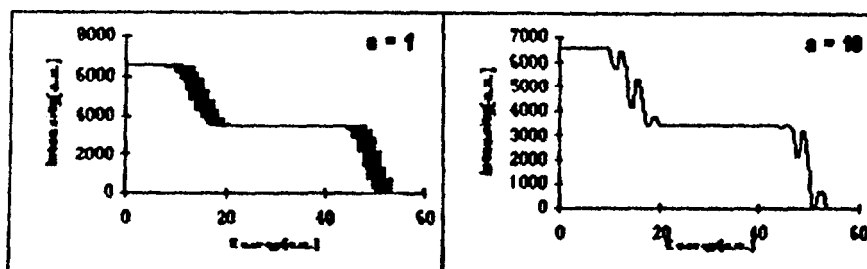


Fig. (2) Ramping voltage slopes ( $a = 1, a = 10$ ) applied to a parent spectrum, shows different modulated daughters.

order to study its effect on the spectrum peaks. The effect of that variation on the collected spectrum is shown in figure(2). The steps appearing on the ramping sides come from the fact that the retarding voltage is taken in step time much greater than the time base of the applied sine wave. This effect deforms the modulated spectrum peaks. In order to eliminate this effect the time of these steps must be less or equal to the inverse of the sine wave frequency.

The resolution of the retarding field analyzer and in turn the spectrum of the collected electrons is affected by the increase or the decrease of the ramping voltage slope (a) (fig.2). It is found that the optimum condition of that slope is when  $a = 1$ .

The frequency of the modulating signal must fulfill two conditions:

- to be limited to small values , otherwise the collected spectrum will suffer a complexity in the modulation technique (fig.3). More over the locking stage will not be able to lock the modulated spectrum to the reference frequency .

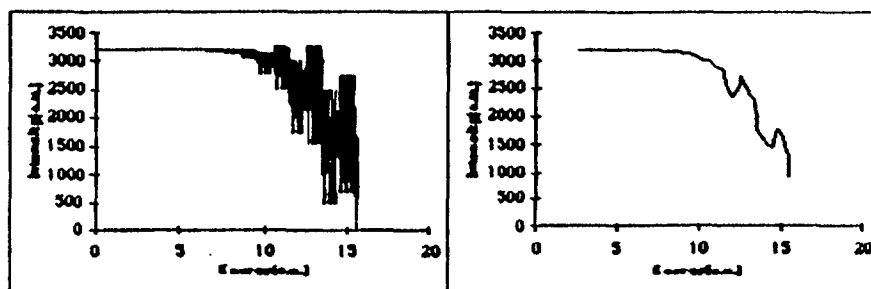


Fig.(3) The left diagram shows a modulated peak, the right one shows its demodulation at relatively high modulation frequency.

- to take values far from the noise spectrum of the environmental background of the laboratory.

The obtained spectrum depends also upon the FWHM of the collected electron peaks and the amplitude of the modulating signal . Not all values of the signal amplitude ( $A_m$ ) can give a good recognition of the detected peaks .It is found that best results can be taken if we follow the equation:

$$A_m = FW / 4.72$$

This comes from the fact that for an ideal Gaussian distribution  $FWHM = 2.36 \sigma$ , and in order to get maximum

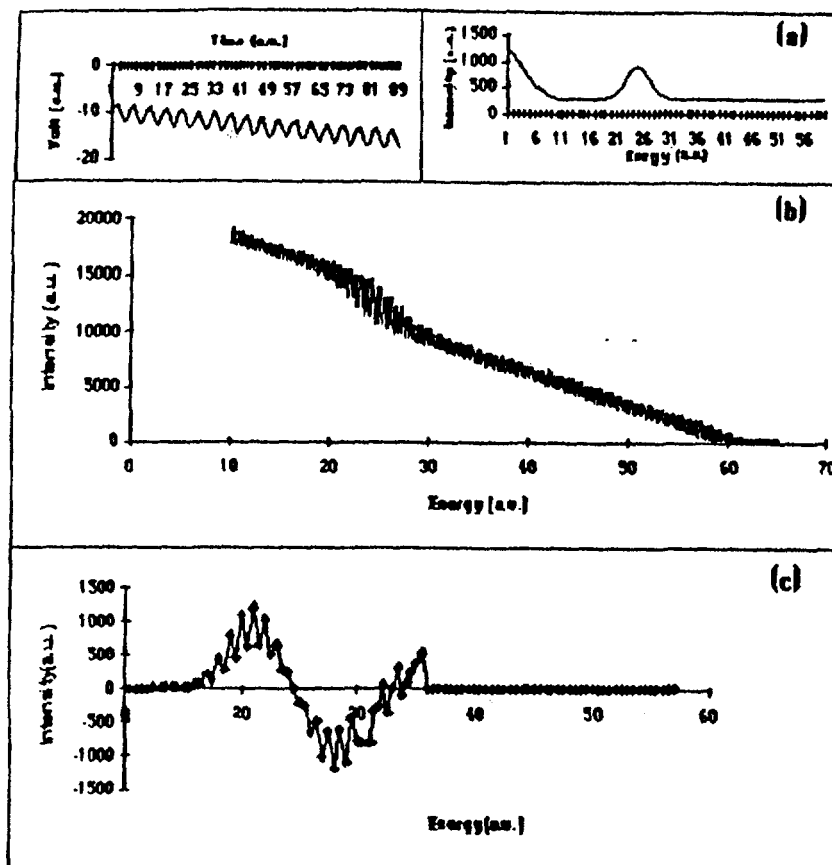


Fig. (4) (a)Created spectrum, (b)Modulated spectrum, (c)Second derivative. The effect of the parameter "b" is shown on the modulated spectrum and the second derivative is free from background .

amplitude of current in the fundamental peak it has been found<sup>[3]</sup> that  $A_m = \sigma/2$ . These results agree with the experimental work done before<sup>[4]</sup> .

The program succeeded to filter out noises and all background levels that are present in the parent spectrum fig.(4). The modulation signal will modulate only our Auger electrons and as a consequence only these electrons will be detected by the lock frequency at the demodulation stage . All undesirable spectrum components having frequencies other than the reference frequency will be rejected.

If the collected spectrum suffers from peaks that will

produce confusion on the low energy side of the spectrum they can be cut by beginning the ramping voltage with a value slightly bigger than the energy of the undesirable peaks we want to cut as shown in figure(4).

**Conclusion:**

The simulation of the Auger electron spectroscopy using AC modulation technique has revealed the behavior of different parameters governing the Auger electron technique that can be used to ensure a best fit for obtaining well defined spectrum peaks .

The frequency is chosen in a way to be small ,offering the possibility to omit the environmental noises.

The step time of the ramping voltage must be smaller or equal to the inverse of the frequency applied to the retarding voltage .

The slope of the ramping voltage versus time (V/s) is better to be equal to 1.

As an optimum condition the amplitude of the modulating signal ( $A_m$ ) must satisfy the relation  $A_m = FW/4.72$ .

This method of computer simulation has offered the advantage that in future work the experimentally collected Auger spectrum can be fed to the program and the output data can be compared to that of the lock-in results .

**Acknowledgment:**

The authors would like to appreciate the efforts of Mr.H.T.Mohsen and Mr.W.A.A.Ghaly demonstrators in Accel.& Ion Sources Dept., for their willing assistance in computer data acquisition of the present work.

**References:**

- [1] Ragheb M.S., Ph.D.Thesis, Alexandria University, Egypt(1992).
- [2] Bakr M.H.S.and Huwait M.R.A. Arab J.of Nucl. Sc.& Appl. 18, 153(1985).
- [3] Chatardji D., "The Theory Of Auger Transitions", Academic press,London(1976).
- [4] Ragheb M.S.and Bakr M.H.S.,Radiat.Phys. Chem., Vol.47, 673(1996).



EG970012\*

## A preparation of thin flat target for RD lifetime measurements.

A. M. El-Badry, Sh. Abdel samie, A. S. Hassan and A. A. Ahmed

Department of physics, Faculty of science, El Minia University,

El Minia, Egypt

and

T.kuroyanagi, and S. Morinobu

Tandem Accelerator laboratory

Department of physics, Kyushu University, 812 Japan

### Abstract

An extreme flatness of a target surface is one of the most important requirements for recoil distance method (RDM) device in the lifetime measurements. A suitable technique was used for preparing a La target. The  $^{139}\text{La}$  target of thickness  $0.22 \text{ mg/cm}^2$  was evaporated onto a very flat soft Au foil of thickness  $2 \text{ mg/cm}^2$ . The capacity measurement was performed to determine the shortest distance between the flat target and the stopper. The prepared target was successfully used for lifetime measurements in the range of  $10^{-9}$  to  $10^{-12}$  sec of the excited nuclear states in  $^{145}\text{Sm}$  nucleus through the nuclear  $^{139}\text{La}(^{10}\text{B}, n)^{145}\text{Sm}$  reaction.

## 1 Introduction

This paper is concerned with the preparation of the flat target surface for use in RD lifetime measurements. This type of measurement is the most suitable one for the lifetime range of  $10^{-9}$  to  $10^{-12}$  sec [1]. However, the lower limit of the measurable lifetime depends on the mechanical precision to achieve the shortest distance between the target and the stopper and the velocity of the recoiling nuclei [2]. Thus very flat target foils are required.

## 2 Preparing of the target

A target assembly consists of 5 parts, as shown schematically in Fig. 1(a); a guard ring, a Teflon ring, a main cylindrical tube, an inner cylinder and a locking screw. A picture of these parts can be seen in Fig.1(b).

A very soft Au foil of  $2 \text{ mg/cm}^2$  in thickness and  $1.7 \times 1.7 \text{ cm}^2$  in area was placed on the end of the cylindrical tube (stainless steel) with an inner diameter of 8 mm. The Teflon ring of 6 mm in thickness is placed carefully onto it surrounding the backed foil surface so that the foil is held as flat as possible. Then the Teflon ring is fixed to the main cylinder by four M2 screws. To achieve a further flatness of the foil surface, the stainless steel inner cylinder with an inner diameter of 6 mm is inserted into the main cylinder from the beam entrance side to give a tension to the Au foil. The position of the inner cylinder was controlled by the M10 locking screw with a beam hole of 7 mm in diameter along the axis. Therefore, the end of the inner cylinder gives a tension to the target foil so that a flat surface of the foil can be realized. In addition to these pieces, there is an Al guard ring fixed to the outer face of the Teflon ring using M2 screws. The guard ring is normally grounded to avoid leakage currents in the measurement of the capacitance between the target and the stopper. The photographic picture of Fig.2 (a) shows the target assembly with the flat surface of the Au backing foil mounted.

The La target was prepared by vacuum evaporation of isotopically enriched  $^{139}\text{La}$  metal. A very thin  $^{139}\text{La}$  film was formed on the Au backing foil in a circular area of 6 mm in diameter. The La target thickness was measured

using method of KX-ray fluorescence by irradiating the foil with  $\gamma$  rays from a  $^{241}\text{Am}$  source. The thickness was obtained to be  $0.22(5) \text{ mg/cm}^2$  which was a suitable value for the lifetime measurements by RDM. This target was used in the lifetime measurements for  $^{145}\text{Sm}$  [4] using the  $^{139}\text{La}(^{10}\text{B}, 4n)^{145}\text{Sm}$  reaction at 49 MeV bombarding energy. The picture of the La target after the beam bombardment is shown in Fig.2(b). The photograph was taken after the lifetime measurements in which about 5 pA of  $^{10}\text{B}$  beam bombarded the target for about 130 h. It can be seen that the foil is still flat and undamaged.

### 3 Recoil velocity, velocity distribution and energy loss straggling

The recoil velocity from the kinematic of the reaction, taken into account the energy losses of both the projectile and  $^{145}\text{Sm}$  in the La target and the Au backing, was calculated to be  $1.76(2) \text{ mm/ns}$ . The width of the velocity or the energy distributions of both the beam and the recoils were estimated. The energy loss straggling of the  $^{10}\text{B}$  projectile in the Au backing, the kinematic of the compound nucleus reactions, and the angular and energy spreads of the recoiling nuclei were calculated. The energy loss of the beam in the  $2 \text{ mg/cm}^2$  Au backing was 1.6 MeV and the actual beam energy was estimated to be 47.4 MeV on the front surface of the La target. The energy loss of the beam in the La target was 0.18 MeV. The spread of the beam direction due to the La target ( $0.22(5) \text{ mg/cm}^2$ ) was calculated to be less than  $1^\circ$  ( $0.09^\circ$ ).

The recoil energy of the  $^{145}\text{Sm}$  recoil was estimated to be 3.1 MeV and the energy loss in the La target to be 1.03 MeV. The width of the kinematical energy of the recoils due to the straggling (electronic collisions) were estimated to be 7.5%. The spread in angle of the recoils was calculated to be as large as  $14^\circ$ . This spread, however, is rather small to cause a serious broadening in the recoil velocity component along the axis of the measurement.

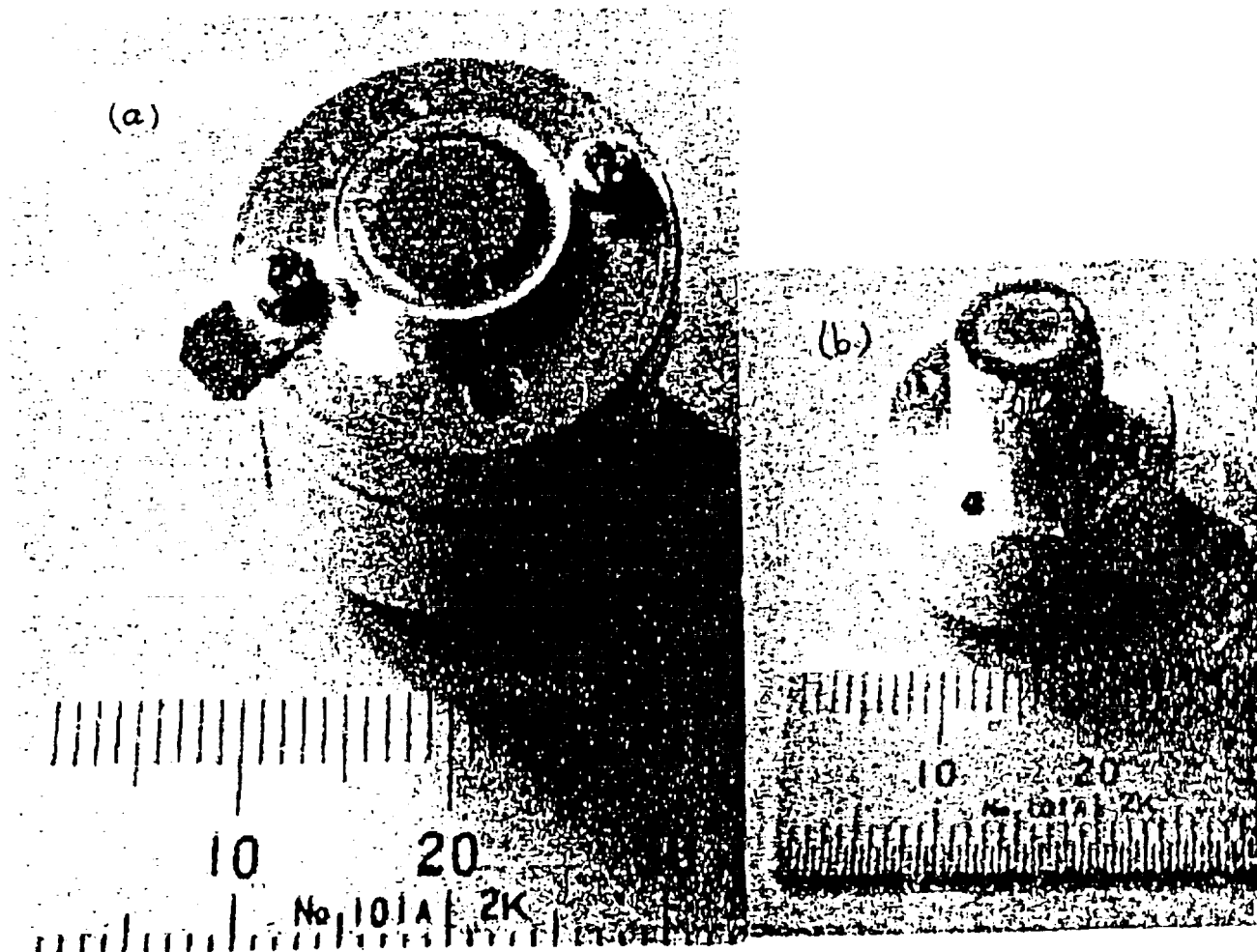


Figure 1: A photographic picture showing the flat surface of the Au backing foil before the La evaporation (a), and for the La target after bombardment by  $^{10}\text{B}$  (b)

## 4 Capacitance measurement between target and stopper

A measurement of the electric capacitance between the target and the stopper was carried out. A schematic diagram illustrating the method of the measurement is shown in Fig.3. If a step function input with a constant voltage  $V_i$  is applied to the stopper, then charge  $Q$  that equals to  $C_t V_i$  is induced on the target foil. The charge sensitive preamplifier converts the charge  $Q$  into voltage  $V_0$ , according to a simple relation [1]:

$$V_0 = k C_t V_i \propto 1/d,$$

where  $k$  is a conversion gain of the preamplifier and  $d$  is a distance between the stopper and the target. Fig. 3 shows the typical plot of  $1/V_0$  versus the micrometer reading. The expected linear relation is found and the zero point of the micrometer reading can be obtained easily by an extrapolation of the straight line to  $1/V_0 = 0$ . On the other hand, the mechanical contact of the target to the stopper was detected by measuring the electrical conduction between the two plates. Difference between the micrometer reading for the electric contact and the extrapolated zero point gives a measure of the relative angle of the target foil.

Generally, the above difference was found as small as  $10 \mu\text{m}$ . If we assume the electrical contact is caused at the edge of the target foil of  $7 \text{ mm}$  in diameter, the observed difference of  $10 \mu\text{m}$  between the contact point and the extrapolated zero point corresponds to the relative angle of  $0.01/7 = 1.5 \text{ m rad}$ , roughly in a agreement with the mechanical ambiguity in the tilting angle of the target in horizontal plane of  $2 \text{ m rad}$  [3]. This ambiguity in angle causes about  $5 \mu\text{m}$  ambiguity in the target -stopper distance over the beam spot area with a size of  $3 \text{ mm}$  in diameter.

## 5 Conclusion

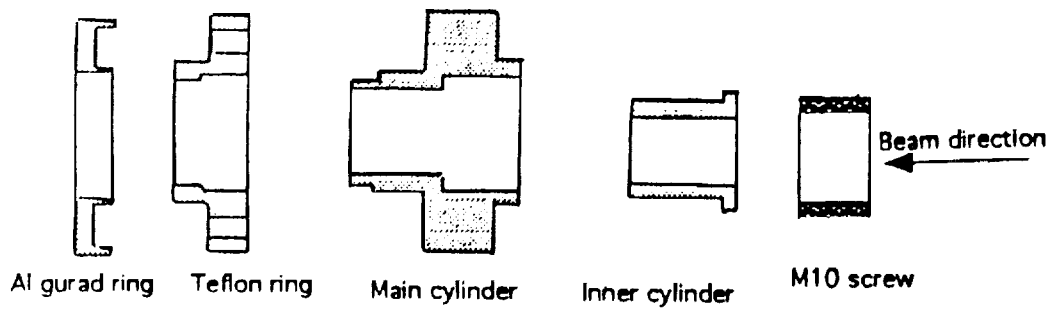
The flat target was prepared for using in the RDM. The measured target thickness of  $0.22 \text{ mg/cm}^2$  is thin enough to permit the recoils with sufficient

yield and suitable velocity. The lower limit of the lifetime was estimated to be 2.5 ps from the minimum distance between the target and the stopper for  $^{139}\text{Lu}(^{10}\text{B}, 4n)^{145}\text{Sm}$  reaction. The prepared target was successively used in lifetime measurement for  $^{145}\text{Sm}$  at beam energy 49 MeV for about 130 hour without damage. Therefore, the production of very flat target foils with suitable thickness is necessary in the RD lifetime measurement. Also the target must remain flat under beam bombardment.

## References

- [1] T. K. Alexander and A. Bell, Nucl. Inst. and methods 81,22(1970)
- [2] J. L. Gallant, Nucl. Inst. and methods 81,27(1970)
- [3] Azza M. El-Badry et al. KUTL Report5,137(1995)
- [4] Azza M. El-Badry et al. Proc. of the six workshop on topics in Nuclear radiation detection, Hiroshima Univ., March(1995).

( a ) target assemblies



( b )

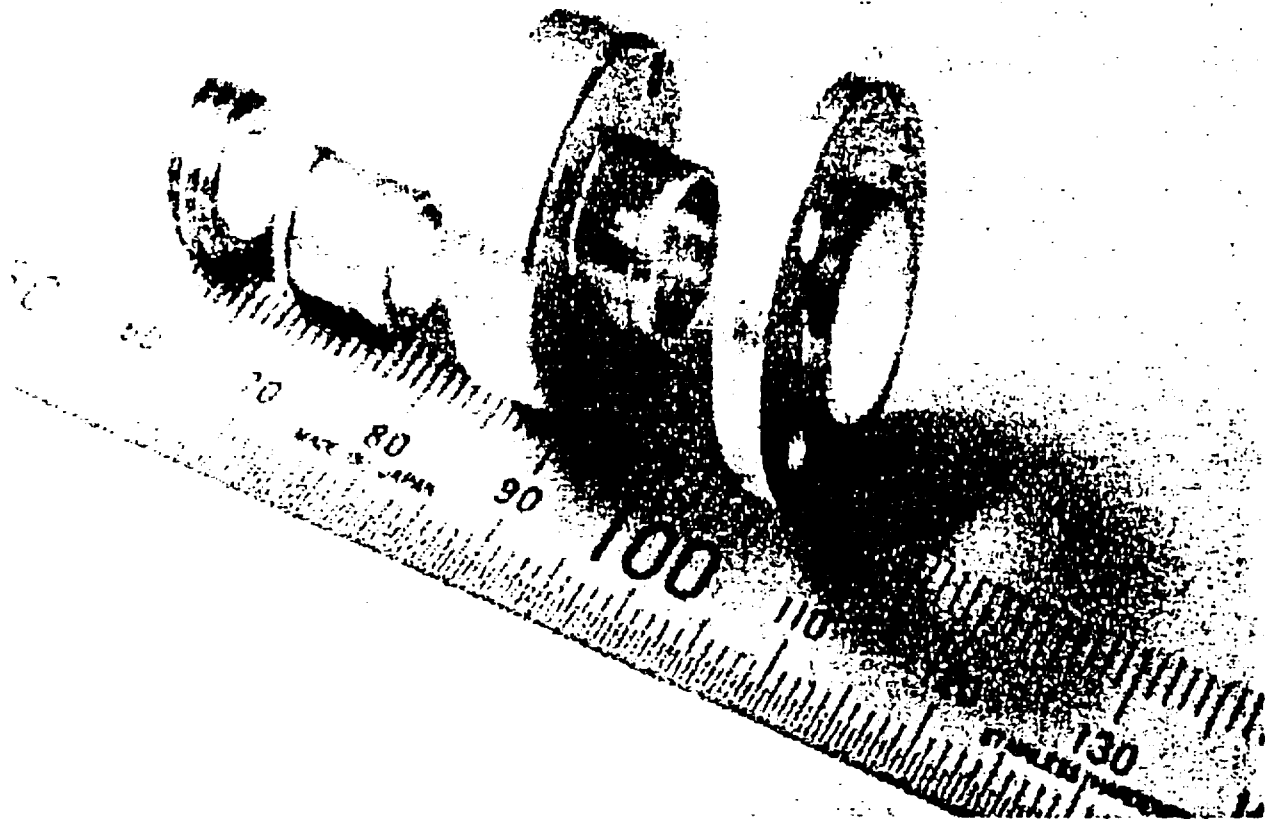


Figure 2. Target assemblies ( a ) and picture of these parts are shown in ( b ).

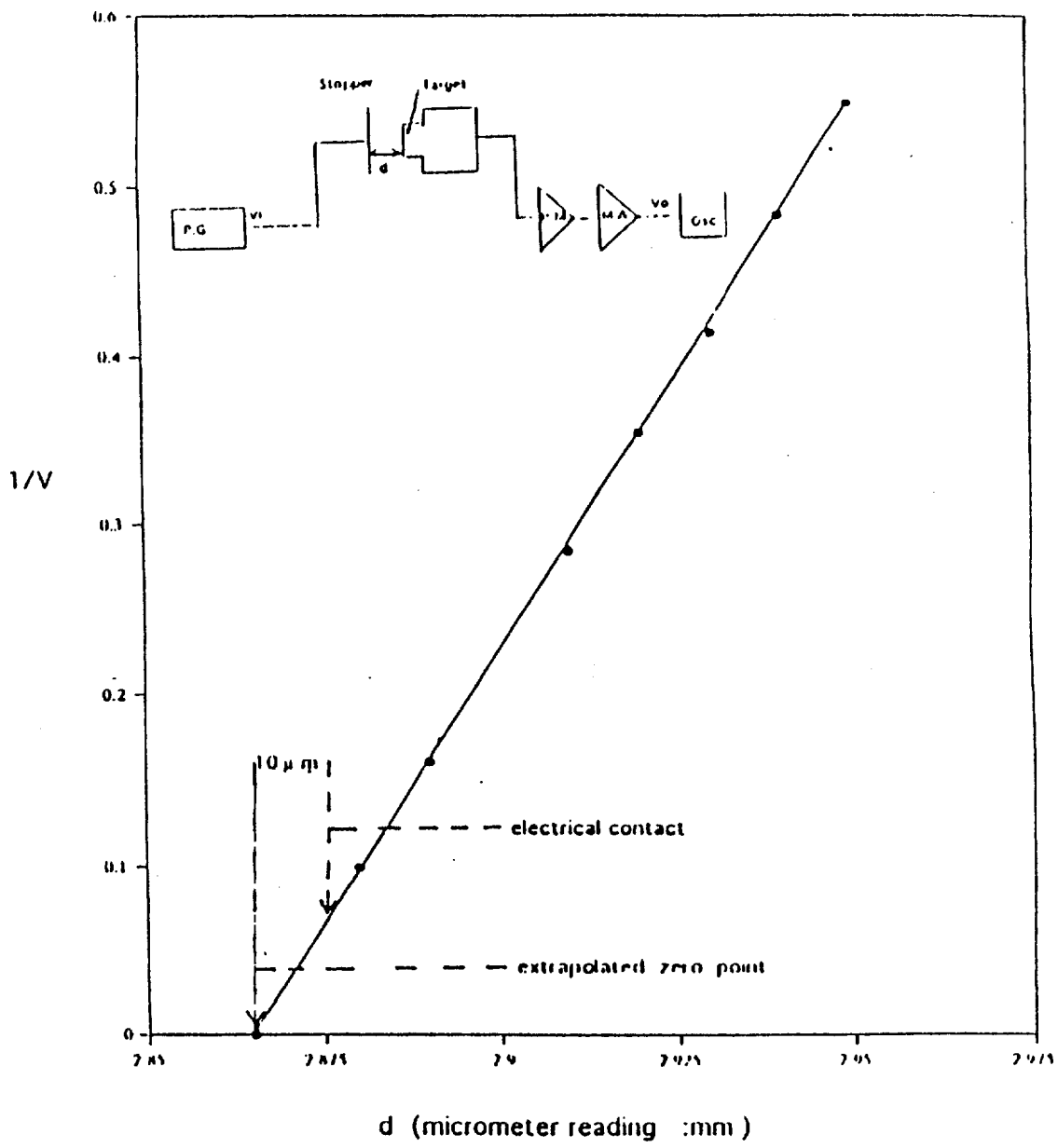


Figure 3. The electronic circuit and the measurements of capacitance between the target and the stopper to determine zero distance on the micrometer scale.

**SCIENTIFIC SESSION (12)**

**HIGH ENERGY PHYSICS**

*Keynote Lecture*

**INTERMEDIATE AND HIGH ENERGY NUCLEAR REACTIONS AT  
THE HADRONIC STRUCTURAL LEVEL**

**B. Slowinski**

**Institute of Physics, Warsaw, University of Technology, Poland  
Institute of Atomic Energy, Swierk, Poland**

**ABSTRACT**

From tens of MeV to several hundred of GeV is stretched out quite a large interval of energy when the interaction between hadrons (for instance, pion/nucleon-nucleus and nucleus-nucleus reactions) can be described by the considerably simplified way with still acceptable accuracy.

This happens because in this energy region hadrons (i.e. pions, nucleons etc.) remain quasiparticles of nuclear matter mostly without revealing any internal structure, their de Broglie's wavelength is much shorter as compared to the average intranuclear nucleon's distance, and the energy transfers in the reaction are, on the average, significantly greater than the binding energy of nucleons inside nuclei. Consequently an approach to the analysis of these phenomena based on simple geometric and probabilistic considerations is justifiable, especially for many practical purposes, in particular, for shielding and dosimetric estimations, material behaviour prediction, as well as for the approximate evaluation of electronuclear breeding effects in different composites of target materials, for nuclear passivation problems and so on.

In this work basic physical reasons of such a simplified picture of intermediate and high energy nuclear reactions are presented. The most usual phenomenological models of hadronic multiple emission/production and recent results of the cascade evaporation type models, are also discussed.

fragments track diameter method and found to be strongly dependent on both C and N. Two semi-empirical formula for  $V_B$  were developed and successfully used to cover all values studied of concentration and temperatures. The corresponding value of etching activation energy was found to be of the order of 1.0 eV. The response function  $V(R)$  and  $V(REL)_{350}$  were calculated at different alpha particle energies, resulting in linearity relation. Optimal etching and efficiency conditions are discussed.

**A NEW METHOD FOR DETERMINING THE RADON EMANATION COEFFICIENTS AND RADON PRODUCTION RATES FROM DIFFERENT BUILDING MATERIALS USING SOLID STATE NUCLEAR TRACK DETECTORS.**

**M. A. Misdaq, H. Moustaidine, K. Fahde, A. Ktata, and H. Khajmi**

**Nuclear Physics and Techniques Laboratory, Faculty of Sciences Semlalia,  
BP S15, University Cadi Ayyad, Marrakech, Morocco**

**ABSTRACT**

Radon alpha-activity concentrations have been measured from various building materials by combining a calculational method with solid state nuclear track detector (SSNTD) technique. Radon emanation coefficients of the materials studied have been evaluated. A new calibration method for determining the radium ( $^{226}\text{Ra}$ ) and thorium ( $^{232}\text{Th}$ ) specific activities of the building materials considered have been developed. The radon production rates per unit volume of the materials studied have been evaluated. The influence of material porosity on the radon emanation coefficient and radon production rate were investigated.

Contributed Papers

**DISTRIBUTION, SCALING, AND CORRELATIONS  
IN PROTON - EMULSION INTERACTIONS AT 400 GEV**

**M. El-Nadi\*, M.S. El-Nagdy\*\*, S.M. Abdel Halim\*\*\*  
and M.N. Yasin\*\*\*\***

\*Phys. Dep., Faculty of Science, Cairo University, Giza, Egypt

\*\*Basic Science Dep. Faculty of Petroleum Engin. Suez Canal University, Egypt

\*\*\*Phys. Dept., Faculty of Science, Zagazig University-Benha Branch, Egypt.

\*\*\*\*Phys. Dept., Faculty of Education, Cairo University-Fayoum Branch, Egypt

**ABSTRACT**

In this paper, the measurements of the hadrons produced in inelastic events of 400 GeV protons in nuclear emulsion are reported. The secondary particles produced in P-P as well as p-nucleus collisions obey KNO scaling. Multiplicity distributions of secondary particles are given and compared with the results of proton interactions at different energies. The correlation dependencies between every two kinds of tracks were also investigated.

**EMISSION OF INTERMEDIATE ENERGY NEUTRONS FROM  
PIONNUCLEUS REACTIONS AT SEVERAL GEV**

**N. Hassan\*, B. Slowinski\*\***

\*Al-Minia University, Egypt

\*\*Institute of Physics, Warsaw University of Technology.  
Institute of Atomic Energy, Swierk, Poland

**ABSTRACT**

The detection of fast neutrons ( $> 100$  MeV) appearing as a result of high energy nuclear reactions still remain a difficult problem. Nevertheless, such neutrons are abundantly emitted in these reactions within the energy range of primary hadrons between several hundred of MeV to several GeV, being of special interest for some practical purposes. For example, in connection with the problem of electrobreeding processes, material and electronic devices behavior when exposed to nuclear radiation as well as nuclear radioactivity passivation problems.

In the work, a method of the registration of prompt neutrons accompanying the reaction of 3.5 GeV/  $\pi^-$  - mesons with Xenon nuclei using the 180 litre Xenon Bubble Chamber of the Institute to Theoretical and Experimental Physics (Moscow) is described. With the help of this method, experimental information about multiplicity distribution of such neutrons has been obtained and compared to similar information concerning the proton component of this reaction.

**ELASTIC SCATTERING OF  $^{12}\text{C}$  BY  $^{12}\text{C}$  AT  
INTERMEDIATE ENERGIES**

**S. A. E. Khallaf\*, M. A. Abdel- Rahman\*\*, S. k. Abdel - Raheem\*\*  
And S. W. Z. Mahmoud\*\***

\* Department of Physics, Faculty of Science, Assiut University, Assiut, Egypt

\*\* Department of Physics, Faculty of Science, El-Minia University, El-Minia, Egypt

**ABSTRACT**

Using the double folding model (DF), the real part of the central optical potential for  $^{12}\text{C} + ^{12}\text{C}$  system is derived. This potential as well as the single folding cluster model potential (SFC) were used to calculate the total and differential cross sections for  $^{12}\text{C}$  elastically scattered on  $^{12}\text{C}$  at three laboratory energies;  $E_{\text{lab}} = 300, 344.5$  and  $360$  MeV.

The calculations were carried out using five sets of nucleon nucleon (NN) interaction of the integrable Gaussian form and two sets of parameters for the nuclear matter density of the harmonic oscillator form. The transparency of the target nucleus was found to increase as the projectile energy increases. Good fits between the present calculations and the experimental data as well as the previously published calculations were obtained.

The present simple methods used to calculate the real part of the optical potential stand on equal footing with the density dependent (DDM 3Y) procedure and it reduces the potential computing time enormously. The suitable choice of NN interaction as well as nuclear matter densities is important.

**CHARACTERISTICS OF THE COSMIC RAY SOLAR DIURNAL  
VARIATION ASSUMING TWO-WAY ANISOTROPY**

**I. Sabbah, A.A. Darwish, and A.A. Bishara**  
Physics Dept., Faculty of Science, Alexandria University, Egypt

**ABSTRACT**

In an attempt to understand the deviation of the solar diurnal anisotropy vector from the 18h direction. The assumption of two-way anisotropy in free space was used. Neutron monitor station located at Deep River and underground muon telescopes located at Socoro and Nagoya have been used in this analysis. The median primary rigidity of response ( $R_m$ ) of the detectors used in our analysis cover a wide range;  $16\text{GV} \leq R \leq 299\text{GV}$ , while the vertical rigidities  $R_0$  of these stations cover the range  $1,0\text{GV} < R_0 < 45\text{GV}$ . Amplitudes, directions, and the upper cut-off rigidity of both anisotropies have been calculated using the least squares method over the time interval 1968-1992. This period covers two complete solar activity cycles (20,21), and part of the cycle 22. The interplanetary magnetic field (IMF) reverse polarity during 1969-1971. The IMF pointed away from the Sun in the northern hemisphere during 1972-1979. It reverses polarity again during 1980 and 1990-1991.

**AN EXPECTATION OF A BACKBENDING FOR  $N \geq 98$   
OF A RARE EARTH NUCLEI**

**M. M. Salah\*, and H. Elgebaly\*\***

\* Physics Dept., Faculty of Science, Minia University

\*\* Physics Dept., Faculty of Science, Cairo University

**ABSTRACT**

The backbending of three neighboring earth nuclei [Er-Yb-Hf] with their isotopes has been studied through the cubic polynomial (CP) theoretical model in addition to  $[E_x \text{ vs. } I(I+1)]$  and  $[\theta \text{ vs. } \omega^2]$  plots, at high energy angular momentum in nuclear rotational bands according to the values of  $R_4$ . Also the rotational nuclei are divided into soft and hard rotors by studying the softness  $S$ . We expected that there may be a backbending for nuclei of  $N \geq 98$ , but with a

high angular momentum, which were not expected before by studying the effect of  $I(I+1)$  at the critical spin of a backbending. The work includes study of the effective moment of inertia  $\theta_{eff}$  for these nuclei, and the theoretical treatment to reduce the error in energy calculation of (CP) model.

INTERMEDIATE AND HIGH ENERGY NUCLEAR REACTIONS AT  
THE HADRONIC STRUCTURAL LEVEL

B. Słowiński

Institute of Physics, Warsaw University of Technology, Poland  
Institute of Atomic Energy, Świerk, Poland

## Abstract

From tens of MeV to several hundred of GeV is stretched out quite a large interval of energy when the interaction between hadrons (for instance, pion/nucleon-nucleus and nucleus-nucleus reactions) can be described by the considerably simplified way with still acceptable accuracy. It so happens because in this energy region hadrons (i.e. pions, nucleons etc.) remain quasiparticles of nuclear matter mostly without revealing any internal structure, their de Broglie's wavelength is much shorter as compared to the average intranuclear nucleon's distance, and the energy transfers in the reaction are, on the average, significantly greater than the binding energy of nucleons inside nuclei. Consequently an approach to the analysis of these phenomena based on simple geometric and probabilistic considerations is justifiable and quite reasonable, especially for many practical purposes, in particular, for shielding and dosimetric estimations, material behaviour prediction, as well as for the approximate evaluation of electronuclear breeding effects in different composites of target materials.

In the work a simple approach to the problem of interaction of fast hadrons with atomic nuclei founded on geometrical and statistical conceptions are briefly discussed and some conclusions following from recent results of the cascade evaporation type models have been drawn. Several remarks are also made concerning the phenomenological way in the subject.

## INTRODUCTION

The interaction of high enough energy (i.e. above about 100 MeV) hadrons and nuclei with nuclear targets is a very complex process involving - to different extent - a great variety of phenomena: quantum structural, wave (diffraction, interference, coherence), collective, statistic, relativistic, microscopic and (quasi)macroscopic, subhadronic etc. At the same time it may reveal different space character, most often volume, surface, tube-linear or local and displays hadronic (barionic, mesonic, resonance such as the  $\Delta(1232)$  and cluster) and quark-gluon degrees of freedom. Finally, it can give rise to particle absorption and emission, excitation of resonance states of nuclei, nucleons and clusters knock-out, partial or even total disintegration of colliding nuclei and - as a rule - it leads to particle production (mostly  $\pi$  mesons). Our knowledge about this process comes mainly to ample experimental information, predominantly on cross sections of different channels of the reaction and multiplicity, energy, momenta and angular distributions of produced and emitted particles. Because of vast and intricate diversity of the phenomena under discussion there is no till now any common consistent and reliable approach to the problem of intermediate and high energy nuclear reactions although recently founded quantum hadrodynamics [1] is just called to play such a part, at least in what it concerns the description of nuclei as relativistic nuclear many-body systems. Nevertheless, for some practical purposes (i.e. for dosimetry, radiation protection and radiation damage) it is quite satisfactory to use sufficiently simple and at the same time general enough models allowing to get quantitative information about main properties of secondary particles produced and/or emitted in these reactions, as well as about the characteristics of residual nuclei. Such models are often based on the quasiclassical analogy to the process of penetration of particles through extended medium using a notion of the trajectory of particles and the classical probabilistic nature of their interaction in nuclear matter. (For a fundamental discussion about the representation of that kind we refer the reader to ref.[2]). Roughly speaking, with increasing energy of interacting particles and consequently, on the average, the momentum transfer between colliding hadrons, all quantum effects vanish rapidly and subhadronic degrees of freedom begin to

reveal. A corresponding quantitative criterion has been introduced by A.M.Baldin [3], based on the four-velocity transfer,  $b_{ik}$ , between interacting and produced particles. In particular, according to this classification hadrons are no more quasi-particles of nuclear matter when  $b_{ik} \gg 1$  and nuclei should be then considered as quark-gluon systems. It has been found experimentally that this domain begin as early as at energy  $\sim 3.5$  GeV/A of primary hadrons initiated interactions [4] and the phenomenon, called the cumulative effect, has a local character. Moreover, it is commonly believed that at much higher energy (i.e. far above 1 GeV/A in the center-of-mass system) a quark gluon plasma may be created in head-on collisions of two heavy nuclei [5], although there exist suggestions that such a phase transition is already available at about  $E_{lab} = 30$  GeV/A and even at  $E_{lab} = 3-5$  GeV/A, at least to the mixed phase of nuclear matter [6].

In the present work we briefly discuss some typical and still actual models of interaction of fast hadrons with nuclear targets based on simple geometrical and probabilistic conceptions.

### QUASIFREE INTERACTIONS

Among the multiplicity of channels of the reaction of fast hadrons with nuclei quasifree channels are the simplest ones having at the same time special practical value. They may be defined as such [7] when a projectile particle (for instance, a proton or  $\pi$  meson) impinging on a target nucleus with the radius  $R$  at the impact parameter  $r_0$  experiences only one inelastic collision with an intranuclear (quasifree) nucleon and the particles produced in this collision leave the nucleus without any inelastic scattering inside it, as shown schematically in Fig.1.

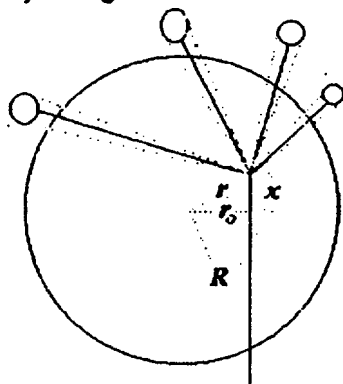


Fig.1.

The probability density function for such event is [7]:

$$f(r_0) = 2\sigma_N \int_0^{\sqrt{R^2 - r_0^2}} \rho(\sqrt{r_0^2 + x^2}) \exp\{-2[\sigma_N \int_0^x \rho(\sqrt{r_0^2 + x^2}) dx + \sum_i f_i(r_0)]\} dx \quad (1)$$

Here  $\sigma_N$  is the total cross section for interaction of the primary particle with a nucleon,  $\sigma_N^{(i)}$  is the total cross section for inelastic interactions of the  $i$ -th particle produced in the collision,  $(\varphi_i, \psi_i)$  are emission and azimuthal angles of the trajectory of the  $i$ -th produced particle,  $\rho(r)$  is the single nucleon density distribution (SNDD) in the target nucleus, and

$$f(r_0) = \sigma_N^{(i)} \int_{(\varphi, \theta, z)} \rho(\sqrt{r_0^2 + x^2}) dx, \quad (2)$$

In consequence of considerable similarity of a shape of SNDD of intermediate and heavy nuclei and relatively weak energy dependence of total inelastic cross sections for hadron-nucleon interactions at energy above ~1 GeV (for instance, [8]) the behaviour of the function (1) does not change practically with energy and atomic number. Moreover, the effect of increasing multiplicity of secondary particles at higher energy is also efficiently compensated by the narrowing a cone  $(\varphi, \theta)$  within which these particles are emitted. It is easy to see it when considering the fraction  $P$  of quasifree interactions expressed by the function  $f(r_0)$  (1) and the total cross section  $\sigma_m^{tot}$  for inelastic channels as:

$$P = \frac{2\pi}{\sigma_m^{tot}} \int_0^R f(r_0) r_0 dr_0 \quad (3)$$

The calculated value of this quantity is  $0.30 \pm 0.01$  for  $\pi$ -Xe interactions in the interval of primary pions energy of ~2-9 GeV, which is in good agreement with the experimental value  $0.30 \pm 0.03$  for these interactions, and, in particular, for  $\pi$ -Em interactions at much higher energy, too [7]. Space localization of quasifree interactions is such that half of all them occur in the region of impact parameters  $r_0 \geq 0.8R$ . As an example the function  $f(r_0)$  for the probability of quasifree interactions of  $\pi^+$  mesons with xenon nuclei at 2.34 GeV/c [7] is displayed in Fig.2.

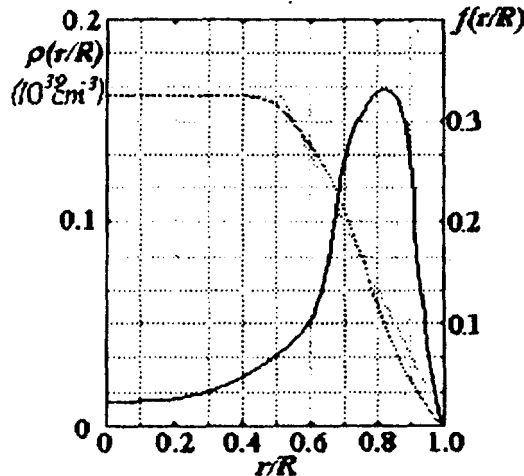


Fig.2.

In this figure plotted is also the single nucleon distribution  $\rho(r/R)$  in the nucleus  $^{54}\text{Xe}^{131}$  as a function of relative radius  $r/R$  and its trapezoidal simplified approximation used for concrete calculation. One can easily see that if we substitute zero for  $\sigma_N^{(i)}$  in (1) and 1 for  $P$  in (3) we obtain a simple expression of total inelastic cross section of hadron-nucleus interactions:

$$\sigma_m^{tot} = 2\pi \int_0^R \{1 - \exp[-2\sigma_N \int_0^{\sqrt{R^2 - r_0^2}} \rho(\sqrt{r_0^2 + x^2}) dx]\} r_0 dr_0 \quad (4)$$

which coincides with the similar formula deduced from the optical model. From Eq.(4) it follows, at least for heavy nuclei with a sharp boundary and at high enough energy, that  $\sigma_{in}^{tot} \sim (4/3)\pi \langle \rho \rangle R_0^3 A \sigma_N$ , i.e. energy dependence of  $\sigma_{in}^{tot}$  should be approximately the same as for  $\sigma_N$ . Experimental data do not contradict such an energy behavior of cross sections within several percents of accuracy [8] (here  $\langle \rho \rangle$  means an averaged nuclear density and  $R_0 \sim 1.2$ fm). One can also note that the form of the probability density function  $f(r_0)$  (1) does not depend remarkably on the specific channel of quasifree hadron-nucleon interactions although the maximum of this function slightly shifts towards the larger values of impact parameters  $r_0$  with increasing the multiplicity of produced particles in the channel and at the same time the width of this maximum becomes lower. Such a property of quasifree interactions may be useful for the experimental estimation of momentum distribution function of intranuclear nucleons at different depths in a target nucleus even when hadronic probes are applied. In this way a high momentum component of peripheral neutrons and protons of xenon nuclei has been estimated [9] starting from experimental information about quasi-two-body  $\pi^+N(Xe)$  reactions at 2.34 GeV/c.

A remark should be made too that it is easy to generalize the formula (1) for the probability density function of quasifree interactions about any type of hadron-nucleus (and, similarly, nucleus-nucleus collisions) by means of setting recurrently instead of  $f_i(r_{0i})$  again a function of the form  $f(r_0)$  but numbered by  $i$ -th step of intranuclear interaction and so on, till the contribution from the subsequent substitution is to be neglected. This way we get a simplified (i.e. based on geometric and probabilistic conceptions) analytic version of the intranuclear cascade model. But as we have not by now any reliable analytic approximations to calculate the expressions of the form  $\sum f_j^{(i)}(r_{0j})$  (here  $j$  numbers a subsequent act of intranuclear collision) the only practical way to get concrete numerical information is to use the so-called Monte-Carlo method, which is at the same time a method of numerical solution of various mathematical problems and a method of computer simulation of many diverse physical processes.

## CASCADE EVAPORATION MODEL

There exist many versions of the cascade evaporation model (CEM) taking into account - to some extent - all investigated up to now or being discussed dynamical and structural effects accompanying the process of intermediate and high energy hadron/nucleus interaction with nuclei (for example, [5, 10-12]). We want to stress here only that:

1. the CEM is, in principle, free of any shortcomings (except for computer time and memory) and so it seems to be the most general approach to the problem of nuclear reactions within very large range of energy of colliding particles;
2. this model is open, in principle, for including any new effect;
3. using the CEM we can adjust the results to concrete conditions of an experiment;
4. there is achieved this way a good agreement with experimental data but mostly for integral characteristics of the process;
5. the flexibility of the CEM makes it especially preferable to searching for new phenomena (for example, for a transition to other structural phase of a system created in the interaction region).

It should be also noted that in order to describe experimental data more correctly, particularly in the case of nucleus-nucleus collisions, the CEM needs to be improved in what

it concerns the particle cascading process at highly destructing nuclei, as well as the mechanism of excitation transfer to the residual nucleus and the problem of relaxation of highly excited nuclei [11].

## PHENOMENOLOGICAL APPROACH

For many practical purposes it is quite sufficient to have reliable enough formulas approximating experimental data on different characteristics of hadron/nucleus-nucleus collisions without going into the mechanism of the process although every formula can be considered as some model of the phenomenon it concerns.

Among various characteristics of high energy hadron/nucleus-nucleus collisions which are investigated both experimentally and theoretically multiplicity distribution of produced and/or emitted particles is the simplest one. To parametrize relevant experimental information a Poisson transform (for example, [13,14]):

$$P_n = \int_0^{\infty} dx f(x) \frac{(x\bar{m})^n e^{-x\bar{m}}}{n!} \quad (5)$$

being a positive weight  $f(x)$  superposition of Poisson distributions is often used (for example, [14,15]). In particular,  $P_n$  is a simple Poisson distribution when  $f(x)=\delta(x-1)$  and a Bose-Einstein distribution at  $f(x)=\exp(-x)$ , whereas for gamma weight function  $P_n$  is a negative binomial distribution. A superposition and a sequence of binomial distributions is also applied [15].

Another important and often investigated characteristic is an energy dependence of inclusive relativistic invariant cross sections of secondary particles which reveal interesting scaling properties [16-20]. It is successful parametrized by an exponential (i.e. Boltzman) dependence being the limiting case for nondegenerated both fermionic and bosonic systems.

## CONCLUDING REMARKS

Although the process of interaction of fast hadrons and nuclei with a nuclear target is, in principle, very complicated involving multiplicity of diverse phenomena, its main features may be understood, at least on the qualitative level and within a large enough energy range from several tens of MeV up to several hundred of GeV, starting from simple geometrical and statistical considerations. Such an approach being convenient for concrete realization may be also very useful for many practical purposes.

## References

1. B.D.Serot. Rep.Progr.Phys. 55(1992)1855.
2. A.A.Tyapkin. Hadronic Journal 17(1994)553.
3. A.M.Baldin et al. Zeitschrift fur Physik C33(1987)363.
4. A.M.Baldin and A.I.Malakhov. JINR Rapid Communications No.3(60)-93, p.52.
5. K.Geiger. Phys.Rep. 258(1995)237-379.
6. A.A.Shanenko, V.D.Toneev. JINR Rapid Communications No.5(73)-95,21-30.
7. B.Słowiński. Sov.J.Nucl.Phys., 1974, v.19, N.3, p.301.
8. V.S.Barashenkov. Cross sections for interaction of particles and nuclei with nuclei (*in Russian*). Dubna, 1993.
9. B.Słowiński, A.Tomaszewicz. Sov.J.Nucl.Phys., Vol.19, No.3 (1974) 301.
10. V.S.Barashenkov, V.D.Toneev. Interactions of high energy particles and atomic nuclei with nuclei (*in Russian*). Moscow, Atomizdat, 1972.

11. V.V.Uzhinskii, A.S.Pak. JINR Communication, P2-95-253. Dubna, 1995.
12. V.V.Uzhinskii et al. JINR Communication, E2-95-296. Dubna, 1995.
13. P.Carruthers, C.C.Shih. Intern.Journal of Mod.Physics A, Vol.2, No.5(1987)1447-1547.
14. R.Szwed, G.Wrochna, A.K.Wróblewski. Warsaw University Preprint IFD/3/87.
15. Z.Strugalski. JINR Report E1-85-230. Dubna, 1985.
16. L.S.Okhrimenko, B.Słowiński, Z.S.Strugalski, A.Tomaszewicz. Sov.J.Nucl.Phys., vol.19, No.6, (1974) 646.
17. B.Słowiński, Z.Strugalski. J.of Nucl.Phys., vol.25, No.3 (1977) 613.
18. B.Słowiński, E.Mulas. J.of Nucl.Phys. vol.34, No.3(9) (1981)777.
19. V.B.Gavrilov, G.A.Leksin. In: X School of ITEP, No.1 (1983)346.
20. A.G.Litvinenko, A.I.Malakhov, P.I.Zarubin. JINR Rapid Communications No.1(58)-93,27.



EG9700126

ELASTIC SCATTERING OF  $^{12}\text{C}$  BY  $^{12}\text{C}$  AT INTERMEDIATE ENERGIES

S. A. E. Khallaf<sup>\*</sup>, M. A. Abdel-Rahman<sup>\*\*</sup>, S. K. Abdel-Raheem<sup>\*\*</sup>  
and S. W. Z. Mahmoud<sup>\*\*</sup>

\* Department of physics, Faculty of science, Assiut University, Assiut, Egypt.

\*\* Department of physics, Faculty of science, El-Minia University, El-Minia, Egypt.

## Abstract:

Using the double folding model DF, the real part of the central optical potential for  $^{12}\text{C} + ^{12}\text{C}$  system is derived. This potential as well as the single folding cluster model potential SFC are used to calculate the total and differential cross sections for  $^{12}\text{C}$  elastically scattered on  $^{12}\text{C}$  at three laboratory energies  $E_{\text{lab.}} = 300, 344.5$  and  $360$  MeV. The calculations are carried out with five sets of nucleon nucleon NN interaction of the integrable Gaussian form and two sets of parameters for the nuclear matter density of the harmonic oscillator form. The transparency of the target nucleus is found to increase as the projectile energy increases. Good fits between the present calculations and the experimental data as well as the previous calculations are obtained. The present simple methods for calculating the real part of the optical potential stand on the same foot as density dependent DDM3Y procedure but the present methods reduce the potential computing time enormously. The suitable choice of NN interaction as well as nuclear matter densities is important.

## 1. Introduction

Recently, the  $^{12}\text{C} + ^{12}\text{C}$  system has been extensively studied for many years over a wide range of energies below 30 MeV up to 1200 MeV in the center of mass (c.m.) frame. Rohlen et al.<sup>[1]</sup> have measured the elastic and inelastic

scattering of  $^{12}\text{C}$  by  $^{12}\text{C}$  in the angular range between  $2.0^\circ$  and  $22.35^\circ$  c.m. system at  $E_{\text{lab.}} = 300$  MeV. Optical model calculations have been performed with Woods-Saxon (WS) and double Folding (DF) potentials, the ground state and the first  $2^+$ -state were coupled in the calculations. The large cross sections of the elastic scattering at large angles is related to the nuclear rainbow scattering, which is centered at about  $56^\circ$ . This requires a potential depth of 100 MeV at a distance of 3 fm, the fit to the data is sensitive down to this region. The calculations using the DF potential with a  $\delta$ -function potential required renormalization factor,  $N_r = 0.5$  to fit the data and show a better agreement with the data than those with the WS shape. Satchler et al.<sup>[2]</sup> have measured the elastic scattering of  $^{12}\text{C} + ^{12}\text{C}$  at 344.5 MeV in the angular range from  $6.23^\circ$  to  $22.35^\circ$  c.m.. The data were analyzed using two versions of the optical model: (1) a potential with a WS form for both the real and imaginary parts, (2) a folded potential for the real part based on the density and energy dependent DDM3Y interaction supplemented by an imaginary potential of a WS form. The renormalization constant required for the real folded potential to fit the data was unity. Buenerd et al.<sup>[3]</sup> have measured the elastic and inelastic scattering at  $E_{\text{lab.}} = 360$  and 1016 MeV for the  $^{12}\text{C} + ^{12}\text{C}$  system. An optical model analysis was reported and nuclear surface transparency effects were discussed, together with the energy dependence of nuclear potential.

In the present work we are interested in driving the analytical real potential of  $^{12}\text{C} + ^{12}\text{C}$  elastic scattering at intermediate energies, namely at 300, 344.5 and 360 MeV, using the DF model. The success of this model will be checked against the measured elastic scattering cross sections of this system. The NN interaction employed in the DF model is that of Gaussian form and is discussed according to five sets of parameters. This is done in order to find the best set which gives the best fit with the experimental data at the forementioned values of energy. The nuclear matter density distribution of  $^{12}\text{C}$  nucleus is taken in the oscillator shell-model form with two sets of parameters, as will be shown later.

The derivation of the Single Folding Cluster (SFC) potential by Khalaf et al.<sup>[4]</sup> for  $^{12}\text{C} + ^{12}\text{C}$  elastic scattering at lower energy (127 MeV) is used to calculate SFC potential at energies  $\geq 300$  MeV and using two different sets of parameters for the nuclear matter density distribution of  $^{12}\text{C}$  nucleus, along

with the parameter  $\mu$  of the internal wave function of  $^{12}\text{C}$  nucleus. Then it will be determined how successful this potential would be in reproducing the measured elastic scattering cross sections for the same system at  $E \geq 300$  MeV.

## 2. The Folding Potentials

### 2.1. The double-folding model potential (DF)

The real part of the optical potential is calculated from a more fundamental basis by the folding method in which the NN interaction  $V_{NN}(r)$ , is folded into the densities of both the projectile and target nuclei [5].

$$V^{DF}(R) = N_r \int \rho_t(\bar{r}_2) \rho_p(\bar{r}_1) V_{NN}(|\bar{R} + \bar{r}_2 - \bar{r}_1|) d\bar{r}_1 d\bar{r}_2 \quad (1)$$

where  $N_r$  is a free renormalization factor,  $\rho_p(\bar{r}_1)$  and  $\rho_t(\bar{r}_2)$  are the nuclear matter density distributions of both the projectile and target nuclei, respectively, and  $V_{NN}(|\bar{R} + \bar{r}_2 - \bar{r}_1|)$  is the NN potential.

The effective NN interaction considered has the Gaussian form [6] ;

$$V_{NN}(\bar{r}) = \sum_{i=1}^2 v_i \exp(-K_i r^2) + d \delta(\bar{r}) \quad (2)$$

where, the parameters  $v_i$ ,  $a_i$ ,  $K_i$  and  $d$  are given in table (1).

The nuclear matter density distribution of  $^{12}\text{C}$  nucleus given by Ref. [4] is;

$$\rho(r) = \rho_{oc} (1 + \alpha r^2) e^{-\beta r^2} \quad (3)$$

with  $\alpha = 0.4987 \text{ fm}^{-2}$ ,  $\beta = 0.37408 \text{ fm}^{-2}$  and  $\rho_{oc}$  can be evaluated from the normalization condition;

$$\int \rho(r) d\bar{r} = 12 \quad (4)$$

These parameters are named as set 1

Another form of the nuclear matter density distribution for  $^{12}\text{C}$  nucleus is given by<sup>[12]</sup> :

$$\rho(r) = \left[ \frac{\rho_0 a^3}{8 S^3} \right] \left[ 1 + \left( \frac{3\gamma}{2} \right) - \left( \frac{3\gamma a^3}{8 S^3} \right) + \left( \frac{\gamma a^2 r^2}{16 S^4} \right) \right] \exp \left[ \frac{-r^2}{4 S^2} \right] \quad (5)$$

This equation can be written in the form:

$$\rho(r) = \rho_{oc} \left[ 1 + \alpha r^2 \right] \exp \left[ -\beta r^2 \right] \quad (6)$$

With

$$\beta = 1/4S^2$$

$$\alpha = \left[ \frac{\gamma a^2}{16 S^4} \right] \left[ \frac{1}{1 + \left( \frac{3\gamma}{2} \right) - \left( \frac{3\gamma a^2}{8 S^2} \right)} \right]$$

and

$$\rho_{oc} = \frac{12 \beta^{5/2}}{\pi^{3/2} \left( \beta + \frac{3\alpha}{2} \right)}$$

where the parameters  $S^2$ ,  $\gamma$  and  $a$  are taken as those given in reference [12]

as follows:

$$S^2 = \frac{a^2}{4} - \frac{r_n^2}{6}, \quad r_n = 0.87 \text{ fm}, \quad \gamma = 1.247 \text{ fm} \text{ and } a = 1.649 \text{ fm}.$$

The collection of these parameters is termed as set 2.

Substituting Eqns.(3) and (2) into Eqn.(1) and performing the volume

integration over  $\bar{r}_1$  and  $\bar{r}_2$  we get:

$$v^{DF}(R) = N_r \left[ \sum_{i=1}^2 v_i I_i + d I_3 \right] \quad (7)$$

where  $I_1$  and  $I_3$  are given as:

$$I_i = S_{0i} [ S_{1i} + S_{2i} R^2 + S_{3i} R^4 ] \exp(-S_i^2 R^2), \quad i=1,2 \quad (8)$$

and

$$I_3 = S_{03} [ S_4 + S_5 R^2 + S_6 R^4 ] \exp(-\beta R^2/2) \quad (9)$$

respectively. In Eqns.(8) and (9)  $S_i, S_{0i}$  and  $S_{03}$  have the form

$$S_i = W_i - \frac{W_i^2}{Z_i}$$

$$S_{0i} = \frac{\rho_{oc}^2 \pi^3}{(G_i Z_i)^{3/2}}$$

and

$$S_{03} = \rho_{oc}^2 \left[ \frac{\pi}{2\beta} \right]^{3/2}$$

In terms of  $K, \beta$  and  $\alpha$  one can define  $G_i, W_i$  and  $Z_i$  as follows:

$$G_i = \beta + K_i, \quad W_i = K_i - \frac{K_i^2}{G_i} \quad \text{and} \quad Z_i = \beta + W_i$$

Then, respectively  $S_{11}, S_{21}, S_{31}, S_4, S_5$  and  $S_6$  can be written as

$$S_{11} = \left( 1 + \frac{3\alpha}{2\sigma_1} \right) + \frac{3\alpha}{2z_1} \left( 1 + \frac{3\alpha}{2\sigma_1} + \frac{K_1^2}{\sigma_1^2} + \frac{5\alpha K_1^2}{2z_1\sigma_1^2} \right).$$

$$S_{21} = \frac{\alpha W_1^2}{z_1} \left( 1 + \frac{3\alpha}{2\sigma_1} + \frac{\alpha K_1^2}{\sigma_1^2} + \frac{3\alpha K_1^2 z_1}{2\sigma_1^2 W_1^2} + \frac{K_1^2 z_1^2}{W_1^2 \sigma_1^2} \right. \\ \left. + \frac{5\alpha K_1^2}{z_1 \sigma_1^2} - \frac{5\alpha K_1^2}{W_1 \sigma_1^2} - \frac{2\alpha K_1^2 z_1}{W_1 \sigma_1^2} \right),$$

$$S_{31} = \frac{\alpha^2 K_1^2 W_1^2}{z_1^2 \sigma_1^2} \left( 1 + \frac{W_1^2}{z_1^2} - \frac{2W_1^2}{z_1} \right),$$

$$S_4 = 1 + \frac{3\alpha}{2\beta} + \frac{15\alpha^2}{16\beta^2},$$

$$S_5 = \frac{\alpha^2}{8\beta} \left( 1 + \frac{4\beta}{\alpha} \right),$$

and

$$S_6 = \frac{\alpha^2}{16}$$

2.2. The single-folding cluster model potential (SFC)

The real part of the central optical potential for  $^{12}\text{C} + ^{12}\text{C}$  elastic scattering has been derived by Khallaf et al.<sup>[4]</sup> using the single folding cluster model in the form:

$$V^{\text{SFC}}(R) = N_r \left[ X_{01} \left( X_1 + X_2 R^2 \right) \right] \exp \left[ -X R^2 \right] \quad (10)$$

Where, the constants  $X$ ,  $X_{01}$ ,  $X_1$  and  $X_2$  are:

$$X = \lambda_1 - \frac{4 \lambda_1^2}{9 \lambda_2},$$

$$X_{01} = -24 \rho_{oc} V_o \left[ \frac{\pi \mu}{\lambda \lambda_2} \right]^{\frac{3}{2}},$$

$$X_1 = \left[ 1 + \frac{3 \alpha}{2 \lambda} + \frac{2 \alpha K^2}{3 \lambda^2 \lambda_2} \right],$$

$$X_2 = \frac{\alpha K^2}{\lambda^2} \left[ 1 - \frac{8 \lambda_1}{9 \lambda_2} + \frac{16 \lambda_1^2}{81 \lambda_2^2} \right],$$

where

$$\lambda_2 = \frac{4 \lambda_1}{9} + 4 \mu, \quad \lambda_1 = K - \frac{K^2}{\lambda}, \quad \lambda = \beta + K,$$

$$K = 0.25 \text{ fm}^{-2} \text{ and } V_o = -37 \text{ MeV}$$

with  $\mu=0.02967$ <sup>[13]</sup>,  $\mu=0.04667$ <sup>[14]</sup> or  $\mu=0.0884$ <sup>[15]</sup>

### 3. Numerical Results and Discussion

The analysis of the experimental data of  $^{12}\text{C} + ^{12}\text{C}$  elastic scattering at different intermediate energies (300 , 344.5 and 360 Mev) has been done using DWUCK4 program<sup>[16]</sup> feeded with either WS form<sup>[2]</sup> for both the real and imaginary parts of the nuclear optical potential, or by the DF or SFC real potentials obtained by expressions (7) or (10), respectively with a WS imaginary potential of parameters fixed to those shown in table (2). Coulomb potential used is that due to uniform spherical distribution of charges of radius  $R_c = 1.3(A_p^{1/3} + A_t^{1/3}) \text{ fm}$ <sup>[3]</sup> where  $A_p$  and  $A_t$  are the mass numbers of the projectile and target nuclei, respectively.

The data are first fitted using set 1 of parameters of the nuclear matter density distribution of  $^{12}\text{C}$  nucleus along with each set of NN interaction parameters (A, B, C, D and E) shown in table 1 independently. The renormalization constant of the DF potential,  $N_r$  is varied in order to obtain the best fit for each case of NN interaction. The results are shown in Figs.(1), (2) and (3) compared with the experimental data taken from Fig.(2) of Ref.[1], from Ref.[2] and from Fig.(4) of Ref.[3] at 300, 344.5 and 360 MeV respectively as well as the phenomenological WS calculations are also shown in these figures . It can be noticed that all sets of NN interaction give a good fit with the experimental data at different renormalization constants  $N_r$  corresponding to the five different sets. The best value of  $N_r$  which is close to unity results from set B of NN interaction. When set 2 is used instead of set 1 the results are shown in Figs.(4), (5) and (6) for the three energies 300, 344.5 and 360 MeV, respectively. From these figures, it can be noticed that the values of  $N_r$  corresponding to the best fit for all chosen sets of NN interactions are greater than those obtained in case of set 1 i.e. more close to unity. The DF calculations carried out using set 2 of parameters of the nuclear matter density of  $^{12}\text{C}$  nucleus with set B of parameters of NN interaction give  $N_r = 0.86$  at 300 MeV which is much better than that obtained from DF model analysis with a  $\delta$ -function potential of the same data where  $N_r = 0.5$ <sup>[1]</sup>. For the 344.5 Mev data  $N_r = 1$ , the same value, which was obtained from the previous DF model analysis with DDM3Y interaction<sup>[2]</sup> and for the 360 Mev data  $N_r = 0.81$  which is nearly the same value obtained from the previous DF model analysis with DDM3Y Interaction in

which  $N_r = 0.83^{1-2}$ .

Figs.(7), (8) and (9) show the calculated elastic scattering cross sections for the system under consideration using SFC potential given by Eqn.(10) and set 1 of parameters of the nuclear matter density distribution of  $^{12}\text{C}$  nucleus along with each value of the parameter  $\mu$  of the internal wave function of  $^{12}\text{C}$  nucleus independently. For each of the energies considered, the best fit is obtained with different  $N_r$  less than unity corresponding to a certain value of the parameter  $\mu$ . The best value of  $N_r$  which approaches the unity is achieved when  $\mu=0.0884$ . When set 2 is used instead of set 1 the SFC results are shown in Figs.(10), (11) and (12). It has been found that the values of  $N_r$  are greater than those obtained using set 1, i.e. more close to unity, specially when  $\mu=0.0884$ . An immediate conclusion can be drawn from this: set 2 along with  $\mu=0.0884$  fit well the data better than set 1.

The reaction cross section,  $\sigma_A$  is calculated directly by DWUCK4 program using WS, DF and SFC potentials in all cases we have analyzed and is included in table 2 as well as Figs. (1-6), for the DF analysis and in Figs. (7-12) for the SFC model analysis. The DF and SFC model analysis with set 2 of parameters of the nuclear matter density of  $^{12}\text{C}$  nucleus gives  $\sigma_A$  nearly equal to those obtained in the case of WS calculations. But parameters of set 1 results in a higher  $\sigma_A$  except for the case of 344.5 Mev where the value of  $\sigma_A$  is the same as that obtained using set 2.

In Figs. (13-18) the renormalised DF real potentials calculated from Eqn.(7) using set 1 and set 2 of parameters of the nuclear matter density distribution of  $^{12}\text{C}$  nucleus along with each set of NN interaction (A, B, C., D and E) are compared with the real WS potential of parameters given in table (2) at each energy. Figs.(19-24) show the renormalised SFC real potential calculated from Eqn.(10) using set 1 and set 2 of parameters of the nuclear matter density distribution of  $^{12}\text{C}$  nucleus along with each value of the parameter  $\mu$  of the internal wave function of  $^{12}\text{C}$  nucleus compared with the real WS potentials of table 2. In all cases, the use of set 1 make the strengths of these potentials rather similar to the WS one especially in the region of strong absorption (4-6 fm), but a significant difference occurs in both the interior and the tail regions, as it can be seen from Figs.(13-15) and Figs.(19-21). This difference is reduced when set 2 is used instead,

Figs.(16-18). and Figs.(22-24) illustrate these reductions.

Figs.(13-18) and Figs.(19-24) show that the real WS, DF and SFC potentials touch or cross each other in the region  $4 \leq r \leq 6$  fm with a mean value  $R_s \approx 5$  fm. We found that the calculated cross sections in the present work are sensitive to the potential magnitudes around  $R_s$ . This region of  $r$  (the separating distance between the colliding nuclei) is known as the sensitive radial region and  $R_s$  is called the sensitive radius<sup>[17]</sup>. Defining  $R_s = r_s (A_t^{1/3} + A_p^{1/3})$  yields  $r_s = 1.092$  fm with  $R_s = 5$  fm. This value of the radius parameter  $r_s$  equals the value of the same parameter deduced by Buenerd et al.<sup>[3]</sup> for the system  $^{12}\text{C} + ^{12}\text{C}$  at 360 MeV, while they found  $r_s = 0.98$  fm for the same system at 1016 MeV. This means that the sensitive radius  $R_s$  decreases as energy of the projectile increases.

On the other hand, the strong absorption radius  $R_{1/2}$  is defined as the distance between colliding nuclei for which the transmission coefficient  $T_L = 1/2$ , i.e. the distance where the incident particle has the 50% probability of being absorbed by the target nucleus. The computer program DWUCK4<sup>[16]</sup> used in the present analysis calculates the transmission coefficient  $T_L$  as a function of the partial wave angular momentum  $L$  as well as the Sommerfeld parameter  $\zeta$  and the projectile wave number  $K_0$ . The relation between  $R_{1/2}$  and  $K_0$ ,  $\zeta$  and  $L_{1/2}$  where  $L_{1/2}$  is the partial wave angular momentum corresponding to  $T_{1/2}$  is:<sup>[3,17]</sup>

$$R_{1/2} = \frac{1}{K_0} \left[ \zeta + \left( \zeta^2 + L_{1/2}(L_{1/2} + 1) \right)^{1/2} \right] \quad (11)$$

Table (3) shows  $R_{1/2}$  deduced at different energies using Eqn.(11) for WS, DF and SFC used in the present work as well as the calculated reaction cross section  $\sigma_A$  where  $T_L$  is taken as near to 0.5 as possible. Also table (3) includes such results at 70, 1016, 1449 and 2400 MeV<sup>[3,17,18]</sup> for comparison. From this table it can be seen that  $R_{1/2}$ ,  $\sigma_A$  and the real and imaginary potentials at the sensitive radius  $R_s$  decrease as energy increases. Except at  $E=344.5$  MeV where the real and imaginary potentials at  $R_s$  do not follow this behavior. This may be due to the narrow angular range of the 344.5 MeV experimental data compared with the 300 and 360 MeV data. The same behavior

of  $\sigma_A$  has been observed in a previous work<sup>[19]</sup>. The weakening of the absorption radius, strength of the real potentials at  $R_s$  and the reaction cross sections as the energy increases indicates that the interacting nuclei interpenetrate deeper without being absorbed i.e. the nuclear surface of the target nucleus is more transparent. This agrees well with the results of phenomenological analysis of  $^{12}\text{C} + ^{12}\text{C}$  elastic scattering at intermediate energies<sup>[3,17]</sup>.

Finally, it may be concluded that the present simple methods for calculating the real central part of the optical potential for  $^{12}\text{C} + ^{12}\text{C}$  system at intermediate energies stand on the same foot as the density-dependent DDM3Y procedure, whereas the present methods reduce the potential computing time enormously. The suitable choice of NN interaction as well as nuclear matter density distribution forms is important.

Table (1): Parameters of NN interaction defined by Eqn.(2).

Inter- action	$V_1$ MeV	$V_2$ (MeV)	$K_1$ (fm) <sup>-2</sup>	$K_2$ (fm) <sup>-2</sup>	$d$ (MeV.fm <sup>3</sup> )	Ref.
Set A	-20.97	---	0.4627	---	---	[7]
Set B	-553.18	1781.4	1.5625	4.0	---	[8]
Set C	-601.99	2256.4	1.5625	4.0	-276(1-0.005E/A)	[9]
Set D	-22.332	---	0.46	---	---	[10]
Set E	-5.447	-12.448	0.292	0.415	---	[11]

Table (2): Best fit optical potential parameters (WS) for  $^{12}\text{C}+^{12}\text{C}$  at different energies . The potential has the form given in Ref.[2].

E MeV	V MeV	$r_o$ fm	$a_o$ fm	$W_o$ MeV	$r_w$ fm	$a_w$ fm	$\sigma_A$ (mb)		Ref.
							present work	previous work	
300	250	0.679	0.75	600.0	0.411	0.850	1420	1420	[1]
344.5	335	0.639	0.8	80.00	0.900	0.692	1340	1342	[2]
360	300	0.62	0.76	62.50	0.910	0.690	1270	1264	[3]

Table (3): The values of V, W and the renormalized  $v^{DF}$  and  $v^{SFC}$  at sensitive radius  $R_s=5$  fm,  $L_{1/2}$ ,  $R_{1/2}$  and  $\sigma_A$  at different energies . For the meaning of these symbols see the text.

E MeV	V(5) MeV	W(5) MeV	$v^{DF}(5)$ MeV	$v^{SFC}(5)$ MeV	$L_{1/2}$	$R_{1/2}$ fm	$\sigma_A$ (mb)			Ref
							WS	DF	SFC	
70	—	—	—	—	—	7	—	—	—	[18]
300	18.6	14.93	19.45	19.03	42	6.65	1420	1420	1420	Present work
344.5	23.3	17.54	21.90	23.20	44	6.48	1340	1330	1340	„
360	16.5	14.38	16.80	17.80	44	6.33	1270	1260	1270	„
1016	13.5	10.00	—	—	66	5.56	996	—	—	[3]
1449	13.0	9.00	—	—	—	5.10	907	—	—	[17]
2400	6.5	5.70	—	—	—	4.5	806	—	—	[17]

Figure captions

- Figure (1): Comparison between the differential cross sections as ratio to Rutherford for the elastic scattering of  $^{12}\text{C}$  on  $^{12}\text{C}$  at  $E = 300$  MeV calculated with DF real central potential using sets A, B, C, D and E of NN interaction and set 1 of parameters of the nuclear matter density distribution of  $^{12}\text{C}$  nucleus and the imaginary WS potential of parameters given in table (2). Solid curves are the WS calculations, dashed-curves are the DF calculations and the solid points are the experimental data taken from Ref.[1].
- Figure (2): The same as fig. (1) but for  $E=344.5$  MeV. The experimental data are taken from Ref.[2].
- Figure (3): The same as fig. (1) but for  $E = 360$  MeV. The experimental data are taken from Ref.[3].
- Figure (4): The same as fig. (1) but using set 2 of parameters of the nuclear matter density distribution of  $^{12}\text{C}$  nucleus .
- Figure (5): The same as fig. (1) but for  $E = 344.5$  MeV and DF calculations with set 2 of parameters of the nuclear matter density distribution of  $^{12}\text{C}$  nucleus.
- Figure (6): The same as fig. (1) but for  $E = 360$  MeV and DF calculations with set 2 of parameters of the nuclear matter density distribution of  $^{12}\text{C}$  nucleus .
- Figure (7): Comparison between the differential cross sections as ratio to Rutherford for the elastic scattering of  $^{12}\text{C}$  by  $^{12}\text{C}$  at  $E=300$  MeV calculated with SFC real potential using different values of the parameter  $\mu$  of the internal wave function of  $^{12}\text{C}$  nucleus and set1 of parameters of the nuclear matter density distribution of  $^{12}\text{C}$  nucleus and the imaginary WS potential of parameters given in table (2). The solid curves are the WS calculations, dashed curves are the SFC calculations and the solid points are the experimental data taken from Ref.[1].
- Figure (8): The same as Fig.(7) but for  $E=344.5$  MeV. The experimental data are taken from Ref.[2].
- Figure (9): The same as Fig.(7) but for  $E=360$  MeV and SFC. The experimental data are taken from Ref.[3].
- Figure (10): The same as Fig.(7) but using set 2 of parameters of the nuclear matter density distribution of  $^{12}\text{C}$  nucleus.

- Figure (11): The same as Fig.(7) but for  $E=344.5$  MeV and using set 2 of parameters of the nuclear matter density distribution of  $^{12}\text{C}$  nucleus.
- Figure (12): The same as Fig.(7) but for  $E=360$  MeV and using set 2 of parameters of the nuclear matter density distribution of  $^{12}\text{C}$  nucleus.
- Figure (13): Comparison of the WS and DF real potentials for  $^{12}\text{C} + ^{12}\text{C}$  elastic scattering at  $E=300$  MeV for the different sets of NN interaction and set 1 of parameters of the nuclear matter density of  $^{12}\text{C}$  nucleus. The solid curves are the WS real potentials of parameters given in table (2) and the dashed-curves are the renormalised DF potentials.
- Figure (14): The same as Fig.(13) but for  $E= 344.5$  MeV.
- Figure (15): The same as Fig.(13) but for  $E=360$  MeV.
- Figure (16): The same as fig.(13) but for DF real potentials with set 2 of parameters of the nuclear matter density distribution of  $^{12}\text{C}$  nucleus.
- Figure (17): The same as Fig.(13) but for  $E= 344.5$  MeV and DF real potentials with set 2 of parameters of the nuclear matter density distribution of  $^{12}\text{C}$  nucleus.
- Figure (18): The same as Fig.(13) but for  $E= 360$  MeV and DF real potentials with set 2 of parameters of the nuclear matter density distribution of  $^{12}\text{C}$  nucleus.
- Figure (19): Comparison of the WS and SFC real potentials for  $^{12}\text{C} + ^{12}\text{C}$  elastic scattering at  $E=300$  MeV for different values of the parameter  $\mu$  of the internal wave function of  $^{12}\text{C}$  nucleus with set 1 of parameters of the nuclear matter density distribution given by eqn.(3). The solid curves are the WS real potentials of parameters given in table (2) and the dashed curves are the renormalized SFC potentials.
- Figure (20): The same as Fig.(19) but for  $E=344.5$  MeV.
- Figure (21): The same as Fig.(19) but for  $E=360$  MeV.
- Figure (22): The same as Fig.(19) but for the renormalized SFC real potentials with set 2 of parameters of the nuclear matter density distribution of  $^{12}\text{C}$  nucleus given by eqn.(6).
- Figure (23): The same as Fig.(19) but for  $E=344.5$  MeV and the renormalized SFC real potentials with set 2 of parameters of the nuclear

matter density distribution of  $^{12}\text{C}$  nucleus.

Figure (24): The same as Fig.(19) but for  $E=360$  MeV and the renormalized SFC real potentials with set 2 of parameters of the nuclear matter density distribution of  $^{12}\text{C}$  nucleus.

REFERENCES

- [1] H. G. Bohlen, M. R. Clover, G. Ingold, H. Lettau, and W. von Oertzen, *Z. Phys.* A308 (1982) 121.
- [2] L. Jarczyk, B. Kamys, A. Magiera, R. Sludak, A. Strzalkowski, B. Styczen, J. Hebenstreit, W. Oelert, P. Von Rossen, H. Seyfarth and G. R. Satchler, *Nucl. Phys.* A518 (1990) 583;  
R. Sludak, private communication.
- [3] M. Buenerd, A. Lounis, J. Chauvin, D. Lebrun, P. Martin, G. Duhamel, J. C. Gondrand and P. De Saintligno, *Nucl. Phys.* A424 (1984) 313.
- [4] S. A. E. Khallaf, A. L. Elattar and M. El-Azab Farid, *Fizika* 15 (1983) 125.
- [5] G. R. Satchler and W. G. Love, *Phys. Rep.* 55 No. 3 (1979) 183.
- [6] O.M. Knyazkov and E.F. Hefter, *Z. Phys.* A301 (1981) 277.
- [7] E.W. Schmid and K. Wildermuth, *Nucl. Phys.* 26 (1961) 463.
- [8] G. Bertsch, J. Borysowicz, H. Mc Manus and W. G. Love, *Nucl. Phys.* A284 (1977) 399.
- [9] G.R. Satchler and W.G. Love, *Phys. Lett.* 65B (1976) 415.
- [10] W. G. Greenless, G. J. Pyle and Y. C. Tang, *Phys. Rev.* 171
- [11] I. Reichstein and Y.C. Tang, *Nucl. Phys.* A139 (1969) 144.
- [12] W. W. Buck, J. W. Norbury, L. W. Townsend and J. W. Wilson, *Phys. Rev.* C33 (1986) 234.
- [13] S. A. E. Khallaf, A. L. Elattar and M. El-Azab Farid, *J. phys.* 08 (1982) 1721.
- [14] S. A. E. Khallaf and M. El-Azab Farid, *Atomkernenergie / Kerntechnik* 37 (1981) 294.
- [15] M. W. Kermode, *Proc. Phys. Soc.* 84 (1964) 554.
- [16] P.D. Kunz, DWUCK4 program, University Of Colorado (1969) (unpublished)
- [17] J. Y. Hostachy, M. Buenerd, J. Chauvin, D. Lebrun, Ph. Martin, B. Bonin, G. Bruge, J. C. Lugol, L. Papineau, P. Roussel, J. Arvieux and C. Cerruti, *Phys. Lett.* 184B (1987) 139. ; J. Y. Hostachy M. Buenerd, J. Chauvin, D. Lebrun, Ph. Martin, J. C. Lugol, L. Papineau, P. Roussel, N. Alamanos, J. Arvieux and C. Cerruti, *Nucl. Phys.* A490 (1988) 441.
- [18] R. M. Wiedland R. G. Stokstad, G. R. Satchler and L. D. Rickertsen, *Phys. Rev. Lett.* 37 (1976) 1458; R. G. Stokstad, R. M. Wiedland, G. R. Satchler, C. B. Fulmer, D. C. Hensley, S. Raman L. D. Rickertsen, A. H. Snell and P. H. Stelson, *Phys. Rev.* C20 (1979) 655.
- [19] M. El Shabshiry, *Indian J. Phys.* 66A (1992) 363.

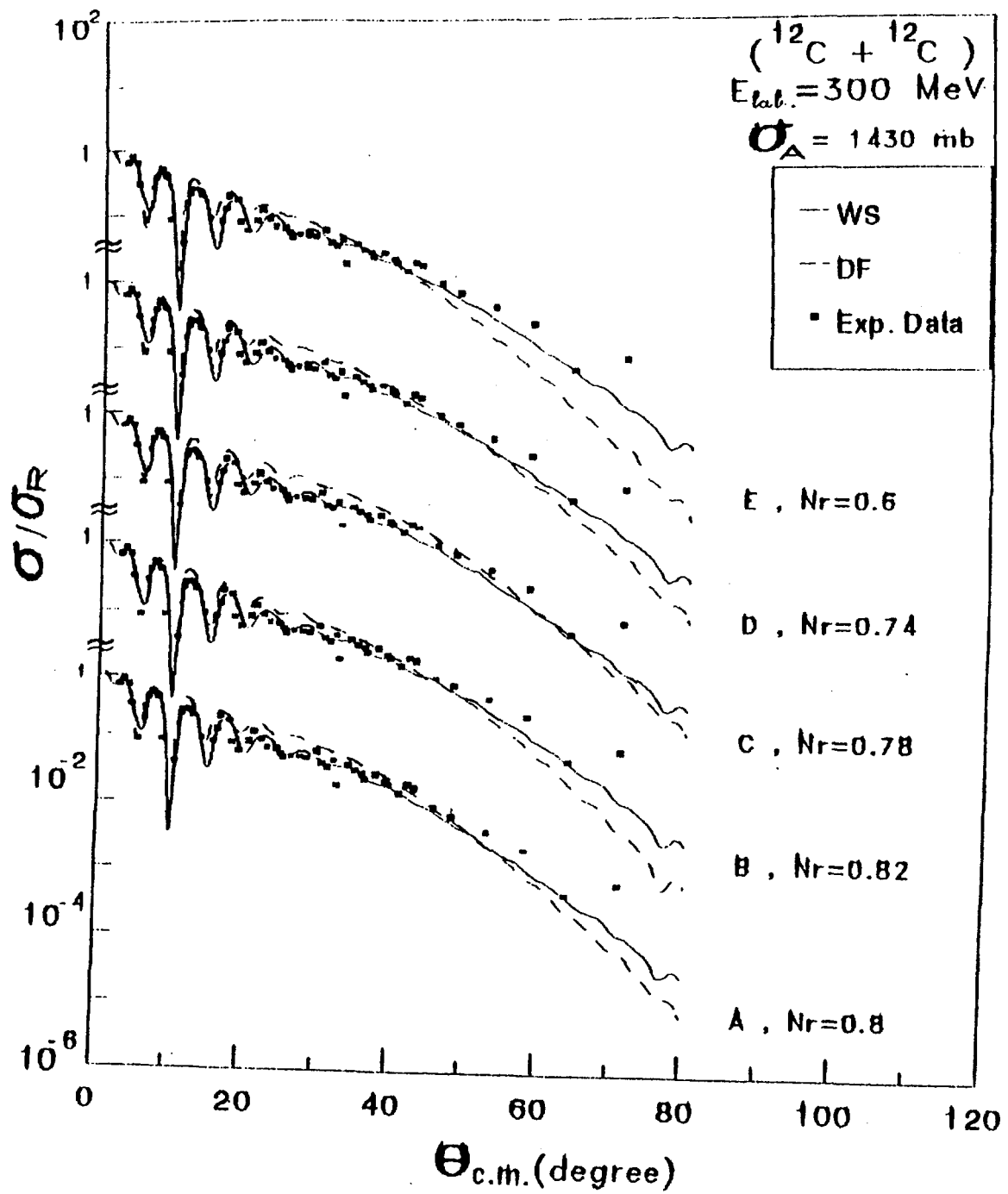


Fig. (1)

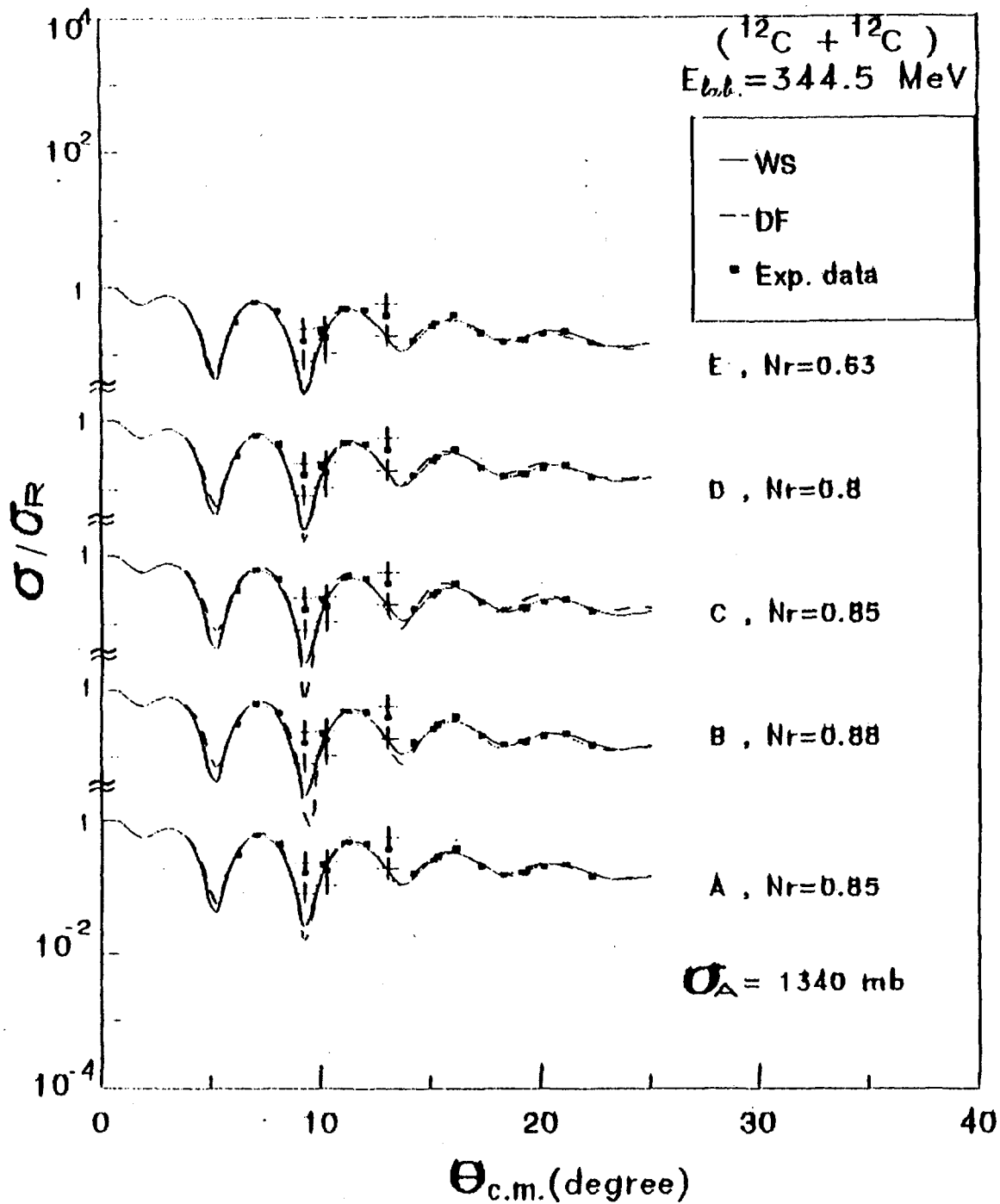


Fig. (2)

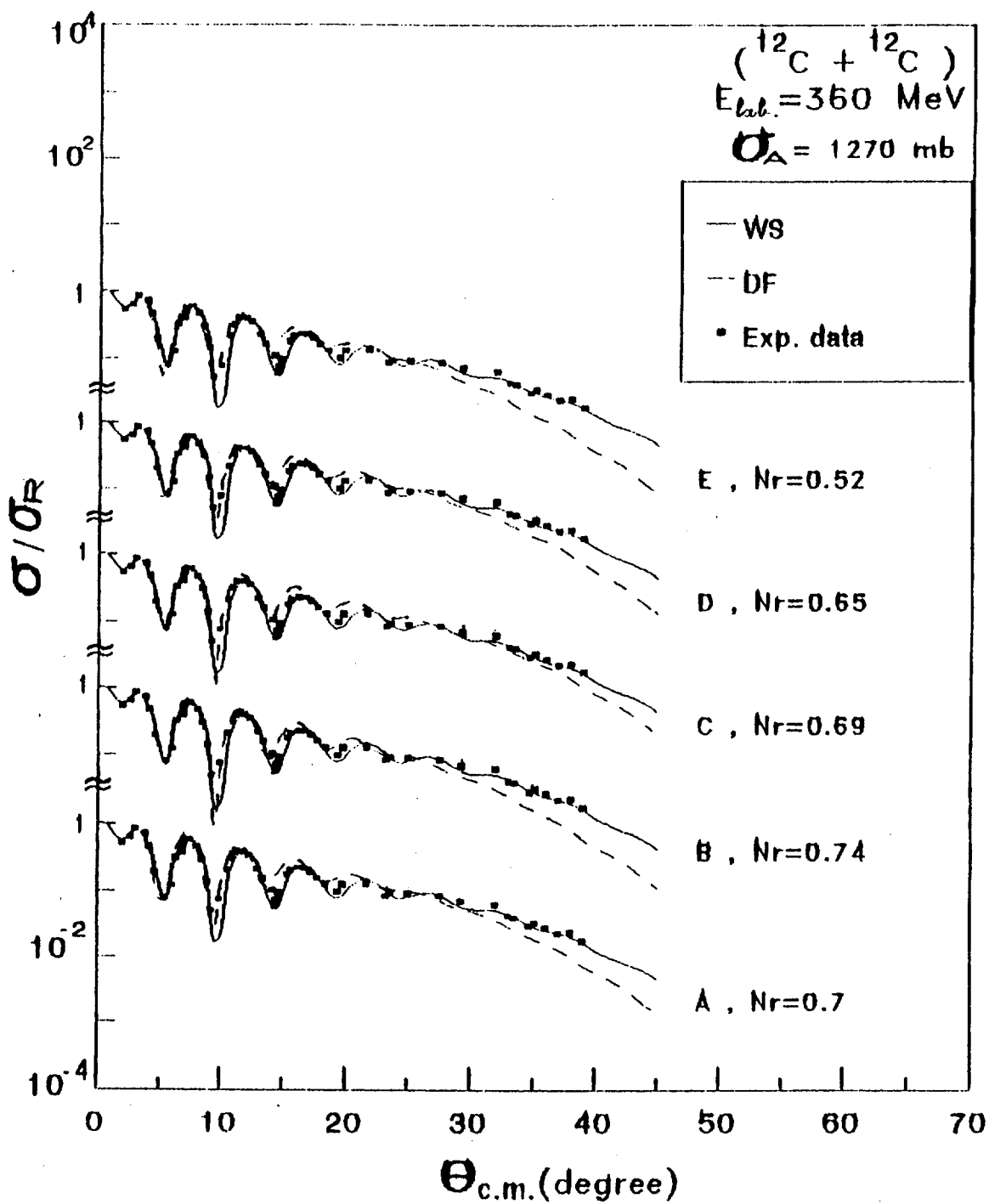


Fig. (3)

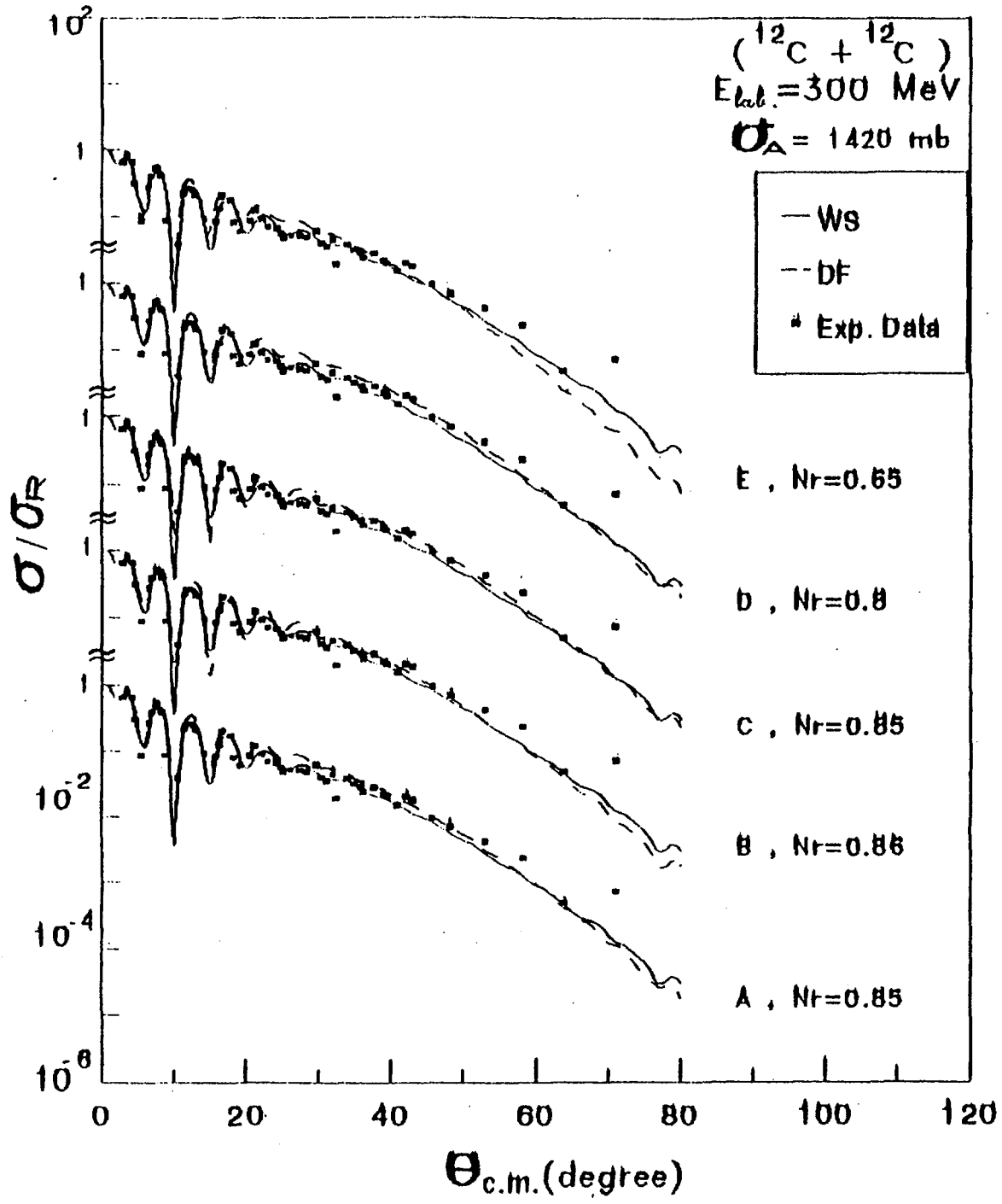


Fig. (4)

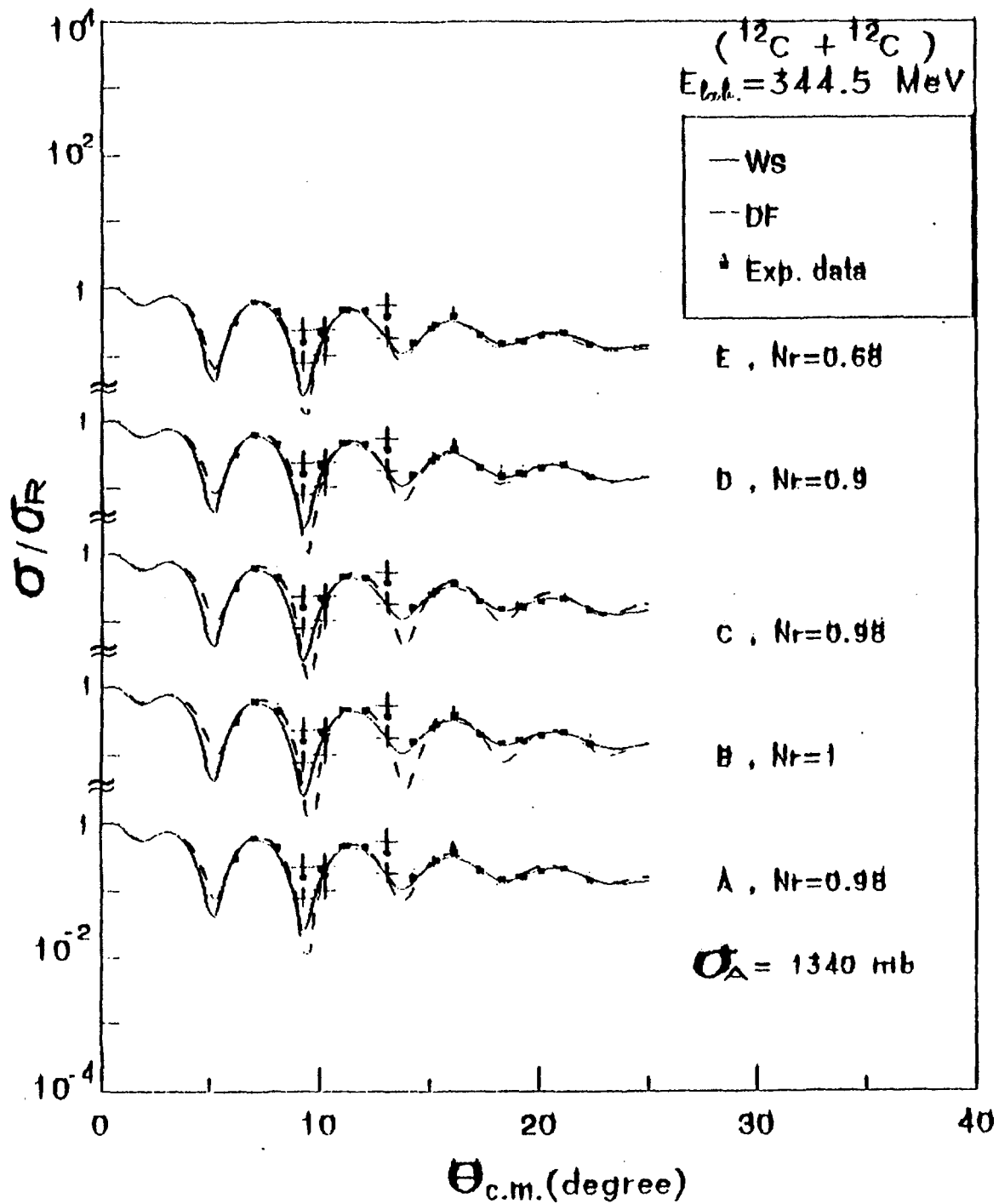


Fig. (5)

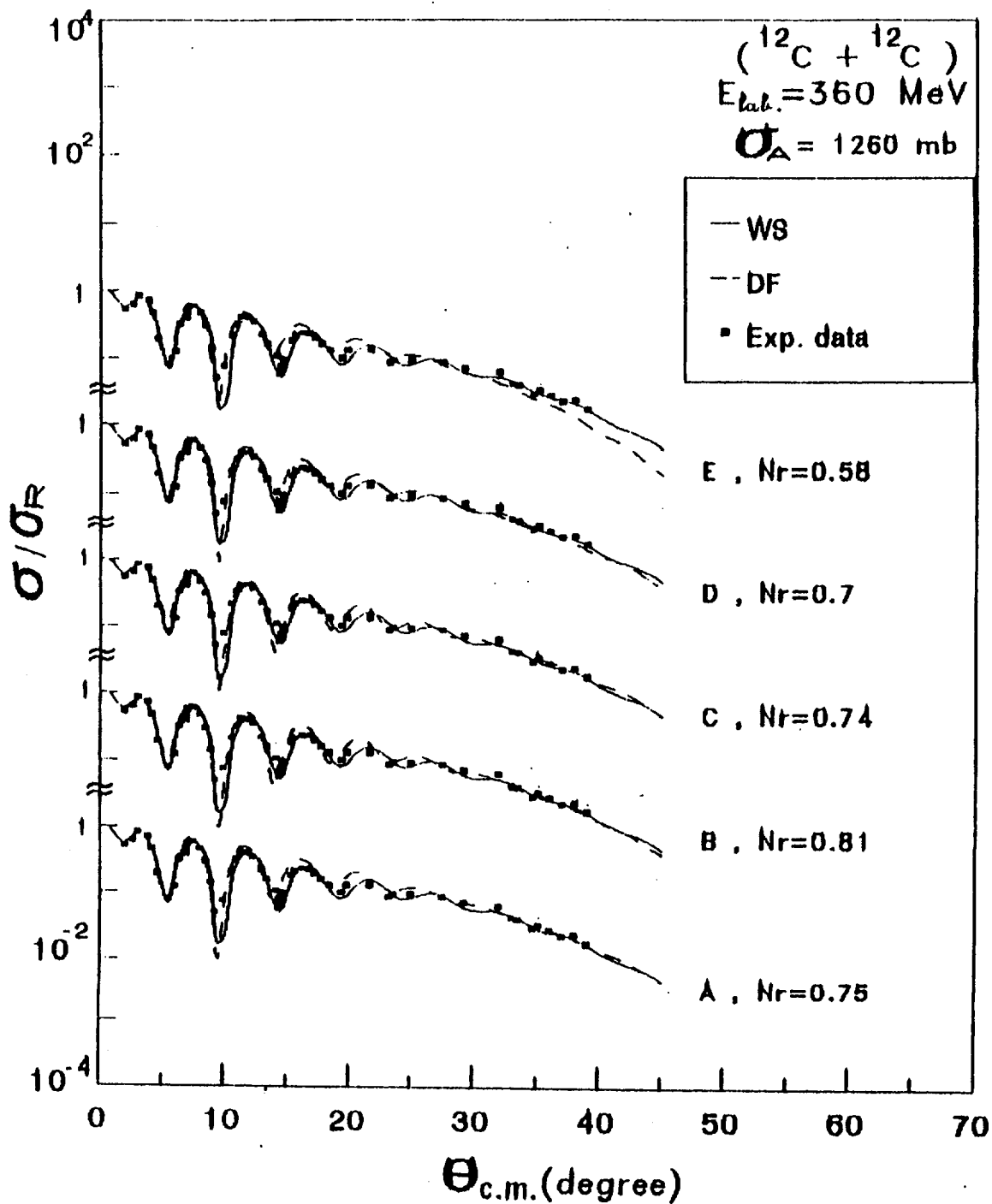


Fig. (6)

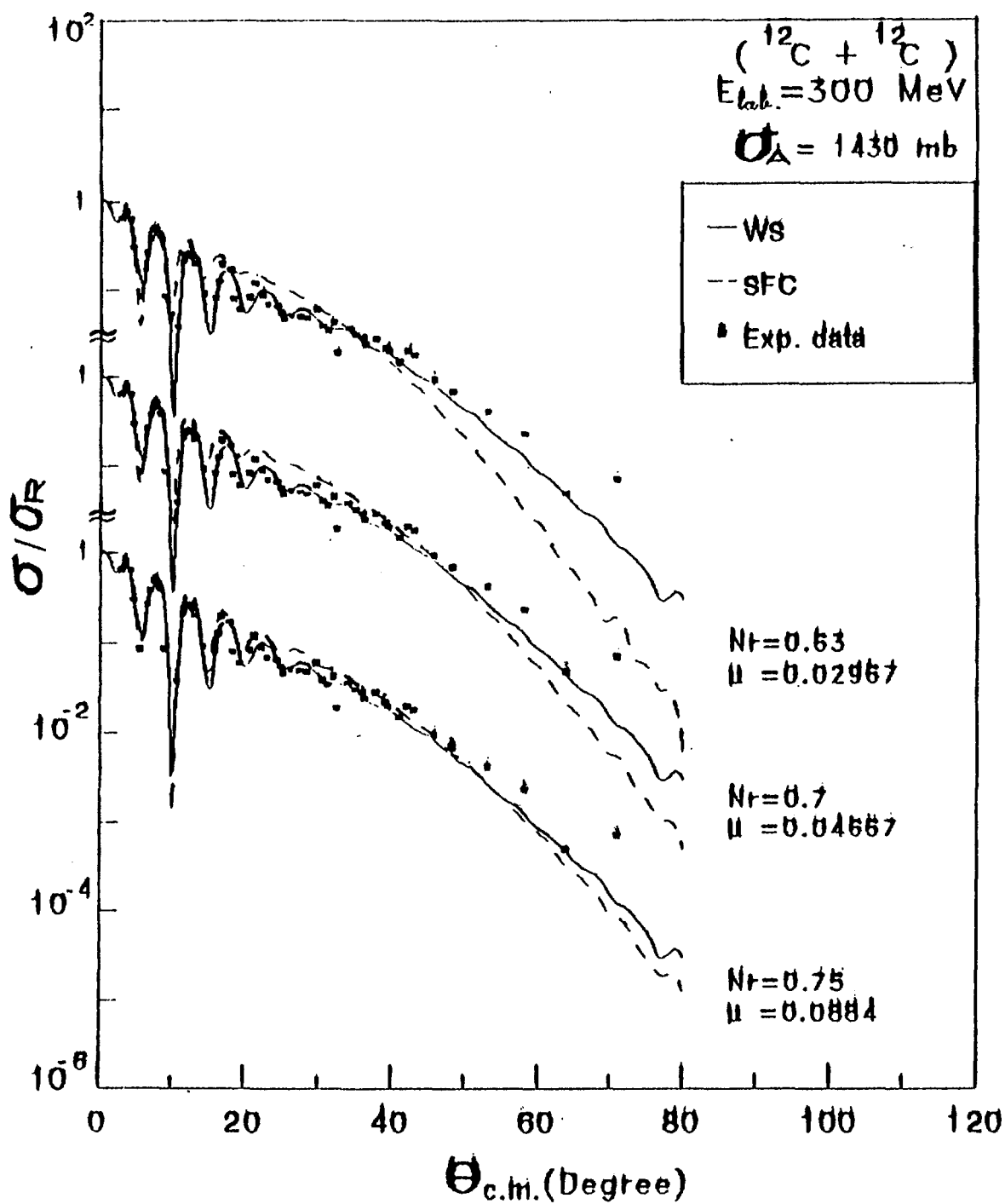


Fig. (7)

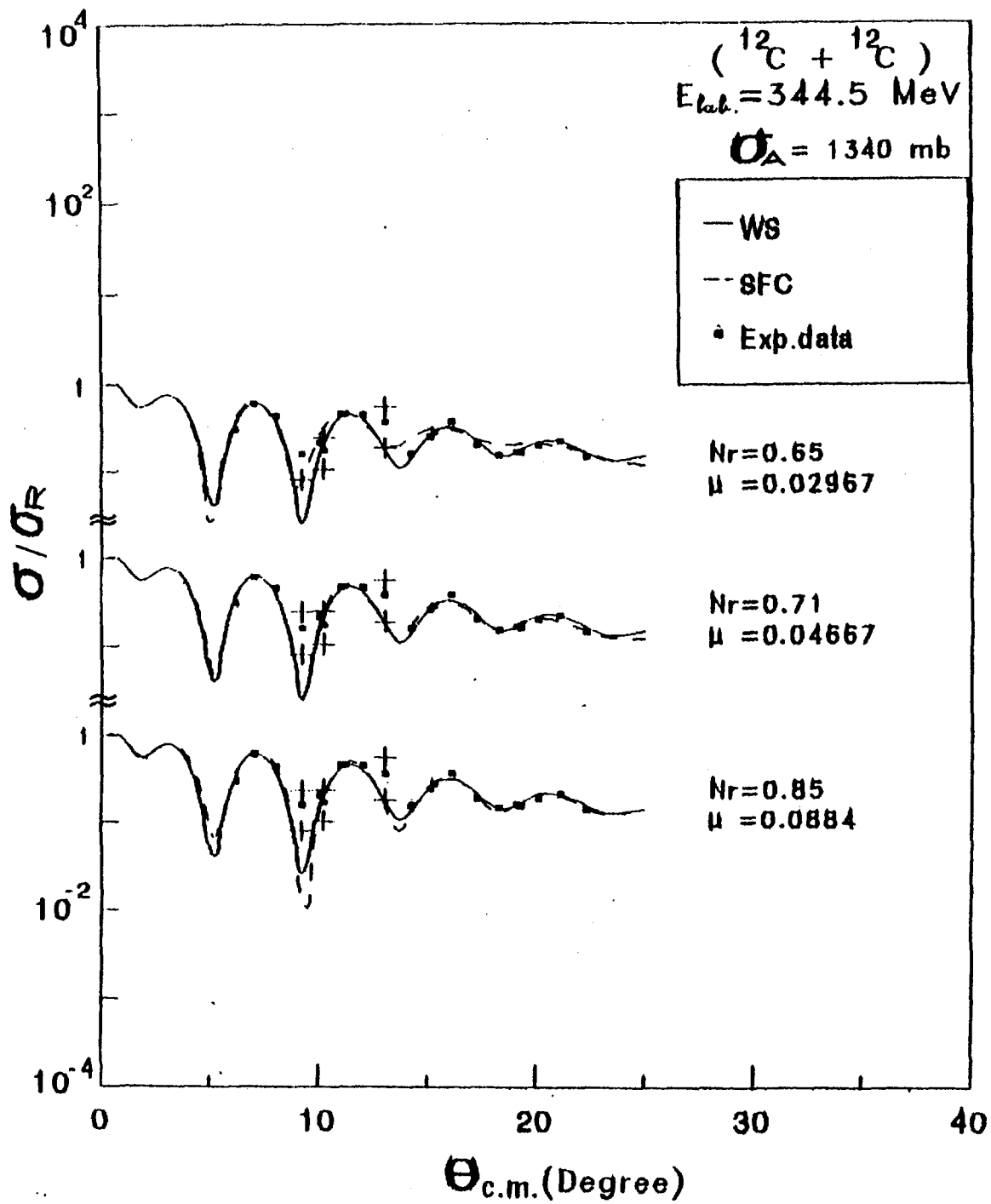


Fig. (8)

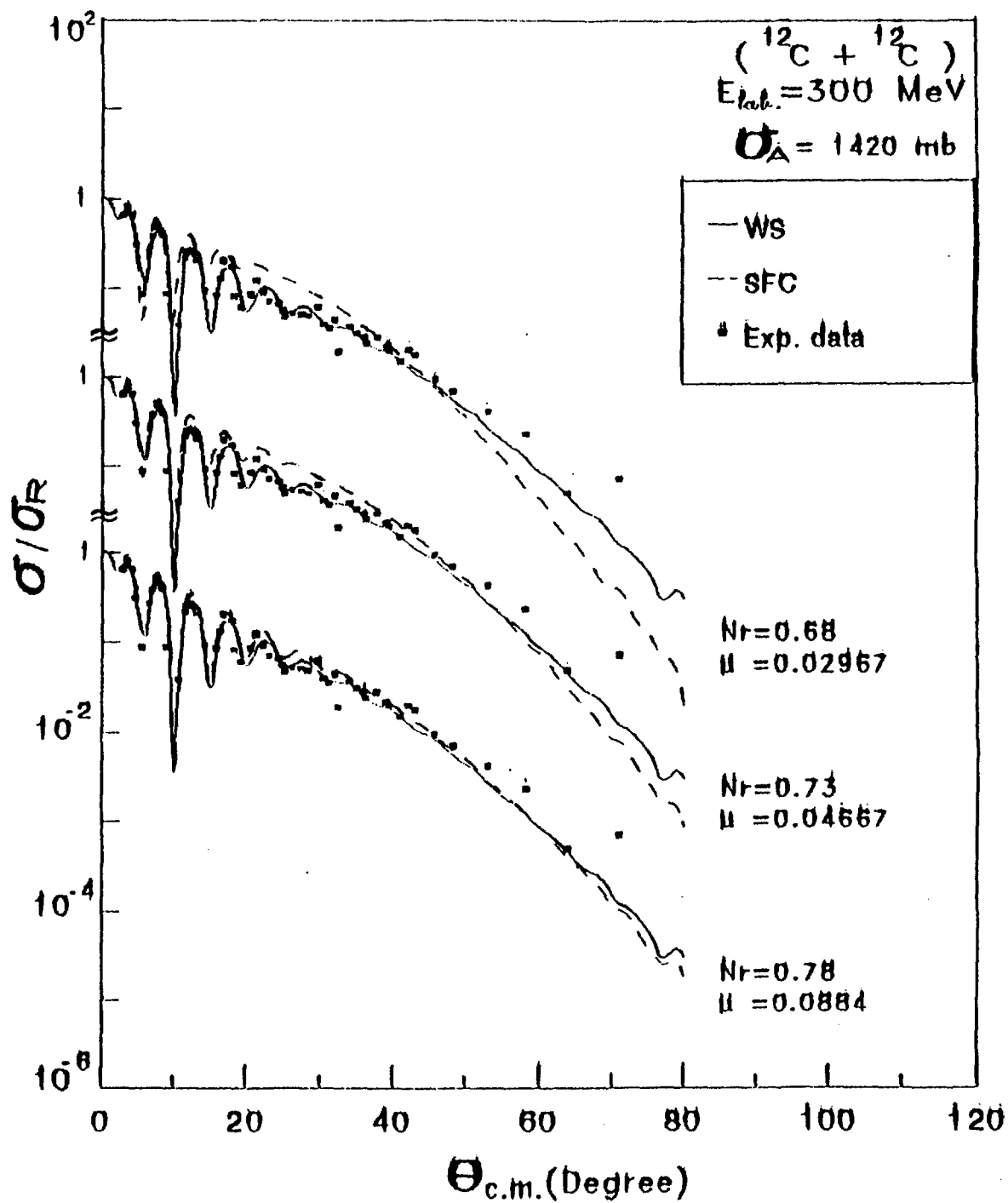


Fig. (10)

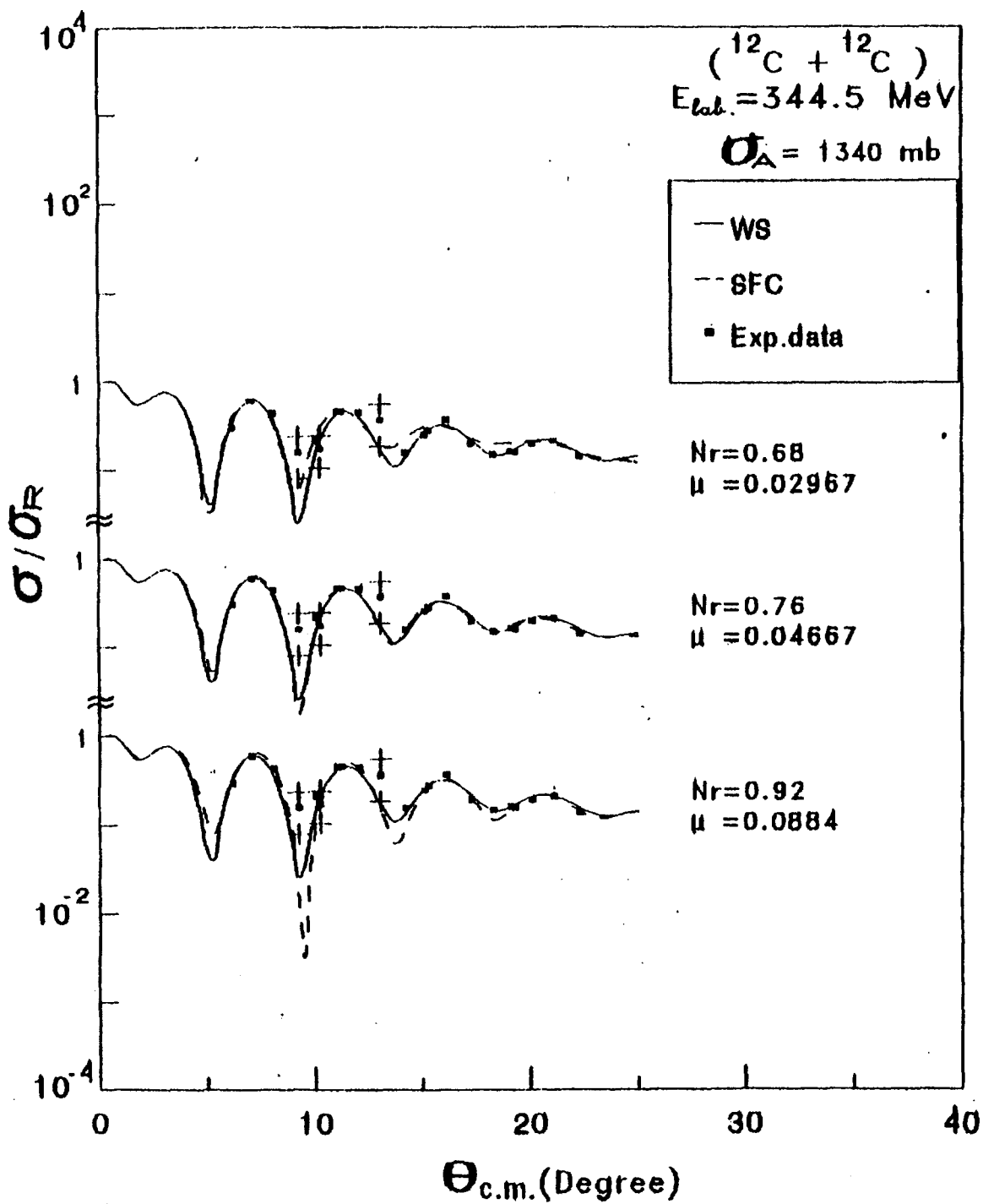


Fig. (11)

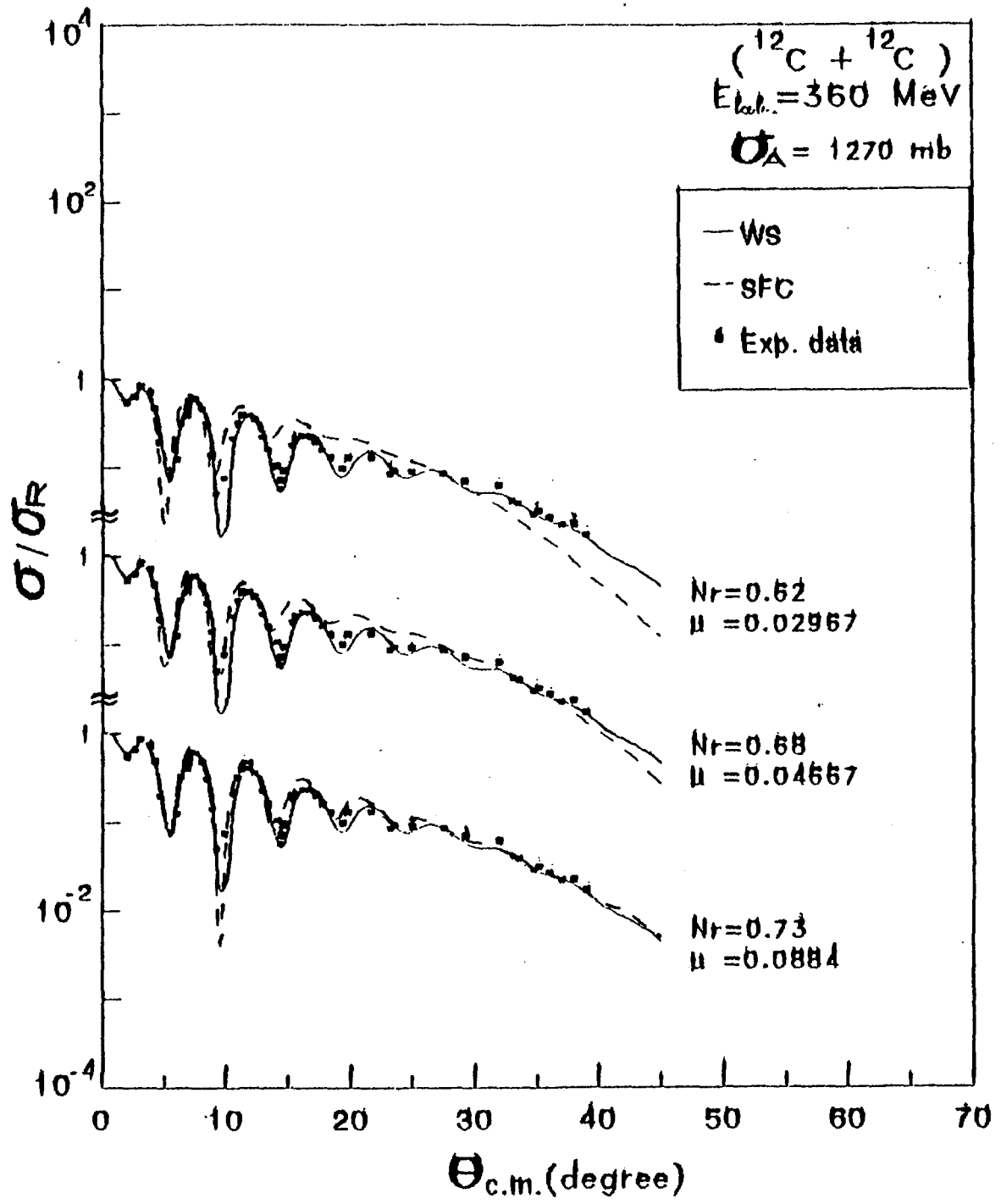


Fig. (12)

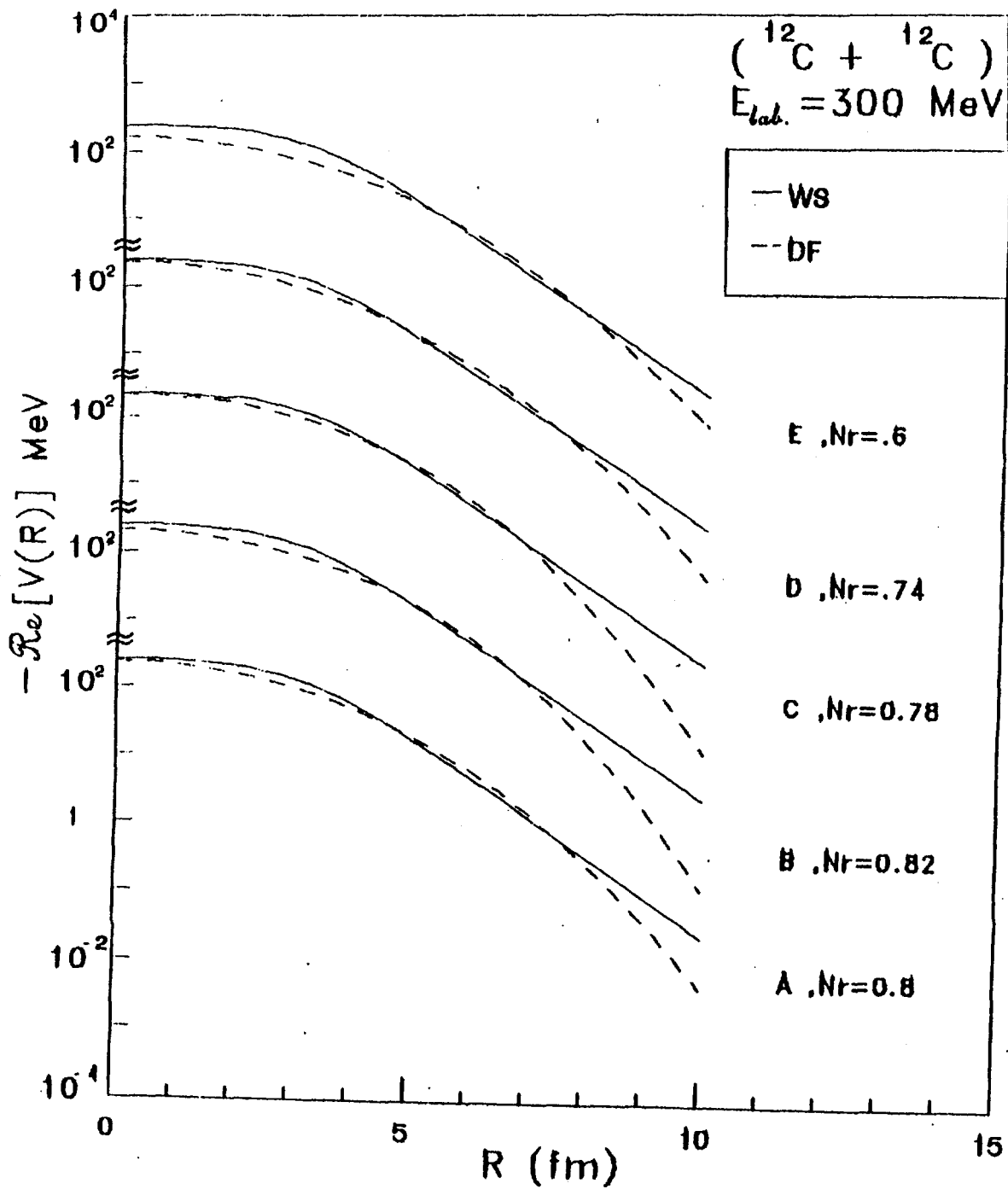
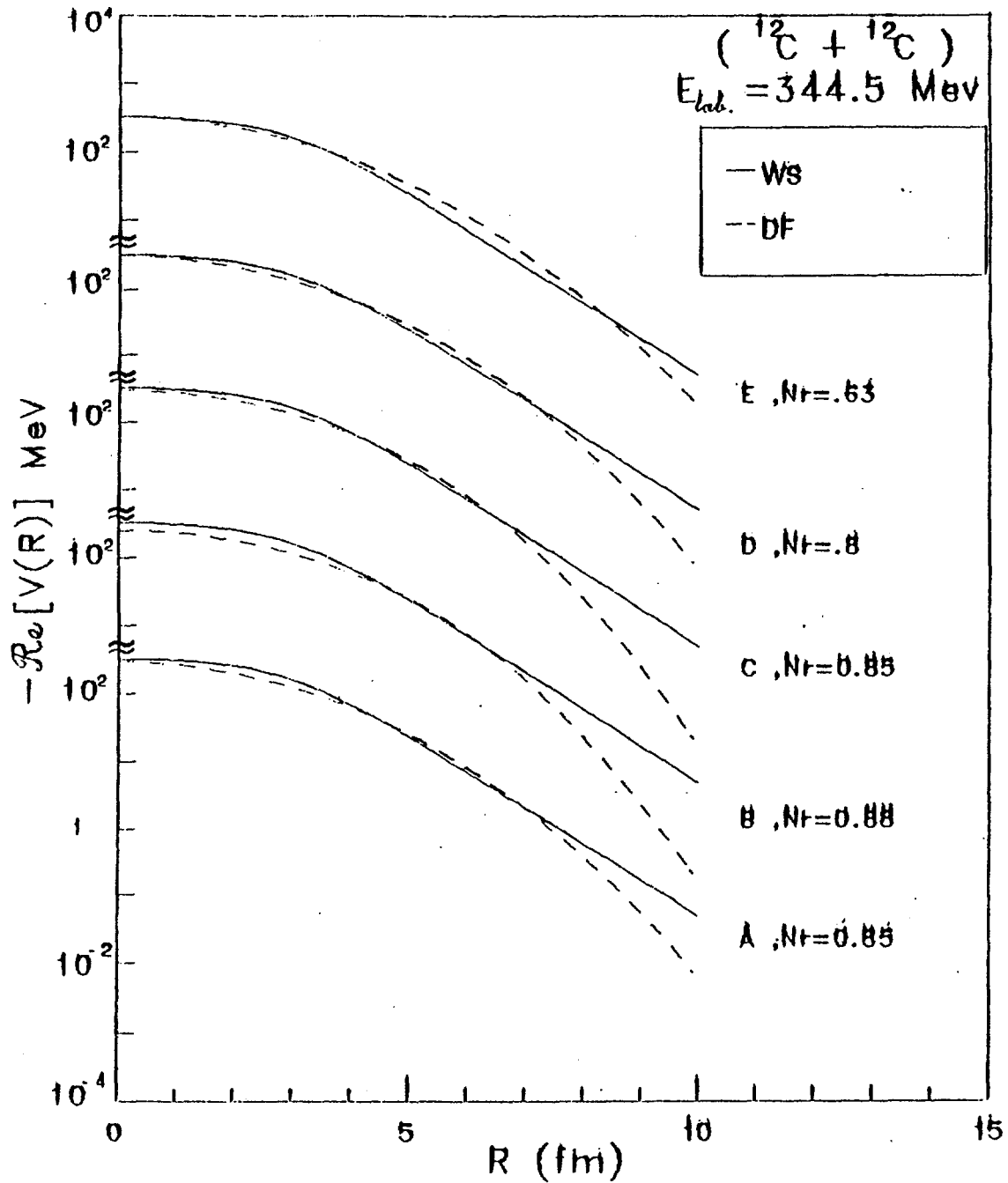


Fig.(13)



*Fig. (14)*

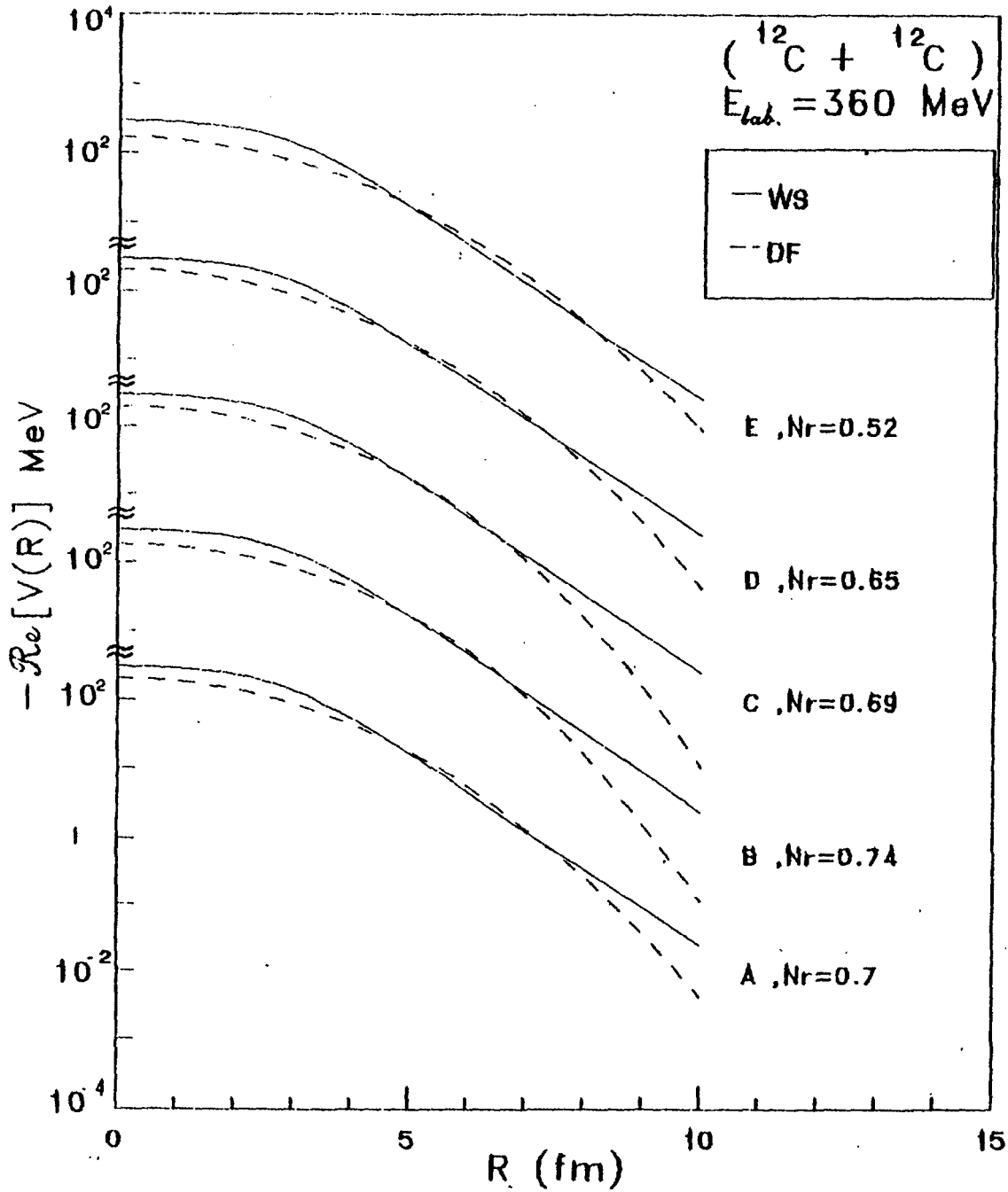
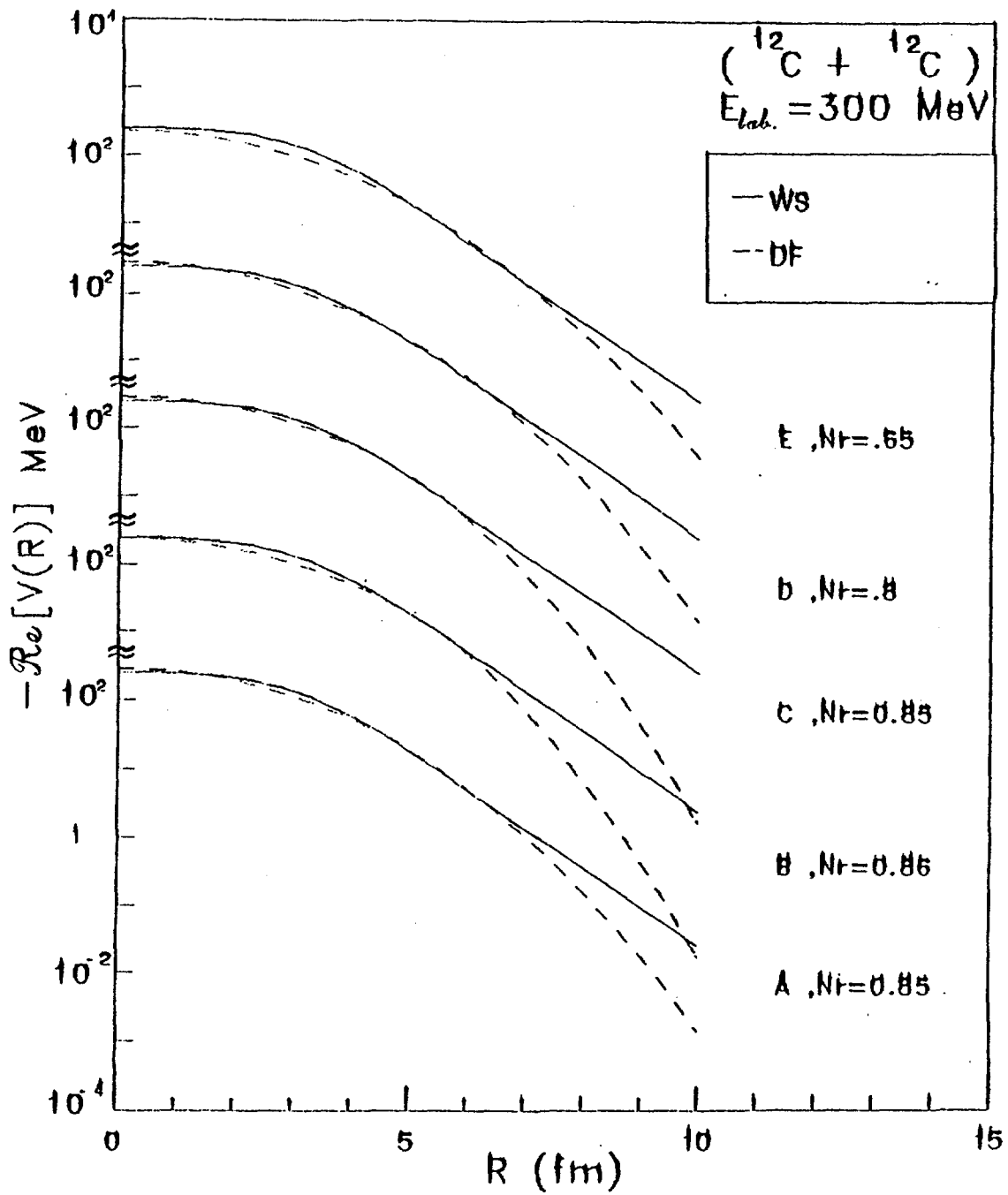


Fig. (15)



*Fig. (16)*

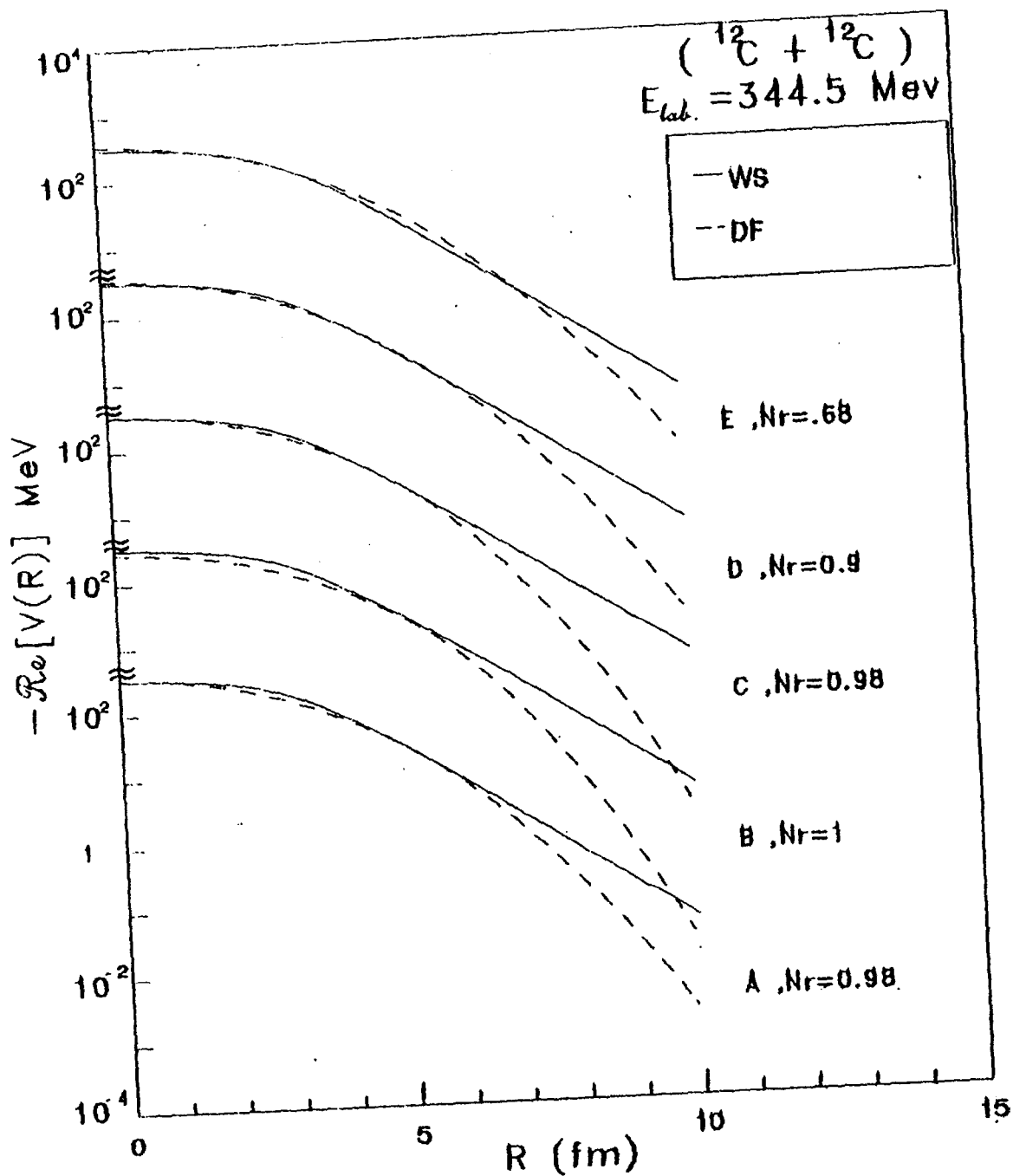
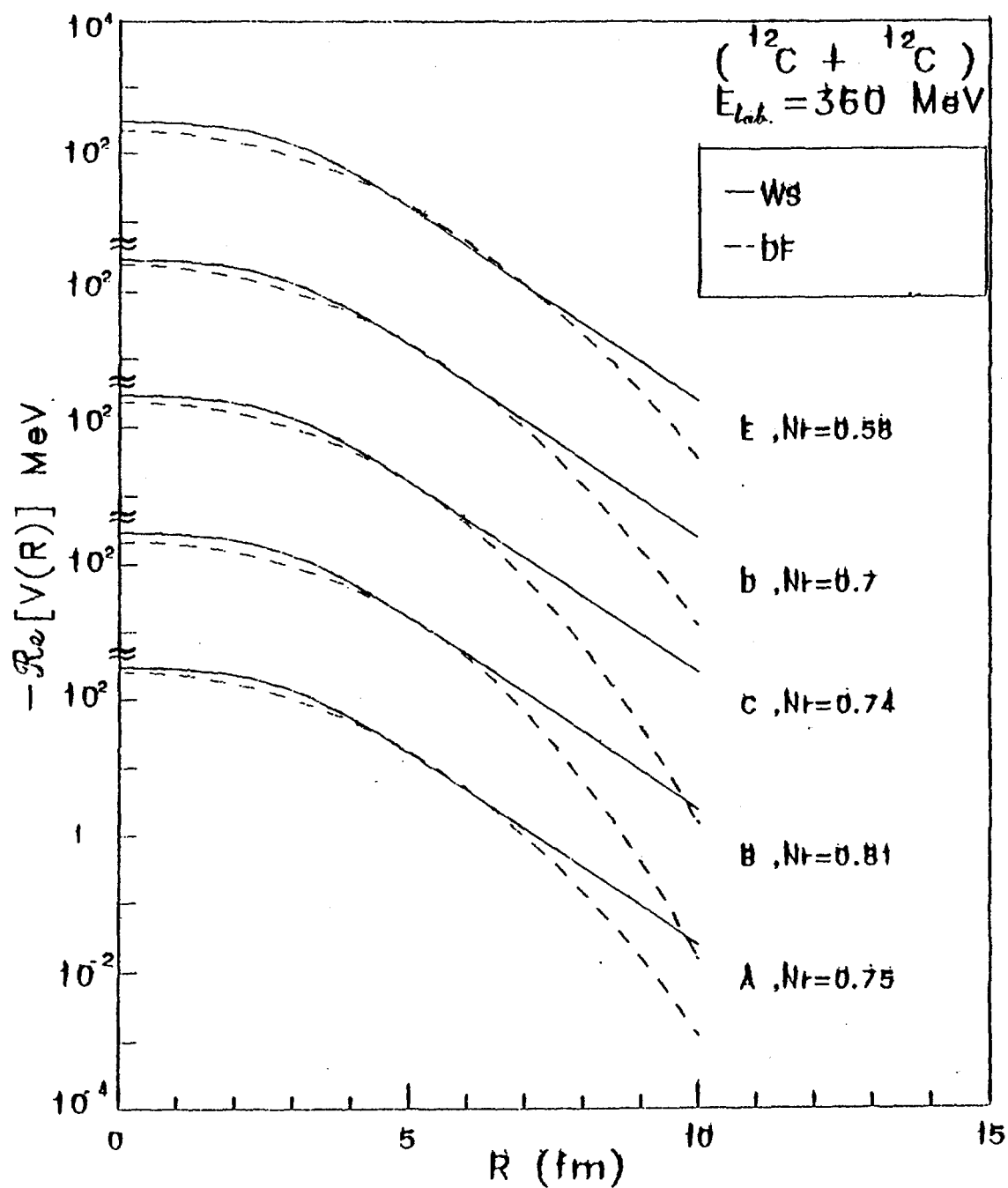


Fig. (17)



*Fig. (18)*

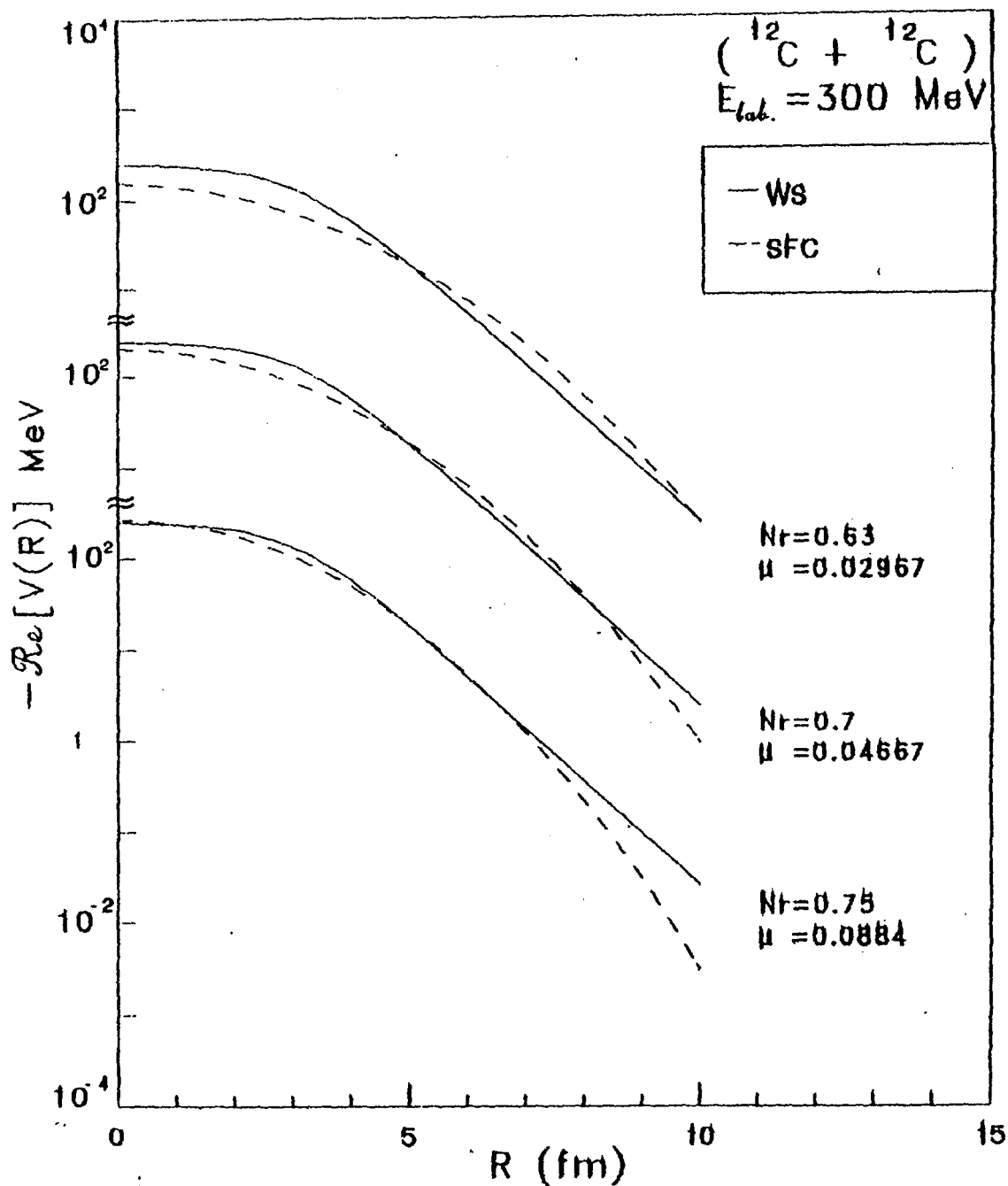


Fig. (19)

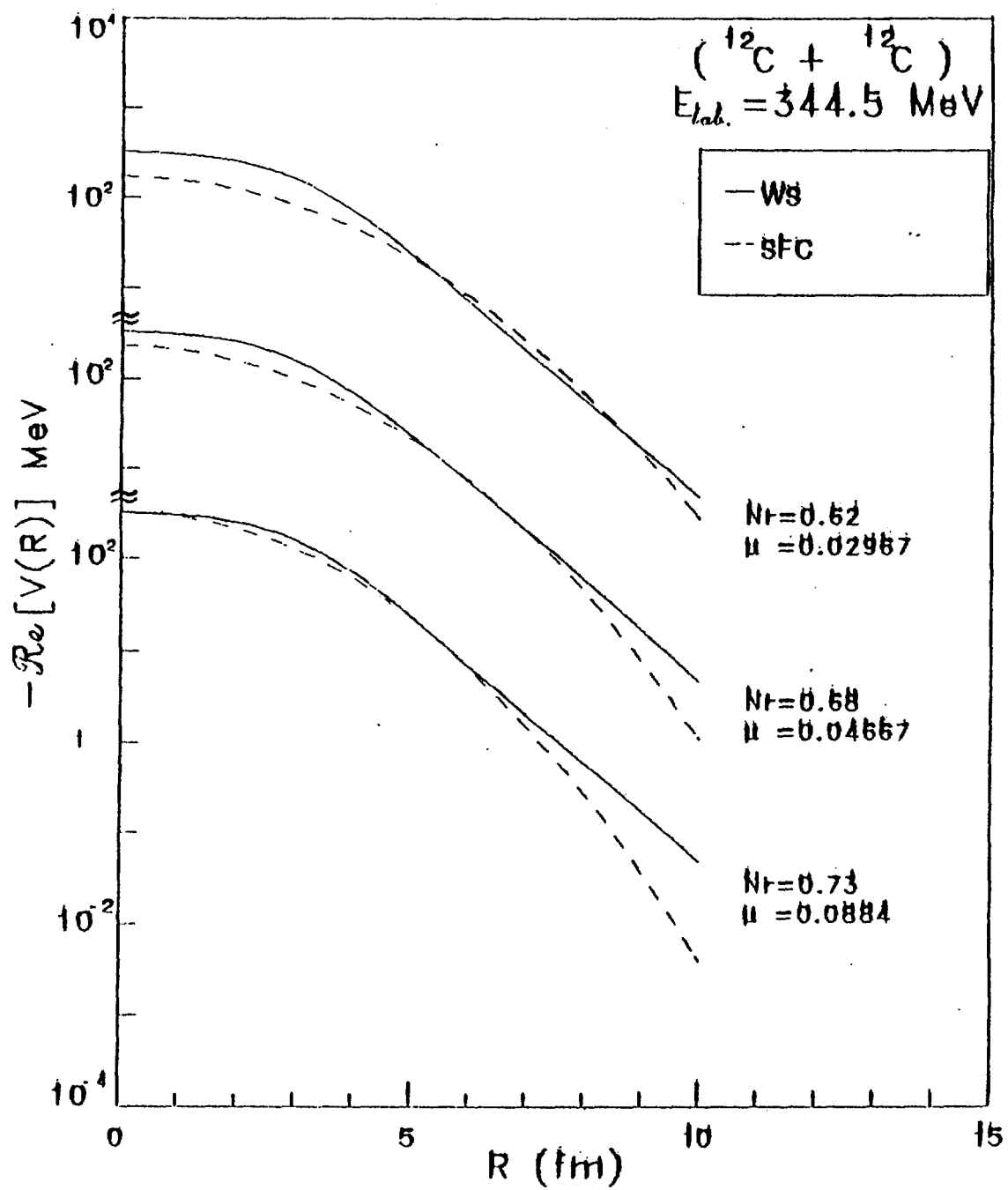


Fig. (20)

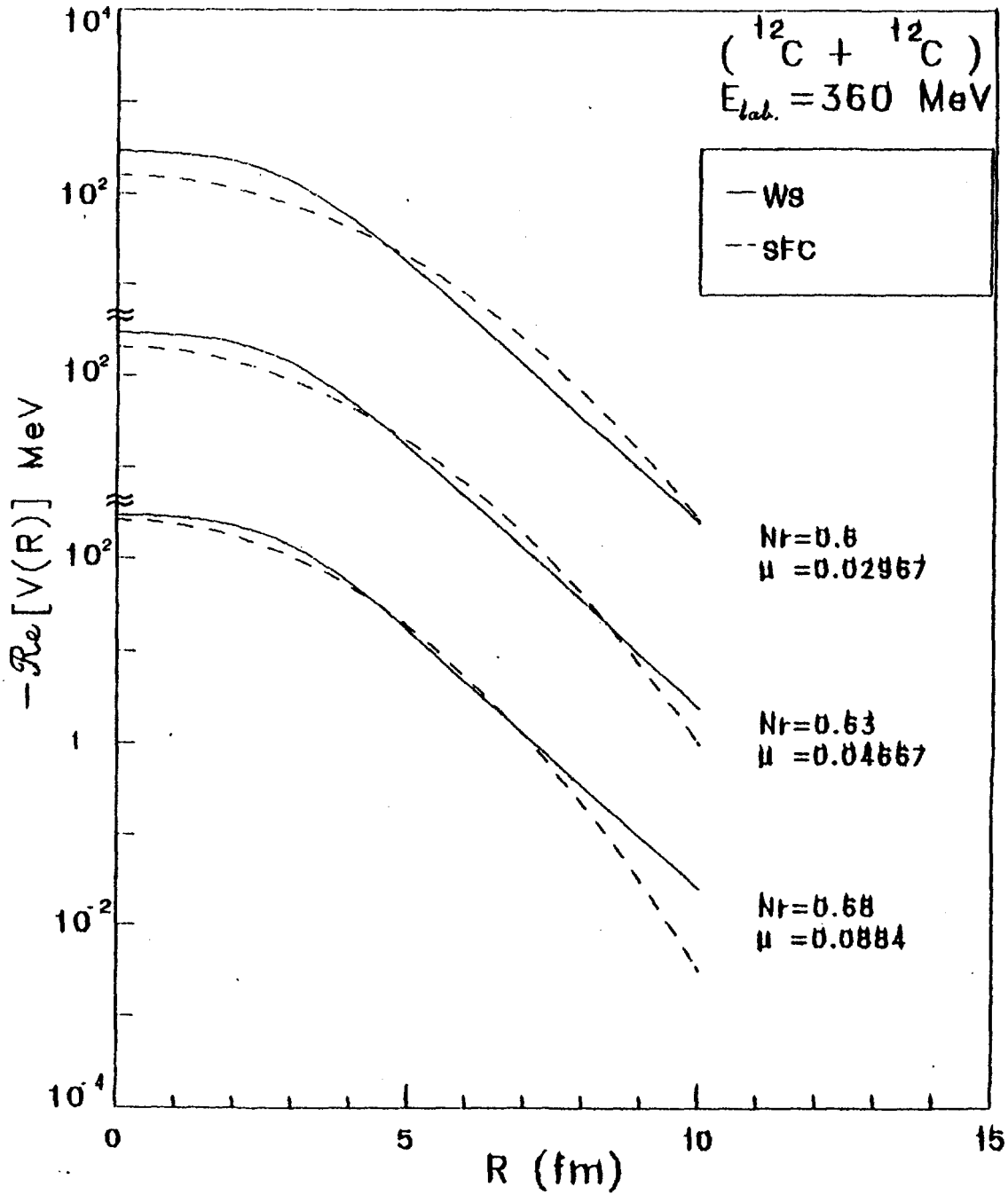


Fig. (21)

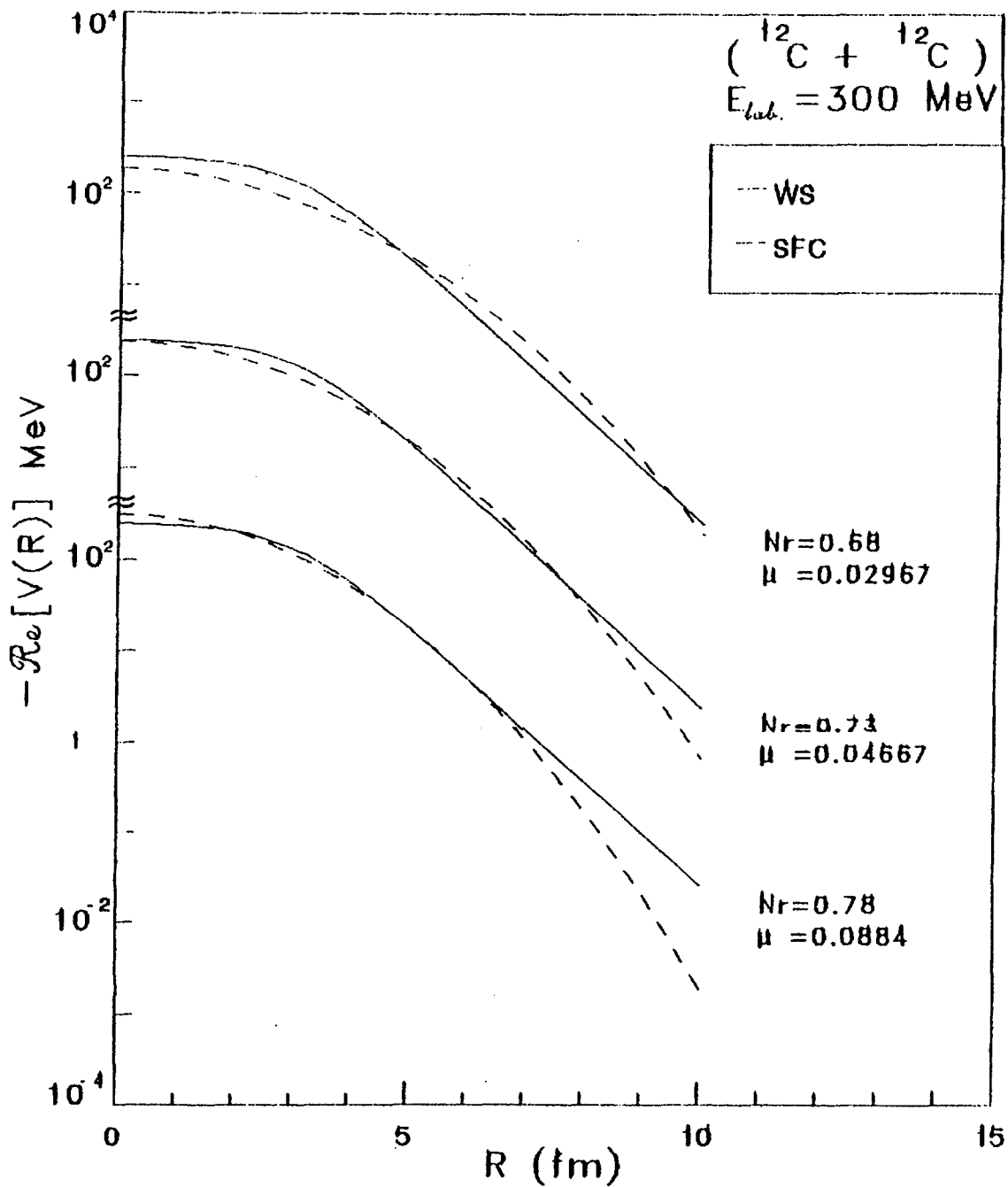


Fig. (22)

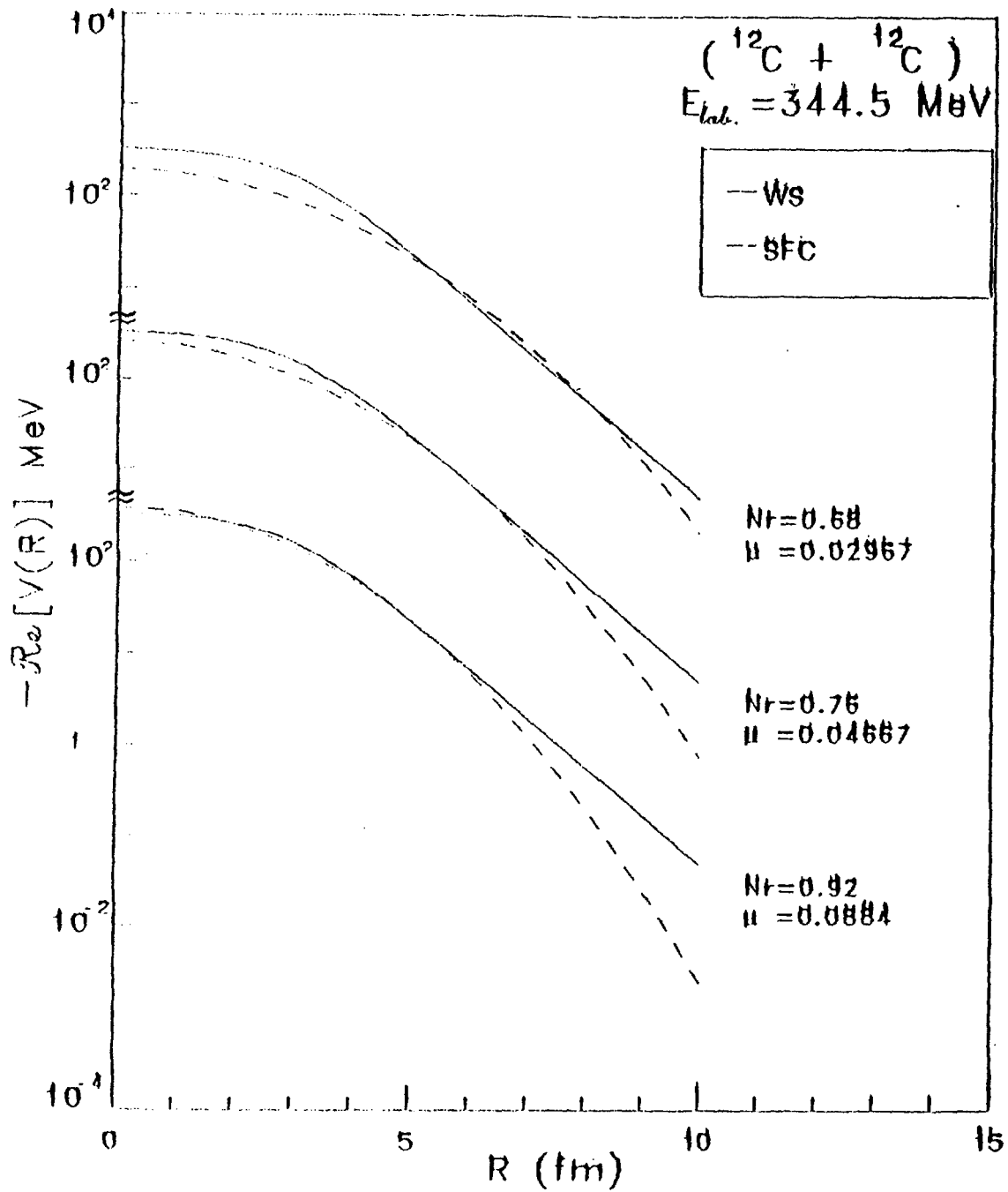


Fig. (23)

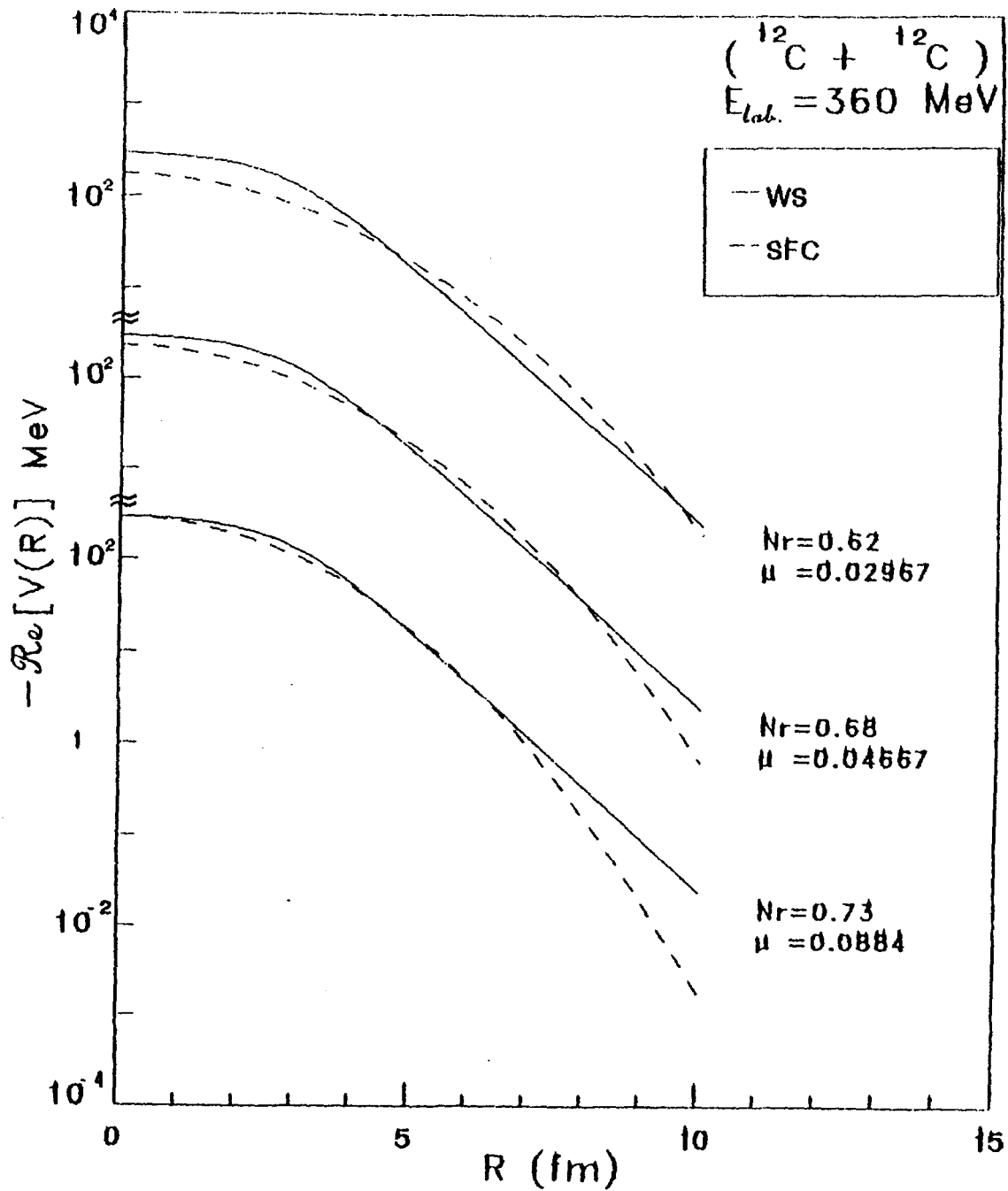


Fig. (24)



EG9700127

## AN EXPECTATION OF A BACKBENDING FOR $N \geq 98$ OF RARE-EARTH NUCLEI

M.M. SALAH

Physics Dept., Faculty of Science, Minia University

H. Elgebaly

Physics Dept., Faculty of Science, Cairo University

### Abstract:

The backbending of three neighboring rare-earth nuclei [Er-YB-Hf] with their isotopes has been studied through the cubic polynomial (CP) theoretical model. Also, from the experimental data, the nuclear moment of inertia  $\mathcal{I}(I)$ , and the squared rotational frequency  $\omega^2(I)$  [as  $(\mathcal{I} - \omega^2)$  plots of a backbending], in addition to the relation of excitation energy  $E_x$ , and the total angular momentum  $I(I+1)$  [as  $E_x - I(I+1)$  plots], have been studied at high energy angular momentum in nuclear rotational bands. The rotational nuclei were divided into soft and hard rotors by studying the softness  $S$  as a function of the ratio  $R_4 = \frac{E(4)}{E(2)}$ . The effective moment of inertia  $\mathcal{I}_{\text{eff}}$  for these nuclei was considered. We expected that there may be a backbending for nuclei of  $N \geq 98$ , but with high angular momentum, which were not expected before, by studying the effect of  $I(I+1)$  at the critical spin of a backbending.

Introduction :

Significant progress, both experimental and theoretical, has recently been achieved in the understanding of the nuclear behavior for rare-earth nuclei at high spin. For example, multiple band structure has been observed in the well-deformed nuclei  $^{160}\text{Yb}$ , and the existence of the second backbending for some rare-earth nuclei.<sup>(1,2)</sup>

It is generally believed that, the backbending is caused by band crossing of the ground band with other rotational bands induced by single-particle degrees of freedom. In other words, some valence particle pairs are decoupled from the collective core and align their angular momentum along the rotational axis. The aligned pair may produce rotational states that are energetically favored as compared with the ground state rotational band states. As a result, band crossing happens, and the aligned pair states become the yrast state<sup>(3)</sup>. So it is suggested that, the backbending in the rare-earth region is due to the breaking of an  $i_{13/2}$  neutron pair and aligned its along the rotational axis.

M.M. King Yen, et al.<sup>(4)</sup>, suggested that the disappearance of the backbending for  $^{166}\text{Er}$  with neutron number  $N=98$ , agrees with announcement made by S.A. Ryde, et al.<sup>(5)</sup>, that no backbending should be expected for nuclei with  $N \geq 98$ . But the level scheme of  $^{170}\text{Yb}$ <sup>(6)</sup> with  $N=100$ , shows that, there is a backbending, Fig.(1). Over again, R. Bengtsson et al.<sup>(7)</sup>, suggested that for  $N \geq 100$ , no backbending must be found, and the low values of  $I$  for  $^{170}\text{Yb}$  is due to the deficiency of the analysis of the data.

The aim of this work is to inquire "Dose a relation between the theoretical critical spin  $I_c$  calculated from the cubic polynomial (CP)<sup>(8)</sup> model for nuclei having no explicit backbending, (due to upbending or no enough data at high energy), and the experimental  $I_c$  exist?", "Dose the experimental  $I_c$  value for  $^{170}\text{Yb}$  agree with the other backbending

critical spins of the surrounding nuclei?" and "Is a backbending for nuclei with  $N \geq 100$  feasible?"

Even-even isotopes of three neighboring rare-earth nuclei (Er- Yb- Hf) at  $N = 84 - 106$  have been studied as a backbending phenomenon, through three conjugate steps:

a) From the experimental data, the nuclear moment of inertia  $\mathcal{I}(I)$ , and the squared rotational frequency  $\omega^2(I)$ , have been studied as  $(\mathcal{I} - \omega^2)$  plots of a backbending<sup>(9,10,11,12)</sup>.

b) The backbending of these nuclei were also studied as a function of excitation energy  $E_x$  versus the total angular momentum  $I(I+1)$ <sup>(13)</sup>.

and

c) The theoretical expression for backbending phenomena according to the cubic polynomial (CP) model were executed for these nuclei.

By studying the effect of  $I_c(I_c + 1)$  at the critical spin of a backbending, we expected that, there will be a backbending for nuclei of  $N \geq 98$ , but with a high angular momentum, which were not observed before.

### Calculations and Analysis :-

The nuclei in our investigation can be divided into three groups according to the values of the  $R_4$ <sup>(14)</sup>, as can be seen in table (1). Also, the softness  $S$ <sup>(8)</sup> of these nuclei are studied, and are shown in Fig.(2) which indicate that the rotational nuclei are very close to each other. As can be seen the rotational nuclei are divided into two groups, "stretching nuclei" with positive  $S$  values, as soft rotors, and "shrinking nuclei" with negative  $S$  values as hard rotors. So, it is clear that, a great part of the nuclei under investigation lie in the rotational region.

Table (I):

The nuclei in our investigation can be divided into three groups according to the values of the  $R_4^{(14)}$ , where :

Region (I) ;  $2.0 \leq R_4 \leq 2.4$  ; for vibration nuclei

Region (II) ;  $2.4 \leq R_4 \leq 3.0$  ; for transition nuclei

Region(III) ;  $3.0 \leq R_4 \leq 10/3$  ; for rotational nuclei

Nuclei	Groups		
	I	II	III
<b>Er</b>	N = 86 - 88	90	92-102
<b>Yb</b>	N = 86 - 88	90-92	94 - 106
<b>Hf</b>	N = 88	90-94	96-106

The backbending ( $\partial-\omega^2$ ) experimental plots for  $_{68}\text{Er}$ ,  $_{70}\text{Yb}$ , and  $_{72}\text{Hf}$  isotopes with  $N=84-106$  have been studied. They included plots for 23 nuclei, can be seen in Fig.(1), distributed as follows:  $^{150}\text{Er}$ ,  $^{158, 162, 166, 170}\text{Yb}$ , and  $^{166,168}\text{Hf}$ ;  $^{(6,15,16)}$  show explicit first backbending in the yrast band at the critical spin values  $I_c=12;10,12,14,16$  ;12,12 respectively,  $^{168}\text{Yb}$  and  $^{170}\text{Hf}^{(6,16,17)}$  with  $N=98$  exhibit just upbending in the yrast band. A second backbending, in addition to the first backbending appeared for  $^{158,160}\text{Er}$ ,  $^{156,160,164}\text{Yb}$ ,  $^{160,162}\text{Hf}^{(10,5,7,17,18,19,20,21)}$ , at  $I_c= 12,14;4,10,12;10,10$  respectively for the first backbending and at  $I_c= 16,16;10,14,16; 14,14$  respectively for the second backbending. For  $^{164,168,170}\text{Er}$ ,  $^{172,174,176}\text{Yb}$ , and  $^{178}\text{Hf}^{(6)}$ , the available data are up to spin  $I = 12,12,12$  ;12,18,18 ;14 respectively, and through this region no backbending appeared. From above, one can say that, for nuclei of  $N = 90$ , and its neighbors, the first backbending is

around  $I_c=12$ , and a second backbending with  $I_c$  not far from 14. For nuclei with  $N \geq 102$ , no backbending appeared. Also, there are some deformation were happened at  $I=16$  for  $N=98$  caused upbending phenomena.

The theoretical approach to the  $(\vartheta-\omega^2)$  experimental plots, for the ground band of even-even nuclei, is the cubic polynomial (CP) model, which applies to the experimental energy levels, as given by Sood<sup>(3)</sup>. The results are shown in Fig.(1).

The becbending is studied also through plots of excitation energy  $E_x$  versus  $I(I+1)$ . The critical spin values  $I_c$  for (Er-Yb-Hf) isotopes deduced by this method are equivalent (or very close), to those deduced from the  $(\vartheta-\omega^2)$  plots. Examples of these plots can be seen in Fig. (3). The effective moments of inertia  $\vartheta_{eff}^{(22)}$  for angular moment below  $I_c$  are calculated. It is clear that,  $\vartheta_{eff}$  decreases as the atomic number  $Z$  increases, while it increases as the neutron number  $N$  increases. This is shown in Fig.(4).

The rotational energy depends on the factor  $I(I+1)$ <sup>(23,24)</sup>. This factor is studied at a critical spin  $I_c$  of a backbending obtained from the theoretical and experimental data by plotting this factor versus the neutron number  $N$ , for the three neighboring nuclei [Er-Yb-Hf] isotopes. This can be seen in Fig. (5). We find that, for  $N \geq 100$ , the theoretical and experimental data exhibit a peak, with a wing as a tail of a peak at small  $N$ . Below  $N \leq 94$  the tail behaves linear. At  $N=88$  and  $96$ , there are humpedges where its peaks linearly decrease with increasing  $Z$ . We think this edge is due to the quadruple deformation increase, and hence the Fermi energy moves below the  $i_{1/2}$  which costs more energy to excite a pair of quasiparticles into these states. This effect increases the critical frequency. For  $N \geq 100$ , data exhibit a peak, which means that, the nucleus rotates rapidly, giving a large deformation. The curvature of a peak is at  $N=102$  for Er, at  $N=$

104 for Yb, and at  $N \geq 104$  for Hf, where at this  $N$  value the orbit  $i_{13/2}$  tends to be filled up to a saturation number  $N$ , ( $N_{sat}$ ). The wing of the peak has a higher value for Er, than for Yb, which in turn both have higher values than Hf. This agrees with the behavior of  $\mathcal{D}_{rot}$  which decreases by increasing the atomic number  $Z$ . For  $N=98$ , which exhibits upbending, in Fig. (1), while the factor  $I_c(I_c+1)$  seems to agree to complete the wings of this peak at the linearly smooth part. Also  $^{158}\text{Er}$ ,  $^{160}\text{Yb}$  with  $N=90$ , and  $^{164}\text{Yb}$  with  $N=94$ , (the neighboring nuclei to the bump edge at  $N=88, 96$ ), lie at the tail of the peak. This means that, the Fermi surface lies at the same place in the  $i_{13/2}$  neutron shell. It is clear for  $^{168,170}\text{Yb}$  and  $^{166}\text{Er}$  which go up to agree and complete the wing. Any change of  $I_c$  for  $^{170}\text{Yb}$  will change its point place on the curve, up or down, which will make some falsification for the smoothing of the curve. So the behavior of this curve gives us an expectation that a backbending happens for  $98 \leq N \leq N_{sat}$  but at high angular momentum. Also we believe that, the  $I_c$  experimental data for  $^{170}\text{Yb}$ , with  $N=100$  agree with our curve.

Comparing the Fig.(2) for the softness  $S$ , and the three curves of a peak, Fig.(5), illustrate that the nuclei with positive  $S$  values (soft rotors), behave in  $I_c(I_c+1)$  curve as a linear part, and those nuclei with negative  $S$  values (hard rotors), behave as a peak in the  $I_c(I_c+1)$  curve. So, stretching nuclei may have a first and a second backbending but the shrinking nuclei may have only one backbending at high energy level for isotopes having  $N \leq N_{sat}$ .

The authors would like to express their thanks to **Prof. Dr. A. H. SALEH**, Physics Dept., Faculty of Science, Cairo University for his discussions and comments on various aspects of this work.

References

- 1- Y.S. Chen, S. Frauendorf, and L.L. Riedinger, *Physics Letters B*, Vol. 171, No. 1, (1986), p. 7
- 2- J. Simpson, M.A. Riley, J.R. Cresswell, P.D. Forsyth, D. Howe, B.M. Nyako, and J.F. Sharpey-Schafer, *Physical Rev. Letters*, Vol. 53, No. 7, (1984), p. 648.
- 3- J.D. Garrett, *Nuclear Phys., A* 409, (1983), p. 259
- 4- M.M. King Yen, S.T. Hsieh, and H.C. Chiang, *Journal of Physical Society of Japan*, Vol. 61, No. 1, (1992), p. 102.
- 5- Ryde, S.A. Hjorth, D. Barncoud, A. Johnsen, G.B. Hagemann, and B. Herskind, *Nucl. Phys., A* 207, (1973), p. 513.
- 6- T. Venkova, and W. Anderjtscheff, *Atomic Data and Nuclear Data Tables*, 26, (1981), p.93.
- 7- R. Bengtsson, and S. Frauendorf, *Nuclear Phys., A* 405, (1983), p. 27
- 8- A.N. Mantri and P.C. Sood, *Physical Rev. C*, Vol. 9, No. 5, (1974), p. 2076.
- 9- M.A. Deleplanque, C.W. Beausang, J. Burde, R.M. Diamond, F.S. Stephens, R.J. McDonald, and J.E. Draper, *Physical Rev. C*, Vol. 39, No. 4, (1989), p. 1651.
- 10- Rainer M. Lieder, *Nuclear Phys., A* 347, (1980), p. 69.
- 11- E.S. Stephens, and R.S. Simon, *Nuclear Phys., A* 183, (1972), p. 257.
- 12- H.J. Mang, *Nuclear Phys.*, (1982), p. 149.
- 13- G. Sletten, S. Bjornholm, J. Borggreen, J. Pedersen, P. Chowdhury, H. Emling, D. Frekers, R.V.F. Janssens, T.L. Khoo, Y.H. Chung, and M. Kortelahti, *Physics Letters*, Vol. 135, No. 1,2,3, (1984), p. 33
- 14- D. Bonatsos, and A. Klein, *Physical Rev. C*, Vol. 29, No. 5, (1984), p. 1879.

# Proc *Third Radiation Physics Conf., Al-Minia, 13 - 17 Nov., 1996*

---

- 15-F.K. McGowan, N.R. Johnson, C. Baktash, I.Y. Lee, Y. Schutz, J.C. Wells, and A. Larabee, *Nuclear Phys.*, A 539, (1992), p. 276 .
- 16-D. Bonatsos, *Physical Rev. C*, Vol. 31, No. 6, (1985), p. 2256 .
- 17-J.P.Sweeney, R. Chapman, S. Arraddad, J. Copnell, A. Fitzpatrick, S.J. Freeman, F. Liden, J.C.Lisle, A.G. Smith, D.M. Thompson, S. Warburton, J.Simpson, S. Clark, P.D. Forsyth, S.Gale, P.M. Jones, J.F. Sharpey-Schafer, J. Smith, M.A. Bentley, A.M. Bruce, and D.M. Cullen, *Nuclear Physics Annual Report (1992-1993)*, p. 38, p. 40 .
- 18-M. Oshima, N.R.Johnson, F.K. McGowan, C.Baktash, I. Y. Lee, Y. Schutz, R.V. Ribas, and J.C. Wells, *Physical Rev.C*, Vol. 33, No. 6, (1986), p. 1988 .
- 19-J.Simpson, M.A. Riley, J.R. Cresswell, D.V. Elenkov, P.D. Forsyth, G.B. Hagemann, D. Howe, B.M. Ngako, S. Ogaza, J.C. Lisle, and J.F. Sharpey - Schafer, *Journal of Nuclear Phys.*, 31, (1987), p. 847 .
- 20-M. Murzel, U. Birkental, K.P. Blume, S. Hppner, H. Hubel, J. Recht, W. Schmitz, K. Theine, H. Kluge, A.Kuhnert, K.H. Maier, G.Hebbinghaus and H.Schnare, *Nuclear Phys.*, A 516, (1990), p.189 .
- 21-H.Hubel, M.Murzel, E.M. Beck, H.Klug, A.Kuhnert, K.H. Maier, J.C.Bacelar, M.A.Deleplanque, R.M. Diamond, and F.S. Stephens, *Z.Phys. A, Atomic Nuclei* 329,(1988), p. 289 .
- 22-A. Pieke, N. Mansour, A. Moussavi, H. Sanchez, H. Strecker, K.Grotz, J.Metzinger, and H.V. Klapdor, *Nuclear Phys.*, A 486, (1988), p. 335 .
- 23-S. Gil, R.Vandenbosch, A.J.Lazzarini, D.K. Lock, and A.Ray, *Physical Rev. C*, Vol. 31. No. 5, (1985), 1752 .
- 24-P.Aguer,G.Bastin, J.P. Thibaud, D.Barneoud, J.Boutet,and C. Foin, *Z. Physik, A* 285. (1978), p. 59 .

**FIGURE CAPTIONS**

**Figure ( 1 ) :**

The backbending ( $\theta - \omega^2$ ) plots for **Er**, **Yb**, and **Hf**. The dashed curve is for the (CP) model calculated values and the solid curve is for the experimental data.

**Figure ( 2 ) :**

Softness **S** as a function of the energy ratio  $R_4 = E(4)/E(2)$  for nuclides in the isotopic sequence of **Er**, **Yb**, and **Hf**. The positive **S** expressed as a stretching nuclei (soft rotors), and the negative **S** expressed as a shrinking nuclei (hard rotors).

**Figure (3) :**

The backbending plots as excitation energies  $E_x$  of the yrast states versus  $I(I+1)$ , for the even-even neighboring nuclei **Er**, **Yb**, and **Hf**.

**Figure (4) :**

The effective moment of inertia versus atomic number **Z** and the neutron number **N** for the three neighboring nuclei (**Er-Yb-Hf**).

**Figure (5) :**

The total angular momentum  $I_c(I_c+1)$ , at the critical angular momentum of the backbending  $I_c$ , versus the the neutron number **N** for [**Er-Yb-Hf**] isotopes.

- 349 -

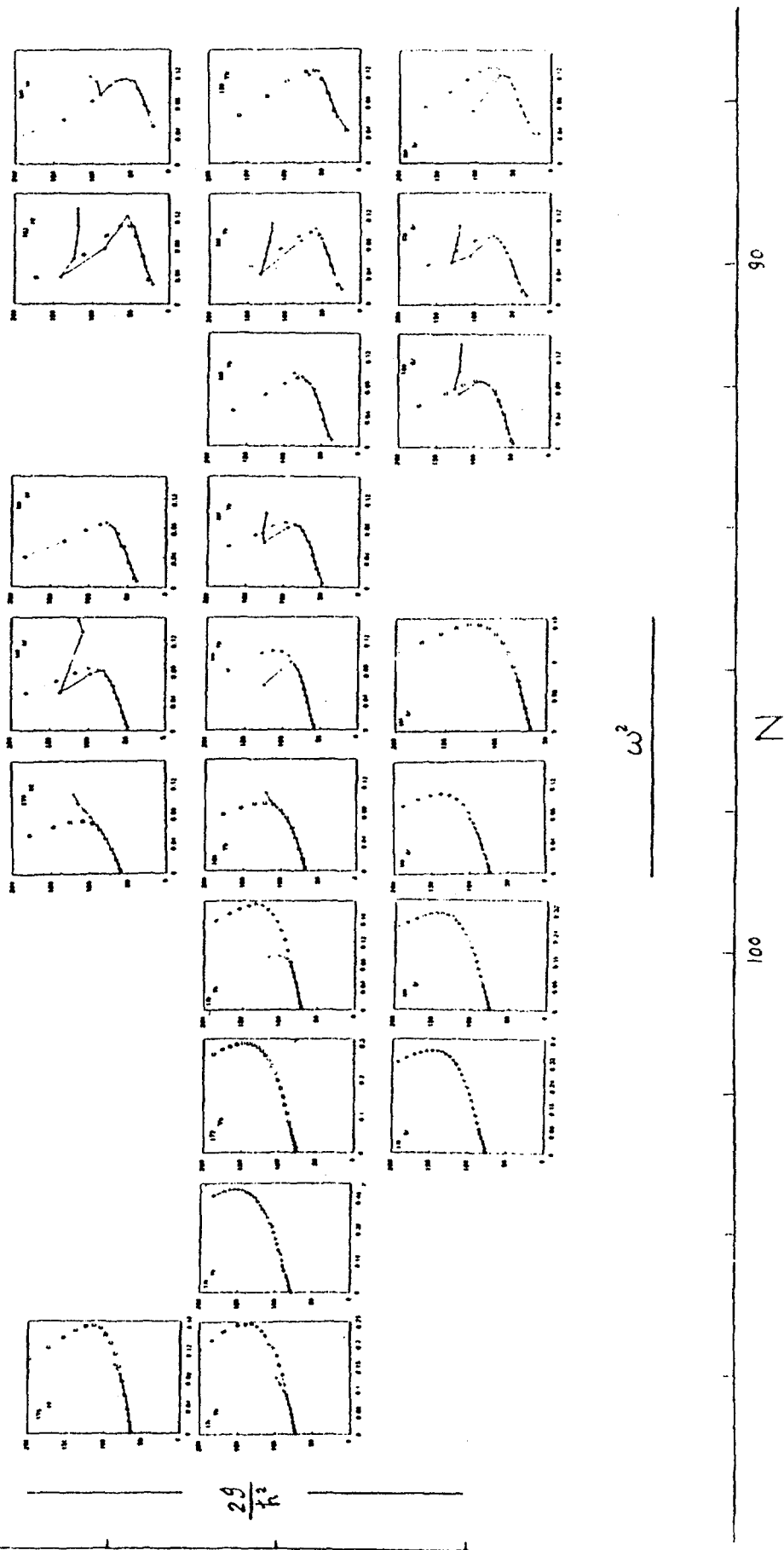
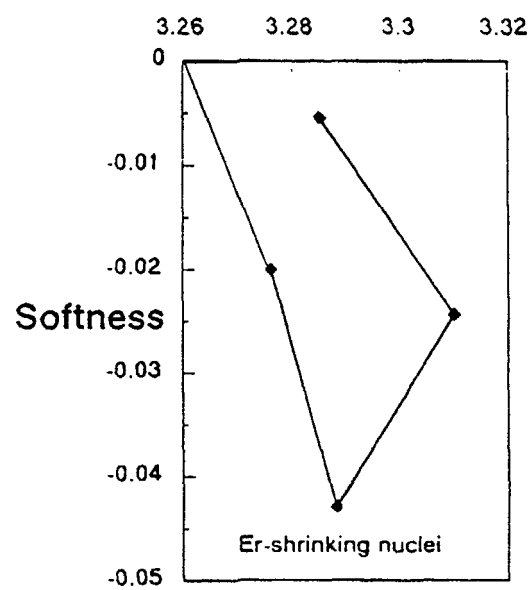
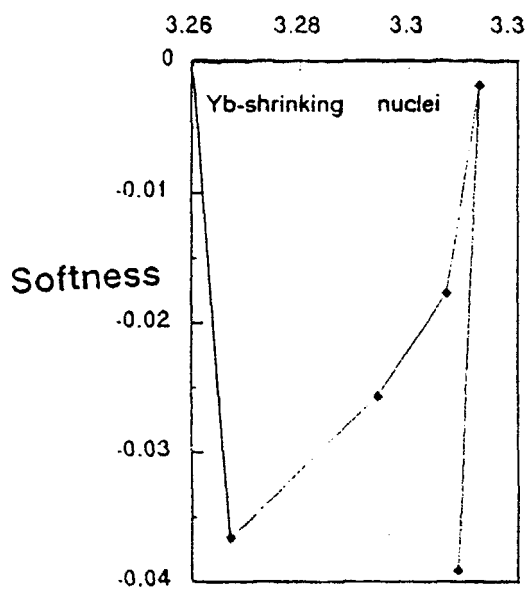
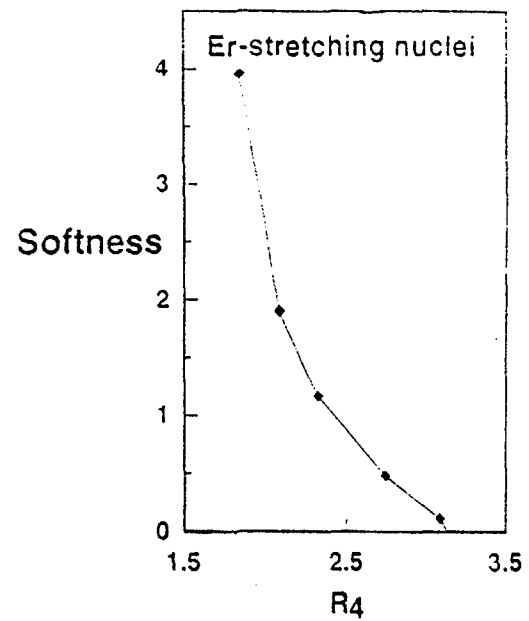
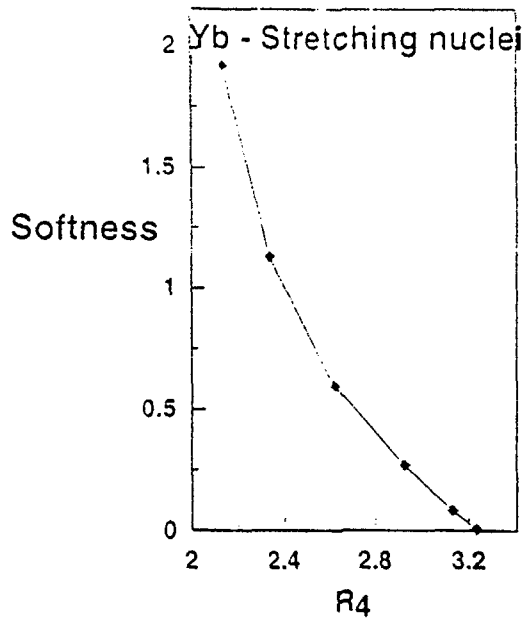
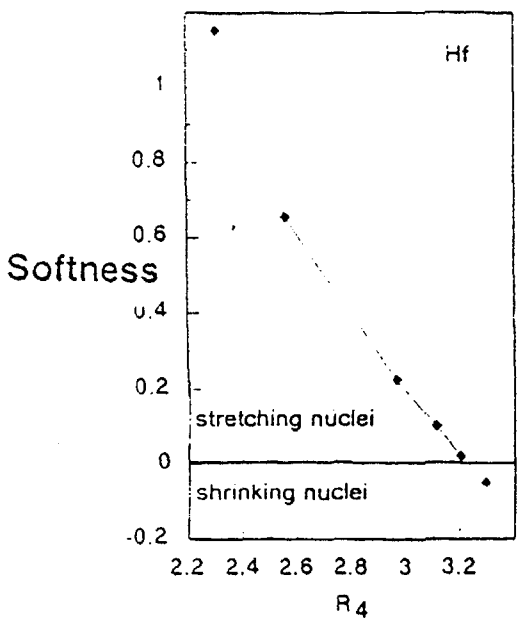


Figure (1)

- 350 -



- 3.51 -

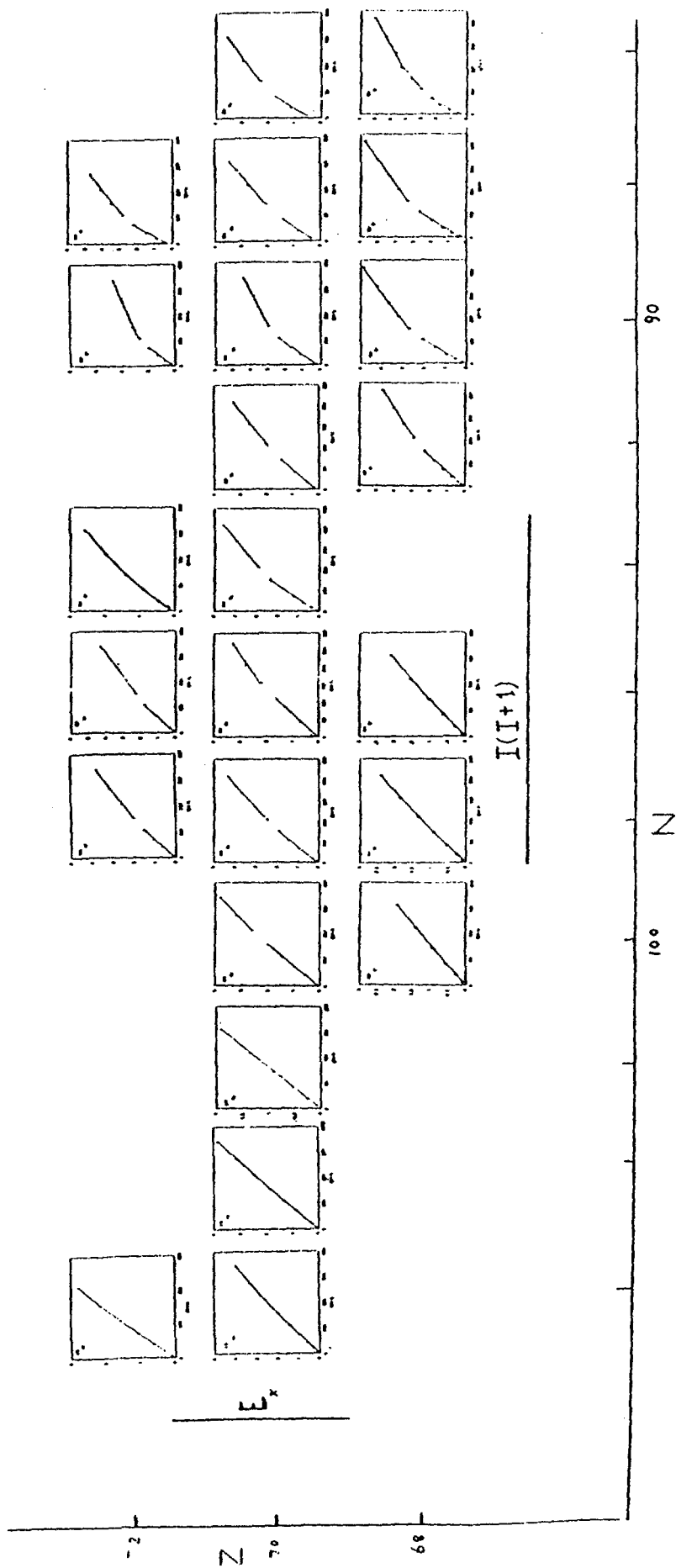


Figure (3)

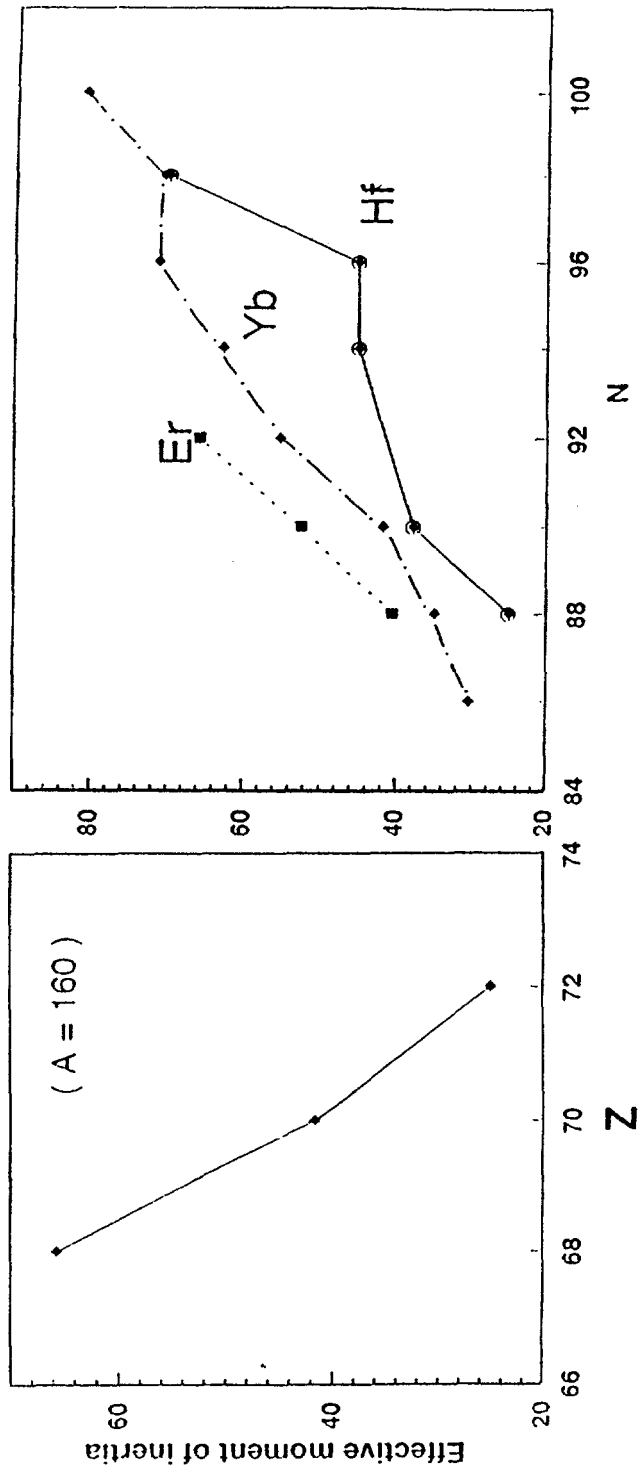


Figure (4)

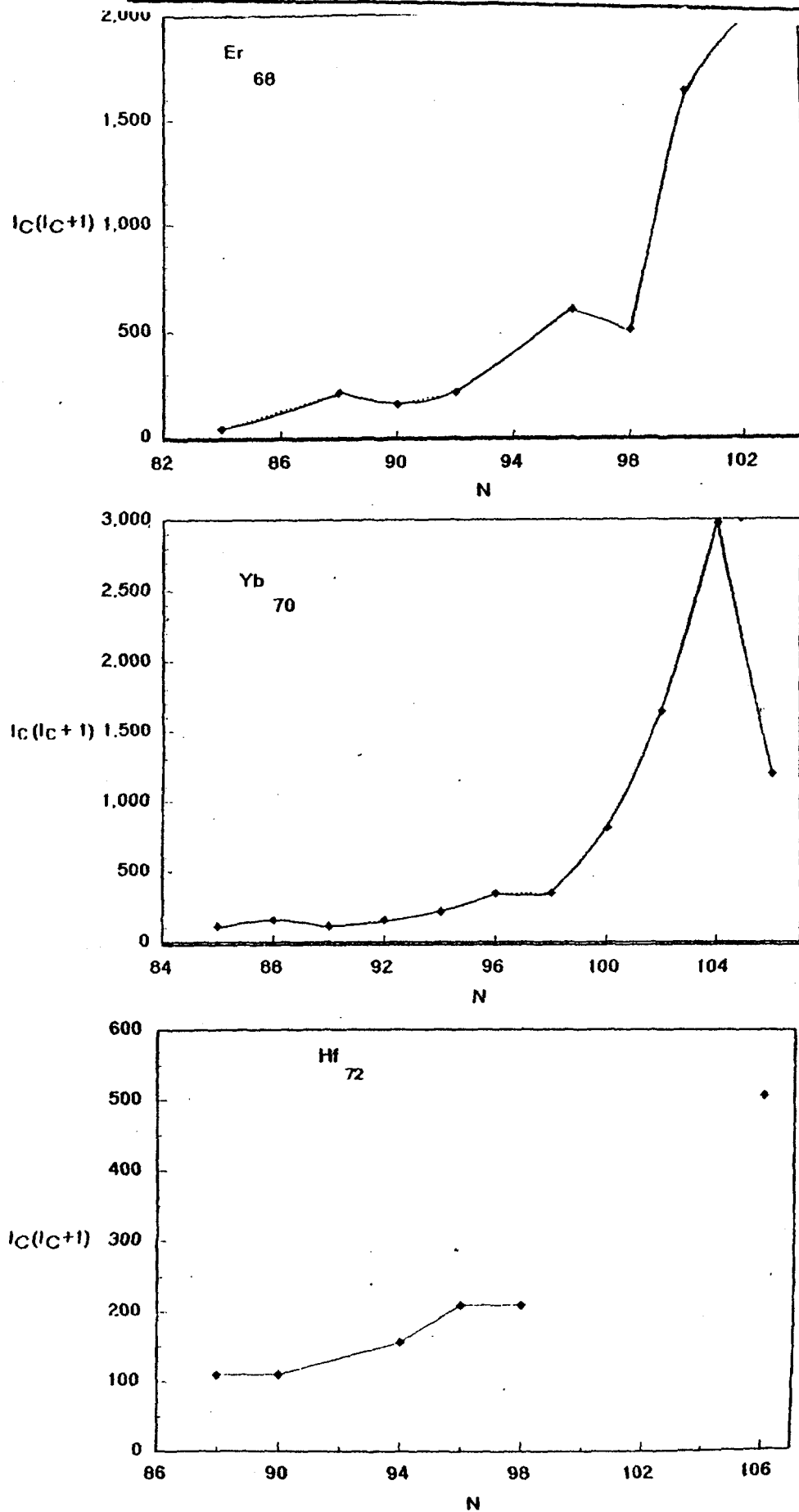


Figure (5F)

**SCIENTIFIC SESSION (13)**

**ENVIRONMENT**

*Keynote Lecture*

**COMPARATIVE ASSESSMENT OF ENVIRONMENTAL IMPACT OF  
DIFFERENT ELECTRICITY SOURCES**

**S. M. Rashad**

**National Center For Nuclear Safety and Radiation Control  
Atomic Energy Authority, Cairo, Egypt**

**ABSTRACT**

Nuclear power is a proven technology that makes an important contribution to energy supply. Given expected population increases, world total primary energy demand is expected to grow at 2.1% per year over the next 20 years, even if energy intensity improvements of 1% per year taken into account. Additional electricity generation is projected to amount to 8400 TWh. Coal and nuclear power are the only discernible supply alternative for responding to the bulk of this demand, while renewable sources have the potential to cover only a minor percentage of it. Expansion of nuclear power, which now provides about 7% of the world's commercial energy and 17% of its electricity, could provide at least an important part of the solution to the problem of increasing energy supply without increasing emissions. All fuel cycles within the electricity generating systems involve some health risks and lead to some environmental impacts, with both nuclear power and renewable energy systems tending to be in the lower spectrum of health risks. The effects of radiation exposures due to nuclear power production are much better known and more strictly limited than the effects of pollutants from other energy cycles. Furthermore, the costs of minimizing these impacts are largely internalized in nuclear power generation costs. In summary, all major energy sources be it coal, oil, natural gas, nuclear or hydropower, have a potential health and environmental impact. A consequent risk comparison between different energy sources has to include all phases of the whole energy cycle. Coal mine accidents have resulted in several 10000 acute deaths over the years.

Then came hydropower, also resulting in many catastrophes and losses of human lives, followed by oil and gas energy industry whose tribute in acute fatalities is expressed by more than 1000 lives lost. No estimate is available concerning later fatalities. Latest in the list is commercial nuclear energy, badly illustrated by the Chernobyl accident resulting officially in 31 acute fatalities, 145 latent fatalities and 135000 evacuated individuals, other health injuries resulting from, for example, radiophobia are not possible to quantify. Global population growth and economic development will continue during the coming decades, to result in an increased energy demand. This increasing demand will be partly coincident with the need to renew a significant part of current electricity generating installations.

Contributed Papers

**KINETIC STUDY ON THE SORPTION OF CESIUM  
ON SOME EGYPTIAN SOILS**

**A. S. Ibrahim\*, W.S. Hegazi\*, W. E. W. Abdel Malik \*\*,  
and N. H. M. Kamel\*\***

\* University College for Girls, Ain Shams University, Calro, Egypt

\*\* Radiation Protection Department, Nuclear Research Center,  
Atomic Energy, Authority, Calro, Egypt

**ABSTRACT**

Soil samples were collected from different locations of the Egyptian desert and were subjected to physical, chemical, mineralogical and sorption studies. Kinetic analysis were made on the sorption of radiocesium by these soil samples. Two models of analysis were treated namely; the one step first order model (the integer model), and the sum of the exponential components (the compartmental model). Statistical treatment of the results obtained showed that. For the one step first order model, samples having the lowest rate constant showed the longest reaction half life  $t^{1/2}$  (771 to 121 minutes), while the samples having higher rate constant the reaction half life decreased markedly ranging from 56 to 14 minutes. The compartmental model of analysis showed that the sorption of cesium of the soil samples involved two or three steps represented by two or three exponential equations. The equation of each step was calculated.

**PARTITIONING OF RADIOACTIVE CESIUM IN  
AQUATIC ENVIRONMENT**

**Tarek A. Ewais\*, Alaistar Grant,\*\* and A. T. , Abdel Fattah**

**\*Nuclear Power Plant Authority, Cairo, Egypt**

**\*\* University of East Anglia, School of Environment, UK**

**\*\*\*Atomic Energy Authority , Cairo, Egypt**

**ABSTRACT**

Scavenging of radionuclides by intertidal estuarine sediment are affected by several factors. Such sediment collected from sea coast of Norfolk county, UK, were subjected to specific analytical study to illustrate their physico-chemical properties on their sorption behavior of  $^{134}\text{Cs}$ . Clay fraction showed high uptake or  $K_d$  values compared to other sediment fractions. Kinetic analysis of the uptake curves showed a very fast followed by a vary slow one. On the other hand, the noticeable uptake by sand fraction (63-90  $\mu\text{m}$ ) was referred to the fine clay particles coating the sand particles. Other environmental factors affecting the  $K_d$  values such as water salinity, grain size, sediment treatment, and pH are disussed in the text.

**LEACHING OF RA-226 CONTAMINATED  
GRAVEL USING DIFFERENT AQUEOUS TREATMENTS**

**Abdel Megid Mamoon, Waleed H. Abulfaraj, and Moustafa A. Sohsah,**

**King Abdulaziz University, Jeddah, Saudi Arabia**

**ABSTRACT**

Investigation of the efficiencies of different aqueous leaching treatments was carried out on gravel artificially contaminated with Ra-226. The extent of leaching efficiency was determined in terms of Ra-226 and its daughter Rn-222. Liquid scintillation counting using high efficiency mineral oil based liquid scintillator was the technique adopted for measuring Ra-226 and Rn-222 leached off the contaminated gravel. Water, dilute solutions of barium chloride and HCL were used as leachants. Different masses of gravel were leached with 200 mL of leachant for various contact time periods. The leached Rn-222 activity measured was plotted vs the decay factor  $e^{-\lambda t}$ ; from which Rn-222 and Ra-226 originally present in the smaple were determined.

Several leaching parameters were tested; namely type of leachant, leachant volume/gravel mass ratio, leachant contact time, effect of varying Ba Cl<sub>2</sub> concentration, and successive leachings.

Optimization of the leaching parameters for desorption of Ra-226 off the contaminated gravel under laboratory conditions may help determine the ideal conditions for remediating soil contaminated with radium or chemically similar radionuclides.

### **OPERATION OF TEMPORARY RADIOACTIVE WASTE STORAGE FACILITY**

**Abdul Raheem A. Kinsara, Waleed H. Abulfaraj, Moustafa A. Sohsah,  
Salah El-Din M. Kamal, and Abdel Megid Mamoon**

**Nuclear Engineering Department, Faculty of Engineering, King Abdulaziz University  
Jeddah - 21413, Saudi Arabia**

#### **ABSTRACT**

Radionuclides of various half lives have been in use for several years at different departments of king Abdulaziz University, the University hospital, and Research Center. The use of unsealed radionuclides in many laboratories, resulted in considerable amounts of solid and liquid radwaste, mainly radiopharmaceuticals.

To avoid accumulation of radwastes in working areas, a temporary radioactive waste storage facility was built. Segregation of radwastes according to type was carried out, followed by collection into appropriate containers and transfer to the storage facility. Average radiation dose rate inside the store was maintained at about 75  $\mu\text{Sv h}^{-1}$  through use of appropriate shielding. The dose rates at points one meter outside the store walls were maintained at about 15-20  $\mu\text{Sv h}^{-1}$ . Utilization of radioisotopes during the period of 1991-1995 resulted in a volume of about 1.8m<sup>3</sup> of solid radwaste and about 200 L of liquid radwaste.

Records of the store inventory are maintained in a computer database, listing dates, types, activities and packaging data pertinent to the radwastes delivered to the store. Quality assurance procedures are implemented during the different stages of the radwaste collection, transportation, and storage.

Construction and operation of the storage facility comply with radiation safety requirements for the workers handling the radwastes, the public and the environment. The capacity of the storage facility is such that it will accommodate storage of generated radwastes of long half life up to year 2016. Permanent disposal of such radwastes may be indicated afterwards.

### **INFLUENCE OF HUMIC SUBSTANCES OF FIXATION OF FISSION PRODUCTS IN SILICATE MEDIA**

**I. S. Shaban, F. Macàsek**

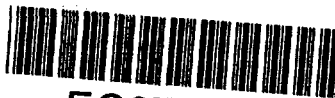
**Department of Nuclear Chemistry, Faculty of Natural Sciences,  
Comenius University, Bratislava, Slovakia**

#### **ABSTRACT**

Clay minerals are exploited in both the land and sea emplacement and as backfill materials for the storage of radioactive waste to increase their radioactive safety. In addition, the influence of inorganic constituents, humic substances may modify the speciation of pollutant cations by solubilisation of metal ions and formation of organic coatings which may block the ion-exchange sites of clays.

The objective of the present work was to characterize the effect of humic acid addition on the capacity of inorganic sorbents to sorb radioactive caesium and strontium. Montmorillonite has been Particularly studied because the high cation exchange capacity and swelling properties make them suitable for waste disposal.

However, an accumulation of humic acid on disposal containers during the time of waste treatment may change the mobility of fission products. The results are treated in respect of sorption isotherms both of humic substances and sorbed ions.



**KINETIC STUDY ON THE SORPTION OF CESIUM  
ON SOME EGYPTIAN SOILS**

A.S.Ibrahim, W.S.Hegazi \* W.E.Y.Abdel Malik and N.H.Kamel  
Radiation Protection Department, Nuclear Research Center, Atomic Energy Authority  
P.O 13759 Cairo, Egypt and \* University College for Girls, Ain. Shams Cairo Egypt .

Soil samples were collected from different locations of the Egyptian desert and were subjected to physical , chemical, mineralogical and sorption studies. In this work the kinetic analysis were made on the sorption of radiocesium by these soil samples . Two models of analysis were used in this study namely ;the one step first order model (integer method) and the sum of the exponential components (compartmental model) . Statistical analysis of the obtained experimental results showed that :

a) for the first order model : samples having the lowest rate constant showed the longest reaction half-life time  $t_{1/2}$  ( 771 to 121 minutes )while the  $t_{1/2}$  ranged from 14.5 to 47 minutes for sampled of higher rate constant .

b) The compartmental model of analysis showed that the sorption of cesium on the soil samples involved two or three steps represented by two or three exponential equations ( except two samples ; their sorption reaction proceeded in four steps ) .

**INTRODUCTION**

Many studies have been carried out to determine the factors affecting the extent of sorbing the radionuclides on the clay materials<sup>(1-5)</sup> . The mineralogical and chemical composition of the clay materials play an important role in the sorption process<sup>(6-8)</sup> . The unexpanding clay ; illite and micas sorb more Cs than the expanded layer silicates , montmorillonite and vermiculite while sorption of Cs on quartz is negligible in comparison to mica<sup>(9)</sup> . The competing ions and the pH of the system were found to have variable effects on the sorption depending on the radionuclide and the soil composition<sup>(10-12)</sup> . The particle size of the clay material has great effect on the sorption of the radionuclides<sup>(4,13,14)</sup> . The time needed for equilibrium to be attained depends upon the mechanism by which the radionuclide is transferred to the solid phase ranging from milliseconds up to years <sup>(15-18)</sup> .

The present work is dealing with the study of the effect of the contact time on the sorption of radiocesium on some Egyptian soil sediments. Statistical analysis of the different phases of these reactions is included in this study. This study may help in the selection of some kinds of the Egyptian soil sediments as cheap natural materials for the removal of the radionuchdes from the liquid radioactive wastes.

### EXPERIMENTAL

The effect of contact time on the sorption of  $^{134}\text{Cs}$  on the soil samples (collected from different locations of the Egyptian deserts) was investigated by mixing 0.5 g of the sample with 100 ml of 0.01 M  $\text{CsCl}$  solution traced by  $^{134}\text{Cs}$  in polyethylene bottles and the suspension was mixed thoroughly. After different time intervals, ranging from 1, 2, 3, ..., 60 minutes and up to 7 days, the bottles were centrifuged at 2000 rpm, and 3 ml from the liquid in each bottle were withdrawn and counted to represent the cesium concentration in liquid phase at time  $t$  ( $C$ ), and returned back into the bottle to keep the volume constant. A blank solution was prepared under the same conditions but without the soil sample, and its counting rate was considered to be equivalent to the original zero time concentration, ( $C_0$ )

The percentage uptake at a certain time can be calculated from the relation :

$$\text{The percentage uptake} = \frac{C_0 - C}{C_0} \times 100 \quad (1)$$

### RESULTS AND DISCUSSION

The change in the percentage of Cs uptake by the soil samples with contact time was plotted on a semilog scale as shown in Figure (1). More than 50 % of the initial Cs concentration has been sorbed over the first 60 minutes for most of the examined samples then further increase of 30-45 % over the next two to three hours, after which, it remained fairly constant. (exceptions are samples WR-15, Q2 and 78-A, where the maximum uptake hardly reached 50 %, while sample Q7 showed uptake just above 20 %)

Two models were used to interpret the sorption mechanism of Cs on the soil samples namely ;

- a) The one step first order model of analysis (integer method), and
- b) The compartmental model of analysis.

#### a- The One Step First Order Model of Analysis

The distribution of the radionuclide between the soil and the aqueous phase is expressed by the sorption coefficient ( $R$ );

$$R = \frac{C_0 - C}{C} \times \frac{V}{m} \quad (2)$$

Where;

$C_0$  and  $C$  are the initial and equilibrium concentrations of the radionuclide in the aqueous phase, respectively.  $V$  is the volume of the aqueous solution and  $m$  is the mass of the soil sample .

Applying the first order kinetic equation<sup>(10)</sup> of the sorption coefficient :

$$R_t = R_\infty (1 - e^{-kt}) \quad (3)$$

where,

$R_t$  is the sorption coefficient at time  $t$  .

$R_\infty$  is the sorption coefficient at infinite time (steady state) ,

$t$  is the time of the reaction in minutes, and

k is the rate constant of the reaction (in minutes<sup>-1</sup>).

Equation (3) is linearized as;

$$\ln \left( 1 - \frac{R_t}{R_\infty} \right) = -kt \quad (4)$$

By plotting  $\ln \left( 1 - \frac{R_t}{R_\infty} \right)$  against the contact time ,t, till the sorption coefficient ( $R_t$ ) was nearly constant, straight lines have been obtained. Figure (2) show the fitting of the experimental data to the first order sorption reaction equation. This indicates that the sorption of Cs by the soil samples can be treated using the first order kinetic model. The time limit for this model to be applied was found to be ranged from 60 up to 240 minutes for the different samples. The rate constant (k) as well as the half life times ( $t_{1/2}$ ) of the reactions were calculated from the slope of the straight lines as shown in table (1).

It could be shown from table (1) that, the samples having the lowest rate constant showed the longest half time ( $t_{1/2}$ ) as recorded for the samples V-1 and WR-15 (771 and 121 minutes, respectively) while the shortest  $t_{1/2}$  was observed for sample 63.

Generally, the extent of sorption over a long period is attributed to limiting rates of diffusion of radionuclides into internal rock pores or slow chemical reaction (mineralization) between rock surface and surface-mobile sorbed nuclide<sup>(19)</sup>. Moreover, Sawhney<sup>(20)</sup> reported similar results on applying the first order kinetic model for sorption of Cs with Ca-vermiculite, the equilibrium was reached after 500 hours. Aksoyoglu<sup>(10)</sup> found that sorption of Cs by kaolonite samples is a rapid reversible process, due to the large ionic radii of Cs ions which do not permit Cs to penetrate the interlattice structure. The influence of contact time on the sorption of Cs and Sr by smectite samples has been studied by Abou-Jamous<sup>(13)</sup>, who showed that Cs sorption was slower than Sr sorption. Also, kinetic studies of radiocesium uptake by fresh water-solids showed that the Cs uptake attained equilibrium after contact times ranging from minutes to hours<sup>(5,21,22)</sup>.

**b-The Sum of the Exponential Components (Compartmental Model)**

The compartmental model is based on the movement of certain molecules successfully between the different components of a system in different steps, e.g. certain ions move from solution to the surface of the clay, then to the hydrated layer, diffused to the inter layer crystal structure, then reacts and exchanges with other ions...etc. each step of the reaction proceeds with a constant rate and is known as a compartment or a component. The number of compartments determines the number of variables or phases of reactions. This number of variables determines the minimum number of exponential terms occurs in the system.

Solomon<sup>(23)</sup> constructed an equation governing the movement of a tracer between the compartment which follows the first order kinetics equation in its steady state, in which the exponential components are expressed in series and represented as:

$$Y = A_1 e^{-k_1 t} + A_2 e^{-k_2 t} + \dots + A_\infty e^{-k_\infty t} \quad (5)$$

170

# PROC *Third Radiation Physics Conf., Al-Minia, 13 - 17 Nov., 1996*

4

Where.

$A_1, A_2, \dots, A_\infty$  are the individual components describing the different phases of Cs sorption on the soil samples, having different rate constants  $k_1, k_2, \dots, k_\infty$  respectively. The  $t_{1/2}$  for each step of the reactions could be determined from the equation  $t_{1/2} = 0.693 / k$ .

This compartmental model was carried out by analysis of the curves in (Figure 3) resulting from plotting the percentage of Cs remained in the aqueous phase as a function of contact time. The values of the coefficient ( $k$ ) and the exponent for each term were given in Table(2). To explain the method of analysis, Sample 63 is chosen as an example. The curve obtained in (Figure 4) of sample 63 is graphically found to follow the equation;

$$Y = 0.284 e^{-1.45 \times 10^{-2} t} + 0.144 e^{-2.25 \times 10^{-3} t} + 1.539 e^{-3.18 \times 10^{-7} t}$$

This equation described the total sorption reaction as three distinct first order reactions.

Table (2) shows that the sorption of Cs by the soil samples involves two or three reaction steps represented by two or three exponential equations (except sample 46-48 km and K-S, showed four reaction steps). The half life times for each reaction step were calculated and summarized in Table (3).

Comparing the results obtained from the kinetic treatment and the mineralogical analysis of the samples, previously reported by the authors<sup>(24)</sup>, it can be seen that the samples consisting of high amount of kaolonite showed the smallest number of reaction steps as in the case of sample Q7. On the other hand, the samples of higher percentage of smectite or vermiculite showed the highest number of sorption reaction steps as in the case of K-S & 46-48 Km and V-1 samples.

The fast step of the reactions is extended to a few seconds or minutes, and may be attributed to the adsorption of Cs ions from the bulk solution onto the surface of the particles (physical adsorption). While the other slower steps may be due to diffusion of Cs ions from the surface of the particles of the soil to the external and internal lattice structure.

The slow steps of the reactions extended from hours to several days. Similar findings were reported by Benez<sup>(5)</sup> and Aksoyoglu<sup>(10)</sup> with some difference in the number of the reaction steps and their half times. This differences may be due to the different composition of the solid phases used (soil samples). Benez<sup>(5)</sup> interpreted his data by sequential three steps of exchange of radiocesium between the bulk solution, hydration shell around the sediment grain surface and the interior of grains. Austin and Nathaniel<sup>(25)</sup> and Filipovic et al.<sup>(26)</sup> assumed a rapid exchange of radiocesium on the surface sites of suspended solids followed by slower absorption into the solid. Sawhney<sup>(20)</sup> found that. Cs sorption by vermiculite and montmorillonite is started initially at the interlayer edges and then through the channels spaces between the layers, where as Cs can diffuse into the minerals interlayers. Thus, all exchange sites in montmorillonite remain equally available and an exchange equilibrium is attained quickly.

**REFERENCES**

- 1- Beck C.W. ,1978, *J. of Archaeological Science* 5:343- 354 .
- 2- Aksoyoglu S. ,1990, " Sorption of Cs on Marl " Progress Report (Paul Scherrer Institute ) PSI Technical Report TM-43-90-53 Swetzerland .
- 3- Gutierrez M., Funes H.R.,1991, *J. Environment Radiochemica* 13:271- 282 .
- 4- Coleman N.T., Grang D., Lewis R.T. ,1963, *Soil Sci. Soc. Amer. Proc.* 27: 278- 289 .
- 5- Benez P. ,1992, *J. of Radioanal. and Nuclear Chemistry Articles* 132(2) : 225- 239 .
- 6- Jacobs D.G. ,1960, *Health Physics* 4: 157-163 .
- 7-Tamura T. 1963 , *Clays and Clay Minerals* , 5 : 389 - 398 .
- 8- Allard B., Kipatsi H.Rudgerg J. ,1977, "Sorption of Long-Lived Radionuclides by Clay and Rock " KBS Technical Report 55 Sweden .
- 9- Lieser K.H.,Stienkoff T. ,1989, *Radiochemica Acta* 46: 39- 47 .
- 10- Aksoyoglu S. ,1989, *J. Radioanal. Nuclear Chemistry* 140(2) : 301-313 .
- 11-Anderson K. and Allard B. ,1983 , "Sorption of Radionuclides on Geologic Media - a Literature Survey 1- Fission Products, KSB Technical Report 83-07 Sweden .
- 12-Benez P. , Borvec Z., Strejc P. ,1986, *J. of Radioanal. and Nuclear Chemistry Articles* 99:407 .
- 13-Abu-Jamous J. Kh, 1992, *J. of Radioanal. and Nuclear Chemistry Aricles* ,99:407 .
- 14-Tamura T. , Jacobs D.G. ,1961 , *Health Physics* 5: 149 - 154 .
- 15- Fukui M. ,1978, *Health Physics* 35 :555- 562 .
- 16- Parker J.C., Valocchi A.J. ,1986, *Water Research Resources* 22: 399- 407 .
- 17- Jacob R. ,1983 , *Water Resources Research* 19(5) : 1231-
- 18- FujikawY. , Fukui M. ,1990, *J. Contaminant Hydrology* 6: 85- 102 .
- 19- Mc Kinley I.G. , Alexander R. , 1993, . of Contaminant Hydrology 13(2) : 249- 259 Amestrdam.
- 20- Sawhney B.L. ,1967, *Soil Sci Soc. Amer. Proc.* 31: 181 - 183 .
- 21- Yousef Y.A. ,1970, *Radioactivity Transport in Water " Summary Report* ORO - 490- 20 .
- 22-Garder , O. S. , 1964 , *Inter. J. Air and Water Pollut.* 8: 229 .
- 23- Conar C. L. , ,1960 , " Mineral metabolism " VI part A , Solomon , A . K . , compartemental methods of kinetic analysis , Chapter 5 p . 119 - 166 .
- 24- Abdel Malik W.E.Y. , Heegazy W.S. , Ibrahim A.S. and Kamel N.H.M. , 1992, *Proc. Symp. of the 5th Conf. Nucl. Sci & Appl. ,Cairo ,Egypt* 16-20 Feb 1992, vol I, p. 496-503.
- 25- Austin H.T., Nathaniel T. ,1952 , *J. Amer. Chem. Soc.* 74:4169-4173 .
- 26- Filipovic N. , Vincekovic Li , Brevic D. ,1990, *J. of Radioanal. and Nuclear Chemistry Articles* . 139(2) : 239- 247 .

**Table (1)**

**The Half Times for the First Order Kinetic Equation of Cs Sorption By the Soil Samples**

Sample	First Order Kinetic Equation		Time Limit (min.)
	K	T <sub>1/2</sub> (min)	
V-1	-0.000898	771.72	240.00
46-48Km	-0.025680	26.99	120.00
K-S	-0.023840	29.07	240.00
74-B	-0.015180	45.65	240.00
78-C	-0.020480	33.84	240.00
Fay-B2	-0.014580	47.53	180.00
63	-0.047910	14.46	120.00
S11	-0.012400	55.89	180.00
WR-15	-0.005720	121.15	120.00
Q2	-0.022124	31.32	240.00
78-A	-0.019500	35.54	240.00
Q7	-0.023210	29.86	60.00

**Table( 2 )**  
**Equations of The Different Steps For Cs Sorption on The Soil Samples**

SAMPLES	SORPTION EQUATION
V-1	$Y = 0.141e^{-3.45 \times 10^{-3} t} + 0.514e^{-2.50 \times 10^{-3} t} + 1.341e^{-4.90 \times 10^{-5} t}$
46-48 km	$Y = 0.202e^{-2.67 \times 10^{-2} t} + 0.355e^{-1.11 \times 10^{-2} t} + 0.261 e^{-2.18 \times 10^{-3} t} + 1.227 e^{-1.18 \times 10^{-5} t}$
K-S	$Y = 0.306e^{-1.53 \times 10^{-2} t} + 0.314e^{-4.34 \times 10^{-3} t} + 0.039 e^{-1.59 \times 10^{-4} t} + 1.311 e^{-6.59 \times 10^{-8} t}$
74-B	$Y = 0.350e^{-1.05 \times 10^{-2} t} + 0.206e^{-1.14 \times 10^{-3} t} + 1.419e^{-2.48 \times 10^{-8} t}$
78-C	$Y = 0.354e^{-1.11 \times 10^{-2} t} + 0.197e^{-1.06 \times 10^{-3} t} + 1.417e^{-1.97 \times 10^{-6} t}$
FAY-B2	$Y = 0.218e^{-6.41 \times 10^{-3} t} + 0.216e^{-1.17 \times 10^{-3} t} + 1.553e^{-1.48 \times 10^{-8} t}$
63	$Y = 0.284e^{-1.45 \times 10^{-2} t} + 0.144e^{-2.25 \times 10^{-3} t} + 1.539e^{-3.18 \times 10^{-7} t}$
S-11	$Y = 0.149e^{-4.41 \times 10^{-3} t} + 0.238e^{-1.69 \times 10^{-3} t} + 1.603e^{-2.36 \times 10^{-6} t}$
WR-15	$Y = 0.166e^{-1.94 \times 10^{-3} t} + 0.132e^{-2.62 \times 10^{-4} t} + 1.696e^{-3.09 \times 10^{-6} t}$
Q-2	$Y = 0.162e^{-4.81 \times 10^{-3} t} + 0.111e^{-5.99 \times 10^{-4} t} + 1.717e^{-8.28 \times 10^{-8} t}$
78-A	$Y = 0.167e^{-3.78 \times 10^{-3} t} + 0.089e^{-4.74 \times 10^{-4} t} + 1.728e^{-1.35 \times 10^{-7} t}$
Q-7	$Y = 0.101e^{-1.47 \times 10^{-3} t} + 1.891e^{-2.22 \times 10^{-7} t}$

- 365 -

**Table (3)**  
**The Half Times of the Different Steps of Cs Sorption**  
**( Applying the Compartmental Method of Analysis)**

Sample	Fast step	Slow steps		
	step 1 ( $t_1$ min)	step 2 ( $t_2$ min)	step 3 ( $t_3$ min)	step 4 ( $t_4$ min)
V-1	87.25	124.86	6076.57	-
46-48 Km	11.26	27.1	317.89	25501
K-S	19.71	69.33	1892.53	4564803.6
74-B	28.71	263.95	1213354.25	-
78-C	27.1	283.72	152661.89	-
Fay-B2	47.02	256.53	203306.46	-
63	20.7	133.97	946263.69	-
S11	68.17	177.18	128139.75	-
WR-15	155.22	148.52	97455	-
Q2	62.56	502.36	8368251.36	-
78-A	79.61	634.84	2213547.45	-
Q7	203.87	134.94	-	-

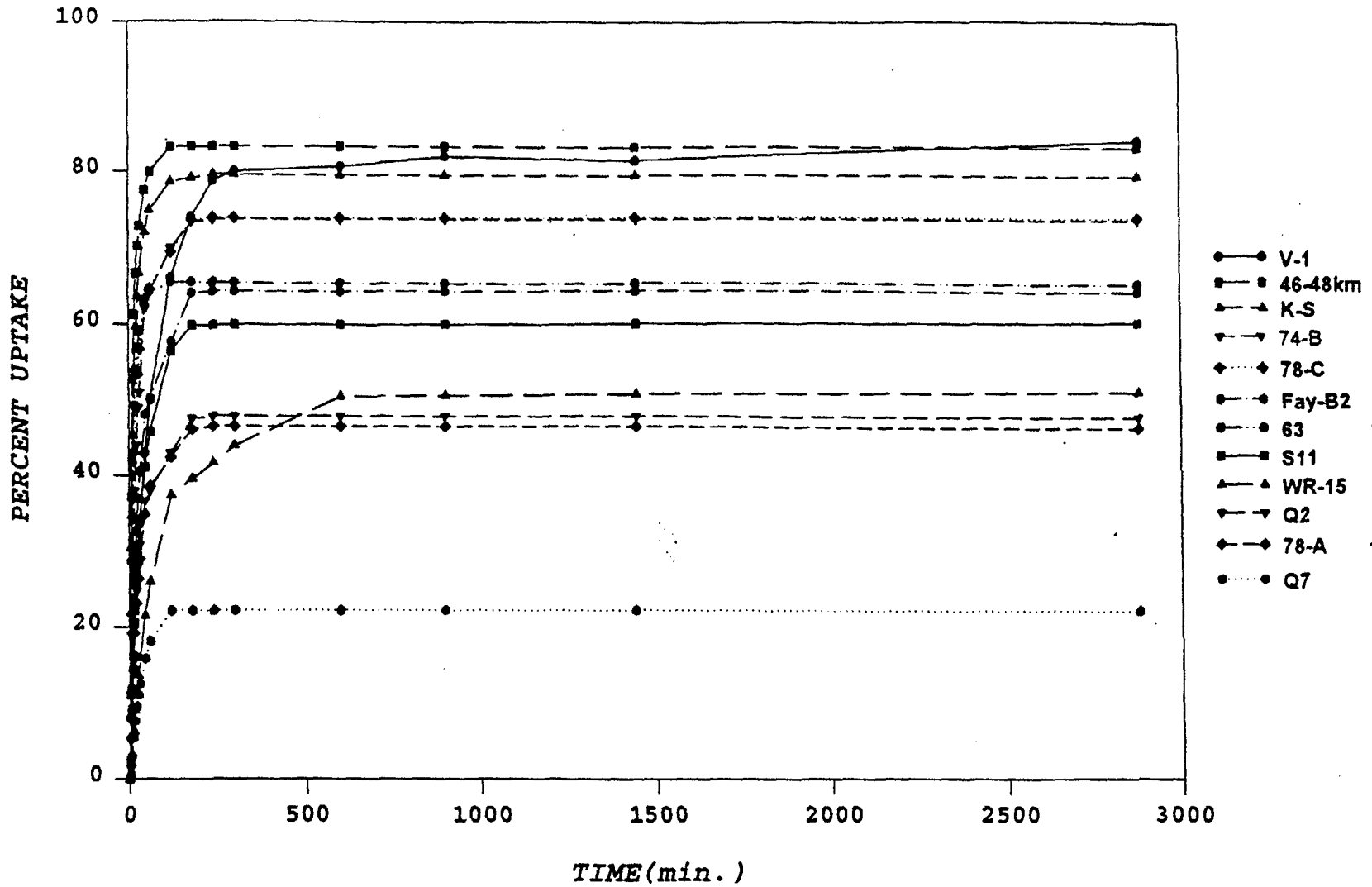
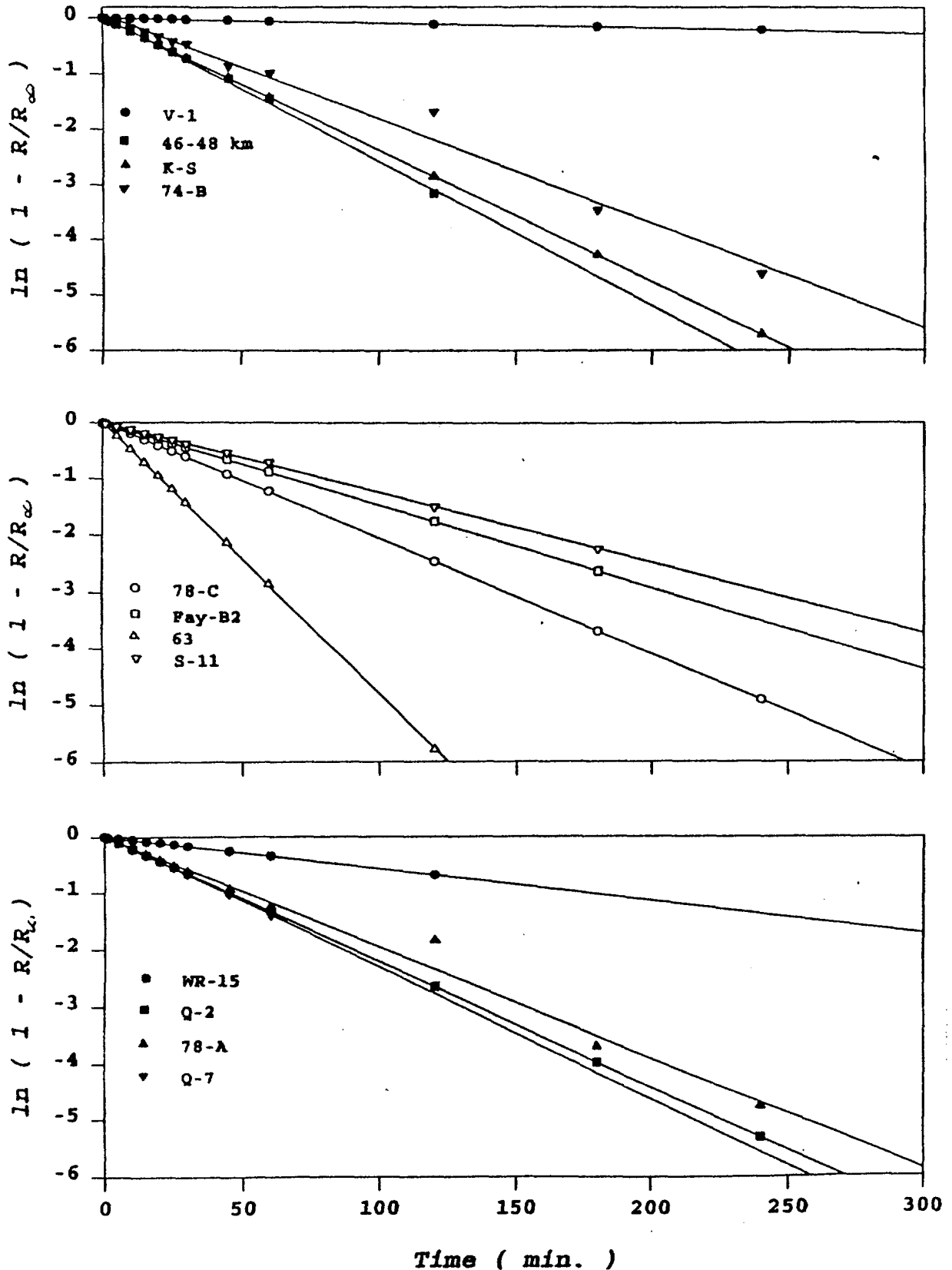


Fig. (1): Sorption Of Cs By The Soil Samples As a Function Of Contact Time .

# Proc Third Radiation Physics Conf, Al-Minia, 13 - 17 Nov, 1996



Fig(2): First Order Sorption Model For The Studied Soil Samples .

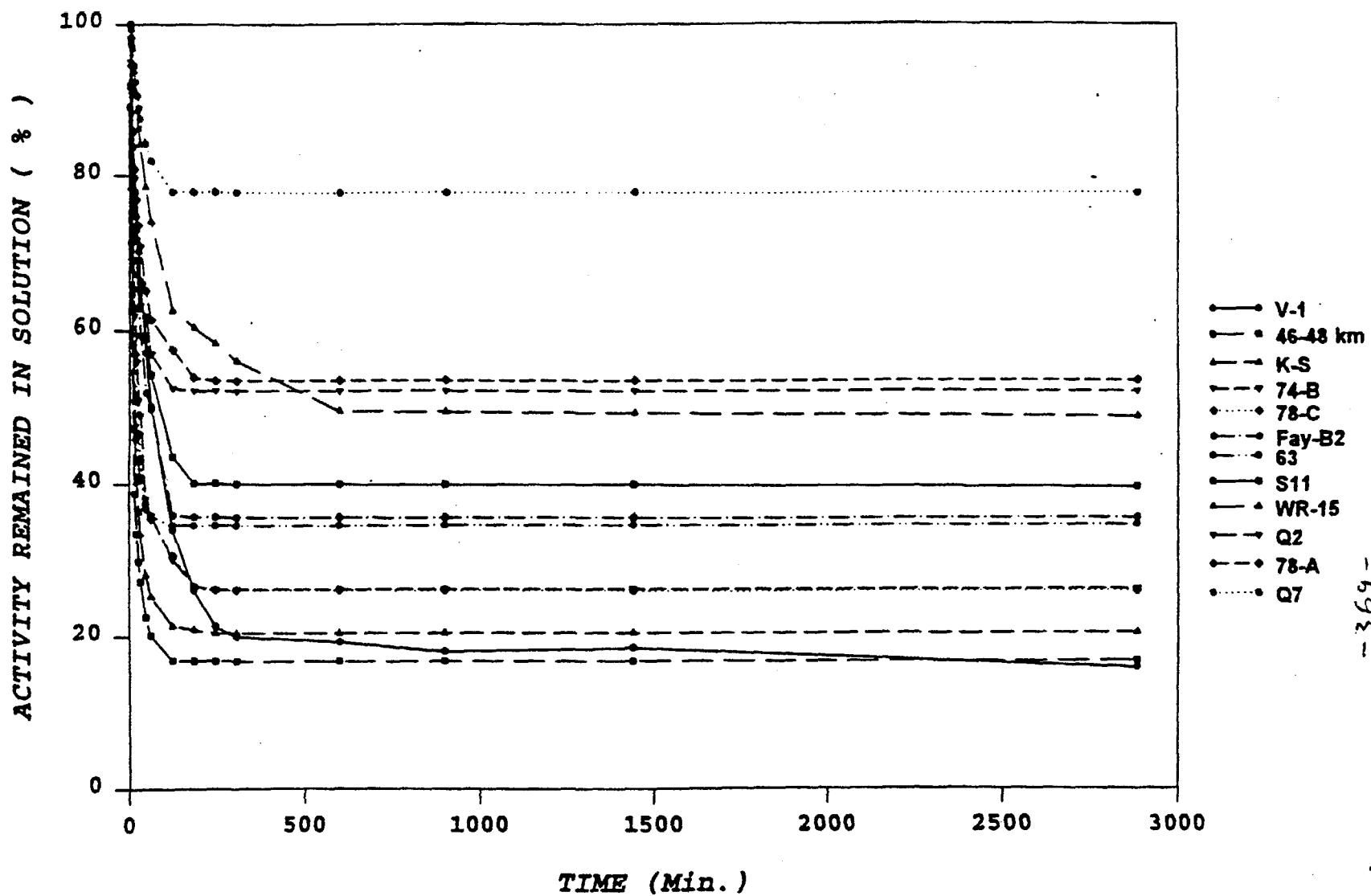


Fig. (3): Percentage of Cs Remained In The Aqueous Phase As a Function Of Contact Time .

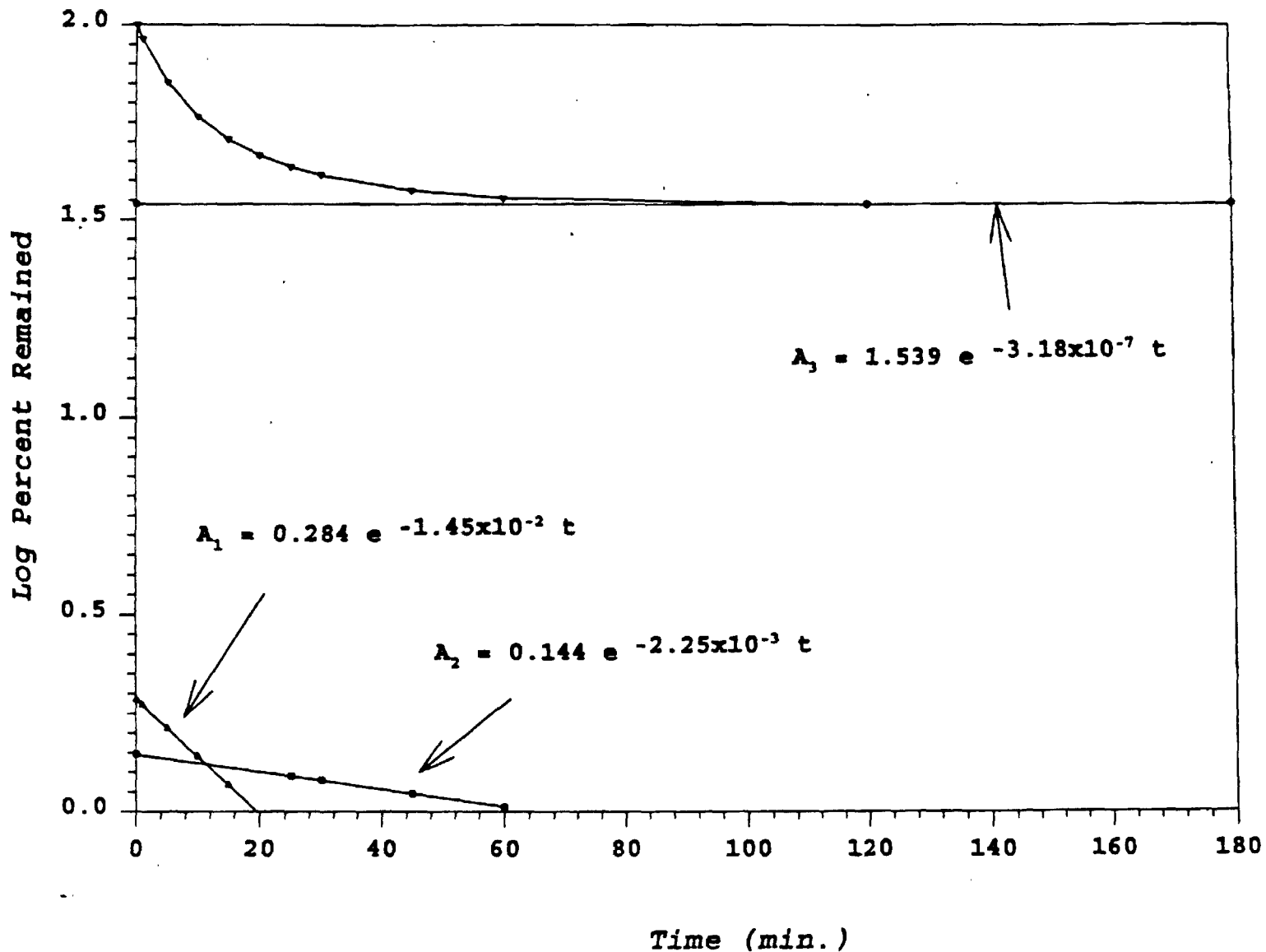


Fig.(4): The Compartamental Model of Analysis for Cs<sup>+</sup> Sorption on Sample 63 .

## PARTITIONING OF RADIOACTIVE CESIUM IN AQUATIC ENVIRONMENT

BY

Tarek A. Ewais, NPPA, Cairo, Egypt  
Alastair Grant, Univ. of East Anglia, School of ENV. UK  
<sup>1</sup>Abdel Fattah A. T., AEA, Cairo, Egypt

### ABSTRACT

*Scavenging of radionuclides by intertidal estuarine sediment are affected by several factors. Such sediment collected from sea coast of Norfolk county, UK, were subjected to specific analytical study to illustrate their physico-chemical properties on their sorption behavior of  $^{134}\text{Cs}$ . Clay fraction, as expected, showed high uptake or  $K_d$  values compared to other sediment fractions. Kinetic analysis of the uptake curves showed a very fast step followed by a very slow one. On the other hand, the noticeable uptake by sand fraction (63-90 $\mu\text{m}$ ) was referred to the fine clay particles coating the sand particles. Other environmental factors affecting the  $K_d$  values can be arranged according to their magnitude in the following descending order: water salinity, grain size, sediment treatment and pH.*

### INTRODUCTION

The principal sources of artificial radionuclides are fallout from nuclear detonation, direct and indirect wastes from nuclear reactor operations, wastes from medical, scientific and industrial uses of radionuclides. As the world moves into the twenty-first century, more demands for energy are created. To satisfy this need, nuclear energy will play an increasingly role and will present an increasing problem to society.

Due to radioactive releases from nuclear installations into the water sources either through normal or accidental operation and from fallout, the sea is considered the ultimate reservoir for these releases. Thus, the marine ecological system is a critical

---

<sup>1</sup>Correspondance Address:  
Prof. Ahmed Taher Bdel Fattah  
NPPA, P.O.Box 108 Abbasia  
Post No. 11381 Cairo, Egypt

pathway for transporting the radioactivity via the food-chain to man (Hamilton et al 1993)

Radionuclides can be removed from the sea, to a certain extent, by biota and sedimentary particles. Such phenomena of sedimentary particles known as sorption capacity is affected by different factors including: the physico-chemical state of the sediment, the radionuclides and the reaction medium (seawater) (Mackinley and Alexander, 1992).

Distribution or partitioning coefficients referred to as ( $K_d$ ) is generally used to describe the reaction between radionuclides concentrations in sediment and water (Duursma and Gross, 19971, Mckinley and Alexander 1992).

The aim of the present work is to obtain information for predicting the fate of radiocesium that may be released into the aquatic environment. Such information include accumulation of radionuclides by sediments in marine estuarine and fresh water system, and the main factors effecting the  $K_d$  which might be considered when modeling the transport of radionuclides.

## EXPERIMENTAL

### Sample preparation:

The study area is south to London by 120 km on the eastern coast called Great Yarmouth of Norfolk county. At this site 3 rivers: Yare, Waveney and Bure drain 2/3 of Norfolk county at Yarmouth. Samples were divided into subsurface layer (below 5 cm) and surface layer (above 5 cm).

Sediment grains were dispersed by high speed mixing in distilled water (150-200 mg dry weight /1500 ml distilled water) for 30 minutes and ultrasonic wave applied to a nest of 20 cm diameter sieve. The fine fractions ( $<32 \mu\text{m}$ ) were further separated according to Stokes's law at different settling times respective to the grain diameters of: 2-8  $\mu\text{m}$ , 8-20  $\mu\text{m}$  and 20-32  $\mu\text{m}$ .

Sand fraction (63-90  $\mu\text{m}$ ) was treated in two different ways. The first way was to remove relatively loosely attached particles. One gram of sand was mixed with 50 ml deionised water and placed in ultrasonic bath for 4 hours. The second way was to remove surface coating. One gram of sand was mixed with 50 ml 0.5 N HCl and treated in the same way as before.

Aliquots of dried sediment fractions samples were prepared for examinations by Scanning Electron Microscope (SEM). For examination of sand particles surface, the particles were mounted on double-sided sticky tape. For examination of cross section the grains were embedded in aradite resin, polished and then coated with carbon. Elemental analysis was carried out using an energy disperseve X-ray analyzer (Phillips PW 17710 Diffraction).

#### **Adsorption studies:**

The adsorption studies of  $^{134}\text{Cs}$  by prepared sediment samples were carried out using the batch technique. This technique is known to yield the most consistent result (Schell et al. 1981). The choice was made of a standard sediment concentration (4 g/l) at which the  $K_d$  did not change with change sediment concentration. Comparing this to other worker: it was 0.04 g/l (Aston and Duursma 1973 and Clayton et al., 1981), 10 g/l (Erten et al., 1988) and 0.1 g/l (Comans et al., 1991).

50 ml centrifuge tubes, screw top, were used. The aqueous phase was either seawater or river water after filtration with 0.45  $\mu\text{m}$  filter. Deionised water may be used.

Aliquots of 25 ml of water were transferred to the centrifuge tube, dilute tracer ( $^{134}\text{Cs}$ ) was added and the pH was adjusted at pH 8 using diluted HCl or NaOH. 0.1 gram of sediment sample was added, the tubes were closed and placed in a shaker water bath for predetermined periods of time. Two replicate were made for each sediment sample together with two blank tubes i.e. without sediment. The tubes were

then centrifuged for 30 minutes at 2400 g and radionuclide concentration was radioassayed and referred to their concentration in the blank tubes.

Radioassay of  $^{134}\text{Cs}$  was carried out using a GeLi detector 11% efficiency and 1.75 KeV resolution at 1.33 Mev (ED&GOrtec model No. 8112-11185-5) attached with 1024' channel analyzer (Model 7450). The counting system was calibrated using suitable sources and geometry of the same sample.

The results are expressed in term of the apparent distribution coefficient (Kd). The Kd is replaced by the formula:

$$Kd = \frac{A_0 - A}{A} \quad V/M$$

Where

- $A_0$  is the initial activity in the aqueous solution before addition of soil sample (plank tubes).
- $A$  is the activity in the supernatant after the elapse of experimental time.
- $V$  is the volume of the aqueous solution (25 ml)
- $M$  is the dry sediment sample (~ 0.1g).

The percentage adsorption or uptake is given by

$$\% \text{ adsorption} = (A_0 - A/A_0) * 100$$

The batch technique was used here to determine the different environmental effect such as pH, salinity, grain size and sediment treatment.

In case of studding the effect of salinity on the uptake of Cs, many authers (Stanners and Aston, 1981, Aston and Duursma, 1973) had focused on the values between 5-30 ‰ salinity. To simulate an estuarine environment where river water (0.08 ‰) is meeting seawater (34.2‰) mixtures were made from seawater and river water in the proportions needed to get the required salinity. To study of the effect of pH value on Kd, the experiments were carried out with fixed temperature (25°C),

sediment concentration as before i.e. 4 g/l and contact time of one day. The reaction medium was either seawater or river water.

## RESULTS & DISCUSSION

### Sand grain studies:

The sand grains surface micromorphological study by scanning electron microscope (SEM), shown in Fig. 2 and 3, illustrates very clearly cavities in these grains which may represent a suitable environment for accumulation of fine clay particles. The X-ray analysis of untreated sand samples, seen in Fig. 4, indicated the presence of some coating elements: Al (most probably of clay minerals), Fe, Ca, K and Cu. For treated sand sample i.e. ultrasonic, acidification and polishing indicate the presence of Si only, which confirms that the clay minerals detected represents a coating around the sand grains.

The measured  $K_d$  values for sand samples are shown in Table 1. It is obvious from this table that ultrasonic and acid + ultrasonic treatment significantly decreased the  $K_d$  values. The  $K_d$  values using  $^{65}\text{Zn}$  and  $^{60}\text{Co}$  were included in this Table which indicates that  $K_d$  in case of  $^{134}\text{Cs}$  was greatly affected compared to that of the other two radionuclides.

### Adsorption studies:

For all size fractions of sediment, the equilibrium was nearly achieved after 1 day for  $^{134}\text{Cs}$  (Fig. 5). The  $K_d$  and the percent uptake of  $^{134}\text{Cs}$  can be arranged in the following order of magnitude:

	clay >>	silt >	sand
grain size :	(<2 $\mu\text{m}$ )	(2-38 $\mu\text{m}$ )	(63-90 $\mu\text{m}$ )
$K_d$	$5 \cdot 10^2$	$\sim 1 \cdot 10^2$	$0.52 \cdot 10^2$
% uptake	68%	$\sim 30\%$	17%

- 325 -

The effect of contact time for short interval up to 12 hours (Fig. 6) using seawater and deionized water with natural sediment showed that the reaction consists of a very fast step followed by a very slow one and the  $K_d$  (or the uptake %) is much higher in case of deionized water than in case of seawater due to presence of competing ions.

The effect of salinity is illustrated in (Fig. 7). These results indicate that the  $K_d$  suddenly drops from  $2.5 \times 10^3$  (91% uptake) to  $8.0 \times 10^2$  (=76% uptake) with change of salinity from 0.08 ‰ to 2.13‰ then slowly from  $5.0 \times 10^2$  (=66% uptake) to  $1.3 \times 10^2$  (35 % uptake) with change of salinity from 4.3 to 34.2‰. The major cation in seawater ( $K^+$ ) compete with Cs for the active sites in the sediment mainly clay minerals. This competition decreases as the salinity decreases. It also seems that there are two mechanisms of adsorption. First adsorption on the low selective sites which may be the outer charged surface of clay minerals and this mechanisms dominate at salinities from 0.08 to 2.13 ‰. Second adsorption on the high active sites which may represent the interlayer of clay minerals and this mechanisms dominates when the salinity increases from 8.5 to 34‰.

Results of pH effect on  $K_d$  are seen in (Fig. 8 and 9). For seawater and fresh water reaction media respectively. In case of seawater (Fig. 8) there was a little effect of pH on  $K_d$ . This indicates that  $H^+$  poorly competes with Cs +: 33% uptake maximum at pH 6 and 27 % uptake minimum at pH 14. In fresh water system (Fig. 9) % uptake also slightly changed from 90.6 % minimum at pH 8 to 94.8 maximum at pH 10. These results are in agreement with those obtained by (Onishi et al., 1981 and Schell et al., 1981).

## CONCLUSION

Clay minerals and perhaps organic matter coating sand particles were found to increase the  $K_d$  value of  $^{134}\text{Cs}$  since both ultrasonic and acid treatment reduced significantly the  $K_d$  value for sand fractions.

Kinetic analysis of  $^{134}\text{Cs}$  uptake curves either by natural sediment or different size fractions indicated that they considered of a very fast step followed by a very slow one. The reaction reached equilibrium after 3 hours in seawater and in few minutes in case of deionized water.

The effect of salinity on the adsorption  $K_d$  suggested that there might be two adsorption mechanisms. The first might be adsorption to the less active sites and easily accessible ones on surface of clay minerals at low salinity (0.08-4.2 ‰). The reaction is fast and the adsorbed Cs ions are easily desorbed. The second mechanisms dominates at high salinity (4.2-34.2 ‰) in which Cs ions are adsorbed onto highly selective sites (interlayer sites of micaceous clay minerals). Changing of pH does not significantly affect the adsorption of  $^{134}\text{Cs}$ .

Table 1

Effect of ultrasonic and acid treatment on the Kd values of sand fraction (63-90  $\mu\text{m}$ ) using radionuclides of  $^{134}\text{Cs}$ ,  $^{65}\text{Zn}$  and  $^{60}\text{Co}$

Radionuclides	Untreated sand fraction	Ultrasonic treatment	Ultrasonic and acid treatment
$^{134}\text{Cs}$	$41 \pm 3$	$29 \pm 2$	$9 \pm 2$
$^{65}\text{Zn}$	$234 \pm 40$	$232 \pm 25$	$200 \pm 5$
$^{60}\text{Co}$	$419 \pm 45$	$418 \pm 32$	$365 \pm 15$

- 328 -

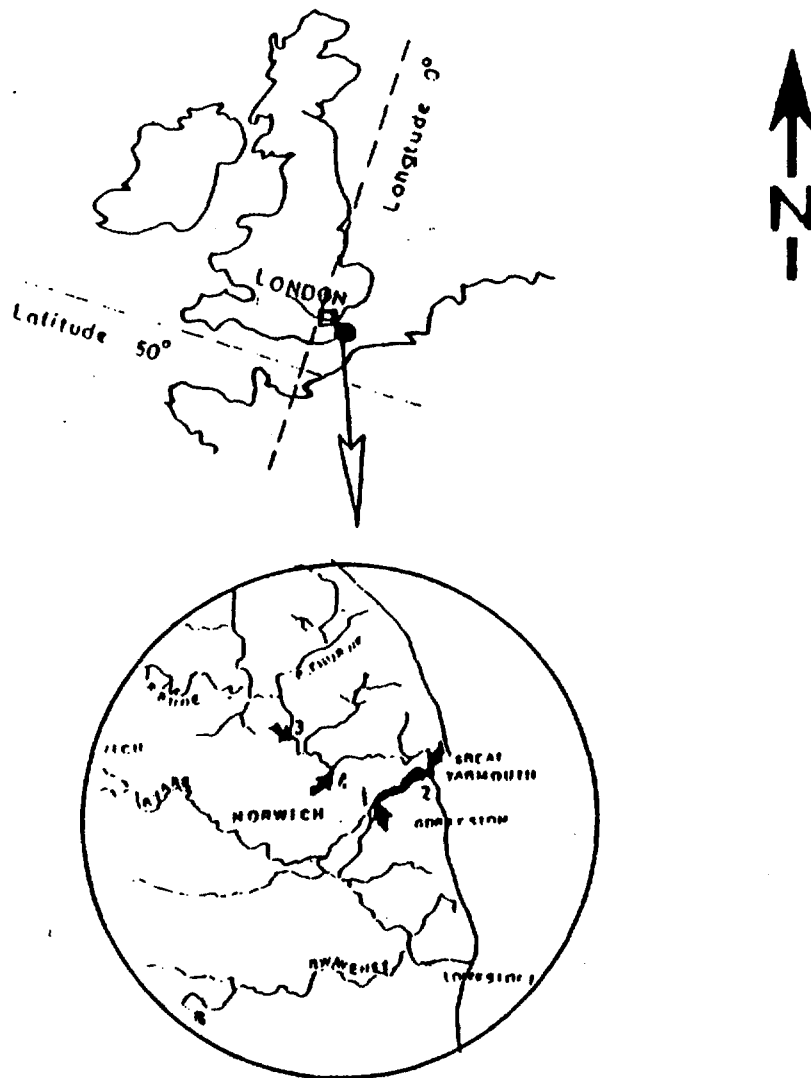


Fig.( 1 ) Study Area: NORWICH UK.



**Fig 2. Observation of Sand Grain by SEM**



**Fig 3. Observation of Sand Grain by SEM  
(Highly Magnified), Showing Fine Grain Inclusions**

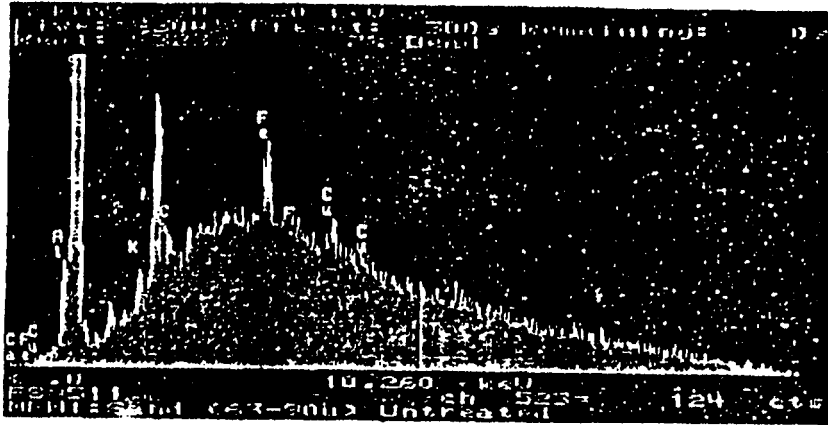


Fig. 4. x-ray analysis of untreated sand ( 63-90  $\mu\text{m}$  ) indicating the presence of some coating elements

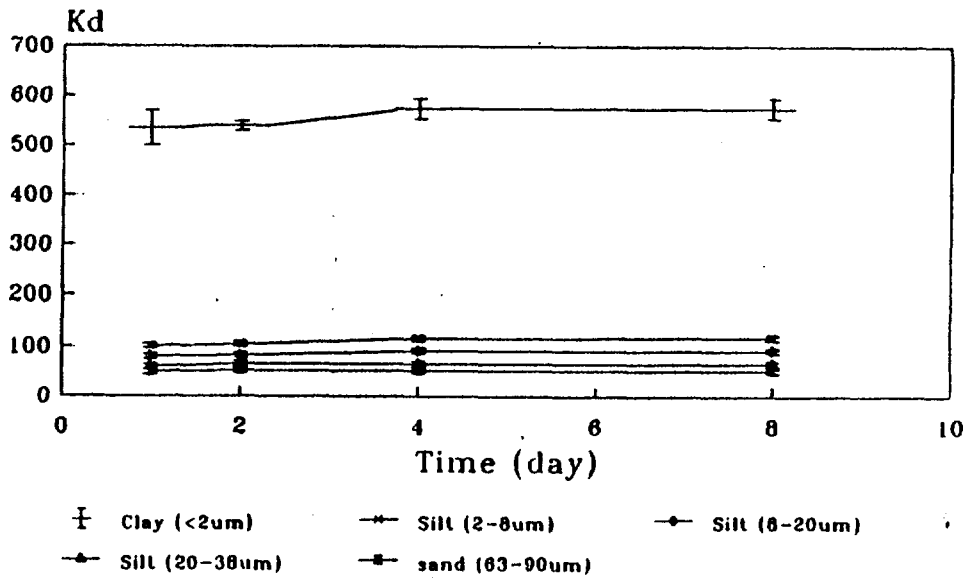


Fig. 5. Effect of size fraction on the Kd by <sup>134</sup>Cs

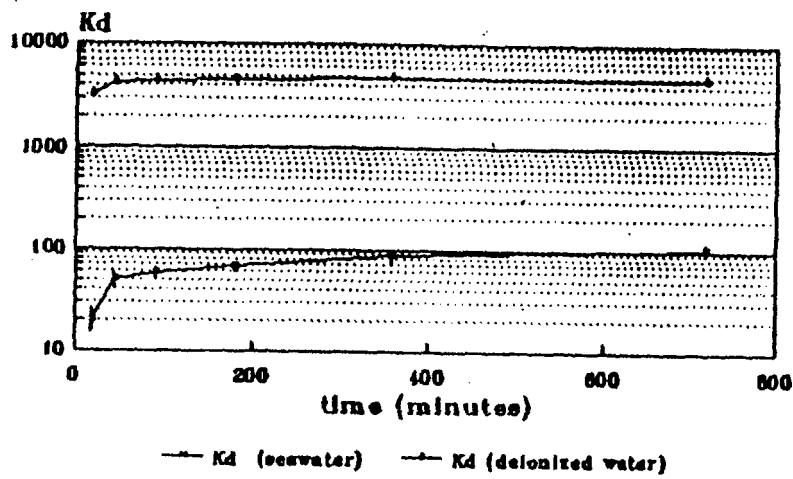


Fig. 6.a Effect of contact time on the Kd of  $^{134}\text{Cs}$  by natural sediment

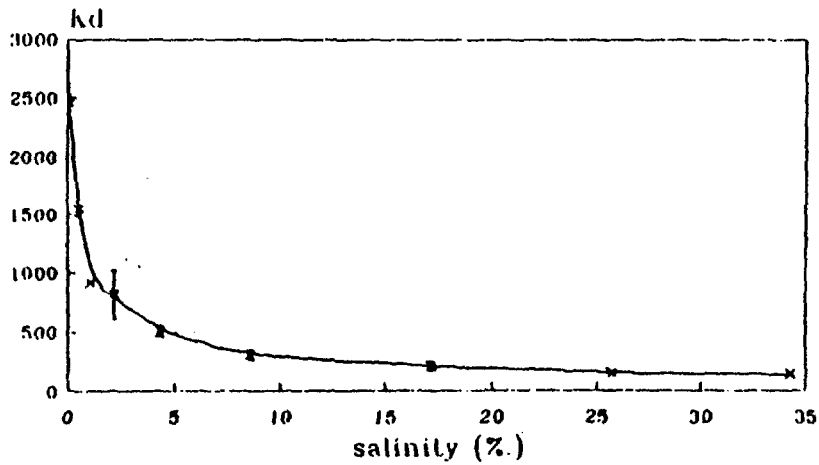


Fig 7. Effect of salinity on adsorption (Kd) of  $^{134}\text{Cs}$  by natural sediment

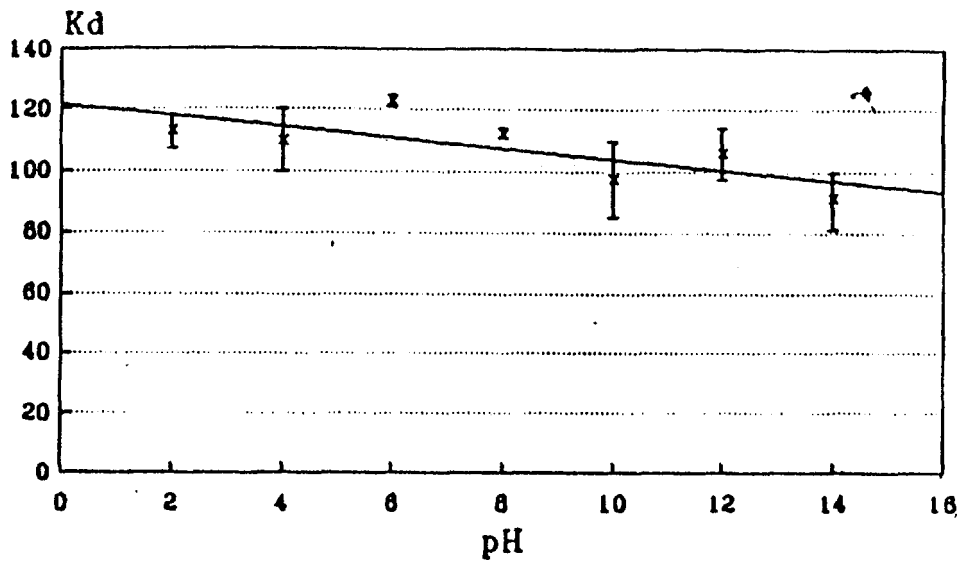


Fig. 8 Effect of pH on the Kd using sediment and seawater

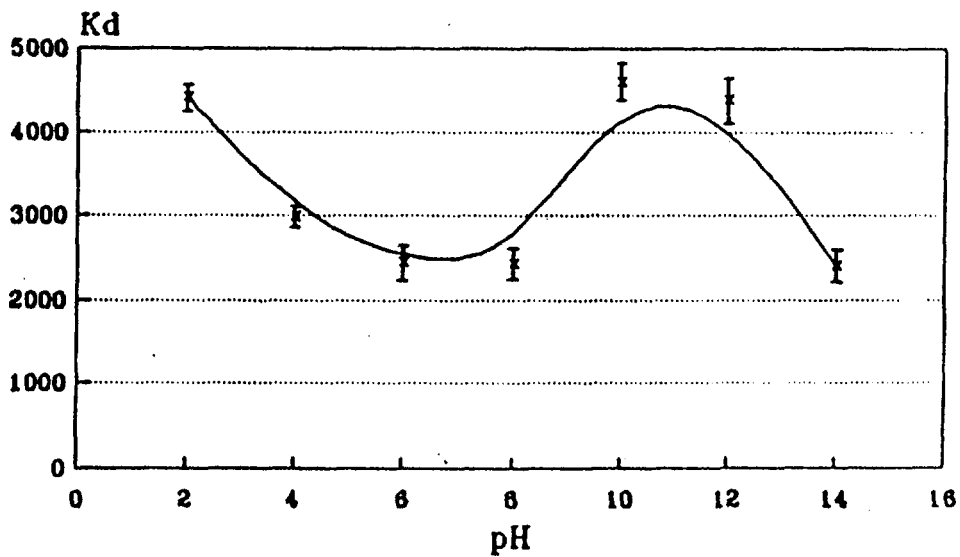


Fig. 9 Effect of pH on the Kd using natural sediment and river (fresh) water

**REFERENCES**

- Aston S. R. and Duursma E. K. (1973): Concentration effects on  $^{137}\text{Cs}$ ,  $^{65}\text{Zn}$ ,  $^{60}\text{Co}$  and  $^{106}\text{Ru}$  sorption by marine sediment with geochemical implication, *Neth. J. Sea Res*, 6, 225-240.
- Camans R. N. J., Haller M. and De Preter P. (1991): Sorption of Cs on illite: non-equilibrium behavior and reversibility. *Geochim. Cosmochim. Acta*, 55, 433-440.
- Clayton J. R., Sibley T. H. and Schell W. R. (1981): Distribution Coefficients of radionuclide for radionuclides in aquatic environment of dissolved organic compounds on the distribution coefficients of  $^{57}\text{Co}$ ,  $^{106}\text{Ru}$ ,  $^{137}\text{Cs}$  and  $^{241}\text{Am}$ . NUREG/CR-1853, Vol 1, 31p.
- Duursma E. K. and Gross M. G. (1971): Marine sediments and radioactivity. In *Radioactivity in the Marine Environment*: 147-160 Nat. Acad. Sciences. Washington, DC., USA.
- Erten N. N., Aksoyoglu S. and Gokturk H. (1988): Sorption/desorption of Cs on clay soil fractions from various regions of Turkey. *Sci. Total Environ.*, 69, 269-296.
- Hamilton-Taylor J. and 19 other (1993): Radionuclides aquatic pathways. In Warner F., and Harrison R. M. (Eds). *Radioecology after Chernobyl: Biological Pathways of Artificial Radionuclides*: 101-176 John Wiley and Sons, New York.
- Livens F. R., Baxter M. S. (1988): Particle size and radionuclide levels in some west Cumbrian Soils. *Sci. Tot. Environ.*, 70, 1-17.
- Mckinley I. G., and Alexander W. R. (1992): Constrains on the applicability of in situ distribution coefficient values. *J. Environ. Radioactivity*. 15, 19-34.
- Onishi Y., Sern R. J., Arnold E. M., Cowan C. E. and Thompson F. L. (1981): Critical Review: Radiation Transport, Sediment Transport and Water Quality Mathematical Modeling and Radionuclide Adsorption/Desorption Mechanism. US Nuclear Regulatory Commission NUREG/CR-1322; PNL 2901. Washington DC. USA.
- Schell W. R., Sanchez A. L. and Sibley T. H. (1981): Distribution coefficient for radionuclides in aquatic environments: Adsorption and Desorption Studies of  $^{137}\text{Cs}$ . US Nuclear Regulatory Commission NUREG/CR-1852 Vol. 2, 49p.
- Stanners D. A. and Aston S. R. (1981): Factors controlling the interaction of  $^{137}\text{Cs}$  with suspended and deposited sediments in estuarine and coastal environments. In *Impact of Radionuclide Releases into Marine Environment*: 131-141. Proc. Symp., IAEA Vienna.

- 384 -



EG9700130

## Leaching Of Ra-226 Contaminated Gravel Using Different Aqueous Treatments

Abdel Megid Mamoon, Waleed H. Abulfaraj & Moustafa A. Sohsah  
College of Engineering, P.O.Box 9027, King Abdulaziz  
University, Jeddah-21413, Saudi Arabia

**Abstract** - Gravel contaminated with Ra-226 is leached with several aqueous leachants, namely water, dilute solutions of HCl aqueous solutions of barium chloride of different molarities and acidified solutions of barium chloride. The effects of leachant volume, leachant temperature, mass of gravel being leached, duration of leaching or contact time and the surface area of gravel being leached were investigated at the laboratory scale level. The study is intended to generate data that help approximate the behavior of large scale pilot studies under field conditions.

**Introduction** - Phosphate deposits occur in economic quantities in different parts of the Kingdom. Phosphate rock is known to embody U-238 series radionuclides in different concentrations depending upon the nature of the phosphate ore. A phosphate processing plant is planned to operate in the near future. Phosphate plants release waste waters that contain radionuclides such as Ra-226 and Rn-222 to the environment, and the surrounding soil can get contaminated with these radionuclides [1,2]. Since there is much dependance on ground water for drinking and irrigation in some parts of Saudi Arabia, there exists then a potential for contaminating such waters in areas in the vicinity of an operating phosphate processing plant, from the

released waste waters. Ra-226 ions, however, have a tendency to get adsorbed on various surfaces such as soil particles, gravel etc. Leachability of the adsorbed radium by various aqueous treatments needs to be investigated. This is due to that the leachate containing radioactive nuclides has the potential of filtering down to the ground water level and contaminating it. Potable ground water contaminated with Ra-226 and its daughter nuclides presents considerable health hazards for people using this water [3]. Potentiality for leachability of gravel contaminated with Ra-226 is tested in the following series of experiments on artificially Ra-226 contaminated gravel leached with different leachants under different experimental conditions. The goal of this study is specifically to find out the factors that lead to maximum leaching of the contaminated gravel.

**Materials and Methods** - a) Ra-226 contaminated gravel was prepared by prolonged exposure of sandy gravel (about 2-3 mm in diameter) to dilute solutions of Ra-226 for several months. Leaching of the contaminated gravel with the different leachants under the various experimental conditions was carried out in glass beakers of different sizes. Leachant volume was 100 ml unless otherwise indicated. Gravel mass used was 20 gram unless otherwise indicated. The leaching was conducted at room temperature, the only exception being one leaching experiment conducted at approximately 90 °C.

b) Water, 0.1N HCl, BaCl<sub>2</sub> of different molarities and acidified solutions of BaCl<sub>2</sub> were used as leachants.

c) Liquid scintillation counter type LSC2 (NE Technology), scaler/rate meter type SR8 (NE Technology), high efficiency mineral oil based liquid scintillator (Du Pont de Nemours Co.), borosilicate scintillation vials and certified Ra-226 standard solutions. The scintillations produced in the scintillator fluid are caused by three alphas and two betas from the decay of Rn-222 and its daughters. The counting efficiency of the counter was determined by counting the Ra-226 standard under identical conditions.

d) Scintillation counting [4]. A known volume of distilled water, 0.1 N HCl, BaCl<sub>2</sub> of different molarities or acidified BaCl<sub>2</sub> solutions is added to a known mass of the Ra-226 contaminated gravel. After a certain contact time, 10 ml of the leachant is transferred to a scintillation vial, preloaded with 10 ml of the liquid scintillator. Measurement of Ra-226 in the leachate is carried out through measurement of its daughter, Rn-222, in the leachate. The Rn-222 in the leachate is composed of Rn-222 already present in it at the time of sampling plus Rn-222 newly generated by Ra-226 in the leachate sample. In the closed system of the leachate sample in the scintillation vial, amount of Rn-222 generated over time depends on the duration of generation and hence upon the extent of achieving the secular equilibrium between Ra-226 and Rn-222. Activity measurements of the total Rn-222 were carried out after secular equilibrium is attained between Rn-222 and its decay products. It should be noted that any Ra-226 in the leachate will remain almost all in the aqueous phase and will not contribute significantly to the scintillations produced in the organic or scintillator phase floating on top of the aqueous phase

and alone facing the window of the photomultipliers. Rn-222 present in the aqueous phase (the leachate sample) will diffuse to the organic phase. The total measured Rn-222 in the scintillator phase is composed of the initial Rn-222 which must have decayed some since leaching, and the newly generated Rn-222 from the leached Ra-226 present in the aqueous sample and both radons diffusing upwards to the scintillator phase in the scintillation vial. The activity of Rn-222 and Ra-226 in the leachate could be obtained from the measured total Rn-222 activity by graphically plotting the equation (Fig. 1):

$$Rn_t = Ra + (Rn_{t_0} - Ra) e^{-\lambda_{Rn}t}$$

where  $Rn_t$ ,  $Rn_{t_0}$  are the total Rn-222 activity measured at time  $t$  and the initial Rn-222 activity respectively and  $\lambda_{Rn}$  is the decay constant for Rn-222. Each leachate sample is counted over several Rn-222 half lives and the total measured activity is plotted against  $e^{-\lambda t}$ .

**Results and Discussion** - Fig. 2 shows while pure water has practically no leaching effect on Ra-226, 0.2 N BaCl<sub>2</sub> in 0.1 N HCl has maximum leaching effect on the adsorbed Ra-226, while 0.1 N HCl or 0.2 N BaCl<sub>2</sub> by itself has limited leaching capacity.

Fig. 4 shows the effect of varying the leachant volume with respect to a fixed mass of 20 grams of gravel, with 100 ml leachant volume, whether water or 0.1 N HCl appearing to be the optimum volume/mass ratio in terms of leaching efficiency whether for Ra-226 or Rn-222 under the used experimental conditions.

Fig. 5 shows the effect of changing the molarity of  $\text{BaCl}_2$  as the leachant on the release of Rn-222 and Ra-226. While there appears to be practically no effect on the activity of Rn-222 leached at the different molarities, the leaching effect of increased  $\text{BaCl}_2$  molarity on Ra-226 release is evident, but again the increased release appears to stop at about 0.3 molar  $\text{BaCl}_2$ .

Fig. 6 shows the effect of increasing the surface area of a constant mass of gravel (in different diameter beakers) that is exposed to the leachant on the Ra-226 and Rn-222 leached from the gravel. It is obvious that both radionuclides are increasingly leached with increasing surface area of the mass of gravel being leached, more so with respect to Rn-222 perhaps because it is a gas that can easily diffuse from the gravel bed into the leachant.

Fig. 7 shows that the maximum relative leaching of adsorbed Ra-226 and Rn-222 takes place in the first leaching followed by lesser and lesser relative leachings in the successive subsequent trials in an apparently exponential pattern. It is also obvious in this figure the effect of the temperature of the leachant, this leaching being conducted at a temperature of 90 °C. Much more Ra-226 is leached at this temperature with 0.1 N HCl than at room temperature by the same leachant as shown in Fig. 2.

**Conclusions** - It can be concluded from the series of experiments conducted in this study that:

1. Acidified  $\text{BaCl}_2$  solutions are the better leachants of radium from radium contaminated gravel, compared with water or  $\text{BaCl}_2$  alone.

2. Increasing the molarity of  $\text{BaCl}_2$  increased the leaching of radium but up to a level, 0.3 molar, after which apparently competing reactions, for instance, increased adsorption of released radium on the walls of glass beakers, masks further increases in the leaching of radium with increase in  $\text{BaCl}_2$  molarity. Ba is chemically similar to Ra and competes with the Ra ion in many reactions.
3. Increase in the duration of contact time of the leachant with the contaminated gravel, and in the mass of gravel increase the released Ra-226, but again up to a limit, due perhaps to increased effect of adsorption reactions of released Ra-226 on the surfaces of the container.
4. Increase in the volume of leachant used, 0.1 N HCl, has a pronounced effect on Rn-222 released, up to about 100 ml leachant volume for a 20 gram mass of gravel, with decrease in the leaching effectiveness of both Rn-222 and Ra-226 with greater leachant volumes.
5. Increase in the surface area of a constant mass gravel being leached with a constant volume of leachant increases the leached Ra-226 and Rn-222 apparently without limit. However it should be noted here that there are actually two variables operating, not just one, the surface area increase and along with it decrease in the thickness (or depth) of the gravel layer making it more efficiently leached.
6. Successive leachings increase the total Ra-226 leached but the largest fraction leached occurs in the first leaching and

then decreases apparently in an exponential fashion. Also leaching at higher temperatures (90 °C) produces a dramatic increase in the effectiveness of leaching.

In this study a worst case scenarios regarding factors that lead to maximum leachability of Ra-226 off contaminated gravel was investigated under laboratory conditions. The Ra-226 contaminated gravel is used to simulate gravel in the vicinity of a phosphate plant releasing waste water carrying uranium series decay products some of them such as Ra-226 being adsorbed by the gravel. The factors affecting the leachability of Ra-226 and Rn-222 off the gravel are a combination of chemical and physical factors, either related to the gravel itself or to the leachant used. Acid rain and ground water of increased salinity would be expected to be effective leaching agents in the natural environment. However it should be noted that when coarse gravel has fine clay underneath it, in the particular geoenvironment concerned, the clay material, known to be strong adsorber of various elements, might bind some of the released Ra-226 before it reaches ground water levels.

### References

1. Menzel, R.G., "Uranium, radium and thorium content in phosphate rods and their possible radiation hazard", *J. Agric. Food Chem.*, 16, 231, 1968.
2. Roessler, C.E.; Smith, Z.A.; Bloch, W.E. and Prince, J.R., "Uranium and radium-226 in Florida phosphate materials", *Health Physics*, 37, 269, 1979.
3. Cothorn, C.R. and Rebers, P.A., "Radon, Radium and Uranium in Drinking Water", editors, Lewis Publishers, 1990.

4. Prichard, H.M. and Gesell, T.F.; "Rapid measurements of Rn-222 concentrations in water with a commercial liquid scintillation counter", *Health Physics*, 33, pp. 577-581, 1977.

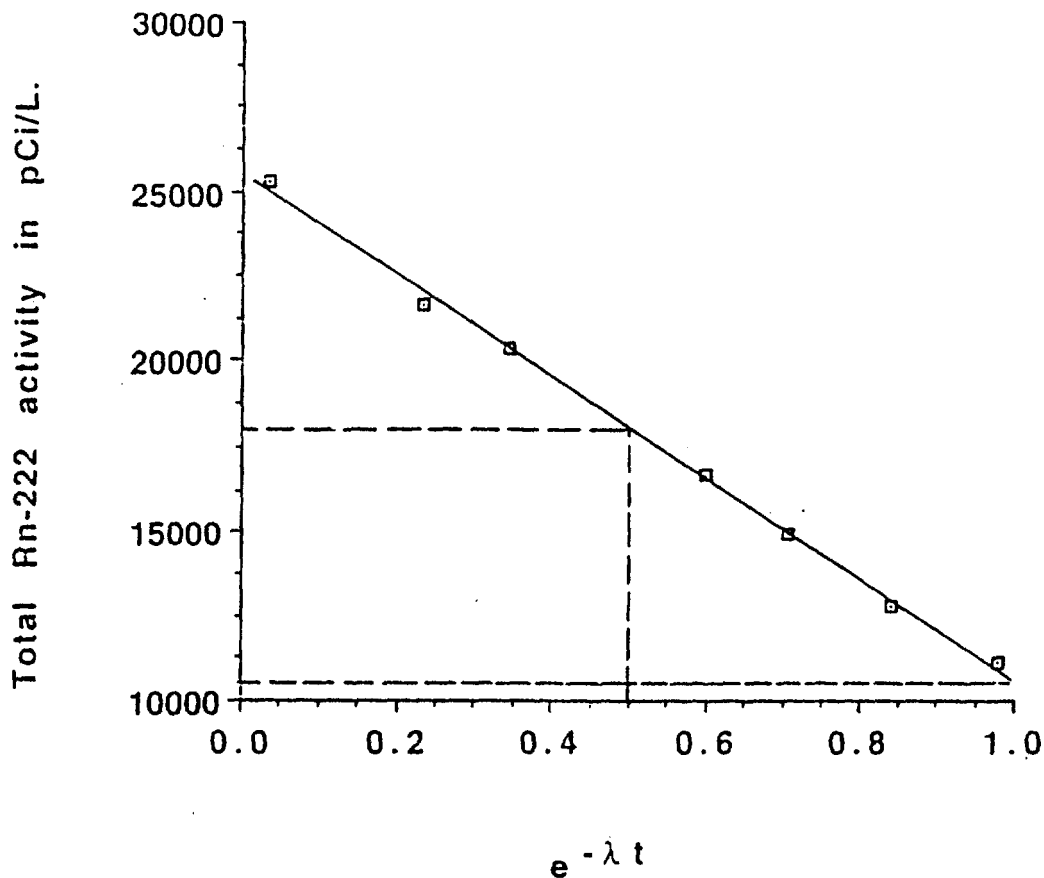


Fig ( 1 ) Estimation of Ra-226 and Rn-222 in an aqueous sample. The time ( t ) is in Rn-222 half lives. After one Rn-222 half life  $e^{-\lambda t} = 0.5$  and the measured activity should be equal to half the secular equilibrium value and hence also equal to half the activity of Ra-226 present in the leachate sample. Added to this is half of the initial Rn-222 activity in this sample. Initial Rn-222 activity was approximately 10400 pCi/L and the Ra-226 activity in this leachate sample was approximately then  $=17750 - 5200 = 12550 \times 2 = 25100$  pCi/L.

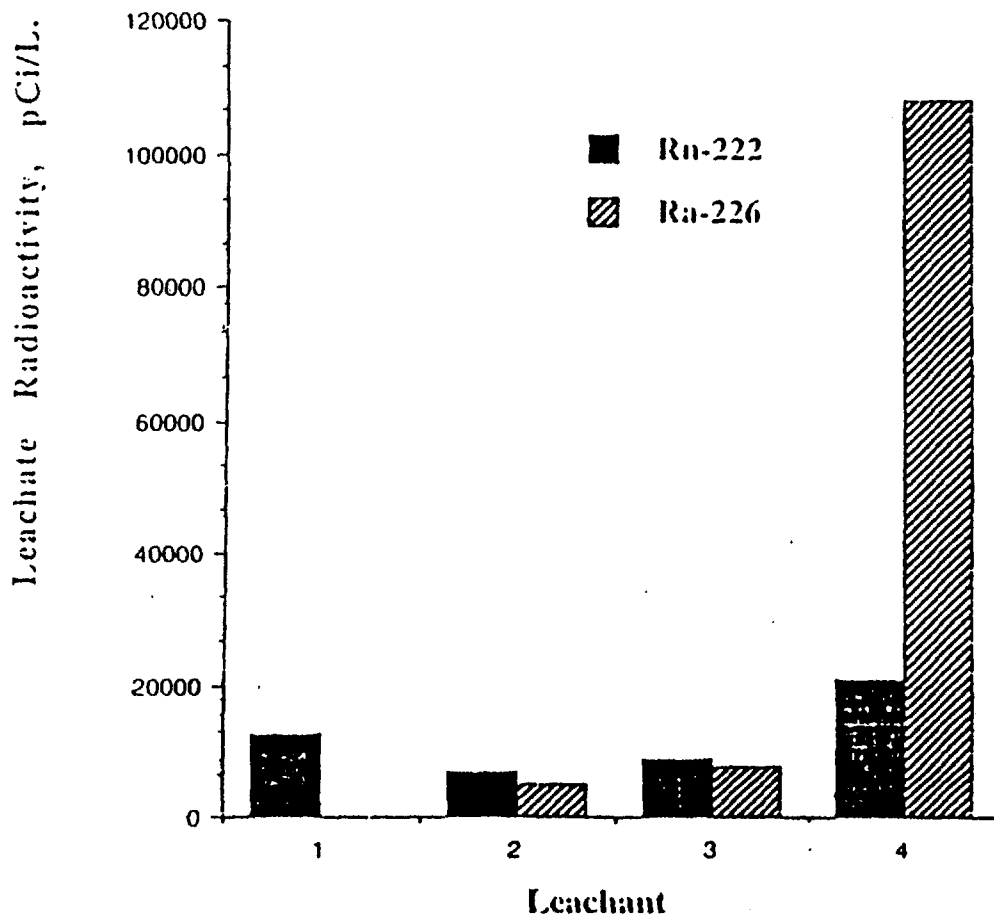
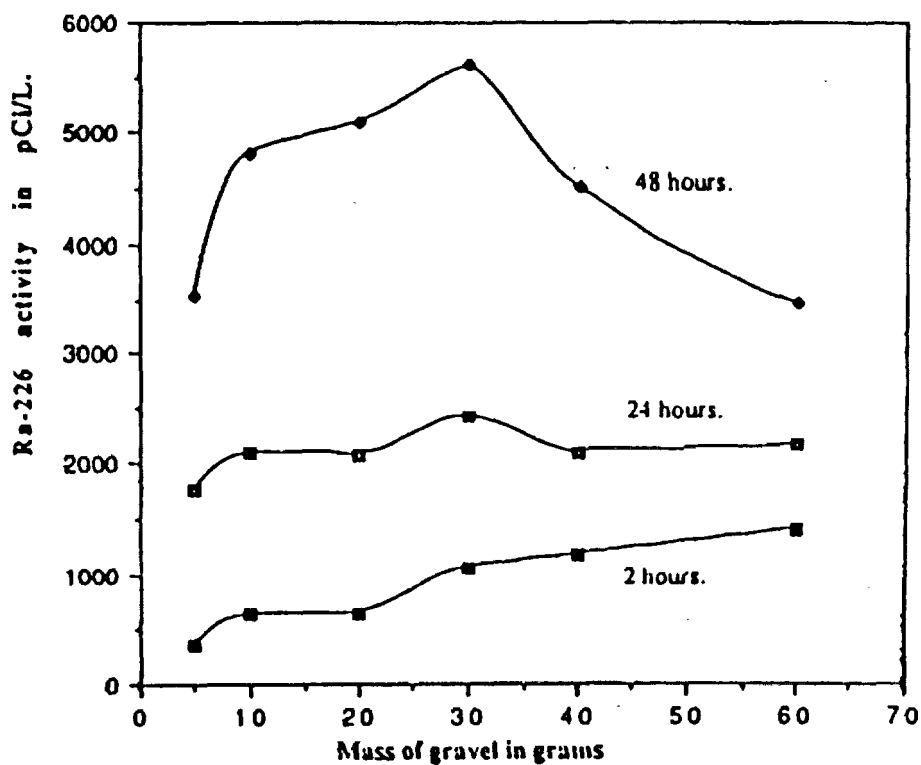
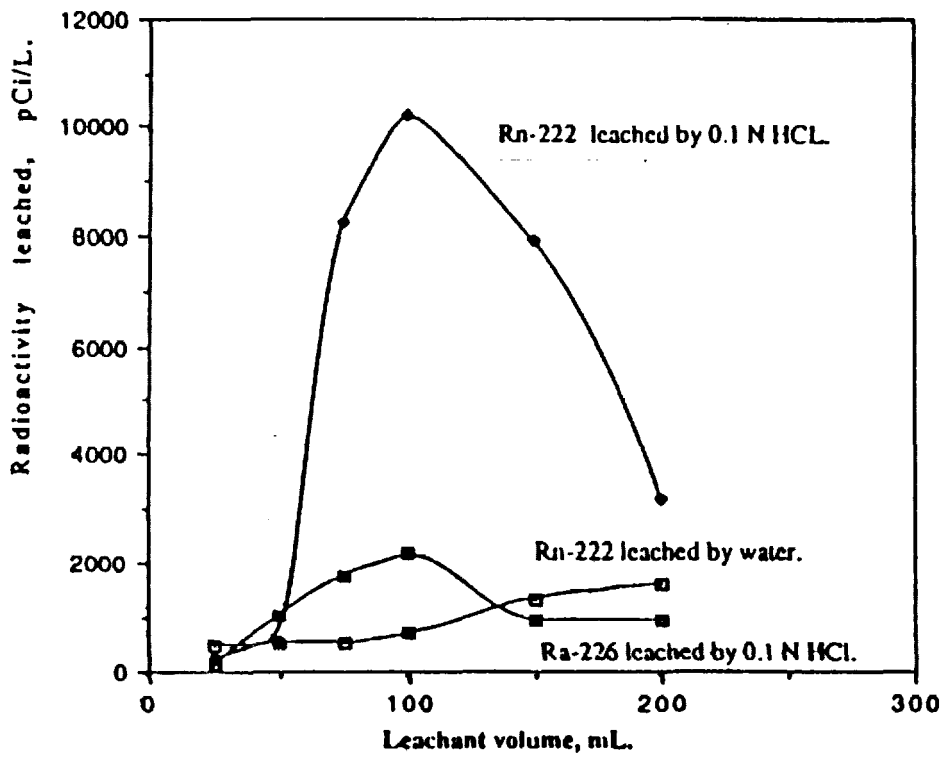


Fig. ( 2 ) Radium contaminated gravel leached with:  
1- water 2- 0.1 N HCl 3- 0.2 N barium chloride  
4- 0.2 N barium chloride in 0.1 N HCl.



**Fig. ( 3 ) Ra-226 activity leached by 0.1 N HCl from various masses of Ra-226 contaminated gravel.**



**Fig. ( 4 )** Ra-226 and Rn-222 activities leached from 20 g. of Ra-226 contaminated gravel by different volumes of water or acid.

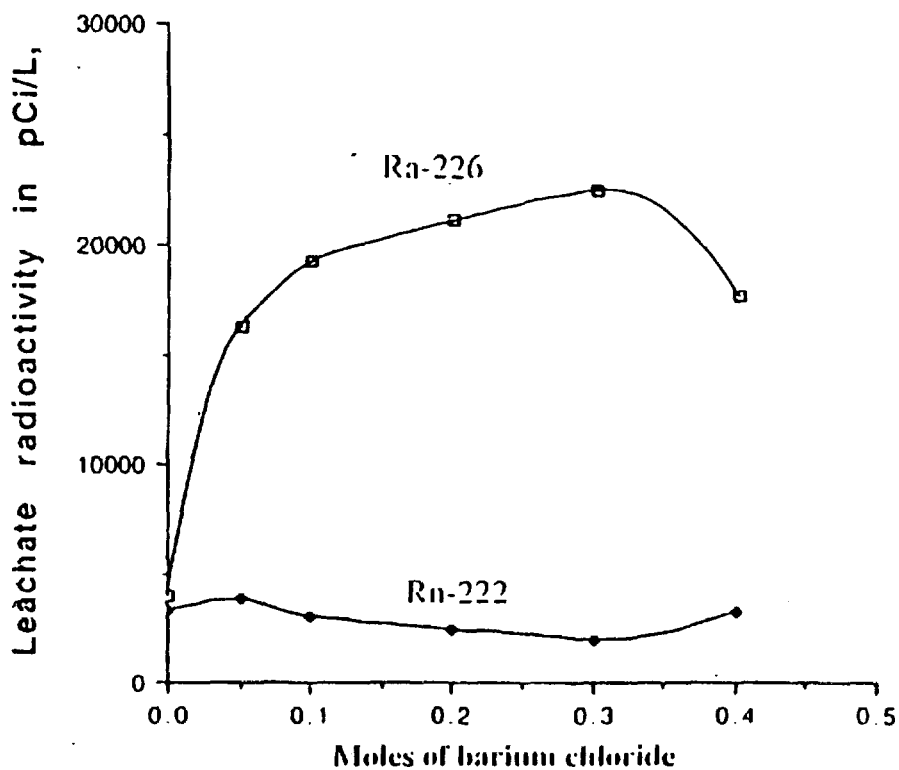


**Fig. ( 5 ) Ra-226 and Rn-222 leached from contaminated gravel with different molarities of barium chloride.**

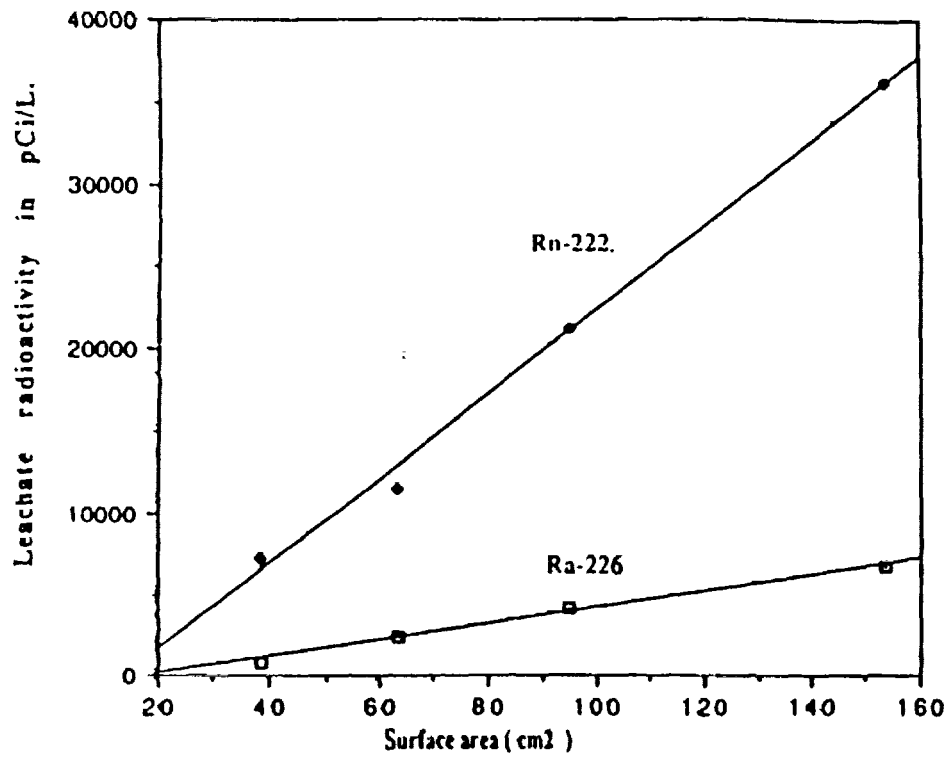


**Fig. ( 6 ) Ra-226 and Rn-222 activities leached from various surface areas of Ra-226 contaminated gravel with 0.1 N HCl.**

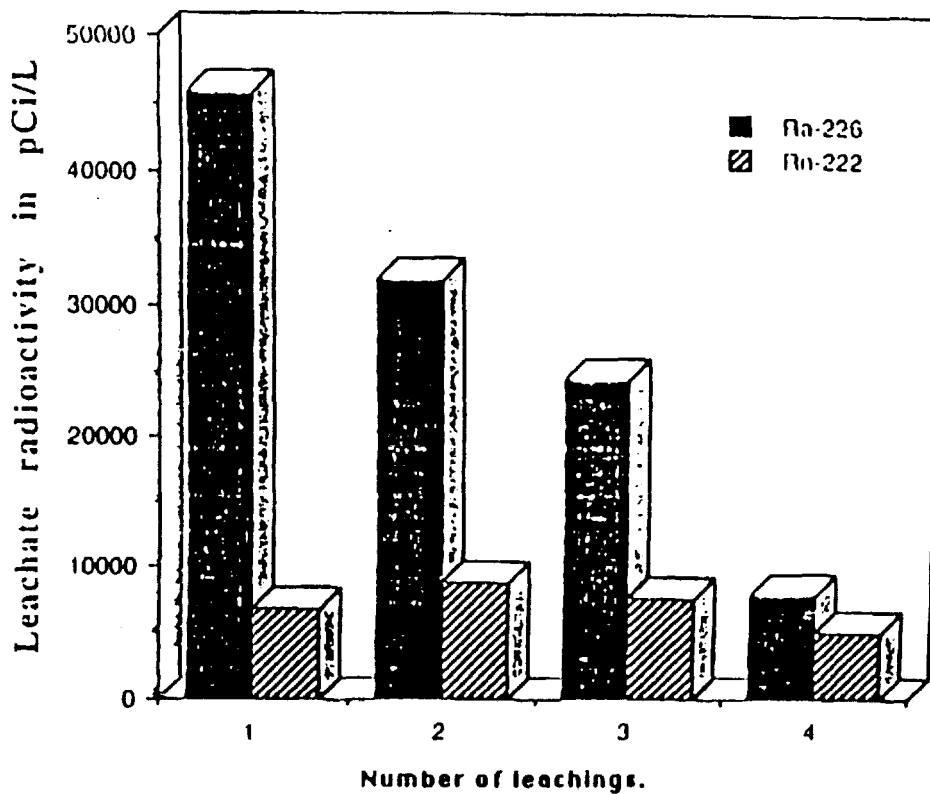


**Fig. ( 7 ) Ra-226 and Rn-222 activities leached with 0.1 N HCl at 90C from Ra-226 cotaminated gravel.**



EG9700131

## Operation of Temporary Radioactive Waste Storage Facility

Abdul Raheem A. Kinsara, Waleed H. Abulfaraj, Moustafa A. Sohsah,  
Salah El-Din M. Kamal and Abdel Megid Mamoon

Nuclear Engineering Department, Faculty of Engineering, King Abdulaziz University and  
Radiation Protection Department, Nuclear Research Center, Cairo, Egypt.  
P.O.Box 9027, Jeddah - 21413, Saudi Arabia

### Summary:

Radionuclides of different half lives have been in use for several years now, in different departments of King Abdulaziz University ( KAAU ). In particular the use of various unsealed radionuclides in many laboratories, resulted in considerable amounts of solid and liquid radwastes. In order to avoid the accumulation of radwastes in working areas and to keep the exposure of workers to radiation as low as reasonably achievable, a temporary radioactive waste storage facility was built in 1991. Segregation of radwastes according to type was carried out, followed by collection into appropriate containers and transfer to the storage facility. Average radiation dose rate inside the storage facility has been maintained at about  $0.75 \mu\text{Sv h}^{-1}$  (  $75 \mu\text{R h}^{-1}$  ) through use of appropriate shielding. The dose rates at points one meter outside the store walls were maintained at about  $0.15 - 0.20 \mu\text{Sv h}^{-1}$  (  $15 - 20 \mu\text{R h}^{-1}$  ) which is compatible with background dose rate in this area. The stored radwastes with reasonably short half lives have been managed by the practice of delay and decay in the storage area. Usage of radioisotopes in the period of 1991-1995 resulted in a volume of about  $1.8 \text{ m}^3$  of solid radwaste and about 200 L of liquid radwaste. The capacity of the storage facility is such that it will accommodate storage of generated radwastes of long half life for up to 20 years from now. Permanent disposal of such radwastes may be indicated afterwards.

Records of the store inventory are maintained in a special computer database listing dates, types, activities and packaging data pertinent to the radwastes delivered to the store. The database is utilized for easy localization and identification of every stored radwaste package.

Safety criteria such as 1. checking the integrity of radwaste containers for early detection of solid or liquid leaks, 2. checking radiation levels inside and outside the storage facility, are implemented on regular basis. Both construction and operation of the storage facility comply with radiation safety requirements for the workers handling the radwastes, for the public and for the bioenvironment.

## 1. INTRODUCTION :

The design and construction of a temporary radioactive waste storage facility for King Abdulaziz University ( KAAU ) campus has been published elsewhere [ Abulfaraj et al 1994 ]. The storage facility built is above ground and has a 40 m<sup>2</sup> floor space and 20 cm concrete walls. Similar works were also reported elsewhere [ Emery et al 1992, Vetter 1992 and Dlouhy 1982. ] .

The university, inspite of still being young in years , has many active research departments, medical research center and university hospital which are using increasing activities of various short and long half life isotopes, both open and sealed sources. However active use of the radwaste storage facility did not start until basic safety related - conditions were satisfied as stipulated by the University Radiation Safety Committee ( URSC ). Firstly, an inventory was made of the sources of radwastes on the campus since the beginning of radioisotope use in the year 1986. Secondly the impact of the accumulated radwaste on the handlers and the public outside of the storage facility was taken in consideration and was ascertained to comply with ICRP and IAEA recommendations [ ICRP,1991 and IAEA , 1995 ]. Thirdly, efficient planning was made for efficient documentation of accumulated radwastes, namely record keeping of arrival dates of the radwastes, its type, packaging, associated dose rates, approximate activities and volumes, anticipated time of release to the environment ( sewers or refuse landfills ). Fourthly, the release limits to the environment recommended by IAEA were implemented, [IAEA, S.S.No.77, 1986 and U.S.A. Code of federal regulations,1993 ].

## 2.Inventory of Radwaste in KAAU in period 1991-1995

Radionuclides are in use in KAAU campus since 1980's. Radwaste have been continuously generated and accumulated at the site of their generation up until 1991, the date of employment of the storage facility. Waste arising were mainly liquid radiopharmaceuticals of different types associated with some contaminated glassware, disposable articles,cloth and paper. Most radionuclides in use were of low level specific activity and short half lives. Radioactive material users producing relative active solid waste are the users in colleges of science and engineering. Their generated radwaste was mostly of long half life but of low specific activity. These radwastes were provided with sufficient shielding inside the storage facility. Fig. ( 1 ) illustrates the inventory of accumulated radwastes , the waste material origin and their volumes in the period of 1991 - 1995. For decay in storage, radionuclides with half-lives of less than 65 days, are kept in storage for 10 half-lives. The 65 days criterion was applied in the light of the fact that most open sources used have short half-lives less than 65 days .

### 3. The need for Radwaste Management in KAAU

Radiation protection is mainly concerned with the protection of workers and members of the public and the bioenvironment against the harmful effects of ionizing radiations such as radiations emitted from generated radwastes. Low level radwastes (LLRW) are being generated in ever increasing amounts in the different institutions and are generating lot of concern for being stored at the producing institution, inspite of their low dose rates. This is because of the adopted radiation protection principle of no threshold for radiation biological effects [ OECD - 1994 ]. Therefore, to overcome the problem of accumulation of radwastes in working areas and for keeping the exposure of workers to radiation to as low as reasonably achievable (ALARA principle) and to maintain noncontamination of the environment, the URSC has built a temporary storage facility. Typical LLRW are Mo-99 ( 66.0 h ) , I-131 ( 8.0 d ) , I - 125 ( 60 d ) and Ir-192 ( 73.8 d ) [ IAEA, Tech-272 and IAEA- 1982 ] .

### 4. Adopted Radwaste Management Strategy

The LLRW generated at KAAU may be solid, Liquid or biological materials (animal carcasses for example ) . It can be sealed or open sources. Since the university generation of radwastes is still relatively small in volume and mostly of short half life radionuclides, the management of the wastes involves only the basic treatments of separation at the site of generation of the radwastes from other types of chemical or hazardous wastes, followed by segregation into liquid ( scintillation fluids and aqueous solutions ) , solid ( syringes, paper, glasses..etc) and biological materials ( animal carcasses ) . These groups of radwastes are collected in large cans covered by double non porous black bags, care being taken at this stage to separate short from long half life wastes, i.e. less than 65 days half life and long half life wastes. For short half life wastes decay storage is adopted and then the wastes are released with municipal refuse. For long half life radwastes , carcasses are kept in deep freeze and solids are packaged in containers ( drum ) for prolonged storage till final disposal in a repository. Aqueous long half life radwastes are treated by dilution followed by flushing into sewers with sufficient volume of water to bring radionuclide concentrations to exemptible levels [IAEA, S.S.No.77, 1986 and U.S.A. Code,1993 ]. Table ( 1 ) illustrates monthly average concentration for different radionuclides that can be released in water in microcurie / ml. Organic liquids like scintillation fluid are still very small in volumes and are kept in prolonged storage pending eventual disposal by incineration or by other appropriate methods.

TABLE ( 1 )  
 Monthly Average Concentration For Different Radionuclides  
 ( in water. microcurie/ml ) , [IAEA. S.S.No.77, 1986 and U.S.A. Code,1993 ]

Radionuclides	Z-No.	Concentration ( in microcurie/ml )	Radionuclides	Z-No.	Concentration ( in microcurie:ml )
Americium-241	95	2E-7	Iron-59	26	1E-4
Barium-131	56	4E-4	Lead-210	82	1E-7
Barium-133	56	4E-4	Nickel-63	28	1E-3
Bismuth-207	83	1E-4	Phosphorus-32	15	9E-5
Cadmium-109	48	6E-5	Plutonium-238	94	2E-7
Calcium-45	20	2E-4	Polonium-203	94	3E-3
Californium-252	98	2E-7	Polonium-210	84	4E-7
Carbon-14	6	3E-4	Radium-226	88	6E-7
Cesium-135	55	1E-4	Ruthenium-106	44	3E-5
Cesium-137	55	1E-5	Selenium-75	34	7E-5
Chlorine-36	17	2E-4	Sodium-22	11	6E-5
Chromium-51	24	5E-3	Strontium-89	38	8E-5
Cobalt-57	27	6E-4	Strontium-90	38	5E-6
Cobalt-58	27	2E-4	Sulfur-35	16	1E-3
Cobalt-60	27	3E-5	Technetium-99m	43	1E-2
Europium-152	63	1E-4	Thallium-201	81	2E-3
Gadolinium-153	64	6E-4	Thallium-204	81	2E-4
Gallium-67	31	1E-3	Thorium-228	90	2E-6
Hydrogen-3	1	1E-2	Thorium-230	90	1E-6
Indium-111	49	6E-4	Thorium-232	90	3E-7
Iodin-125	53	2E-5	Titanium-44	22	4E-5
Iodin-129	53	2E-6	Tungsten-185	74	4E-3
Iodin-135	53	3E-4	Yttrium-88	39	1E-4
Iridium-192	77	1E-4	Zinc-65	30	5E-5
Iron-55	26	1E-3			

It should be mentioned here that in view of that the university campus area is somewhat large, transportation of these wastes, packaged in clearly marked packages, is carried out by authorized persons from URSC, in a special small car used

exclusively for this purpose. The storage room is easily accessible from all parts of the campus and potential for accidents during transportation is negligible.

Fig. ( 2 ) summarizes the various options for treating the radwastes transported to the storage room. Decay storage can be followed by release with municipal refuse or in case of aqueous radwastes by release to the sewers. Table ( 2 ) gives the duration of time needed for reduction in activity to certain levels. This is generated from applying the following formula :

$$T = \ln R / \lambda$$

where  $T$  = time in years,  
 $\lambda$  = the decay constant  $y^{-1}$  ,  
 $R$  = reduction factor in  $10^n$  .

e.g. for P-32 :

$$T = \ln 10^6 / 1.8 \times 10^1 = 0.767528$$

$$= 7.8 \times 10^{-1} \text{ a}$$

$$= 7.8 \times 10^{-1} \times 365$$

$$= 284 \text{ days.}$$

So, for P-32 of half life  $3.9 \times 10^{-2}$  year, a period of 284 days is required for a  $10^6$  reduction in its activity .

TABLE ( 2 )  
 The duration of time needed for reduction in activity to certain levels [ IAEA-TECDOC-653 ]

Racionuclide	Decay Constant $a^{-1}$	Time for Reduction in Activity by a Factor of					
		$10^1$	$10^2$	$10^3$	$10^4$	$10^5$	$10^6$
P-32	$1.8 \times 10^1$	$1.3 \times 10^{-1} \text{ y}$ [47.5 d]	$2.6 \times 10^{-1} \text{ y}$ [94.9d]	$3.9 \times 10^{-1} \text{ y}$ [142.4d]	$5.2 \times 10^{-1} \text{ y}$ [189.8d]	$6.5 \times 10^{-1} \text{ y}$ [237.3d]	$7.8 \times 10^{-1} \text{ y}$ [284.7d]
Ca-45	1.5	1.5 y [547.5d]	3 y [1095d]	4.5 y [1642.5d]	6 y [2190d]	7.5 y [2555]	9 y [3285d]
Tc-99m	$1.0 \times 10^3$	$2.3 \times 10^{-3} \text{ y}$ [0.84d]	$4.6 \times 10^{-3} \text{ y}$ [1.68d]	$6.9 \times 10^{-3} \text{ y}$ [2.5d]	$9.2 \times 10^{-3} \text{ y}$ [3.4d]	$1.2 \times 10^{-2} \text{ y}$ [4.4d]	$1.4 \times 10^{-2} \text{ y}$ [5.1d]
I-125	4.1	$5.5 \times 10^{-1} \text{ y}$ [204.4d]	1.1 y [401.5d]	1.7 y [620.5d]	23 y [839.5d]	28 y [1022d]	3.4 y [1241d]
I-131	$3.2 \times 10^1$	$1.7 \times 10^{-1} \text{ y}$ [52.05d]	$3.4 \times 10^{-1} \text{ y}$ [124.1d]	$5.0 \times 10^{-1} \text{ y}$ [182.5d]	$6.7 \times 10^{-1} \text{ y}$ [244.6d]	$8.4 \times 10^{-1} \text{ y}$ [306.6 d]	1.0 y [365d]

y : years                      d: days

Table ( 3 ) presents the clearance or exemption level adopted by URSC for release to ordinary refuse [ IAEA - TECDOC - 653, 1992 ]. For solid waste it is

recommended . that radwastes contaminated by traces of short lived radionuclides not exceeding  $74 \text{ Bq g}^{-1}$  can be sent to ordinary refuse for disposal . Total activity ( per disposal ) must be less than :

- 3.7 KBq for radionuclides of very high toxicity .
- 37 KBq for radionuclides of high toxicity .
- 370 KBq for radionuclides of moderate toxicity .
- 3700 KBq for radionuclides of low toxicity .

**TABLE ( 3 )**  
The Recommended Clearance Levels for the Surface  
Activity Concentration [ IAEA-TECDOC-653 ]

Type of activity	Clearance level for the mass activity concentration	Clearance level for the surface activity concentration
Beta, gamma	1 Bq/g averaged over a maximum mass of 1000 kg <sup>a</sup>	0.4 Bq/cm <sup>2</sup> for non-fixed contamination on accessible surface <sup>b</sup>
Alpha	N / A <sup>c</sup>	

**a** no single item may exceed 10 Bq / g .

**b** averaged over any area of 300 cm<sup>2</sup> of any part of the surface.

**c** non applicable ( N/A ) : no value is recommended .

#### 5. Estimation of future generated radwastes :

It is of obvious important to attempt to assess volume of future generation of radwastes. Because of the complexity of such forecasting due to potential changes in the extent of use of radionuclide activities and hence generated wastes, simplifying assumptions were adopted. The university generated radwastes over 5 years ( 1991 - 1995 ) is 1.8 m<sup>3</sup> of solid wastes and about 200 L of liquid radwaste. The mean annual solid waste and liquid waste volumes are estimated as  $1.8 \text{ m}^3 / 5 \text{ y.} = 0.36 \text{ m}^3 / \text{y}$  and  $200\text{L} / 5 = 40 \text{ L} / \text{y}$  .Then if we assume that the factors increasing the use of radionuclides on the campus and hence increasing the volume of generated waste are balanced by the general tendency to use less and less activity per application ( to decrease radwaste generation ) then we can consider that the mean annual solid waste generation rate will stay the same. Hence in 20 years time ( the expected life span for the temporary storage room ) there will be accumulated in the storage room about  $0.36 \text{ m}^3 / \text{y} \times 20 = 7.2 \text{ m}^3$  of solid waste. That is assuming that all the generated solid waste is long half life, i.e. worst case scenario, and that non has

decayed enough during that period. Regarding the liquid wastes, judging by the currently generated wastes, the mean annual volume generated is taken as 40 L. Now if we assume that all the collected liquid waste is of long half life then again in 20 y there will have accumulated in the storage room  $20 \text{ y} \times 40 \text{ y} = 800 \text{ L}$ . The accumulated long half life solid and liquid radwastes will then be managed by the appropriate volume reduction methods ( compaction or incineration ..etc) and then immobilized in a waste form such as cement and made ready for disposal in a repository.

## 6. CONCLUSION

It can be concluded that the LLRW radwaste generated currently and in the near future, up to 2016, from the use of radionuclides in KAAU laboratories, hospital and research center can be safety managed by the standard basic management treatments. Regarding very long half life wastes, these will have eventually to be subjected to disposal in a repository. A national repository is planned for the near future.

## 7. REFERENCES

- Abulfaraj W.H., Samman T. A. and Kamal S. M. ( 1994 ); " Design of a Temporary Radioactive Waste Storage Facility " Radiat. Phys. Chem. 44, no. 1/2, 149 - 156 .
- Emery R., Jeannte M. and Sprau D. (1992) Characte-rization of Low Level Radioactive Waste Generated by a Large University / Hospital Complex, Health Phys. 62 (2), 183 - 185.
- Vetter R.J. (1992) Incineration of Biomedical Low - Level Radoactive Waste, Heath Phys. 62 (2), 121-122.
- International Commission on Radiological Protection (1991) Publication 60, Ann. ICRP 21 ( 1-3 ) , Annal of the ICRP .
- International Atomic Energy Agency, (1996) Basic Safety Standards, Safety Series No. 115, IAEA, Vienna, p 60..
- Nuclear Energy Agency Organization for Economic Co-Operation and Development, OECD 1994, " Radiation Protection Today and Tomorrow " , France.
- International Atomic Energy Agency. (1986 )Principles for Limiting Releases of Radioactive Effluents into the Environment, Safety Series No. 77, IAEA, Vienna.
- U.S.A. Code of Federal Regulations : Appendix B to C.F. 20. 1001 - 20.2402, Office of Federal Register National Archives and Records Administration, U.S.A., 1993.
- International Atomic Energy Agency, (1992 ), " Storage of radioactive wastes " IAEA-TECDOC- 653, Vienna,

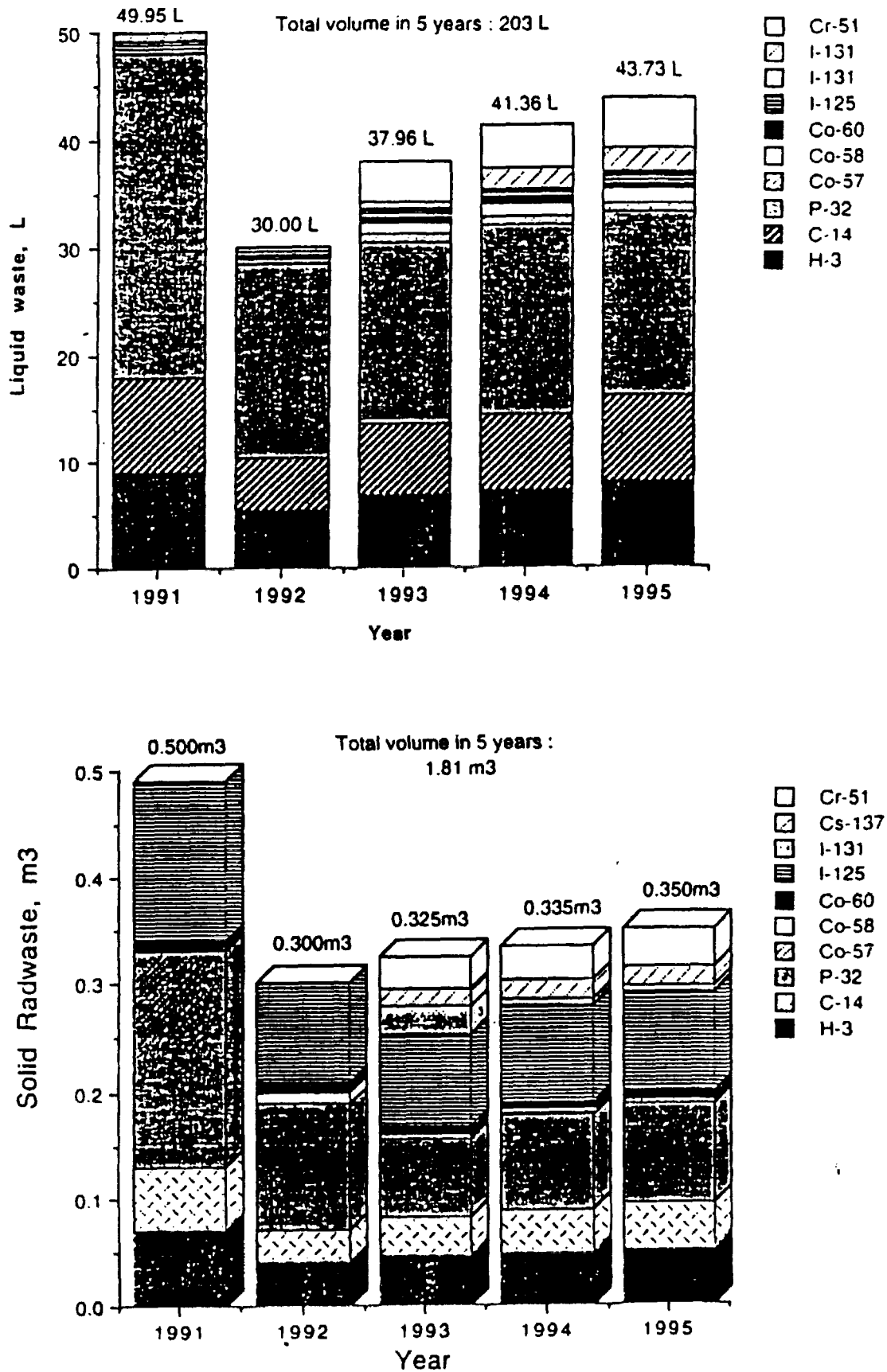


Fig. ( 1 ) Inventory of radwaste stored in KAAU storage facility in period 1991 - 1995 .

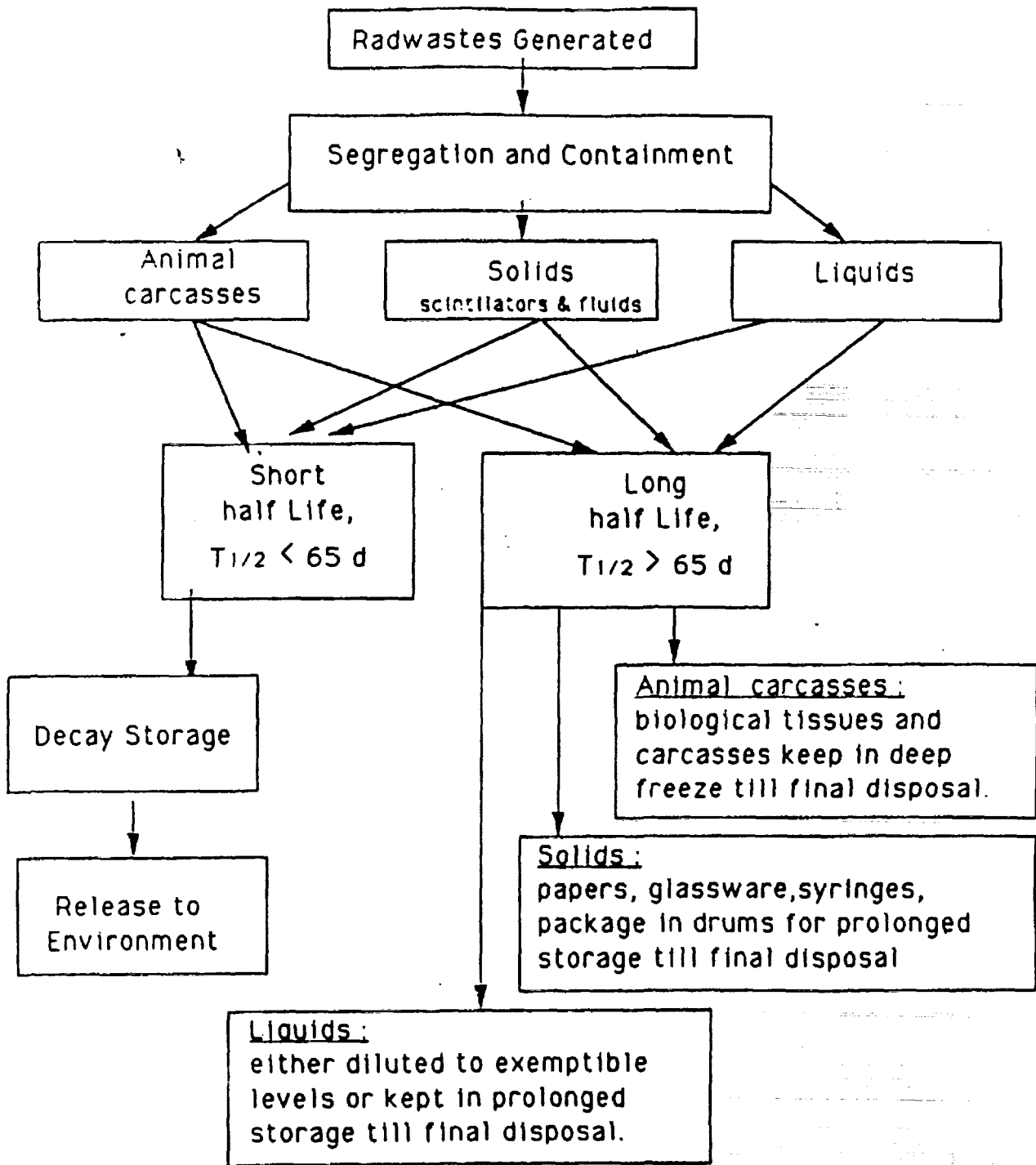


Fig.( 2 ) KAAU Waste Management Strategy



## INFLUENCE OF HUMIC SUBSTANCES ON FIXATION OF FISSION PRODUCTS IN SILICATE MEDIA

Ibrahim S. Shaban<sup>\*</sup>, Fedor Macáček

*Department of Nuclear Chemistry, Faculty of Natural Sciences,  
Comenius University, SK-842 15 Bratislava, Slovakia*

### ABSTRACT

The effect of humic acid addition on the capacity of inorganic sorbents to sorb radioactive cesium and strontium was studied on silica gel, silica gel modified with nickel ferrocyanide, zeolite, and montmorillonite. The Sips isotherm for humic acid sorption and multisite distribution model of ion sorption were found to suit well for description of mobility of ions as a function of humic acid concentration as a single variable at given pH and type of silicate. Complexation of the ions was of minor importance at the conditions investigated.

### INTRODUCTION

Clay minerals are exploited in both the land and sea emplacement and as backfill materials for the storage of radioactive waste to increase their radioactive safety. Mobility and fixation of ions may be affected by blocking of sorption sites of silicates and by solubilisation of metal ions in pore water by humic substances.

The interaction of radionuclides with natural organic materials is relatively poorly understood, despite the potential importance of such processes in the transport and retardation of radionuclides<sup>1</sup>. Particular attention has recently been focused up on this problem by high degree of mobility and availability of Chernobyl radio-caesium and -strontium deposited on organic soils<sup>2,3,4</sup>, which clearly demonstrated that an improved understanding of their mobility in horizontal and vertical directions of geosphere.

The aim of present work was to establish a model describing sorption behavior of radionuclides on various silicate sorbents as a function of concentration of humic acid in solution both considering

<sup>\*</sup> Permanent adress: Nuclear Research Center, P.O.Box 30878, Tajura, Tripoli, Libya

- (i) the blocking of sorbent surface by humic acid and changing its sorption properties (a negative but also positive effect on radionuclide sorption can be expected),
- (ii) complexation of radionuclide ion in solution with humic acid ligands (negative effect is most probable).

## EXPERIMENTAL

**Materials:** Four sorbents were used; Zeolite 0.8-1.0 mm Nalsit (gift of the Slovnaft VURUP, Bratislava), Silica gel 0.8-1.0 mm and nickel ferrocyanide (7%) modified silica gel, NiFeCN-SiO<sub>2</sub> (Institute of Polymers Slovak Academy of Sciences, Bratislava), and montmorillonite isolated by sedimentation from water suspension of bentonite (Stará Kremnička-Jeľšovský potok, Slovakia), gift of Prof. V. Fajnor, Department of Inorganic Chemistry of our faculty. Two humic acids (HA) have been studied; a commercial humic acid (Aldrich), further HHA and a soil HA extracted from peat Hrobonová, Slovakia (gift of Prof. J. Kandráč, Department of Analytical Chemistry), further AHA. Strontium-85 and cesium-137 were products of Dupont de Nemours (Brussels, Belgium) of Polatom (Otwock-Swierk, Poland) respectively.

All used chemicals were of analytical grade (Lachema Brno, Czech Republic). The metal chlorides carrier concentration in either case of Cs and Sr was  $10^{-4}$  mol.dm<sup>-3</sup>

**Techniques:** Dilute aqueous suspensions of each sorbent were shaken for 2 hours at constant temperature (20 °C) under aerobic conditions. It was found that two hours were sufficient for equilibration<sup>3</sup>. pH of humic acid solutions was adjusted to 7.0 (digital pH-meter OP-211/1 Radelkis, Hungary) with a few drops of concentrated NaOH or HCl before volume concentration adjustment. After separation of the solid and liquid phases by centrifugation 10 min at 4000 rpm, the supernatant solutions were analyzed: <sup>137</sup>Cs and <sup>85</sup>Sr by radiometric method using NaI(Tl) detector (automatic gamma-spectrometric system Packard 5330) and HA by UV-VIS Spectrophotometry (Specord UV-VIS Zeiss Jena) in 1 cm quartz cuvettes. For spectrophotometric assessment of humic acid, five values  $\lambda = 270, 285, 350, 465$  and  $665$  nm were permanently used in present work to inspect deviations from average humic acid composition in course of sorption. A constant ratio of absorbancies at 465 and 665 nm was checked in particular and the ratio value of derived supernatant concentration varied between 0.97 to 1.04. Wave length 350 nm appeared the most representative analytical line. Sorbed amounts of humic acid and distribution ratio of radionuclides

were evaluated and fitted to various sorption isotherms by use of Sigma Plot 5.0 (Jandel Scientific, San Rafael, USA).

Parameters of calibration curves for these are given in Table 1.

**Table 1. Slope parameters ( $L\ g^{-1}\ cm^{-1}$ ) linear calibration graphs for humic acids at pH 7.0 (square root of the coefficient of determination  $r^2$  is always above 0.999)**

$\lambda(nm)=$	270	285	350	465	665
HHA	21.24	19.45	8.74	2.25	0.403
AHA	19.97	17.98	9.55	2.86	0.404

### RESULTS

The original data on measurement of humic acids in original and supernatant solutions are presented in Table 2, except the data for NiFCN-SiO<sub>2</sub> where a strong interference appeared at wave lengths 266 and 285 nm probably due to leaching of some organics from the sorbent prepared by sol-gel method.

For each wave length, the sorbed amount of humic acid ( $\Gamma$ , mg/g) was calculated as

$$\Gamma = c_0(1 - kA / k_0A_0)V / m \quad (1)$$

where  $c_0$  is initial concentration of humic acid (g/L) in volume  $V$  (mL) contacted with amount  $m$  (g) of sorbent,  $A_0$  and  $A$  are absorbancies of initial and equilibrated solution and  $k$  and  $k_0$  are dilution values used before spectrophotometric analysis.

Combined uncertainty of  $\Gamma$  was estimated from relative uncertainties of absorbancies ( $\delta_A$ ) as:

$$\delta_{\Gamma} = \sqrt{\delta_A^2 + \delta_V^2 + \delta_m^2} \quad (2)$$

Distribution ratio of radionuclide ( $D$ , L/g) was calculated from the specific (volume) activities of initial and resulting solutions,  $a_0$  and  $a$ :

$$D = (a_0 / a - 1)V / m \quad (3)$$

where  $V$  and  $m$  have the same meaning as above. Uncertainty of  $D$  was found from relative uncertainties of  $a$ ,  $V$  and  $m$ ,

$$\delta_{D\delta} = \sqrt{\delta_a^2 + \delta_{a_0}^2 + \delta_V^2 + \delta_m^2} \quad (4)$$

**Table 2: Spectrophotometric data (1cm quartz cell) of equilibrated solutions of humic acid above sorbents at pH 7.0 and batch factor V/m=0.02 L/g (a) HHA; (b) AHA.**

Sorbent	C <sub>HA</sub> , g/l	Wave Length (λ), nm				
		270	285	350	465	665
Montmorillonite	(a)					
	0.100	0.320	0.290	0.100	0.030	0.010
	0.200	0.568	0.505	0.200	0.055	0.015
	0.250	0.720	0.625	0.245	0.070	0.020
	0.300	0.980	0.870	0.360	0.100	0.025
	0.400	1.600	1.420	0.620	0.190	0.040
Silica gel	0.100	1.440	1.320	0.640	0.200	0.050
	0.200	0.380*	0.330*	1.400	0.420	0.100
	0.250	0.470*	0.420*	1.800	0.550	0.150
	0.300	0.520*	0.480*	2.200	0.700	0.200
	0.400	0.650*	0.620*	3.100	0.900	0.250
	0.600	1.010*	0.960*	0.470*	1.400	0.400
Zeolite	0.100	1.920	1.750	0.820	0.240	0.050
	0.200	0.400*	0.360*	0.170*	0.500	0.100
	0.250	0.500*	0.460*	0.220*	0.600	0.200
	0.300	0.600*	0.560*	0.260*	0.800	0.300
	0.400	0.810*	0.760*	0.350*	1.000	0.350
	0.600	1.230*	1.140*	0.530*	1.600	0.400
NiFeCN-SiO <sub>2</sub>	0.100	0.470*	0.310*	0.100*	0.300	0.100
	0.200	0.660*	0.495*	0.195*	0.600	0.150
	0.250	0.780*	0.600*	0.245*	0.700	0.200
	0.300	1.000*	0.780*	0.320*	0.900	0.250
	0.400	1.220*	1.000*	0.415*	1.200	0.300
	0.600	1.680*	1.420*	0.630*	1.800	0.400
Sorbent	C <sub>HA</sub> , g/l	Wave Length (λ), nm				
		270	285	350	465	665
Montmorillonite	(b)					
	0.100	0.465	0.395	0.145	0.035	0.007
	0.200	0.720	0.615	0.240	0.051	0.008
	0.250	0.985	0.805	0.360	0.080	0.010
	0.300	1.095	0.940	0.395	0.084	0.012
	0.400	1.420	1.230	0.540	0.127	0.022
Silica gel	0.500	1.820	1.600	0.710	0.159	0.026
	0.100	1.825	1.600	0.771	0.222	0.035
	0.200	0.346*	0.308*	1.52	0.450	0.081
	0.250	0.425*	0.380*	1.893	0.580	0.090
	0.300	0.543*	0.485*	2.46	0.720	0.096
	0.400	0.713*	0.638*	0.325*	0.966	0.139
0.500	0.919*	0.825*	0.430*	1.324	0.208	

\*1) Diluted in ten times

## DISCUSSION

The distribution ratio of ionic solute M<sup>n+</sup>, which complexity function <sup>6</sup> in solution is X, on the surface possessing several homogeneous sites <sup>7</sup> (x<sub>i</sub>=m<sub>i</sub>/m being the fraction of the i-th sort of binding site and D<sub>i</sub> = c<sub>i</sub>/c is the distribution ratio on the latter) is

$$D = [M^{n+}]_s / X[M^{n+}] = \frac{\sum c_{i,m} / m}{c} = \sum x_i D_i \quad (5)$$

and if there are two such sites, the free one (x<sub>0</sub>) and the occupied by humic acid (x<sub>h</sub>),

$$D = x_s D_s + x_h D_h \quad (6)$$

Because  $x_s + x_h = 1$ , from Eq. (6) there follows a linear dependence of gross distribution ratio on the fraction of the surface occupied by absorbed humic acid:

$$D = D_s + (D_h - D_s) x_s \quad (7)$$

The fraction  $x_s$  should be established from humic acid absorption data which in principle can be presented by various types of sorption isotherms <sup>6</sup>, the Freundlich isotherm

$$\Gamma = k c^{n_s} \quad (8)$$

the Langmuir isotherm

$$\Gamma = k_1 c / (k_2 + c) \quad (9)$$

or combined Langmuir-Freundlich isotherm

$$\Gamma = k_1 c^{n_s} / (k_2 + c^{n_s}) \quad (10)$$

Similar to the last one is the Sips isotherm <sup>8</sup>

$$\Gamma = k_1 [c / (k_2 + c)]^{n_s} \quad (11)$$

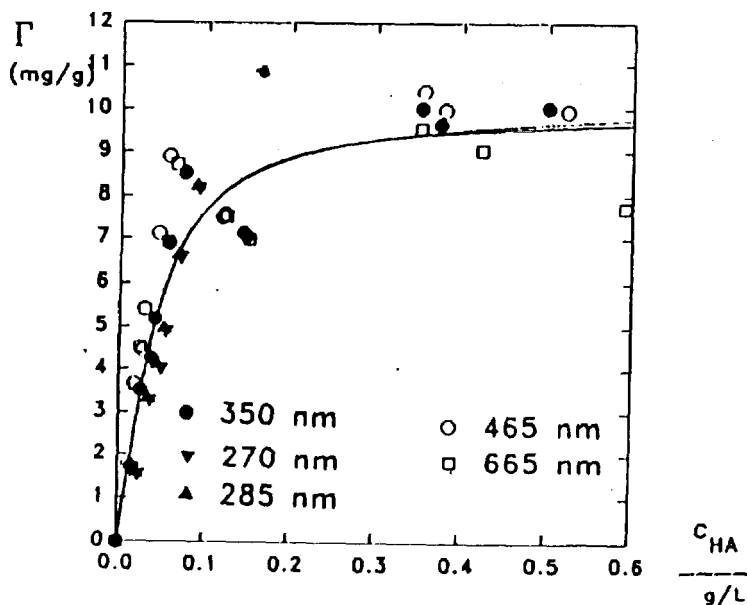


**Fig.1. Sorption isotherm of Aldrich humic acid on montmorillonite derived from spectrophotometric data.**

It means that two or three unknown sorption parameters should be found to describe experimental data (Fig.1) and in last three cases the constant  $k_1$  represents sorption

capacity of the sorbent in respect to humic acid. Therefore, the fraction of the sorbent occupied by humic acid can be obtained as

$$x_s = s = \Gamma / k_1 \quad (12)$$

The sorption data from various light transparency regions (Table 2) were treated by each of these four models and the parameters obtained and summarized in Table 3:

**Table 3. Fitted parameters of isotherms ( $k_1$  mg/g,  $k_2$  mg/L,  $n_0$  dimensionless).**

MODEL		HHA silica gel	HHA zeolite	HHA montmori- llonite	AHA silica gel	AHA montmori- llonite
Eq.(8)	$k$	$2.6 \pm 0.3$	$0.58 \pm 0.17$	$16.8 \pm 1.5$	$1.6 \pm 0.4$	$109 \pm 22$
	$n_0$	$0.56 \pm 0.06$	$0.36 \pm 0.28$	$0.39 \pm 0.03$	$0.34 \pm 0.17$	$0.98 \pm 0.07$
Eq.(10)	$k_1$	12	4100	$8.1 \pm 0.6$	$10.9 \pm 0.12$	$9.9 \pm 0.8$
	$k_2$	3.7	4230	$1.1 \pm 0.6$	$2.0 \pm 0.7$	$1.2 \pm 0.9$
	$n_0$	0.56	0.57	$1.26 \pm 0.16$	$2.7 \pm 0.8$	$1.37 \pm 0.25$
Eq.(11)	$k_1$	5.8	8.6	$8.6 \pm 0.5$	$1.4 \pm 0.4$	$10.3 \pm 0.7$
	$k_2$	3	53	$3.3 \pm 0.3$	$8.8 \pm 1.1$	$5.1 \pm 0.2$
	$n_0$	0.58	0.55	$6.3 \pm 0.6$	$10.6 \pm 1.3$	5.9

The three-parameters Sips isotherm appeared to be the best fit for most systems and therefore

$$s = [c / (k_2 + c)]^{n_0} \quad (13)$$

The data plotted in  $D$  vs.  $s$  coordinates (Fig.2) give for absorption of cesium and strontium on montmorillonite the values:

	$D_s$ L/g	$D_h$ L/g
cesium	$0.57 \pm 0.04$	$0.28 \pm 0.13$
strontium	$1.09 \pm 0.10$	$0.25 \pm 0.07$

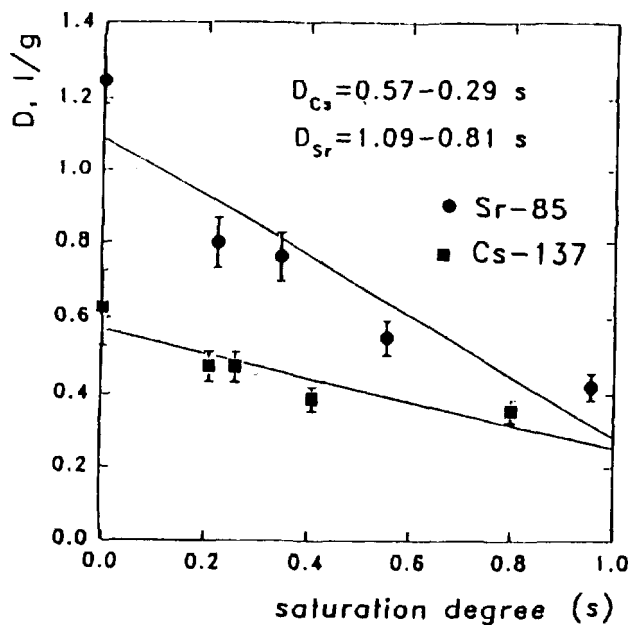


**Fig.2. Distribution ratios (D) of cesium and strontium as a function of saturation degree of montmorillonite by humic acid (s) - Eqs. (7) and (13).**

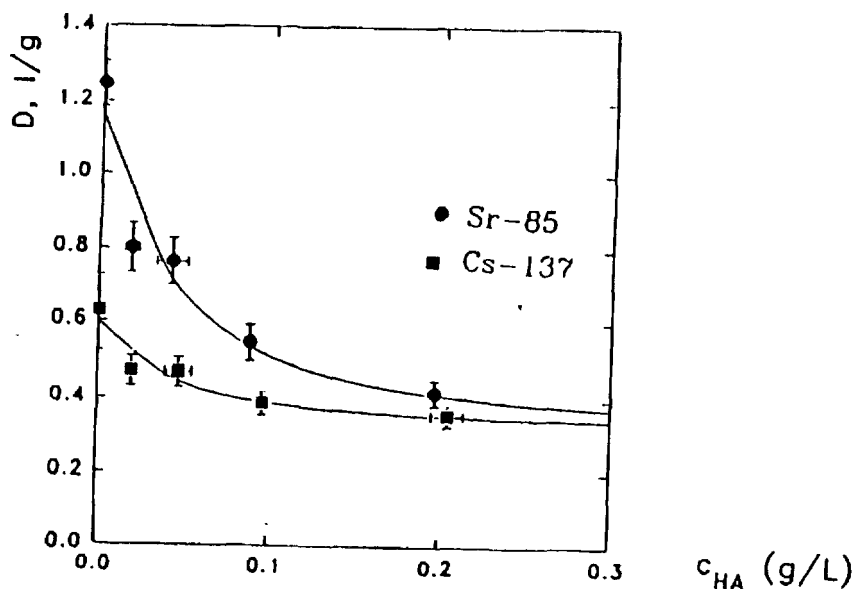
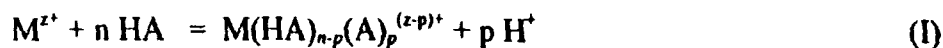


**Fig.3 Two-site distribution models of cesium and strontium adsorption with complexation in aqueous phase - Eq.(16).**

The difference between distribution ratios of the ions on the free and „humified“ surface is less than expected from known data. Moreover, if a fraction of surface remains unavailable for bulky humic acid molecules, a true value of  $D_h$  can be even higher than presented here. Therefore, the influence of humic acid on mobility of the ions may be less expressed than usually considered.

Another explanation of lower  $D_h$  can be sought in complexation of ion by humic acid ligand in solution, e.g.



to which an apparent equilibrium constant (quotient) at constant pH value,

$$\beta_h = \beta_{no}/[H^+]^p = [M(HA)_{n-p}(A)_p^{(z-p)+}]/[M^{z+}][HA]^n \quad (14)$$

corresponds and the concentration of ion solute in solution is

$$c = [M^{z+}] + [M(HA)_{n-p}(A)_p^{(z-p)+}] = [M^{z+}](1 + \beta_h [HA]^n) = [M^{z+}](1 + \beta_h c^n) \quad (15)$$

Then from Eqs (5), (7), (13) and (14) there is

$$D = \frac{D_i + (D_h - D_i)[c/(k_2 + c)]^{n_2}}{1 + \beta_h c^n} \quad (16)$$

However, the treatment of sorption data of cesium and strontium in this way (Fig.3) did not differ from those obtained from Eqs. (7) and (13) what indicates only minor influence of complexation of  $Cs^+$  and  $Sr^{2+}$  ions in humic acid solutions at pH 7: evaluated  $\beta$  value for cesium is  $\beta_1 < 3 \text{ L/g}$  and for strontium  $\beta_2 < 8 \text{ L}^2/\text{g}^2$ .

## REFERENCES

1. Choppin, G.R., *Radiochim. Acta*, **44/45**, 23 (1988).
2. Livens, F.R. and Loveland, P.J., *Soil Use & Managem.* **4**, 69 (1988).
3. Livens, F.R. and Rimmer, D.L., *Soil Use & Managem.* **4**, 63 (1988).
4. Sugden, C.L. and Farmer, J.G., *Proceedings of the 8th Int. Conf. on Heavy Metals in the Environment*, CEP Consultants, Edinburgh, p.90 (1991).
5. Shaban, I.S. and Mikulaj, V., *J. Radioanal. Nucl. Chem., Articles* **208**, 603 (1996).
6. Macášek, F. and Navratil, J.D., *Separation Chemistry*, E. Horwood, New York, pp.116-118 (1992).
7. Barrer, R.M. and Klinowski, J., *J. Chem. Soc. Faraday Trans. I*, **68**, 73 (1972).
8. Sips, R., *J. Chem. Phys.* **18**, 1024 (1950).
9. Shaban, I.S., *Influence of Humic Acid on Mobility of some Radionuclides in Environment [Review]*, Comenius University, Bratislava (1996).

**SCIENTIFIC SESSION (14)**

**RADIATION DOSIMETRY -2**

**APPLICATIONS OF DEVELOPED TECHNIQUES FOR OBTAINING TRAP  
PARAMETERS OF OVERLAPPED THERMOLUMINESCENCE  
GLOW PEAKS**

**M. S. Rasheedy**

**Physics Department, Faculty of Science, Assiut University  
Assiut, Egypt**

**ABSTRACT**

Several recent techniques have been described to obtain the trap parameters of an isolated thermoluminescence (TL) glow peak and of complex glow curve that includes several peaks. In case of isolated peaks, an equation has been derived to estimate the order of kinetics (b) in terms of temperatures and areas at different portions of the increasing and decreasing part of the peak. In case of a complex glow curve, two equations were derived which give the value of (b) by using the decreasing part of the higher temperature peak. Thereafter, the other trap parameters of the glow peak are determined in sequence. This technique is applied here to obtain the trap parameters of the TL glow curve from TLD-200 (Ca F<sub>2</sub> : Dy), which includes four overlapped glow peaks appearing at 125°C, 150°C, 195°C, and 245°C when 2°C/S heating rate is used. A procedure is suggested to check the isolation and singularity of the TL glow peak. This depends on obtaining (b) at several portions of the glow peak. The peak is considered fairly isolated if all values of (b) are given.

**CONSTRUCTING ISODOSE CURVES USING TL DOSIMETERS**

**M. A. El-Fiki, Nadia R. Khalil, H. Soliman**

**Radiation Dept. National Institute for Standards, Egypt**

**ABSTRACT**

Measurements of the depth dose and the dose distribution of 10 & 20 MeV high energy photon beams from a Siemens Mevatron KD-77 linear accelerator were made. A comparison was made between the central axis depth dose data

obtained by TLDs (LiF-700 chips) and those obtained using the Markus flat ionization chamber (as a reference) for the photon beams studied. The isodose charts obtained of the high energy photon beams using LiF-700 are presented in a 3 dimensional plots. The results showed that the TLD system could be successfully used for constructing isodose charts for high energy photon beams.

### **RADIATION DOSE TO PATIENT IN SOME DIAGNOSTIC X-RAY PROCEDURES**

**N. El-Sherbiny\*, A. Hamed \*\*, and M. H. Nassef\*\***

**\*Radiology Dept. Faculty of Medicine, Calor University**

**\*\* National Center for Nuclear Safety and Radiation control, AEA, Egypt.**

#### **ABSTRACT**

X-ray machines located at different hospitals were investigated for the measurements of dose to the patient in every type of examination.

From these measurements of dose for every type of examination selected optimized values for the physical parameters of tube potential, time of exposure, and other parameters for every investigation were evaluated. These predicted, which could be considered a reference for the X-ray diagnostic procedures suitable for Egypt.

### **COMPARISON OF SOME PHYSICAL PARAMETERS OF HIGH ENERGY PHOTON BEAMS**

**N. A. El-Sherbini, \*A.A. El Said\*\*, and M. A. Sherif\*\*\***

**\* Radiotherapy Dep., faculty of medicine, Cairo Univ.**

**\*\* Biophysics Dep., Faculty of Science, Cairo Univ.**

**\*\*\*Radiation Dep. National Institute for Standards**

#### **ABSTRACT**

Some physical parameters of high energy photon beams such as beam sharpness, beam angulation, beam uniformity and phantom inhomogeneity effects were investigated. These parameters were measured at different photon beam energies namely MeV 1.25, 6 MeV, 10MeV, & 20MeV using flat ionization Chamber (markus) with a perspex phantom. The effects of the

parameters on dose distribution revealed that degree of sharpness at the beam boundary depend not only on photon beam energy but also on collimating system, flattening filter and dosimetry system used. Beam homogeneity was related to beam energy and phantom separation. Beam uniformity could be distorted due to beam angulation especially with beam angle more than 30°. Heterogeneity region in the phantom could give rise to what is called build down and build up when the phantom is irradiated. These were more severe with increasing energy.

**APPLICATION OF TLD IN RADIOTHERAPY  
TREATMENT PLANNING**

**M.A. El- Fiki, Nadia R. Khalil, H. Soliman**

**Radiation Dept. National Institute for Standards, Egypt**

**ABSTRACT**

The manual isodose curves to calculate the dose distribution in pelvis were compared with the measurements of the dose distributions using TLD system. The finding of deviation between the measurements and calculation is accepted according to the ICRU 23, 1973.